The Development of *in vitro* Corneal Infection Models for Antimicrobial Drug Testing

A Thesis Submitted for the Degree of Doctor of Philosophy

Lucy Urwin

Supervisors: Professor Peter Monk, Dr Lynda Partridge, Dr Luke Green and formerly, Dr Rahaf Issa

Department of Infection, Immunity and Cardiovascular Disease (IICD)
Faculty of Medicine, Dentistry and Health (MDH)
University of Sheffield

May 2022

DECLARATION

The work presented in the thesis is the work of the candidate with the following exceptions:

1. **Chapter 1** contains text and figures from the published review, 'Corneal Infection Models: Tools to Investigate the Role of Biofilms in Bacterial Keratitis' (Urwin et al., 2020). Whilst the majority of work was completed by first and corresponding author, Lucy Urwin, 9 co-authors contributed and/or provided feedback. Of note, clinical symptoms of bacterial keratitis were described by Dr Prashant Garg (LV Prasad Eye Institute (LVPEI), India), H&E staining of the human cornea was provided by Dr Sanhita Roy (LVPEI, India) and significant contributions to *ex vivo* and *in vivo* modelling sections were provided by Kasia Emery (Chemical & Biological Engineering (CBE), University of Sheffield (UoS)). This work was published under a Creative Commons license.

2. Whole genome sequencing was performed using Illumina at Microbes NG (Birmingham, UK) or by Dr Naveen Kumar (Christian Medical College (CMC), Vellore, India) using a MinION sequencer.

3. Isolation and differentiation of mouse bone marrow-derived macrophages was performed by Dr Emma Smith (Sheffield Institute for Translational Neuroscience (SITran), UoS).

ACKNOWLEDGEMENTS

and fellow PhD students in the LU128 office for providing much needed coffee breaks and companionship in the labs. Similarly, I am very thankful to my former housemates at Westbrook Bank for helping me relax outside of the lab and for making the COVID-19 lockdowns so much more bearable.

Possibly the biggest thanks go to my parents, for their continued support throughout my time in higher education and for providing much-needed weekends at home when burn-out was looming. I would also like to thank my sister Kate for her help using Vectorworks to produce figures and my partner Frazer, for his continued understanding when our weekend plans were disrupted by lab work.

TABLE OF CONTENTS

LIST OF FIGURES

LIST OF TABLES

ABSTRACT

Bacterial keratitis is a corneal infection, which causes permanent corneal scarring and loss of vision. The most common causative agents of bacterial keratitis are *Staphylococcus aureus* and *Pseudomonas aeruginosa* and increasing rates of antibiotic resistance mean that new ophthalmic antimicrobials are desperately required. One of the major obstacles to drug development is an absence of suitable test models. In this thesis, two novel *in vitro* models of the human corneal epithelium are presented that have been used to simulate bacterial keratitis. Both models were developed using the HCE2 human corneal epithelial cell line and my first model utilises transwell inserts to culture HCE2 cells at air-liquid interface. Extensive optimisation of transwell culture conditions was required but characterisation studies confirmed the presence of differentiated multilayers with strong epithelial barrier integrity under defined conditions. The second model utilises the BioFlux microfluidic system to study HCE2 monolayers under physiological flow conditions. This model represents the first of its kind and aims to mimic shear stress due to blinking. Genotypic and phenotypic analysis of clinical bacterial keratitis isolates was also performed, allowing me to study trends in the infective population and identify isolates of interest. Infection studies provided new insights into bacterial pathogenesis at the ocular surface. *S. aureus* caused destruction of HCE2 multilayers and was able to traverse corneal epithelial cell layers, most likely due to *S. aureus* proteases and cytolytic toxins. Furthermore, *S. aureus* traversal was increased in the presence of HCE2 multilayers compared to no cell conditions and this is a previously unreported phenomenon that cannot be explained by bacterial transcytosis. Despite this, phagocytosis studies showed that HCE2 cells internalise high numbers of *S. aureus* bacteria and that these bacteria persist intracellularly, evading intracellular killing. Finally, *in vitro* infection models were used to test novel anti-adhesion therapies and unfractionated heparin was shown to significantly reduce *S. aureus* and *P. aeruginosa* adhesion to HCE2 monolayers under static conditions. However, no inhibition of *P. aeruginosa* adhesion was observed under flow conditions. This demonstrates the importance of using physiologically relevant infection models for antimicrobial drug testing and further validates the aims of this thesis.

ABBREVIATIONS

A549	Human airway epithelial cell line
aa	Amino acid
ADPRT	Adenosine diphosphate ribosyl transferase
Agr	Accessory genome locus
ALI	Air-liquid interface
AMP	Anti-microbial peptide
ANGPTL7	Angiopoietin Like 7
AR	Antibiotic resistance
AUC	Area under the curve
BAEC	Bovine aortic endothelial cell line
Bbp	Bone sialo-binding protein
BLAST	Basic local alignment search tool
BMDM	Bone marrow-derived macrophage
BPE	Bovine pituitary extract
BSA	Bovine serum albumin
CARD: RGI	Comprehensive antibiotic resistance database: resistance gene identifier
CBE	Chemical & Biological Engineering (University of Sheffield)
CCL20	Chemokine ligand 20
CDC	Centers for Disease Control and Prevention
cDNA	Complementary DNA
CDS	Cell dissociation solution
CFU	Colony forming units
cGMP	Cyclic guanosine monophosphate
CHO	Chinese hamster ovary cell line
ClfA/B	Clumping factor A/B
CLU	Clusterin
CMC	Christian Medical College (Vellore, India)
Cna	Collagen adhesin
CS	Chondroitin sulphate
Ct	Cycle threshold
cUMP	Cyclic uridine monophosphate
CV	Crystal violet
CWA	Cell wall anchored proteins
Cyclic-di-GMP	Cyclic-di-guanosine monophosphate
DAPI	4',6-diamidino-2-phenylindole
DLL	Dock, lock, latch
DMEM: F12	Dulbecco's modified eagle medium: nutrient mixture F-12 ham
DMEM	Dulbecco's modified eagle's medium
DMSO	Dimethyl sulfoxide
DNA	Deoxyribonucleic acid
ECAM-1	Epithelial cell adhesion molecule 1
ECM	Extracellular matrix
EGF	Epidermal growth factor
EMEM	Eagle's minimum essential medium
ERM	Ezrin, radixin and moesin proteins
EU	European Union
EUCAST	European Committee on Antimicrobial Susceptibility Testing
Exo	Exotoxin

FAST	Feature-assisted segmenter/tracker
FBS	Foetal bovine serum
FITC	Fluorescein isothiocyanate
Fn	Fibronectin
FnBPA/B	Fibronectin binding protein A/B
Fro	Flow-regulated operon
GAG	Glycosaminoglycan
GAP	GTPase activating protein
GAPDH	Glyceraldehyde 3-phosphate dehydrogenase
GFP	Green fluorescent protein
H&E	Haematoxylin and eosin staining
HaCaT	Human keratinocyte cell line
HBSS	Hank's balanced salt solution
HCE/HCEC	Human corneal epithelial cell
HCE2	Human corneal epithelial cell 2 cell line
HS	Heparan sulphate
HSPG	Heparan sulphate proteoglycan
Ig	Immunoglobulin
IgG	Immunoglobulin G
IgM	Immunoglobulin M
IICD	Dept. Infection, Immunity & Cardiovascular Disease (University of Sheffield)
IL-6	Interleukin 6
IL-8	Interleukin 8
K	Keratin
KSFM	Keratinocyte serum free medium
LB	Lysogeny broth
LCIS	Live cell imaging solution
LDH	Lactate dehydrogenase
LVPEI	LV Prasad Eye Institute (Hyderabad, India)
MDCK	Madin-Darby canine kidney cell line
MDR	Multi-drug resistant
MEC	Mammary epithelial cell line
MFI	Median fluorescence intensity
MGE	Mobile genetic element
MH	Mueller Hinton
MIC	Minimum inhibitory concentration
MOI	Multiplicity of infection
mRNA	Messenger RNA
MRSA	Methicillin resistant *Staphylococcus aureus*
MSCRAMM	Microbial surface components recognising adhesive matrix molecules
MUC	Mucin
NCBI	National Center for Biotechnology Information
NF-κB	Nuclear factor kappa B
NGH	Northern General Hospital (Sheffield, UK)
OD	Optical density
PASP	*Pseudomonas aeruginosa* small protease
PBS	Phosphate buffered saline
PET	Polyethylene terephthalate/polyester
PFA	Paraformaldehyde
PI	Propidium iodide
PIV	Type IV serine protease

PMN	Polymorphonuclear leukocyte
PubMLST	Public databases for molecular typing and microbial genome diversity
QC	Quality Control
QUAST	Quality assessment tool
RNA	Ribonucleic acid
RND	Resistance nodulation division
ROS	Reactive oxygen species
Rot	Repressor of toxins
RT4	Human bladder epithelial cell line
RT	Room temperature
Rt	Reverse transcriptase
RT-PCR	Reverse transcription polymerase chain reaction
RT-qPCR	Real-time quantitative polymerase chain reaction
SCR	Scrambled (peptide)
SDC	Syndecan
sIgA	Secretory immunoglobulin A
SITraN	Sheffield Institute for Translational Neuroscience (University of Sheffield)
SP-A	Surfactant protein A
SP-D	Surfactant protein D
SRB	Sulforhodamine B
SSL1	*Staphylococcus aureus* superantigen-like protein
T1SS	Type I secretion system
T2SS	Type II secretion system
T3SS	Type III secretion system
T5SS	Type V secretion system
T6SS	Type VI secretion system
TAK1	Transforming growth factor β-activated kinase 1
TCF	Total cell fluorescence
TEER	Trans-epithelial electrical resistance
TEM	Transmission electron microscopy
TEMs	Tetraspanin enriched microdomains
TJP	Tight junction protein
TLR	Toll-like receptor
TM	Transmembrane
TNFα	Tumour necrosis factor α
TSB	Tryptone soya broth
TX-100	Triton X-100
UFH	Unfractionated heparin
UoS	UoS= University of Sheffield
VF	VF= Virulence factor
VFDB	VFDB= Virulence factor database
WHO	WHO= World Health Organization
ZO1	ZO1= Zonula occludens-1
α-SMA	α-SMA= α-smooth muscle actin

CHAPTER 1: INTRODUCTION

1.1. Cornea

The cornea is the outermost layer of the human eye, and it is composed of avascularised, transparent tissue that forms a thin protective lens over the rest of the eye (Navaratnam et al., 2015). The corneal tissue is composed of six distinct layers: corneal epithelium, Bowman's membrane, stroma, pre-Descemet's layer, Descemet's membrane and endothelium (**Figure 1-1**) and the highly ordered nature of these layers is essential in maintaining corneal transparency (Krachmer et al., 2010, Dua et al., 2013). The cornea plays a critical role in eyesight by facilitating the transmission and refraction of incident light and the corneal lens is estimated to account for two thirds of the total dioptric power of the eye (Meek et al., 2003). This means that if corneal topography or transparency become compromised, eyesight may be significantly impaired. In order to prevent this, the cornea is equipped with various ocular defence and immune tolerance mechanisms, which protect against infection and inflammation respectively.
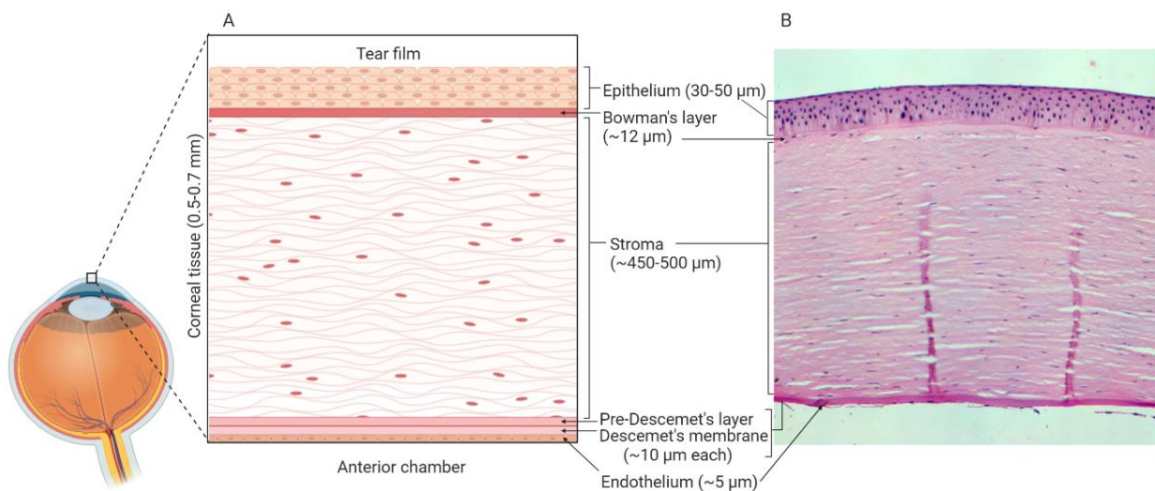
Figure 1-1. Layers of the human cornea.
(A) Schematic representation (B) Haematoxylin and eosin staining.
The human cornea is composed of six distinct layers. The outermost layer is the corneal epithelium, which is made up of 5-7 rows of tightly packed corneal epithelial cells. These cells lie on an acellular, collagenous layer named the Bowman's layer and together the epithelium and Bowman's layer are essential in the protection of the underlying stromal tissue. The stroma constitutes 90% of the overall thickness of the cornea and is composed of mainly type I collagen and differentiated keratocytes. Beneath the stroma is the Pre-Descemet's layer (also known as Dua's layer) and the Descemet's membrane. These collagen-rich, acellular layers separate the stromal tissue from the endothelium. The endothelium is composed of a single layer of cells, which are mainly hexagonal in shape. This layer is adjacent to the anterior chamber and constitutes the final layer of the cornea. Created with Biorender.com and published previously (Urwin et al., 2020).

1.1.1. Ocular Defence Mechanisms

The cornea is described as a site of 'immune privilege'. This term was first coined by Sir Peter Medawar in the 1940s, following his observation that skin allografts are rapidly rejected by tissues such as the skin, but not by the anterior chamber of the eye (Medawar, 1948). For many years, the cornea was believed to be devoid of all immune cells, but this is not the case. In fact, there is a resident immune population consisting of mast cells, Langerhans, macrophages, γδ T lymphocytes, and innate lymphoid cells (Liu and Li, 2021). However, these immune cells are separated from the rest of the body by the blood-ocular barrier and are driven towards an anti-inflammatory response by immunosuppressive factors such as thrombospondin, Fas Ligand (FasL) and Transforming Growth Factor β (TGFβ) (Taylor, 2016, Livingston et al., 2019). There is also an infiltrating immune population and neutrophil influx may be observed following corneal trauma and/or severe infection (Sahu et al., 2018). However, in the absence of severe infection immunosuppression is vital as ocular inflammation may cause corneal scarring and subsequent loss of vision (Livingston et al., 2019). In order to compensate for the inhibition of immune cell functions and protect against infection, the cornea has a plethora of alternative defence mechanisms. One of the major defence mechanisms is the physical barrier function of the cornea. The presence of tight cell junctions limits bacterial passage across the epithelium and regular shedding of superficial epithelial cells removes adherent bacteria at the ocular surface (Ren and Wilson, 1996, Sosnova-Netukova et al., 2007). The Bowman's membrane also contributes to barrier function and *in vivo* mouse infection studies have shown that *P. aeruginosa* is unable to traverse this acellular layer without prior wounding (Alarcon et al., 2009b). Another ocular defence mechanism is the tear film, which contains over 1,500 proteins (Zhou et al., 2012). These proteins play important roles in immunosuppression and wound healing and many of the components of tear film have antimicrobial activity (**Figure 1-2**) (McDermott, 2013, O'Callaghan, 2018, Pflugfelder and Stern, 2020, Argueso et al., 2021). Finally, blinking has important dual functionality by lubricating the cornea and washing away foreign particles such as microbes.
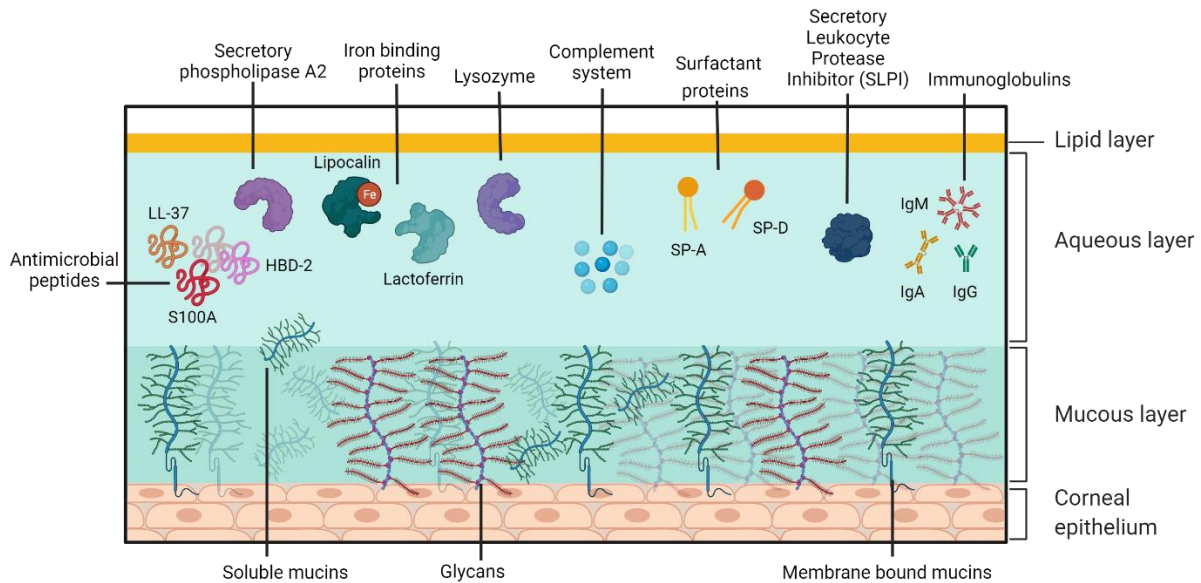
Figure 1-2. Composition of human tear film.

The tear film is composed of three layers, the mucous layer, aqueous layer and lipid layer. The mucous layer is in direct contact with the corneal epithelium and the epithelial cell glycocalyx protrudes into this layer. The glycocalyx is a carbohydrate rich coating comprised of membrane bound mucins and glycans such as proteoglycans and glycosphingolipids. This carbohydrate-rich matrix acts as a physical barrier but may also reduce adhesion by providing decoy receptors and attenuating virulence factors. Soluble mucins are found within the mucous and aqueous layers. The aqueous layer contains a vast array of proteins with antimicrobial activities. Antimicrobial peptides have broad spectrum activity but commonly bind bacterial membranes, triggering pore formation and rapid cell death. Secretory phospholipase A2 lyses the cell membranes of Gram positive bacteria. Lipocalin and lactoferrin bind to free iron, helping to reduce bacterial growth. Lysozyme enzymatically cleaves bacterial peptidoglycan. The complement system enhances phagocytosis via interactions with antibodies and immune cells. Surfactant proteins promote phagocytosis by binding and aggregating bacteria. Secretory Leukocyte Protease Inhibitor (SLPI) inhibits bacterial proteases and elicits bacterial killing by binding bacterial membranes. Immunoglobulins bind antigens and mediate bacterial clearance. Secretory IgA, IgG and IgM are all found within the tear fluid but sIgA is most abundant. The final layer of the tear film is the lipid layer. This is a thin layer comprised of polar and non-polar lipids, which reduce the surface tension of the tear film. This layer also generates a smooth optical surface and prevents evaporation of the tear fluid. Created with Biorender.com.

1.2. Bacterial Keratitis

Bacterial keratitis is a potentially sight-threatening eye infection, localised to the cornea. The infection is characterised by the presence of replicating bacteria on the ocular surface, which disrupt the integrity of the corneal epithelium and result in inflammation of the corneal stroma (Keay et al., 2006). Early symptoms include pain, redness, excessive lacrimation, light sensitivity and blurred vision. Examination of the eye reveals lid oedema, congestion of conjunctiva, corneal haze and a variable degree of inflammation of the anterior chamber. The condition results in corneal scarring or in extreme cases, corneal perforation and loss of the eye (Keay et al., 2009). According to the World

Health Organization, corneal blindness is currently the 4th largest contributor to global blindness (Pascolini and Mariotti, 2012) and instances of ocular trauma/corneal ulceration have been estimated to cause 1.5-2 million new cases of monocular blindness per year (Whitcher et al., 2001). Following ocular surface trauma, the cornea becomes highly susceptible to infection and so many of these cases involve an infection component. Corneal infections may be caused by bacteria, fungi, viruses or protozoans (collectively termed 'microbial keratitis') (Collier et al., 2014) but this thesis is focussed solely on bacterial keratitis.

1.2.1. Predisposing Risk Factors

The healthy cornea is highly resistant to infection and so microbial keratitis rarely occurs in the absence of predisposing risk factors (Fleiszig et al., 2019). Reported risk factors include corneal trauma, contact lens-wear, chronic ocular surface disease, ocular surgery and systemic diseases associated with an immunocompromised state (Bourcier et al., 2003, Ng et al., 2015). These factors compromise the resistance mechanisms employed by the cornea, rendering it newly susceptible to infection (Fleiszig et al., 2019). Although microbial keratitis occurs in both developed and developing countries, there are large differences in the disease epidemiology and aetiology (Ung et al., 2019). In developing countries, corneal trauma constitutes the major risk factor in the development of microbial keratitis. This is thought to reflect the increased size of the agricultural workforce in these countries, e.g., rice stalks and thorns are a common cause of ocular injury for farmers in South India (Bharathi et al., 2007, Al-Mujaini et al., 2009). Support for this is provided by a recent epidemiological study, conducted in South India (n=252). Ocular trauma was reported for 72% of microbial keratitis infections and 63% of patients were employed as agriculturists (Chidambaram et al., 2018). In contrast, contact lens-wear constitutes the major risk factor in the development of microbial keratitis in more developed countries. Studies conducted in France and Sweden identified contact-lens wear as the major risk factor in ~50% of cases (Bourcier et al., 2003, Sagerfors et al., 2019) and steep rises in the incidence of microbial keratitis in developed countries have been linked to the increased popularity of contact lenses. In Minnesota, a 435% increase in microbial keratitis was recorded over a 39-year period, following the introduction of contact-lenses (Erie et al., 1993).

1.3. Pathogens

Both Gram positive and Gram negative species of bacteria have been implicated in corneal infections. The most common causative agents are *Staphylococcus aureus* and *Pseudomonas aeruginosa*, although geographic variations in predominance have been reported (Neumann and Sjostrand, 1993,

Alexandrakis et al., 2000, Houang et al., 2001). *P. aeruginosa* is especially dominant in contact lens-related keratitis (Stapleton and Carnt, 2012, Green et al., 2019).

1.3.1. *Staphylococcus aureus*

Staphylococcus aureus is a Gram positive, coccoid bacterium that can colonise the human body as a harmless commensal or pathogen, depending on the host environment. *S. aureus* commonly colonises the throat and/or anterior nares and ~30% of individuals are reported to act as intermittent, asymptomatic carriers of *S. aureus* (Wertheim et al., 2005). Asymptomatic carriage is further increased in hospital workers, with one study reporting that 50-70% of front-line workers were colonised by *S. aureus* (Rashid et al., 2012). This opportunistic pathogen is responsible for a wide range of infections, affecting multiple sites within the body. Examples include common skin infections such as impetigo, boils and cellulitis but *S. aureus* can also cause life threatening infections such as pneumonia, endocarditis, toxic shock syndrome and sepsis (Coates et al., 2014). Compared to *P. aeruginosa*, the *S. aureus* genome is relatively small at approximately 2.8 MB (Chua et al., 2013). However, considerable genome plasticity is conferred by Mobile Genetic Elements (MGE), which account for approximately 15-20% of the *S. aureus* genome. An MGE can be defined as "any intra chromosomal or extra chromosomal DNA segment that can be independently mobilized within or between *S. aureus* cells" and mobilizable plasmids and phage constitute the major MGEs in *S. aureus* (Copin et al., 2018). MGEs are highly problematic in the treatment of *S. aureus* infections as they allow genes encoding antibiotic resistance and/or novel virulence determinants to be transferred between strains. Insertion of a transposable element into the *rot* promoter of USA500 has been shown to induce hypervirulence (Benson et al., 2014) and multiple MGEs have been implicated in the evolution of USA300, an epidemic clone of Community-Acquired Methicillin-Resistant *Staphylococcus aureus* (CA-MRSA) (Diep et al., 2006). Therefore, MGEs are a significant contributor to the severity of *S. aureus* infections and play an important role in virulence. *S. aureus* produces a diverse array of virulence factors but toxin production is the major staphylococcal virulence mechanism (Kong et al., 2016). *S. aureus* toxins include the hemolysins (e.g., α and β toxin), leukotoxins (e.g., Panton-Valentine leukocidin), staphylococcal exfoliative toxins and Toxic-Shock Syndrome Toxin-1 (TSST-1). Many of these toxins are pore-forming toxins that induce host cell damage via cytolytic activity (Oliveira et al., 2018). Additional *S. aureus* virulence mechanisms include complex regulatory networks, e.g., the Accessory gene regulator (Agr) system, which modulates expression of virulence factors in response to quorum sensing; bacterial enzymes that damage host tissues, e.g., bacterial coagulases and proteases; and Cell Wall Anchored (CWA) proteins, which have multiple functions in immune evasion, biofilm formation and host cell adhesion (Kong et al., 2016, Jenul and Horswill, 2019, Speziale and Pietrocola, 2020).

1.3.1.1. *Staphylococcus aureus* Adhesins

Many of the Cell Wall Anchored (CWA) proteins are important *S. aureus* adhesins (**Table 1-1**). CWAs are bacterial cell surface proteins that are covalently linked to the peptidoglycan cell wall, and they share common structural features. All CWAs contain a wall-spanning region, as well as an N-terminal signal sequence and C-terminal sorting signal. The signal sequence facilitates Sec-dependent protein secretion, whereas the sorting signal prevents complete extrusion of protein by covalently anchoring the C-terminal region to the peptidoglycan cell wall (Schneewind and Missiakas, 2014). Additional domains are involved in host-binding interactions and structure-function studies have been used to classify CWAs into 4 main groups (Foster et al., 2014). These are the Microbial Surface Components Recognising Adhesive Matrix Molecules (MSCRAMM), NEAT motif family, G5-E repeat family and three-helical bundle proteins (i.e., Protein A). The MSCRAMMs are the largest group of CWA proteins and they play an important role in bacterial adhesion to the host Extracellular Matrix (ECM). MSCRAMMs are classified by the presence of an A region, which contains IgG-like subdomains (N1, N2, N3) and MSCRAMMs involved in bacterial adhesion include Clumping factors A and B (ClfA/B), Fibronectin Binding Proteins A and B (FnBPA/B), Collagen adhesin (Cna) and Bone sialo-binding protein (Bbp; SdrE isoform) (**Figure 1-3**) (Ponnuraj et al., 2003, Foster et al., 2014, Speziale and Pietrocola, 2020). These CWAs enable bacteria to bind major components of the ECM, e.g., fibronectin, fibrinogen and collagen, thereby facilitating initial attachment, but they also influence infection outcome. For instance, Cna has been shown to play an important role in corneal virulence. Infection of rabbit corneas with Cna mutant bacteria does not induce corneal inflammation and histology revealed minimal neutrophil infiltration (Rhem et al., 2000). Furthermore, a study which used *S. aureus* CWA mutants to induce bacteraemia in mice, showed that bacterial load at 5 days post-infection was significantly reduced in mice infected with ClfA, ClfB, IsdA or SasG mutants (Cheng et al., 2009). Finally, FnBPs are of particular interest, due to their dual functionality in bacterial adhesion and invasion. FnBPs possess 10 (FnBPB) or 11 (FnBPA) fibronectin binding repeats, located downstream of the IgG-like receptor binding domains (Speziale and Pietrocola, 2020). These repeat regions are able to bind multiple fibronectin molecules with varying affinities and each FnBP protein is estimated to bind between 6 and 9 fibronectin molecules (Meenan et al., 2007). Studies involving FnBPA have been used to propose an internalisation mechanism and central to this mechanism is the observation that host integrin, α5β1, binds fibronectin via an RGD motif (Pytela et al., 1985, Fowler et al., 2000). By binding and clustering fibronectin at the host cell surface, *S. aureus* promotes the clustering of integrins. This causes phosphorylation of integrin cytoplasmic domains and activates a signalling cascade which triggers endocytosis (Schwarz-Linek et al., 2004). Adherent *S. aureus* become internalised and therefore CWA proteins also play a role in the intracellular virulence mechanisms of *S. aureus*.

Table 1-1. *S. aureus* CWA adhesins and corresponding host targets.

CWA family	Adhesin	Receptor/binding site	Reference
Microbial Surface Components Recognising Adhesive Matrix Molecules (MSCRAMM) family	ClfA	Immobilised and/or soluble fibrinogen	(Deivanayagam et al., 2002)
	ClfB	Fibrinogen, keratin-10 and loricrin. Adhesion to desquamated epithelial cells and nasal colonisation.	(Eidhin et al., 1998)
	FnBPA	Receptors include fibrinogen, elastin, fibronectin, and plasmin. Adhesion to ECM.	(Flock et al., 1987, Speziale and Pietrocola, 2020)
	FnBPB	Receptors include fibrinogen, elastin, fibronectin, and plasmin. Adhesion to ECM.	(Jonsson et al., 1991, Speziale and Pietrocola, 2020)
	Cna	Collagen triple helix, adhesion to collagen-rich tissue	(Zong et al., 2005)
	Bbp (SdrE isoform)	Binds fibrinogen and potentially collagen IV. Adhesion to ECM.	(Vazquez et al., 2011)
NEAT motif family	IsdA	Receptors include haem, fibrinogen, fibronectin, cytokeratin 10 and loricrin. Binds desquamated epithelial cells.	(Clarke et al., 2009)
G5-E repeat family	SasG	Unknown receptor, binds desquamated epithelial cells	(Roche et al., 2003)
Structurally uncharacterised	SasX	Unknown receptor, nasal colonisation	(Li et al., 2012)
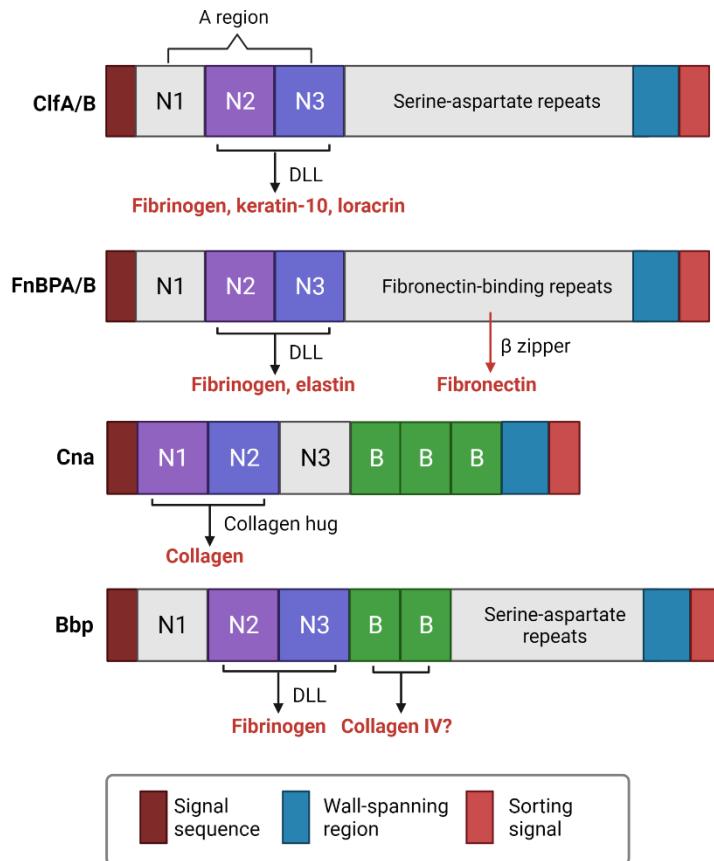
Figure 1-3. Comparing the structure and ECM binding sites of MSCRAMMs involved in *S. aureus* adhesion. MSCRAMMs contain a signal sequence, wall spanning region, sorting signal and 'A region' containing three distinct subdomains (N1, N2 and N3). Subdomains shown in purple possess IgG-like folds that facilitate ECM binding. ClfA/B, FnBPA/B and Bbp bind ECM targets via the Dock, Lock, Latch (DLL) mechanism. The N2/N3 subdomains possess an open conformation in the unbound apoprotein but following ligand docking, a structural rearrangement occurs which locks the ligand in place. Additional interactions between bacterial domains further stabilise the structure and ligand and receptor become latched together. Cna binding to collagen is mediated by the collagen hug, a variation of the DLL mechanism involving N1/N2. With the exception of Cna, the MSCRAMMs possess a flexible linker region which connects the A domain and wall spanning regions. In ClfA/B and Bbp, this region is made up of serine-aspartate repeats (SD region) and in FnBPA/B, this region contains 10-11 fibronectin binding repeats. These repeats facilitate FnBP binding to fibronectin via a β-zipper mechanism, whereby the fibronectin binding region forms a β-strand and aligns itself anti-parallel with the N terminal binding modules within fibronectin. Cna and Bbp contain additional regions of repetitive sequence known as B domains and unlike SD regions, these domains are highly rigid. B domains have been shown to facilitate collagen IV binding in SdrF, a *Staphylococcus epidermis* protein that is closely related to Bbp and so it has been suggested that *S. aureus* Bbp may also bind collagen in this way. Created with Biorender.com and adapted from Foster et al., 2014.

1.3.2. *Pseudomonas aeruginosa*

Pseudomonas aeruginosa is a Gram negative, rod-shaped bacterium commonly found in the environment. Due to its metabolic flexibility, *P. aeruginosa* is able to thrive in diverse ecological niches and is commonly found in soil and water. However, this environmental species also acts as an opportunistic pathogen and causes a range of human infections. *P. aeruginosa* commonly affects immunocompromised individuals or those with chronic health conditions (e.g., cystic fibrosis, chronic obstructive pulmonary disease and cancer patients) (Winstanley et al., 2016, Garcia-Nunez et al., 2017, Hilliam et al., 2020). However, infections can also occur in relatively healthy individuals following invasive procedures or wounding (e.g., catheter use or microbial keratitis) (Hilliam et al., 2020, Rossi et al., 2021). As a result, these infections are a huge problem in hospitals and *P. aeruginosa* is estimated to account for 10% of all nosocomial infections in the EU (de Bentzmann and Plésiat 2011). One of the reasons *P. aeruginosa* is such a successful pathogen is its genomic plasticity. The *P. aeruginosa* genome is very large (5.5-7 MB) and consists of a core and accessory genome (Rossi et al., 2021). The core genome refers to essential genes possessed by all *P. aeruginosa* strains, whereas the accessory genome is considerably larger and consists of non-essential genes. A recent study utilising 1,311 *P. aeruginosa* bacterial genomes, identified only 665 core genes, representing less than 1% of the entire pan-genome (Freschi et al., 2019). The large *P. aeruginosa* genome means that this pathogen has a huge toolbox of virulence factors at its disposal and the presence of multiple regulatory pathways allows *P. aeruginosa* to quickly adapt to the host environment and circumvent the immune system (Silby et al., 2011). The major virulence mechanisms utilised by *P. aeruginosa* can be divided into several groups. These mechanisms include the ability of *P. aeruginosa* to form biofilms; the sophisticated regulation of gene expression via quorum sensing; bacterial appendages such as the flagellum and type IV pili; iron acquisition mechanisms; the complex structure and function of the outer membrane; and the presence of multiple secretion systems that release proteases, lipolytic enzymes and other deleterious toxins into the host environment (Jurado-Martin et al., 2021).

1.3.2.1. *P. aeruginosa* Adhesins

P. aeruginosa possesses multiple virulence factors that are involved in adhesion to host cells (**Table 1-2**). The two major *P. aeruginosa* adhesins are the flagellum and type IV pili, which also play key roles in motility. The flagellum is responsible for swimming motility and in *P. aeruginosa* there is just one flagellum per bacterium, which is polarly located (Haiko and Westerlund-Wikstrom, 2013). The flagellum is composed of over 20 different proteins, but the major subunit is FliC (flagellin). Polymerisation of FliC proteins generates the flagellar filament and this filament is capped at the distal end by the FliD protein (Chevance and Hughes, 2008). It is FliC and FliD that have been implicated in

flagellum-mediated adhesion. FliC has been shown to bind to the heparan sulphate chains of Heparan Sulphate Proteoglycans (HSPGs) and binding is increased following the upregulation of HSPGs in an epithelial injury model (Bucior et al., 2012). FliC has also been shown to bind Surfactant Protein A (SP-A) from bronchoalveolar lavage fluid (Ketko et al., 2013) and glycolipid GM1 in cell membranes, although the latter was shown to be a rare event in CHO Lec-2 epithelial cells (Feldman et al., 1998). There is also evidence to suggest that the flagellum binds the host mucin protein, MUC1. However, there are conflicting reports regarding the importance of FliC and FliD in this interaction (Arora et al., 1998, Scharfman et al., 2001, Lillehoj et al., 2002). The second major *P. aeruginosa* adhesin is the type IV pili. These are polarly localised bacterial appendages that facilitate twitching motility via the rapid assembly and disassembly of pili fibres (Mattick, 2002). These fibres are helical structures, predominantly composed of PilA (pilin) protein. However, minor pilin proteins (e.g., PilV and PilW) and the PilY1 protein are essential for filament assembly and may also be incorporated into pili fibres, most likely at the distal tip (Leighton et al., 2015). There is evidence to suggest that PilA acts as the type IV pilin adhesin, as it has been shown to bind host N-glycans (Bucior et al., 2012) and asialo-GM1/GM2 glycolipids (Lee et al., 1994). However, *P. aeruginosa* is known to preferentially bind to the basolateral surface of epithelial cells and since both of these host cell receptors are localised to the apical cell surface, they are unlikely to represent the primary adhesion pathway (Heiniger et al., 2010). Furthermore, preliminary experiments demonstrating an interaction between PilA and the GM1/GM2 glycolipids used purified pilin proteins and this binding interaction was not observed using piliated *P. aeruginosa* (Emam et al., 2006). More recently, PilY1 has been proposed as the major adhesin. Support for this is provided by structural similarities between PilY1 and PilC, the known type IV pili adhesin for *Neisseria gonorrhoeae* (Orans et al., 2010). PilY1 has been shown to be necessary for *P. aeruginosa* adhesion to the basolateral surface of epithelial cells (Heiniger et al., 2010) and more recently, a potential host receptor and PilY1 binding site were identified. PilY1 has been shown to contain an integrin binding RGD motif and interaction between purified PY1 and host integrin protein was demonstrated *in vitro* (Johnson et al., 2011). This interaction was shown to be calcium dependent, and a novel calcium binding site was identified upstream of the RGD motif. Finally, outer membrane proteins, OprF and OprQ have been proposed to play a role in adhesion to host cells, although these proteins are not regarded as major adhesins. *P. aeruginosa* binding to human alveolar epithelial cells was shown to be reduced by 43% in an OprF mutant strain (Azghani et al., 2002) and OprQ has been shown to bind plasmatic fibronectin *in vitro* (Arhin and Boucher, 2010). Fibronectin (Fn) is commonly exploited for bacterial adhesion and so OprQ-Fn binding could represent an additional adhesion mechanism.

Table 1-2. *P. aeruginosa* **adhesins and corresponding host targets.**

Bacterial structure	Adhesin	Receptor/binding site	Reference
Flagella	FliC	Monosialylated glycolipid GM1 in cell membranes	(Feldman et al., 1998)
	FliC	Heparan sulphate proteoglycans on the basolateral surface of epithelial cells	(Bucior et al., 2012)
	FliC	SP-A pulmonary surfactant protein	(Ketko et al., 2013)
	FliC/D	Mucin protein, MUC1	(Arora et al., 1998, Scharfman et al., 2001, Lillehoj et al., 2002)
Type IV pili	PilA	Glycolipid asialo-GM1 and GM2	(Lee et al., 1994)
	PilA	N-glycans on the apical surface of epithelial cells	(Bucior et al., 2012)
	PilY1	Host receptor on basolateral surface of epithelial cells	(Heiniger et al., 2010)
	PilY1	Integrins	(Johnson et al., 2011)
Outer membrane	OprF	Human alveolar epithelial cells	(Askarian et al., 2018)
	OprQ	Human fibronectin	(Arhin and Boucher, 2010)

1.3.2.2. *P. aeruginosa* Secretion Systems

P. aeruginosa possesses five secretion systems, namely Type I (T1SS), Type II (T2SS), Type III (T3SS), Type V (T5SS) and Type VI (T6SS). These secretion systems are responsible for translocating virulence factors across cell membranes and secreted effectors have a range of functions that are deleterious to the host and/or other bacteria (**Table 1-3**) (Filloux, 2011, Jurado-Martin et al., 2021). T1SS, T2SS and T5SS release virulence factors into the extracellular environment whereas T3SS and T6SS inject secreted products directly into the cytosol of target cells (Jurado-Martin et al., 2021). In the context of corneal infections, T2SS and T3SS are most important. The T2SS secretes a number of different proteolytic enzymes such as LasA and LasB, which damage the corneal tissue but are not essential for corneal virulence (Kreger and Gray, 1978, Hobden, 2002, O'Callaghan et al., 2019). In contrast, type IV serine protease (PIV) and *P. aeruginosa* Small Protease (PASP) are major virulence determinants in corneal infections, and this is evidenced by their conservation in clinical keratitis isolates (Caballero et al., 2004, Tang et al., 2009, Dave et al., 2020). *P. aeruginosa* PIV mutants display reduced corneal virulence and *Pseudomonas putida*, a non-ocular pathogen that does not secrete active proteases, has been shown to acquire corneal virulence following transformation with a pPIV plasmid (Traidej et al., 2003, O'Callaghan et al., 2019). PASP was more recently discovered and possesses additional proteolytic activity against collagens IV and I. The PASP-mediated degradation of collagen fibrils causes corneal erosions and infection of rabbit corneas with a PASP-deficient mutant has been shown to cause a significant reduction in pathology (Marquart et al., 2005, Tang et al., 2013). Hence, the T2SS plays a significant role in bacterial keratitis via its secretion of these proteins. The T3SS is equally

11

important and is responsible for the secretion of ExoU, ExoY, ExoT and ExoS. These exoproteins circumvent host clearance mechanisms and induce rapid cell death via a number of different pathways (**Figure 1-4**) (Kazmierczak and Engel, 2002, Epelman et al., 2004, Angus et al., 2010, de Lima et al., 2012, Beckert et al., 2014, Anantharajah et al., 2016, He et al., 2017, Jurado-Martin et al., 2021). There is variable expression of the T3SS effector genes within the *P. aeruginosa* population and *exoS* and *exoU* are often considered to be mutually exclusive, as isolates possessing both or neither of these genes are highly uncommon (Zhu et al., 2006, Borkar et al., 2013). These genes are used to assign isolates to different pathotypes, based on the virulence mechanisms of ExoS and ExoU and *exoS* +ve isolates are described as invasive, whereas *exoU* +ve isolates are classed as cytotoxic. Pathotype appears to affect the clinical features of bacterial keratitis, as evidenced by the Steroids for Corneal Ulcers Trial (SCUT). In this trial, invasive isolates were associated with larger corneal ulcers and prolonged healing times but at 3 months post-infection, these patients presented with better visual acuity (Borkar et al., 2013). The trial also revealed differences in the efficacy of corticosteroids for treating corneal ulcers depending on pathotype. This suggests consideration of pathotype and the T3SS could be important in the development of new therapeutics.

Table 1-3. *P. aeruginosa* secretion systems and their associated effector proteins.

Secretion system	Effectors	Function
Type 1 (T1SS)	AprA	Alkaline protease
	AprX	Unknown function
	HasAp	Haemophore
	TesG	Suppresses the host inflammatory response
Type 2 (T2SS)	ToxA	Exotoxin A-ADP ribosyl transferase
	LasA, LasB	Elastase
	PrpL	Type IV protease (PIV)
	PasP	*Pseudomonas aeruginosa* Small Protease (PASP)
	PmpA	Unknown function, putative protease
	PaAp	Aminopeptidase
	PhoA, LapA	Alkaline phosphatase
	LipA, LipC	Lipase
	PlcB, PlcN	Phospholipase
	PlcH	Haemolytic phospholipase C
	CbpD	Chitin binding protein
	LoxA	Lipoxygenase
	Pyocyanin	Phenazine
Type 3 (T3SS)	ExoU	Phospholipase A2 activity
	ExoY	Nucleotidyl cyclase
	ExoT	GTPase Activating Protein (GAP) and Adenosine Diphosphate Ribosyl Transferase (ADPRT) activity
	ExoS	GAP and ADPRT activity
Type 5 (T5SS)	EstA	Esterase
	PlpD	Lipolytic enzyme
	CdrA	Extracellular adhesin
	CupB5	Unknown function, putative adhesin
	LepA	Protease
Type 6 (T6SS)	Tse1-3	Bacterial toxins
	ChiC	Chitinase

Figure 1-4. Exoproteins secreted by the Type III Secretion System (T3SS) and their role in the pathogenicity of *P. aeruginosa*.

The T3SS injects toxic exoproteins directly into the cytosol of host cells. Secreted exoproteins include ExoU, ExoY, ExoS and ExoT. These proteins induce cell death or dysfunction via several different pathways. ExoU has phospholipase A2 activity, which lyses host cell membranes and causes irreversible damage to host cells. It also activates the NF-κB pathway, which promotes IL-8 secretion. Increased production of pro-inflammatory eicosanoids induces expression of inflammatory genes. ExoY is a nucleotidyl cyclase responsible for the production of cyclic nucleotides, with a preference for cGMP and cUMP production. These secondary messengers activate protein kinases, which ultimately trigger microtubule disassembly. By reducing activation of Transforming growth factor β-Activated Kinase 1 (TAK1), ExoY also reduces secretion of pro-inflammatory cytokines and inhibits the innate immune response. ExoS and ExoT have highly similar effects, as they both possess GTPase Activating Protein (GAP) and Adenosine Diphosphate Ribosyl Transferase (ADPRT) protein domains. Together, these domains significantly impede phagocytosis. For ExoS, this may be mediated by ADP-ribosylation of Ras, which prevents production of Reactive Oxygen Species (ROS) in neutrophils. For ExoS and ExoT, GAP activity causes inactivation of the GTPases normally responsible for maintaining the actin cytoskeleton. Consequently, cell migration and cell division are disrupted, and widespread cell detachment occurs. Additional functions of ExoS include activation of the TLR2/4 signalling pathways and disruption of important cell functions such as DNA synthesis, cell trafficking, maintenance of cell shape, motility and adhesion. Many of these effects are mediated by ADP-ribosylation of the Ezrin, Radixin and Moesin (ERM) proteins. Finally, the ADPRT domain of ExoS also helps to promote intracellular survival of *P. aeruginosa* by inducing membrane bleb formation. Created with Biorender.com.

1.4. Biofilms

One major obstacle in the treatment of bacterial keratitis is the formation of biofilms. A biofilm has been defined as "a microbially derived sessile community characterised by cells that are irreversibly attached to a substratum or interface or to each other, are embedded in a matrix of extracellular polymeric substances that they have produced, and exhibit an altered phenotype with respect to growth rate and gene transcription" (Donlan and Costerton, 2002). Biofilms form on both biotic and abiotic surfaces and are ubiquitous in infection. It is estimated that over 80% of microbial infections affecting the human body involve a biofilm component (Veerachamy et al., 2014) and this includes various ocular infections (Zegans et al., 2005, Bispo et al., 2015). Biofilm formation has been directly visualised at the corneal surface during experimental corneal infection (Saraswathi and Beuerman, 2015) and bacteria obtained from corneal infections display biofilm forming activity (Zegans et al., 2016, Dave et al., 2020). The biofilm life-cycle can be divided into 3 main stages: Initial attachment, biofilm maturation and dissemination (O'Toole et al., 2000) and the process of dissemination creates particular challenges in the treatment of biofilm infections, as it allows biofilm bacteria to regain their planktonic characteristics and colonise distal sites within the body. As a result, many biofilm infections become chronic and are recurrent in nature (Hoiby et al., 2011) and eradication of biofilms is further complicated by an enhanced resistance phenotype (Stewart and Costerton, 2001, Hanke and Kielian, 2012, Rybtke et al., 2015). Biofilm literature is currently dominated by abiotic models which lack any living cells (Buhmann et al., 2016). Numerous studies have investigated biofilm formation on contact lenses/lens cases, as well as the efficacy with which different lens materials and disinfecting solutions can be used to reduce bioburden (Henriques et al., 2005, Dutta et al., 2012, Kackar et al., 2017, Hsiao et al., 2018, Cho and Boost, 2019). However, these models lack the crucial interaction between bacteria and mammalian tissue. To understand bacterial biofilms and their true role in infections, it is imperative that co-culture models investigating biofilm formation on biotic surfaces (such as the cornea) are developed.

1.5. Antibiotic Resistance

Another major concern for the treatment of bacterial keratitis is the emergence of antibiotic resistance. Two of the most common causative agents, *S. aureus* and *P. aeruginosa*, are ESKAPE pathogens, an acronym used by the Infectious Diseases Society of America to describe 6 major pathogens (*Enterococcus faecium, Staphylococcus aureus, Klebsiella pneumoniae, Acinetobacter baumannii, Pseudomonas aeruginosa,* and *Enterobacter* species) that commonly cause nosocomial infections and that utilise various antibiotic resistance mechanisms (Pendleton et al., 2013, Santajit and Indrawattana, 2016). Furthermore, *S. aureus* and *P. aeruginosa* have been identified by the World

Health Organization as 'High' and 'Critical' priority targets, in the development of new antibiotics (WHO, 2017). Evidence of increasing antibiotic resistance amongst ocular isolates is provided by longitudinal studies (Chang et al., 2015, Tam et al., 2017) and of particular concern is the observation that resistance to fluoroquinolones is increasing for both Methicillin Susceptible (MSSA) and Methicillin Resistant (MRSA) *S. aureus* strains (Chang et al., 2015). In the UK, fluoroquinolones are currently used as the first-line antibiotic in the treatment of bacterial keratitis (Tuft and Burton, 2013). Antibiotic resistance data for *P. aeruginosa* ocular isolates is varied, with studies reporting Multi-Drug Resistant (MDR) isolates in the range of 6.52-42.9% (Saffari et al., 2017, Heidari et al., 2018). Overall, the US Department of Health and Human Services has reported that MDR *P. aeruginosa* constitutes 13% of all *P. aeruginosa* infections (n= 6700) (CDC, 2013). Infections involving antibiotic resistant bacteria are difficult to treat and often require combination antibiotics in high doses (fortified therapy) instead of the standard fluoroquinolone monotherapy. Furthermore, increased levels of antibiotic resistance have been linked to poorer clinical outcomes, with one study reporting a significant association between the Minimum Inhibitory Concentration (MIC) of the treatment antibiotic(s) and the length of healing time for corneal ulcers (Kaye et al., 2010).

1.5.1. Biofilm-Specific Antibiotic Resistance

In order to tackle the growing threat of antibiotic resistance, it is important that we understand the antibiotic resistance mechanisms used by bacteria. Resistance is largely attributable to genetic mutations and the acquisition of specific antibiotic resistance genes by horizontal gene transfer. Common genetic mechanisms include the presence/overexpression of efflux pumps that remove antibiotics, stimulation of modifying enzymes that inactivate antibiotics and the modification of bacterial target sites (Walsh, 2000). The formation of biofilms has also been associated with an increased resistance to antimicrobials (Stewart and Costerton, 2001). However, biofilm-specific antimicrobial resistance does not appear to be governed by the same genetic elements that confer resistance in planktonic bacteria and dissemination of bacterial biofilms has been associated with a return in susceptibility to antimicrobials (Anwar et al., 1989). This suggests that the multicellular nature of biofilms is central in explaining biofilm-specific antibiotic resistance and three main hypotheses that acknowledge the importance of multicellularity have been proposed. These include limited antimicrobial penetration in the presence of biofilm, the existence of altered chemical microenvironments within biofilms and the presence of persister cells (Olsen, 2015, Hall and Mah, 2017). The resistance phenotype of biofilms and the mechanisms which underpin it are discussed in more detail in my review (Urwin et al., 2020).

1.6. Modelling Bacterial Keratitis Infections

A critical tool for bacterial keratitis research is the existence of suitable infection models. It is important that these models encompass the complexity of the cornea, e.g., the presence of epithelial barrier functions, the production of ocular defence proteins such as antimicrobial peptides and the existence of shear stress conditions at the ocular surface due to blinking. It is also important that pathogens are studied in a physiologically relevant way. Bacteria have been shown to colonise the cornea as biofilm populations during bacterial keratitis and yet the majority of corneal biofilm research has been conducted using abiotic models. These models do not allow host-pathogen interactions to be studied and this represents a significant gap in the literature. A number of corneal infection models that utilise *in vitro*, *ex vivo* or *in vivo* systems have now been reported and biotic biofilm models are beginning to emerge. In this section, the various advantages and disadvantages (**Table 1-5**) associated with each of these models will be discussed, with special focus on biofilm studies.

1.6.1. *In vitro* Models

In vitro models use well-defined cell culture techniques to generate 3D corneal constructs. These models are a popular choice for ophthalmological research due to their relative cost-effectiveness and limited use of animals. The human cornea is composed of 6 distinct layers (**Figure 1-1**) and as the outermost layer, the corneal epithelium constitutes the first line of defence against external pathogens and acts as the major barrier against ocular drug penetration (Sosnova-Netukova et al., 2007). Therefore, many *in vitro* models have focussed solely on the cultivation of human corneal epithelial cell (HCE) multilayers (Ranta et al., 2003, Toropainen, 2007). However, 3D organotypic models have also been developed which incorporate epithelial, stromal and endothelial cells, providing whole-tissue models (Builles et al., 2007, Zorn-Kruppa et al., 2005). Another source of model diversity is the use of primary cells versus immortalised cell lines.

Primary cells are extracted directly from donor corneal tissue. As a result, these cells share the same phenotypic and genotypic characteristics as the donor tissue. The drawback is that these cells have a finite lifespan and reach senescence after only a few passages (Kahn et al., 1993). Furthermore, the availability of human corneal tissue is highly limited as healthy tissue is generally reserved for keratoplasty. This means animal corneas are often used as a source of primary corneal epithelial cells. The production of an immortalised cell line involves transfection/transformation of cells with a virus or plasmid that induces the cells to enter a continuously growing state by activating telomere maintenance mechanisms (Ouellette et al., 2000). As a result, these cells may be continuously passaged, and cell lines are commercially available. Numerous corneal epithelial cell lines have been reported in the literature (**Table 1-4**), including the commercially available HCE2 cell line that was used

throughout this project. It should be noted that HCE2 and HCE-T cell lines use the same methodology to generate immortalised cells, but HCE2 was coined for commercial production. It should also be noted that previous papers have used HCE and HCEC interchangeably, to refer to cell lines of multiple origin. Immortalised cell lines make attractive model systems, as they are easy to assemble and economical. However, the underlying assumption that cell lines mimic all aspects of the normal cornea has not been proven and with each passage, genetic drift occurs, causing cells to become phenotypically distinct from the original cell population (Hughes et al., 2007). A study comparing the gene expression profile of the HCE-T cell line to gene expression in the healthy human cornea, found changes in gene expression for 36% of probed genes (Greco et al., 2010). This is a reminder of the importance of characterising cell lines to ensure they remain suitably representative of the ocular surface *in vivo*.

Table 1-4. Immortalised human corneal epithelial cell lines.

'K' has been used to denote members of the keratin protein family. Keratin proteins are obligate heterodimers that form intermediate filaments. Differentiated corneal epithelial cells express K3/K12. Limbal stem cells may differentiate to become corneal transient amplifying cells. These progenitor cells co-express K5/K14 and K3/K12 (Kao et al., 1996).

Cell line	How cell line was produced	Characteristics of cell line	Reference
CEP1/ CEP1-17-CL4	Primary HCEs were infected with a recombinant SV40 T antigen retroviral vector.	▪ Cobblestone morphology. ▪ Cells could be passaged >200 times. ▪ Strong positive staining for K8, K18, K19 and weak positive staining for K3, K13, and K17. ▪ Negative staining for K4, K7 and K14. ▪ Expression of cytokines, growth factors and cytochrome p450 enzymes that is similar to that of primary HCE cells from biopsy tissue. ▪ Deemed metabolically competent.	(Sharif et al., 1997)
HCE (SV40)	Primary HCEs were infected with a recombinant SV40-adenovirus vector.	▪ Cobblestone morphology. ▪ Cells could be passaged >400 times. ▪ Development of desmosomes and microvilli was observed. ▪ Positive staining for K3. ▪ Cells differentiate to form multi-layers in the presence of an Air-Liquid Interface (ALI).	(Arakisasaki et al., 1995)
HCE-T/ HCE2	Primary HCEs were infected with Adeno 12-SV40 hybrid virus or transfected using RSV-T plasmid.	▪ Cobblestone morphology. ▪ Confluent monolayers do not differentiate under submerged media conditions. ▪ 3D, tissue-like morphology develops in the presence of an ALI. ▪ Highly migratory.	(Kahn et al., 1993, Kahn and Rhim, 1996)

		▪ Positive staining for K3.	
		▪ Cell monolayers exhibit barrier function.	
HPV16-E6/E7	Primary HCEs were infected with HPV16-E6/E7 retrovirus.	▪ Cells form multi-layered, stratified structures in the presence of an ALI. ▪ Multi-layers are 5-7 cell layers thick. ▪ Morphology of organelles is generally normal, but a small number of giant cells were observed. ▪ Cell proliferation is tightly regulated. ▪ Expression of K3. ▪ Morphology and growth rate of cells is affected by calcium concentration (slower growth observed at a higher calcium concentration). ▪ Cell monolayers exhibit significant barrier function.	(Mohan et al., 2003)
hTERT/ hTCEpi	Primary cells are infected with a retroviral vector encoding human telomerase reverse transcriptase (hTERT). Infected cells are termed hTCEpi cells.	▪ Over 240 cell doublings recorded. ▪ Cells differentiate to form multi-layers (5-7 cell layers thick) in the presence of an ALI. ▪ High calcium medium induces stratification of cells. ▪ Expression of K3, K5, K12 and K14. ▪ Expression of K5/14 increases when cells are grown submerged in media. ▪ Expression of K3 increases in the presence of an ALI. ▪ Positive staining for the ZO1 tight junction protein. ▪ Expression of MUC1, MUC4 and MUC16 (but at lower levels than in native corneal tissue).	(Gipson et al., 2003, Robertson et al., 2005)

1.6.1.1. Existing *in vitro* Infection Models

Drug permeation studies have been a key driver in the development of *in vitro* corneal models. Curved filters have been used to produce monolayers that share the curvature of the cornea (Postnikoff et al., 2014) and optimisation of cell culture conditions has led to the development of corneal models with tight cell junctions, epithelial barrier integrity and permeation profiles comparable to those of the excised cornea (Toropainen et al., 2001, Toropainen et al., 2003). The development of *in vitro* models for studying corneal absorption has been reviewed previously (Dey, 2011, Reichl et al., 2011) and optimised cell culture techniques are transferable to the development of *in vitro* infection models. Such models have been used to investigate host-pathogen interactions at the corneal epithelial surface. Immortalised HCE cell lines have been used to investigate receptor-mediated adhesion mechanisms and identify key bacterial Virulence Factors (VFs) involved in invasion (Jett and Gilmore,

2002, Garcia et al., 2016). Modulation of the host response has also been studied, with a recent study demonstrating that the Type-III Secretion System (T3SS) of *P. aeruginosa* is involved in subversion of Anti-Microbial Peptide (AMP) expression (Sharma et al., 2018). Furthermore, *in vitro* studies have demonstrated the importance of host cell defences such as cell surface mucins and tear fluid. Knockdown of MUC16 in the HCLE cell line causes significant decreases in epithelial barrier function (Gipson et al., 2014) and exposure of primary rabbit corneal epithelial cells to human tear fluid has been shown to confer significant cytoprotective effects, as well as reducing the translocation of *P. aeruginosa* (Fleiszig et al., 2003, Kwong et al., 2007). These *in vitro* infection models have helped to progress our understanding of bacterial keratitis, but they are limited by the absence of a biofilm component. To the best of my knowledge, an *in vitro* model that combines live HCE cells and the formation of bacterial biofilm is yet to be reported. In contrast, multiple keratitis studies have investigated biofilm formation on abiotic surfaces in the absence of cells (Doroshenko et al., 2018, Ponce-Angulo et al., 2020). As *in vitro* modelling techniques continue to improve, co-culture models may be reported but there are various limitations associated with the use of *in vitro* systems for studying biofilm infections (Roberts et al., 2015). For instance, characteristics of the biofilm microenvironment (e.g., nutritional cues, presence of immune cells) (Palmer et al., 2007, Bjarnsholt et al., 2013, Kolpen et al., 2014), have been shown to influence biofilm morphology and so differences in specific biofilm-forming conditions may limit model applicability.

1.6.1.2. Evaluation of *in vitro* Infection Models

It seems likely that the absence of *in vitro* HCE-biofilm models can be attributed to the reduced viability of corneal epithelial cells *in vitro*. Cell viability data was reported for an *in vitro* study using primary rabbit corneal epithelial cells infected with 10^6 CFU/ml *P. aeruginosa* and bacteria were shown to induce significant cell death after only 3 hrs (Fleiszig et al., 2003). In contrast, *ex vivo* models often rely on scarification or stromal injection for infection to become established and the same group reported use of an inoculum up to 5-log more concentrated for *ex vivo* infection work (Fleiszig et al., 2019). The increased susceptibility of *in vitro* models can be attributed to a reduced number of host defences. The conjunctiva, tear fluid, blinking and resident/infiltrative immune cells all contribute to immune defence *in vivo* (Fleiszig et al., 2019) and are absent from standard *in vitro* models. However, a number of host defences are orchestrated by corneal epithelial cells and are present in cell culture models. Corneal epithelial cells express protective mucins, AMPs and pro-inflammatory cytokines (Mantelli and Argueso, 2008, Mohammed et al., 2017) and expression levels are sensitive to bacterial antigens, providing evidence of functional PRR signalling pathways in the *in vitro* environment (Xue et al., 2000, Maltseva et al., 2007, Redfern et al., 2011). Furthermore, HCE cell lines express microRNAs

that are capable of regulating innate immune defence genes (Mun et al., 2013) and use of the gelatinous basement membrane preparation, Matrigel, has been shown to decrease bacterial translocation, mimicking the barrier integrity of the corneal epithelium (Alarcon et al., 2009b). Therefore, many host defence mechanisms remain investigable *in vitro*.

Another limitation of *in vitro* models is their suitability for studying biofilms. As *in vitro* modelling techniques continue to improve, corneal cell monolayers with an enhanced resistance to bacterial infection are likely to be reported. This could yield the development of *in vitro* co-culture models that display mature biofilm architecture. However, there are various drawbacks associated with *in vitro* biofilm infection models (Roberts et al., 2015). Firstly, there are large differences in the morphology of *in vitro* biofilms and biofilms observed in real-life infections. Biofilms observed *in vivo* are generally much smaller and do not share the same structural characteristics as their *in vitro* counterparts (Bjarnsholt et al., 2013). The absence of immune cells is also likely to affect biofilm growth *in vitro*. For instance, polymorphonuclear leukocytes (PMNs) have been shown to influence the biofilm micro-environment via their oxygen consumption. This generates gradients of oxygen availability within the biofilm and causes metabolic heterogeneity to arise (Kolpen et al., 2014). Another problem with *in vitro* biofilm models is that they are typically used to study biofilm formation under static conditions. Due to the combined effects of tear fluid and blinking, the corneal surface is continually exposed to shear stress and therefore static biofilm models can never be truly representative of the ocular surface (Masterton and Ahearne, 2018).

1.6.2. *Ex vivo* Models

Ex vivo studies make use of whole, excised corneas that are maintained in an artificial environment before experimentation. Animal corneas are often used due to the limited availability of human corneas and so interspecies variation is one of the main problems with *ex vivo* studies. A lack of standardised methods and paucity of information on animal models means comparing *ex vivo* studies can be difficult and there is dispute regarding the suitability of different animal models. *Ex vivo* models used to investigate bacterial keratitis include mice (Sullivan et al., 2015, Zhu et al., 2016, Metruccio et al., 2017, Zhu et al., 2017, Metruccio et al., 2019), rabbits (Lawinbrussel et al., 1993, Ren et al., 1997, Hume et al., 2001, Zhu et al., 2016, Pinnock et al., 2017, Robertson et al., 2017, Zhu et al., 2017), goats (Madhu et al., 2018), cows (Chu et al., 2013) and pigs (Vermeltfoort et al., 2005, Brothers et al., 2015, Okurowska et al., 2020). It is currently unknown if interspecies differences in the thickness of the corneal epithelium (Krachmer et al., 2010, Agarwal and Rupenthal, 2016) and stroma (Ehlers et al., 2010, Hatami-Marbini et al., 2013, Abhari et al., 2018) play a major role in development and

progression of infection in the *ex vivo* cornea. Morphological aspects that may affect the development of infection between species have been discussed previously (Marquart, 2011) but many questions remain unanswered. Of particular importance is the presence or absence of the Bowman's layer. The Bowman's layer is typically found in primate species but has not been found in all animals (Merindano et al., 2002, Wilson, 2020) and there is evidence that it functions as an additional barrier to bacterial traversal (Alarcon et al., 2009b). The importance of this layer is influenced by the method of infection. Popular infection methods include corneal scarification or intrastromal injection, which bypass the Bowman's layer and provide direct access to the corneal stroma. In these instances, the protective role of the Bowman's layer is less important but other studies have used contact lenses or blotting paper to introduce bacteria without prior wounding of the cornea. Such methods are important for studying intrinsic corneal resistance and/or initial bacterial adhesion and in these studies, interspecies differences in the Bowman's layer may compromise model suitability. There are conflicting reports for rabbit and porcine corneas with some studies claiming the Bowman's layer is absent (Ojeda et al., 2001, Jay et al., 2008, Batista et al., 2016, Crespo-Moral et al., 2020) whilst others report it as present (Hayashi et al., 2002, Lai and Tang, 2014). Given the popularity of these two animal models, it is important that resolution be reached on this topic.

1.6.2.1. Existing *ex vivo* Infection Models

Various techniques have been used to induce bacterial infection in *ex vivo* corneas, including prolonged exposure to bacteria (Ramphal et al., 1981, Vallas et al., 1996), use of infected contact lenses (Vermeltfoort et al., 2005), superficial injury (e.g., tissue paper blotting) (Klotz et al., 1989), corneal scarification (Robertson et al., 2017, Madhu et al., 2018, Okurowska et al., 2020) and intrastromal injection (Pinnock et al., 2017). Differences in infection method, inoculum size, culturing techniques, incubation times and bacterial strains mean that comparing *ex vivo* studies is challenging. For example, Pinnock et al. (Pinnock et al., 2017), found that more bacteria are recovered after injecting the inoculum into the stroma than after corneal wounding. In contrast, similar infection outcomes were reported for both rabbit and human corneas. Colony Forming Units (CFU) were measured following 24 or 48 hr infection and variations in CFU were small despite differences in bacteria and handling techniques for each model (Pinnock et al., 2017). In agreement with Pinnock et al., it was recently demonstrated that there was no significant difference in viable cell count between *ex vivo* porcine and rabbit cornea models after 24 hr infection, nor when two different strains of *P. aeruginosa* were used (Okurowska et al., 2020). Furthermore, whilst some studies have reported that infection in *ex vivo* corneas is easy to establish and that progress is visible within less than 24 hrs (Vallas et al., 1996, Pinnock et al., 2017, Okurowska et al., 2020), Madhu et al. found that incubation

time could be extended by a few days if a smaller inoculum was used (Madhu et al., 2018). Despite issues with standardisation, *ex vivo* models have been used to study various aspects of bacterial keratitis. This includes epithelial barrier function (Augustin et al., 2011, Metruccio et al., 2017), effect of bacteria on epithelial cell migration (Brothers et al., 2015), bacterial transmission from contact lenses (Ren and Wilson, 1997, Vermeltfoort et al., 2005, Ubani-Ukoma et al., 2019), bacterial adherence to corneal epithelium (Klotz et al., 1989), movement of bacteria in stroma (Robertson et al., 2017), role of virulence factors (Sullivan et al., 2015, Madhu et al., 2018) and drug testing of new ophthalmic antimicrobials (Chu et al., 2013, Doroshenko et al., 2018).

1.6.2.2. Evaluation of *ex vivo* Infection Models

The existence of co-culture models that display mature biofilm architecture provides a strong argument for the use of *ex vivo* modelling in keratitis research. Another strength of these models is the presence of a more complete host immune response (as compared to simple, *in vitro* systems). The same innate immune defences described for *in vitro* models (e.g., mucins, AMPs) are present *ex vivo*, alongside additional host defences. These defences include the presence of resident immune cells e.g., CD11c +ve (dendritic) cells, which contribute to epithelial barrier function during health (Metruccio et al., 2017) and additional cell layers, e.g., the Bowman's layer, which impede bacterial traversal (Alarcon et al., 2011). However, not all animal models possess a Bowman's layer and there are interspecies differences in the thickness/structural organisation of this layer which must be considered (Lai and Tang, 2014). Furthermore, the absence of a complete immune response means there are elements of clinical keratitis infections that cannot be investigated *ex vivo*. For instance, CD11c +ve cell response has been shown to differ between *ex vivo* and *in vivo* settings (Metruccio et al., 2017). Following bacterial challenge *in vivo*, CD11c +ve dendritic cells migrate to the site of infection where they co-localise with adherent bacteria and undergo significant changes in morphology. This response is not observed *ex vivo*, showing that control of this system extends beyond the cornea (e.g., lymphatic vessels, corneal nerves). Infiltrative PMNs are also absent from *ex vivo* models. These immune cells are involved in ulcer formation and are largely responsible for inflammatory damage to the cornea (Livingston et al., 2019). Inflammation is one of the key hallmarks of bacterial keratitis and so the full extent of infection cannot be mimicked in the absence of PMN recruitment. Another problem with *ex vivo* models is potential interspecies differences in immune defence. For example, significant differences in mucin expression have been reported for rabbit versus human corneas (Leonard et al., 2016). Mucins have been implicated in a range of functions including tear fluid dynamics, signal transduction and glycocalyx-mediated defence (Gipson and Argueso, 2003) and MUC1 has been shown to directly interact with *P. aeruginosa* at the surface of airway epithelial

cells (Kato et al., 2010). Therefore, it seems likely that differences in mucin expression could affect host-pathogen interactions at the corneal surface.

Despite potential problems with interspecies variation, *ex vivo* systems have been described as ideal models for studying biofilm formation. This is because they incorporate desirable attributes from both *in vitro* and *in vivo* systems (Roberts et al., 2015). The human cornea has a complex, 3D surface topology made up of multiple different cell-types, making it extremely difficult to mimic *in vitro*. The use of excised tissue eliminates this problem by providing a biotic surface that should be highly representative of the *in vivo* tissue. However, there are still likely to be differences in biofilm formation due to differences in the corneal environment. For instance, the tear film is absent *ex vivo* and this layer contains multiple antimicrobial compounds (e.g., secretory immunoglobulin A, lactoferrin, lysozyme) which have been shown to influence bacterial colonisation *in vivo* (Kwong et al., 2007). Furthermore, excised corneas are often maintained in an artificial tissue culture medium, which may not reflect the nutritional environment *in vivo*. This is important as nutritional cues can impose significant effects on biofilm growth (Palmer et al., 2007). Finally, the dynamic conditions present at the cornea (due to blinking, tear flow etc.) are not present *ex vivo*. *Ex vivo* models that mimic features of the ocular environment (e.g., intraocular pressure, flow conditions) have been reported (Rowe et al., 2010, Guindolet et al., 2017), with one study even utilising artificial tears (Elbadawy et al., 2015) but these models are yet to be trialled in the context of infection.

1.6.3. *In vivo* Models

In vivo modelling involves the use of live animals. Rat (Tam et al., 2010) and rabbit (Venkatesh et al., 2017, Tang et al., 2018, Jian et al., 2020) models have been reported but mouse models currently dominate the literature (Saraswathi et al., 2013, Metruccio et al., 2016, Metruccio et al., 2017, Kugadas et al., 2019, Metruccio et al., 2019, Li et al., 2020, Ponce-Angulo et al., 2020). Despite its smaller size, the murine cornea contains more corneal epithelial cell layers than the human cornea and the ratio of epithelial to stromal cells is larger (Henriksson et al., 2009). As with other animal models, there is a dispute regarding the presence of a Bowman's layer (Hayashi et al., 2002, Lai and Tang, 2014) and there are large interspecies differences in immune response that must be considered (Zschaler et al., 2014). However, murine models remain a popular choice for *in vivo* work because of their small size, ease of breeding and the existence of large genetic mutant libraries. Various techniques have been developed for studying bacterial keratitis *in vivo*. Animals are first anesthetised so that corneal wounding/bacterial inoculation can be performed, and infection progresses in the living model. Following scarification, eyes are enucleated and analysed *ex vivo* or alternatively,

intravital imaging techniques have now been reported which allow microscopic analysis to be conducted *in vivo* (Tam et al., 2011). *In vivo* corneal models are ideal for studies of host immune defences, inflammation and corneal healing processes. However, these models are not suitable for studying the early stages of infection, as the healthy, intact cornea is difficult to infect unless contaminated contact lenses are used (Mun et al., 2009, Metruccio et al., 2019, Wan et al., 2020). Additionally, initiating and developing infection takes days and is not always guaranteed (Mun et al., 2009).

1.6.3.1. Existing *in vivo* Infection Models

Increasing interest in ocular biofilms over the past decade has resulted in the development of an established *in vivo* cornea model (Saraswathi et al., 2013), followed by improved methods of imaging bacteria and biofilm formation (Tam et al., 2011, Saraswathi and Beuerman, 2015, Sullivan et al., 2015, Metruccio et al., 2017, Kugadas et al., 2019, Ponce-Angulo et al., 2020). This has led to further publications focusing on: biofilm formation on contact lenses in rabbit (Jian et al., 2020) and in mice (Li et al., 2020); host-pathogen interactions on ocular samples using proteomics (Sewell et al., 2014, Yeung et al., 2020); activation of immune signalling pathways (Sun et al., 2010); the role of virulence factors in keratitis (Hume et al., 2001, Metruccio et al., 2016, Suzuki et al., 2018, Tang et al., 2018); and drug testing of new ophthalmic antimicrobials (Clemens et al., 2017, Venkatesh et al., 2017, Kugadas et al., 2019). Drug testing has included synthetic analogues of host antimicrobial peptides, with one study reporting reduced corneal bioburden and improved ocular scores following treatment with their lead peptide (Clemens et al., 2017). This suggests that synthetic AMP analogues could provide valuable alternatives/adjuncts to antibiotics and highlights the importance of ocular surface proteins in defence against bacterial keratitis (Ni et al., 2008, Augustin et al., 2011, Metruccio et al., 2017). For instance, Surfactant Protein D (SP-D) present in tear fluid has been shown to take part in clearing *P. aeruginosa* from the murine ocular surface (Mun et al., 2009) while exogenous vasoactive intestinal peptide regulates expression of other proteins involved in infection (Jiang et al., 2012). However, it was recently found that there are differences in protein expression between human and mouse stroma in vascularised and healthy corneas (Barbariga et al., 2019). These differences are likely to affect pathophysiology between species and may limit the clinical relevance of murine *in vivo* models.

1.6.3.2. Evaluation of *in vivo* Infection Models

The major advantage of *in vivo* infection models is the presence of a complete immune response. This includes numerous host systems which have the potential to influence infection outcome, but which

are absent from *in vitro*/*ex vivo* models, e.g., the tear film, lacrimal glands, conjunctiva, lymphatic vessels, infiltrative immune cells and the role of blinking. However, differences between the murine and human immune response may compromise the suitability of these models (Zschaler et al., 2014). For instance, although the presence of a lacrimal gland provides a functional tear film, the nature of lacrimal gland secretions differs between species (Schechter et al., 2010). This gland is responsible for the production of lipid binding proteins, chemokines, secretory IgA and growth factors and therefore differences in the lacrimal gland secretions are likely to affect host-pathogen interactions at the corneal surface. Furthermore, there are large differences in white blood cell composition between humans and mice. In humans, PMNs are the most abundant leukocyte, comprising 50-70% of total white blood cells (Haley, 2003). In the C57BL/6 mouse model, PMNs are much less abundant at 10-25% and lymphocytes constitute 75-90% of total leukocytes (Doeing et al., 2003). These differences in leukocyte populations are likely to reflect large differences in the nature of the immune response and limit the clinical relevance of murine models.

The suitability of *in vivo* systems for investigating chronic biofilm infections has been praised (Roberts et al., 2015). In contrast to *in vitro*/*ex vivo* biofilm studies, we can expect biofilm morphology to be highly representative of the true infectious scenario, as similar growth conditions (e.g., specific nutritional cues and oxygen gradients) are present. Furthermore, the dynamic, shear stress conditions of the cornea are present, although this may be affected by differences in blinking frequency between species (Hayes et al., 2007). One general criticism of *in vivo* biofilm models is a lack of species diversity. Chronic wound infections have been well studied in the context of biofilms and one study reported the presence of 5 or more bacterial species in 30% of diabetic foot infections (Peters et al., 2012). However, it is important to note that species diversity amongst infectious agents closely matched that of the natural skin flora. In contrast, the human corneal surface does not possess a resident microbiome and microbial diversity in the nearby conjunctiva is very low compared to other sites in the body (Doan et al., 2016). Therefore, multi-species infections are less relevant to corneal biofilm studies, although mixed infection models have been reported (Ponce-Angulo et al., 2020).

Table 1-5. Evaluation of *in vitro*, *ex vivo* and *in vivo* corneal models for the study of bacterial keratitis infections. Previously published as part of my review (Urwin et al., 2020).

	Advantages	Disadvantages
***In vitro* cell culture models**	- Economical. - Reduced use of animals. - Cell lines can be used continuously. 3D organotypic models can be developed using multiple cell lines. - Many host defence mechanisms remain investigable, e.g., expression of mucins, AMPs, pro-inflammatory cytokines and microRNAs, investigation of cell surface receptors and PRR signalling pathways.	- Problems with cell lines and genetic drift. - Primary cells reach senescence after a few passages. - Reduced cell viability and increased susceptibility to infection. - Absence of resident and infiltrative immune cells. - Absence of conjunctiva. - Absence of tear fluid and lacrimal glands. - Infection normally occurs under static conditions. - Differences in the biofilm microenvironment (e.g., nutritional cues, absence of immune cells) may affect biofilm morphology.
***Ex vivo* models**	- Whole-tissue model. - Complex 3D surface topology of the cornea is preserved. - Increased cell viability facilitates longer infection periods. - Presence of resident immune cells.	- Low availability of human corneas means animal models are commonly used. - Lack of standardised infection methods - Dispute regarding corneal anatomy of animal models. - Interspecies differences in corneal anatomy, functional characteristics and immune response may affect applicability to human infections. - Absence of infiltrative immune cells. - Absence of conjunctiva. - Absence of tear fluid and lacrimal glands. - Infection normally occurs under static conditions. - Differences in the biofilm microenvironment (e.g., nutritional cues, absence of immune cells) may affect biofilm morphology.
***In vivo* models**	- Complete immune response (resident/infiltrative immune cells, tear film, conjunctiva and lymphatic vessels). - Infection occurs under dynamic, shear stress conditions. - Biofilm morphology should be highly similar to the true infectious scenario.	- Animal models must be used, raising ethical issues. - Interspecies differences in corneal anatomy, functional characteristics and immune response may affect applicability to human infections. - Expensive. - Time-consuming. - Infections can be difficult to establish, and prior wounding of the cornea is often required.

1.7. Physiological Flow Models

One of the major problems with *in vitro* and *ex vivo* corneal models is that they are generally used to study bacterial keratitis under highly controlled, static conditions, which are not representative of the ocular surface. The human cornea is exposed to various mechanical stimuli, including tear film, eyelid movement, intraocular pressure and contact lens-wear and corneal cells detect and respond to these mechanical signals via a process known as mechanotransduction (Masterton and Ahearne, 2018). This phenomenon has important biological implications for the cornea. For instance, axial strain has been shown to affect α-Smooth Muscle Actin (α-SMA) production in rabbit corneal fibroblasts and under physiological strain conditions, α-SMA production is downregulated (Leonard et al., 2012). This is proposed to play an important role in maintaining corneal transparency. Another important mechanical signal, which specifically affects corneal epithelial cells, is shear stress. Shear stress can be defined as the frictional force that "arises from the friction between two virtual layers in a fluid, and is induced by the difference in movement of the two layers and the 'roughness' (or viscosity) between these layers" (Helderman et al., 2007). Corneal shear stress is a by-product of physiological flow conditions at the ocular surface, and it is generated by the movement of tear film over the corneal epithelium. The magnitude of shear stress is influenced by two parameters, shear rate and solution viscosity (Sanfilippo et al., 2019) and therefore shear stress can calculated using the following equation:

$$\text{Shear stress (dyn/cm}^2) = \text{Shear rate (1/s)} \times \text{Dynamic viscosity (dyn} \times \text{s/cm}^2)$$

'Shear rate' describes the change in velocity as a fluid passes over an adjacent layer and 'dynamic viscosity' refers to the fluidity of the solution. The importance of shear stress has been well documented in other model systems, e.g., shear stress generated by the bloodstream is highly influential in the structure and function of the vascular system, with certain cardiovascular diseases linked to defects in mechanosensing (Humphrey et al., 2015). Therefore, it is important that physiological shear stress conditions are investigated in the context of the cornea. Fortunately, corneal flow models are beginning to emerge but there is considerable diversity in experimental conditions (**Table 1-6**). This can be explained by a lack of data for *in vivo* shear stress values. Kang et al. estimated that corneal shear stress is 0.05 dyn/cm^2, based on a blink rate of 20 blinks/min and tear volume turnover rate of 0.31 ml/min (Mathers and Daley, 1996, Kang et al., 2014). However, another group previously provided a much higher estimate of 14 dyn/cm^2 (Srinivas et al., 2002). Shear stress calculations are further complicated by individual differences. Various factors such as blink rate, tear film thickness and composition of the tear film, affect shear stress values (Masterton and Ahearne, 2018). This makes calculating average values for the human cornea difficult, especially because these characteristics are often altered in individuals with ocular diseases (e.g., dry eye disease) and in

response to therapeutics (e.g., artificial tears) (Rolando and Zierhut, 2001, Schmidl et al., 2015). Therefore, calculating *in vivo* shear stress values poses a significant challenge in the field.

1.7.1. Existing Physiological Flow Models

Despite uncertainty regarding *in vivo* shear stress conditions, various groups have developed models for investigating the corneal epithelium under flow conditions (**Table 1-6**). One emerging technology is the use of cornea-on-a-chip models (Bennet et al., 2018, Yu et al., 2021). These models contain a porous polycarbonate membrane, which divides a microfluidic chip into two chambers. The polycarbonate membrane is coated with ECM reagents (e.g., fibronectin or collagen) to mimic the basement membrane and corneal epithelial cells are seeded onto the coated membrane. Yu et al. also incorporated endothelial cells into their model. These cells were seeded into the lower chamber and the inclusion of multiple cell types represents an important step in the development of organ-on-a-chip models. Furthermore, the presence of two microfluidic channels, above and below the membrane, allows independent flow rates to be established and corneal epithelial cells can be cultured at air-liquid interface by removing media from the upper channel. This is important as air-lifting has been shown to promote differentiation of corneal epithelial cells (Greco et al., 2010). Cornea-on-a-chip models represent an exciting advancement in microfluidics, and it will be interesting to see how they are applied in future years. Other physiological flow models have provided a range of interesting findings. In studies involving rabbit corneas, cell shedding was shown to be increased in the presence of shear stress (Ren and Wilson, 1997) and ATP production was increased in primary rabbit corneal epithelial cells (Srinivas et al., 2002). Significant changes in cell morphology have also been associated with shear stress conditions. Molladavoodi et al. showed that HCECs cultured under high (8 dyn/cm^2) or low (4 dyn/cm^2) shear stress conditions produced highly organised, elongated filamentous actin. These cytoskeletal changes were time-dependent, with most significant changes in morphology occurring at 24 hrs. Scratch assays were used to assess cell proliferation and migration and these behaviours were significantly increased following 24 hr shear stress exposure (Molladavoodi et al., 2017). This suggests shear stresses at the ocular surface may play an important role in corneal wound healing. Hampel et al. also investigated cytoskeletal changes in response to shear stress and they employed continuous (14 dyn/cm^2) and oscillatory (0-50 dyn/cm^2) flow conditions. Under oscillatory shear stress conditions, hTCEpi cells adopted a flattened, polygonal morphology, highly similar to the stratified corneal epithelium observed *in vivo*. Increased mRNA expression of E-cadherin and Tight Junction Protein-1 (ZO1) was observed and increased expression of occludin was recorded at both the RNA and protein level. Rose-Bengal staining was used to assess barrier function and whilst no significant changes were observed under oscillatory flow, uptake was significantly diminished

under continuous flow conditions (Hampel et al., 2018). Taken together, these findings illustrate the importance of shear stress in tight junction formation and stratification of the corneal epithelium.

Table 1-6. Previously reported *in vitro* and *ex vivo* flow models for studying the corneal epithelium.

Cell type	Flow system	Shear stress conditions	Reference
Whole rabbit eyes	Whole eye perfusion model	Stirred solution (continuous, circular flow, 3000 rpm) 6 hrs	(Ren and Wilson, 1997)
Primary rabbit corneal epithelial cells	Rotating disk model	0.34 dyn/cm^2 20 seconds	(Srinivas et al., 2002)
SV-40 immortalised corneal epithelial cells (HCE-T)	Microfluidic flow channel	1 dyn/cm^2 40 minutes	(Pretor et al., 2015)
Porcine cornea	Bioreactor	Medium flow (5 µl/min) in endothelial chamber, epithelial chamber subject to air-lifting (exposed to air for 30 seconds, then media for 1 second). 7 days	(Guindolet et al., 2017)
HPV-immortalised human corneal epithelial cells (HCECs)	Parallel plate flow channel	4 or 8 dyn/cm^2 6, 14 and 24 hrs	(Molladavoodi et al., 2017)
Human telomerase-immortalised corneal epithelial cells (hTCEpi)	Cornea-on-a-chip	No flow; continuous flow (0.0198 cm/s); and blinking associated pulsatile flow model (17 blinks per minute). 300 minutes	(Bennet et al., 2018)
Human telomerase-immortalised corneal epithelial cells (hTCEpi)	Ibidi pump system	Unidirectional, continuous flow at 14 dyn/cm^2 or oscillatory, discontinuous flow at 0-50 dyn/cm^2 72 hrs	(Hampel et al., 2018)
Human telomerase-immortalised corneal epithelial cells (hTCEpi)	Ibidi pump system	0, 0.22, 0.4 and 0.8 dyn/cm^2 24 hrs	(Cha et al., 2019)
Immortalised human corneal epithelial (HCEpi) and endothelial (HCEnd) cells	Cornea-on-a-chip	Continuous, volumetric flow rate of 100 µl/h, shear stress value not provided Up to 14 days	(Yu et al., 2021)

1.7.2. Existing Physiological Flow Models: Infection Studies

Despite advancements in physiological flow models, use of these models for studying bacterial keratitis has been limited and there appears to be only one publication on this topic (Lakkis et al., 2001). In this study, a simple corneal flow model was used to investigate the cytotoxicity of *P. aeruginosa* against rabbit corneal epithelial cells and trypan blue staining was measured in the presence of static versus shear stress conditions (50-134 dyn/cm^2). Cytotoxicity was reduced but not completely eliminated under shear stress conditions and shear stress values above the reported range were associated with epithelial cell damage. The experimental setup was highly simplistic and involved

culturing corneal epithelial cells on a rocker apparatus to induce shear stress. More sophisticated models have been used to study host-pathogen interactions under flow conditions in other cell types. For example, the BioFlux200 system has been used to study adhesion and biofilm formation of pathogenic *Escherichia coli* on human colorectal (HRT-18) cell monolayers, providing a model for high-throughput screening of putative adhesion mutants (Tremblay et al., 2015). However, this model was limited by the absence of high-resolution, live-cell imaging. One of the most popular cell-types for microfluidic research is endothelial cells and host-pathogen interactions at the endothelium have been studied in the context of bacterial (Soyer and Dumenil, 2012), fungal (Grubb et al., 2009), viral (DuRose et al., 2012) and parasitic (Maksimov et al., 2016) infections. Endothelial infection models have provided crucial insight into the effects of shear stress. For example, the role of mechanosensitive proteins such as von Willebrand factor in mediating bacterial adhesion (Steinert et al., 2020) and the ablation of staphylococcal FnBP binding mechanisms under shear stress conditions (Reddy and Ross, 2001). These findings may have relevance in bacterial keratitis and further investigation is crucial. Previously reported corneal flow models have demonstrated changes in mammalian cell behaviour in response to shear stress and infection outcome is further complicated by the observation that bacteria also modulate their behaviour in this way. For example, the adhesion characteristics of *P. aeruginosa* are altered in response to shear stress and the residence time of adherent bacteria on glass and PDMS, increases with increasing shear stress (0-35 dyn/cm^2) (Lecuyer et al., 2011). Furthermore, biofilm morphology may be influenced by shear stress. Self-aggregating, suspension biofilms are observed under low shear conditions whereas surface attached *P. aeruginosa* biofilms form under high shear stress (Crabbe et al., 2008). Shear-induced changes in bacterial phenotype, alongside shear-induced changes in host cell behaviour are likely to affect infection outcome and therefore it is imperative that bacterial keratitis be investigated under physiological flow conditions.

1.8. Testing Novel Antimicrobials

A key incentive in the development of *in vitro* infection models is their potential application in antimicrobial drug testing, particularly anti-adhesion therapies, which target the initial binding interactions between host and bacteria. Bacterial adhesion represents the first stage of pathogenesis and so by disrupting this process, anti-adhesins have the potential to prevent new infections and/or disrupt the colonisation of distal sites within the body. During this project, the anti-adhesion effects of CD9-derived tetraspanin peptides and unfractionated heparin were investigated. CD9 peptides and UFH are both proposed to reduce bacterial adhesion by altering the cell surface profile of mammalian

host cells (**Figure 1-6**). Additive effects are not observed when the treatments are used in combination and so they are believed to act on similar bacterial adhesion pathways (Green et al., unpublished data).

1.8.1. CD9-Derived Tetraspanin Peptides

The CD9 peptides are novel anti-infective peptides, derived from the CD9 tetraspanin. The tetraspanins are a superfamily of four-span membrane proteins that are highly conserved and widely distributed throughout multicellular organisms (Charrin et al., 2014). Mammals possess 33 tetraspanin proteins, including CD9, and these proteins share a number of conserved structural features, including the presence of four transmembrane domains, one intracellular loop and two extracellular loops, termed EC1 and EC2, respectively (**Figure 1-5**) (Monk and Partridge, 2012). The EC2 domain is highly variable in terms of its size and amino acid composition and nearly all known protein interaction sites have been mapped to this region (Seigneuret et al., 2001, Hemler, 2005). Therefore, differences in tetraspanin specificity are generally attributed to the EC2 domain. Despite EC2 diversity, tetraspanins generally lack specialised functions and instead play overlapping roles in basic cell functions such as cell adhesion, motility, membrane trafficking and cell to cell fusion. For example, CD9 and CD81 play overlapping roles in multiple cell fusion events including muscle cell fusion, multinucleated giant cell formation and sperm-egg fusion (Fanaei et al., 2011) and at least six different tetraspanins, referred to as the TspanC8 subgroup, have been shown to interact with ADAM10 metalloproteinase, altering its subcellular localisation and modulating important cell signalling events such as Notch activation (Jouannet et al., 2016). Another important characteristic of the tetraspanins is their propensity to form large protein clusters in the cell membrane. These clusters are termed Tetraspanin Enriched Microdomains (TEMs), and they arise when tetraspanins form lateral associations with each other and with other proteins in the plasma membrane (Yanez-Mo et al., 2009). Through the formation of TEMs, the tetraspanins act as molecular organisers, assembling membrane proteins in close proximity and facilitating cell membrane functions (Halova and Draber, 2016). It has been suggested that bacteria are able to exploit TEMs as a means of infecting host cells (Monk and Partridge, 2012). Many of the host cell proteins found within TEMs act as receptors for bacterial adhesins, e.g., the CD46 complement receptor, HSPGs and integrins, are all found within TEMs and have been shown to facilitate bacterial adhesion (Hauck, 2002, Gill and Atkinson, 2004, Umeda et al., 2020). Hence, TEMs have been likened to "sticky platforms" and it was hypothesised that disruption of TEMs could be used as an anti-adhesion therapy (Monk and Partridge, 2012). Previous work by our group showed that CD9, CD63 and CD151 antibodies, as well as recombinant tetraspanin proteins, were able to reduce adhesion of *Neisseria meningitidis* to epithelial cell lines by as much as 90% (Green et al., 2011). The CD9 tetraspanin became of particular interest due to its high expression at host cell membranes and

short peptides that share amino acid sequence with the CD9 tetraspanin were designed. These CD9-derived tetraspanin peptides were later shown to specifically interact with endogenous CD9 and cause disruption of TEM clustering (Issa et al., unpublished data). As a result, these CD9 peptides have potent anti-infective effects and have been shown to reduce adhesion of *S. aureus* to human keratinocytes by as much as 60% (Ventress et al., 2016). More recently, the CD9 peptides have been shown to reduce adhesion of *S. aureus* and *P. aeruginosa* to immortalised cell lines, including human keratinocytes and corneal epithelial cells (Issa et al., unpublished data). *S. aureus* and *P. aeruginosa* are common causative agents of bacterial keratitis and so CD9-derived peptides could act as valuable therapeutics in the treatment of corneal infections. However, previous studies have utilised highly simplistic infection models, with short infection times and therefore further investigation is required.
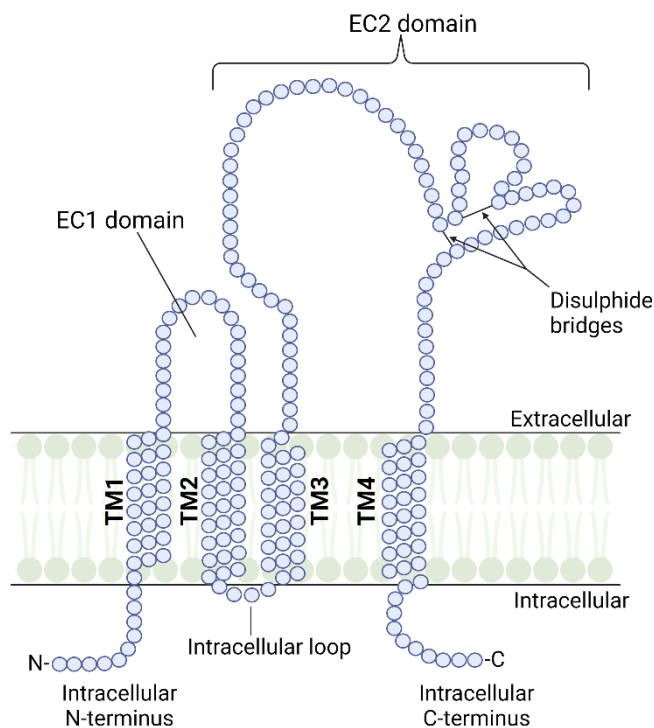
Figure 1-5. Structural features of the tetraspanin superfamily.
Members of the tetraspanin superfamily possess 4 transmembrane domains (TM1-4) that contain charged residues. Both the N and C-termini are intracellularly located and TM2 and TM3 are connected by a small intracellular loop. There are also two extracellular loops and the smaller of these loops is termed EC1. The large extracellular loop is termed EC2, and this domain is responsible for forming protein-protein interactions. Within the EC2 loop is a conserved Cys-Cys-Gly sequence motif and an additional 2-6 cysteine residues can be found downstream of this motif. These residues facilitate the formation of disulphide bridges.
Created with Biorender.com and adapted from Ventress et al., 2016.

1.8.2. Heparin

Mammalian cells produce a diverse array of glycoproteins which are found in the host ECM or embedded in the plasma membrane (Varki et al., 1999). These glycoproteins are composed of one core protein, which is covalently linked to one or more glycosaminoglycan (GAG) chains. GAGs are formed of repeating disaccharide units that generate linear chains with highly anionic charge. GAGs may be divided into separate groups based on their disaccharide composition and examples include Chondroitin Sulphate (CS) and Heparan Sulphate (HS) chains (Aquino and Park, 2016). Membrane proteoglycans generally possess HS chains and are referred to as Heparan Sulphate Proteoglycans (HSPGs); however, there is large diversity in the nature and number of GAGs possessed by HSPGs. One well-studied group of HSPGs is the syndecan (SDC) family, which consist of SDC1-4 (Gondelaud and Ricard-Blum, 2019). Syndecans possess both CS and HS chains and these GAGs act as important binding factors for cytokines, growth factors and ECM components. However, multiple species of bacteria have been shown to subvert host GAGs during infection. For instance, *N. gonorrhoeae* binds directly to HSPGs (Vanputten and Paul, 1995) and SDC-1 is known to play an important role in the adhesion of *S. aureus* and *S. pneumoniae* to corneal epithelial cells, although direct interactions between SDC-1 and bacterial adhesins have not been observed (Hayashida et al., 2011, Jinno et al., 2020). Furthermore, *S. aureus* and *P. aeruginosa* have been shown to induce HSPG shedding via α/β toxin and LasA, respectively (Chen et al., 2008). The shed HSPG ectodomains have inhibitory effects on host AMPs, helping to reduce bacterial clearance. Interestingly, endogenous HS and HS mimics such as heparin, have been shown to significantly reduce bacterial adhesion to the HCE2 human corneal epithelial cell line (Garcia et al., 2016), as well as lung epithelial (A549) and fibroblast (MRC5) cell lines (Rajas et al., 2017). Heparin is a soluble analogue of heparan sulphate, and these GAGs are composed of the same disaccharide units, although heparin is more heavily sulphated. Also, whereas HS is expressed by virtually all cells in the body, heparin is mainly produced by mast cells and is more commonly known for its pharmaceutical use as an anti-coagulant (Varki et al., 1999). For many years, the mechanism by which heparin disrupts the indirect interactions between HSPGs and bacteria has remained unclear, but there is increasing evidence for the role of fibronectin. Syndecans have been shown to bind fibronectin via HepII domains (Gong et al., 2008) and SDC-1/2 have been implicated in integrin-dependent fibronectin fibrillogenesis at the cell surface (Yang and Friedl, 2016). More recently, a mechanism for the inhibition of *S. aureus* adhesion by heparin was proposed (Green et al., unpublished data). In this model, HSPGs such as SDC-1 bind fibronectin and generate "adhesion nets" composed of fibrillar fibronectin. *S. aureus* is then able to bind fibronectin and interact with other bacterial adhesion receptors, such as α5β1 integrin, via the localisation of HSPGs to TEMs. In the presence of heparin, fibronectin is displaced from the cell surface and/or interactions between

bacteria and fibronectin are blocked. This prevents the formation of fibronectin "adhesion nets" and subsequent association with TEMs. This area of research has exciting implications for drug development as fibronectin is commonly exploited during bacterial infections. Therefore, heparin has potential use as a broad-spectrum antimicrobial compound.
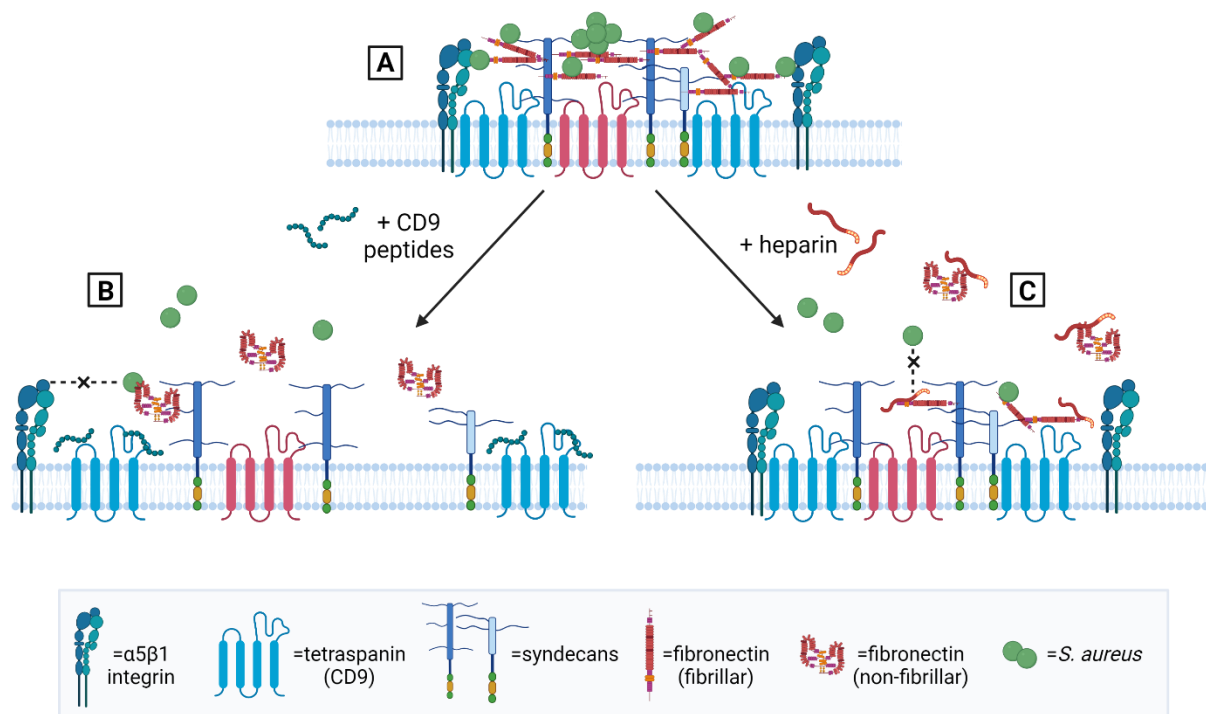
Figure 1-6. Proposed mechanism of action for novel anti-adhesion therapies.
(A) No treatment: Densely packed Tetraspanin Enriched Microdomains (TEMs) exist in host cell membranes. These TEMs cluster bacterial adhesion receptors in close proximity and fibronectin "adhesion nets" are formed by the activity of syndecans and integrin proteins. Bacteria such as *S. aureus* are able to bind fibronectin nets.
(B) CD9-derived tetraspanin peptides: Peptides specifically interact with CD9 tetraspanins in the host cell membrane. This blocks interactions between the CD9 and other TEM proteins and TEMs increase in size, becoming more dispersed. The separation of TEM proteins prevents fibronectin fibrillogenesis and prevents adherent bacteria from making secondary interactions with other proteins. **(C) Heparin:** Heparin displaces fibronectin from the host cell surface and blocks fibronectin binding. This prevents bacteria from making initial binding interactions. Created with Biorender.com.

1.9. Concluding Remarks

Bacterial keratitis is a potentially sight-threatening corneal infection, which remains a major cause of corneal blindness worldwide. The most common causative agents of bacterial keratitis are *Staphylococcus aureus* and *Pseudomonas aeruginosa,* and these bacteria possess characteristics that

threaten to compromise existing antibiotic treatments. Firstly, these bacteria can colonise the cornea as biofilm populations, which display a strong resistance phenotype compared to their planktonic counterparts. This phenotype includes an increased resistance to antimicrobials and reduced clearance by the host immune system. Furthermore, *S. aureus* and *P. aeruginosa* have been identified by the World Health Organization as 'High' and 'Critical' priority targets respectively, for the development of new antibiotics, due to the increasing prevalence of antibiotic resistance amongst these bacteria. Consequently, new ophthalmic antimicrobials are desperately required. In order to improve our understanding of bacterial keratitis and develop new antimicrobials, realistic corneal infection models are needed. *In vitro*, *ex vivo* and *in vivo* corneal infection models have all been reported previously but these models possess various limitations. One of the major problems with *ex vivo* and *in vivo models* is that these models generally require the use of animals and there are concerns that interspecies differences may affect applicability to human infections. *In vitro* models have the potential to overcome this problem via the use of immortalised cell lines or primary cells extracted from the human cornea. However, these models are currently limited by the absence of a biofilm component, as well as the static nature of infection conditions, which are unrepresentative of physiological flow conditions at the ocular surface. Therefore, it is essential that we continue to optimise corneal infection models. These models currently act as critical tools in antimicrobial drug testing and by developing more realistic infection models, we will be better equipped to predict efficacy in humans.

1.10. Hypothesis

I hypothesise that the HCE2, human corneal epithelial cell line can be used to develop sophisticated *in vitro* models of the infected corneal epithelium, with valuable applications in antimicrobial drug testing.

1.11. Aims

The primary focus of this thesis is bacterial keratitis, a potentially sight-threatening bacterial infection localised to the cornea, which remains a major cause of blindness worldwide. Clinicians currently depend on antibiotics to resolve bacterial keratitis infections but increasing rates of antibiotic resistance mean that new ophthalmic antimicrobials are desperately required. In order to tackle this problem, we must improve our understanding of corneal epithelial cell functions, the bacterial characteristics that contribute to pathogenicity and the complex host-pathogen interactions that occur between them. It is also important that we continue to improve corneal infection models so

that they better mimic real-life infections by incorporating important host characteristics such as epithelial barrier function and physiological flow conditions into *in vitro* corneal infection models. This will be critical for antimicrobial drug testing, as it will provide early-stage models that are better able to predict efficacy in humans. In this PhD thesis, I seek to address current gaps in the literature and contribute to the development of novel therapeutics, via the following aims:

i. To develop an *in vitro* cell culture model of the differentiated corneal epithelium, using the HCE2 human corneal epithelial cell line.

ii. To study clinical bacterial isolates obtained from bacterial keratitis patients.

iii. To use *in vitro* HCE2 models to simulate bacterial keratitis and test novel antimicrobials.
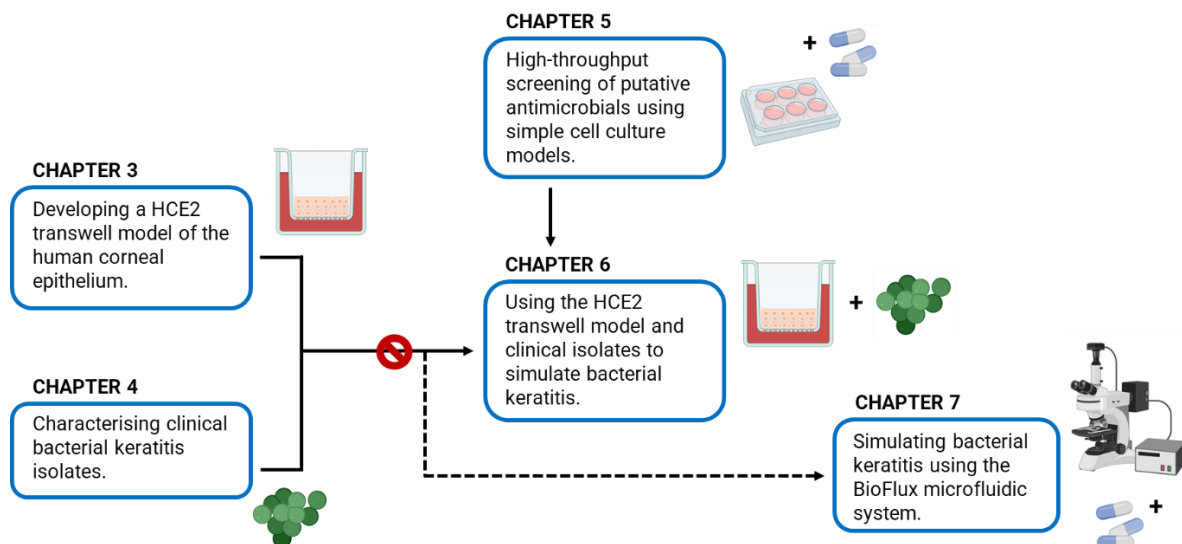
Figure 1-7. Overview of thesis chapters.
The original project plan involved developing a HCE2 transwell model of the corneal epithelium and characterising bacterial keratitis isolates from the LV Prasad Eye Institute (India), in parallel. These two elements of work would then be brought together, to simulate bacterial keratitis by infecting the optimised HCE2 transwell model with clinical isolates of interest. Once the transwell infection model had been established, it would be used to test putative antimicrobial compounds. These compounds, as well as optimum treatment concentrations, were to be identified by preliminary testing involving simple cell culture models. Unfortunately, disruption caused by the COVID-19 pandemic and supply problems involving transwell inserts, highly limited the number of transwell infection studies that could be performed. Therefore, many of the intended experiments (e.g., use of clinical bacterial keratitis isolates and antimicrobial drug testing) could not be performed. To overcome problems with the HCE2 transwell model, an alternative HCE2 infection model involving the BioFlux microfluidic system was developed. This model was used to perform a small number of antimicrobial studies. Created with Microsoft PowerPoint and Biorender.com.

CHAPTER 2: MATERIALS & METHODS

2.1. Materials

2.1.1. Buffers & solutions

1X trypsin was prepared by diluting 10X trypsin (BioWhittaker BE02-007E) in Hank's Balanced Salt Solution (HBSS) containing no Ca^{2+} or Mg^{2+} ions (BioWhittaker 10-547F). HBSS containing Ca^{2+} and Mg^{2+} (BioWhittaker 10-527F) was used in all other instances. 5% Bovine Serum Albumin (BSA) was prepared by dissolving BSA (Sigma A6003) in HBSS and 2% saponin was prepared by dissolving saponin (Sigma 47036) in PBS. 5% BSA and 2% saponin were subsequently filter-sterilised using 0.2 µm syringe filters. BBN solution was prepared by adding 1% BSA and 0.5% sodium azide to HBSS (BioWhittaker 10-527F). Phosphate Buffered Saline (PBS) was prepared by dissolving PBS tablets (Sigma P4417-100TAB) in sterile water.

2.1.2. Antibodies, sera & staining reagents

Table 2-1. Antibodies, sera & staining reagents.

Antibody/serum	Clone	Host species	Category no.	Manufacturer
Anti-human CD9	602.29	Mouse	-	In-house preparation
Mouse IgG1 isotype control	JC1	Mouse	-	In-house preparation
Anti-mouse IgG-FITC	Polyclonal	Goat	F5897	Sigma
FITC anti-human CD9	H19a	Mouse	312104	BioLegend
FITC mouse IgG1, κ isotype control	MOPC-21	Mouse	400108	BioLegend
Anti-human occludin	Polyclonal	Rabbit	71-1500	Invitrogen
Anti-human ZO1	Polyclonal	Rabbit	61-7300	Invitrogen
Rabbit serum control	Serum	Rabbit	R9133	Sigma
Anti-rabbit IgG-FITC	Polyclonal	Goat	F9887	Sigma
Anti-human CD49e (Integrin α5)	P1D6	Mouse	921704	BioLegend
Anti-human CD29 (Integrin β1)	Lia 1/2	Mouse	GTX44230	GeneTex

Staining reagent	Source	Category no.	Manufacturer
Texas Red-X Phalloidin	*Amanita phalloides* toxin	T7471	Invitrogen
CellMask Deep Red Plasma Membrane Stain	-	C10046	ThermoFisher

2.1.3. Antibiotics

Antibiotics from each of the main antibiotic classes were used for Minimum Inhibitory Concentration testing. Beta-lactams: Flucloxacillin Sodium (Sigma 32353), Meropenem Trihydrate (Sigma M2574), Penicillin G (Sigma PEN-NA). Fluoroquinolones: Ciprofloxacin (Sigma 17850). Polymyxins: Colistin sulfate salt (Sigma C4461). Tetracyclines: Doxycycline hyclate (Sigma 33429), Tetracycline (Sigma T-3383). Macrolides: Erythromycin (Sigma E-6376). Aminoglycosides: Gentamicin (Sigma G1272),

Tobramycin (Sigma T4014). Glycopeptides: Vancomycin (Sigma V2002). Chloramphenicol (Sigma C0378).

2.1.4. Peptides

Short-chain (16 amino acid) peptides, 800-cap, 800ii and 800-SCR, were synthesised using solid phase Fmoc chemistry (Genscript, New Jersey, USA). The 800-cap peptide shares its sequence with a 16-aa region of the EC2 domain of human CD9 tetraspanin. The amino acid sequence of 800ii peptide is almost identical to 800-cap but alanine residues (A) have been replaced with an (S)-2-(4-pentenyl) alanine staple (X) to improve peptide stability. 800-SCR is a scrambled control peptide, randomly generated from the 800-cap sequence.

Table 2-2. Peptide sequences.

Peptide	Amino acid sequence
800-cap	DEPQRETLKAIHYALN
800ii	DEPQRETLK**X**IHY**X**LN
800-SCR	QEALKYNRAETPLDIH

2.1.5. Heparin

Unfractionated heparin (Leo, 1000 U/ml) was obtained from the Royal Hallamshire Hospital Pharmacy, UK. Once opened, heparin was used or replaced within 6 months.

2.1.6. Primers

Table 2-3. Primer sequences.

Primer name	Sequence (5'-3')
PAX6 F	AAGCAAGAATACAGGTATGGTTTTC
PAX6 R	TCTGGCTGGGGACTGGG
IL-6 F	CTCCTTCTCCACAAGCGCCTTC
IL-6 R	GCGCAGAATGAGATGAGTTGTC
IL-8 F	GCAGTTTTGCCAAGGAGTGCTA
IL-8 R	GCATCTGGCAACCCTACAACAAG
TNFα F	GAAAGCATGATCCGGGACGTG
TNFα R	GATGGCAGAGAGGAGGTTGAC
CCL20 F	GAATCAGAAGCAGCAAGCAACTTTG
CCL20 R	GAAGCCCACAATAAATTTAGGATGA
GAPDH F	TGCACCACCAACTGCTTAGC
GAPDH R	GGCATGGACTGTGGTCATGAG

2.2. Cell culture techniques

2.2.1. Immortalised cell lines

The HCE2 [50.B1] human corneal epithelial cell line was provided by ATCC (CRL-11135). HCE2 cells have been immortalised using the Adeno-12/SV40 viral sequences (Kahn and Rhim, 1996). The spontaneously immortalised HaCaT human keratinocyte cell line (Boukamp et al., 1988) was provided by Cell Lines Service GmbH (Eppelheim, Germany) and used for comparison with HCE2 cells.

2.2.2. Primary cells

Primary Bone Marrow-Derived-Macrophages (BMDMs) were harvested and differentiated by Dr Emma Smith (SITraN, UoS). BMDM precursors were isolated from wild type C57BL/6 mice at 8-10 weeks of age and differentiated into BMDM according to a protocol modified from Marim et al (Marim et al., 2010). Briefly, mice were euthanized and whole legs dissected from the hip joint. The femur and tibia were dissected by separation at the knee and ankle joints. Muscle and connective tissue were removed. Following removal of the epiphyses, BMDM precursors were flushed from both femur and tibia using a 25 G needle in BMDM flush medium (Dulbecco's Modified Eagle's Medium (DMEM) supplemented with 10 % FBS, 100 IU/ml penicillin and 100 mg/ml streptomycin) and kept on ice. Primary BMDM were differentiated by plating 500,000 BMDM precursors into a 10 cm dish in 10 ml BMDM growth medium (DMEM supplemented with 10 % FBS, 15 % L929 conditioned medium, 100 IU/ml penicillin and 100 mg/ml streptomycin in a 37 °C, 5% CO_2 incubator. L929 conditioned medium was used as a source of M-CSF to stimulate BMDM differentiation. An additional 10 ml BMDM growth medium was added on DIV1 and BMDM were allowed to adhere and proliferate until DIV5. On DIV5, non-adherent cells were removed and the adherent BMDM cultured further until DIV11 with regular feeding. For infection assays, penicillin and streptomycin were removed from the BMDM growth medium from DIV5. On DIV11, BMDM were detached from the dishes in ice cold PBS and re-plated for assays at 500-800,000 cells/ml. BMDM were used in assays at DIV12-14. The differentiation of bone marrow precursors into BMDM was confirmed by F4/80 (ab6640 (abcam), 1:1000) immunostaining.

2.2.3. HCE2 coating media

Coating media is required for prolonged culture of HCE2s on tissue culture surfaces. HCE2 cells were maintained in tissue culture flasks coated with the standard fibronectin coating medium: 0.01 mg/ml fibronectin (Sigma F2006), 0.03 mg/ml bovine collagen type I (PureCol, Advanced Biomatrix 5005),

0.01 mg/ml BSA (Sigma A8022), prepared in Eagle's Minimum Essential Medium (EMEM) (Lonza BE12-611F). When preparing the standard fibronectin coating medium, collagen was always added last to prevent clumping. For HCE2 experiments, a reduced coating medium of 0.1 mg/ml bovine collagen type I was prepared in HBSS. Coating volumes reflected cell seeding area and following addition of coating media, coated tissue culture plastic was incubated overnight at 37°C, 5% CO_2. Fibronectin-coated flasks were stored in the dark, at Room-Temperature (RT) and collagen-coated plates were stored at 4°C. Coating media was aspirated prior to cell seeding and a 1x wash with PBS was carried out for collagen-coated plastics.

2.2.4. Cell culture media

Keratinocyte Serum-Free Medium (KSFM) (Gibco 17005-042) was used for standard cell culture and maintenance of HCE2 cells. KSFM was supplemented with frozen additives, Bovine Pituitary Extract (BPE) and Epidermal Growth Factor (EGF), supplied with KSFM. BPE and EGF were present at a final concentration of 0.05 ng/ml and 5 ng/ml, respectively. Additional supplements, 500 ng/ml hydrocortisone (Sigma H0396) and 0.005 mg/ml insulin (Sigma 91077-C) were also added. Dulbecco's Modified Eagle's Medium: nutrient mixture F-12 ham (DMEM: F12) ((Sigma D6421) was used to induce differentiation of HCE2 cells. DMEM: F12 medium was supplemented with 1% L-Glutamine (BioWhittaker 17-605E) and Foetal Bovine Serum (FBS) (Labtech FCS-EU) was used as a supplement at varying concentrations of 2%, 5% and 10%. HaCaT cells were cultured in Dulbecco's Modified Eagle's Medium (DMEM) (Gibco 41965-039), supplemented with 10% FBS.

2.2.5. Maintenance & passage of cells

Mammalian cell lines were maintained as sub-confluent monolayers in T-75 flasks at 37°C, 5% CO_2. Cells were passaged every 3-4 days using standard cell harvesting procedures. Medium was removed and cells were washed 2x with PBS. To detach the cells, 1X trypsin was added and flasks were incubated at 37°C. A light microscope was used to monitor cell detachment and once cells had completely detached, fresh medium was added to neutralise the trypsin. Flask contents were transferred to a falcon tube and centrifuged at 400 $\times g$ for 5 mins. Supernatant was decanted and cell pellets were re-suspended in 1 ml medium per input flask. A cell count was completed, and cells were seeded into fresh tissue culture flasks or plates at the required seeding density. Cell counts were performed using Cell Counting Slides (Bio-Rad 145-0011) and the Bio-Rad TC20 Automated Cell Counter.

2.2.6. Optimised transwell culture protocol

Corning Transwells (Costar 3460) were used for all experiments aside from PAX6 expression studies. These plates possess 12 mm polyester membrane inserts, with a 0.4 µm pore size. 250 µl collagen coating medium was used per transwell. Following removal of coating medium, 0.5 ml or 1.5 ml KSFM was added to apical and basal chambers respectively. Plates were incubated at 37°C for 30 mins to equilibrate inserts and cells were harvested from confluent T-75 flasks. KSFM was removed from apical chambers and HCE2s were seeded at 250-300,000 cells/per insert, 0.5 ml final volume. Plates were placed on an analogue roller mixer (33 rpm) for 5 mins to improve transwell coverage and then left on laboratory benchtop for 10 mins to allow cells to adhere. Plates were then incubated at 37°C, 5% CO_2 for 72 hrs. After 72 hrs, old media was removed and apical and basal chambers were washed 1x with HBSS. 1.5 ml DMEM: F12 + 10% FBS was added to each of the basal chambers and apical chambers were left free of media, introducing an Air-Liquid Interface (ALI). Following media switch (Day 0); plates were returned to incubator for a further 6 days. Media in basal chambers was replaced on alternate days and flow-through in apical chambers was carefully aspirated daily.

2.2.7. Preparation of frozen stocks of mammalian cells

Mammalian cell lines were stored at -80°C using cryogenic storage vials. Confluent T-75 flasks were harvested to generate frozen stocks and cell pellets were resuspended in the appropriate freezing medium. Freezing medium consisted of 85% cell culture medium, 10% FBS and 5% Dimethyl Sulfoxide (DMSO) (Sigma 41639). 2 ml freezing medium was used per flask and stocks were stored as 1 ml aliquots.

2.3. Bacterial culture techniques

2.3.1. Bacterial strains

2.3.1.1. Laboratory strains

Staphylococcus aureus SH1000 and SH1000-GFP were provided by Professor Simon Foster, School of Biosciences, UoS. SH1000-GFP is derived from RN4220 and contains the pSK5487 plasmid. This plasmid confers resistance to chloramphenicol at 10 µg/ml and expresses GFP protein. PAO1 is a wild-type *Pseudomonas aeruginosa* strain (Holloway, 1955). PAO1 (PAO1 strain 1) and PAO1-GFP were provided by Dr Mark Thomas, Dept. Infection, Immunity & Cardiovascular Disease (IICD), UoS. PAO1-GFP contains the non-mobilizable pIN25 plasmid, which confers resistance to chloramphenicol at 50 µg/ml. A second PAO1 sample (PAO1 strain 2) was obtained by Dr Rahaf Issa during research at

the University of Brighton. PAOMW1 is a double mutant derivative of PAO1 (PAO-MW1: rhlI::Tn501 lasI::tetA) and was obtained by Dr Rahaf Issa during research at the University of Brighton. This strain was originally provided by Peter Greenberg, University of Washington, USA. The PAOMW1 mutant was generated by mutagenesis of *lasI* in the *rhlI* deletion mutant of PAO1. There is no detectable production of the LasI and RhlI signalling auto inducers, 3-oxo-C12-HSL and C4-HSL, by this mutant (Whiteley et al., 1999). *P. aeruginosa* wild type PA14 was provided by Ms Kasia Emery (Dr Esther Karunakaran group), CBE, UoS. This strain was gifted to Dr Esther Karunakaran by Professor Urs Jenal, University of Basel, Switzerland. Reference strains, *S. aureus* ATCC 29213 and *P. aeruginosa* ATCC 27853 were purchased from ATCC.

2.3.1.2. Clinical strains

Six clinical isolates of Methicillin-Resistant *Staphylococcus aureus* (MRSA) were provided by Sue Whittaker, Senior Biomedical Scientist at Northern General Hospital (NGH), Sheffield. MRSA isolates were retrieved from skin infections in patients at the hospital. Several isolates from bacterial keratitis infections were also provided by NGH, Sheffield. These were isolated from corneal scrapings and provided by Dr Simon Tazzyman, Research Coordinator and Mark Tovey, Biomedical Scientist. Numerous clinical isolates were provided by collaborators at LV Prasad Eye Institute (LVPEI), Hyderabad, India. LV Prasad isolates were retrieved from patients with corneal infections and collected aseptically via corneal scrapings.

Table 2-4. Bacterial clinical isolates.

Isolate name	Bacterial species	Type of infection	Source	Total no. of isolates
MRSA1-6	Methicillin Resistant *Staphylococcus aureus*	Skin	NGH, Sheffield, UK	6
NGH Sa	Coagulase negative *Staphylococcus aureus*	Bacterial keratitis	NGH, Sheffield, UK	1
NGH Ko	*Klebsiella oxytoca*	Bacterial keratitis	NGH, Sheffield, UK	1
NGH Pm	*Proteus mirabilis*	Bacterial keratitis	NGH, Sheffield, UK	1
NGH Pa	*Pseudomonas aeruginosa*	Bacterial keratitis	NGH, Sheffield, UK	1
LVP1-6, LVP8, LVP9, LVP25-36, LVP38-45, LVP49, LVP59-61, LVP64-69, LVP71	*Pseudomonas aeruginosa*	Bacterial keratitis	LVPEI, Hyderabad, India	39
LVP10	*Staphylococcus haemolyticus* (Originally believed to be *Staphylococcus aureus*)	Bacterial keratitis	LVPEI, Hyderabad, India	1
LVP11, LVP13	*Staphylococcus aureus*	Bacterial keratitis	LVPEI, Hyderabad, India	2

2.3.2. Standard bacterial growth media and conditions

Lysogeny Broth (LB) (Fisher BioReagents Lennox BP1427-500) was used as the standard growth medium for *P. aeruginosa*, *Klebsiella oxytoca*, *Proteus mirabilis* and all staphylococcal strains. Bacterial cultures were maintained on LB agar plates between experiments and these plates were prepared in-house (Sigma A6686, Lennox BP1427-500). All strains were grown in aerobic conditions at 37°C, in the absence of CO_2.

2.3.3. Biofilm promoting media

Tryptone Soya Broth (TSB) (Oxoid CM0129), supplemented with 0.5% glucose (Sigma G6152) was used as the biofilm promoting medium for staphylococcal strains. For *P. aeruginosa* strains, M63 minimal medium, supplemented with 0.4% arginine (Fisher BioReagents BP370-100) and 1 mM $MgSO_4$ (BDH Laboratory Supplies 101514Y) was used. M63 minimal medium was prepared in distilled water using 110 mM KH_2PO_4 (VWR Chemicals 26936.260), 200 mM K_2HPO_4 (Fisher Chemicals P/5240/53) and 75 mM $(NH_4)_2SO_4$ (Sigma A-2939).

2.3.4. Preparing overnight cultures

To prepare overnight cultures, 2-3 colonies of the desired strain were looped from an agar streak plate and inoculated in 10 ml growth medium. Cultures were incubated overnight, under shaking conditions (110 rpm used as standard).

2.3.5. Preparation of bacterial stocks

Bacterial strains were stored at -80°C in growth medium supplemented with glycerol (Sigma G5516). Glycerol was present at a final concentration of 15%. Frozen mid-log stocks were used in *S. aureus* infection experiments. To prepare infection stocks, overnight cultures were set up and diluted to OD 0.05 (600 nm) the following day. Diluted cultures were incubated at 37°C under shaking conditions until an OD of ~1.4 was reached. Bacterial cultures were then supplemented with glycerol and stored as 1 ml aliquots in Eppendorf tubes. Prior to infection work, frozen stocks were thawed and centrifuged at 16,000 *xg* for 3 mins to pellet the cells. The supernatant was then removed and bacterial pellet resuspended in 1 ml PBS. Stocks were re-centrifuged to wash the cells, the supernatant was removed and pellets were resuspended in 1 ml of the appropriate tissue culture medium. These suspensions were used to prepare the desired inoculum. Colony Forming Units (CFU) were calculated for each bacterial stock by performing 1:10 serial dilutions in PBS and plating dilutions onto agar.

2.3.6. Preparation of fresh mid-log cultures

Fresh mid-log cultures were used in *P. aeruginosa* infection experiments. To prepare infection stocks, overnight cultures were set up and diluted to OD 0.05 (600 nm) the following day. Diluted cultures were incubated at 37°C under shaking conditions until the desired OD was reached. The mid-log culture was mixed by vortexing and a 1 ml aliquot was used to prepare the inoculum as described for frozen mid-log stocks.

2.3.7. Colony Forming Unit calculations

The Miles-Misra method was used to quantify bacterial numbers as Colony Forming Units (CFU) (Miles et al., 1938). Bacterial suspensions were serially diluted 1:10 in PBS (neat to 10^{-7}) and 10 µl aliquots of the chosen dilutions were plated onto agar. Plates were incubated at 37°C for 12-14 hrs (*P. aeruginosa*) or 16-18 hrs (*S. aureus*) and then colony counts were performed at the most appropriate dilution (10-100 colonies). CFU/ml values were calculated using the following equation:

$$CFU/ml = Average\ no.\ of\ colonies\ x\ \frac{1}{Volume\ plated\ (ml)} \times Dilution\ factor$$

CFU/ml values were then converted to CFU/well based on the well volume (e.g., in 96-well plate assays a well volume of 100 µl was used and so CFU/ml values were divided by 10 to provide CFU/well).

2.3.8. Multiplicity of Infection (MOI)

Multiplicity of Infection (MOI) is a ratio that describes the number of bacteria present per host cell during an infection. Prior to infection experiments, cell counts were performed, and bacterial stocks were plated out. These values were used when preparing the bacterial inoculum to ensure the actual MOI was as close to the desired MOI as possible.

2.4. HCE2 assays

2.4.1. FITC-Dextran permeability assay

Transwell inserts were prepared using the standard transwell culture protocol but various media and time point conditions were trialled. On the day of the media switch (Day 0), five different media conditions were introduced: KSFM; DMEM: F12 no FBS; DMEM: F12 + 2% FBS; DMEM: F12 +5% FBS; DMEM: F12 + 10% FBS. Following introduction of ALI, plates were returned to the incubator for 0, 2, 4, 6, 8 or 10 days and then permeability measurements were taken. To measure permeability,

selected transwells were transferred to a new 12-well plate and old media was removed. Both apical and basal chambers were washed 1x with HBSS, 1.5 ml fresh HBSS was added to basal chambers and 0.5 ml 2 mg/ml FITC-Dextran (prepared in HBSS) (Sigma FD4) was added to apical chambers. Plates were incubated at 37°C for 2 hrs in the dark. After 2 hrs, 2x 100 µl aliquots were collected from basal chambers. Varioskan™ LUX multimode microplate reader was used to measure excitation (485 nm) and emission (530 nm).

2.4.1.1. Permeability coefficient calculations

Steady state flux values were calculated using a dilution curve, which provided fluorescence values associated with different FITC-Dextran concentrations (**Figure 2-1**). Transwell inserts had a surface area of 1.12 cm^2 and an initial FITC-Dextran concentration of 500 µM was estimated based on an average molecular weight of 4000 gmol^{-1}. Permeability coefficients were then calculated using the following equation (Hubatsch et al., 2007):

$$Permeability\ coefficient\ (P_{app}) = (\frac{dQ}{dt})(\frac{1}{AC_0})$$

P_{app}= permeability coefficient (cm s^{-1})
dQ/dt= steady state flux (µmol s^{-1})
A= surface area of filter (cm^2)
C_0= initial concentration in apical chamber (µM)
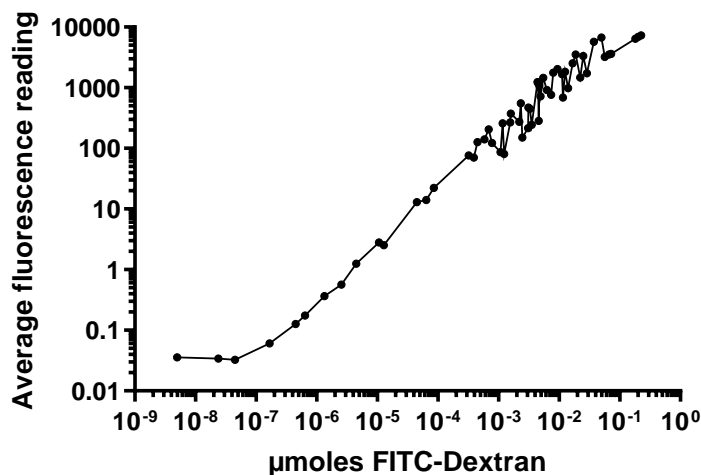
Figure 2-1. Plotting µmoles FITC-Dextran against fluorescence to calculate steady state flux.
Known concentrations of FITC-Dextran were serially diluted in a 96-well plate and fluorescence readings were measured. Concentrations were then converted to µmoles and plotted against fluorescence. A non-linear fit was performed which enabled interpolation of x-values using experimental fluorescence readings.

2.4.2. Standard immunofluorescence staining protocol

Cell culture medium was removed and cells were washed 1x with BBN. 4% paraformaldehyde (PFA) (prepared in-house by IICD technician, Mr Jonathan Kilby) was added and plates were incubated at RT for 20 mins to fix the cells. Wells were washed 3x with PBS and if cells needed to be permeabilised, 0.1% Triton X-100 (TX-100) (prepared in PBS) (Sigma X100) was added. Plates were incubated, on ice, for 10 mins following addition of TX-100 and then washed 2x with PBS. 5% BSA was then added to wells and plates were incubated at RT for 30 mins to block non-specific binding. Wells were washed 2x with PBS and then the primary antibody (prepared in BBN) was added. Plates were incubated for 1 hr at RT under humid conditions, in the dark. After 1 hr, wells were washed 2x with PBS and then a final wash was carried out using the maximum volume of PBS. For final wash, plates were left on shaker (set to 100 rpm) for 15 mins. PBS was removed and the secondary antibody (prepared in BBN) was added. Plates were incubated for 30 mins at RT under humid conditions, in the dark and then wash steps were carried out as described previously. If cells had been permeabilised and Texas red-X phalloidin (prepared in PBS, 1% BSA) was required, this was then added to cells and plates were incubated for 45 mins at RT under humid conditions, in the dark. Wells were washed 3x with PBS and the final wash was left on for 5 mins. A small volume of PBS was added to cover the wells and slide preparation was carried out. Samples were fixed to slides using Vectashield mounting medium containing DAPI (Vector, H-1200) and allowed to air-dry under dark conditions. Nail varnish was used to seal sample edges and dry samples were stored at 4°C in the dark until examination by fluorescence microscopy.

2.4.2.1. Detection of expression of CD9 tetraspanin proteins

Sterile coverslips were transferred to a 24-well plate and coated with the desired coating medium. HCE2s were seeded in KSFM at 100,000 cells/coverslip, 1 ml final volume and plates were incubated overnight at 37°C, 5% CO_2. The standard immunofluorescence staining protocol was then performed using the following antibodies: 250 μl mouse anti-human CD9 (100 μg/ml); 250 μl mouse IgG1 control (100 μg/ml); 250 μl goat anti-mouse IgG-FITC (1:200). Slides were visualised using the Olympus Epifluorescence microscope.

2.4.2.2. Detection of expression of tight junction proteins on transwell inserts

 Transwell cultures were prepared using the standard transwell culture protocol but various media and time point conditions were trialled. On the day of the media switch (Day 0), two different media conditions were introduced: KSFM or DMEM: F12 + 10% FBS. Following introduction of ALI, plates were returned to the incubator for 4, 6 or 8 days and then immunofluorescence staining was

performed using the standard protocol. The following antibodies/staining reagents were used: 250 µl rabbit anti-human occludin (2 µg/ml); 250 µl rabbit anti-human ZO1 (1.5 µg/ml); 250 µl rabbit serum control (2 or 1.5 µg/ml); 250 µl goat anti-rabbit IgG-FITC (1:200 for anti-occludin staining, 1:250 for anti-ZO1); 200 µl Texas Red-X phalloidin (1:50). During slide preparation, transwell inserts were excised using a scalpel and placed cell-side-up on the slides. Coverslips were then fixed to inserts using Vectashield and slides were visualised using the Nikon A1 confocal microscope.

2.4.2.3. Image analysis

Image analysis was carried out using ImageJ (National Institutes of Health, Bethesda, MD, USA). Integrated density, area and mean fluorescence were recorded for each image using the Analyze, Set Measurements tool and total cell fluorescence was calculated using the following equation:

Total fluorescence= Integrated density - (Area × Mean fluorescence of background)

Background fluorescence measurements were obtained by selecting three 'empty' regions within each microscopy image, i.e., regions with no cells or visible fluorescence. Fluorescence measurements were recorded for each region and values were averaged to provide mean fluorescence of background.

2.4.3. Standard flow cytometry protocol for measuring protein expression

Cells were harvested using standard cell culture techniques. Early experiments used trypsin to detach cells, but this was replaced by Cell Dissociation Solution (CDS) (Biological Industries, 03-071-1B) in later work. However, supplementary data shows flow cytometry values are not affected by choice of cell detachment technique (see **Appendix A**). Once cells had been detached and centrifuged, the cell pellet was washed 2x using BBN and centrifugation at 400 *xg* for 5 mins. A cell count was performed, and cells were resuspended in BBN to give the desired volume of sample, at a cell density of 0.5 x 10^6 cells/ml. The cell suspension was then dispensed into round bottomed plastic tubes, as 1 ml aliquots and sample tubes were centrifuged at 400 *xg* for 5 mins. Supernatant was carefully aspirated and 50 µl of primary antibody (prepared in BBN) was added directly to the cell pellets. Samples were mixed by vortexing and then placed on ice to incubate for 1 hr. Cells were then resuspended in 1 ml BBN, centrifuged at 400 *xg* for 5 mins and supernatant was aspirated. BBN wash was repeated once and then 50 µl of secondary antibody (prepared in BBN) was added directly to cell pellets. Samples were mixed by pipetting and then placed on ice to incubate for 45 mins. Samples were washed 2x in BBN as previously described and the final cell pellets were resuspended in 300 µl BBN and stored on ice until sample processing. For longer term storage of samples (up to

48 hrs), pellets were resuspended in 300 µl 2% PFA (prepared in PBS using 4% PFA stock) and stored at 4°C. Samples were run on the BD™ LLSRII flow cytometer.

2.4.3.1. Measuring expression of CD9 in uninfected cells

In experiments investigating effects of coating media and cell media conditions, cells were cultured in T-75 flasks prior to cell harvesting. Cells were seeded in KSFM at a cell seeding density of 1,500,000 cells/flask and then incubated at 37°C, 5% CO_2 for 3 (coating media experiments) or 7 days (culture media experiments). For 7-day incubations, a media switch was completed on day 3. KSFM was removed, flasks were washed 1x with HBSS and five different media conditions were introduced: KSFM; DMEM: F12 no FBS; DMEM: F12 + 2% FBS; DMEM: F12 +5% FBS; DMEM: F12 + 10% FBS. Media was then replaced on alternate days until cell harvesting. The standard flow cytometry protocol was followed for each experiment, but different antibodies were used. For coating media studies, separate primary and secondary antibodies were used: mouse anti-human CD9 (20 µg/ml), mouse IgG1 isotype control (20 µg/ml) and goat anti-mouse IgG-FITC (1:64). For cell media studies, FITC-conjugated primary antibodies were used: FITC anti-human CD9 (20 µg/ml) and FITC mouse IgG1, kappa isotype control (20 µg/ml). The use of conjugated antibodies necessitated only one antibody incubation step. Samples were incubated for 30 minutes on ice before BBN washing and resuspension in BBN/2% PFA as described previously.

2.4.3.2. Measuring expression of CD9 following infection

A 6-well plate format was used for these experiments and HCE2s were seeded onto collagen-coated plastic at 700,000 cells/well, 3 ml final volume. Plates were incubated at 37°C, 5% CO_2 overnight, to achieve 80-85% confluency by the following day. Cells were washed 1x with HBSS and 5% BSA was added to each well. Plates were incubated for 1 hr at 37°C and the chosen bacteria was prepared. For studies with *S. aureus* LVP11, frozen mid-log stocks were used at MOI 50. For studies with *P. aeruginosa* LVP3, fresh mid-log cultures (OD 0.25-0.35) were used at MOI 10. Bacterial inoculates were prepared using basal KSFM (containing no additional supplements) and 1 ml of the inoculum/uninfected medium control was added to each well. Plates were incubated at 37°C for 2 hrs and then the inoculum was removed. Wells were washed 4x with PBS. Infected cells were harvested using cell dissociation solution and the standard flow cytometry protocol was followed. FITC-conjugated antibodies, FITC anti-human CD9 (20 µg/ml) and FITC mouse IgG1, kappa isotype control (20 µg/ml) were used, as described previously.

2.4.3.3. Flow cytometric analysis

Analysis was completed using the batch analysis tool in BD FACSDiva software. Two separate gates were applied to select populations of interest (**Figure 2-2**). The same gates were applied to all samples within an experiment, unless different cell lines were used.
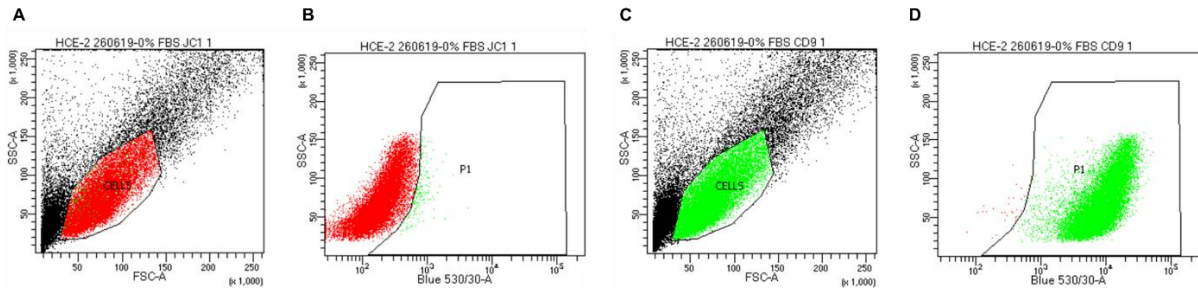
Figure 2-2. Gating method for protein expression experiments.
An FSC vs SSC plot was used to gate the main cell population and exclude cell debris (A and C). Isotype samples were used to gate for no/non-specific binding of the secondary antibody (B) and a gate (P1) was drawn upstream of this population. Events recorded within the gate represent specific binding of the secondary antibody and therefore cells that express the protein of interest (D).

2.4.4. RNA extraction and Real Time quantitative Polymerase Chain Reaction (RT-qPCR)

2.4.4.1. Preparation of cells for PAX6 expression studies

Cells were cultured using collagen-coated, Corning 6-well transwell plates (Costar 3450). The optimised transwell culture protocol was followed, and volumes were adjusted accordingly. HCE2s were seeded in KSFM at 1,000,000 cells/well, 1.5 ml final volume and 2.5 ml medium was used for basal chambers. On the day of the media switch (Day 0), two different media conditions were introduced: KSFM or DMEM: F12 + 10% FBS. Plates were incubated at ALI for 6 days before cell harvesting with trypsin. Cells were also harvested from confluent, T-75 flasks (submerged, KSFM culture) as a control. All cell pellets were resuspended in 1 ml PBS and transferred to RNase free Eppendorfs. Samples were centrifuged at 200-400 *xg* for 5 mins and supernatant was removed. Pellets were stored at -80°C prior to RNA extraction.

2.4.4.2. Preparation of cells for cytokine expression studies

Cells were cultured using collagen-coated, 6-well plates. HCE2s were seeded in KSFM at 1,000,000 cells/well, 2.5 ml final volume and then incubated at 37°C, 5% CO_2 overnight. The standard infection protocol for measuring bacterial adhesion was followed and cells were infected at MOI 5. However, infection length was increased to 3.5 hrs and treatment conditions (100 nM 800-cap, 100 nM 800-

SCR or 10 U/ml UFH) were included in the bacterial inoculum. After 3.5 hrs, wells were washed 3x with PBS and 20 µg/ml lysostaphin (Sigma L7386) was prepared using basal KSFM. Lysostaphin was added to wells and plates were incubated at 37°C for 30 mins to kill extracellular bacteria. Lysostaphin was removed, wells were washed 3x with PBS and RNA extraction was performed.

2.4.4.3. RNA extraction

Total RNA was extracted using the RNeasy Mini Kit (Qiagen, 74104) and instructions for purification of total RNA from animal cells were followed. In PAX6 expression studies, cells were harvested prior to RNA extraction and RLT Plus was added to cell pellets. In cytokine studies, RLT Plus was added directly to cell monolayers. A few minor changes were made to the Qiagen protocol. Cells were homogenised by passing the RLT Plus lysate through a 20-gauge needle 15 times and prior to RNA elution, RNase-free water was left to soak into the column membrane for 2-3 minutes. The eluted RNA was then quantified using NanoPhotometer N60 Touch (Implen). A_{260}/A_{280} and A_{260}/A_{230} values were recorded to assess quality of RNA samples.

2.4.4.4. cDNA conversion

RNA samples were diluted to the desired concentration using RNase free water and then converted to cDNA using the High-Capacity cDNA Reverse Transcription Kit (Applied Biosystems, 4368813). In PAX6 studies, RNA was used at 50 ng/µl. In cytokine studies, RNA was used at 5 ng/µl. For each biological replicate, control samples containing no reverse transcriptase (Rt) or no RNA template were included. The total volume of cDNA synthesis reactions ranged from 10-20 µl depending on volume of cDNA required, but reagent ratios remained constant.

Table 2-5. cDNA synthesis components.

Materials	Test sample Volume (µl)	No Rt control Volume (µl)	No RNA control Volume (µl)
10X RT Buffer	2.0	1.5	1.5
10X RT random primer	2.0	1.5	1.5
25X dNTP mix	0.8	0.6	0.6
Reverse transcriptase	1.0	0	0.75
Nuclease-free H_2O	4.2	3.9	10.65
RNA sample	10	7.5	0
Total	20	15	15

Table 2-6. Thermocycler steps for cDNA synthesis.

Thermocycler steps	Step 1	Step 2	Step 3	Step 4
Temperature	25°C	40°C	86°C	4°C
Time	10 minutes	120 minutes	5 minutes	Hold

2.4.4.5. Quantitative Polymerase Chain Reaction (qPCR)

RT-qPCR was performed by SYBR Green assay (ROX passive reference) using the PrecisionPLUS OneStep RT-qPCR Master Mix (Primerdesign) but final composition of the qPCR mastermix varied between PAX6 and cytokine expression experiments (**Table 2-7**). In cytokine studies, 5.6 μl of the mastermix was added to the wells first and then 5 μl diluted cDNA was added to the opposite side of each well. Stages of the qPCR reaction remained the same throughout experiments (**Table 2-8**), but different qPCR machines were used. The Abi Prism 7900 HT PCR system was used for PAX6 expression studies, and the QuantStudio 5 Real-Time PCR system was used for cytokine expression studies. In both studies, expression of the housekeeping gene, Glyceraldehyde 3-Phosphate Dehydrogenase (*GAPDH*), was measured as an internal control.

Table 2-7. qPCR master mix components.

(A) PAX6 expression studies

Materials	Volume (μl)
PrecisionPLUS OneStep RT-qPCR Master Mix	5
Forward primer (100 μM)	0.5
Reverse primer (100 μM)	0.5
Nuclease free H$_2$0	3
cDNA (25 ng/μl)	1
Total volume	10

(B) Cytokine expression studies.

Master mix		cDNA samples	
Materials	Volume (μl)	Materials	Volume (μl)
PrecisionPLUS OneStep RT-qPCR Master Mix	5	Nuclease free H$_2$0	4
Forward primer (10 μM)	0.3	cDNA (2.5 ng/μl)	1
Reverse primer (10 μM)	0.3		
Total volume	5.6	Total volume	5

Table 2-8. Stages of the qPCR reaction.

Reaction stage	Enzyme activation		Denaturation		Melt curve		
Step	1	2	1	2	1	2	3
Temperature	50°C	95°C	95°C	60°C	95°C	60°C	95°C
Time	2 min	10 min	15 sec	1 min	15 sec	15 sec	1 sec
No. of cycles	X1		X40		X1		

2.4.4.6. RT-qPCR analysis

The following equations were used for RT-qPCR analysis:

ΔCt Value (Control) (ΔCTC) = Average control Ct Value (test gene) - Average control Ct value (housekeeping gene)
ΔCt value experimental (ΔCTE) = Average experimental Ct value (test gene) - Average experimental Ct value (housekeeping gene)
Delta Delta Ct value (ΔΔCt) = ΔCTE – ΔCTC
Relative fold change in gene expression (ΔΔCq) = $2^{-\Delta\Delta Ct}$

In PAX6 studies, CT values for HCE2s cultured in flasks (i.e., undifferentiated cells), were considered the control. In cytokine studies, CT values for infected HCE2s that were not treated with peptide/UFH were considered the control condition.

2.4.5. Sulforhodamine B (SRB) staining

SRB staining was carried out using a protocol modified from Skehan et al (Skehan et al., 1990). Cell monolayers were fixed by layering 40% trichloroacetic acid (TCA) on top of tissue culture medium to give a final concentration of 10%. Plates were incubated at RT for 5 minutes and then at 4°C for a further 1 hr. Medium was removed, and plates were washed 5x with 200 µl water. To stain for cellular protein, 100 µl 0.4% sulforhodamine B sodium salt solution (Sigma, S901) (prepared in 1% acetic acid) was added to each of the wells and plates were incubated at RT for 30 mins. After 30 mins, SRB was removed and 4x quick wash steps were carried out using 100 µl of 1% acetic acid. Plates were allowed to air dry completely and then any bound SRB dye was solubilised by adding 50 µl 10 mM unbuffered Tris-base (pH 10.5) to each well. Plates were incubated at RT for 5 mins, agitating gently and then OD was measured at 570 nm using the Varioskan™ LUX multimode microplate reader.

2.5. Characterisation of bacterial isolates

2.5.1. Bacterial growth curves

Overnight cultures were prepared and diluted to an OD of ~0.05 (600 nm) the following day. Precise OD values were recorded at 0 hrs and repeat OD measurements were taken each hour for 8 hours. A final OD measurement was taken at 24 hrs. For each bacterial strain, the standard growth medium and conditions were used.

2.5.2. Crystal violet biofilm formation assays

Overnight cultures were prepared and diluted to an OD of 0.02 (600 nm) using the appropriate biofilm promoting medium or basal DMEM: F12 (containing no L-glutamine or FBS). 100 µl aliquots of diluted cultures (plus medium-only controls) were transferred to a 96-well plate and incubated at 37°C for 22 hrs. After 22 hrs, medium was carefully aspirated, and wells were washed 1x with 150 µl PBS. Plates were left to air-dry and then 150 µl, 95% methanol was added to each well to fix bacteria. Methanol was immediately removed, and plates left to air-dry. Crystal Violet (CV) solution was prepared at 0.01-0.1% using sterile water and 150 µl was added to each well. Plates were incubated at RT for 15 mins, then CV was removed, and wells were washed 3x with 200 µl water. Once plates were completely dry, CV was solubilised by adding 200 µl DMSO to each well and plates were incubated with DMSO at RT for 15 mins. Samples were diluted 2-fold with DMSO, and absorbance readings were recorded at 595 nm using the Varioskan™ LUX multimode microplate reader.

2.5.3. Determining Minimum Inhibitory Concentrations

Minimum Inhibitory Concentrations (MICs) were determined by broth microdilution, using guidelines provided by European Committee on Antimicrobial Susceptibility Testing (EUCAST). Bacterial suspensions were prepared from overnight cultures and a fixed starting OD of 0.02 (600 nm) was used in each experiment. LB was used to prepare bacteria and antibiotic dilutions. Microdilution plates were incubated at 37°C for 22 hrs and absorbance readings were collected at 600 nm using the Varioskan™ LUX multimode microplate reader. Negative (LB only) control values were subtracted from sample wells and the MIC was selected as the lowest concentration at which absorbance readings were ≤ 0.01.

2.5.4. DNA extraction

DNA extraction was performed using mid-log cultures of the following isolates: LVP3-6, LVP10, LVP11, LVP13 and MRSA1-6. The Qiagen DNeasy Blood and Tissue kit (69504) was used and the manufacturer's protocols for Gram-Positive and Gram-Negative bacteria were followed. Changes to the protocol were required for high-yield extraction of DNA from Gram-Positive isolates. Bacteria were harvested directly from agar plates instead of broth cultures, incubation with Proteinase K and buffer AL was increased to 45 minutes and composition of lysis buffer was altered. Optimised lysis buffer contained 20 mM Tris-Cl (pH 8), 2 mM disodium EDTA (pH 8), 1.2% TX-100 and 100 µg/ml lysostaphin. Samples were incubated at 37°C for 2 hrs. Eluted DNA was quantified using the NanoPhotometer N60 Touch (Implen). A_{260}/A_{280} and A_{260}/A_{230} values were recorded to assess quality

of DNA samples. All samples were diluted to 30 ng/µl using buffer EB (Qiagen, 19086) and stored at -20°C.

2.5.5. Whole Genome Sequencing

Bacterial DNA extracted at the University of Sheffield was sent to Microbes NG and Illumina sequencing was performed. Additional isolates were sequenced by Dr Naveen Kumar using the MinION sequencer (Oxford Nanopore Technologies) at CMC, Vellore, India.

2.5.5.1. MinION Library preparation

Library preparation was performed using SQK-LSK108 Kit R9 version (Oxford Nanopore Technologies, Oxford, UK). The 1D sequencing protocol provided by the manufacturer was followed. Sequencing was performed using FLO-MIN106 R9 flow cell in MinION Mk 1B sequencer. The initial amount of DNA used for sequencing was greater than 100 ng. DNA was purified using 1x AMPure beads (Agencourt, Beckman Coulter, Brea CA, USA) and then dA-tailing was performed with NEBNext dA-Tailing Module (New England Biolabs). Ligation to leader and hairpin sequencing adapters (Oxford Nanopore Technologies) was carried out using Blunt TA Ligase master mix (New England Biolabs) and then clean-up was performed with 1x AMPure beads. Barcode adapter mix, BAM 1D (Oxford Nanopore Technologies) was used for adapter ligation, followed by clean-up with 0.4x AMPure beads. Recovery of the DNA library was achieved using 15 µl of Elution Buffer (Oxford Nanopore Technologies) and the prepared DNA was loaded onto the flow cells as per manufacturer's instructions.

2.5.5.2. MinION sequencing

The sequencing run parameters are configured using Oxford Nanopore's MINKNOW software. While the sequencer runs, base calling takes place in real-time using Oxford Nanopore's Metrichor cloud service. The sequence data can be analysed using either 1D or 2D workflows. This workflow generally uses a hairpin like adaptor, which links the top and bottom strands of double-stranded DNA into one strand. The base caller recognizes the hairpin sequence and aligns both strands of the template molecule for improving sequencing accuracy.

2.5.5.3. MinION assembly

The Fast5 files were generated from MinION sequencing and the reads were base called with Albacore 2.0.1 (https://nanoporetech.com/about-us/news/new-basecaller-now-performs-raw-

basecalling-improved-sequencing-accuracy). After base calling, low quality reads were removed using Nanofilt (https://github.com/wdecoster/nanofilt). Error correction was done using Canu 1.7. The quality of the MinION reads was assessed using MinIONQC (https://github.com/roblanf/minion_qc). The filtered fastq files were assembled with Canu 1.7 with corresponding size of each isolate. The assembled genomes were aligned using minimap2 and polished with Nanopolish version 0.8.1 (https://github.com/jts/nanopolish). nanopolish_makerange.py was used to split the assembled sequence into 50 kb segments and all segments were polished in parallel using Nanopolish (https://github.com/jts/nanopolish). Finally, the polished genome fragments were merged to generate complete genome assembly. Contigs were manually circularized by confirming the overlap regions at the ends of each contigs.

2.5.6. Analysis of sequencing data

Antibiotic Resistance (AR) genes were identified using the Comprehensive Antibiotic Resistance Database Resistance Gene Identifier (CARD: RGI) (McArthur et al., 2013). This database was last accessed on 11/02/2022. Details of perfect/strict CARD-RGI hits can be accessed via the University of Sheffield data repository, ORDA (https://orda.shef.ac.uk/): 10.15131/shef.data.19169657. Only 28 of the 39 clinical *P. aeruginosa* isolates from LVPEI were included in AR gene analysis. Isolates LVP1, 2, 8, 32, 33, 40, 41, 43, 44, 59 and 60, were excluded. Excluded isolates were sequenced later during the project and the Quality Assessment Tool (QUAST) for genome assemblies (Gurevich et al., 2013) revealed genome assemblies for these isolates were of lower quality than earlier isolates (**Table 2-9**). Genes encoding common virulence factors were identified using the Virulence Factor Database (VFDB) (Chen et al., 2005) and/or the Basic Local Alignment Search Tool (BLAST) (Altschul et al., 1990). To perform BLAST, genome sequence data was uploaded to the public databases for molecular typing and microbial genome diversity (PubMLST) and reference sequences were obtained from the National Center for Biotechnology Information (NCBI) Gene (**Table 2-10**). All 39 clinical *P. aeruginosa* isolates from LVPEI were included in VF analysis.

Table 2-9. QUAST metrics for *P. aeruginosa* clinical isolates.

Isolates excluded from AR gene analysis are shown in red. Descriptions of QUAST metrics were obtained from the QUAST 5.05 manual: http://quast.sourceforge.net/docs/manual.html.

Isolate	No. contigs	Largest contig (bp)	Total length (bp)[1]	N50[2]	L50[3]	Mismatches
LVP1	42	1,034,167	6,356,930	304,468	7	100
LVP2	132	550,393	6,078,677	98,091	18	0
LVP3	1	6,404,360	6,404,360	6,404,360	1	0
LVP4	1	6,303,169	6,303,169	6,303,169	1	0
LVP5	1	6,301,690	6,301,690	6,301,690	1	0
LVP6	1	6,419,639	6,419,639	6,419,639	1	0
LVP8	97	457,538	6,355,516	101,959	19	0
LVP9	1	6,337,693	6,337,693	6,337,693	1	0
LVP25	9	7,010,888	7,067,473	7,010,888	1	0
LVP26	1	6,590,950	6,590,950	6,590,950	1	0
LVP27	4	7,640,525	7,836,348	7,640,525	1	0
LVP28	5	6,667,016	7,164,579	6,667,016	1	0
LVP29	8	2,571,039	7,579,426	1,469,672	2	0
LVP30	2	6,364,648	6,411,986	6,364,648	1	0
LVP31	5	4,468,060	6,444,858	4,468,060	1	0
LVP32	119	213,583	5,609,322	75,963	25	100
LVP33	56	705,116	6,460,122	196,075	11	200
LVP34	1	6,507,168	6,507,168	6,507,168	1	0
LVP35	1	6,356,408	6,356,408	6,356,408	1	0
LVP36	6	6,322,282	6,517,590	6,322,282	1	0
LVP38	1	6,345,898	6 345,898	6,345,898	1	0
LVP39	2	6,487,315	6,500,016	6,487,315	1	0
LVP40	83	498,750	6,389,596	169,985	13	100
LVP41	30	897,178	7,069,250	569,715	5	0
LVP42	2	6,680,738	6,690,011	6,680,738	1	0
LVP43	78	551,601	6,734,391	134,287	14	0
LVP44	20	1,346,789	6,348,191	925,188	3	0
LVP45	2	6,358,277	6,450,423	6,358,277	1	0
LVP49	1	6,443,191	6,443,191	6,443,191	1	0
LVP59	81	433,841	6,397,127	149,267	13	100
LVP60	11	1,546,143	6,605,338	862,310	3	0
LVP61	1	6,421,782	6,421,782	6,421,782	1	0
LVP64	3	6,389,352	6,432,918	6,389,352	1	0
LVP65	1	6,409,686	6,409,686	6,409,686	1	0
LVP66	1	6,734,962	6,734,962	6,734,962	1	0
LVP67	2	6,427,942	6,500,972	6,427,942	1	0
LVP68	9	6,537,169	7,174,217	6,537,169	1	0
LVP69	30	6,574,730	7,837,103	6,574,730	1	0
LVP71	78	6,707,540	9,865,711	6,707,540	1	0

[1] Total length= The total number of bases in the assembly.

[2] N50= The length for which the collection of all contigs of that length or longer covers at least half an assembly.

[3] L50= The number of contigs equal to or longer than N50 (i.e., the minimal number of contigs that cover half the assembly).

Table 2-10. Reference sequences for *P. aeruginosa* virulence factor genes.

Gene name	NCBI reference sequence	Gene ID/GenBank code
exoS	NC_002516.2	Gene ID: 879837
exoT	NC_002516.2	Gene ID: 878350
exoY	NC_002516.2	Gene ID: 879421
exoU	NC_017549.1	Gene ID: 12571634
lasA	NC_002516.2	Gene ID: 878260
lasB	NC_002516.2	Gene ID: 880368
aprA	N/A	GenBank: JX853450.1
prpL	N/A	GenBank: DQ351524.1
pasP	NC_002516.2	Gene ID: 877902
fliC a-type	NC_017549.1	Gene ID: 12571749
fliC b-type	NC_002516.2	Gene ID: 882052

2.6. Standard tissue culture plate infection protocols

2.6.1. Optimised infection protocol for measuring bacterial adhesion

Cell monolayers at ~95% confluency were used for bacterial adhesion assays. Wells containing no cells were also included to measure non-specific binding to tissue culture plastic. On the date of infection, tissue culture medium was removed, and wells were washed 1x with HBSS. 5% BSA was then added to each of the wells and plates were incubated at 37°C for 1 hr. Following removal of BSA, wells were washed 1x with PBS and anti-adhesion pre-treatments were carried out. CD9:EC2 peptides were used at a range of concentrations (20-200 nM), UFH was used at 10 U/ml. Treatments were prepared in basal tissue culture medium, and untreated control wells were included. Plates were incubated in the treatment medium at 37°C for 1 hr and then medium was removed. During this incubation, bacteria was prepared from frozen mid-log stocks. The inoculum was prepared at the chosen MOI using basal tissue culture medium and plates were incubated at 37°C for 1 hr. Inoculum was removed and wells were washed 4x with PBS. For 96-well plate assays, a shaker was used to perform wash steps at 130 rpm for 1 minute. An increased volume of PBS was used for the final wash. 2% saponin was added to wells and plates were incubated at 37°C for 20 minutes. An equal volume of PBS was added and wells were vigorously scraped using pipette tips. Once cell lysis had been achieved, lysates were pipetted up and down and transferred to a fresh 96-well plate so that bacteria could be quantified in CFU/well.

2.6.2. Phagocytosis by flow

6-well plates were used for phagocytosis assays. HCE2s were seeded on collagen-coated plastic at 1,000,000 cells/well, 2.5 ml final volume. HaCaTs and mouse BMDMs were seeded on uncoated plastic at 700,000 cells/well and 500-800,000 cells/well respectively. Following seeding, plates were

incubated overnight at 37°C, 5% CO_2. The following day, medium was removed, and wells were washed 1x with HBSS. SH1000-GFP was prepared from frozen mid-log stocks and 1 ml of the desired inoculum was added to each well. Uninfected controls were also included. Following infection, plates were centrifuged at 150 *xg* for 5 minutes and then incubated at 37°C for 2 hrs. Inoculum was removed and wells were washed 2x with PBS. 2 ml of 20 µg/ml lysostaphin (prepared in basal tissue culture medium) was added to each well and plates were incubated at 37°C for 30 mins to kill extracellular bacteria.

2.6.2.1. Measuring bacterial uptake

To measure bacterial uptake, lysostaphin was removed and wells were washed 2x with PBS. Cells were harvested and centrifuged at 400 *xg* for 5 mins to pellet the cells. Supernatant was removed and cells were resuspended in 500 µl PBS. Cell suspensions were transferred to Eppendorfs and centrifuged at 400 *xg* for 5 mins to wash the cells. PBS was removed and cells were resuspended in 250 µl 4% PFA. Samples were incubated at 4°C for 1 hr and then centrifuged at 400 *xg* for 5 mins to remove PFA. An additional wash step was carried out using 500 µl PBS and pellets were resuspended in 250 µl BBN. Samples were stored on ice until sample processing. Immediately before processing, 250 µl 0.2% trypan blue (prepared in PBS) (Sigma T8154) was added to quench extracellular fluorescence. Samples were run on the BD™ LLSRII flow cytometer.

2.6.2.2. Measuring bacterial clearance

To measure bacterial clearance, 20 µg/ml lysostaphin solution was removed and replaced with 2.5 ml of 2 µg/ml lysostaphin, prepared in basal tissue culture medium. Plates were returned to the incubator at 37°C, for 4 hrs. After this additional incubation, lysostaphin-containing medium was removed and the protocol for measuring bacterial uptake was followed.

2.6.6.3. Flow cytometric analysis

Analysis was completed using the BD FlowJo software. Three separate gates were applied to select populations of interest (**Figure 2-3**). The same gates were applied to all samples within an experiment, unless different cell lines were used.
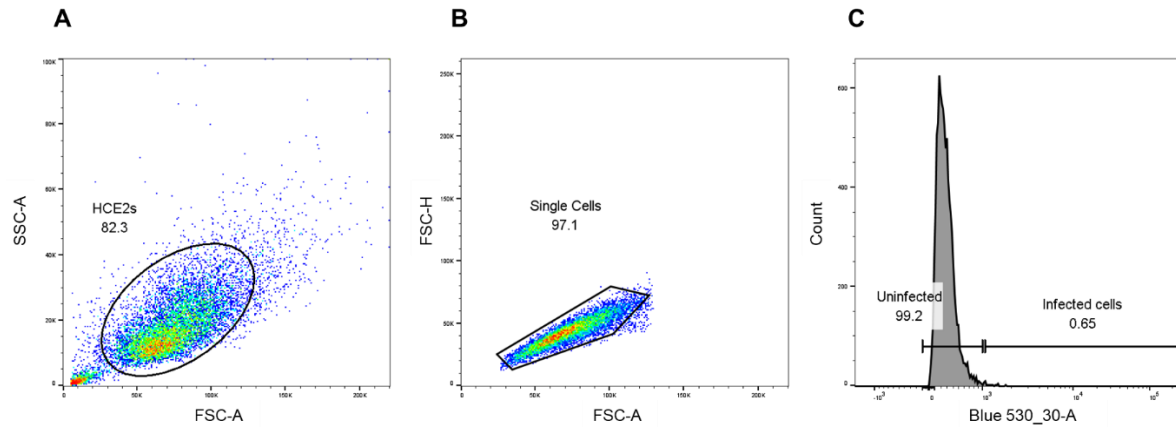
Figure 2-3. Gating method for phagocytosis experiments.
An FSC vs SSC plot was used to gate the main cell population and exclude cell debris (A). An FSC-A vs FSC-H was then used to gate for single cells only (B). Finally, the uninfected cell population was used to gate fluorescence readings (C). Events recorded outside of the 'Uninfected' gate represent cells containing SH1000-GFP.

2.7. Infection studies using the HCE2 transwell model

2.7.1. Transwell infection protocol

Transwell cultures were prepared using the optimised transwell culture protocol and infection studies were carried out on day 6 at ALI. Media was removed from both apical and basal chambers and wash steps were performed. Apical chambers were washed 2x and basal chambers washed 1x with HBSS. 5% BSA was then added to block non-specific binding; volumes of 1 ml and 1.5 ml were used for apical and basal chambers respectively. Plates were then incubated at 37°C for 1 hr and bacteria were prepared. Frozen mid-log stocks were used as described previously. Following removal of BSA, apical and basal chambers were washed 2x with PBS. 1.5 ml basal DMEM: F12 (containing no L- glutamine or FBS) was added to basal chambers and 250 µl of the chosen bacterial inoculum, basal DMEM: F12 or 1% TX-100 was added to the allotted wells. Plates were then incubated at 37°C for 1 hr. Supernatants were then transferred from apical and basal chambers into individual, sterile Eppendorfs and stored on ice for use in CFU/well calculations and LDH assays. Apical chambers were washed 2x with HBSS and DMEM: F12 medium was replaced. 0.5 ml fresh medium was added to apical chambers and 1.5 ml medium was added to basal chambers. Plates were then returned to the incubator at 37°C, 5% CO_2 for 4-8 hrs. After 4 hrs, supernatants were collected and stored on ice as described previously. For 8 hr plates, DMEM: F12 medium was replaced, and plates were returned to incubator for 4 hrs. For 4 hr plates, transwells were prepared for microscopy or used for quantification of adherent bacteria. Note: the 4 and 8 hr plates represent 5 and 9 hrs post-infection, respectively.

2.7.2. Quantifying bacteria in transwell supernatants

Eppendorfs containing transwell supernatants were removed from ice and inverted to mix. 100 µl of each supernatant was transferred to a 96-well plate and 1:10 serial dilutions were performed. Dilutions were plated and used to calculate CFU/well as described previously.

2.7.3. Lactate Dehydrogenase (LDH) assays

Eppendorfs containing transwell supernatants were centrifuged at 200 *xg* for 5 minutes. 200 µl or 100 µl aliquots (depending on the volume of sample) were removed from the top of the Eppendorf and transferred to new tubes. Samples were stored at -80°C. LDH assays were performed using the Promega CytoTox 96 Non-Radioactive cytotoxicity assay (G1780) and the manufacturer's cytotoxicity assay protocol was followed. Transwells treated with TX-100 (detergent) were used to provide a value for maximum LDH release and absorbance readings were recorded at 490 nm.

2.7.3.1. Cytotoxicity calculations

$$\% \, cytotoxicity = \frac{(Experimental \; LDH \; release - media \; background)}{(Maximum \; LDH \; release - media \; background)} \times 100$$

Absorbance readings for corresponding apical and basal chambers were combined to provide a single value for each transwell. Absorbance readings for transwells containing no cells were used to measure bacterial LDH and these values were subtracted from values for cells before calculating % cytotoxicity. In % cytotoxicity calculations, TX-100-treated cells represent maximum LDH release and wells containing only media represent media background.

2.7.4. Quantification of adherent bacteria

Following removal of transwell supernatants at 4 or 8 hrs, apical chambers were washed 2x with HBSS. 250 µl 2% saponin was then added to apical chambers and plates were incubated at 37°C for 30 minutes to lyse mammalian cells. Transwell membranes were then scraped with P200 pipette tips and cell lysates were pipetted up and down to ensure complete destruction of cell multilayers. Lysates were then transferred to a 96-well plate and 1:10 serial dilutions were performed. Dilutions were plated and used to calculate CFU/well as described previously.

2.7.5. Preparation for confocal microscopy

Following removal of transwell supernatants at 4 or 8 hrs, apical chambers were washed 2x with HBSS. 250 μl CellMask Deep Red Plasma membrane stain (1:1000, prepared in PBS) was added to apical chambers and plates were wrapped in foil before incubation at 37°C for 30 minutes. Inserts were washed 3x with PBS and 250 μl 2% PFA (prepared in PBS using 4% PFA stock) was added to each well. Plates were incubated at RT for 30 mins to fix the cells and then wells were washed 3x with PBS. 250 μl PBS was added to each well and plates were stored at 4°C until slide preparation. Slides were visualised using the Zeiss LSM880 AiryScan Confocal microscope.

2.7.6. Electron Microscopy

Following removal of transwell supernatants at 4 or 8 hrs, apical chambers were washed 2x with HBSS. 250 μl fixative (2.5% Glutaldehyde/0.1M Sodium Cacodylate buffer) was added to apical chambers and plates were incubated at 4°C overnight. The following day, plates were given to Chris Hill (Cryo-Electron Microscopy Facility, UoS) who carried out further sample processing and microscopy. Samples were post-fixed in 2% aqueous Osmium Tetroxide, dehydrated through a graded series of ethanol, cleared in epoxypropane (EPP) and then infiltrated in 50/50 mix, of Araldite resin: EPP mixture overnight on a rotor. This mixture was replaced twice over 8 hours with fresh Araldite resin mixture before being embedded and cured in a 60 °C oven for 48-72 hours. Ultrathin sections (approx. 85 nm) were cut using a Leica UC6 ultramicrotome onto 200 mesh copper grids, stained with saturated aqueous Uranyl Acetate followed by Reynold's Lead Citrate and examined using an FEI Tecnai Transmission Electron Microscope at an accelerating voltage of 80 Kv. Electron micrographs were recorded using Gatan Orius 1000B digital camera and Gatan Digital Micrograph software.

2.7.7. Adapted transwell infection protocol for measuring bacterial traversal

A simplified version of the transwell infection protocol was used to measure bacterial traversal. Bacterial inoculum in apical chambers was removed following 1 hr infection and wells were washed 2x with HBSS. However, media in basal chambers was not replaced at 1 hr and neither the media in apical nor basal chambers was replaced at later time points. Instead, 50 μl aliquots were removed from the apical chambers and 100 μl aliquots were removed from the basal chambers at 1, 4 and 8 hrs post-infection. Aliquots were transferred to a 96-well plate and used to calculate CFU/well as described previously.

2.7.7.1. Treatment conditions

4% PFA was used to fix HCE2 multilayers before the infection protocol. 250 µl was added to apical chambers and pates were incubated at 37°C for 30 minutes. Apical chambers were then washed 3x with PBS and basal chambers washed 1x. Cytochalasin D was prepared at 0.5 µg/ml in DMEM: F12. Following the BSA block step, 500 µl was added to apical chambers and plates were incubated at 37°C for 1 hr. Cytochalasin D was also included in the bacterial inoculum and replacement apical medium. In coating experiments, the standard collagen coating medium (0.1 mg/ml) was used as a control. Fibronectin was prepared in EMEM at 10 µg/ml. ECM gel from Engelbreth-Holm-Swarm murine sarcoma (Sigma E6909) was prepared in DMEM at 1:20. Following addition of 250 µl coating media, plates were incubated overnight at 37°C, 5% CO_2. Excess coating media was removed before addition of cell culture media. Since, no cells were included in coating media experiments, transwells were only incubated in DMEM: F12 + 10% FBS overnight.

2.8. BioFlux assays

Preliminary BioFlux experiments were completed using the BioFlux™ 1000z in the Dept. Chemical and Biological Engineering (CBE), UoS. Optimisation of infection protocols and high-resolution imaging was completed using the BioFlux™ 200 in the School of Biosciences. 48 well low-shear plates with glass channels were used for all experiments. Protocols for coating BioFlux plates, BioFlux cell seeding, and the preliminary BioFlux infection protocol were developed by Dr Mahendra Raut (CBE), using the BioFlux 1000z system.

2.8.1. Coating BioFlux plates

BioFlux plates were coated with the standard fibronectin coating medium. To introduce medium into channels, 150 µl coating medium was added to inlet wells and continuous flow at 1 dyn/cm^2 was initiated in the inlet to outlet direction, for 10 minutes. Coated plates were incubated overnight at 37°C, 5%.

2.8.2. BioFlux cell seeding

Prior to cell seeding, excess coating medium was removed, and channels were washed 1x with PBS. 150 µl PBS was added to outlet wells and continuous flow at 1 dyn/cm^2 was initiated in the outlet to inlet direction, for 10 minutes. Excess PBS was removed, and inlet and outlet wells were washed 1x with 1 ml PBS. PBS was removed so that only a droplet remained in the centre of each well. HCE2s were harvested using standard cell culture techniques and a cell suspension containing 1.6 x10^7

cells/ml was prepared in KSFM. To seed cells into channels, 30 µl cell suspension was added to the PBS droplet in outlet wells and continuous flow was initiated at 5 dyn/cm^2 for 1-2 seconds in the outlet to inlet direction. Leftover cell suspension was removed from outlet wells and outlet wells were washed 3x with 1 ml PBS. 1 ml KSFM was added to inlet wells and 100 µl KSFM was added to outlet wells. Plates were incubated at 37°C, 5% for 18-24 hrs.

2.8.3. Preparation of bacteria

PAO1-GFP or SH1000-GFP were used throughout BioFlux experiments. In preliminary experiments, overnight cultures of PAO1-GFP were prepared and incubated at 37°C, under shaking conditions (150 rpm). Following a 20-22 hr incubation period, overnight cultures were diluted to an OD of 0.05-0.06 (600 nm) and used in stationary phase. In the optimised protocol, overnight cultures were prepared and diluted to an OD of 0.05 the following day. Diluted cultures were incubated at 37°C, under shaking conditions (180 rpm) for 2.5 hrs (PAO1-GFP) or 3 hrs (SH1000-GFP). Mid-log cultures were centrifuged at 4,000 *xg* for 5 mins and bacterial pellets were washed twice by centrifugation with PBS. The final cell pellet was resuspended in the appropriate tissue culture medium. An OD measurement was taken at 600 nm and the culture was diluted to the chosen OD using tissue culture medium. In the optimised protocol, SH1000-GFP bacteria were prepared at a final OD of 0.03-0.04 and OD 0.1-0.12 was used for PAO1-GFP.

2.8.4. Preliminary BioFlux infection protocol

BioFlux channels were visualised to check host cell confluency. If a healthy cell monolayer was present, continuous flow was initiated at 1 dyn/cm^2 for 3 minutes, in the inlet to outlet direction to remove any dead cells/debris. Excess KSFM was removed and 250 µl fresh KSFM (with/without 800 nM peptides) was added to outlet wells. Continuous flow was initiated at 1 dyn/cm^2 for 1 hr, in the outlet to inlet direction and the bacterial inoculum was prepared using basal KSFM. After the 1 hr incubation, excess medium was removed so that a small droplet remained in the centre of each well. 15 µl of the bacterial inoculum was added to the KSFM droplet in outlet wells and continuous flow was initiated at 1 dyn/cm^2 for 3 seconds, in the outlet to inlet direction. Plates were incubated in the BioFlux at 37°C, 5% CO_2 under static conditions for 1 hr. Leftover inoculum was removed and replaced with fresh KSFM. 1 ml KSFM was added to inlet wells and 100 µl KSFM was added to outlet wells. Plate was returned to the BioFlux, and oscillatory flow (**Figure 2-4A**) was initiated at 1 dyn/cm^2 for 16-24 hrs. Infection progression was monitored by imaging every 15 minutes and plates were incubated at 37°C, 5% CO_2, with overall flow in the inlet to outlet direction.

2.8.4.1. Microscopy

All BioFlux 1000z experiments were performed using the Zeiss Axio Observer microscope with a Hamamatsu orca flash LT 4.0 camera and 20X objective. The BioFlux Montage software was used for image capture.

2.8.5. Optimised BioFlux infection protocols

BioFlux channels were visualised to check host cell confluency. If a healthy cell monolayer was present, continuous flow was initiated at 1 dyn/cm^2 for 3 minutes, in the inlet to outlet direction to remove any dead cells/debris. Excess KSFM was removed and 250 µl fresh medium (with/without unfractionated heparin (UFH)) was added to outlet wells. UFH was prepared at 10 U/ml using tissue culture media. For bacterial adhesion assays and phase microscopy, Live Cell Imaging Solution (LCIS) (Invitrogen A14291DJ) was used. For microcolony formation assays, CO_2 Independent Medium (Gibco 18045088) was used. Continuous flow was initiated at 1 dyn/cm^2 for 1 hr, in the outlet to inlet direction and the bacterial inoculum was prepared.

2.8.5.1. Measuring bacterial adhesion

Following pre-treatment, excess medium was removed so that a small droplet remained in the centre of each well. 500 µl of the inoculum (prepared in LCIS) was added to each of the inlet wells and 500 µl fresh LCIS was added to each of the outlet wells. Plate was returned to the BioFlux so that 0 hr images could be collected and continuous flow was initiated at 0.2 dyn/cm^2 for 2 hrs, in the inlet to outlet direction. Infection progression was monitored by imaging every 15 minutes and plates were incubated at 37°C.

2.8.5.2. Measuring microcolony formation

Following pre-treatment, excess medium was removed so that a small droplet remained in the centre of each well. 100 µl of the inoculum (prepared in CO_2 independent medium) was added to each of the inlet wells and 100 µl fresh CO_2 independent medium was added to each of the outlet wells. Continuous flow was initiated at 0.2 dyn/cm^2 for 6 minutes, in the inlet to outlet direction. Plates were then incubated in the BioFlux at 37°C, under static conditions for 30 mins. After 30 mins, excess medium was removed from both wells. 1 ml CO_2 independent medium was added to outlet wells and 100 µl medium was added to inlet wells. Plate was returned to the BioFlux so that 0 hr images could be collected, and then pulsatile flow (**Figure 2-4B**) was initiated at 1 dyn/cm^2 for 8 hrs.

Infection progression was monitored by imaging every 15 minutes and plates were incubated at 37°C.
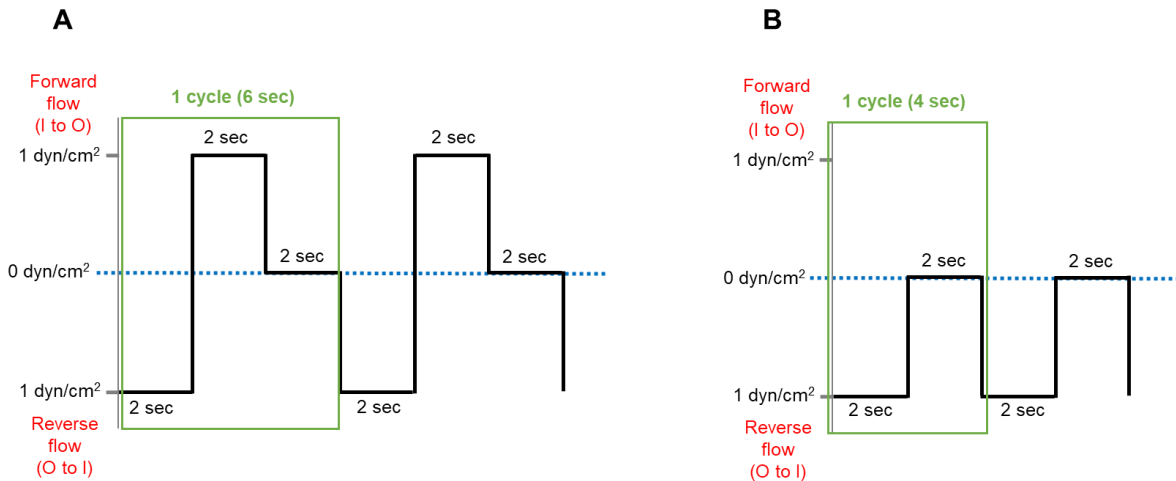
Figure 2-4. Flow conditions used for BioFlux experiments.
(A) Oscillatory flow: 2 seconds flow in outlet to inlet direction, 2 seconds flow in the inlet to outlet direction, 2 seconds no flow (gravity flow only). There is overall flow in the inlet to outlet direction. **(B) Pulsatile flow**: 2 seconds flow in the outlet to inlet direction, 2 seconds no flow (gravity flow only). There is overall flow in the outlet to inlet direction.

2.8.5.3. Microscopy

All BioFlux 200 experiments were performed using the Nikon Ti-E inverted microscope with a Hamamatsu Flash 4.0 v2 camera and Nikon Perfect Focus system. The Nikon 20X Plan Apochromat objective was used for time-lapse images. The Nikon 100X Plan Apochromat Phase objective and Ph3 phase ring were used for phase microscopy. The Nikon NIS-Elements imaging software was used for image capture. In each experiment, images were collected at three channel positions within the BioFlux viewing window (start, middle and end). Equivalent channel positions were used for control and treatment conditions. In early experiments, time-lapse images were collected using a single z-plane. The base of the microfluidic channel was considered 0 μm and images were collected approximately 2-3 μm above this. In later experiments, images were collected in multiple z-planes (0 and 2 μm or 0, 2 and 4 μm).

2.8.5.4. Image processing

Image processing was carried out using ImageJ (National Institutes of Health, Bethesda, MD, USA). Time-lapse images were stabilized using the Image Stabilizer Plugin, translation transformation was

performed using 500 maximum iterations and an error tolerance of 1×10^{-9}. The Integral Image Filters Plugin was used to normalise local contrast. All Brightfield images were processed using a standard deviation value of 2 (standard) or 4 (phase microscopy). For fluorescence images, a value of 15 was used but only in data sets showing individual bacteria. The subtract background function was also performed for early time point fluorescence images, a rolling ball radius of 7 was selected and smoothing was disabled. If images were collected in multiple z-planes (0, 2, 4 µm), the imageCalculator add function was used to combine 0 and 2 µm images, images collected at 4 µm were excluded from quantitative analysis. A Fiji macro was written to perform batch processing of bacterial adhesion images, with help from Dr James Wheeler, School of Biosciences, UoS.

2.8.5.5. Quantitative image analysis

Quantitative analysis was performed using MATLAB (The MathWorks Inc, Natick, MA, USA) and the MATLAB-based tracking platform, FAST (Feature-Assisted Segmenter/Tracker). FAST can be accessed at: https://doi.org/10.5281/zenodo.4323627 and was used to perform segmentation and feature extraction. Analysis of channel images was carried out in duplicate, using images taken at the 'start' and 'middle' of the BioFlux viewing window under all conditions. NB. When using the BioFlux 200 system, images of the channel were inverted. Therefore, 'start' refers to the section of the viewing window closest to the outlet well. Additional MATLAB code was used to perform batch processing (provided by Dr Oliver J. Meacock, University of Oxford) and extraction of the count data (provided by Dr James Wheeler, School of Biosciences, UoS).

2.8.5.6. Access to ImageJ and MATLAB code

The code used to perform batch processing and extraction of FAST data, can be accessed via the University of Sheffield data repository, ORDA (https://orda.shef.ac.uk/): 10.15131/shef.data.19213785.

2.9. Statistical analysis

All statistical analysis was performed using GraphPad Prism 9. Where possible, a minimum of three biological repeats (n=3) were performed and statistical significance was only calculated for experiments where n ≥ 3. Each biological replicate was calculated by averaging a minimum of two technical replicates but in some studies, significantly more technical repeats were performed, e.g., eight technical replicates were used in biofilm formation studies. For normally distributed data, an unpaired t-test was used to compare two groups and ANOVA was used to compare three or more

groups. One-way ANOVA with multiple comparisons was used to analyse datasets with one independent variable and two-way ANOVA with multiple comparisons was used to analyse datasets with two independent variables. Non-normally distributed datasets were identified using the Shapiro Wilk normality test and the non-parametric Mann-Whitney test was used to compare two groups of non-normally distributed data.

CHAPTER 3: DEVELOPING A TRANSWELL MODEL OF THE CORNEAL EPITHELIUM

3.1. Introduction

This chapter describes the development of an *in vitro* model of the human corneal epithelium, using the HCE2 human corneal epithelial cell line. The HCE2 cell line has been immortalised using Adeno-12/SV40 viral sequences (Kahn and Rhim, 1996) and these cells are commercially available from ATCC (CRL-11135). The commercial availability of the HCE2 cell line was the initial reason these cells were selected, as the in-house generation of immortalised cell lines can be highly time-consuming and by using a commercially available cell line, I am able to directly compare my findings with those of other researchers. However, before HCE2s could be implemented in infection studies, characterisation studies were required to assess their suitability for *in vitro* modelling. HCE2s were tested for a number of desirable characteristics, including expression of CD9 tetraspanin, the ability to form differentiated cell multilayers and retention of corneal epithelial cell identity. During model development stages, transwell inserts were used to culture HCE2 cells at Air-Liquid Interface (ALI) (**Figure 3-1**), as air-lifting has been shown to promote the differentiation of human corneal epithelial cells (Greco et al., 2010, Toropainen et al., 2001).
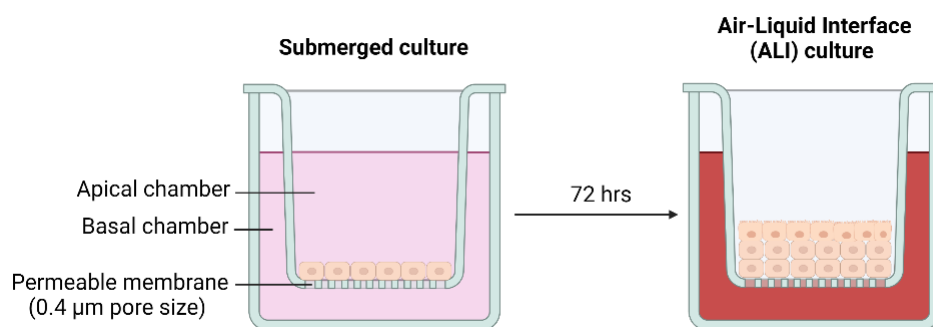
Figure 3-1. The use of transwell inserts for culturing HCE2 cells at air-liquid interface.
Transwell culture consists of two stages: (1) submerged culture and (2) culture at air-liquid interface. (1) HCE2 cells are seeded onto collagen-coated transwell inserts and incubated at 37°C, 5% CO_2 for 72 hrs. During this stage, both the apical and basal chambers are supplied with KSFM, and cells are completely submerged in medium. (2) Media is removed from apical chambers and superficial corneal epithelial cells are exposed to the air. Basal chambers are still supplied with media but under optimised conditions, a media switch from KSFM to DMEM: F12 +10% FBS is performed. Created with Biorender.com.

3.1.1. Expression of CD9 tetraspanin

CD9 is a 21-24 kDa membrane protein belonging to the tetraspanin superfamily (Reyes et al., 2018). This tetraspanin is widely expressed throughout the body, with high levels of expression in the skin and cardiovascular system, but expression of CD9 is not ubiquitous (Sincock et al., 1997). CD9 and other tetraspanins play overlapping roles in important cell functions such as cell migration, adhesion, proliferation, cell fusion and intracellular signalling (Reyes et al., 2018) and many of these functions are mediated by Tetraspanin-Enriched Microdomains (TEMs), which arise when tetraspanins form lateral associations with other proteins in the plasma membrane (Yanez-Mo et al., 2009). Many of the partner proteins found within TEMs are receptors for bacterial adhesins and so it has been suggested that TEMs act as "sticky platforms" for bacterial adhesion (Monk and Partridge, 2012). In order to test this hypothesis, putative anti-adhesion therapies were developed to disrupt TEM formation. Preliminary studies utilised anti-tetraspanin antibodies but low antigenicity of human tetraspanins meant tetraspanin studies were historically limited by a lack of suitable antibodies. Therefore, recombinant GST fusion proteins and short peptides were designed, which share amino acid sequence with the EC2 domain of target tetraspanins. The EC2 domain is a large extracellular loop that mediates protein-protein interactions in TEMs (Seigneuret et al., 2001). Therefore, EC2 derivatives are proposed to disrupt TEM formation by interacting with endogenous EC2 domains and blocking further protein-protein interactions. This concept has since been demonstrated in various model systems. Recombinant EC2 domains of CD9, CD63 and CD151 tetraspanins have been shown to reduce meningococcal adhesion to human epithelial cells (Green et al., 2011) and CD9-derived peptides have been shown to reduce staphylococcal adhesion to human keratinocytes by as much as 60% (Ventress et al., 2016). In recent years, CD9 has become the major tetraspanin of interest due to its observed effects on bacterial adhesion and its high expression at host cell membranes (Green et al., 2011). CD9-derived peptides could have potential applications in the treatment of bacterial keratitis, but these peptides cannot be tested using HCE2 models unless CD9 tetraspanin is expressed by the HCE2 cell line.

3.1.2. Formation of differentiated cell multilayers

One of the major aims of the project was to develop an *in vitro* model of the corneal epithelium that is more representative of the *in vivo* cornea than standard cell culture models. Therefore, it was essential that HCE2 cells are able to form differentiated cell multilayers which share characteristics with the human cornea. The human corneal epithelium consists of 5-7 cell layers and there are three subsets of corneal epithelial cells, named the basal, wing and superficial corneal epithelial cells (Sridhar, 2018). Terminally differentiated superficial cells form the outermost layer of the corneal

epithelium and these cells possess microvilli (Pfister, 1973), which stabilise the tear film and maximise nutrient exchange (Collin and Collin, 2000). The presence of cell multilayers and multiple cell types may influence host-pathogen interactions *in vivo* and so it is important these characteristics are replicated *in vitro*. Another important characteristic of the corneal epithelium is the presence of tight cell junctions, which confer epithelial barrier integrity and protect the healthy cornea against infection (Fleiszig et al., 2019). The stratified human corneal epithelium expresses the three major classes of tight junction protein (TJP), and these are occludin, Zonula Occludens (ZO1, ZO2, ZO3) and members of the claudin family (claudin 1, 2, 3, 7, 9, 14 and 15) (Leong and Tong, 2015). The importance of TJPs has been demonstrated using *P. aeruginosa* lipopolysaccharide (LPS) (Yi et al., 2000) and human interleukin 1 beta (IL-1β) (Kimura et al., 2009), which reduce expression of TJPs at the corneal cell surface and have been shown to impair epithelial barrier function. Therefore, it is essential that HCE2 cells are able to form tight cell junctions. This can be assessed using multiple techniques, including immunofluorescence staining for TJPs and paracellular permeability studies, as the formation of tight cell junctions has been associated with reduced paracellular permeability *in vitro* (Toropainen et al., 2001).

3.1.3. Maintenance of corneal epithelial cell identity

It is important that HCE2 cells maintain the identity of corneal epithelial cells, despite the occurrence of genetic drift in cell lines (Hughes et al., 2007). This can be determined by measuring the expression of corneal epithelial cell-specific markers such as PAX6. The *PAX6* gene encodes a positive transcription factor and is proposed to play a role in corneal epithelium lineage specific differentiation (Li and Lu, 2005). PAX6 expression is detected in mature ocular cell types, including retinal, lenticular and corneal cells and CRISPR-Cas mediated knockout of *PAX6* in primary corneal epithelial cells has been associated with several changes in gene expression, including downregulation of Keratin 3 (K3), Keratin 12 (K12), Clusterin (CLU) and Angiopoietin-Like 7 (ANGPTL7) (Kitazawa et al., 2017). K3/K12 are corneal specific differentiation markers which play an important role in maintaining the structural integrity of the corneal epithelium (Kao et al., 1996), whereas CLU and ANGPTL7 prevent keratinization (Nakamura et al., 2002) and neovascularisation (Toyono et al., 2015), respectively. Therefore, PAX6 is considered a key regulator of corneal epithelial cell identity and if HCE2 cells retain the identity of a human corneal epithelial cell, they should express the *PAX6* gene.

3.2. Aims

1. To develop an *in vitro* model of the corneal epithelium using the HCE2 cell line, which displays strong epithelial barrier integrity and possesses cell multilayers.

2. To determine if CD9 tetraspanin is expressed by the HCE2 cell line and whether expression is altered in response to cell culture conditions.

3. To determine if the corneal epithelial cell marker, PAX6, is expressed by the HCE2 cell line and whether mRNA expression is altered in response to cell culture conditions.

3.3. Results

3.3.1. CD9 tetraspanin is expressed by the HCE2 cell line and expression is unaffected by coating reagents.

CD9 expression by the HCE2 human corneal epithelial cell line, was detected using an in-house preparation of anti-human CD9 antibody (**Figure 3-2**). Cells treated with mouse IgG1 isotype control antibody presented with minimal FITC-fluorescence (**Figure 3-2B, D**), confirming the specificity of the anti-CD9 antibody. The immunofluorescence staining pattern for anti-CD9 (**Figure 3-2A, C**) indicates that CD9 is highly expressed at HCE2 cell membranes, as cells were not permeabilised prior to immunofluorescence staining. HCE2s were cultured on coated-coverslips for microscopy as HCE2 cells would not adhere effectively to uncoated glass and the absence of coating media was associated with abnormal cell morphology. Potential fibronectin and collagen coating conditions were selected prior to this project and use of either condition did not appear to affect CD9 expression (**Figure 3-2A, C**). This was confirmed by flow cytometry (**Figure 3-3**). Following the subtraction of mouse IgG1 control values (**Figure 3-3B**), Median Fluorescence Intensity (MFI) values for anti-CD9 antibody-treated cells were compared for cells cultured on different coating reagents: uncoated plastic (441.3 ± 215.9), fibronectin-coated plastic (467.0 ± 250.0) or collagen-coated plastic (476.3 ± 227.4). There was no significant difference in MFI between conditions ($p > 0.05$ in all cases, n=3, one-way ANOVA with Tukey's multiple comparisons test), confirming that CD9 expression in HCE2 cells is unaffected by coating reagents. The human keratinocyte cell line, HaCaT, was also included in flow cytometric analysis as this cell line has previosuly been shown to express CD9 (Ventress et al., 2016). CD9 expression levels were similar between HaCaT cells (574.5 ± 34.7) and HCE2 cells (461.6 ± 201.1).

3.3.1.1. HCE2 CD9 expression is altered by choice of tissue culture media.

CD9 expression in HCE2 cells was investigated by flow cytometry, using HCE2 monolayers cultured under different media conditions (**Figure 3-4**). The chosen media conditions were under consideration

72

for use in the HCE2 transwell model. MFI values for anti-CD9 antibody-treated cells were compared between media conditions: DMEM: F12 +0% FBS (8005.3 ± 399.4); DMEM: F12 +2% FBS (6755.5 ± 611.3); DMEM: F12 +5% FBS (6994.2 ± 763.9); DMEM: F12 + 10% FBS (7968.3 ± 689.0); and KSFM (11543.5 ± 1440.8). There was a significant increase in MFI for the KSFM condition, as compared to all other DMEM: F12 conditions (p ≤ 0.01 for 2% and 5% FBS, p ≤ 0.001 for 0% and 10% FBS, n=3, one-way ANOVA with Tukey's multiple comparisons test). Conversely, there was no significant difference in MFI between any of the DMEM: F12 conditions (p > 0.05 in all cases).
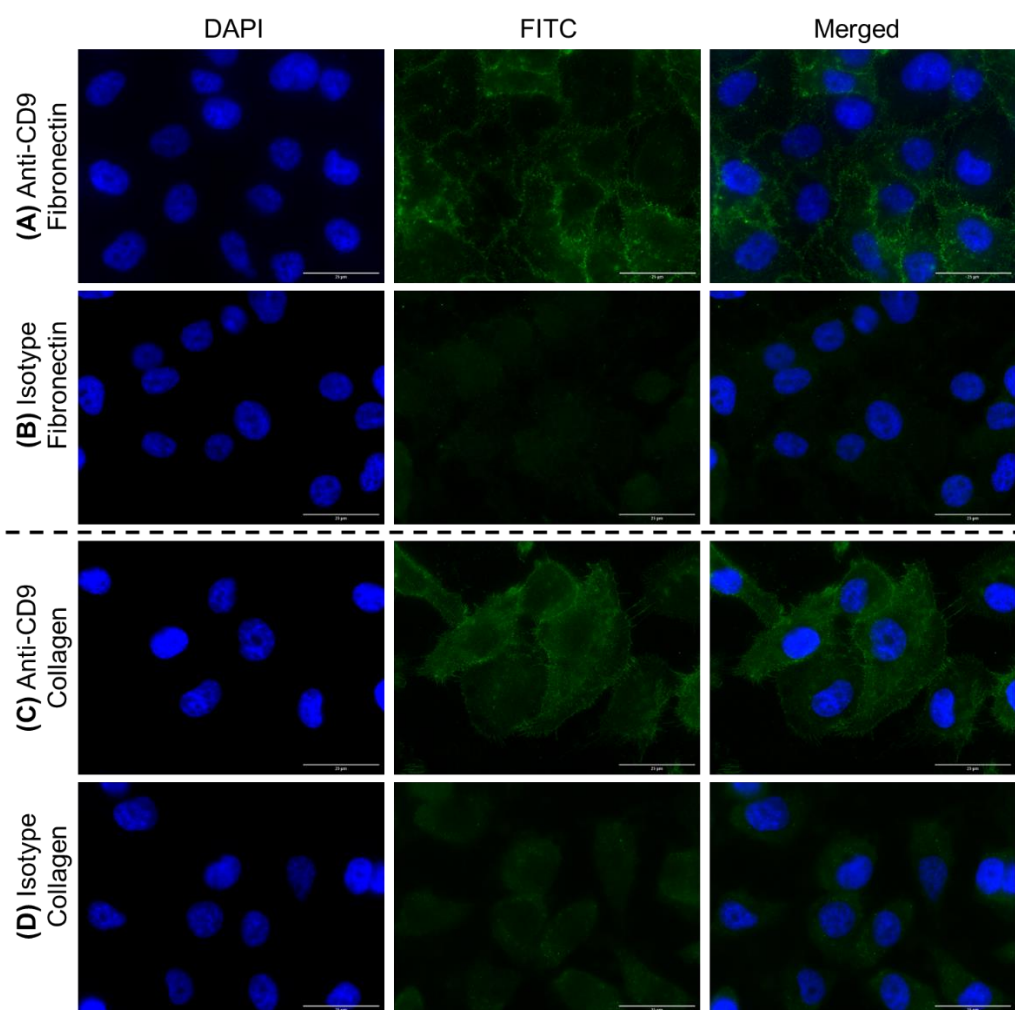
Figure 3-2. Immunofluorescence staining for CD9 expression in the HCE2 cell line.
HCE2 cells were seeded onto fibronectin-coated (A-B) or collagen-coated (C-D) coverslips and cultured in KSFM overnight. DAPI was used to stain cell nuclei (blue) and FITC-conjugated secondary antibody was used to label anti-CD9 antibody (green). Mouse IgG1 isotype control antibody was included to assess non-specific antibody binding (green). Scale bars represent 25 µm.

73

(A)

(B)
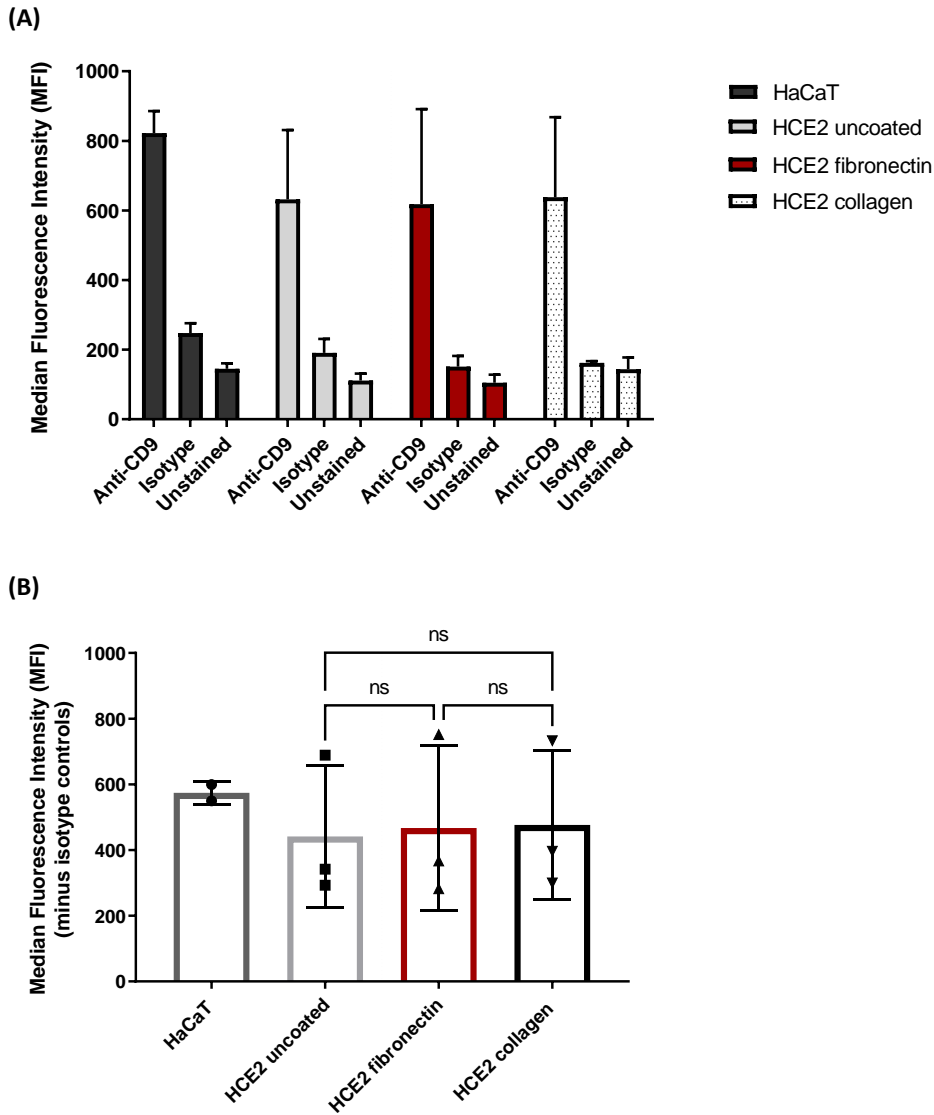
Figure 3-3. CD9 expression in HaCaT versus HCE2 cell lines and in the presence of different HCE2 coating reagents.

(A) MFI values for anti-CD9 antibody-treated cells and negative controls. Negative controls include cells treated with mouse IgG1 isotype control antibody and unstained cells. (B) Net MFI values following subtraction of isotype control antibody values. CD9 expression was quantified by flow cytometry. HCE2s were harvested from confluent T-75 flasks after 72 hr culture in KSFM. Flasks were either uncoated, coated with the standard fibronectin coating medium (0.01 mg/ml fibronectin, 0.03 mg/ml bovine collagen type I, 0.01 mg/ml BSA) or collagen coated (0.1 mg/ml bovine collagen type I). HaCaT cells were included as a positive control as these cells are known to express CD9. Data represent mean ± SD; for HCE2 cells, n=3 and for HaCaT cells, n=2. HCE2 data was analysed using one-way ANOVA with Tukey's multiple comparisons test, ns= not significant ($p > 0.05$).
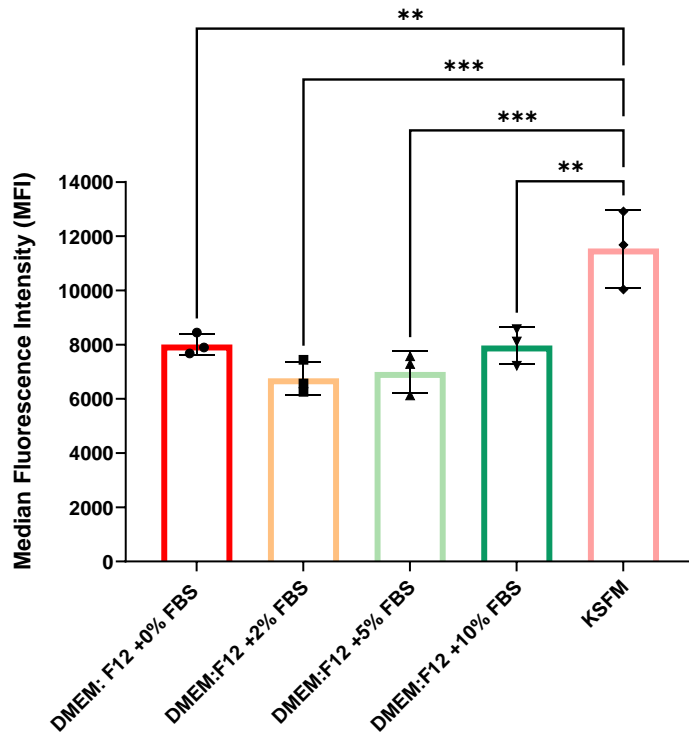
Figure 3-4. CD9 expression in HCE2s under different media conditions.

CD9 expression in HCE2s was quantified by flow cytometry. HCE2s were harvested from confluent T-75 flasks following 7-day culture under different media conditions. All flasks were fibronectin coated and HCE2s were grown in submerged culture conditions but different media conditions (KSFM or DMEM: F12 supplemented with 0%, 2%, 5% or 10% FBS) were introduced on day 3. MFI values for HCE2 cells treated with mouse IgG1 isotype control antibody have been subtracted from MFI values for anti-CD9 antibody-treated cells. Data represent mean ±SD, n=3. The data was analysed using one-way ANOVA with Tukey's multiple comparisons test, $**p \leq$ 0.01 $***p \leq 0.001$.

3.3.2. Paracellular permeability assays reveal differences in epithelial barrier integrity under different transwell culture conditions.

In the aforementioned studies, HCE2 cells were studied as monolayer cultures, grown under submerged conditions using T-75 flasks or standard cell culture plates. Experiments described in the remainder of this Chapter were performed using specialised transwell inserts, which allowed HCE2 cells to be cultured at air liquid interface. Paracellular permeability assays were used to compare the epithelial barrier integrity of HCE2 multilayers under different transwell culture conditions. Paracellular transport of FITC-Dextran (molecular weight 3000-5000 gmol^{-1}) was reduced in the presence of HCE2 multilayers, as indicated by reduced basal chamber fluorescence readings for cells versus no cell conditions (**Figure 3-5A**). Furthermore, paracellular permeability of HCE2 multilayers was influenced by media composition and length of culture at ALI (**Figure 3-5A**). Following the introduction of ALI (day 0), the DMEM: F12 +0% FBS and KSFM media conditions were consistently associated with reduced barrier function and therefore the highest % permeability values (**Figure 3-5B**). Conversely, HCE2 multilayers cultured in DMEM: F12 containing FBS, were associated with increased barrier function, showing the lowest % permeability values. This trend persisted until day 10, when a decline in barrier function was observed for all HCE2 multilayers cultured in FBS. Lowest % permeability values were observed on day 6 for the 5% FBS (19.2% ± 2.7) and 10% FBS (19.9% ± 2.6) DMEM: F12 conditions. Under these conditions, a significant decrease in permeability was observed (**Figure 3-6**), as compared to HCE2 multilayers cultured in DMEM: F12 with no FBS (46.7% ± 8.9) (p=0.0247 for 5% FBS, p= 0.0288 for 10% FBS, n=3, one-way ANOVA with Tukey's multiple comparisons test). This was mirrored by day 6 permeability coefficient calculations (**Table 3-1**), with decreasing values corresponding to reduced traversal of cell layers by FITC-Dextran and improved barrier function: No cells (1.76 x 10^{-11} cm s^{-1}), DMEM: F12 +0% FBS (6.69 x 10^{-12} cm s^{-1}), KSFM (6.59 x 10^{-12} cm s^{-1}), DMEM: F12 +2% FBS (2.10 x 10^{-12} cm s^{-1}), DMEM: F12 +10% FBS (1.55 x 10^{-12} cm s^{-1}), DMEM: F12 +5% FBS (1.46 x 10^{-12} cm s^{-1}).

(A)

(B)
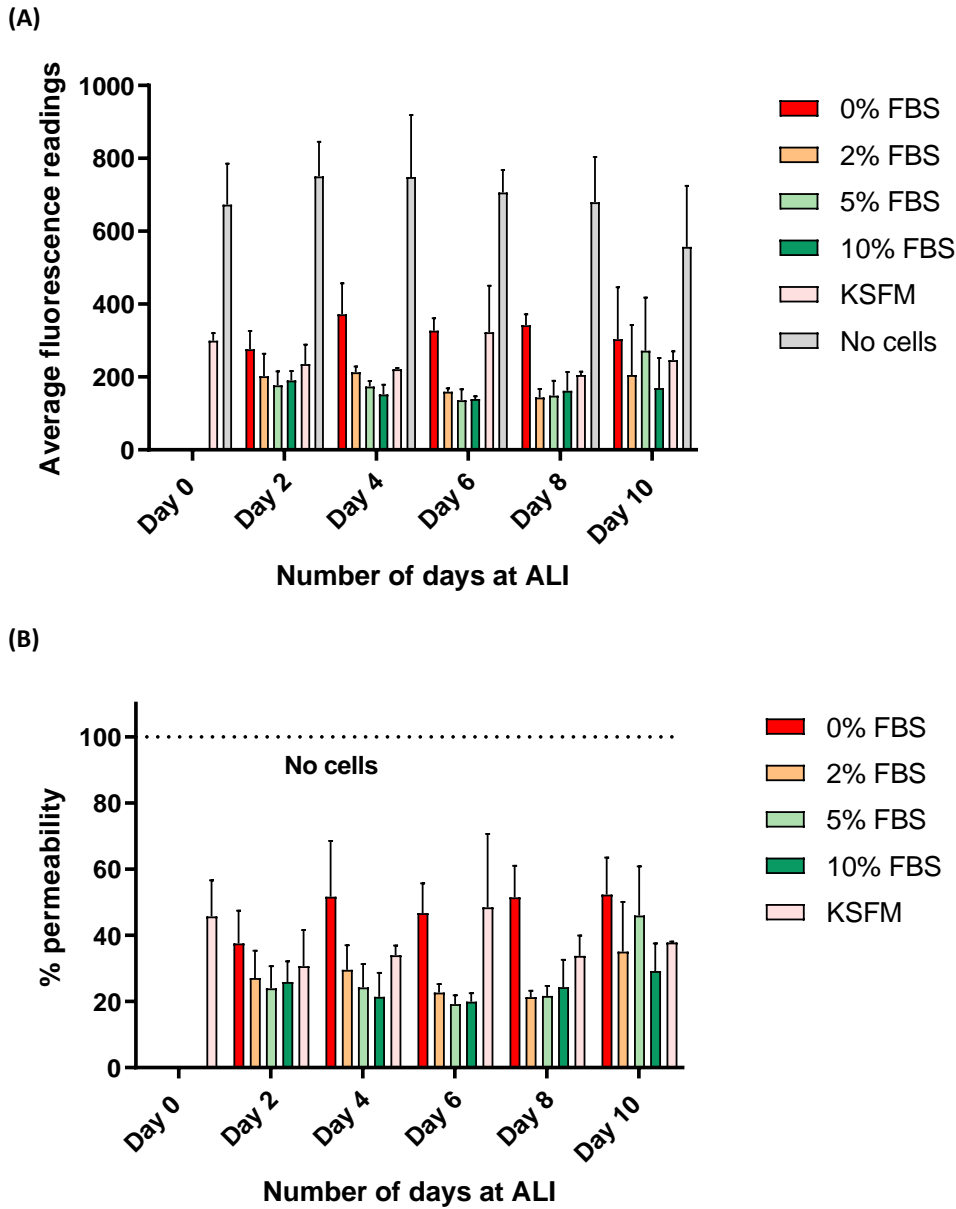
Figure 3-5. Permeability of HCE2 multilayers to FITC-Dextran under different cell culture conditions. HCE2s were cultured on transwell inserts using different media conditions and various lengths of culture at ALI. No cell controls were also included. To measure paracellular permeability, FITC-Dextran was added to the apical chambers and plates were incubated at 37 °C for 2 hrs. After 2 hrs, aliquots were collected from basal chambers and fluorescence measured (excitation 485 nm, emission 530 nm). Data represent mean ±SD, n=2 to 3. **(A) Average fluorescence readings for all conditions (B) Relative permeability of HCE2 monolayers compared to no cell conditions.** Data has been expressed as a % of the average no cells value for each experiment.

77
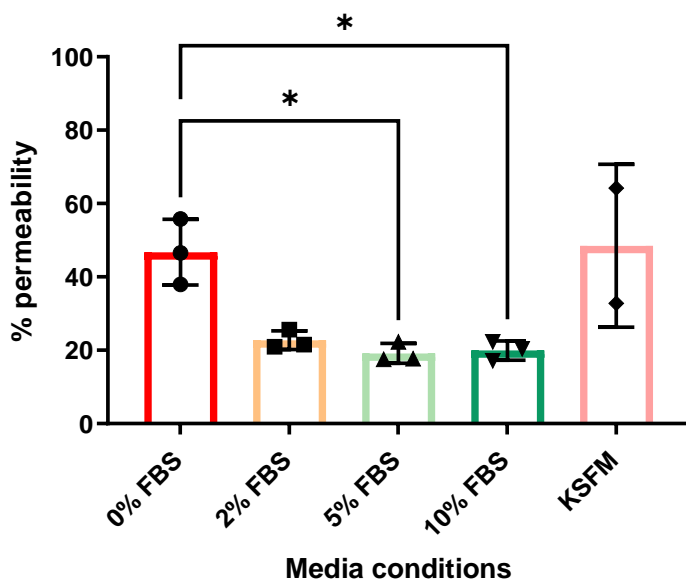
Figure 3-6. Permeability data collected on day 6 of culture at ALI.
Relative permeability data from day 6 at ALI is shown as this time point was associated with the lowest permeability values. Data represent mean ±SD, n=3 for DMEM: F12 conditions. Data was analysed using a one-way ANOVA with Tukey's multiple comparisons test, *p ≤ 0.05, KSFM was excluded from statistical analysis as n=2 for this condition.

Table 3-1. Permeability coefficients for FITC-Dextran on day 6 of culture at ALI.
Permeability coefficients have been calculated using average fluorescence readings on day 6 at ALI. Number of mmoles were interpolated from a dilution curve of FITC-Dextran fluorescence (see **section 2.4.1.1**).

	Fluorescence	Moles (mmoles)	Steady state flux (dQ/dt)	Permeability coefficient (Papp) (cm s^{-1})
0% FBS	327	1.80×10^{-6}	2.50×10^{-10}	6.69×10^{-12}
2% FBS	160	5.64×10^{-7}	7.83×10^{-11}	2.10×10^{-12}
5% FBS	136	3.93×10^{-7}	5.46×10^{-11}	1.46×10^{-12}
10% FBS	140	4.18×10^{-7}	5.80×10^{-11}	1.55×10^{-12}
KSFM	323	1.77×10^{-6}	2.46×10^{-10}	6.59×10^{-12}
No cells	707	4.73×10^{-6}	6.57×10^{-10}	1.76×10^{-11}

3.3.3. Immunofluorescence staining for tight-junction proteins can be used to identify optimum transwell culture conditions.

3.3.3.1. Immunofluorescence staining for occludin

Anti-occludin antibody was used to detect HCE2 expression of the tight junction protein, occludin, under different media conditions (**Figure 3-7)**. On day 8 of ALI culture, occludin expression was observed under both DMEM: F12 +10% FBS and KSFM culture conditions. F-actin was also expressed under all conditions and differences in the cortical actin staining pattern for HCE2s cultured in DMEM: F12 +10% FBS versus KSFM, illustrate morphological differences associated with choice of cell culture medium. In the DMEM: F12 condition, HCE2 cells appear elongated whereas cells cultured in KSFM were smaller and more rounded. The use of DMEM: F12 +10% FBS was also associated with improved cell viability and increased transwell coverage following 8-day ALI culture. Poor transwell coverage was observed for HCE2 cells cultured in KSFM and this was particularly striking for HCE2s treated with rabbit serum control (**Figure 3-7B**). Colocalisation of occludin and cortical actin filaments was not observed and instead, colocalisation of occludin and DAPI-stained cell nuclei was visible for anti-occludin antibody-treated HCE2s. The selected antibodies demonstrated only partial specificity as there was non-specific FITC staining for DMEM: F12 cultured cells treated with the rabbit serum control. However, no FITC staining was observed for KSFM cultured cells treated using the same serum control. Total cell fluorescence calculations showed an increase in occludin-staining for anti-occludin antibody-treated cells that were cultured in DMEM: F12 (5.77×10^5), as compared to KSFM (3.69×10^5) (**Figure 3-8**). However, this trend was reversed following subtraction of control values and net cell fluorescence was larger for KSFM (3.69×10^5) than the DMEM: F12 +10% FBS (2.61×10^5) condition.

3.3.3.2. Immunofluorescence staining for Zonula Occludens 1 (ZO1)

Anti-ZO1 antibody was used to investigate HCE2 expression of the tight junction protein, ZO1, under different transwell culture conditions (**Figure 3-9**). ZO1 expression was observed under both DMEM: F12 +10% FBS and KSFM culture conditions and ZO1-staining was visible on days 4, 6 and 8 of transwell culture at ALI. On day 4, anti-ZO1 antibody-treated cells displayed ZO1-staining and there was moderate colocalisation of ZO1 and cortical actin filaments under both DMEM: F12 and KSFM conditions (**Figure 3-9A**). On day 6, the DMEM: F12 condition displayed increased ZO1 expression and this was associated with an increase in ZO1-actin colocalisation (**Figure 3-9B**). In contrast, there was a decrease in ZO1 staining for the KSFM condition and whilst colocalisation of ZO1 and actin was observed, it was greatly reduced compared to the DMEM: F12 condition. DAPI-staining was also reduced for HCE2 cells cultured in KSFM, as cell numbers were reduced and cell nuclei appeared smaller and less distinct. On day 8, ZO1 expression persisted in the DMEM: F12 condition but

colocalisation of ZO1 and actin at cell membranes was no longer visible (**Figure 3-9C**). For the KSFM condition, ZO1-staining remained similar between days 6 and day 8 but the HCE2 population was no longer viable and DAPI-staining revealed widespread degradation of cell nuclei. As noted in earlier experiments, F-actin was expressed under all culture conditions and differences in the staining pattern for DMEM: F12 versus KSFM are indicative of differences in the HCE2 actin cytoskeleton. Rabbit serum control was used to assess non-specific antibody binding and non-specific, FITC-staining was observed for all cell culture conditions. However, the extent of non-specific binding varied between conditions. Background binding was consistently higher for cells cultured in KSFM, versus DMEM: F12, as measured by Total Cell Fluorescence (TCF) (**Figure 3-10A**). Following subtraction of control values, total cell fluorescence was consistently higher for HCE2s cultured in DMEM: F12 versus KSFM (**Figure 3-10B**). The difference in TCF for DMEM: F12 (4.79×10^7) versus KSFM (2.90×10^7) was smallest on day 4, with a fold difference of approximately 1.7. On day 6, a dramatic decrease in TCF for KSFM was observed, resulting in a 20-fold difference between DMEM: F12 (4.71×10^7) and KSFM (2.51×10^6). On day 8, average TCF values for KSFM increased, resulting in a 10-fold difference between DMEM: F12 (5.18×10^7) and KSFM (4.66×10^6). Average TCF values for the DMEM: F12 condition remained relatively consistent between days 4 and day 8, with the highest TCF value reported on day 8 (5.18×10^7).

(A)

(B)
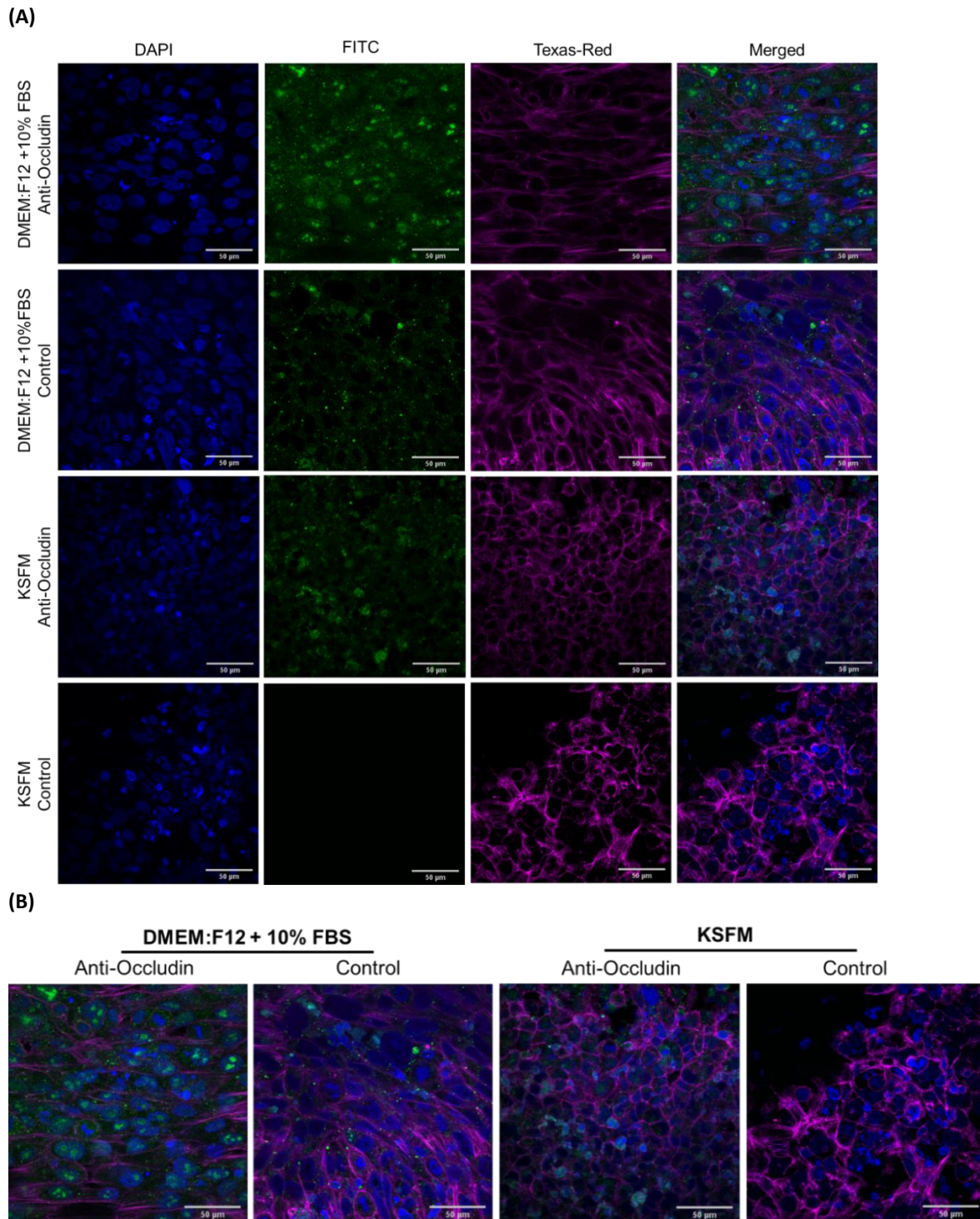
Figure 3-7. Immunofluorescence staining for Occludin under different media conditions, on day 8 of culture at ALI.

(A) DAPI, FITC, Texas-Red, Merged (left to right) (B) Merged images only. HCE2s were cultured on transwell inserts. After 72 hrs submerged culture in KSFM, ALI was introduced and KSFM was replaced with DMEM: F12 + 10% FBS or KSFM (Day 0). Immunofluorescence staining was carried out on day 8 of culture at ALI. DAPI was used to stain cell nuclei (blue) and FITC-conjugated secondary antibody was used to label anti-occludin antibody (green). Texas-Red X phalloidin has been used to stain actin filaments (magenta). Rabbit serum control was included to assess non-specific antibody binding (green). The same brightness and contrast settings have been used for all images collected in the same channel. Scale bars represent 50 μm.

81
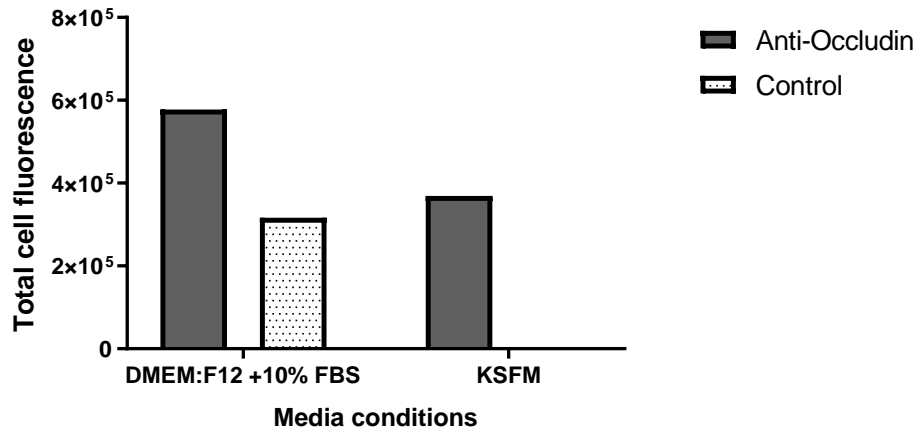
Figure 3-8. Total cell fluorescence values for HCE2 multilayers treated with anti-occludin antibody.
Total cell fluorescence has been calculated using FITC fluorescence values from the previously shown images (**Figure 3-7**). The total area of each image was used. TCF values for HCE2 cells treated with rabbit serum control are shown to display non-specific antibody binding.

(A)

(B)

(C)

(D)

Figure 3-9. Immunofluorescence staining for ZO1 under different time points and media conditions.
(A) Day 4 at ALI (B) Day 6 at ALI (C) Day 8 at ALI (A-C) DAPI, FITC, Texas-Red, Merged (left to right). (D) All time points, merged images only. HCE2s were cultured on transwell inserts. After 72 hrs submerged culture in KSFM, ALI was introduced and KSFM was replaced with DMEM: F12 + 10% FBS or KSFM (Day 0). Immunofluorescence staining was carried out on days 4, 6 or 8 of culture at ALI. DAPI was used to stain cell nuclei (blue) and FITC-conjugated secondary antibody was used to label anti-ZO1 antibody (green). Texas-Red X phalloidin has been used to stain actin filaments (red). Rabbit serum control was included to assess non-specific antibody binding (green). Regions of co-localisation between FITC and Texas-Red are visible (yellow). The same brightness and contrast settings have been used for all images collected in the same channel, with the exception of Day 8 DAPI-staining **(C-D)** where the brightness of KSFM images has been reduced to improve visibility. Scale bars represent 50 μm. This data set can be viewed as blue, green and magenta in **Appendix B**.

(A)

(B)
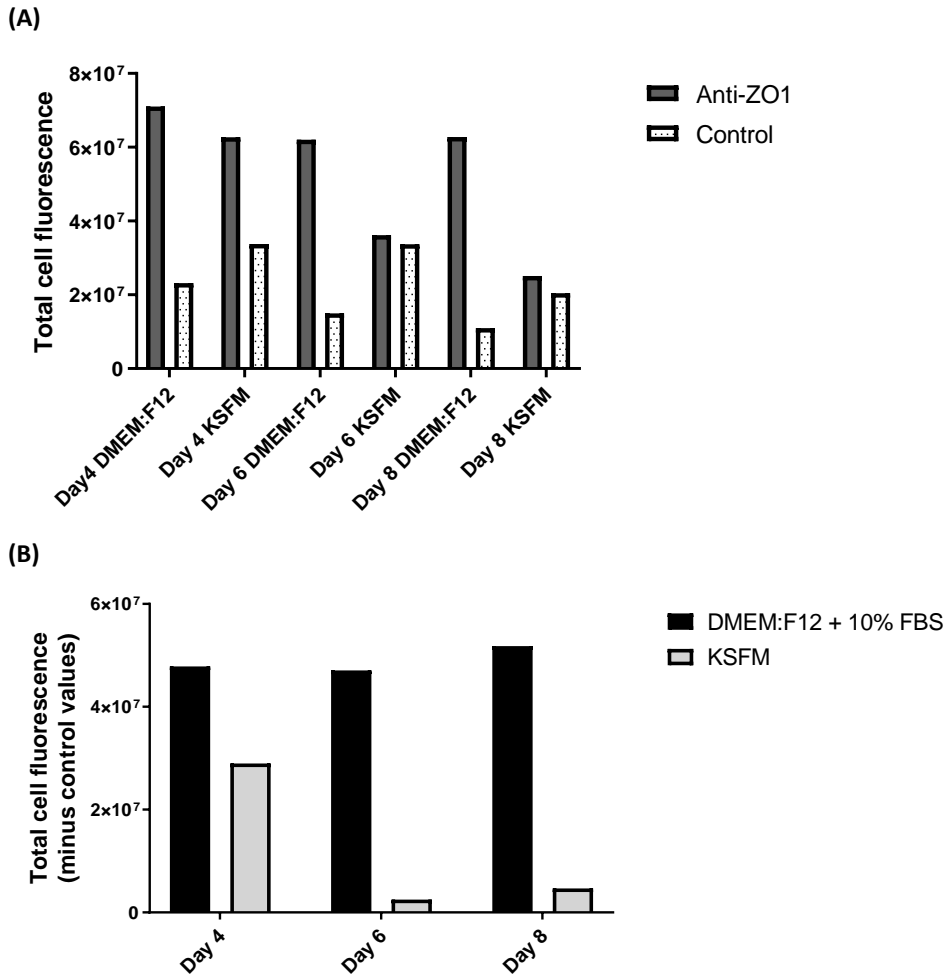
Figure 3-10. Total cell fluorescence values for HCE2 multilayers treated with anti-ZO1 antibody.
(A) **Total cell fluorescence values for HCE2 multilayers treated with anti-ZO1 antibody and rabbit serum control (B) Net cell fluorescence following subtraction of serum control values.**
Total cell fluorescence was calculated using FITC fluorescence values from the previously shown images (**Figure 3-9**). An additional set of technical replicates was also included. The total area of each image was used to calculate TCF and each bar represents mean TCF. TCF values for HCE2 cells treated with rabbit serum control are shown to display non-specific antibody binding.

3.3.4. Transmission electron microscopy reveals architecture of HCE2 multilayers.

Transmission electron microscopy was used to visualise HCE2 cell multilayers cultured on transwell inserts, under the optimised ALI conditions (**Figure 3-11**). Approximately 3-4 cell layers were observed, as well as the presence of essential organelles such as cell nuclei, mitochondria, and lysosomes (**Figure 3-11A**). Transwell structures were clearly visible, including the transwell membrane and 0.4 μm pores (**Figure 3-11A, B**). Microvilli could be observed protruding from HCE2 cells at the apical surface and were not observed in lower cell layers (**Figure 3-11C, D**).
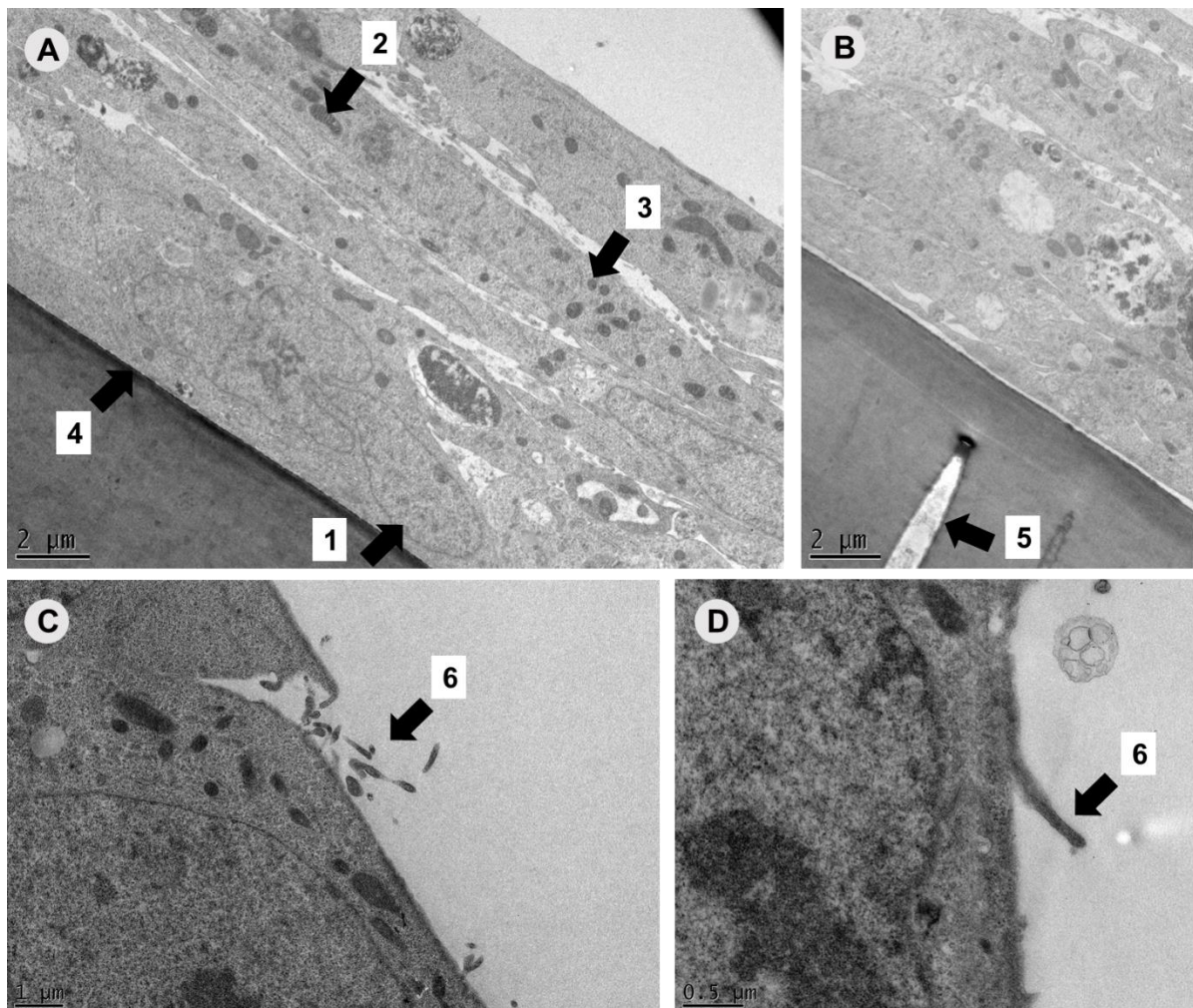
Figure 3-11. Transmission Electron Micrographs of air lifted HCE2 multilayers cultured on transwell inserts using optimised techniques.

HCE2s were cultured on transwell inserts for 6 days at ALI, using DMEM: F12 + 10% FBS. **A-B** show uninfected multilayers. **C-D** show multilayers that have been infected with SH1000-GFP at MOI 10. Images were collected 5 hrs post-infection, multilayers remain in-tact and no bacteria are visible in these images. Three to four cell layers can be observed in the differentiated HCE2 multilayers and features of interest have been labelled (black arrows): (1) nucleus (2) mitochondrion (3) lysosomes (4) semi-permeable PET membrane (5) transwell pore (0.4 μm pore size) and (6) microvilli. Scale bars represent 2 μm for **A-B**, 1 μm for **C** and 0.5 μm for **D**. Microscopy was performed by Chris Hill (Cryo-Electron Microscopy Facility, UoS).

3.3.5. PAX6 mRNA is expressed by the HCE2 cell line under multiple culture conditions.

HCE2 expression of mRNA transcripts for PAX6 and Glyceraldehyde-3-Phosphate Dehydrogenase (GAPDH) was investigated by qPCR under multiple cell culture conditions (**Figure 3-12**). Expression was determined using cycle threshold (C_t) values, which are inversely related to mRNA expression (**Figure 3-12A**). HCE2 expression of PAX6 and GAPDH mRNA was observed under all conditions. For PAX6, there was no significant difference in C_t values for HCE2s cultured at ALI compared to the no ALI control (24.9 ± 0.2), but PAX6 expression was influenced by choice of medium at ALI. C_t values were significantly higher for HCE2s cultured at ALI in the presence of DMEM: F12 +10% FBS (26.4 ± 0.8), as compared to HCE2s cultured at ALI in KSFM (24.2 ± 1.6), indicating increased expression of PAX6 mRNA in the KSFM condition (p= 0.0107, n=3, two-way ANOVA with Tukey's multiple comparisons test). Conversely, there was no significant difference in C_t values for GAPDH (p > 0.05 in all cases). C_t values for GAPDH were significantly lower than PAX6 C_t values, with an overall average C_t value of 15.6 for GAPDH. Low C_t values for GAPDH indicate high levels of mRNA expression and support its use as an endogenous control. Negative controls containing no reverse transcriptase (Rt), or RNA were included in all experiments (data not shown). C_t values for negative controls were consistently higher than samples, with an overall average C_t value of 30.8 for no Rt controls. For no RNA controls, C_t values were predominantly undetermined (i.e., C_t >40). A control condition using HCE2 cells cultured in KSFM, without ALI was used to represent undifferentiated HCE2s whereas HCE2s cultured at ALI are differentiated (see **sections 3.3.2** to **3.3.4**). Relative expression of PAX6 has been calculated for HCE2s cultured at ALI, as compared to PAX6 expression in the control (no ALI) condition (**Figure 3-12B**). For HCE2s cultured in DMEM: F12 +10% FBS, a relative decrease in expression was observed (0.54 ± 0.2), whereas an increase in expression was observed for HCE2s cultured in KSFM (4.2 ± 4.8). Despite a trend towards increased PAX6 expression in KSFM, no significant difference between the two ALI media conditions was reported (p= 0.2504, n=3, unpaired t-test).

(A)

(B)
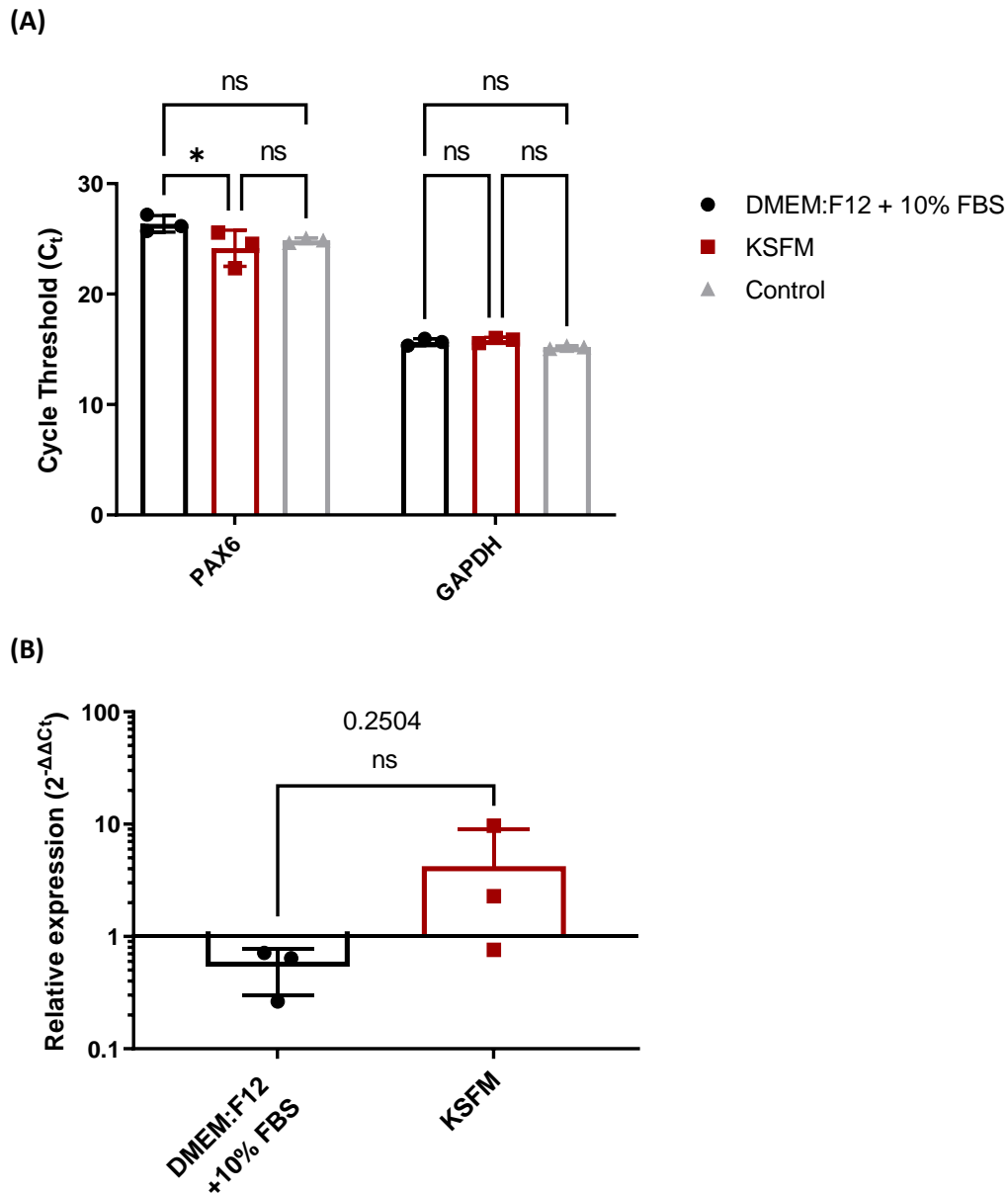
Figure 3-12. mRNA expression of PAX6 in response to different cell culture conditions.
(A) Cycle threshold values. HCE2s were cultured on transwell inserts for 6 days at ALI, using DMEM: F12 + 10% FBS or KSFM. A control condition using HCE2s cultured in T-75 flasks was included. These cells were cultured in KSFM under submerged culture conditions and were representative of an undifferentiated cell type. HCE2s were harvested and total RNA was extracted. RNA was then converted to cDNA so that mRNA expression levels could be determined by RT-qPCR. GAPDH was included as an endogenous control. Data represent mean values ± SD, n=3 for all conditions. Data was analysed using two-way ANOVA with Tukey's multiple comparisons test, *p ≤ 0.05, ns= not significant (p > 0.05).
(B) Relative expression of PAX6 in response to cell culture conditions. Data has been normalised using *GAPDH* expression and is shown relative to mRNA expression in undifferentiated HCE2 cells (=1). Data was analysed by unpaired t-test, ns= not significant.

3.4. Discussion

3.4.1. Summary of results

In this chapter, the development of an *in vitro* model of the human corneal epithelium has been presented. This model utilises the HCE2 human corneal epithelial cell line and transwell inserts were employed to culture HCE2 cells at an air-liquid interface. Optimisation of transwell culture conditions identified DMEM: F12 medium, supplemented with 10% FBS as the optimal medium condition for culturing differentiated HCE2 cells. The effect of altering length of culture at ALI was also investigated and a 6-day ALI culture period was selected for future work. Under these conditions, HCE2s formed multilayers possessing microvilli and paracellular permeability data indicated the formation of tight cell junctions, thus fulfilling my first aim for this chapter. To achieve my second aim, immunofluorescence staining and flow cytometry were used to quantify CD9 expression. CD9 tetraspanin was observed at HCE2 cell membranes and CD9 expression levels were comparable to CD9 expression in the HaCaT keratinocyte cell line used in previous studies (Ventress et al., 2016). Therefore, the HCE2 cell line represents a suitable model for investigating the anti-infective properties of CD9-derived peptides. To achieve my final aim, PAX6 mRNA expression was quantified by qPCR. PAX6 expression was detected under multiple cell culture conditions, thereby confirming retention of corneal epithelial cell identity in the HCE2 cell line.

3.4.2. CD9 expression

In **section 3.3.1,** the CD9 expression profile of the HCE2 cell line was investigated and microscopy revealed expression of CD9 at the plasma membrane. Flow cytometry was used to quantify CD9 expression under different culture conditions and coating media was reported to have no effect on CD9 expression, with similar MFI values reported for HCE2 cells cultured on uncoated plastic, fibronectin-coated plastic, and collagen-coated plastic. Therefore, CD9 expression does not need to be taken into consideration when selecting coating media conditions. Conversely, CD9 expression was altered in response to media conditions and a significant increase in CD9 expression was observed for HCE2 cells cultured in KSFM versus DMEM: F12. However, CD9 expression remained strongly detectable under all conditions and therefore both DMEM: F12 and KSFM media can be used to investigate CD9-related activity in the HCE2 cell line. Data collected for permeability studies (**section 3.3.2**), suggests epithelial barrier integrity is increased when HCE2 cells are cultured in DMEM: F12 + FBS compared to KSFM. Strong epithelial barrier integrity is a marker of cell differentiation and therefore differences in CD9 expression may be linked to differences in cell differentiation profile.

CD9 expression in corneal epithelial cells has been reported previously, using rat models of corneal development and wound healing (Watsky and Geisert, 2007). In this study, wounded adult corneas, control adult corneas and developing corneas from 0 to 20-day old pups, all demonstrated strong CD9 immunoreactivity and CD9 staining was strongest at the corneal surface. Primary corneal epithelial cells were also obtained, and *in vitro* models of the corneal epithelium were highly CD9 positive. I am not aware of any published data on the CD9 expression profile of differentiated versus undifferentiated human corneal epithelial cells. However, this has been investigated using human keratinocytes (Ventress et al., 2016) and in this study, a significant reduction in CD9 expression was observed for differentiated keratinocytes. This provides support for the hypothesis that differences in CD9 expression are linked to cell differentiation profile and CD9 expression may be reduced for HCE2 cells cultured in DMEM: F12 because these cells have begun to differentiate. However, this hypothesis cannot explain why CD9 expression levels in DMEM: F12 appear to be unaffected by FBS concentration, whereas the absence of FBS was associated with a dramatic decrease in epithelial barrier integrity during permeability studies (see **section 3.3.2**).

3.4.3. Optimisation of transwell culture conditions

The main focus of this chapter has been the development of an optimised protocol for culturing HCE2 cells on transwell inserts. Similar protocols have been published previously (Kahn et al., 1993, Toropainen et al., 2001, Hahne and Reichl, 2011), but there is much variation in the literature regarding choice of tissue culture medium and length of culture at ALI. Furthermore, some transwell models have described the use of different media conditions for submerged culture and culture at ALI (Kahn et al., 1993, Postnikoff et al., 2014). KSFM is the ATCC-recommended medium for HCE2 cell culture, and so this medium was used for submerged transwell culture of HCE2s throughout the project. In contrast, different media conditions were trialled for culture at ALI and DMEM: F12 was selected due to its popularity in other HCE models. DMEM: F12 is commonly supplemented with FBS but concentrations ranging from 2% (Postnikoff et al., 2014) to 15% (Verstraelen and Reichl, 2013) have been reported previously and therefore multiple FBS concentrations (0%, 2%, 5% and 10%) were trialled. The suitability of different transwell culture conditions was assessed by permeability assays, immunofluorescence staining, and Transmission Electron Microscopy (TEM) and markers of epithelial barrier integrity were used to guide model development.

Paracellular permeability studies revealed that FITC-Dextran can traverse HCE2 multilayers, but rate of traversal is significantly reduced compared to no cell conditions (**section 3.3.2**). The use of DMEM: F12 medium supplemented with 2%, 5% or 10% FBS was associated with the reduced paracellular

permeability of HCE2 multilayers (as compared to cells cultured in KSFM or DMEM: F12 +0% FBS) and largest reductions in permeability were observed on day 6 of culture at ALI. Permeability coefficients (P_{app}) were calculated using day 6 data and the DMEM: F12 +5% FBS condition, closely followed by DMEM: F12 +10% FBS, provided the lowest permeability coefficients, with P_{app} values of 1.46×10^{-12} cm s^{-1} and 1.55×10^{-12} cm s^{-1} respectively. Low permeability coefficients are indicative of tight junction formation and further support for this was provided by immunofluorescence staining results (**section 3.3.3**). Anti-occludin antibody staining of HCE2 multilayers yielded mixed results. Occludin expression was visible on day 8 of ALI for both KSFM and DMEM: F12 +10% FBS conditions, but occludin was not localised to cell membranes. In contrast, anti-ZO1 antibody staining revealed expression of ZO1 at cell membranes on days 4, 6 and 8 of ALI. ZO1 expression was increased in the presence of DMEM: F12 +10% FBS versus KSFM and day 6 was identified as the optimal cell culture timepoint due to high levels of ZO1-actin colocalisation. Day 6 HCE2 multilayers cultured in the presence of DMEM: F12 +10% FBS were visualised by TEM (**section 3.3.4**), and micrographs revealed the presence of 3-4 cell layers, possessing microvilli. Microvilli were visible at the outermost surface of HCE2 multilayers but were not observed within lower cell layers, suggesting HCE2 cells are able to differentiate into human corneal epithelial cell subsets, including terminally differentiated superficial corneal epithelial cells, which possess microvilli (Sridhar, 2018). Taken together, these data show that use of DMEM: F12 medium, containing FBS, is advantageous for culturing HCE2 multilayers at ALI and this medium should be selected over KSFM. The benefits of DMEM: F12 are dependent on its supplementation with FBS and increasing concentrations of FBS appear to be associated with improved epithelial barrier integrity.

Other groups have reported similar findings relating to FBS. Toropainen et al. reported an inability to culture their HCE cell line at FBS concentrations lower than 15% (Toropainen et al., 2001) and after trialling several serum-free culture conditions, Hahne & Reichl concluded that epithelial barrier integrity measurements were unsatisfactory compared to cultivation of cells in FBS supplemented media (Hahne and Reichl, 2011). In this study, epithelial barrier integrity was measured by Trans-Epithelial Electrical Resistance (TEER), where increasing TEER values correspond to improved barrier function (Srinivasan et al., 2015). TEER values less than 100 Ω cm^2 were reported for cells cultured in serum free DMEM: F12 or the Keratinocyte Medium (K-SFM, ScienCell), whereas TEER values as high as 5500 Ω cm^2 were recorded for cells cultured in serum-supplemented DMEM: F12 (Hahne and Reichl, 2011). Optimisation of serum concentration was conducted using 0.2% to 20% FBS and 15% was identified as the optimal FBS concentration. This group also conducted paracellular permeability studies using FITC-Dextran. However, a co-culture, hemicornea construct containing both human corneal epithelial cells and human corneal keratocytes was used. A permeability coefficient of $4.96 \pm 1.46 \times 10^{-8}$ cm s^{-1} was reported for the hemicornea, which is several magnitudes larger than the

permeability coefficient for my optimal transwell condition (1.46×10^{-12} cm s^{-1}) (**section 3.3.2**). Permeability coefficients of $1.67 \pm 0.43 \times 10^{-8}$ cm s^{-1} and $9.08 \pm 4.88 \times 10^{-8}$, were also reported for the *ex vivo* porcine cornea and rabbit cornea, respectively (Hahne and Reichl, 2011). Low permeability coefficients are associated with improved epithelial barrier function (Hubatsch et al., 2007) and therefore these findings suggest that my HCE2 transwell model possesses increased barrier function compared to the *in vitro* hemicornea model and *ex vivo* animal corneas. However, it should be noted that my experiments were carried out under static conditions, whereas corneal models used by Hahne & Reichl were agitated continuously, using an orbital shaker. The presence of an unstirred liquid layer has been shown to influence paracellular permeability and in the absence of agitation, permeability coefficents may be underestimated (Karlsson and Artursson, 1991, Hubatsch et al., 2007). Therefore, direct comparisons between studies cannot be made but low permeability coefficient values for the HCE2 transwell model are highly encouraging.

Other groups have also investigated expression of tight junction proteins, occludin and ZO1, in human corneal epithelial cells. Immunostaining of human corneas has confirmed the expression of occludin and ZO1 within the stratified corneal epithelium and these TJPs are predominantly expressed by superficial corneal epithelial cells (Ban et al., 2003). Differences in antibody staining were observed for occludin and ZO1, with ZO1 forming a continuous ring around cells whereas occludin expression is non-continuous, forming a dotted pattern. Various corneal epithelial cell lines have also been used to visualise TJP expression (Kimura et al., 2009, Hakkarainen et al., 2016), including use of the HCE2 cell line to visualise ZO1 (Nunez-Alvarez and Osborne, 2019). ZO1 was visualised at HCE2 cell membranes and anti-ZO1 antibody generated distinct rings around HCE2 cells. Although ZO1 was observed at cell membranes in my experiments (**section 3.3.3.2**), a distinct ring staining pattern was not observed and so antibody conditions may require further optimisation to reduce non-specific binding. It would be beneficial to repeat this work using different antibody conditions and/or an alternative antibody labelling technique such as immunoblotting.

I am not aware of any studies in which microscopy has been used to visualise occludin expression in HCE2 cells, but these cells have been used to perform immunoprecipitation experiments and authors identified the presence of ECAM-1/Claudin-1/Occludin tight junctional complexes in HCE-2 cell monolayers (Zhou et al., 2016). However, because immunoprecipitation reactions use whole cell extract, we cannot comment on the specific localisation of occludin within these cell monolayers. In my experiments, occludin was localised to HCE2 cell nuclei rather than cell membranes (**section 3.3.3.1**). This may represent a defect with the HCE2 cell line, or alternatively the selected time point (day 8 at ALI) may have been too late. During optimisation of transwell conditions, transwell inserts

were routinely inspected by light microscopy and deterioration of HCE2 monolayers was observed from day 8 onwards. Although cells still display barrier integrity at this time point (**section 3.3.2**), intracellular trafficking and protein synthesis may be disrupted.

There are various limitations associated with immunofluorescence staining data that must be acknowledged. Firstly, TJP expression was quantified by total cell fluorescence and this measurement is unable to distinguish between junctional and cytosolic proteins. Instead, it would have been more beneficial to use image profile scans to identify junctional peaks in fluorescence. Furthermore, there is a disconnect between immunofluorescence staining and TEM images. Anti-ZO1 staining suggests the formation of tight cell junctions, but these structures were not visible in TEM images. In contrast, clear tight junctions between corneal epithelial cells have been visualised by TEM previously (Seeber et al., 2008). It may be that these HCE cells were visualised at a higher magnification than my samples but this is difficult to confirm due to the absence of scale bars. Regardless, conclusions surrounding tight junction proteins should be made with caution.

3.4.4. PAX6 expression

In **section 3.3.5**, qPCR was used to investigate PAX6 expression in the HCE2 cell line and mRNA transcripts for the major PAX6 variant were detected under all conditions. PAX6 is an important regulator of corneal epithelial cell identity (Kitazawa et al., 2017) (see **section 3.1.3**) and so expression of PAX6 suggests the HCE2 cell line retains the key characteristics of a corneal epithelial cell. Interestingly, PAX6 expression does not appear to be influenced by ALI as there was no significant difference in C_t values for HCE2 cells cultured at ALI and HCE2 cells grown in submerged culture. I had previously speculated that PAX6 expression may be increased at ALI, as air lifting has been shown to promote differentiation of corneal epithelial cells (Greco et al., 2010, Toropainen et al., 2001) and PAX6 controls the expression of corneal specific differentiation markers, keratin 3 and keratin 12 (Kitazawa et al., 2017). However, this is a highly simplified view of cell differentiation and investigation of multiple regulatory pathways, e.g., the Notch signalling pathway (Xin et al., 2010), would likely be required to study corneal epithelial cell differentiation in a meaningful way. Furthermore, the basal expression of K3/K12 in the HCE2 cell line has not been investigated. It may be that these fibrous proteins are already highly expressed and remain relatively unaffected by changes in culture conditions. Another finding from the qPCR study was that choice of ALI culture medium appears to affect PAX6 expression. C_t values were significantly decreased in the presence of KSFM (as compared to DMEM: F12 +10% FBS), revealing increased expression of PAX6 under these conditions. PAX6 controls the expression of multiple corneal epithelial specific genes, including keratin 3, keratin 12,

clusterin and angiopoietin-Like 7 (Kitazawa et al., 2017) and therefore expression of these genes may also be increased under KSFM conditions. These genes have been linked to the structural integrity of the corneal epithelium (Kao et al., 1996), as well as the maintenance of an avascularised, transparent cornea (Nakamura et al., 2002, Toyono et al., 2015) and so this could have important implications for HCE2 function and morphology. However, it should be noted that the PAX6 primers used in this study were designed to recognise the major PAX6 mRNA variant. According to the National Center for Biotechnology Information (NCBI) website, there are at least 51 PAX6 mRNA variants and so this represents a major limitation of the study. Other PAX6 transcripts may have been present that were not amplified by my primers and furthermore, I cannot be certain that increased expression at the RNA level necessarily corresponds to increased expression at the protein level. Therefore, it would be beneficial to carry out additional immunoblot assays to study PAX6 expression at the protein-level.

3.4.5. Future work

Although I am satisfied with my existing HCE2 transwell model, there are a few additional experiments that could be carried out. Firstly, it would be interesting to trial DMEM: F12 +15% FBS in the HCE2 transwell model and monitor its effects on epithelial barrier integrity. Similarly, it could be beneficial to try supplementing the DMEM: F12 medium with DMSO, as this has been shown to improve epithelial barrier integrity in other HCE models (Hahne and Reichl, 2011). Furthermore, immunofluorescence staining studies could be repeated using different antibody conditions and/or alternative techniques such as immunoblotting. In terms of the PAX6 work, it would be useful to expand this study to include RNA extracted from HCE2 cells on days 0, 2 and 4 of ALI culture. Only day 6 is included in the present study and therefore I could be missing changes in PAX6 expression that occur soon after the introduction of ALI. The expression of genes controlled by PAX6 could also be investigated to see whether differences in PAX6 expression affect HCE2 profile at the protein level. For example, flow cytometry could be used to quantify K3/K12 proteins for HCE2 cells cultured at ALI in the presence of DMEM: F12 +10% FBS versus KSFM. PAX6 expression is significantly increased in the presence of KSFM and therefore if K3/K12 expression is upregulated by PAX6, I would expect to see an increase in their expression.

3.4.6. Conclusion

In summary, the HCE2 cell line is suitable for *in vitro* modelling of the human corneal epithelium and an optimised HCE2 transwell culture protocol has been developed by investigating epithelial barrier integrity under different culture conditions. This protocol involves culturing HCE2 cells at ALI for 6 days,

in the presence of DMEM: F12 +10% FBS and the optimised HCE2 transwell model will be used to study host-pathogen interactions in **Chapter 6**.

CHAPTER 4: CHARACTERISING BACTERIAL KERATITIS ISOLATES

4.1. Introduction

In this chapter, clinical bacterial keratitis isolates were characterised based on their biofilm-forming ability, antibiotic susceptibility, and possession of virulence factors. Due to my collaboration with the LV Prasad Eye Institute, I had access to a large number of clinical bacterial keratitis isolates. However, it would have been impractical and expensive to incorporate large numbers of isolates into corneal infection models and so characterisation studies were used to identify of isolates of particular interest. Since my corneal infection models are intended to test novel antimicrobial compounds, I was particularly interested in using clinical isolates with high levels of antibiotic resistance. Increased resistance to antibiotics may be conferred by biofilm formation and/or the possession of antibiotic resistance genes and therefore the biofilm forming activity and antibiotic susceptibility profiles of different isolates were compared. Genome sequencing data was also used to identify antibiotic resistance genes, as well as the presence or absence of certain virulence factor (VF) genes, as certain VFs have been associated with worse infection outcomes in bacterial keratitis (see **section 1.3.2.2**).

4.1.1. Biofilm formation assays

Biofilm formation was measured by crystal violet staining (O'Toole, 2011) and commonly used bacterial strains (i.e., SH1000, PAO1, PAOMW1, PA14) were used for optimisation as the biofilm forming activity of these strains has been characterised previously. *P. aeruginosa* strains, PAOMW1 and PA14, are both expected to exhibit defects in biofilm formation due to mutations affecting important regulatory pathways. PAOMW1 is a double mutant with mutations in the *lasI* and *rhlI* genes, which encode enzymes belonging to the Las and Rhl quorum sensing systems, respectively (Whiteley et al., 1999). Therefore, quorum sensing is significantly perturbed in PAOMW1 mutants (Cady et al., 2012) and since quorum sensing is critical in inducing biofilm formation (Davey and O'Toole, 2000), the biofilm-forming activity of PAOMW1 should also be disrupted. Unlike PAOMW1, PA14 is a wild-type *P. aeruginosa* strain, but it also exhibits aberrant biofilm forming activity due to a mutation in the *ladS* gene, which encodes the LadS sensor kinase (Mikkelsen et al., 2011). This sensor is an important component of the RetS/LadS/GacS signalling cascade, which is responsible for regulating various bacterial functions such as biofilm formation and bacterial virulence (Parkins et al., 2001). Therefore, the PA14 strain is also expected to display reduced biofilm forming activity. In addition to bacterial reference strains, six clinical MRSA isolates were included in initial biofilm formation experiments. These clinical isolates were used by previous laboratory members for skin infection models but their biofilm forming activity remained to be characterised. During biofilm formation studies, bacterial

strains were cultured in a biofilm promoting medium and then in the presence of basal DMEM: F12 tissue culture medium (no FBS). The appropriate biofilm promoting medium for *S. aureus* and *P. aeruginosa* was selected based on the literature (Zmantar et al., 2010, O'Toole, 2011), whereas DMEM: F12 was selected based on my results in **Chapter 3**. In this chapter, DMEM: F12 supplemented with 10% FBS was selected as the optimal medium condition for transwell culture of HCE2 cells and therefore, DMEM: F12 medium was selected for transwell infection work in **Chapter 6**. In order to limit the growth of bacteria, DMEM: F12 used in infection studies did not contain any FBS. Identical media conditions (i.e., DMEM: F12 no FBS) were used in biofilm formation studies to identify clinical isolates capable of forming biofilms in the transwell infection model.

4.1.2. Antimicrobial susceptibility testing

The European Committee on Antimicrobial Susceptibility Testing (EUCAST) (www.eucast.org), provides resources for standardised antimicrobial susceptibility testing and determination of Minimum Inhibitory Concentration (MIC) of antibiotics. Resources include the EUCAST broth microdilution protocol (EUCAST., 2021b), clinical MIC breakpoints for bacteria (EUCAST., 2021a) and Quality Control (QC) tables containing MIC values for QC strains (EUCAST., 2021c). The recommended QC strain for testing Staphylococcus species is *S. aureus* ATCC 29213 and for Pseudomonas species, *P. aeruginosa* ATCC 27853 is recommended. Both of these QC strains display susceptibility to a wide range of antibiotics and have been included as reference strains in MIC experiments. An adapted version of the EUCAST broth microdilution protocol was used and it should be noted that my bacterial isolates were cultured in LB, rather than the recommended Mueller Hinton (MH) broth and MIC values were determined using absorbance readings at 600 nm rather than by eye.

When designing MIC experiments, one or two antibiotics were selected from each of the five main classes of antibiotics. These included beta lactam antibiotics, which disrupt cell wall synthesis by targeting penicillin-binding proteins (i.e., flucloxacillin, meropenem, penicillin); fluoroquinolones, which disrupt DNA synthesis by inhibiting DNA gyrase and topoisomerase IV (i.e., ciprofloxacin); tetracyclines, which disrupt protein synthesis by targeting the 30S ribosomal subunit (i.e., doxycycline, tetracycline); aminoglycosides which disrupt protein synthesis by targeting the 30S ribosomal subunit (i.e., gentamicin, tobramycin); and macrolides, which disrupt protein synthesis by targeting the 50S ribosomal subunit (i.e., erythromycin) (Hutchings et al., 2019). For staphylococcal strains, chloramphenicol and the glycopeptide antibiotic, vancomycin, were also used. These antibiotics impair bacterial activity by targeting the 50S ribosomal subunit or disrupting cell wall synthesis, respectively. For *P. aeruginosa*, colistin was also selected and this polymyxin antibiotic exerts its

bactericidal effects via the disruption of cell membranes. The antibiotics selected for *S. aureus* strains were based on an MIC study conducted by a previous laboratory member but antibiotic choices for *P. aeruginosa* were guided by the literature. It was important to include a polymyxin such as colistin, as colistin is generally considered a "last-resort" antibiotic for *P. aeruginosa* infections (Kaye et al., 2016) and polymyxins have been deemed the most effective antibiotics for combatting multi-drug resistant *P. aeruginosa*. (El Solh and Alhajhusain, 2009, Lim et al., 2011). Similarly, meropenem, tobramycin and ciprofloxacin were also included as these antibiotics have been identified as the most effective agents for treating *P. aeruginosa* infections in the CF lung (Hill et al., 2005).

4.1.3. *P. aeruginosa* virulence factors

The *P. aeruginosa* genome encodes multiple proteases, which act as virulence factors. This has been discussed in more detail in **section 1.3.2.2**, but these proteases include: elastase A (LasA), elastase B (LasB), alkaline protease (AprA), type IV serine protease (PrpL) and *Pseudomonas aeruginosa* Small Protease (PASP) (Jurado-Martin et al., 2021). Of these proteases, PrpL and PASP in particular have been implicated in corneal virulence and mutations in these genes are associated with significant reductions in corneal pathology (O'Callaghan et al., 2019). *P. aeruginosa* also produces four exotoxins, ExoT, ExoY, ExoS and ExoU, which are secreted by the Type III secretion system. ExoS and ExoU are of particular interest as these effector proteins are generally mutually exclusive and can be used to classify *P. aeruginosa* isolates into one of two pathotypes (Hilliam et al., 2020); *exoS* +ve isolates are classified as invasive, whereas *exoU* +ve isolates are described as cytotoxic and there is evidence to suggest that the clinical features of bacterial keratitis may be influenced by pathotype. For example, as part of the Steroids for Corneal Ulcers Trial (SCUT), invasive isolates were associated with larger corneal ulcers and prolonged healing times (Borkar et al., 2013). However, patients that were infected with this pathotype also presented with better visual acuity at 3 months post-infection. Finally, another important *P. aeruginosa* virulence factor is the flagella, and this is predominantly composed of flagellin (FliC) (Haiko and Westerlund-Wikstrom, 2013). This protein is encoded by the *fliC* gene and different alleles (a-type and b-type *fliC*) have been reported. A previous study characterising *P. aeruginosa* isolates obtained from ulcerative keratitis patients, reported an increased prevalence of the a-type allele (Winstanley et al., 2005). This allele was present in 76% of isolates and authors speculated that the prevalence of this gene could be linked to differences in mucin binding specificity between a-type and b-type flagellin. In the aforementioned study, all isolates were collected in the UK whereas my *P. aeruginosa* isolates were obtained from keratitis patients in India. Therefore, I was interested to see if the same trend would be observed in my isolate population.

4.2. Aims

1. To identify clinical bacterial keratitis isolates with biofilm-forming activity for use in corneal biofilm infection models.

2. To identify clinical bacterial keratitis isolates which display high levels of antibiotic resistance, as determined by MIC testing and genome sequence analysis.

3. To determine the presence or absence of *P. aeruginosa* virulence factors of interest.

4.3. Results

4.3.1. Growth curves for laboratory strains and clinical isolates of Staphylococcus and *P. aeruginosa.*

Growth curves were plotted for laboratory strains and clinical isolates of Staphylococcus and *P. aeruginosa*, as determined by OD measurements at 600 nm (**Figure 4-1**). All bacterial strains demonstrated a similar growth pattern. This growth pattern was characterised by a short lag phase (approx. 1 hr) followed by an exponential growth phase (approx. 4-5 hrs), before bacterial growth plateaued, and the bacteria entered stationary phase. Final OD readings at 24 hrs were consistently higher for staphylococcal strains (3.97 ± 0.5) (**Figure 4-1A, C, E**), as compared to *P. aeruginosa* (2.86 ± 0.8) (**Figure 4-1B, D, E**), with staphylococcal strains demonstrating an increased doubling rate during the exponential growth phase. For *P. aeruginosa*, clinical isolates demonstrated a faster growth rate than laboratory strains and the final OD measurement for PA14 (1.08 ± 0.1) (**Figure 4-1B**) was much lower than that of other *P. aeruginosa* strains. For staphylococcal strains, final OD measurements and relative growth rates were similar for all strains. The bacterial growth rates for genetically modified bacteria, SH1000-GFP and PAO1-GFP, were unaffected by the possession of a Green Fluorescent Protein (GFP) tag (**Figure 4-1E**) and similar growth curves were observed for wild-type and GFP-tagged strains of SH1000 and PAO1 (**Figure 4-1A, B, E**).

(A)

SH1000 ■ MRSA1 ▲ MRSA2 ▼ MRSA3
◆ MRSA4 ○ MRSA5 ⊟ MRSA6

(B)

PAO1 strain 1 ■ PAO1 strain 2
▲ PAOMW1 ▼ PA14

(C)

● LVP10 ■ LVP11 ▲ LVP13

(D)

● LVP3 ■ LVP4 ▲ LVP5 ✚ LVP6

(E)

◆ SH1000-GFP ■ PAO1-GFP
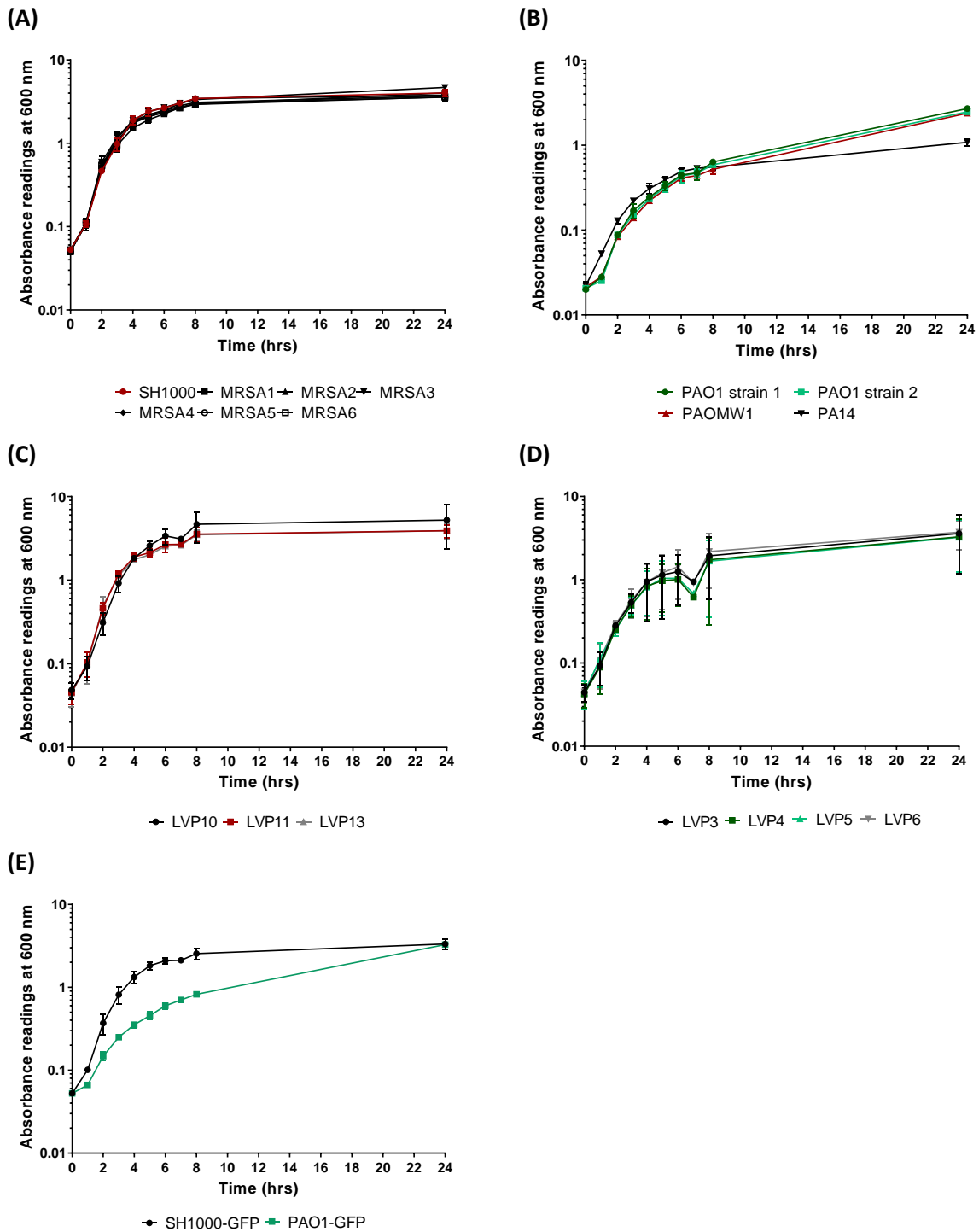
Figure 4-1. Bacterial growth curves.
Overnight cultures were prepared and diluted to an OD of 0.05 using LB. Growth of cultures was measured by absorbance at 600 nm. Absorbance readings were collected every hour for 8 hrs and a final measurement was taken at 24 hrs. Data represent mean ± SD for all strains. *(A) S. aureus* **laboratory strain, SH1000 and clinical skin isolates, MRSA 1-6** n=3 for all strains. **(B)** *P. aeruginosa* **laboratory strains (PAO1, PAOMW1, and PA14)** n=3 for all strains. **(C) Staphylococcal LVPEI clinical isolates (LVP10, 11 and 13)** n=3 for all strains. **(D***) P. aeruginosa* **LVPEI clinical isolates (LVP3-6)** n=3 for all strains. **(E) GFP tagged SH1000 and PAO1** n=2 for both strains.

4.3.2. *S. aureus* and *P. aeruginosa* test strains demonstrate biofilm-forming activity.

4.3.2.1. *S. aureus and P. aeruginosa* test strains form biofilms in the presence of biofilm-promoting media.

The biofilm-forming activity of the *S. aureus* laboratory strain, SH1000, and six clinical isolates of MRSA were measured by crystal violet staining assay in the presence of a biofilm promoting medium (**Figure 4-2**). Tryptone Soya Broth (TSB) supplemented with 0.5% glucose, was used as the biofilm promoting medium for staphylococcal strains. The constituents of bacterial biofilms are stained non-specifically by crystal violet and therefore absorbance readings provide a quantitative measure of biofilm mass. Compared to the medium only control (0.07 ± 0.02), SH1000 (2.69 ± 0.6), MRSA1 (1.23 ± 0.3), MRSA2 (1.37 ± 0.2), MRSA3 (1.15 ± 0.2), MRSA4 (1.69 ± 0.07), MRSA5 (1.10 ± 0.2) and MRSA6 (1.99 ± 0.2) were all associated with significant increases in absorbance ($p \leq 0.01$ in all cases), indicating the formation of bacterial biofilm. In the presence of TSB, *S. aureus* SH1000 was the strongest biofilm former and there was a significant increase in absorbance for this laboratory strain compared to all MRSA strains ($p = 0.0322$ for MRSA6, $p = 0.0010$ for MRSA4, $p \leq 0.0001$ for MRSA1, 2, 3 and 5, n=4, one-way ANOVA with Tukey's multiple comparisons test). Of the MRSA strains, MRSA6 exhibited the strongest biofilm-forming activity and there was a significant increase in absorbance for this isolate compared to MRSA1 ($p = 0.0182$), MRSA3 ($p = 0.0068$) and MRSA5 ($p = 0.0036$).

Crystal violet staining was repeated using *P. aeruginosa* laboratory strains and two biofilm promoting media were compared: (1) TSB medium and (2) M63 minimal medium supplemented with 0.4% arginine and 1 mM MgSO$_4$ (M63) (**Figure 4-3**). Under both TSB and M63 media conditions, a large increase in absorbance was observed for all *P. aeruginosa* strains, as compared to TSB (0.07 ± 0.02) or M63 (0.04 ± 0.003) media only controls, indicating the formation of bacterial biofilm. However, the extent of biofilm formation and the relative biofilm-forming activity of *P. aeruginosa* strains was affected by choice of biofilm promoting medium. Increased absorbance readings were observed in the presence of TSB versus M63 for all *P. aeruginosa* strains. The largest difference was observed for PAOMW1 (2.15 ± 0.2 versus 0.29 ± 0.04), followed by PA14 (2.70 ± 0.6 versus 0.87 ± 0.3) and PAO1 (0.76 ± 0.2 versus 0.50 ± 0.02). There was a trend towards increased biofilm formation by PA14 in the presence of both TSB and M63. However, the relative biofilm-forming ability of PAOMW1 differed largely between conditions. In the presence of TSB, PAOMW1 was the second strongest biofilm former and absorbance readings were approximately 3x higher than those of PAO1. In the presence of M63, PAOMW1 was the weakest biofilm former and absorbance readings were 1.7x lower than those of PAO1. Since PAOMW1 was intended to act as a negative control for biofilm formation, M63 was selected for future biofilm formation studies. Due to low absorbance readings for M63, it was

hypothesised that *P. aeruginosa* biofilms were disrupted by the PBS wash step in the crystal violet staining protocol. A wash study was performed (**Figure 4-4**) and increased absorbance readings were recorded for all *P. aeruginosa* strains following removal of the PBS wash step. However, the relative pattern of results remained the same, indicating that loosely adherent bacteria and not biofilm structures were removed by the PBS wash step. An additional PAO1 strain (PAO1 strain 2) was included to determine whether the low biofilm-forming activity of the original PAO1 strain (PAO1 strain 1) was linked to a defect in this strain. Highly similar readings were recorded for both PAO1 strains and therefore this theory was rejected.
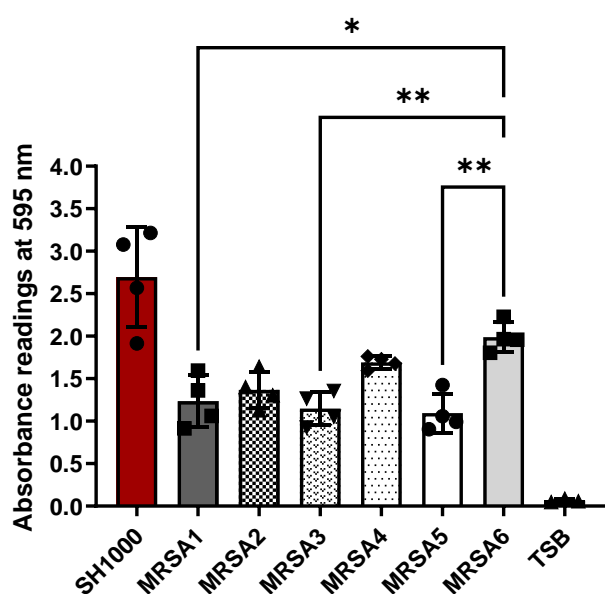
Figure 4-2. Biofilm formation by *S. aureus* test strains in the presence of TSB biofilm promoting medium.
The laboratory strain, SH1000 and 6 clinical skin isolates of MRSA were cultured in TSB + 0.5% glucose at 37°C for 22 hrs. After 22 hrs, bacteria were washed, fixed and stained with 0.1% crystal violet. Biofilm formation was measured by absorbance at 595 nm, using undiluted samples. A medium only control (TSB) was included. Data represent mean ± SD, n=4 for all strains. Data was analysed using one-way ANOVA with Tukey's multiple comparisons test, *p ≤ 0.05, **p ≤ 0.01, ***p ≤ 0.001, ****p ≤ 0.0001. A significant difference in biofilm formation was observed for SH1000 and all MRSA strains. MRSA1-3 (****), MRSA4 (***), MRSA5 (****), MRSA6 (*).
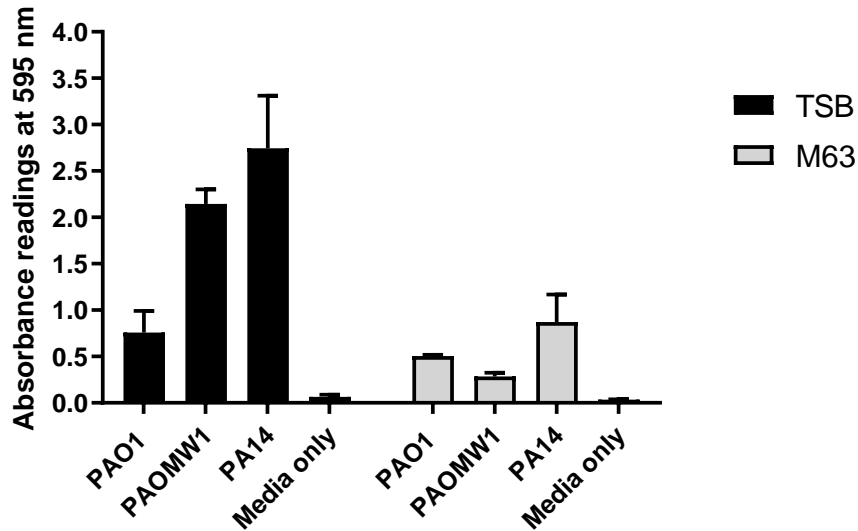
Figure 4-3. Biofilm formation by *P. aeruginosa* laboratory strains in the presence of TSB or M63 biofilm promoting media.

P. aeruginosa PAO1, PAOMW1 and PA14 were cultured using either TSB+ 0.5% glucose or M63 +0.4% arginine +1mM $MgSO_4$. After 22 hrs culture at 37°C, bacteria were washed, fixed and stained with 0.1% crystal violet. Biofilm formation was measured by absorbance at 595 nm, using undiluted samples. TSB and M63 media only controls were included. Data represent mean ± SD, n=3 for TSB (except PA14, n=2), n=2 for M63.
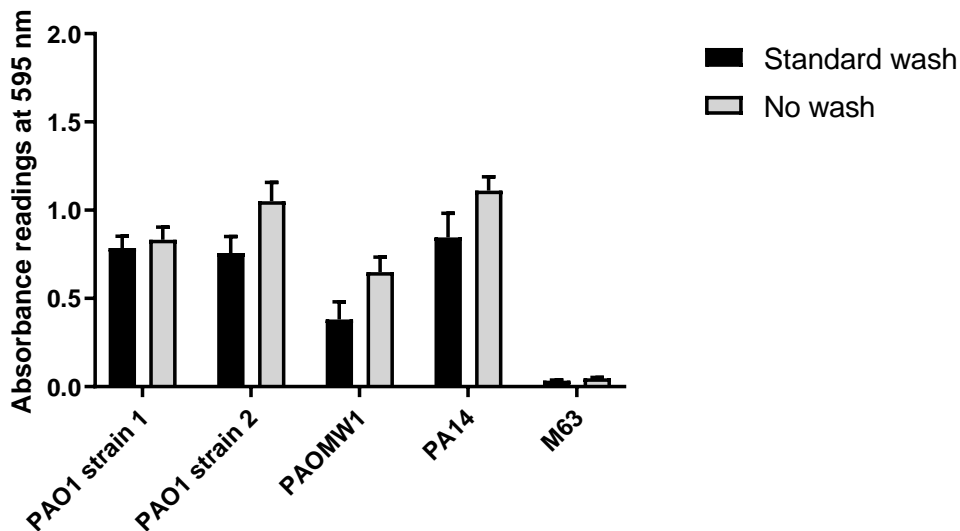
Figure 4-4. Assessing the effect of the PBS wash step during crystal violet staining.

During the standard crystal violet staining protocol, bacteria are washed 1x with PBS to remove non-adherent bacteria. To assess the effect of the wash step, *P. aeruginosa* laboratory strains were cultured in M63 +0.4% arginine +1mM $MgSO_4$ at 37°C for 22 hrs. After 22 hrs, bacteria either were washed 1x with PBS (standard wash) or not washed (no wash). Bacteria were stained using 0.1% crystal violet and biofilm formation was measured by absorbance at 595 nm. A medium only control (M63) was included. Data represent mean ±SD; n=1; 8 technical replicates were performed.

4.3.2.2. *S. aureus* and *P. aeruginosa* test strains form biofilms in the presence of DMEM: F12 tissue culture medium.

The biofilm-forming activity of the *S. aureus* laboratory strain, SH1000, and six clinical isolates of MRSA were measured by crystal violet staining assay in the presence of DMEM: F12 tissue culture medium (**Figure 4-5**). Two crystal violet concentrations were trialled, 0.1% (original concentration) (**Figure 4-5A**) and 0.01% (**Figure 4-5B**). All staphylococcal strains demonstrated biofilm forming activity and similar results were observed for both crystal violet concentrations (**Figure 4-5**). However, the use of 0.01% crystal violet was associated with reduced variation and therefore this concentration was selected for future experiments. Unlike previous experiments involving TSB, there was no significant difference in absorbance readings between staphylococcal strains. However, absorbance readings for SH1000 (0.63 ± 0.05), MRSA1 (0.69 ± 0.10), MRSA2 (0.46 ± 0.05), MRSA3 (0.45 ± 0.17), MRSA4 (0.54 ± 0.02), MRSA5 (0.46 ± 0.05) and MRSA6 (0.49 ± 0.18) were significantly increased compared to the DMEM: F12 medium only control (0.04 ± 0.03) ($p \leq 0.01$ in all cases, n=3, one-way ANOVA with Tukey's multiple comparisons) (**Figure 4-5B**).

Similar findings were observed for *P. aeruginosa*. All *P. aeruginosa* laboratory strains demonstrated biofilm forming activity in the presence of DMEM: F12 tissue culture medium (**Figure 4-6**) and the variability of results was reduced in the presence of 0.01% crystal violet (**Figure 4-6B**). There was no significant difference in absorbance readings between *P. aeruginosa* strains ($p > 0.05$ in all cases) but average absorbance values for PAO1 strain 1 (0.47 ± 0.09), PAO1 strain 2 (0.59 ± 0.04), PAOMW1 (0.80 ± 0.26) and PA14 (0.69 ± 0.19) were significantly increased compared to the DMEM: F12 medium only control (0.04 ± 0.03) ($p \leq 0.05$ in all cases, n=3, one-way ANOVA with Tukey's multiple comparisons) (**Figure 4-6B**). In contrast to previous experiments involving M63, there was a trend towards increased biofilm formation for PAOMW1 in the presence of DMEM: F12.

(A)

(B)
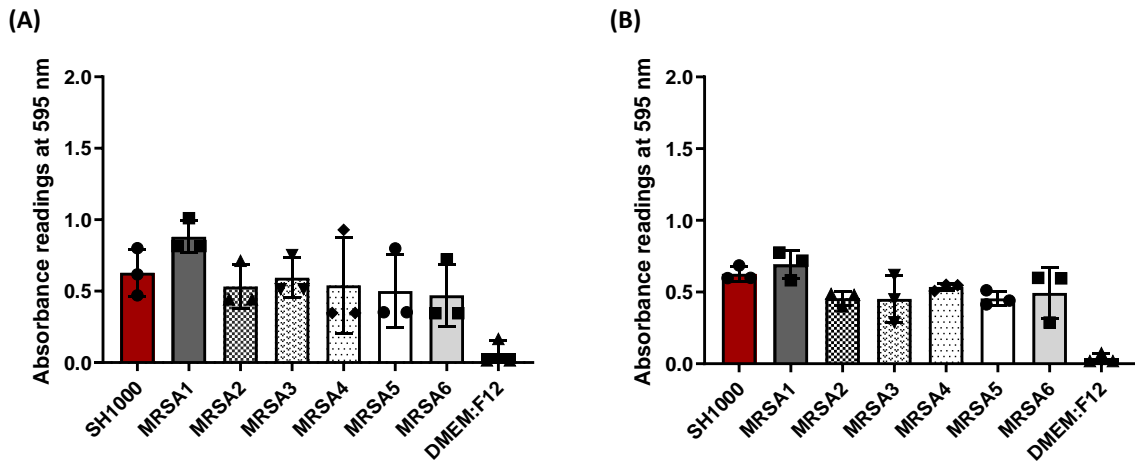
Figure 4-5. Biofilm formation by *S. aureus* test strains in the presence of DMEM: F12 tissue culture medium.
(A) 0.1% crystal violet (B) 0.01% crystal violet. The laboratory strain, SH1000 and 6 clinical skin isolates of MRSA were cultured in basal DMEM: F12 (no FBS) at 37°C for 22 hrs. After 22 hrs, bacteria were washed, fixed and stained with crystal violet at two different concentrations. Biofilm formation was measured by absorbance at 595 nm, using undiluted samples. A medium only control (DMEM: F12) was included. Data represent mean ± SD, n=3.

(A)

(B)
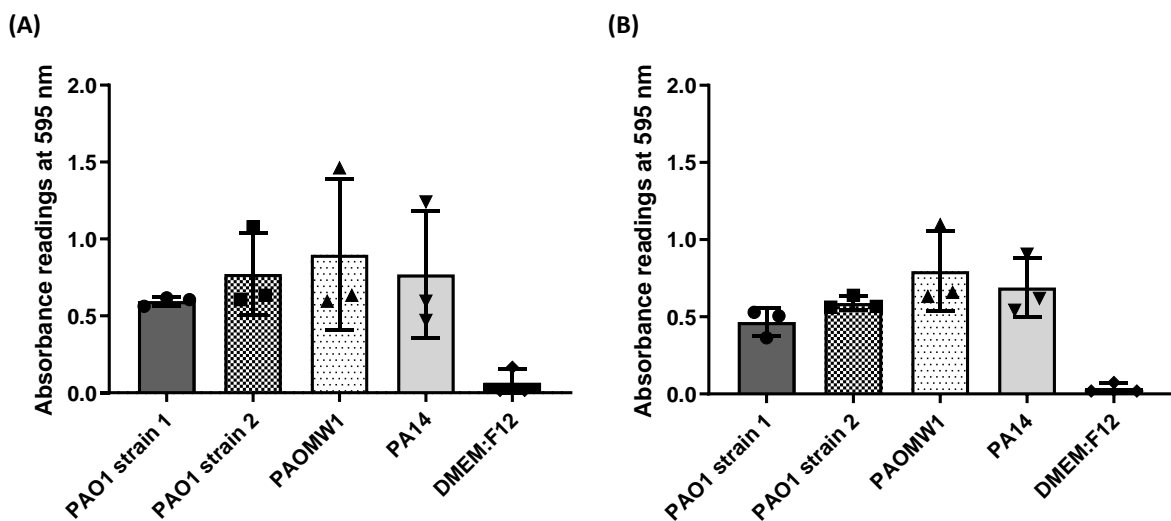
Figure 4-6. Biofilm formation by *P. aeruginosa* laboratory strains in the presence of DMEM: F12 tissue culture medium.
(A) 0.1% crystal violet (B) 0.01% crystal violet. *P. aeruginosa* PAO1, PAOMW1 and PA14 were cultured in basal DMEM: F12 (no FBS) at 37°C for 22 hrs. After 22 hrs, bacteria were washed, fixed and stained with crystal violet at two different concentrations. Biofilm formation was measured by absorbance at 595 nm, using undiluted samples. A medium only control (DMEM: F12) was included. Data represent mean ± SD, n=3.

4.3.2.3. The use of a biofilm-promoting media versus DMEM: F12 tissue culture medium has differing effects on biofilm formation in *S. aureus* and *P. aeruginosa* test strains.

The extent of biofilm formation, as measured by absorbance, was compared for bacterial strains grown in a biofilm promoting medium, and in DMEM: F12 tissue culture medium (**Figure 4-7**). The use of TSB versus DMEM: F12 was associated with a significant increase in biofilm formation for all staphylococcal test strains ($p \leq 0.05$ in all cases), with the exception of MRSA1 ($p = 0.4585$, n=3, two-way ANOVA with Šidák's multiple comparisons test) (**Figure 4-7A**). In contrast, differences in biofilm formation were minimal for *P. aeruginosa* strains cultured in M63 versus DMEM: F12 medium (**Figure 4-7B**). There was a trend towards increased biofilm formation for PAOMW1 in the presence DMEM: F12, whereas absorbance readings for PAO1 and PA14 remained similar under different media conditions. However, it should be noted that only two biological repeats were performed for M63.

Absorbance readings for staphylococcal strains consistently exceeded 1.0 in the presence of TSB. A measurement of 1.0 represents the upper limit for accurately measuring absorbance on a standard spectrophotometer and so serial dilutions were used to check the accuracy of the Varioskan Lux plate reader (**Figure 4-8**). The Varioskan displayed a reasonable degree of accuracy for absorbance readings taken between 1.0 and 4.0 but there was a reduction in accuracy compared to readings taken below 1.0. Therefore, a two-fold dilution step was incorporated into the crystal violet staining protocol in later experiments to ensure absorbance readings were below 1.0.

(A)

(B)
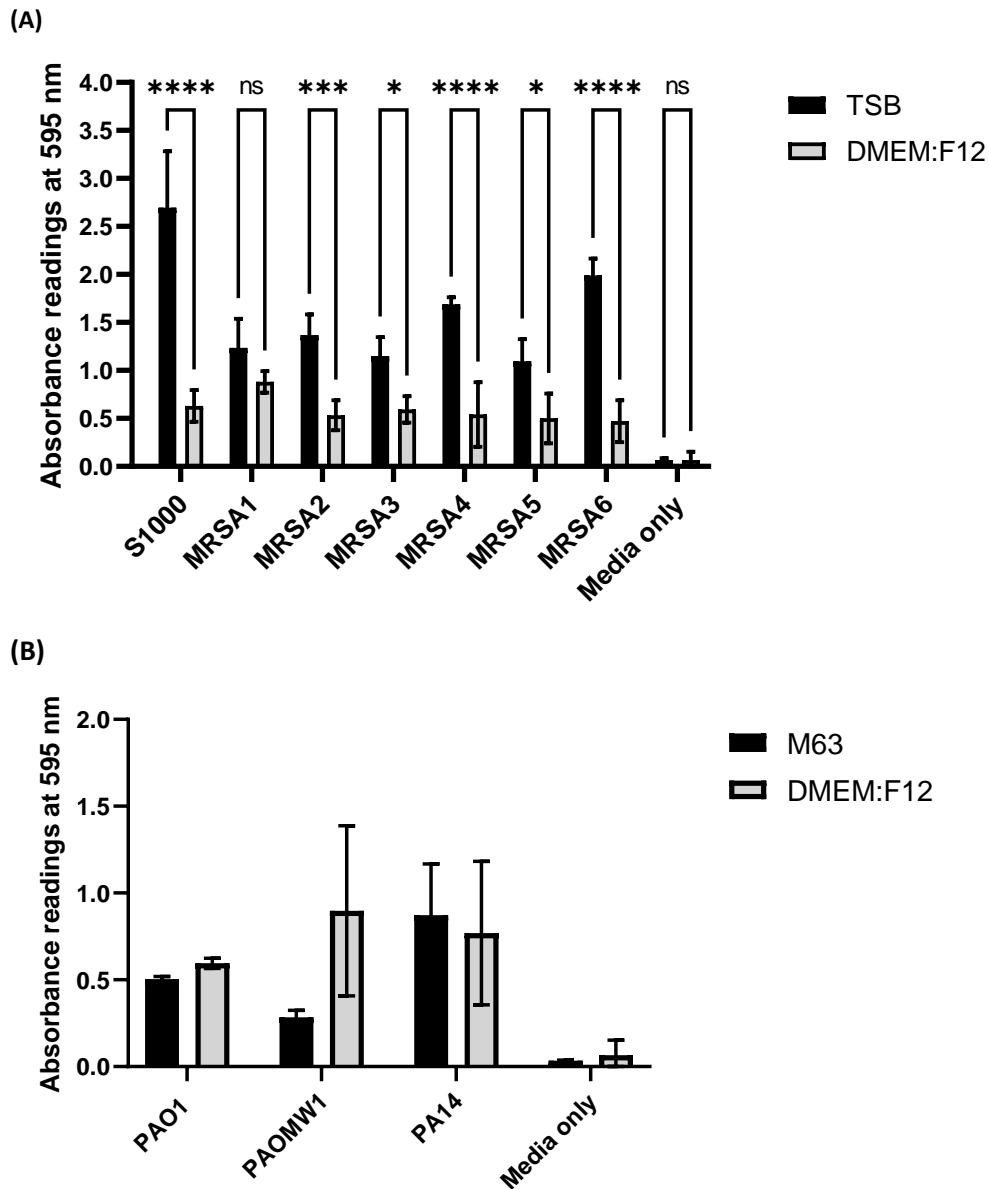
Figure 4-7. A comparison of biofilm formation data for *S. aureus*/*P. aeruginosa* laboratory strains and MRSA clinical isolates in the presence of a biofilm promoting medium versus DMEM: F12 tissue culture medium. Data represent mean ± SD. Data was analysed using two-way ANOVA with Šidák's multiple comparisons test, *p ≤ 0.05, ***p ≤ 0.001, ****p ≤ 0.0001 **(A) *S. aureus*** n=4 for TSB, n=3 for DMEM: F12. **(B) *P. aeruginosa*** n=2 for M63, n=3 for DMEM: F12.
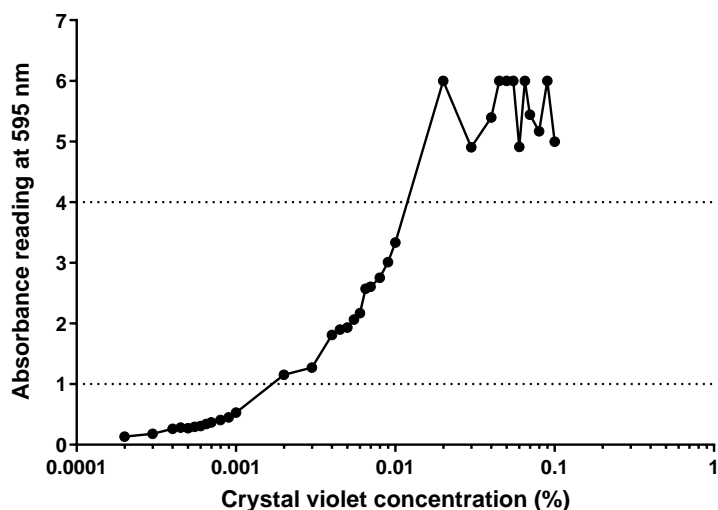
Figure 4-8. Assessing the accuracy of the Varioskan Lux plate reader.
Crystal violet was prepared at multiple concentrations by serial dilution of stock solutions. Twelve stock solutions were prepared, ranging from 0.1% to 0.02%. Absorbance was measured at 595 nm and plotted against crystal violet concentration. The dotted line at 4.0 represents the point at which the Varioskan Lux highlights absorbance readings as inaccurate. The dotted line at 1.0 represents the upper limit for accurately measuring absorbance on a standard spectrophotometer. Data represent mean values, n=1.

4.3.3. Clinical isolates obtained from bacterial keratitis patients demonstrate biofilm-forming activity.

4.3.3.1. Clinical isolates obtained from bacterial keratitis patients form biofilms in the presence of biofilm-promoting media.

The biofilm-forming activity of staphylococcal isolates obtained from bacterial keratitis patients was measured by crystal violet staining assay (**Figure 4-9**). The biofilm-promoting medium, TSB, was used. A significant increase in absorbance was observed for LVP10 (0.94 ± 0.06), LVP11 (0.83 ± 0.06) and LVP13 (0.68 ± 0.07), as compared to the medium only control (0.04 ± 0.03), indicating the formation of bacterial biofilm (p ≤ 0.0001 in all cases). Of the three staphylococcal isolates, *S. haemolyticus* LVP10 displayed the greatest biofilm-forming activity and absorbance readings were significantly increased compared to *S. aureus* LVP13 (p= 0.0031, n=3, one-way ANOVA with Tukey's multiple comparisons test).

Clinical isolates of *P. aeruginosa* also demonstrated biofilm forming activity in the presence of a biofilm-promoting medium (**Figure 4-10**). *P. aeruginosa* strains were grown using M63 medium and average absorbance readings for LVP3 (0.62 ± 0.21), LVP4 (1.06 ± 0.25), LVP5 (1.17 ± 0.21) and LVP6 (0.80 ± 0.15) were significantly increased compared to the M63 medium only control (0.02 ± 0.01) (p ≤ 0.01 in all cases). Of the four *P. aeruginosa* isolates, LVP4 and LVP5 were the strongest biofilm

108

formers and absorbance readings were significantly increased compared to *P. aeruginosa* LVP3 (p= 0.0287 for LVP4, p= 0.0061 for LVP5, n=4, one-way ANOVA with Tukey's multiple comparisons test).
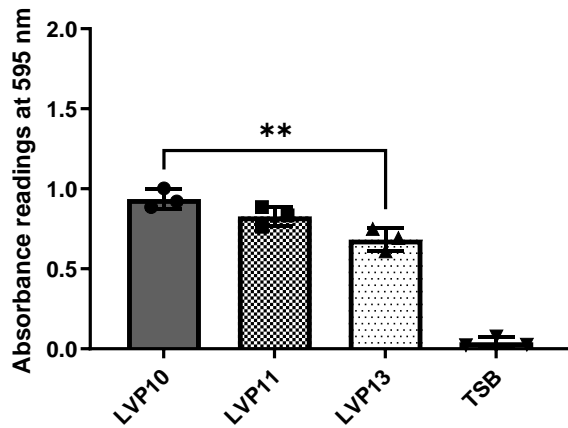
Figure 4-9. Biofilm formation by staphylococcal LVPEI clinical isolates in the presence of TSB biofilm promoting medium.
Clinical isolates of *S. haemolyticus* (LVP10) and *S. aureus* (LVP11 and LVP13) were cultured in TSB + 0.5% glucose at 37°C for 22 hrs. After 22 hrs, bacteria were washed, fixed and stained with 0.01% crystal violet. Biofilm formation was measured by absorbance at 595 nm, using samples diluted 2-fold in DMSO. A medium only control (TSB) was included. Data represent mean ± SD, n=3. Data was analysed using one-way ANOVA with Tukey's multiple comparisons test, **p ≤ 0.01.
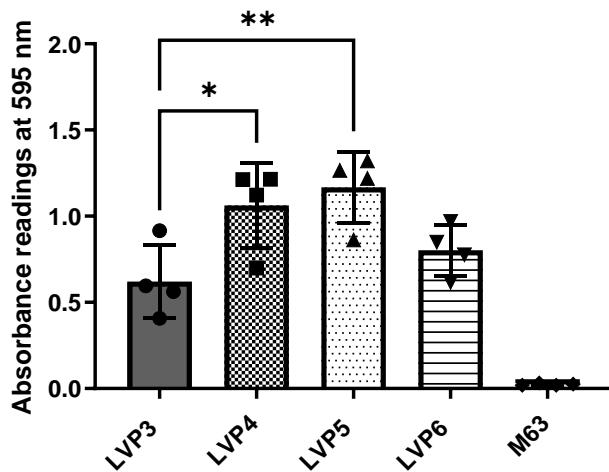
Figure 4-10. Biofilm formation by LVPEI clinical isolates of *P. aeruginosa* in the presence of M63 biofilm promoting medium.
Clinical isolates of *P. aeruginosa* (LVP3-6) were cultured in M63 +0.4% arginine +1mM $MgSO_4$ at 37°C for 22 hrs. After 22 hrs, bacteria were washed, fixed and stained with 0.01% crystal violet. Biofilm formation was measured by absorbance at 595 nm, using samples diluted 2-fold in DMSO. A medium only control (M63) was included. Data represent mean ± SD, n=4. Data was analysed using one-way ANOVA with Tukey's multiple comparisons test, *p ≤ 0.05, **p ≤ 0.01.

4.3.3.2. Clinical isolates obtained from bacterial keratitis patients form biofilms in the presence of DMEM: F12 tissue culture medium.

The biofilm-forming activity of staphylococcal isolates obtained from bacterial keratitis patients was measured by crystal violet staining assay in the presence of DMEM: F12 tissue culture medium (**Figure 4-11**). A significant increase in absorbance was observed for LVP10 (0.93 ± 0.14), LVP11 (0.77 ± 0.17) and LVP13 (0.96 ± 0.08), as compared to the medium only control (0.07 ± 0.03), indicating the formation of bacterial biofilm (p ≤ 0.001 in all cases). Unlike previous experiments involving TSB, there was no significant difference in absorbance readings between staphylococcal strains (p > 0.05 in all cases, n=3, one-way ANOVA with Tukey's multiple comparisons test).

Clinical isolates of *P. aeruginosa* also demonstrated biofilm forming activity in the presence of DMEM: F12 tissue culture medium (**Figure 4-12**). Average absorbance readings for LVP3 (0.51 ± 0.05), LVP4 (0.52 ± 0.06), LVP5 (0.59 ± 0.11) and LVP6 (1.25 ± 0.60) were increased compared to the M63 medium only control (0.07 ± 0.03). However, a significant increase in absorbance compared to the DMEM: F12 control was only observed for LVP6 (p= 0.0026). A significant increase in absorbance was also observed for LVP6 as compared to LVP3 (p= 0.0489) and there was a trend towards increased biofilm formation by LVP6 as compared to LVP4 (p= 0.0551, n=3, one-way ANOVA with Tukey's multiple comparisons test).
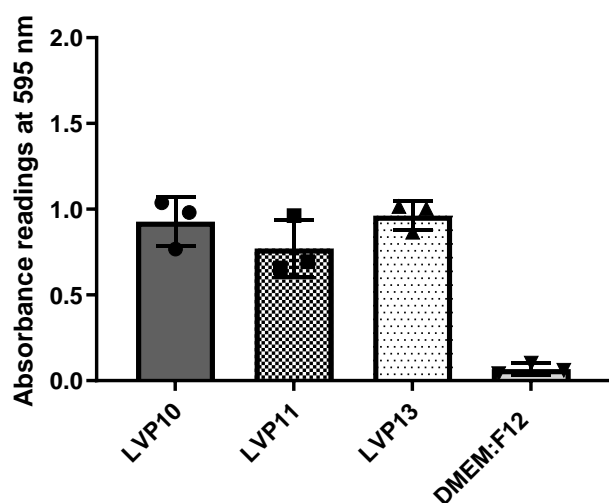
Figure 4-11. Biofilm formation by staphylococcal LVPEI clinical isolates in the presence of DMEM: F12 tissue culture medium.
Clinical isolates of *S. haemolyticus* (LVP10) and *S. aureus* (LVP11 and 13) were cultured in basal DMEM: F12 (no FBS) for 22 hrs. After 22 hrs, bacteria were washed, fixed and stained with 0.01% crystal violet. Biofilm formation was measured by absorbance at 595 nm, using samples diluted 2-fold in DMSO. A medium only control (DMEM: F12) was included. Data represent mean ± SD, n=3. Data was analysed using one-way ANOVA with Tukey's multiple comparisons test.
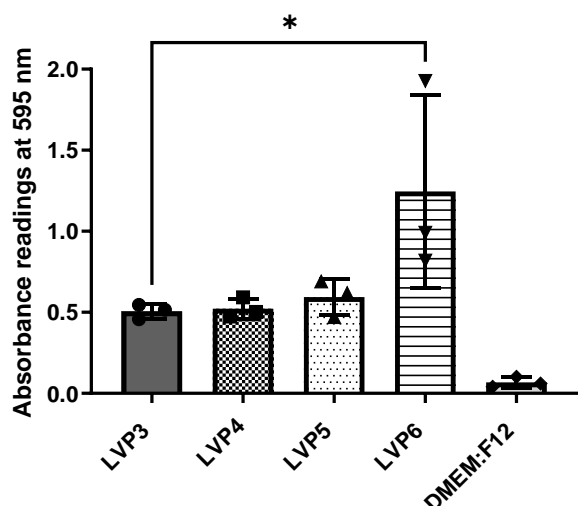
Figure 4-12. Biofilm formation by LVPEI clinical isolates of *P. aeruginosa* in the presence of DMEM: F12 tissue culture medium.

Clinical isolates of *P. aeruginosa* (LVP3-6) were cultured in basal DMEM: F12 (no FBS) for 22 hrs. After 22 hrs, bacteria were washed, fixed and stained with 0.01% crystal violet. Biofilm formation was measured by absorbance at 595 nm, using samples diluted 2-fold in DMSO. A medium only control (DMEM: F12) was included. Data represent mean ± SD, n=3. Data was analysed using one-way ANOVA with Tukey's multiple comparisons test, *p ≤ 0.05.

4.3.3.3. Differences in biofilm formation between biofilm promoting media and DMEM: F12 tissue culture medium are strain specific.

Absorbance readings from crystal violet staining assays were compared for LVPEI clinical isolates grown in a biofilm promoting media (i.e., TSB or M63 media) and DMEM: F12 tissue culture medium (**Figure 4-13**). For staphylococcal isolates (**Figure 4-13A**), there was no significant difference in absorbance readings for *S. haemolyticus* LVP10 or *S. aureus* LVP11, between biofilm promoting and tissue culture conditions (p > 0.05 for both isolates). However, absorbance readings for *S. aureus* LVP13 were significantly increased in the presence of DMEM: F12 compared to TSB medium (p=0.0084, n=3, two-way ANOVA with Šidák's multiple comparisons test). For *P. aeruginosa* isolates (**Figure 4-13B**), absorbance readings were unaffected by media conditions for *P. aeruginosa* LVP3 and LVP6 (p > 0.05 for both isolates). In contrast, absorbance readings were significantly increased for *P. aeruginosa* LVP4 and LVP5 in the presence of M63, as compared to DMEM: F12 (p= 0.0214 for LVP4, p= 0.0131 for LVP5, n=3, two-way ANOVA with Šidák's multiple comparisons test).

(A)

(B)
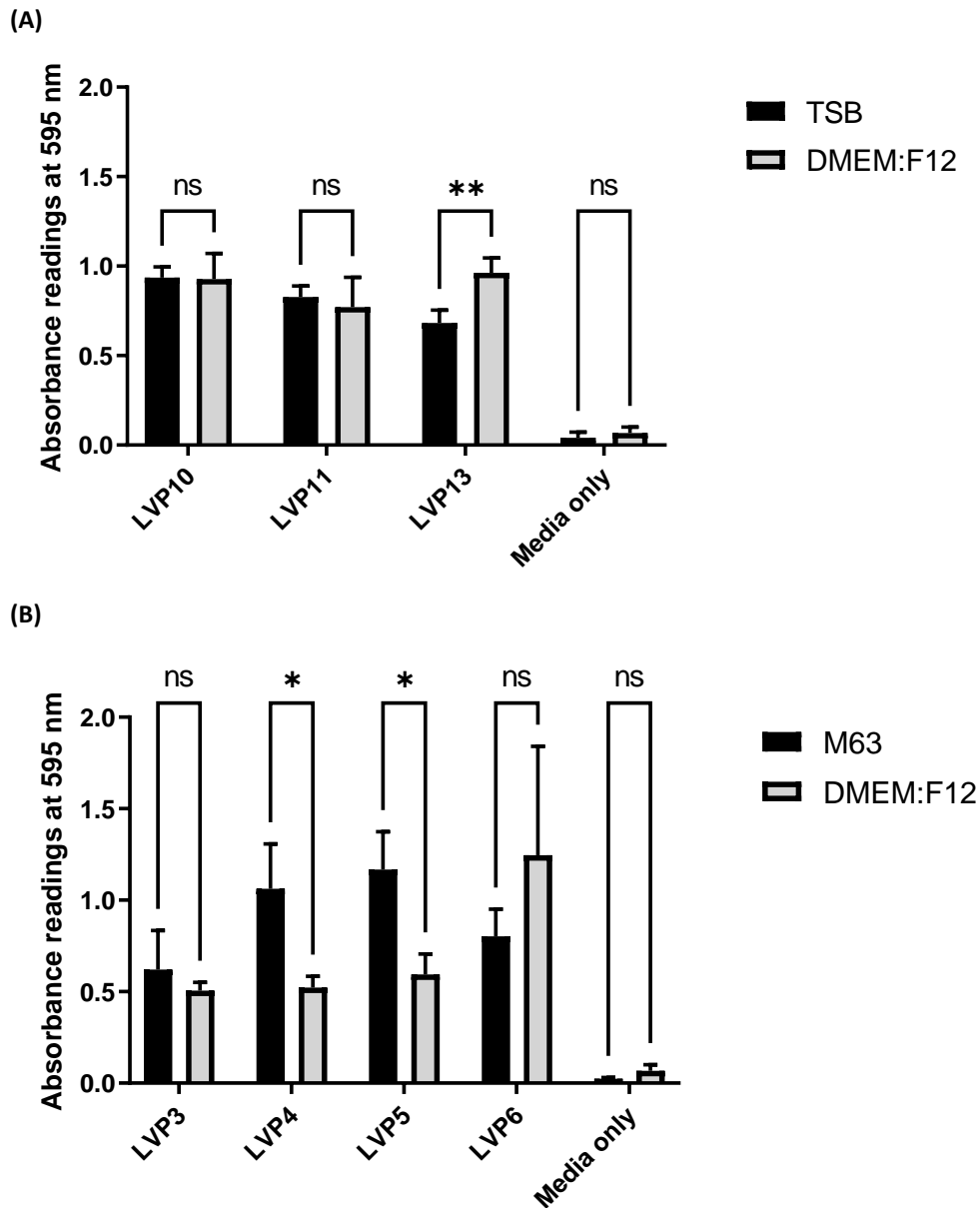
Figure 4-13. A comparison of biofilm formation data for LVPEI staphylococcal/*P. aeruginosa* clinical isolates in the presence of a biofilm promoting media versus DMEM: F12 tissue culture medium.

Data represent mean ± SD. Data was analysed using two-way ANOVA with Šidák's multiple comparisons test, *$p \leq 0.05$, **$p \leq 0.01$, ns= not significant. **(A) Staphylococcal strains** n=3 for all conditions **(B)** *P. aeruginosa* n=4 for M63, n= 3 for DMEM: F12.

112

4.3.3.4. Differences in biofilm formation by LVPEI clinical isolates are not caused by differences in growth rate.

Absorbance readings were collected for LVPEI isolates directly after 22 hr incubation in DMEM: F12 and following crystal violet staining (**Figure 4-14**). Initial absorbance readings provided a measure of bacterial growth, whereas absorbance readings collected after crystal violet staining provided a quantitative measure of biofilm mass. The pattern of absorbance readings differed between measurements, indicating that the extent of biofilm formation is not directly linked to bacterial growth rate. For instance, LVP6 demonstrated the strongest biofilm forming activity (1.41 ± 0.06) but presented with only the fourth largest absorbance reading before crystal violet staining (0.94 ± 0.02). LVP13 was the second strongest biofilm forming strain (0.98 ± 0.13) but provided the lowest initial absorbance reading (0.38 ± 0.03).
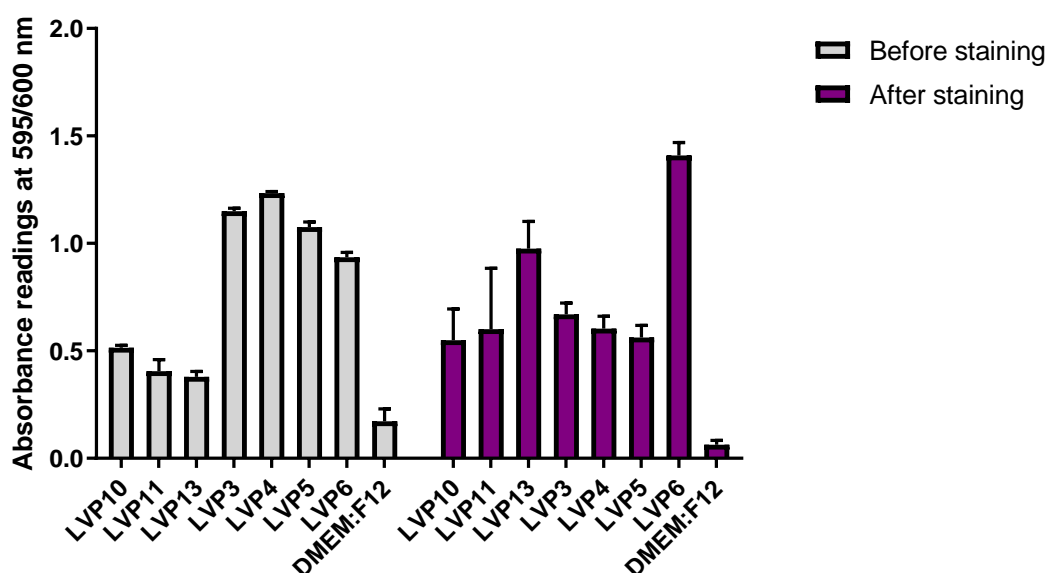
Figure 4-14. A comparison of bacterial growth and biofilm formation in crystal violet staining assays.
LVPEI clinical isolates were cultured in basal DMEM: F12 (no FBS) for 22 hrs. After 22 hrs, bacterial growth was measured by absorbance at 600 nm (before staining). Bacteria were washed, fixed and stained with 0.01% crystal violet. Biofilm formation was measured by absorbance at 595 nm (after staining). Data represent mean ± SD, n=2.

4.3.4. The adapted EUCAST broth microdilution protocol can be used to determine the antibiotic susceptibility of clinical bacterial keratitis isolates.

4.3.4.1. Clinical staphylococcal isolates display varying susceptibilities to antibiotics.

The growth of clinical staphylococcal isolates in the presence of nine different antibiotics was measured using absorbance (**Figure 4-15**). The four clinical staphylococcal strains (LVP10, LVP11, LVP13, NGH Sa) and two *S. aureus* reference strains (SH1000, ATCC 29213) demonstrated susceptibility to flucloxacillin (**C**), tetracycline (**D**), doxycycline (**E**), vancomycin (**F**), gentamicin (**G**) and chloramphenicol (**H**) antibiotics, as demonstrated by absorbance readings ≤ 0.01. Under most antibiotic conditions, a gradual decrease in absorbance was observed with increasing antibiotic concentration before the MIC was reached (**C**, **D**, **E**, **G**, **and H**). In contrast, a sudden decrease in absorbance was observed for vancomycin at the MIC (**F**). The majority of strains demonstrated susceptibility to erythromycin (**A**) but the susceptibility of LVP13 was undetermined due to a lack of data at high concentrations (n=1 for 64 and 128 mg/L). One biological replicate showed erythromycin susceptibility at 32 mg/L whereas a later replicate demonstrated growth of bacteria at 64 and 128 mg/L. Therefore, an MIC of > 32 mg/L has been assigned for LVP13 (**Table 4-1**). All strains apart from SH1000 were resistant to penicillin at the antibiotic concentrations tested (**Figure 4-15B**). For ciprofloxacin (**I**), coagulase negative *S. aureus* (NGH Sa) and *S. aureus* reference strains demonstrated antibiotic susceptibility at low concentrations of ciprofloxacin. In contrast, LVP10 and LVP13 remained resistant to ciprofloxacin until the maximum antibiotic concentration, 256 mg/L, was reached. LVP11 remained resistant to ciprofloxacin at this concentration. A reduced growth rate was observed for coagulase negative *S. aureus* (NGH Sa) compared to other staphylococcal strains, as demonstrated by reduced absorbance readings at low concentrations of antibiotic (**Figure 4-15**). For example, in the presence of penicillin, absorbance readings for LVP11 and LVP13 were approximately 3x higher than absorbance readings for coagulase negative *S. aureus* (**B**).

The Minimum Inhibitory Concentration (MIC) of antibiotic has been defined as the lowest concentration for which absorbance readings were predominantly ≤ 0.01. MIC values for clinical staphylococcal isolates are summarised in **Table 4-1**. MIC values for the SH1000 laboratory strain were always less than or equal to the MIC value for clinical isolates, revealing an increased susceptibility to antibiotics. The only exception was chloramphenicol, where a relatively high MIC was reported for SH1000 (128 mg/L) as compared to clinical isolates (16 to 64 mg/L). The most effective antibiotic against staphylococcal strains was vancomycin, as measured by low MIC values for all strains. Doxycycline was also a highly effective antibiotic and low MIC values were recorded for all strains apart from coagulase negative *S. aureus* (64 mg/L). In contrast, penicillin was the least effective

antibiotic, with MIC values greater than 256 mg/L for all clinical strains. Ciprofloxacin was also highly ineffective against LVPEI staphylococcal strains (≥ 256 mg/L), but low MIC values were recorded for coagulase negative *S. aureus* (2 mg/L) and SH1000 (0.25 mg/L). Of the two *S. aureus,* LVPEI isolates (LVP11 and LVP13), antibiotic susceptibility profiles were highly similar, but MIC values were generally slightly higher for LVP11. There was a considerable difference in antibiotic susceptibility between LVPEI staphylococcal isolates and the NGH coagulase negative *S. aureus* isolate. The NGH isolate demonstrated increased resistance to erythromycin, flucloxacillin and doxycycline, but was susceptible to ciprofloxacin at very low concentrations.
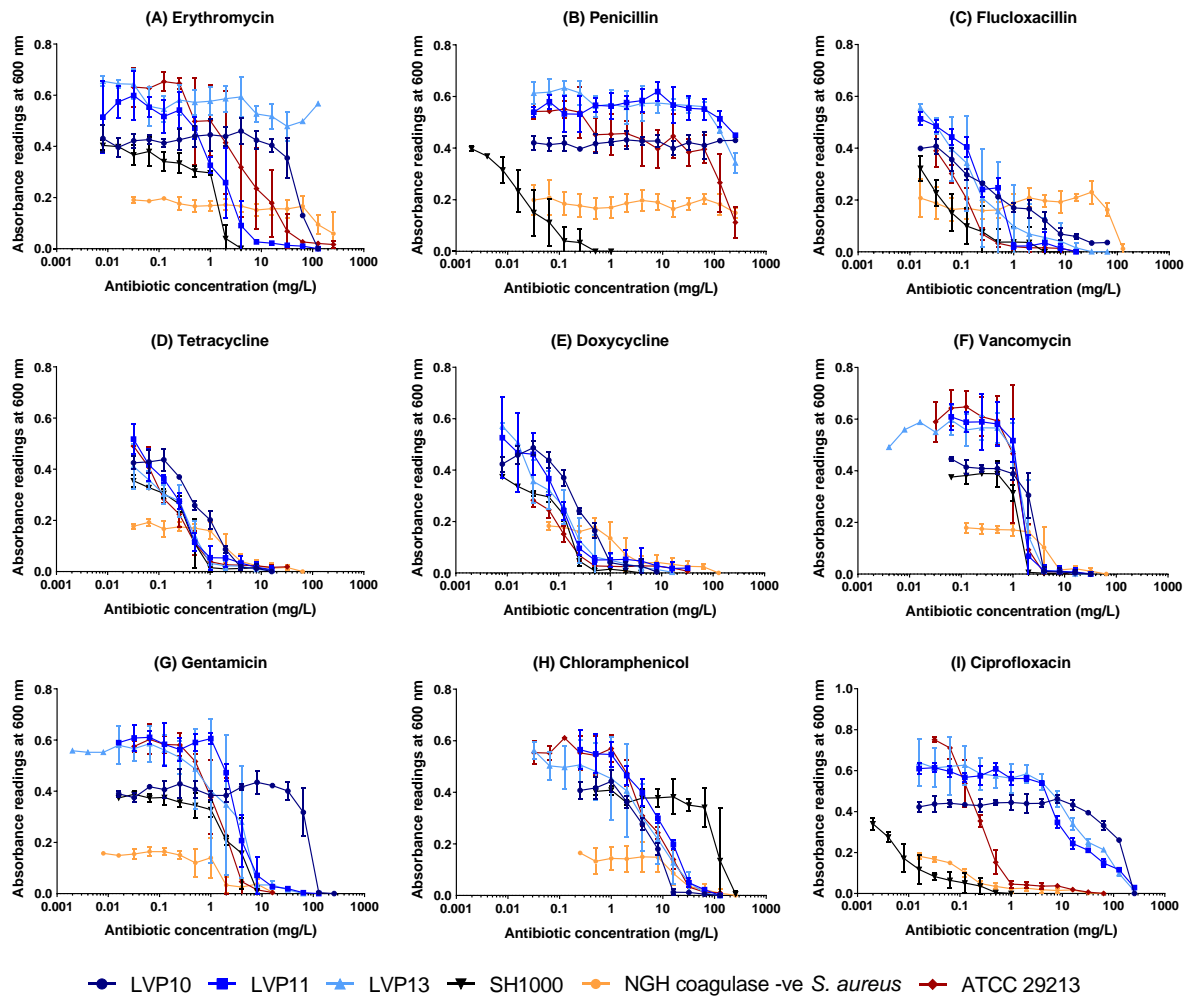
Figure 4-15. Antibiotic susceptibility of staphylococcal clinical isolates obtained from LV Prasad Eye Institute, India and Northern General Hospital, Sheffield.

Clinical isolates of *S. haemolyticus* (LVP10) and *S. aureus* (LVP11, LVP13, NGH Sa) were cultured in LB containing antibiotics to determine the Minimum Inhibitory Concentration (MIC) of nine antibiotics. Antibiotics included Erythromycin (A), Penicillin (B), Flucloxacillin (C), Tetracycline (D), Doxycycline (E), Vancomycin (F), Gentamicin (G), Chloramphenicol (H) and Ciprofloxacin (I). Bacterial growth was measured by absorbance at 600 nm. The *S. aureus* laboratory strain, SH1000 and *S. aureus* reference strain, ATCC 29213 were also included. These strains have known antibiotic susceptibility and MIC data for ATCC 29213 has been published previously. Data represent mean ± SD, n=3 to 7.

Table 4-1. MICs for staphylococcal clinical isolates and the SH1000 laboratory strain.
MIC values are reported in mg/L.

Antibiotic	LVP10	LVP11	LVP13	NGH Sa	SH1000
Erythromycin	128	8	>32	256	4
(Benzyl)Penicillin	>256	>256	>256	>256	0.25
Flucloxacillin	>64	4	2	≥256	1
Doxycycline	2	8	4	64	0.5
Vancomycin	4	4	2	8	2
Gentamicin	128	32	16	8	8
Chloramphenicol	16	64	≥32	64	128
Tetracycline	8	16	2	8	1
Ciprofloxacin	256	>256	256	2	0.25

4.3.4.2. Clinical *P. aeruginosa* isolates display varying susceptibilities to the selected antibiotics.

The growth of clinical *P. aeruginosa* isolates in the presence of seven different antibiotics was measured using absorbance (**Figure 4-16**). The five clinical *P. aeruginosa* strains (LVP3, LVP4, LVP5, LVP6, NGH Pa) and the *P. aeruginosa* reference strain (ATCC 27853) demonstrated susceptibility to meropenem (**A**), ciprofloxacin (**C**), tetracycline (**D**), gentamicin (**E**), tobramycin (**F**) and colistin (**G**) antibiotics, as demonstrated by absorbance readings ≤ 0.01. A gradual decrease in absorbance readings was observed for ciprofloxacin, tetracycline, gentamicin and tobramycin, with increasing concentrations of antibiotic (**C**, **D**, **E**, **and F**). In contrast, a sudden decrease in absorbance was observed for meropenem and colistin once an effective concentration was reached (**A**, **G**). All *P. aeruginosa* strains were resistant to erythromycin at the concentrations tested. Antibiotic susceptibility profiles were highly similar for all LVPEI *P. aeruginosa* isolates. There was also very little difference between isolates obtained from LVPEI and NGH, although the NGH *P. aeruginosa* isolate demonstrated reduced sensitivity to ciprofloxacin at low concentrations of antibiotic (**C**).

MIC values for clinical *P. aeruginosa* isolates are summarised in **Table 4-2**. The most effective antibiotics against *P. aeruginosa* were meropenem and ciprofloxacin, as measured by low MIC values for all strains. Colistin was also a highly effective antibiotic and low MIC values were recorded for all strains apart from LVP3. The least effective antibiotics were erythromycin and tetracycline. MIC values were highly similar for all LVPEI *P. aeruginosa* isolates. However, LVP3 presented with the highest or equal highest MIC values for all antibiotics apart from meropenem. MIC values were highly similar for LVPEI isolates and the *P. aeruginosa* isolate obtained from NGH. The only exceptions were ciprofloxacin and tetracycline. The NGH isolate was more resistant to ciprofloxacin, with an MIC of 16

mg/L (versus 4 to 8 mg/L), whereas this isolate was less resistant to tetracycline, with an MIC of 64 mg/L (versus 128 to 256 mg/L).
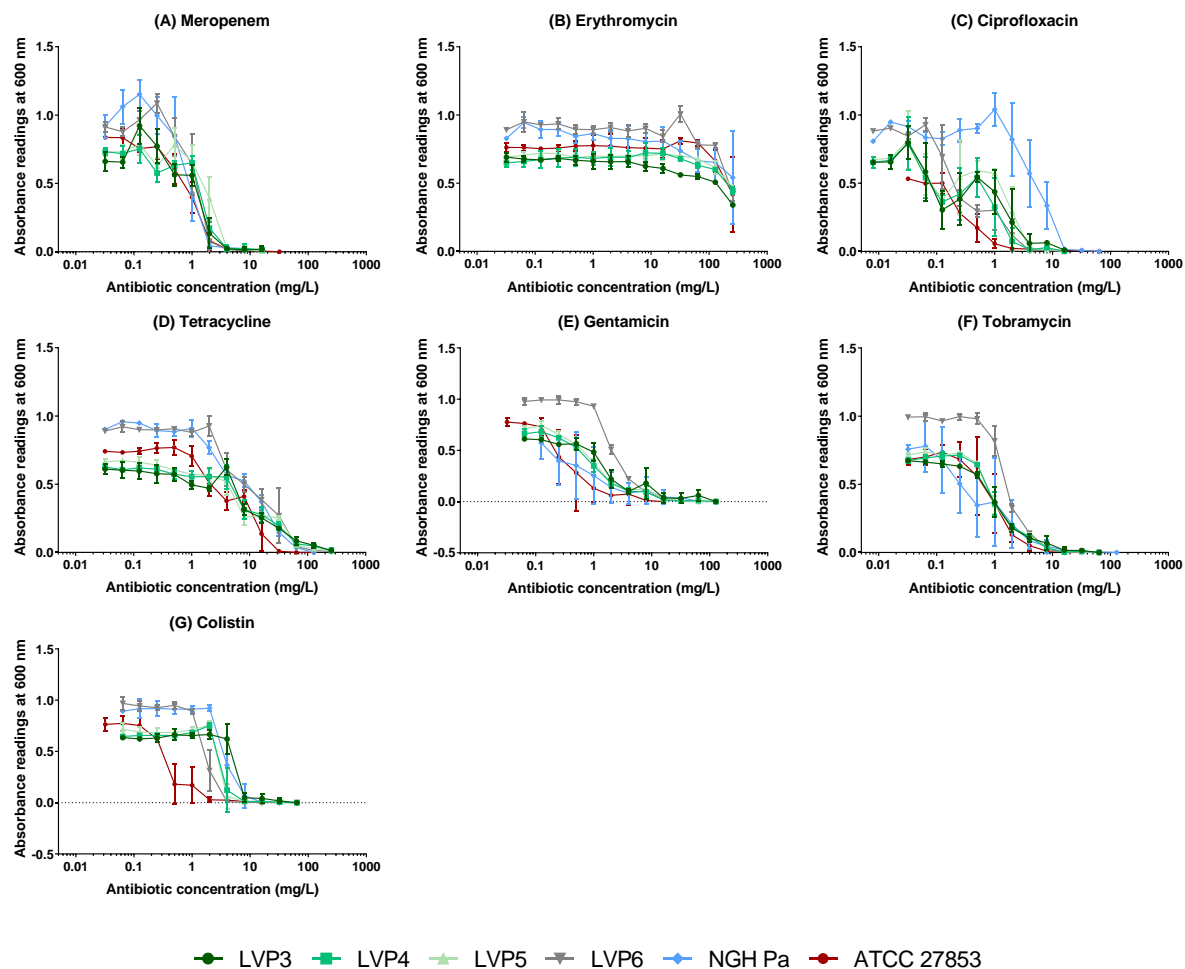
Figure 4-16. Antibiotic susceptibility of *Pseudomonas aeruginosa* clinical isolates obtained from LV Prasad Eye Institute, India and Northern General Hospital, Sheffield.

Clinical isolates of *P. aeruginosa* (LVP3-6) were cultured in LB containing antibiotics to determine the Minimum Inhibitory Concentration (MIC) of seven antibiotics. Antibiotics included Meropenem (A), Erythromycin (B), Ciprofloxacin (C), Tetracycline (D), Gentamicin (E), Tobramycin (F) and Colistin (G). Bacterial growth was measured by absorbance at 600 nm. Reference strain, *P. aeruginosa* ATCC 27853 was included, as this strain has known antibiotic susceptibility and MIC data has been published previously. Data represent mean ± SD, n= 3 to 4.

4.3.4.3. Gram negative clinical isolates display varying susceptibilities to antibiotics.

The growth of Gram negative, clinical isolates was measured in the presence of seven different antibiotics using absorbance (**Figure 4-17**). All Gram negative, clinical isolates (NGH Ko, NGH Pm, NGH Pa) and the *P. aeruginosa* reference strain (ATCC 27853) demonstrated susceptibility to meropenem (**A**), ciprofloxacin (**C**), tetracycline (**D**), gentamicin (**E**) and tobramycin (**F**). In contrast, all isolates were resistant to erythromycin at antibiotic concentrations tested (**B**). For colistin, *P. aeruginosa* and *K. oxytoca* isolates demonstrated antibiotic susceptibility but *P. mirabilis* was resistant to colistin at all concentrations tested (**G**). For antibiotics such as meropenem and erythromycin, similar antibiotic susceptibility profiles were reported for all three NGH isolates (**A**, **B**). In contrast, large differences in antibiotic susceptibility profile were recorded for ciprofloxacin, tetracycline, tobramycin and colistin (**C**, **D**, **F**, **and G**). *P. mirabilis* was resistant to colistin and demonstrated reduced sensitivity to tetracycline and tobramycin, as compared to the other Gram negative isolates. For ciprofloxacin, *P. aeruginosa* demonstrated increased antibiotic resistance.

MIC values for Gram negative, clinical isolates are summarised in **Table 4-2**. The most effective antibiotics against all NGH Gram negative isolates were meropenem and ciprofloxacin, with maximum MIC values of 8 and 16 mg/L, respectively. In contrast, all Gram negative isolates were resistant to erythromycin, with MIC values greater than 256 mg/L. Of the clinical isolates, *P. mirabilis* presented with the highest or equal highest MIC value for the majority of antibiotics tested.
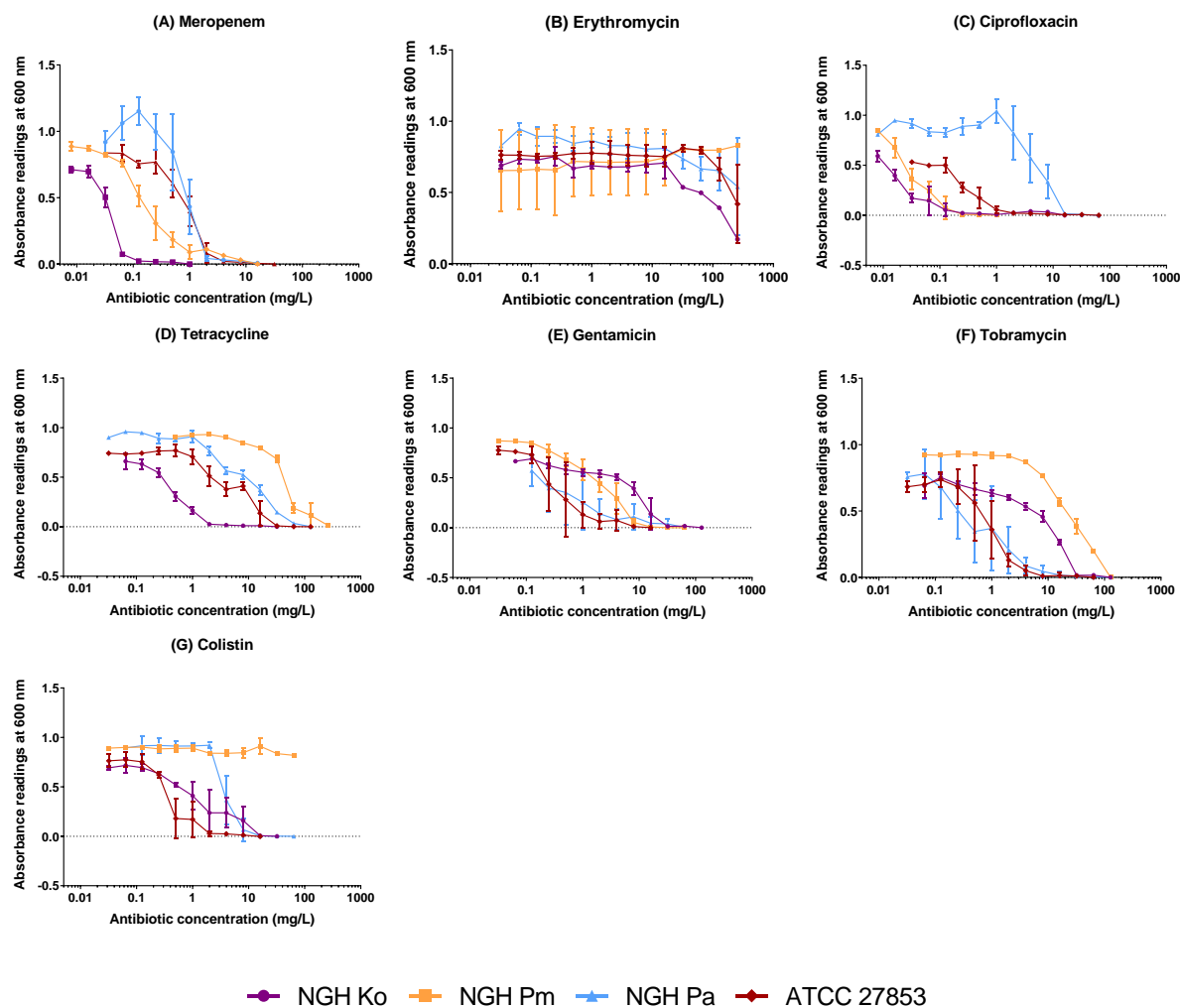
Figure 4-17. Antibiotic susceptibility of Gram negative, clinical isolates obtained from Northern General Hospital, Sheffield.

Clinical isolates of *K. oxytoca* (NGH Ko), *P. mirabilis* (NGH Pm) and *P. aeruginosa* (NGH Pa) were cultured in LB containing antibiotics to determine the Minimum Inhibitory Concentration (MIC) of seven antibiotics. Antibiotics included Meropenem (A), Erythromycin (B), Ciprofloxacin (C), Tetracycline (D), Gentamicin (E), Tobramycin (F) and Colistin (G). Bacterial growth was measured by absorbance at 600 nm. Reference strain, *P. aeruginosa* ATCC 27853 was included, as this strain has known antibiotic susceptibility and MIC data has been published previously. An LVPEI clinical isolate of *P. aeruginosa* (LVP4) has been included for comparison. Data represent mean ± SD, n=3 to 4.

Table 4-2. MICs for Gram negative clinical isolates.
MIC values are reported in mg/L.

Antibiotic	LVP3	LVP4	LVP5	LVP6	NGH Pa	NGH Ko	NGH Pm
Meropenem	4	4	8	4	8	0.25	8
Erythromycin	>256	>256	>256	>256	>256	>256	>256
Ciprofloxacin	8	4	8	4	16	1	0.25
Tetracycline	256	256	256	128	64	4	256
Tobramycin	16	16	8	16	16	32	128
Gentamicin	32	16	16	32	16	32	16
Colistin	32	8	4	4	8	16	>64

4.3.4.4. EUCAST MIC breakpoints should not be used to classify the antibiotic susceptibility of isolates included in this study.

The European Committee on Antimicrobial Susceptibility Testing (EUCAST) provides MIC breakpoints for a range of antibiotics (EUCAST., 2021a). These breakpoints can be used to identify bacterial strains as 'Susceptible' (S), 'Susceptible, increased exposure' (I) or 'Resistant' (R) to antibiotics. In **Table 4-3**, the antibiotic susceptibility of clinical isolates has been classified using MIC breakpoints for *S. aureus*, coagulase negative *S. aureus* and Pseudomonas species. Reference strains were also included for comparison. For *S. aureus*, LVP11 was classified as resistant (R) to all antibiotics and LVP13 was classified as resistant to most antibiotics, with the exception of vancomycin (S) and tetracycline (I). The coagulase negative *S. aureus* isolate was classified as resistant to all antibiotics. For *P. aeruginosa*, all clinical isolates were classified as resistant to tobramycin, ciprofloxacin and colistin, with intermediate (I) resistance reported for meropenem. Upon first inspection of the data, it appeared all clinical isolates were highly antibiotic resistant. However, ATCC reference strains were also classified as resistant to multiple antibiotics using EUCAST breakpoints. These strains were included in experiments because of their antibiotic sensitivity and so it was hypothesised that EUCAST MIC breakpoints could not be applied to my data, because of differences in the way MIC was determined.

In my experiments, MIC values were measured by absorbance, whereas EUCAST recommends selecting MIC by eye. A study was carried out using the ATCC reference strains and MIC values were determined both by eye and by using absorbance (**Table 4-4**). For *S. aureus*, reduced MIC values were reported for all antibiotics apart from vancomycin when measured by eye versus absorbance. Similarly, reduced MIC values were reported for more than half of antibiotics for *P. aeruginosa*. Furthermore, when MICs were determined by eye, many of the ATCC MIC values fell within the range reported by EUCAST. This confirmed my hypothesis that EUCAST breakpoint data cannot be

used to classify the antibiotic susceptibility of the clinical isolates, as the use of absorbance provides higher MIC values than the EUCAST method.

Instead, the relative antibiotic susceptibility of clinical isolates has been compared to ATCC reference strains (**Table 4-5**). For *S. aureus*, MIC values were highly similar between clinical isolates and the ATCC reference strain, but exceptions included ciprofloxacin and erythromycin. For ciprofloxacin, a large increase in MIC was observed for clinical isolates (256 mg/L versus 16 mg/L) and whilst the ATCC reference strain was resistant to erythromycin, LVP11 and LVP13 displayed sensitivity to this antibiotic. For *P. aeruginosa*, clinical isolates displayed increased MIC values for meropenem, tetracycline, tobramycin and gentamicin and there was a particularly large increase in MIC values for tetracycline (128 to 256 mg/L versus 32 mg/L). MIC values for erythromycin, ciprofloxacin and colistin were roughly similar.

Table 4-3. Classification of clinical isolates as Susceptible (S), Susceptible, increased exposure (I) or Resistant (R), according to EUCAST breakpoint data.
(A) *S. aureus*. **(B)** Coagulase negative *S. aureus*. **(C)** *P. aeruginosa*.

S= High likelihood of therapeutic success using a standard dosing regimen of the agent. I= High likelihood of therapeutic success because exposure to the agent is increased by adjusting the dosing regimen or by its concentration at the site of infection. R= High likelihood of therapeutic failure even when there is increased exposure. EUCAST breakpoints in brackets are used to distinguish between organisms with and without acquired resistance mechanisms. IE indicates that there is insufficient evidence that the organism or group is a good target for therapy with the agent. MIC values are reported in mg/L.

(A)

Antibiotic	LVP11	LVP13	SH1000	ATCC 27913	EUCAST MIC breakpoint for *S. aureus*	
					S ≤	R >
Erythromycin	**R** (8)	**R** (>32)	**R** (4)	**R** (>256)	1	2
(Benzyl)Penicillin	**R** (>256)	**R** (>256)	**R** (0.25)	**R** (>256)	0.125	0.125
Doxycycline	**R** (8)	**R** (4)	**S** (0.5)	**R** (8)	1	2
Vancomycin	**R** (4)	**S** (2)	**S** (2)	**S** (2)	2	2
Gentamicin	**R** (32)	**R** (16)	**R** (8)	**R** (8)	(1)[1]	(1)[1]
Chloramphenicol	**R** (64)	**R** (≥32)	**R** (128)	**R** (64)	8	8
Tetracycline	**R** (16)	**I** (2)	**S** (1)	**R** (16)	1	2
Ciprofloxacin	**R** (>256)	**R** (256)	**I** (0.25)	**R** (16)	0.001	1

(B)

Antibiotic	NGH Sa	EUCAST MIC breakpoint for Coagulase negative *S. aureus*	
		S ≤	R >
Erythromycin	**R** (256)	1	1
(Benzyl)Penicillin	**R** (>256)	Resistant to benzyl penicillin	
Doxycycline	**R** (64)	1	2
Vancomycin	**R** (8)	4	4
Gentamicin	**R** (8)	(1)[1]	(1)[1]
Chloramphenicol	**R** (64)	8	8
Tetracycline	**R** (8)	1	2
Ciprofloxacin	**R** (2)	0.001	1

(C)

Antibiotic	LVP3	LVP4	LVP5	LVP6	NGH Pa	ATCC 27853	EUCAST MIC breakpoint for Pseudomonas spp.	
							S ≤	R >
Meropenem	**I** (4)	**I** (4)	**I** (8)	**I** (4)	**I** (8)	**S** (2)	2	8
Ciprofloxacin	**R** (8)	**R** (4)	**R** (8)	**R** (4)	**R** (16)	**R** (8)	0.001	0.5
Tobramycin	**R** (16)	**R** (16)	**R** (8)	**R** (16)	**R** (16)	**R** (8)	(2)[1]	(2)[1]
Gentamicin	- (32)	- (16)	- (16)	- (32)	- (16)	- (4)	IE	IE
Colistin	**R** (32)	**R** (8)	**R** (4)	**R** (4)	**R** (8)	**R** (8)	2	2

Table 4-4. Comparing EUCAST data with my own MIC values for ATCC reference strains, as determined by absorbance and by eye.
(A) *S. aureus* **reference strain, ATCC 29213 (B)** *P. aeruginosa* **reference strain, ATCC 27853.** Red= MIC is greater than EUCAST values; Orange= MIC is equal to EUCAST values; Green= MIC is lower than EUCAST values. MIC values are reported in mg/L.

(A)

Antibiotic	ATCC 29213 Absorbance	ATCC 29213 By eye	EUCAST MIC range for ATCC 29213
Erythromycin	>256	2.0-4.0	0.25-1
(Benzyl)Penicillin	>256	128-256	Range not provided
Flucloxacillin	2	0.25	Range not provided
Doxycycline	8	0.25	0.125-0.5
Vancomycin	2	2.0-4.0	0.5-2
Gentamicin	8	4	0.125-1
Chloramphenicol	64	32	2-16
Tetracycline	16	1	0.125-1
Ciprofloxacin	16	0.5-1	0.125-0.5

(B)

Antibiotic	ATCC 27853 Absorbance	ATCC 27853 By eye	EUCAST MIC range for ATCC 27853
Meropenem	2	2	0.125-1
Erythromycin	>256	>256	Range not provided
Ciprofloxacin	8	0.25-1	0.125-1
Tetracycline	32	32	Range not provided
Tobramycin	8	2	0.25-1
Gentamicin	4	0.25-0.5	0.5-2
Colistin	8	2	0.5-4

124

Table 4-5. Comparing MIC values for clinical isolates against my own MIC data for ATCC reference strains. (A) Staphylococcal clinical isolates vs *S. aureus* ATCC 29213. (B) *P. aeruginosa* clinical isolates vs *P. aeruginosa* ATCC 27853. Red= clinical MIC is greater than MIC of ref. strain; orange= clinical MIC is equal to MIC of ref. strain; green= clinical MIC is lower than MIC of reference strain. MIC values are reported in mg/L.

(A)

Antibiotic	LVP11	LVP13	SH1000	ATCC 29213 reference strain data
Erythromycin	8	>32	4	>256
Penicillin	>256	>256	0.25	>256
Flucloxacillin	4	2	1	2
Doxycycline	8	4	0.5	8
Vancomycin	4	2	2	2
Gentamicin	32	16	8	8
Chloramphenicol	64	≥32	128	64
Tetracycline	16	2	1	16
Ciprofloxacin	>256	256	0.25	16

(B)

Antibiotic	LVP3	LVP4	LVP5	LVP6	NGH Pa	ATCC 27853 reference strain data
Meropenem	4	4	8	4	8	2
Erythromycin	>256	>256	>256	>256	>256	>256
Ciprofloxacin	8	4	8	4	16	8
Tetracycline	256	256	256	128	64	32
Tobramycin	16	16	8	16	16	8
Gentamicin	32	16	16	32	16	4
Colistin	32	8	4	4	8	8

4.3.5. *P. aeruginosa* clinical isolates encode antibiotic resistance genes affecting multiple antibiotic pathways and drug classes.

Genome sequencing data for *P. aeruginosa* isolates was analysed using the Comprehensive Antibiotic Resistance Database Resistance Gene Identifier (CARD: RGI) to identify known Antibiotic Resistance (AR) genes. Only 28 of the 39 clinical *P. aeruginosa* isolates were included due to poor genome assembly scores for 11 of the isolates (see **section 2.5.6**). The perfect/strict hits identified for each isolate can be accessed via the University of Sheffield data repository, ORDA: 10.15131/shef.data.19169657. CARD: RGI identified at least 4 perfect hits (100% sequence identity), 16 strict hits (≥ 90% sequence identity) and over 400 loose hits (< 90% sequence identity) for all *P. aeruginosa* clinical isolates (**Figure 4-18A**). Total number of perfect and strict hits have been combined in **Figure 4-18B** and the largest number of hits was recorded for LVP3, 4, 5, 6 and 27, with 58 or 59 hits for each isolate. In contrast, the lowest number of hits, 33, was recorded for LVP31. Perfect and strict hits were subjected to further analysis and the percentage of AR genes associated with six different antibiotic resistance mechanisms was calculated (**Figure 4-19**). The vast majority of AR genes were associated with antibiotic efflux and these genes accounted for 61.9-84.2% of genes identified by CARD: RGI. AR genes associated with antibiotic inactivation and target alteration were also identified and these genes accounted for 2.6-17.5% and 7.5-15.5% of CARD: RGI hits respectively. Other resistance mechanisms included reduced permeability to antibiotics and AR genes associated with this mechanism were identified for all isolates apart from LVP39. In contrast, AR genes associated with target replacement were only identified for LVP25, 27 and 29 and only LVP27 encoded an AR gene associated with target protection. Perfect and strict hits were also analysed by affected drug class (**Figure 4-20**). AR genes affecting 17 different classes of antibiotic were identified for all *P. aeruginosa* isolates. Of these classes, fluoroquinolone, tetracycline and phenicol antibiotics were associated with the highest number of AR genes and each *P. aeruginosa* isolate encoded somewhere in the region of 18 to 33 AR genes affecting each of these antibiotics.

(A)
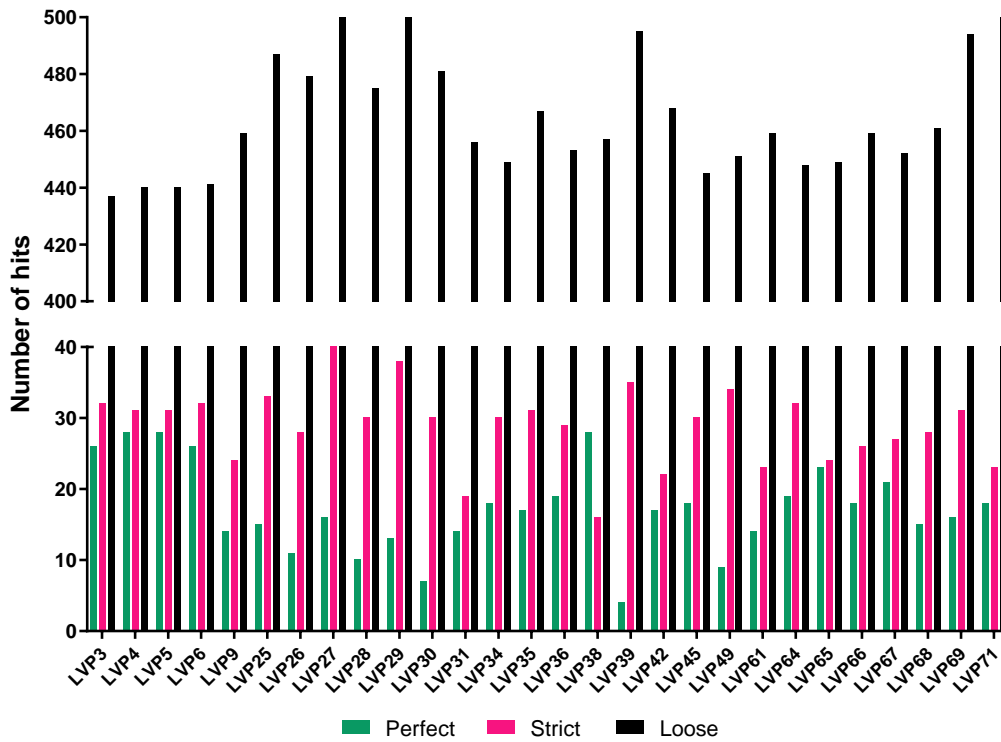
(B)
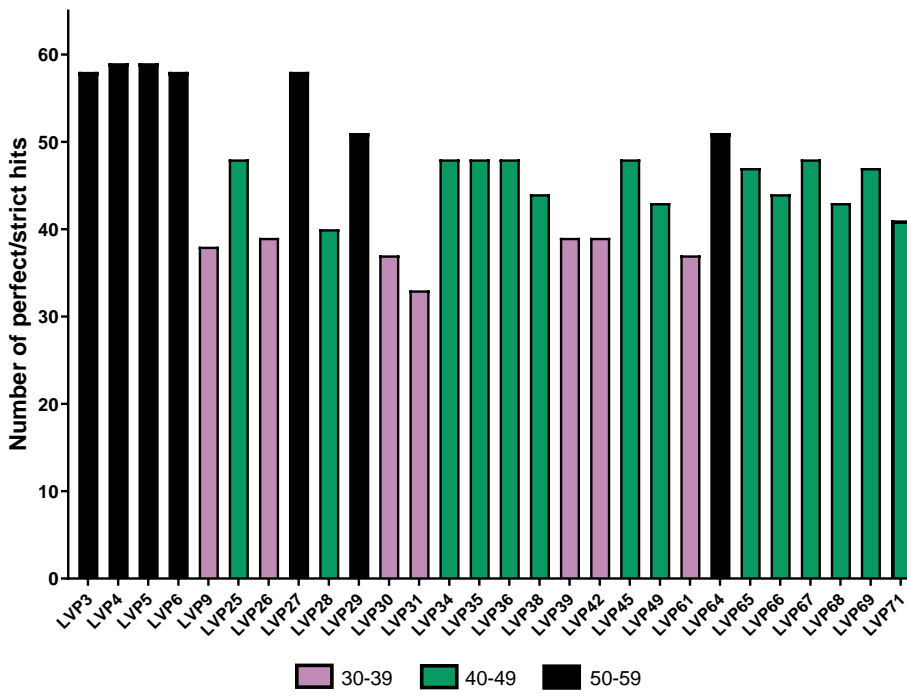
Figure 4-18. Number of antibiotic resistance genes possessed by LVPEI clinical isolates of *P. aeruginosa*, as identified by CARD: RGI.

FASTA files for 37 LVPEI clinical isolates of *P. aeruginosa* were analysed using the Resistance Gene Identifier. **(A) Perfect, strict and loose hits.** Perfect= 100% sequence identity, Strict= ≥ 90% sequence identity, Loose= < 90% sequence identity. **(B) Perfect and strict hits only.**
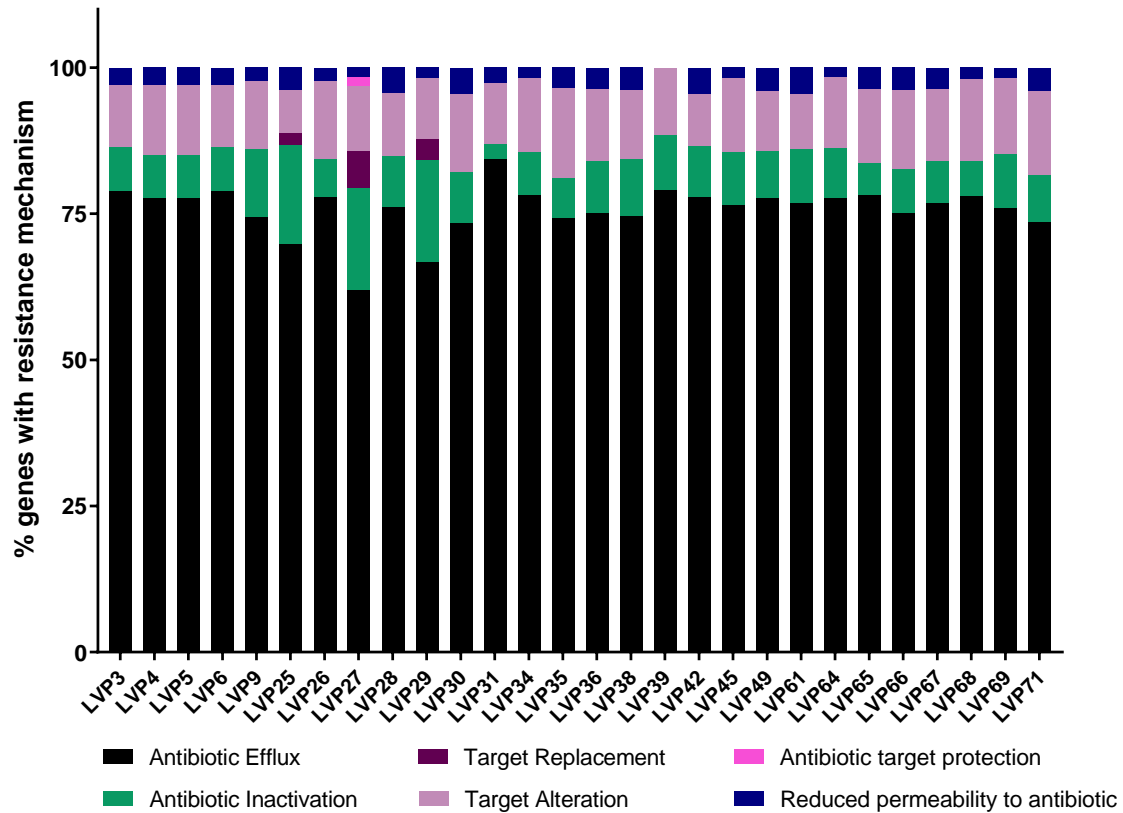
Figure 4-19. Antibiotic resistance mechanisms associated with resistance genes identified by CARD: RGI.
CARD: RGI provides the antibiotic resistance mechanism associated with each known AR gene. AR mechanisms are divided into 6 categories, which include antibiotic efflux, antibiotic inactivation, target replacement, target alteration, antibiotic target protection and reduced permeability to antibiotic. Only data for perfect and strict hits are shown and the total number of genes associated with each mechanism has been expressed as a % of the total number of AR genes.
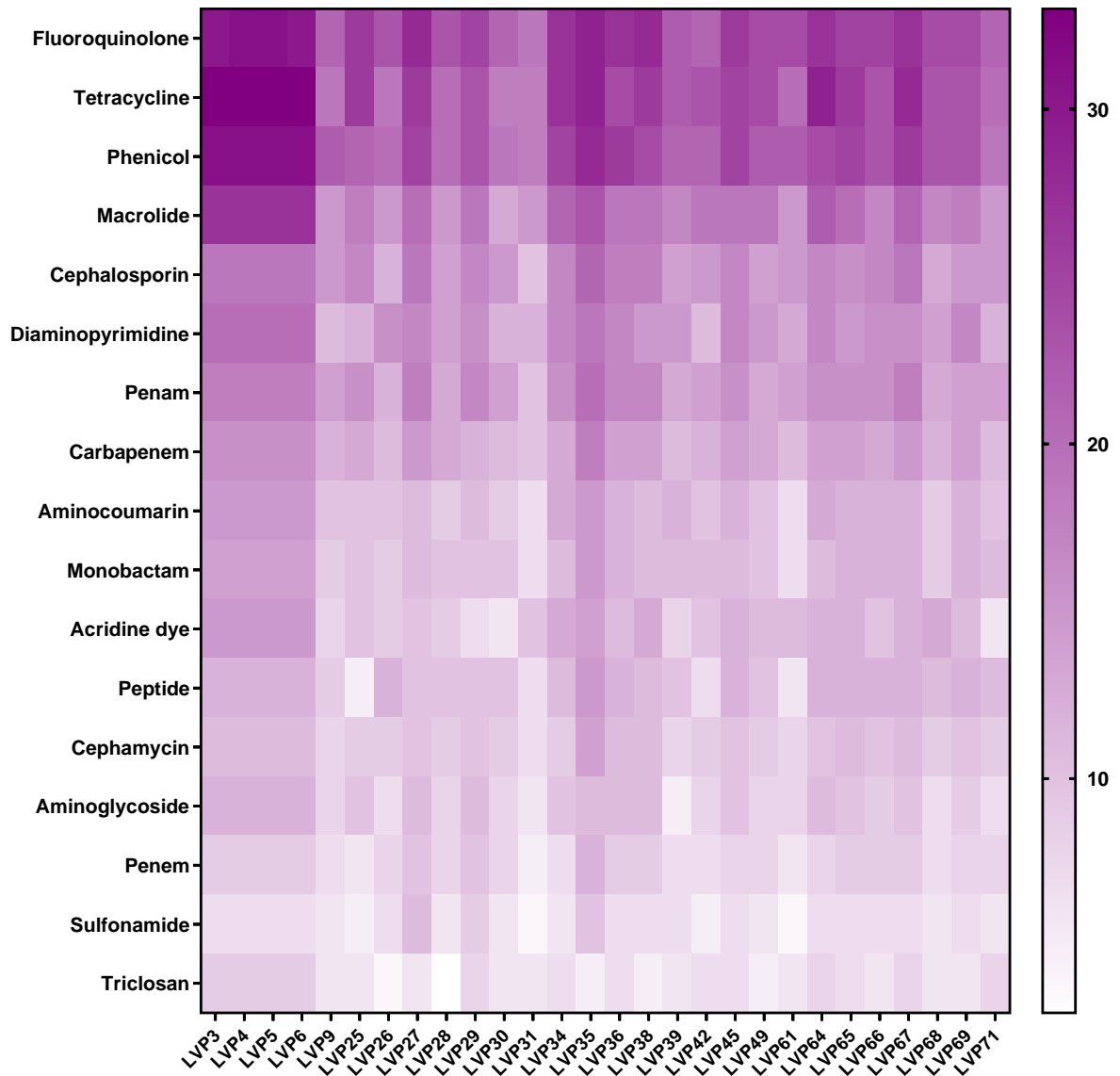
Figure 4-20. Heat map of CARD: RGI data showing the drug classes affected by identified antibiotic resistance genes.

The number of genes that confer resistance to each major drug class has been presented as a heat map. Increasing colour intensity corresponds to an increased number of antibiotic resistance genes. Only data for perfect and strict CARD: RGI hits are shown.

4.3.6. *P. aeruginosa* clinical isolates encode virulence factor genes with varying predominance.

The Basic Local Alignment Search Tool (BLAST) was used to identify the presence or absence of virulence factor (VF) genes in clinical *P. aeruginosa* isolates, based on scores for sequence identity and alignment length (**Table 4-6**). Reference sequences for VF genes were obtained from the National Center for Biotechnology Information (NCBI), using NCBI Gene (see **section 2.5.6**). All clinical *P. aeruginosa* isolates encoded the *lasA* (elastase A), *lasB* (elastase B), *aprA* (alkaline protease) and *prpL* (serine protease IV) genes, with sequence identity values of ≥ 96% for all isolates. The *pasP* (*Pseudomonas aeruginosa* small protease) gene was encoded by all isolates apart from LVP32 and the *fliC* (flagellin) gene was identified for all isolates apart from LVP43. For the *fliC* gene, the b-type allele was more predominant and was encoded by 61.5% of isolates, whereas the a-type allele was encoded by 35.9% of isolates. Of the four *P. aeruginosa* exotoxins, *exoT* was encoded by all isolates and *exoY* was encoded by the majority of isolates (87.2%). Possession of *exoS* (invasive pathotype) and *exoU* (cytotoxic pathotype), was mutually exclusive and all 39 isolates encoded either *exoS* or *exoU*. The *exoS* gene was more widely encoded and 79.5% of isolates were *exoS* +ve, whereas only 20.5% of isolates were *exoU* +ve. Therefore, the invasive pathotype is more common amongst *P. aeruginosa* clinical isolates obtained from LVPEI.

Table 4-6. Important *P. aeruginosa* virulence factors and their presence/absence within LVPEI clinical isolates.

Isolate	*exoS*	*exoT*	*exoY*	*exoU*	Pathotype	*lasA*	*lasB*	*aprA*	*prpL*	*pasP*	*fliC*-type
LVP1	+	+	+	-	Invasive	+	+	+	+	+	b
LVP2	+	+	+	-	Invasive	+	+	+	+	+	b
LVP3	+	+	+	-	Invasive	+	+	+	+	+	b
LVP4	+	+	+	-	Invasive	+	+	+	+	+	b
LVP5	+	+	+	-	Invasive	+	+	+	+	+	b
LVP6	+	+	+	-	Invasive	+	+	+	+	+	b
LVP8	+	+	+	-	Invasive	+	+	+	+	+	b
LVP9	+	+	+	-	Invasive	+	+	+	+	+	a
LVP25	-	+	+	+	Cytotoxic	+	+	+	+	+	a
LVP26	-	+	-	+	Cytotoxic	+	+	+	+	+	b
LVP27	-	+	+	+	Cytotoxic	+	+	+	+	+	a
LVP28	-	+	-	+	Cytotoxic	+	+	+	+	+	b
LVP29	-	+	+	+	Cytotoxic	+	+	+	+	+	a
LVP30	+	+	-	-	Invasive	+	+	+	+	+	a
LVP31	+	+	+	-	Invasive	+	+	+	+	+	a
LVP32	+	+	+	-	Invasive	+	+	+	+	-	b
LVP33	+	+	+	-	Invasive	+	+	+	+	+	b
LVP34	+	+	+	-	Invasive	+	+	+	+	+	b
LVP35	+	+	+	-	Invasive	+	+	+	+	+	b
LVP36	+	+	+	-	Invasive	+	+	+	+	+	b
LVP38	+	+	+	-	Invasive	+	+	+	+	+	b
LVP39	+	+	-	-	Invasive	+	+	+	+	+	a
LVP40	+	+	+	-	Invasive	+	+	+	+	+	a
LVP41	-	+	+	+	Cytotoxic	+	+	+	+	+	a
LVP42	+	+	+	-	Invasive	+	+	+	+	+	b
LVP43	-	+	+	+	Cytotoxic	+	+	+	+	+	Neither
LVP44	+	+	+	-	Invasive	+	+	+	+	+	b
LVP45	+	+	+	-	Invasive	+	+	+	+	+	b
LVP49	+	+	+	-	Invasive	+	+	+	+	+	b
LVP59	+	+	-	-	Invasive	+	+	+	+	+	a
LVP60	-	+	+	+	Cytotoxic	+	+	+	+	+	a
LVP61	+	+	+	-	Invasive	+	+	+	+	+	b
LVP64	+	+	+	-	Invasive	+	+	+	+	+	a
LVP65	+	+	+	-	Invasive	+	+	+	+	+	a
LVP66	+	+	+	-	Invasive	+	+	+	+	+	b
LVP67	+	+	+	-	Invasive	+	+	+	+	+	a
LVP68	+	+	+	-	Invasive	+	+	+	+	+	b
LVP69	+	+	+	-	Invasive	+	+	+	+	+	b
LVP71	+	+	+	-	Invasive	+	+	+	+	+	b

4.4. Discussion

4.4.1. Summary of results

In this chapter, clinical bacterial keratitis isolates were characterised by genotypic and phenotypic analyses. Previously characterised reference strains (e.g., SH1000, PAOMW1 and ATCC 27853) were also included to assist assay optimisation, perform quality control and provide comparison with clinical isolates. The three major aims for this chapter were achieved. Crystal violet staining allowed isolates with biofilm-forming activity to be identified, thereby fulfilling my first aim for this chapter, and all clinical isolates demonstrated biofilm forming activity in DMEM: F12 medium. This permits the use of any of these isolates in biofilm infection models. The second aim was achieved using MIC studies, as these studies allowed me to compare antibiotic resistance profiles between isolates. Although antibiotic resistance profiles were highly similar within species, *S. aureus* LVP11 and *P. aeruginosa* LVP3 were selected for future work as these isolates had the highest MIC values for the antibiotics tested. The resistance phenotype of LVP3 was further validated by genome sequencing as this revealed high numbers of antibiotic resistance genes for LVP3 compared to other *P. aeruginosa* isolates. Finally, use of BLAST allowed me to generate a virulence factor profile for each of the *P. aeruginosa* clinical isolates, with special focus on proteases and T3SS exotoxins, thereby fulfilling the final aim for this chapter. My isolate population was compared against previously sequenced keratitis populations and findings of particular interest included the prevalence of the invasive *P. aeruginosa* pathotype and b-type *fliC* allele.

4.4.2. Biofilm formation

In section **4.3.2**, the biofilm forming activity of *S. aureus* and *P. aeruginosa* reference strains were measured under different media conditions. This work was used to optimise the biofilm formation protocol. TSB supplemented with 0.5% glucose was selected as an appropriate biofilm promoting medium for staphylococcal strains, whereas M63 medium supplemented with 0.4% arginine and 1 mM MgSO$_4$ was selected for *P. aeruginosa*. The M63 medium was selected following comparison of TSB and M63 media conditions. All *P. aeruginosa* strains demonstrated increased crystal violet staining in the presence of TSB but the relative biofilm forming activities of these strains contradicted previous literature findings. PAOMW1 and PA14 were expected to exhibit defects in biofilm formation (**section 4.1.1**) but under TSB conditions, these strains demonstrated increased crystal violet staining compared to PAO1. In contrast, PAOMW1 formed the weakest biofilms under M63 conditions. It was hypothesised that TSB medium promoted the growth of non-biofilm associated *P. aeruginosa* bacteria and therefore M63 medium was selected for future work. In the presence of the optimised biofilm promoting medium, all *S. aureus* and *P. aeruginosa* reference strains formed biofilms. For *S. aureus*,

SH1000 was the strongest biofilm forming strain and for *P. aeruginosa*, there was a trend towards increased biofilm formation by PA14, followed by PAO1 and PAOMW1. All strains also formed biofilms in the presence of DMEM: F12 tissue culture medium, but for *S. aureus*, there was a significant reduction in biofilm formation for most strains and SH1000 biofilm formation was no longer significantly increased compared to MRSA skin isolates. For *P. aeruginosa*, there was no significant difference in biofilm formation between M63 and DMEM: F12 media conditions, but there was a trend towards increased biofilm formation by PAOMW1 in DMEM: F12. During this phase of work, various aspects of the protocol were optimised. Crystal violet concentration was reduced from 0.1% to 0.01% to reduce variability and a two-fold dilution step was introduced to ensure absorbance readings remained below 1.0. These changes reduced variation and improved the accuracy of Varioskan readings, respectively. A wash study was also conducted to determine whether biofilm structures were being disrupted by the PBS wash step. It was concluded that only loosely adherent, non-biofilm bacteria were removed by washing and therefore this step remained in the optimised protocol.

Biofilm formation data for *S. aureus* is supported by previous research findings. TSB supplemented with glucose is commonly used to assess staphylococcal biofilm formation (Cassat et al., 2013) and *S. aureus* SH1000 has been shown to form biofilms under these conditions previously (Corrigan et al., 2007). Whilst the biofilm forming characteristics of MRSA1-6 have not been studied previously, other clinical MRSA isolates have been shown to form biofilms in the presence of TSB (Xu et al., 2016). Xu et al showed that most of their MRSA isolates were weak biofilm formers, providing support for my observation that biofilm formation was significantly reduced in MRSA isolates compared to SH1000. In contrast, biofilm formation data for *P. aeruginosa* contradicts previous literature findings. PAO1 is a well-documented biofilm-forming strain (Li et al., 2015, Periasamy et al., 2015), whereas PA14 and PAOMW1 are expected to exhibit defects in biofilm formation (see **section 4.1.1**). Therefore PAO1 (and not PA14) was expected to display the highest biofilm-forming activity. Unexpectedly high levels of biofilm formation for PA14 may have been due to the presence of 0.4% arginine in M63 medium. *P. aeruginosa* PA14 is highly sensitive to arginine and this amino acid has been shown to increase PA14 biofilm formation by as much as 3-fold (Bernier et al., 2011). In retrospect, biofilm inhibitors would have provided improved negative controls for biofilm formation compared to PA14 and PAOMW1 strains.

Despite the popularity of the crystal violet staining method, few published articles have used this technique to assess biofilm formation in the presence of tissue culture medium. As a result, I was unable to compare my DMEM: F12 data with previous research findings. The scarcity of these studies reflects a much wider problem in *in vitro* modelling, which is an absence of co-culture, host-biofilm

models. Most previously reported biofilm models have investigated biofilm formation in the context of abiotic surfaces or non-living mammalian cell populations (Buhmann et al., 2016) and as such, there has not been a requirement to study biofilm formation under tissue culture conditions.

In section **4.3.3**, the optimised crystal violet staining protocol was used to measure the biofilm forming abilities of clinical bacterial keratitis isolates. All staphylococcal and *P. aeruginosa* isolates demonstrated biofilm forming activity in the presence of a biofilm promoting medium (TSB or M63), as well as in the presence of DMEM: F12 tissue culture medium. Therefore, any of these isolates may be used to model corneal biofilm infections. For staphylococcal strains, LVP10 demonstrated a significant increase in biofilm formation in TSB medium, whereas there was no significant difference in biofilm formation between LVP10, LVP11 and LVP13 in DMEM: F12. *For P. aeruginosa* strains, LVP4 and LVP5 were the strongest biofilm forming strains in the presence of M63 medium but there was no significant difference in biofilm formation between LVP3, LVP4, LVP5 and LVP6 in DMEM: F12. My observation that *P. aeruginosa* clinical isolates LVP3-6, are biofilm forming strains is in agreement with previously published data using these isolates (Dave et al., 2020). Finally, comparison of OD readings collected before and after the crystal violet staining showed that differences in biofilm formation were not linked to differences in bacterial growth rate. In retrospect, it would have been beneficial to collect initial absorbance readings during all experiments as this would have allowed crystal violet measurements to be normalised against bacterial growth. Another limitation of the biofilm formation protocol that must be considered is the specificity of crystal violet. Crystal violet stains proteins and DNA within bacterial biofilms but staining is non-specific and therefore, CV staining can only provide an accurate measurement of biofilm mass if non-biofilm bacteria have been successfully removed. Biofilm markers with increased specificity have been reported, such as anti-Psl antibodies which bind a major polysaccharide within *P. aeruginosa* biofilms (DiGiandomenico et al., 2012). However, antibody techniques are much more expensive, labour intensive and may be complicated by differences in biofilm composition between bacterial strains.

4.4.3. Antibiotic susceptibility testing

In section **4.3.4**, MIC studies were used to determine the antibiotic susceptibility profiles of clinical bacterial keratitis isolates. Clinical staphylococcal isolates (LVP10, LVP11, LVP13 and NGH Sa), demonstrated antibiotic susceptibility to flucloxacillin, tetracycline, doxycycline, vancomycin, gentamicin and chloramphenicol antibiotics and the majority of strains also displayed sensitivity to erythromycin. Of these antibiotics, vancomycin was the most effective and provided low MIC values for all strains. In contrast, all clinical isolates were resistant to penicillin and were either resistant or

highly resistant to ciprofloxacin at concentrations of up to 256 mg/L. With the exception of chloramphenicol, clinical isolates always presented with higher MIC values than the SH1000 laboratory strain and whilst MIC values for *S. aureus* LVP11 and LVP13 were highly similar, MIC values for LVP11 were slightly increased. Clinical *P. aeruginosa* isolates (LVP3, LVP4, LVP5, LVP6 and NGH Pa) demonstrated antibiotic susceptibility to meropenem, ciprofloxacin, tetracycline, gentamicin, tobramycin and colistin and of these antibiotics, meropenem and ciprofloxacin were most effective, with low MIC values for all strains. In contrast, all isolates were resistant to erythromycin. MIC values were similar between clinical isolates but LVP3 provided the highest, or equal highest, MIC value for most antibiotics. When MIC testing of Gram negative isolates was expanded to include *P. mirabilis* and *K. oxytoca*, similar antibiotic susceptibility profiles to NGH *P. aeruginosa* were observed. As with *P. aeruginosa*, these Gram negative isolates were susceptible to meropenem, ciprofloxacin, tetracycline, gentamicin and tobramycin and were resistant to erythromycin. However, *P. mirabilis* also demonstrated resistance to colistin and of the three Gram negative NGH isolates, this isolate provided the highest, or equal highest, MIC values for all antibiotics.

MIC experiments were designed using resources provided by EUCAST. However, differences between my broth microdilution protocol and EUCAST guidelines meant that EUCAST MIC breakpoints could not be used to classify isolates as susceptible or resistant to antibiotics. EUCAST recommend determining MIC by eye, whereas absorbance readings were used to determine MIC in my experiments. When these methods were compared using quality controls strains (ATCC 29213 and ATCC 27853), MIC values were consistently higher using the absorbance method. Therefore, use of EUCAST MIC breakpoint data provided an overestimate of antibiotic resistance in my clinical isolates. Since EUCAST breakpoints could not be used, the relative antibiotic susceptibility of my isolates was assessed by comparison with MIC data for quality control strains. For *S. aureus* strains, MIC values were highly similar for all antibiotics apart from ciprofloxacin. For this antibiotic, clinical isolates presented with much higher MIC values. For *P. aeruginosa* strains, MIC values for meropenem, tetracycline, tobramycin and gentamicin were increased for clinical isolates compared to the ATCC reference strain. A particularly large increase in MIC values was observed for tetracycline.

Deviation from the EUCAST protocol prevents direct comparisons between my MIC data and antibiotic susceptibility data from previous studies. However, I have identified a number of conserved trends, including high levels of ciprofloxacin resistance amongst *S. aureus* isolates. A longitudinal study conducted in South India showed a significant increase in *S. aureus* resistance to fluoroquinolones, including ciprofloxacin, over a 12-year period (Lalitha et al., 2017) and clinicians have warned against the continued use of ciprofloxacin monotherapy for bacterial keratitis due to the emergence of

ciprofloxacin resistant strains (Kunimoto et al., 1999, Sharma et al., 2004). These findings are in agreement with my data, which showed staphylococcal isolates were completely resistant or highly resistant to ciprofloxacin at all concentrations tested. Despite increasing resistance, fluoroquinolones remain a popular treatment for bacterial keratitis due to their broad-spectrum activity and the most commonly prescribed fluoroquinolones are ciprofloxacin, levofloxacin and moxifloxacin (Redgrave et al., 2014). For example, 0.5% levofloxacin is currently prescribed as the first-line treatment for bacterial keratitis at the Royal Hallamshire Hospital in Sheffield. The popularity of fluoroquinolones may explain trends in antibiotic resistance for *P. aeruginosa*. Lalitha et al showed no significant increase in *P. aeruginosa* resistance to ciprofloxacin, levofloxacin, gentamicin, chloramphenicol or tobramycin over a 12-year period (Lalitha et al., 2017), whereas a significant increase in *P. aeruginosa* resistance to moxifloxacin was reported (Das et al., 2019). This may reflect the move from second-generation fluoroquinolones (i.e., ciprofloxacin and levofloxacin) to fourth-generation fluroquinolones (i.e., moxifloxacin) in recent years. Amongst my *P. aeruginosa* isolates, MIC values were notably increased for tetracycline compared to the ATCC reference strain. High levels of tetracycline resistance are well-documented in *P. aeruginosa* strains and tetracycline resistance is largely attributed to intrinsic resistance mechanisms such as the possession of multi-drug efflux pumps (Grossman, 2016). Increased tetracycline resistance in clinical isolates may be explained by additional antibiotic resistance genes, acquired via horizontal gene transfer. A recent study comparing Indian and Australian keratitis isolates revealed increased numbers of acquired antibiotic resistance genes amongst Indian isolates, including the *tetG* tetracycline resistance gene (Khan et al., 2020). This gene encodes a metal-tetracycline/H$^+$ antiporter which removes tetracycline via active efflux and was present in 56% of Indian isolates compared to 0% of Australian isolates. Acquired genes conferring resistance to aminoglycoside antibiotics were also increased in the Indian isolate population. Therefore, high rates of horizontal gene transfer may explain increased resistance to tetracycline and aminoglycoside antibiotics within the clinical isolate population.

4.4.4. Genome sequencing

In section **4.3.5**, genome sequencing data for *P. aeruginosa* clinical isolates was used to identify antibiotic resistance genes. CARD: RGI identified antibiotic resistance genes for all isolates and the most perfect/strict hits (with ≥ 90% sequence identity) were recorded for LVP3, LVP4, LVP5, LVP6 and LVP27. The majority of antibiotic resistance genes were associated with antibiotic efflux and antibiotic drug classes most affected by AR genes included fluoroquinolones, tetracycline and phenicol antibiotics. The number of AR genes identified, and the drug classes affected were highly similar for isolates LVP3-6. This mirrored the MIC data as only small differences in antibiotic susceptibility were

observed for these isolates. Furthermore, the large number of tetracycline resistance genes identified by CARD: RGI explains why these isolates demonstrated such high levels of resistance (128-256 mg/L) to tetracycline antibiotic. However, a large number of antibiotic resistance genes were also identified for fluoroquinolones and LVP3-6 presented with fairly low MIC values for ciprofloxacin (4-16 mg/L).

Antibiotic efflux constitutes a major antibiotic resistance mechanism in *P. aeruginosa* and multiple efflux systems have been reported (Dreier and Ruggerone, 2015). For example, 12 different efflux systems belonging to the Resistance Nodulation Division (RND) family have been identified in *P. aeruginosa* PAO1 and of these, the MexAB-OprM, MexCD-OprJ, MexEF-OprN, and MexXY-OprM systems are known to play a major role in antibiotic resistance (Fernandez and Hancock, 2012). Therefore, it stands to reason that a high proportion of AR genes in the isolate population are linked to antibiotic efflux. There are a number of possible explanations for why large numbers of fluoroquinolone resistance genes did not correspond to high MIC values for ciprofloxacin. Firstly, whilst genome sequencing data confirms the presence or absence of genes, it does not provide expression data. It may be that certain fluoroquinolone resistance genes were not expressed under my experimental conditions and therefore did not provide activity against ciprofloxacin. Secondly, there may be functional redundancy amongst fluoroquinolone resistance genes, whereby multiple genes contribute to the same resistance mechanism with limited additive effects. For example, closer inspection of CARD: RGI hits for LVP3, revealed that all fluoroquinolone resistance genes were associated with the RND family of efflux pumps. In contrast, mutations in *gyrA*, *gyrB*, *parC* and *parE*, were not observed. These genes encode the protein subunits of DNA gyrase and DNA topoisomerase IV and it is these bacterial enzymes that are directly targeted by fluoroquinolone antibiotics (Redgrave et al., 2014). Therefore, mutations in these enzymes are associated with high-level fluoroquinolone resistance. In contrast, antibiotics are still expected to interact with DNA gyrase and/or DNA topoisomerase enzymes in LVP3, resulting in low-level fluoroquinolone resistance.

In section **4.3.6**, genome sequencing data for *P. aeruginosa* clinical isolates were used to identify virulence factor genes of interest. All 39 isolates possessed genes encoding elastase A (*lasA*), elastase B (*lasB*), alkaline protease (*aprA*) and serine protease IV (*prpL*) and all isolates apart from LVP32 encoded the *Pseudomonas aeruginosa* Small Protease (*pasP*). Isolates were classified as invasive or cytotoxic based on the possession of *exoS* or *exoU* respectively, and within my isolate population, the majority of isolates (79.5%) were invasive. There was also variation in the *fliC* gene and both a-type and b-type *fliC* alleles were observed within the population. The b-type allele was more prevalent and was present in 61.5% of isolates.

A number of these findings contradict previous reports on bacterial keratitis isolates. For instance, it has previously been suggested that cytotoxic *P. aeruginosa* strains are the dominant pathotype in *P. aeruginosa* keratitis. A UK-based study showed that *exoU* +ve *P. aeruginosa* strains were predominant within their isolate population, accounting for 59% of *P. aeruginosa* isolates (Winstanley et al., 2005) and comparison between the *P. aeruginosa* keratitis subpopulation and the global *P. aeruginosa* population revealed a strong disequilibrium for certain genetic markers, including *exoU* (Stewart et al., 2011). In contrast, the vast majority of my isolates were *exoS* +ve. This suggests that differences in exotoxin profile may be linked to geographic variations in the *P. aeruginosa* population, rather than differences in corneal virulence between pathotypes. Aetiological differences may also play a role. Contact-lens wear represents the major risk factor for developing bacterial keratitis in more developed countries (e.g., UK), whereas ocular trauma constitutes the major risk factor in countries with a large agricultural workforce (e.g., India) (Bharathi et al., 2007, Ung et al., 2019). Therefore, differences between UK and Indian isolate populations could also represent differences in the infection environment. I propose that whilst different pathotypes may be associated with different clinical symptoms, e.g., invasive isolates have been associated with larger corneal ulcers (Borkar et al., 2013), both pathotypes are equally capable of initiating corneal infections. Winstanley et al also reported an increased prevalence of the a-type *fliC* allele within their isolate population, accounting for 76% of isolates (Winstanley et al., 2005), whereas only 35.9% of my isolates possessed this allele. The vast remainder of isolates encoded the b-type allele, with the exception of LVP43, which possessed neither allele. The *fliC* gene encodes flagellin, the major subunit of the *P. aeruginosa* flagella and non-flagellated mutants have been associated with loss of *P. aeruginosa* virulence (Montie et al., 1982). Therefore, it seems unlikely that *fliC* is absent and instead, the reported absence of this gene may be linked to sequencing errors. This highlights one of the major limitations of MinION sequencing. MinION generates longer reads than traditional Illumina sequencing and this is advantageous for genome assembly as it allows the structural organisation of repetitive regions to be resolved (Wick et al., 2017). However, MinION sequencing is also more prone to sequencing errors and concerns regarding the quality of genome assemblies were raised in **section 2.5.6**, following use of the QUAST Quality Assessment Tool (Gurevich et al., 2013). The QUAST report revealed high contig numbers and low N50 values for a number of isolates, including LVP43, and these metrics are indicative of a poor-quality genome assembly. Similar metrics were reported for LVP32, and this was the only isolate in my *P. aeruginosa* population shown not to possess the *pasP* gene. Therefore, it seems plausible that the absence of *fliC* and *pasP* in LVP43 and LVP32, respectively, may be linked to sequencing errors. The PASP protease has been shown to play an important role in corneal virulence and is highly conserved amongst *P. aeruginosa* keratitis isolates (O'Callaghan et al., 2019), therefore it will be important to

repeat sequencing of LVP32. If LVP32 is a true *pasP* mutant, this isolate could be highly useful in infection studies.

4.4.5. Future work

There are a number of additional experiments that could be performed as part of this chapter. Firstly, if MIC experiments were to be repeated, it would be valuable to determine MIC values by eye and culture bacteria in MH broth instead of LB, so that EUCAST breakpoint data could be used to determine antibiotic susceptibility. It would also be useful to incorporate additional fluoroquinolone antibiotics into MIC experiments, specifically levofloxacin and moxifloxacin. Fluoroquinolones are a popular choice of antibiotic for bacterial keratitis infections and levofloxacin is routinely used at the Royal Hallamshire Hospital. Therefore, MIC data for levofloxacin could have useful clinical implications. It would also be interesting to compare MIC values for levofloxacin and moxifloxacin. Moxifloxacin is a fourth-generation fluoroquinolone and therefore I would expect increased susceptibility to this antibiotic. It would also be clinically valuable to perform Minimum Biofilm Eradication Concentration (MBEC) testing to determine which antibiotics are able to clear *S. aureus*/*P. aeruginosa* biofilms and how these MBEC values compare with MIC values. By the time patients seek treatment for bacterial keratitis, the bacterial infection is likely to be well established and a corneal biofilm may be present. Therefore, MBEC measurements are perhaps more clinically relevant than MIC testing. Finally, it would also be beneficial to repeat genome sequencing for the *P. aeruginosa* LVP32 isolate, as BLAST analysis did not identify the *pasP* gene within this strain. The *pasP* gene encodes *Pseudomonas aeruginosa* Small Protease (PASP), which has been reported to play an important role in corneal virulence. Therefore, if this gene is truly absent, LVP32 would be a highly interesting isolate to incorporate into infection studies.

4.4.6. Conclusion

In summary, a number of clinical bacterial keratitis isolates have been identified which would be interesting to incorporate into the HCE2 transwell infection model (**Chapter 5**) and/or future infection studies. All of the clinical isolates tested demonstrated biofilm forming activity, making them suitable for studying biofilm infections at the cornea and a number of specific isolates (e.g., LVP3 and LVP32) are of particular interest due to their antibiotic resistance profile and possession of virulence factor genes, respectively.

CHAPTER 5: SIMPLE CELL CULTURE INFECTION MODELS

5.1. Introduction

This chapter describes the use of simple cell culture models to study putative anti-adhesion therapies and their effects on infected HCE2 monolayers. Infected HCE2 monolayers were intended to mimic bacterial keratitis infections, and I was particularly interested in disrupting bacterial adhesion, as this is the first stage of infection pathogenesis. Anti-adhesion therapies included CD9-derived tetraspanin peptides and unfractionated heparin (UFH) and simple cell culture models provided a cheap, high-throughput alternative to the transwell and BioFlux infection models described in **Chapters 6** and **7**. Therefore, these models were used to perform preliminary testing stages, identifying effective anti-adhesion treatments and suitable concentrations for future work. Infection studies predominantly involved *S. aureus* SH1000-GFP but *P. aeruginosa* PAO1-GFP was also included in UFH adhesion assays. The majority of experiments described in this chapter are bacterial adhesion assays and there are two main reasons for this. Firstly, CD9 peptides and UFH are both hypothesised to limit infection progression by inhibiting bacterial adhesion to epithelial cells (see **section 1.8**). Therefore, quantification of adherent bacteria constituted the major infection output of interest. Secondly, multiple comparison studies were designed to assess the suitability of the bacterial adhesion protocol. This protocol is difficult to perform and may be compromised by non-specific bacterial binding. Therefore, there were concerns that non-cell associated bacteria could be masking the effects of anti-adhesion treatments. In addition to bacterial adhesion experiments, CD9 expression was investigated following infection and qPCR was used to investigate changes in cytokine expression in response to CD9 peptide/UFH treatment conditions.

5.1.1. Bacterial adhesion assays

The main focus of this chapter was to investigate the effects of CD9-derived tetraspanin peptides and unfractionated heparin (UFH) on bacterial adhesion to HCE2 monolayers. These experiments were performed using a standard 96-well plate format, optimised by previous laboratory members. Prior to infection, HCE2 cells were seeded onto uncoated, 96-well plates at a seeding density of 40,000 cells/well and incubated overnight. The use of uncoated plastic represents a discrepancy between bacterial adhesion assays and all other experiments involving HCE2 cells. However, previous laboratory members had shown that coating reagents were associated with increased non-specific binding and therefore uncoated plastic was used as part of the standard protocol. On the day of infection, HCE2 monolayers were incubated in 5% BSA to reduce non-specific binding and pre-treated with CD9 peptide/UFH/medium only control for 1 hr. Cells were then infected with *S. aureus*/*P.*

aeruginosa under the chosen infection conditions and at the end of the infection period, non-adherent bacteria were removed by washing with PBS. Infected HCE2 monolayers were then incubated in 2% saponin to induce cell lysis and lysates were plated onto agar so that CFU/well calculations could be performed. All bacterial adhesion experiments involved no cell controls that were used to measure non-specific binding to tissue culture plastic, or 'background binding' and adhesion data was rejected if CFU/well values for no cell controls were higher than CFU/well measurements for HCE2 conditions. Data in this chapter has also been presented as % bacterial adhesion values. These values were calculated by subtracting no cell control values from the HCE2 conditions. The remaining CFU/well measurements were then expressed as a percentage of the untreated (i.e., no CD9 peptide or UFH) condition.

5.1.1.1. CD9-derived tetraspanin peptides

The CD9-derived tetraspanin peptides share amino acid sequence with the EC2 domain of CD9 tetraspanin (**Figure 5-1**). Early experiments involved the 800 peptide, and this peptide was shown to reduce staphylococcal adhesion to human keratinocytes by as much as 60% (Ventress et al., 2016). Recent studies have used the 800-cap and 800ii peptides. 800-cap is almost identical to 800 peptide but it contains an additional N-terminal aspartate residue that completes an alpha helical structure in the native EC2 domain. 800ii is a variation of 800-cap in which two alanine residues have been replaced by an (S)-2-(4-pentenyl) alanine staple to improve peptide stability. Previous laboratory members have shown that these CD9 peptides are able to reduce staphylococcal adhesion to A549 human alveolar basal epithelial cells (unpublished data, Green et al.) and Dr Rahaf Issa demonstrated significant reductions in bacterial adhesion to HCE2 monolayers using a range of bacterial pathogens. These HCE2 studies included *S. aureus* SH1000; the clinical skin isolate, MRSA6; and clinical *S. aureus* keratitis isolates (unpublished data). Dr Mahendra Raut also performed bacterial adhesion experiments using MRSA6 and observed significant effects of the 800ii peptide at 200 nM but not 800-cap (unpublished data). Both Dr Rahaf Issa and Dr Mahendra Raut used 1 hr infection conditions. In contrast, experiments involving RT4 human bladder epithelial cells and Uropathogenic *Escherichia coli* (UPEC) have yielded highly variable results (Albaldi, 2022). Dr Fawzyah Albaldi observed minor effects of the 800-cap peptide but reductions in bacterial adhesion were non-significant compared to the 800-SCR control and multiple laboratory members have reported difficulties with the bacterial adhesion protocol due to high levels of background binding.
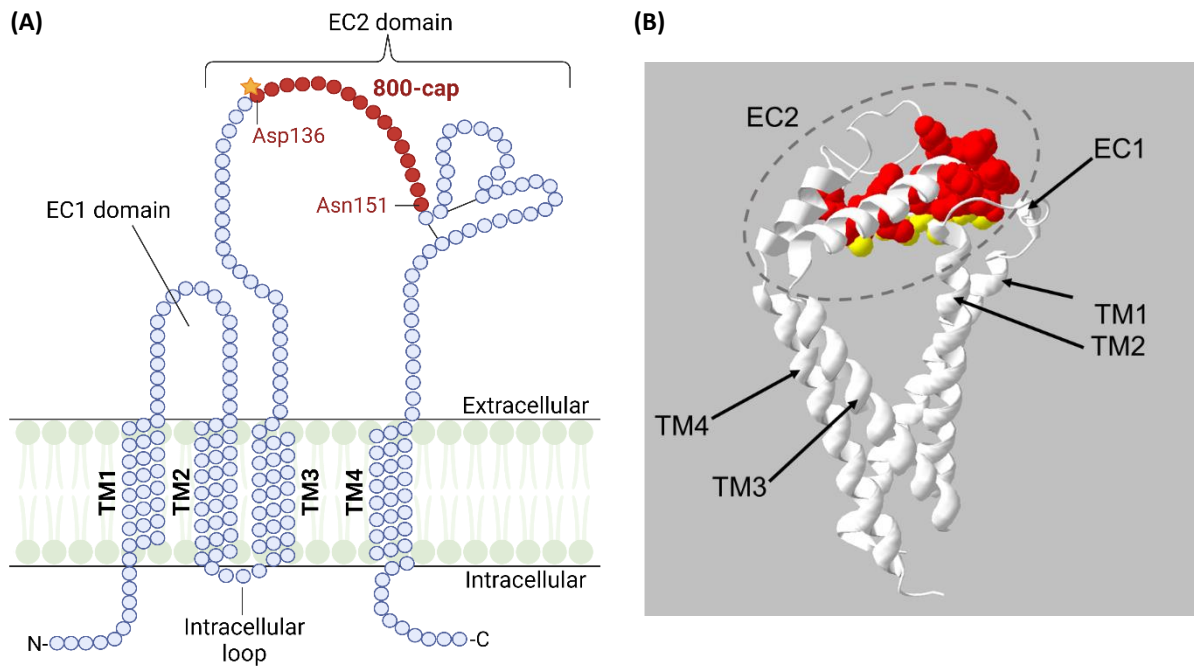
Figure 5-1. Origin of the CD9-derived tetraspanin peptides.
The CD9-derived tetraspanin peptides are derived from the amino acid sequence of the EC2 loop in CD9 tetraspanin. **(A) Schematic of CD9 and 800-cap.** Each circle represents a different amino acid. Red has been used to highlight the 16-aa region which shares its sequence with 800-cap peptide. A star has been used to label the aspartate 'cap'- this amino acid was not included in the original 800 peptide sequence. Created with Biorender.com and adapted from Ventress et al., 2016. **(B) 3D structure of the CD9 tetraspanin protein.** CD9 transmembrane domains (TM1-4) and two extracellular loop regions (EC1/EC2) have been labelled. Amino acids included in the 800-cap sequence are shown in red and yellow. Red represents 'active' residues and yellow represents 'inactive' residues, as identified by Dr Rahaf Issa. Inactive residues can be substituted for other amino acids with no effect on peptide activity and (S)-2-(4-pentenyl) alanine staples in the 800ii peptide were placed in the position of two inactive alanine residues. Created by Professor Peter Monk using structural data for CD9 tetraspanin protein (PDB DOI: 10.2210/pdb6K4J/pdb) (Umeda et al., 2020) in PyMOL (Schrödinger).

5.1.1.2. Unfractionated heparin (UFH)

Heparin is a soluble analogue of heparan sulphate (HS), which is commercially produced and used as an anti-coagulant. Both heparin and heparan sulphate are examples of glycosaminoglycans (GAGs) and heparan sulphate is commonly expressed at the mammalian cell surface as part of membrane proteoglycans (e.g., the heparan sulphate proteoglycans, HSPGs) (see **section 1.8.2**) (Aquino and Park, 2016). Previous researchers have demonstrated the importance of GAGs in bacterial adhesion to mammalian cells and addition of exogenous heparan sulphate has been shown to significantly reduce bacterial adhesion to the HCE2 human corneal epithelial cell line (Garcia et al., 2016), as well as lung epithelial and fibroblast cell lines (Rajas et al., 2017). Furthermore, heparin has been shown to reduce adhesion of *Neisseria gonorrhoeae* to epithelial-like, Chinese Hamster Ovary (CHO) cells (Chen et al.,

142

1995). However, these anti-adhesion effects were only observed at high concentrations with reverse effects observed at low concentrations. In recent years, members of our laboratory have been investigating the effects of medical-grade, unfractionated heparin on staphylococcal adhesion to human cell lines. UFH has been shown to significantly reduce *S. aureus* adhesion to RT4 and A549 epithelial cell lines (Albaldi & Green, unpublished data) and this HS mimic is proposed to block staphylococcal adhesion by displacing fibronectin at the host cell surface (Green et al, unpublished data). However, the inhibitory effects of UFH are biphasic with decreasing efficacy at high concentrations. 10 U/ml UFH was identified as the optimal concentration for inhibiting *S. aureus* adhesion to the A549 cell line and therefore this concentration has been used throughout the project.

5.2. Aims

1. To use simple cell culture models to investigate the effects of CD9-derived tetraspanin peptides (800-cap and 800ii) on bacterial adhesion to HCE2 monolayers.
2. To use simple cell culture models to investigate the effects of unfractionated heparin (UFH) on bacterial adhesion to HCE2 monolayers.
3. To investigate changes in cytokine expression in response to CD9 peptides and UFH.

5.3. Results

5.3.1. CD9 expression in the HCE2 cell line is unaffected by 2 hr infection with *S. aureus* or *P. aeruginosa*.

In the previous chapter uninfected HCE2 cells were shown to express CD9, making these cells a suitable model for testing CD9-derived tetraspanin peptides. However, it was important to confirm that CD9 expression levels were not altered in response to infection. Flow cytometry was used to compare CD9 expression in uninfected HCE2 cells and cells infected with clinical isolates of *S. aureus* (LVP11) and *P. aeruginosa* (LVP3) (**Figure 5-2**). For *S. aureus*, an average MFI value of 9646.5 ± 788 was reported for LVP11-infected cells versus 10277.3 ± 346 for uninfected cells (**Figure 5-2A**). For *P. aeruginosa*, an average MFI value of 12187.7 ± 1083.3 was reported for LVP3-infected cells, whereas uninfected cells had an average MFI value of 12484.3 ± 1316.7 (**Figure 5-2B**). There was no significant difference in MFI between infected and uninfected HCE2 cells for either infection condition ($p > 0.05$ for both conditions, n=3, unpaired t-test).
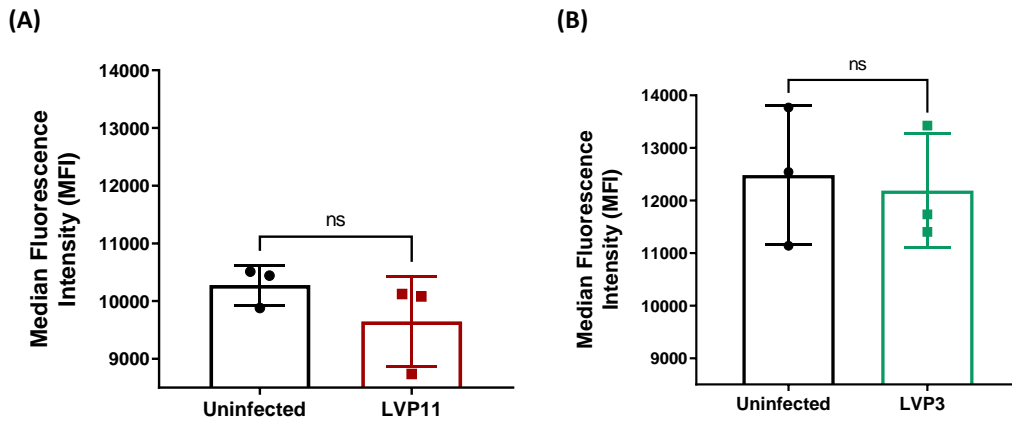
Figure 5-2. CD9 expression in HCE2 cells following bacterial infection.
(A) Infection with clinical *S. aureus* isolate, LVP11 (B) Infection with clinical *P. aeruginosa* isolate, LVP3.
HCE2 monolayers were infected with bacteria for 2 hrs. Uninfected, medium only controls were also included. After 2 hrs, HCE2s were harvested and CD9 expression was quantified by flow cytometry. Data represent mean values ± SD, n=3 for all conditions. Data was analysed by unpaired t-test, ns= not significant.

5.3.2. Pre-treatment of HCE2 cells with 800ii CD9-derived tetraspanin peptide has no significant effect on SH1000-GFP adhesion to HCE2 monolayers under the majority of infection conditions.

Adherence of *S. aureus* bacteria was investigated under multiple infection conditions, including: HCE2 monolayers infected with bacteria; HCE2 monolayers pre-treated with 800ii CD9 peptide and then infected with bacteria; HCE2 monolayers pre-treated with scrambled CD9 peptide and then infected with bacteria; and empty wells infected with bacteria (**Figure 5-3**, **5-4** and **5-5**). A range of peptide concentrations and infection conditions were trialled but the *S. aureus* laboratory strain, SH1000-GFP was used throughout. Pre-treatment of HCE2 monolayers with 200 nM peptide, followed by 4 hr infection with SH1000-GFP, revealed no significant effects of the 800ii peptide (or scrambled control) on bacterial adhesion (**Figure 5-3**). At MOI 5, CFU per well values were significantly reduced under no cell conditions ($9.56 \times 10^5 \pm 2.27 \times 10^5$), as compared to the untreated HCE2 condition ($3.80 \times 10^5 \pm 8.64 \times 10^4$) (p= 0.0003), demonstrating the occurrence of cell-specific binding (**Figure 5-3A**). However, there was no significant difference in CFU/well values for untreated HCE2 cells and 800ii-treated ($9.16 \times 10^5 \pm 1.42 \times 10^5$) or SCR-treated ($8.95 \times 10^5 \pm 4.90 \times 10^4$) HCE2 monolayers (p > 0.05 in all cases, n=3, two-way ANOVA with Tukey's multiple comparisons test). Following % bacterial adhesion calculations, the mean % adhesion value for 800ii-treated cells (90.7% ± 40.0) was lower than that of SCR-treated cells (108.7% ± 33.1). However, neither peptide had a significant effect on bacterial adhesion compared to the untreated control (p= 0.8433 for 800ii, p=0.8619 for SCR, n=5, one-way ANOVA with Dunnett's multiple comparisons test) (**Figure 5-3B**).

Varied results were observed when HCE2 monolayers were infected with SH1000-GFP for 1 hr, then washed and incubated for an additional 3 hrs (**Figure 5-4**) and these findings were influenced by peptide concentration. At 200 nM peptide concentration, CFU per well values were increased for HCE2 infection conditions, as compared to no cell controls, at both MOIs (**Figure 5-4A**). However, statistical analysis was not performed due to low number of repeats (n=1 for MOI 5, n=2 for MOI 10). Following combination of MOI conditions for % bacterial adhesion calculations, a significant reduction in bacterial adhesion was observed for 800ii-treated cells (29.4% ± 8.4) (p= 0.0012) (**Figure 5-4B**). However, a significant reduction was also recorded for SCR-treated cells (41.1% ± 21.7) (p= 0.0031, n=3, one-way ANOVA with Dunnett's multiple comparisons) and one-way ANOVA with Tukey's multiple comparisons showed no significant difference between 800ii and SCR peptide conditions (p= 0.5677, data not shown). This suggests anti-adhesion effects of the peptide were non-specific at this concentration. In contrast, no significant effects of the peptides were observed at 20 nM concentration (**Figure 5-4C**, **D** and **E**). Average CFU/well values were increased for HCE2 infection conditions, as compared to no cell controls at MOI 5, 10 and 20 (**Figure 5-4C**). However, a significant difference in CFU/well values for untreated HCE2 monolayers ($9.04 \times 10^5 \pm 2.34 \times 10^5$) compared to no cell controls ($5.21 \times 10^5 \pm 2.85 \times 10^5$) was only observed at MOI 20 (p= 0.0075, n=4, two-way ANOVA with Dunnett's multiple comparisons) and large variations in bacterial numbers were recorded at all MOIs. Bacterial adhesion calculations revealed no significant difference in SH1000-GFP adhesion to host cells for either peptide (p > 0.05 in all cases) (**Figure 5-4D**, **E**). However, mean % adhesion values were reduced for 800ii compared to scrambled peptide at MOI 5 (67.5% vs 88.7%), MOI 10 (86.3% vs 105.2%) and MOI 20 (100.5% vs 121.5%) (**Figure 5-4D**). Following combination of MOI conditions, an average % bacterial adhesion value of 84.6% ± 35.6 was reported for 800ii-treated cells and a value of 105.1% ± 43.8 was reported for SCR-treated cells (**Figure 5-4E**). Compared to untreated HCE2 monolayers (100%), no significant difference in bacterial adhesion was observed for either peptide condition (p= 0.4432 for 800ii, p= 0.9070 for SCR, n=11, one-way ANOVA with Dunnett's multiple comparisons).

Pre-treatment of HCE2 monolayers with 200 or 20 nM peptide, followed by 1 hr infection, showed no effect of the peptides on bacterial adhesion at either concentration (**Figure 5-5**). At 200 nM peptide concentration, CFU per well values were increased for HCE2 infection conditions, as compared to no cell controls, at MOI 10 and 20 (**Figure 5-5A**). However, statistical analysis was not performed due to low number of repeats (n=2 for MOI 10, n=2 for MOI 20). Following combination of MOI conditions for % bacterial adhesion calculations, values of 92.6% ± 30.1 and 88.6% ± 29.6 were reported for 800ii and SCR-treated cells, respectively (**Figure 5-5B**). No significant difference in bacterial adhesion was observed for either peptide (p= 0.4299 for 800ii, p= 0.6618 for SCR, n=4, one-way ANOVA with

Dunnett's multiple comparisons). At 20 nM concentration, there was a significant difference in CFU/well values for cells versus no cell conditions at MOI 5 (p= 0.0037) and MOI 10 (p= 0.0002, n=3, two-way ANOVA with Dunnett's multiple comparisons) (**Figure 5-5C**). % Bacterial adhesion calculations revealed no significant difference in SH1000-GFP adhesion in the presence of peptide (p > 0.05 in all cases) (**Figure 5-5D**, **E**) and there was large variation in the dataset for MOI 5 (**Figure 5-5D**). Following combination of MOI conditions, a mean % adhesion value of 92.7% ± 29.3 was recorded for 800ii-treated cells and 104.6% ± 37.8 was reported for SCR-treated monolayers (**Figure 5-5E**).

(A)

(B)

HCE2 + SH1000   HCE2 + SH1000 + 800ii   HCE2 + SH1000 + SCR   SH1000
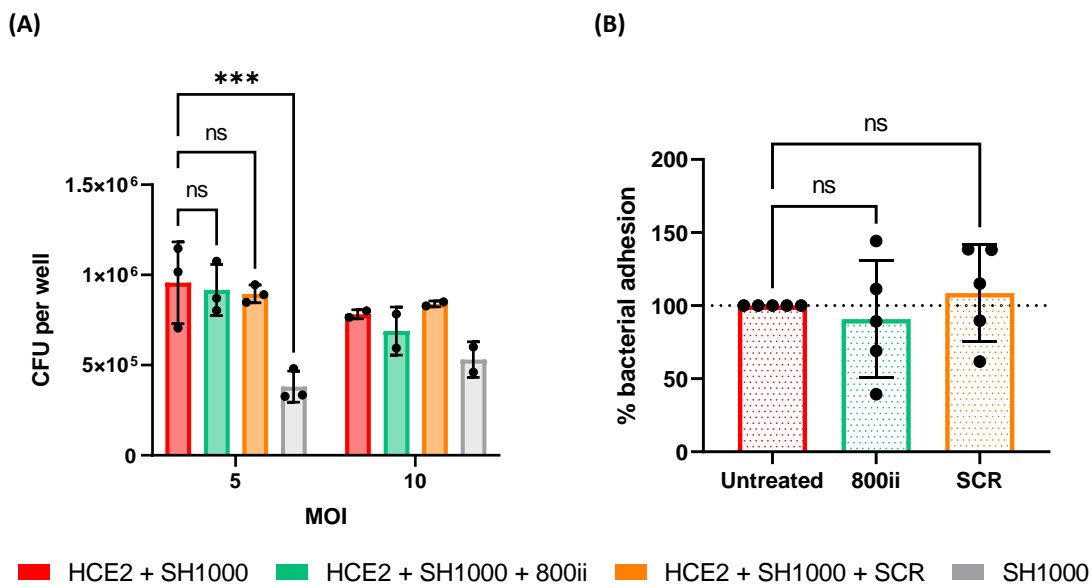
Figure 5-3. Effects of the 800ii CD9 peptide on bacterial adhesion to HCE2 monolayers, following 4 hr continuous infection with SH1000-GFP.
HCE2 cells were pre-treated with 200 nM 800ii peptide, 200 nM scrambled (SCR) peptide or tissue culture medium only and then infected with SH1000-GFP at MOI 5 or 10, for 4 hrs. No HCE2 cell controls were also included. **(A) CFU per well data.** Data represent mean ± SD, n=3 for MOI 5, n=2 for MOI 10. Data was analysed by two-way ANOVA with Dunnett's multiple comparisons test, ***p ≤ 0.001, ns= not significant. **(B) % bacterial adhesion.** Average CFU/well values for the no cell control have been subtracted and values for peptide-treated cells are expressed as a % of the no treatment control. MOI conditions shown in (A) have been combined. Data represent mean ± SD, n=5. Data was analysed by one-way ANOVA with Dunnett's multiple comparisons test.
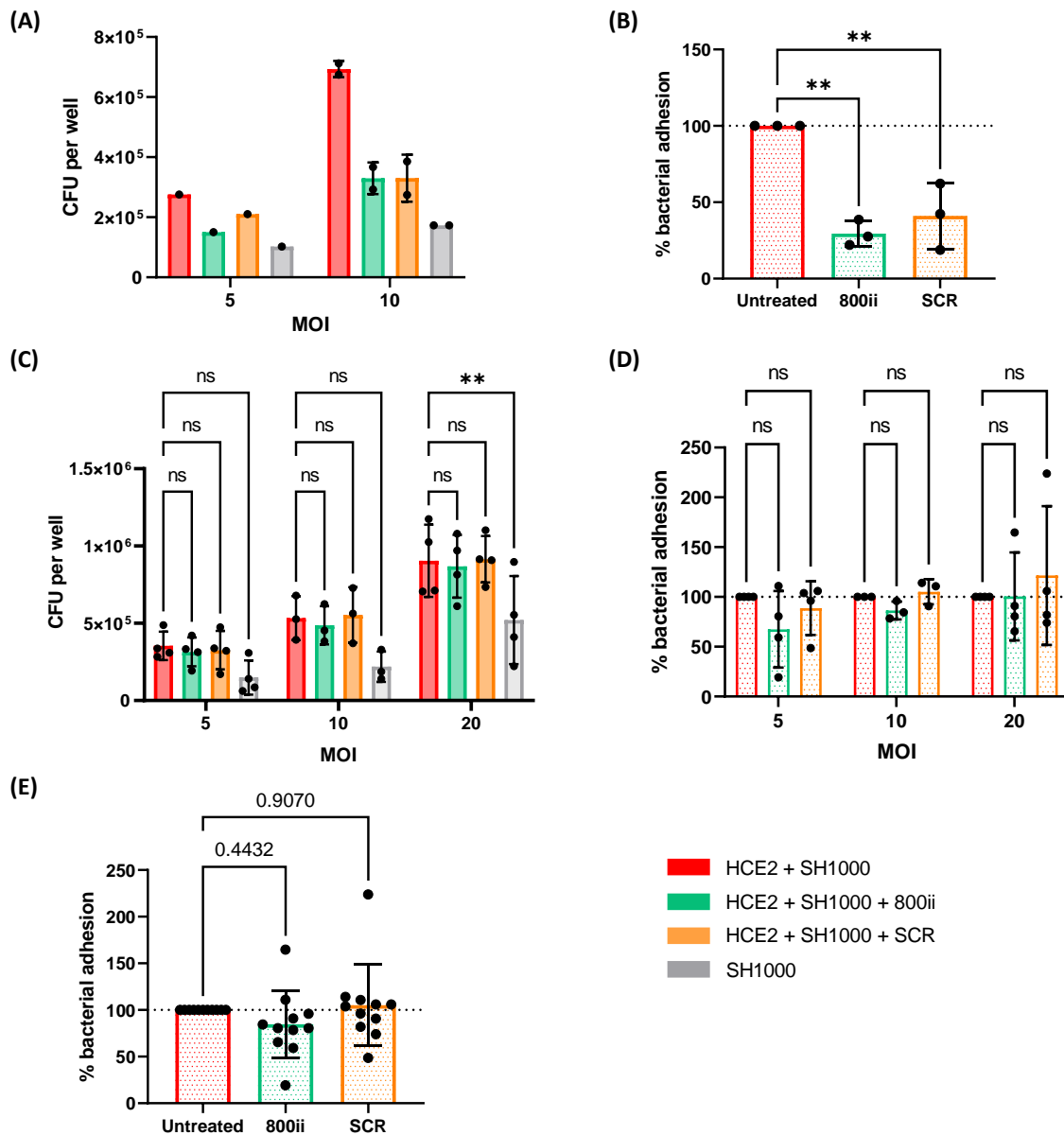
Figure 5-4. Effects of the 800ii CD9 peptide on bacterial adhesion to HCE2 monolayers, following 1 hr initial infection and 3 hrs incubation with SH1000-GFP.

(A-B) 200 nM peptide. (C-E) 20 nM peptide. HCE2 cells were pre-treated with 800ii peptide, scrambled (SCR) peptide or tissue culture medium only and then infected with SH1000-GFP at MOI 5, 10 or 20, for 1 hr. After 1 hr, the bacterial inoculum was removed and well were washed with HBSS. Tissue culture medium (with/without peptides) was replaced, and plates were incubated for an additional 3 hrs. No HCE2 cell controls were also included. **(A) CFU per well data.** Data represent mean ± SD, n=1 for MOI 5, n=2 for MOI 10. **(B) % bacterial adhesion.** Average CFU/well values for the no cell control have been subtracted and values for peptide-treated cells are expressed as a % of the no treatment control. MOI conditions shown in (A) have been combined. Data represent mean ± SD, n=3. Data was analysed by one-way ANOVA with Dunnett's multiple comparisons test, **p ≤ 0.01. **(C) CFU per well data.** Data represent mean ± SD, n=3 for MOI 10, n=4 for MOI 5 and 20. Data was analysed by two-way ANOVA with Dunnett's multiple comparisons test, ns= not significant. **(D) % bacterial adhesion, individual MOIs.** Data represent mean ± SD, n=3 for MOI 10, n=4 for MOI 5 and 20. Data was analysed by two-way ANOVA with Dunnett's multiple comparisons test. **(E) % bacterial adhesion, all MOIs.** MOI conditions shown in (C/D) have been combined. Data represent mean ± SD, n=11. Data was analysed by one-way ANOVA with Dunnett's multiple comparisons test.

147
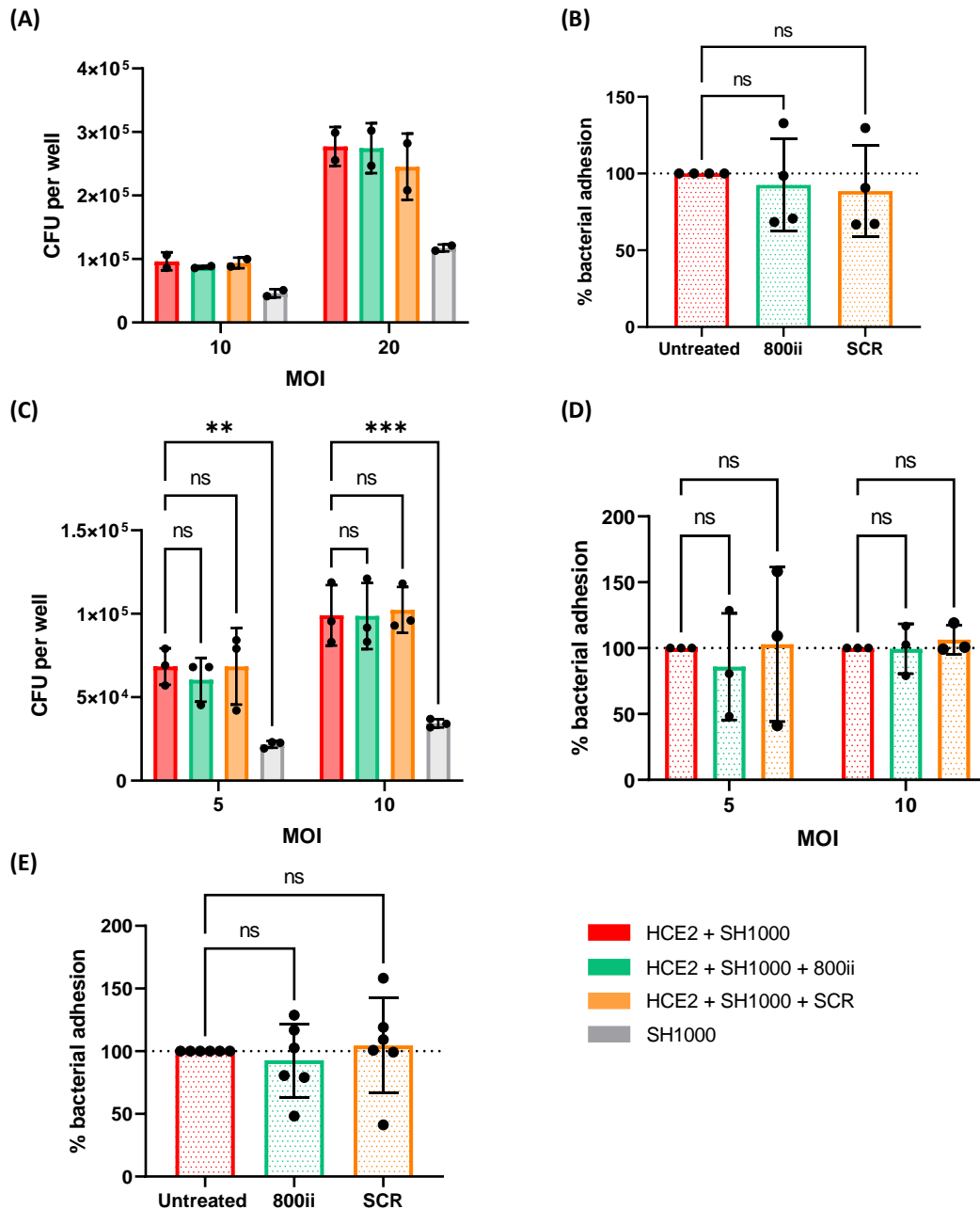
Figure 5-5. Effects of the 800ii CD9 peptide on bacterial adhesion to HCE2 monolayers, following 1 hr infection with SH1000-GFP.

(A-B) 200 nM peptide. (C-E) 20 nM peptide. HCE2 cells were pre-treated with 800ii peptide, scrambled (SCR) peptide or tissue culture medium only and then infected with SH1000-GFP at MOI 5, 10 or 20, for 1 hr. No HCE2 cell controls were also included. **(A) CFU per well data.** Data represent mean ± SD, n=2 for MOI 10 and 20. **(B) % bacterial adhesion.** Average CFU/well values for the no cell control have been subtracted and values for peptide-treated cells are expressed as a % of the no treatment control. MOI conditions shown in (A) have been combined. Data represent mean ± SD, n=4. Data was analysed by one-way ANOVA with Dunnett's multiple comparisons test, ns= not significant. **(C) CFU per well data.** Data represent mean ± SD, n=3 for MOI 5 and 10. Data was analysed by two-way ANOVA with Dunnett's multiple comparisons test, **$p \leq 0.01$, ***$p \leq 0.001$. **(D) % bacterial adhesion, individual MOIs.** Data represent mean ± SD, n=3 for MOI 5 and 10. Data was analysed by two-way ANOVA with Dunnett's multiple comparisons test. **(E) % bacterial adhesion, all MOIs.** MOI conditions shown in (C/D) have been combined. Data represent mean ± SD, n=6. Data was analysed by one-way ANOVA with Dunnett's multiple comparisons test.

148

5.3.2.1. Experimental conditions were validated using comparison studies, but these studies also highlighted problems with non-specific binding.

Due to unexpected results in **section 5.3.2**, which showed limited effects of the 800ii CD9 peptide on bacterial adhesion, a series of comparison studies were conducted to optimise my experimental protocol and/or confirm the suitability of chosen conditions. The 96-well bacterial adhesion protocol involved a series of PBS wash steps, which were performed at the end of the infection period. It was hypothesised that the original washing technique (i.e., swirling each plate 5 times between PBS washes, referred to as wash condition 1) was not removing all non-adherent bacteria and therefore these bacteria were masking the anti-adhesion effects of the 800ii CD9 peptide. To test this hypothesis, three new washing techniques (wash conditions 2, 3 and 4) were trialled and relative differences in bacterial adhesion were measured using CFU/well (**Figure 5-6**). Both HCE2 monolayers and no cell controls were included and there was no significant difference in CFU per well between these conditions for any of the four wash techniques ($p > 0.05$ in all cases, n=4, two-way ANOVA with Šidák's multiple comparisons test) (**Figure 5-6A**). These findings revealed a high degree of background binding under all conditions, caused by bacteria adhering non-specifically to plastic. The difference in CFU/well values for cells versus no cell conditions was compared for each washing condition (**Figure 5-6B**) and statistical analysis revealed no significant difference between conditions ($p > 0.05$ in all cases, n=4, one-way ANOVA with Tukey's multiple comparisons), although wash conditions 3 and 4 were associated with reduced variability. Of these conditions, wash condition 4 (i.e., use of the shaker for all wash steps) was selected as the optimal washing technique, as the difference between cell and no cell conditions was larger for this condition at $8.58 \times 10^4 \pm 2.32 \times 10^4$, as compared to $5.31 \times 10^4 \pm 1.71 \times 10^4$ for condition 3. The effect of different washing conditions on HCE2 cell numbers was also investigated by crystal violet staining (**Figure 5-7**). Absorbance readings revealed no significant difference between wash conditions ($p > 0.05$ in all cases, n=3, two-way ANOVA with Tukey's multiple comparisons test). Since none of the wash conditions were associated with increased disruption of HCE2 monolayers, they were all considered suitable for the bacterial adhesion assay. The effect of using collagen-coated versus uncoated 96-well plates was also investigated (**Figure 5-8** and **5-9**). Throughout the project, HCE2 cells were routinely cultured on fibronectin or collagen-coated plastic. However, uncoated plates were used for bacterial adhesion assays to reduce non-specific binding to tissue culture plates. The relatively short length of time between cell seeding and infection (16-24 hrs), meant normal HCE2 morphology was retained during these conditions. Sulforhodamine B (SRB) staining was used to quantify relative numbers of adherent HCE2 cells under different conditions (**Figure 5-8** and **5-9**) as SRB is a protein-binding dye that stains cellular proteins non-specifically (Skehan et al., 1990). HCE2 cells were seeded onto uncoated or collagen-coated plastic at a range of

149

cell seeding densities and highly similar absorbance readings were recorded following overnight culture of cells (**Figure 5-8**). The effects of using uncoated versus collagen-coated plastic were also investigated following 1 hr infection of HCE2 monolayers with SH1000-GFP and no significant difference was observed between coating conditions (p > 0.05 in all cases, n=3, two-way ANOVA with Šidák's multiple comparisons test) (**Figure 5-9**). Finally, SRB staining was used to compare preparations of 5% BSA and measure potential effects on cell viability (**Figure 5-10**). As part of the bacterial adhesion protocol, HCE2 monolayers were incubated in 5% BSA (prepared in HBSS) to reduce non-specific binding of bacteria to tissue culture plates. Subtle changes in cell morphology were observed during incubation of HCE2 monolayers in 5% BSA. Based on this observation, 5% BSA was prepared using KSFM tissue culture medium and under these conditions, changes in HCE2 morphology were not observed. Therefore, it was hypothesised that 5% BSA prepared in HBSS had detrimental effects on HCE2 cell viability, perhaps causing cell detachment. SRB staining was used to compare HCE2 cell monolayers following 1 hr incubation in different BSA preparations (**Figure 5-10**). However, absorbance readings were highly similar under HBSS (0.730 ± 0.177) and KSFM (0.834 ± 0.396) conditions, refuting the cell detachment hypothesis.
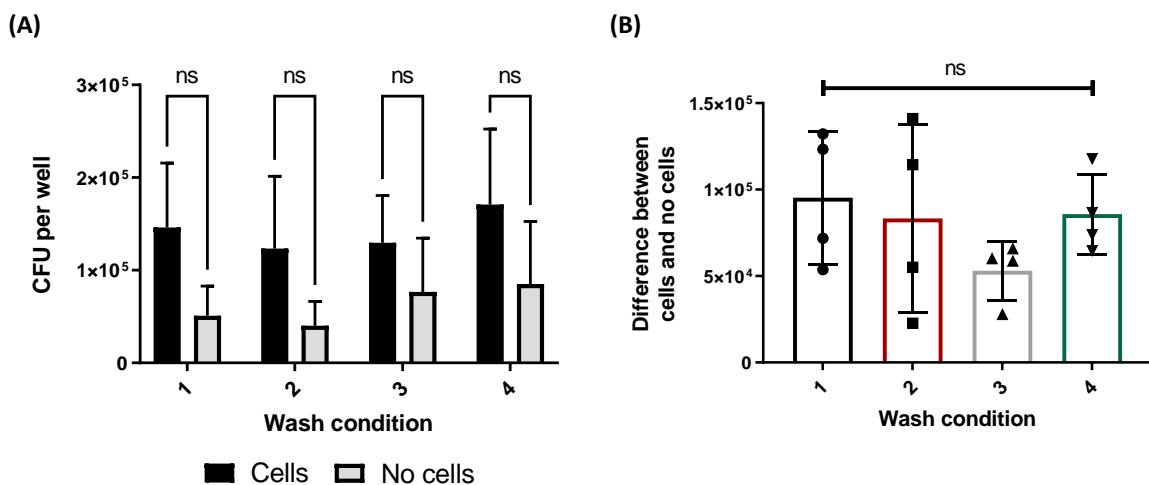
Figure 5-6. Measuring the numbers of adherent bacteria under different wash conditions.
HCE2 monolayers or no cell controls were infected with SH1000-GFP at MOI 20 for 1hr. Four different PBS wash conditions were trialled to remove non adherent bacteria at 1hr. 1= plate is swirled 5 times for each wash (original condition). 2= vigorous swirling, plate is swirled 20 times for each wash. 3= plate is washed 1x on shaker (for 1 min at 130 rpm) and then washed 3x by swirling plate 5 times. 4= shaker is used for each wash step (for 1 min at 130 rpm). Data represent mean ±SD, n=4. **(A) All CFU per well values.** Data was analysed using two-way ANOVA with Šidák's multiple comparisons test, ns= not significant. **(B) Difference between cells and no cell conditions.** CFU/well values for no cell controls have been subtracted. Data was analysed by one-way ANOVA with Tukey's multiple comparisons.
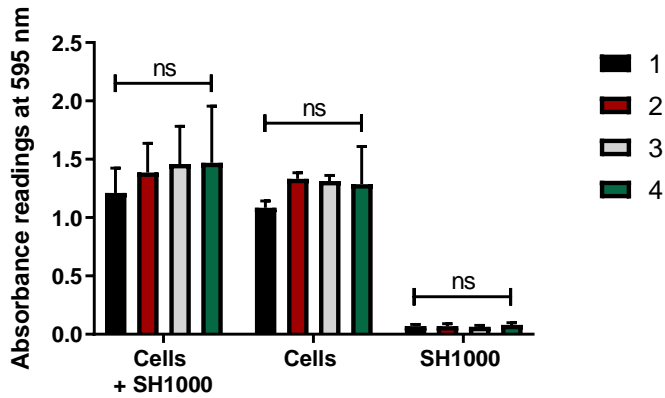
Figure 5-7. The use of crystal violet staining to determine whether HCE2 cell numbers are affected by different wash conditions.

HCE2s were cultured in a 96-well plate and then infected with SH1000-GFP at MOI 20 for 1 hr or incubated with tissue culture medium only. No cell controls were also included (SH1000). Four different wash conditions were trialled. 1= plate is swirled 5 times for each wash (original condition). 2= vigorous swirling, plate is swirled 20 times for each wash. 3= plate is washed 1x on shaker (for 1 min at 130 rpm) and then washed 3x by swirling plate 5 times. 4= shaker is used for each wash step (for 1 min at 130 rpm). After PBS washes, samples were fixed with 4% PFA and stained using 0.01% crystal violet. Data represent mean ±SD, n=3. Data was analysed by two-way ANOVA with Tukey's multiple comparisons test, ns= not significant.
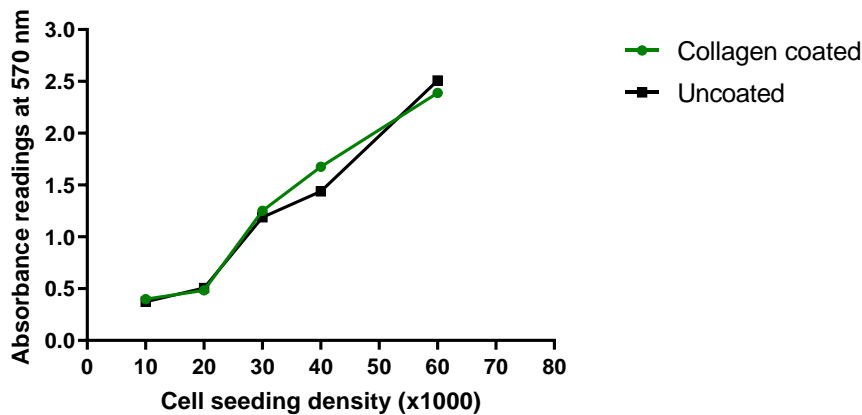
Figure 5-8. Relative numbers of adherent HCE2 cells on collagen coated vs uncoated plastic.

HCE2s were seeded into 96-well plates that had been coated with 0.1 mg/ml bovine collagen type I or left uncoated (standard condition). Different seeding densities, ranging from 10,000- 60,000 cells/well, were trialled and cells were cultured overnight. SRB staining was performed, and cell numbers were quantified, as measured by absorbance at 570 nm. No cell controls were also included; absorbance readings for these wells have been subtracted. Data represent mean values for 3 technical replicates, n=1.
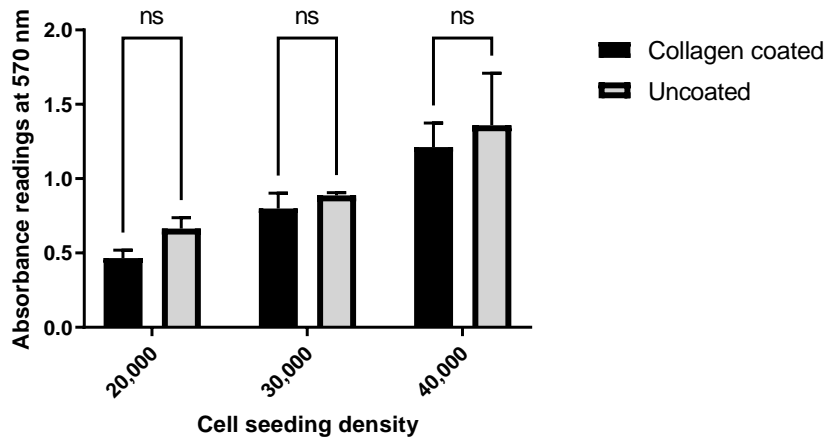
Figure 5-9. Relative numbers of adherent HCE2 cells on collagen coated vs uncoated plastic, following infection with SH1000-GFP.

HCE2s were seeded onto collagen coated or uncoated plastic at a range of seeding densities and then infected with SH1000-GFP at MOI 20 for 1 hr. Wells were washed 4x with PBS and SRB staining was performed. Number of adherent HCE2s is measured by absorbance at 570 nm. No cell controls were also included; absorbance readings for these wells have been subtracted. Data represent mean ±SD, n=3. Data was analysed by two-way ANOVA with Šidák's multiple comparisons test, ns= not significant.
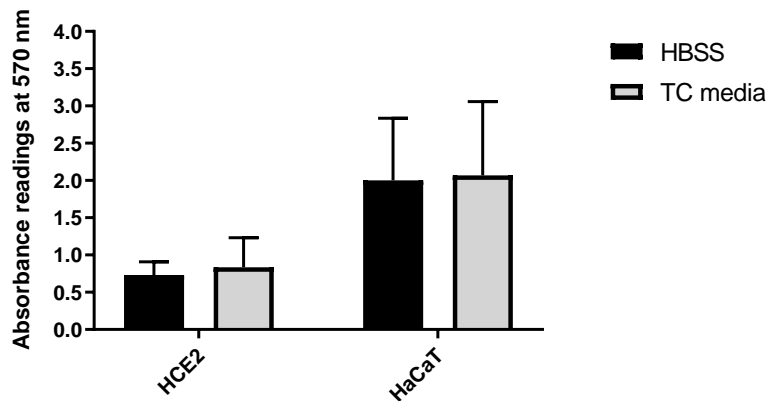
Figure 5-10. Comparing numbers of adherent cells following 1 hr incubation in 5% BSA, prepared using HBSS or cell culture medium.

Cells were seeded onto an uncoated 96-well plate and incubated overnight. The following day cells were washed 1x with HBSS and incubated in 5% BSA for 1 hr. BSA was prepared using HBSS (standard) or the appropriate tissue culture medium. After 1 hr, cells were washed 1x with HBSS and SRB staining was performed. The HaCaT, human keratinocyte cell line was included as a control. Number of adherent cells is measured by absorbance at 570 nm. Data represent mean ±SD, n=2.

5.3.3. Pre-treatment of HCE2 cells with 800-cap CD9-derived tetraspanin peptide had no significant effects on SH1000-GFP adhesion to cells.

Staphylococcal adhesion to HCE2 monolayers was also investigated using the 800-cap CD9-derived tetraspanin peptide (**Figure 5-11**, **5-12**). However, fewer infection conditions were trialled due to time constraints. An initial experiment testing a range of peptide concentrations (0.2-200 nM) was conducted to identify the most effective concentrations for future work (**Figure 5-11**). Average CFU/well values were larger for HCE2 monolayer conditions than no cell controls at all peptide concentrations (**Figure 5-11A**), however there was large variability in the data, particularly under scrambled peptide conditions (**Figure 5-11**). Following % bacterial adhesion calculations, peptide concentrations of 0.2 nM and 2 nM were selected for future work. Under these conditions, average % adhesion values were below 100%, at 83.3% ± 41.3 and 62.4% ± 42.2, respectively. Repeat experiments were carried out almost a year later and so datasets have not been combined due to potential differences in the HCE2 population. One of the major difficulties with using the HCE2 cell line was that frozen stocks were at a high passage number and therefore, freshly thawed cells were only used for 10-15 additional passages (up until P55-P60). Subtle differences in HCE2 morphology were observed between frozen stocks and so biological replicates were always performed using HCE2 cells from the same frozen stock population. Later experiments, utilising 0.2 nM and 2 nM 800-cap peptide, showed no significant effects of the peptide on bacterial adhesion to HCE2 monolayers (**Figure 5-12**). However, variation in CFU per well data was greatly reduced compared to earlier experiments and CFU/well values were significantly reduced under no cell conditions ($2.06 \times 10^4 \pm 4.08 \times 10^3$), as compared to untreated HCE2 monolayers ($4.09 \times 10^4 \pm 4.50 \times 10^3$), indicating a considerable degree of cell-specific binding (p= 0.0039, n=3, one-way ANOVA with Dunnett's multiple comparisons test) (**Figure 5-12A**). % Bacterial adhesion calculations revealed no significant difference between untreated HCE2 monolayers (100%) and any of the peptide conditions (one-way ANOVA with Dunnett's multiple comparisons test) (**Figure 5-12B**) and there was also no significant difference between 800-cap and scrambled peptide conditions at either concentration (p > 0.05 in all cases, n=3, one-way ANOVA with Tukey's multiple comparisons test). However, % bacterial adhesion values were consistently lower for 800-cap compared to the scrambled peptide at peptide concentrations of 2 nM (89.0% ± 12.3 vs 101.0% ± 16.0) and 0.2 nM (89.7% ±27.6 vs 96.5% ± 26.0).

(A)

(B)

■ HCE2 + SH1000   ■ HCE2 + SH1000 + 800-cap   ■ HCE2 + SH1000 + SCR   ■ SH1000
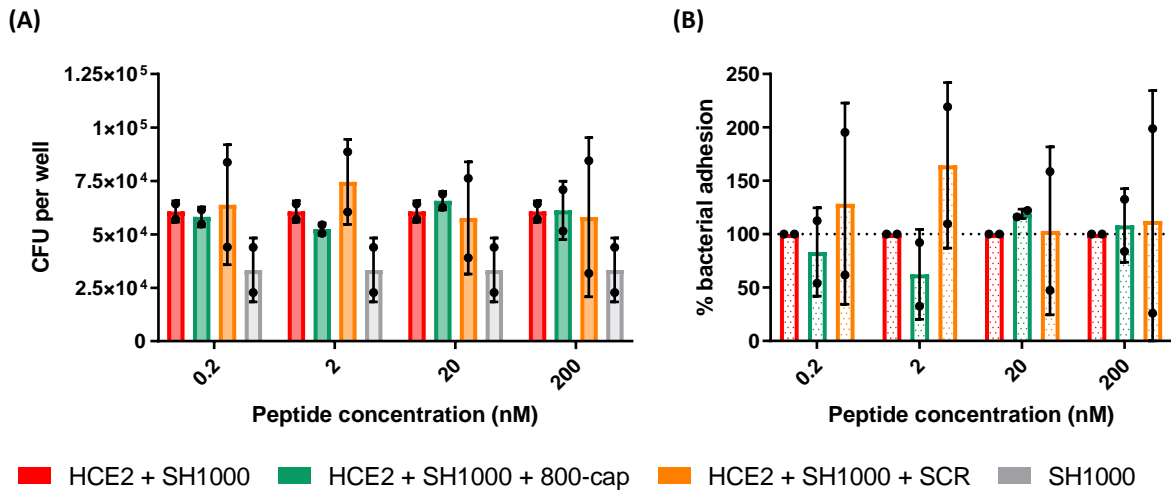
Figure 5-11. Effects of the 800-cap CD9 peptide, at 0.2-200 nM concentration, on bacterial adhesion to HCE2 monolayers following 1 hr infection with SH1000-GFP.
HCE2 cells were pre-treated with 800-cap peptide, scrambled (SCR) peptide or tissue culture medium only control, at a range of concentrations (0.2-200 nM). Pre-treated wells were then infected with SH1000-GFP at MOI 10 for 1 hr. No HCE2 controls were also included. **(A) CFU per well data.** Data represent mean ± SD, n=2. **(B) % bacterial adhesion.** Average CFU/well values for the no cell control have been subtracted and values for peptide-treated cells are expressed as a % of the no treatment control. Data represent mean ± SD, n=2.

(A)

(B)
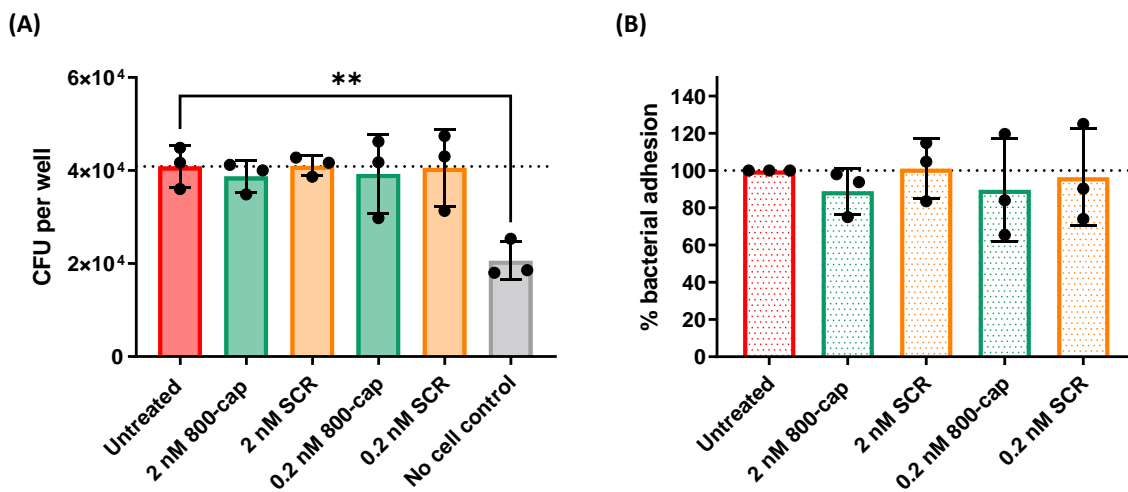
Figure 5-12. Effects of the 800-cap CD9 peptide, at 0.2-2 nM concentration, on bacterial adhesion to HCE2 monolayers following 1 hr infection with SH1000-GFP.
HCE2 cells were pre-treated with 800-cap peptide, scrambled (SCR) peptide or tissue culture medium only control, using 0.2 or 2 nM peptide concentrations. Pre-treated wells were then infected with SH1000-GFP at MOI 5 for 1 hr. No HCE2 controls were also included. Data represent mean ± SD, n=3. **(A) CFU per well.** Data was analysed by one-way ANOVA with Dunnett's multiple comparisons test, **$p ≤ 0.01$. **(B) % Bacterial adhesion.** Average CFU/well values for the no cell control have been subtracted and values for peptide-treated cells are expressed as a % of the no treatment control.

154

5.3.4. Pre-treatment of HCE2 cells with unfractionated heparin (UFH) causes a significant reduction in bacterial adhesion to cells.

Bacterial adhesion was investigated under multiple infection conditions, including: HCE2 monolayers infected with bacteria; HCE2 monolayers pre-treated with 10 U/ml UFH and then infected with bacteria; and empty wells infected with bacteria (**Figure 5-13** and **Figure 5-14**). For 96-well plates infected with the *S. aureus* SH1000-GFP laboratory strain, there was a significant difference between CFU/well values for infected HCE2 monolayers ($6.18 \times 10^4 \pm 1.73 \times 10^4$) and no HCE2 control wells ($3.09 \times 10^4 \pm 1.20 \times 10^4$) (p = 0.0321) (**Figure 5-13A**). There was also a significant difference between infected HCE2 monolayers and infected HCE2 monolayers pre-treated with 10 U/ml UFH ($3.09 \times 10^4 \pm 1.27 \times 10^4$) (p = 0.0318, n=4, one-way ANOVA with Tukey's multiple comparisons test) and CFU/well values for UFH-treated cells closely resembled those of the no HCE2 control. The average CFU/well value for the no HCE2 control was subtracted from the other conditions to account for bacteria that were non-specifically bound to plastic. Remaining bacteria in the UFH condition were expressed as a percentage of the bacteria in the untreated HCE2 condition and a significant reduction in *S. aureus* adhesion was observed for UFH-treated cells (p= 0.0006, n=4, unpaired t-test) (**Figure 5-13B**). The number of adherent bacteria in the UFH condition was approximately 14.7% of bacterial numbers in the untreated condition and therefore an 85.3% reduction in SH1000 adhesion was observed.

For experiments using the *P. aeruginosa* laboratory strain, PAO1-GFP, a significant difference in CFU/well values was observed between infected HCE2 monolayers ($5.03 \times 10^4 \pm 7.30 \times 10^3$) and no HCE2 control wells ($3.78 \times 10^4 \pm 4.97 \times 10^3$) (p = 0.0325) (**Figure 5-14A**). However, there was no significant difference between any other conditions (p > 0.05, n=4, one-way ANOVA with Tukey's multiple comparisons test) and average CFU/well for UFH-treated HCE2 monolayers was $4.13 \times 10^4 \pm 4.72 \times 10^3$. Following subtraction of no HCE2 control values, percentage adhesion calculations displayed a significant reduction in *P. aeruginosa* adhesion for UFH-treated cells (p = 0.0006, n=4, unpaired t-test) (**Figure-14B**). The number of adherent bacteria in the UFH condition was approximately 31.2% of bacterial numbers in the untreated condition and therefore a 68.8% reduction in PAO1 adhesion was observed following pre-treatment of cells with 10 U/ml UFH. It should be noted that intact HCE2 monolayers were observed under all conditions following 1 hr infection with *S. aureus* or *P. aeruginosa*. However, cell viability assays were not performed.

(A)

(B)
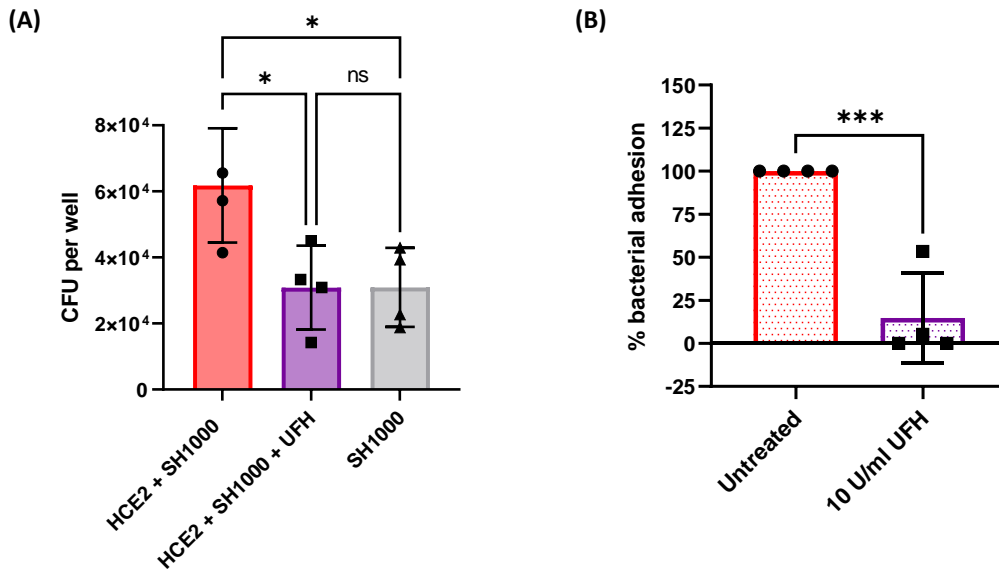
Figure 5-13. The effect of unfractionated heparin on bacterial adhesion of SH1000-GFP to HCE2 cells.
HCE2s were pre-treated with 10 U/ml unfractionated heparin (UFH) for 1 hr and then infected with SH1000-GFP at MOI 5 for 1 hr. The optimised infection protocol for measuring bacterial adhesion was used and no cell controls (SH1000) were included. Data represent mean values ± SD, n=4. **(A) CFU per well data.** Data was analysed by one-way ANOVA with Tukey's multiple comparisons test, *p ≤ 0.05, ns= not significant. **(B) % bacterial adhesion.** Average values for the no cell control have been subtracted and data for UFH-treated cells is expressed as a % of the no treatment control. Negative values are recorded as 0%. Data was analysed by unpaired t-test, ***p ≤ 0.001.

(A)

(B)
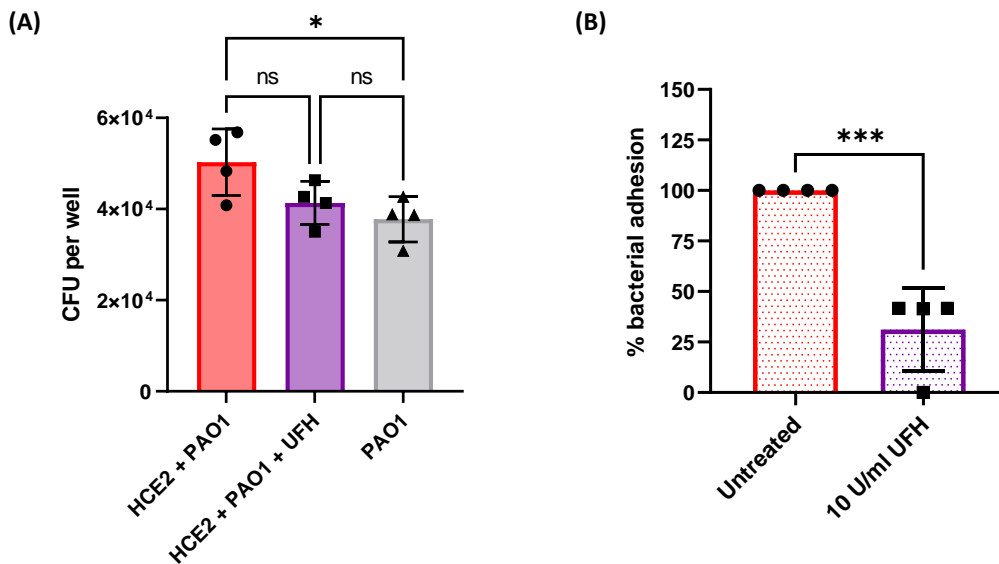
Figure 5-14. The effect of unfractionated heparin on bacterial adhesion of PAO1-GFP to HCE2 cells.
HCE2s were pre-treated with 10 U/ml unfractionated heparin (UFH) for 1 hr and then infected with PAO1-GFP at MOI 1 for 1 hr. The optimised infection protocol for measuring bacterial adhesion was used and no cell controls (PAO1-GFP) were included. Data represent mean values ± SD, n=4. **(A) CFU per well data.** Data was analysed by one-way ANOVA with Tukey's multiple comparisons test, *p ≤ 0.05, ns= not significant. **(B) % bacterial adhesion.** Average values for the no cell control have been subtracted and data for UFH-treated cells is expressed as a % of the no treatment control. Negative values are recorded as 0%. Data was analysed by unpaired t-test, ***p ≤ 0.001.

156

5.3.5. mRNA expression of cytokines in infected HCE2 cells is unaffected by pre-treatment of HCE2 monolayers with CD9-derived peptide or UFH.

HCE2 mRNA expression of interleukin-6 (IL-6), interleukin-8 (IL-8), Tumor Necrosis Factor alpha (TNFα), Chemokine Ligand 20 (CCL20) and Glyceraldehyde-3-Phosphate Dehydrogenase (GAPDH) was investigated under multiple infection conditions, using qPCR. An extended infection period of 3.5 hrs was used to allow sufficient time for changes in gene expression to occur and expression was determined using cycle threshold (Ct) values, which are inversely related to mRNA expression (**Figure 5-15**). An SH1000 only control, containing no HCE2 cells was included as a negative control and Ct values for this condition were used as a benchmark for no expression.

Ct values for IL-6 revealed mRNA expression of this cytokine under all infection conditions: untreated (30.3 ± 2.0), 800-cap-treated (30.5 ± 1.7), 800-SCR-treated (28.1 ± 0.9), UFH-treated (29.3 ± 2.3) (**Figure 5-15A**). There was no significant difference between any of these conditions ($p > 0.05$) but Ct values were significantly reduced compared to the SH1000 only control (36.0 ± 0.04) ($p \leq 0.05$ in all cases). In contrast, IL-6 was not expressed by uninfected HCE2 cells (38.0 ± 1.8) and Ct values were not significantly reduced compared to the SH1000 only control ($p = 0.6733$, n=3, one-way ANOVA with Tukey's multiple comparisons test). Ct values for IL-6 and GAPDH (endogenous control) were used to calculate relative expression of IL-6 under different infection conditions (**Figure 5-16A**). Compared to untreated, infected HCE2 monolayers (=1), there was no significant difference in IL-6 expression for 800-cap-treated (1.8 ± 2.5), 800-SCR-treated (10.0 ± 15.0) or UFH-treated cells (1.8 ± 1.7) ($p > 0.05$ in all cases, n=3, one-way ANOVA with Dunnett's multiple comparisons test).

Similarly, IL-8 expression was not detected for uninfected HCE2 cells (38.5 ± 1.2) but reduced Ct values were observed for infected HCE2 cells under all conditions: untreated (33.4 ± 0.4), 800-cap-treated (32.7 ± 0.2), 800-SCR-treated (34.0 ± 3.4), UFH-treated (35.0 ± 3.4) (**Figure 5-15B**). However, statistical analysis revealed no significance difference between these conditions, nor between infection conditions and the SH1000 only control ($p > 0.05$). However, a significant difference between 800-cap-treated cells and uninfected cells was observed ($p = 0.0380$, n=3, one way ANOVA with Tukey's multiple comparisons test). Therefore, it may be that IL-8 mRNA is present in infected HCE2 cells, but expression levels are very low. Relative expression of IL-8 was calculated under different infection conditions (**Figure 5-16B**) and there was no significant difference in IL-8 expression for 800-cap-treated (1.7 ± 0.6), 800-SCR-treated (1.6 ± 1.8) or UFH-treated cells (0.9 ± 1.1), as compared to untreated cells (=1) ($p > 0.05$ in all cases, n=3, one-way ANOVA with Dunnett's multiple comparisons test).

In contrast, Ct values for TNFα demonstrated clear expression of TNFα-mRNA under all infection conditions: untreated (30.3 ± 1.0), 800-cap-treated (29.6 ± 1.3), 800-SCR-treated (29.4 ± 1.1), UFH-treated (30.3 ± 1.7) (**Figure 5-15C**). There was no significant difference between any of these conditions, but Ct values were significantly reduced compared to the SH1000 only control (36.3 ± 0.6) ($p \leq 0.001$) and uninfected HCE2 cells (35.0 ± 0.6) ($p \leq 0.01$ in all cases). There was no significant difference in Ct values between uninfected HCE2 cells and the SH1000 control (p= 0.6748, n=3, one-way ANOVA with Tukey's multiple comparisons test), confirming TNFα was not expressed by uninfected HCE2 cells. Relative expression of TNFα was calculated under different infection conditions (**Figure 5-16C**) and there was no significant difference in TNFα expression for 800-cap-treated (2.5 ± 2.5), 800-SCR-treated (3.1 ± 4.1) or UFH-treated cells (0.8 ± 0.3), as compared to untreated cells (=1) ($p > 0.05$ in all cases, n=3, one-way ANOVA with Dunnett's multiple comparisons test).

Ct values revealed mRNA expression of CCL20 by uninfected HCE2 cells (30.2 ± 0.7) and infected HCE2 cells under all treatment conditions: untreated (23.1 ± 0.4), 800-cap-treated (23.3 ± 0.6), 800-SCR-treated (22.9 ± 0.4), UFH-treated (23.0 ± 0.6) (**Figure 5-15D**). Ct values were significantly reduced compared to the SH1000 only control (36.3 ± 3.4) for all HCE2 conditions ($p \leq 0.01$). However, CCL20 expression was significantly increased in infected versus uninfected HCE2 cells ($p \leq 0.001$ in all cases, n=3, one-way ANOVA with Tukey's multiple comparisons). Relative expression of CCL20 was calculated under different infection conditions (**Figure 5-16D**) and there was no significant difference in CCL20 expression for 800-cap-treated (0.9 ± 0.4), 800-SCR-treated (1.0 ± 0.4) or UFH-treated cells (0.8 ± 0.4), as compared to untreated cells (=1) ($p > 0.05$ in all cases, n=3, one-way ANOVA with Dunnett's multiple comparisons test).

Expression of GAPDH-mRNA was observed in uninfected HCE2 cells (18.9 ± 0.3) and infected HCE2 cells under all treatment conditions: untreated (19.2 ± 0.3), 800-cap-treated (19.1 ± 0.3), 800-SCR-treated (18.8 ± 0.3), UFH-treated (18.7 ± 0.6) (**Figure 5-15E**). In contrast to findings for IL-6, TNFα and CCL20, there was no significant difference in Ct values for infected and uninfected conditions, confirming its suitability as an endogenous control ($p > 0.05$ in all cases). However, all HCE2 conditions were associated with significant reductions in Ct value, as compared to the SH1000 only control (30.3 ± 1.9) ($p \leq 0.001$ in all cases, n=3, one-way ANOVA with Tukey's multiple comparisons test).
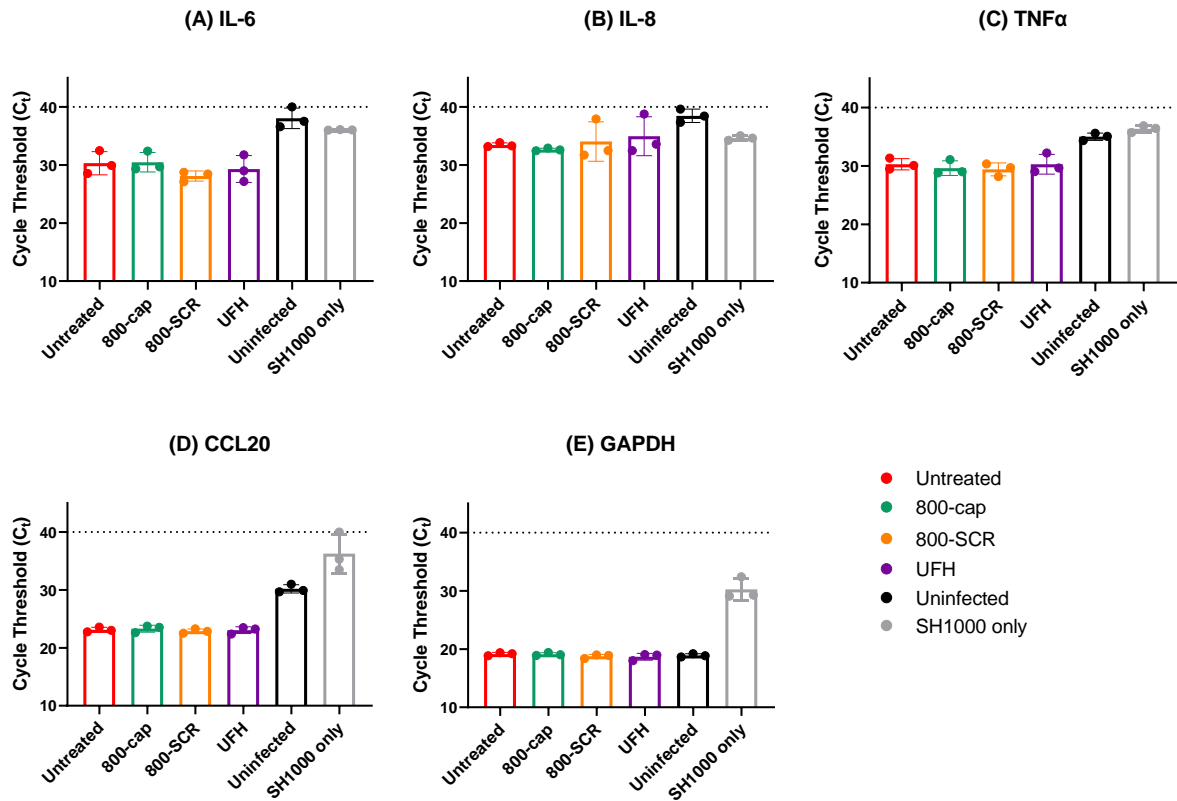
Figure 5-15. mRNA expression of cytokines in response to infection conditions.

HCE2s were pre-treated with 800-cap, 800-SCR, UFH or basal tissue culture medium (untreated control) and infected with SH1000-GFP for 3.5 hrs at MOI 5. Uninfected cells and bacteria-only wells were included as negative controls. Total RNA was extracted and converted to cDNA so that mRNA expression levels could be determined by RT-qPCR. mRNA expression of cytokines IL-6 (A), IL-8 (B), TNFα (C) and CCL20 (D) was investigated. GAPDH (E) was included as an endogenous control. Data represent mean values ± SD, n=3 for all conditions. Data was analysed by one-way ANOVA with Tukey's multiple comparisons test.
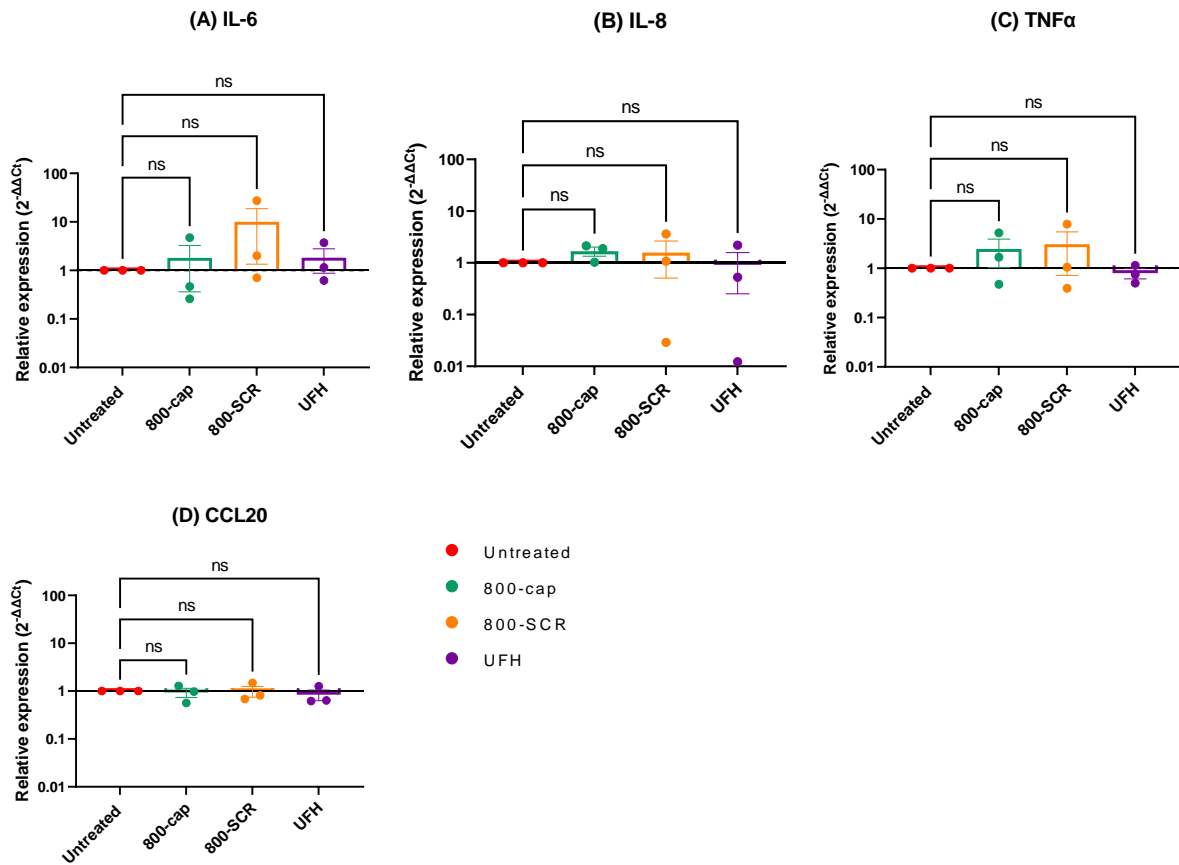
Figure 5-16. Relative expression of cytokines in response to infection conditions.
Data has been normalised using *GAPDH* expression and is shown relative to mRNA expression in untreated HCE2 cells (=1). Data represent mean values ± SD, n=3 for all conditions. Data was analysed by one-way ANOVA with Dunnett's multiple comparisons test, ns= not significant.

5.4. Discussion

5.4.1. Summary of results

In this chapter, infection studies involving simple HCE2 monolayer cultures have been described. These studies were predominantly focussed on bacterial adhesion and the putative anti-adhesion effects of CD9-derived tetraspanin peptides (800-cap and 800ii), and unfractionated heparin (UFH) were investigated. CD9 peptides were shown to have limited effects on staphylococcal adhesion and there were concerns regarding the experimental protocol. Early infection studies involved 800ii and although this peptide was shown to reduce staphylococcal adhesion under certain conditions, its effects were non-specific as reductions in bacterial adhesion were also observed for the 800-SCR control peptide, which does not share sequence homology with CD9 tetraspanin. Based on these findings, 800ii was replaced with 800-cap and optimisation studies were performed. These studies highlighted problems with non-specific bacterial binding and new washing conditions were selected. However, follow-up studies involving 800-cap also revealed no significant effects of the peptide. Due to time constraints, it was not possible to test the 800ii peptide using optimised techniques and it would be beneficial to complete additional CD9 peptide studies using different bacterial strains and/or species. Therefore, although I have begun to investigate the effects of CD9 peptides on bacterial adhesion to HCE2 monolayers, this aim has not been fully achieved. In contrast, bacterial adhesion studies involving UFH were successful and complete datasets were collected for *S. aureus* SH1000-GFP and *P. aeruginosa* PAO1-GFP, thereby achieving my second aim for this chapter. In these studies, 10 U/ml UFH was shown to cause significant reductions in bacterial adhesion to HCE2 monolayers for both bacterial species. The final aim for this chapter was to investigate whether treatment conditions were associated with changes in cytokine expression. This was achieved using qPCR and neither the CD9 peptides nor UFH were shown to alter mRNA expression of cytokines in *S. aureus* infected HCE2 cells. Finally, CD9 expression was investigated in response to infection and no significant difference was observed between infected and uninfected HCE2 cells.

5.4.2. CD9 expression during infection

In **section 5.3.1**, flow cytometry was used to compare CD9 expression in uninfected HCE2 cells and cells infected using clinical isolates of *S. aureus* and *P. aeruginosa*. There was no significant difference in MFI values between uninfected and infected conditions for either bacterial pathogen, leading me to conclude that CD9 expression is not altered in response to infection. Therefore, the HCE2 cell line is suitable for testing CD9-derived tetraspanin peptides and peptide efficacy should not be affected by changes in CD9 expression during infection. To the best of my knowledge, changes in tetraspanin expression in response to *S. aureus*/*P. aeruginosa* expression have not been investigated previously.

However, a significant reduction in CD9 expression was reported for the J774.2 mouse macrophage cell line following 3 hr infection with *Burkholderia thailandensis* (Elgawidi et al., 2020). It should also be noted that only changes in protein expression and not mRNA expression were measured in my experiments. Therefore, it remains possible that changes in CD9 protein expression do occur in response to infection, but these changes are not detectable at the protein-level by 2 hrs post-infection.

5.4.3. Bacterial adhesion assays

5.4.3.1. CD9-derived tetraspanin peptides

In **section 5.3.2**, bacterial adhesion assays were used to investigate the effect of the 800ii CD9 peptide on staphylococcal adhesion to HCE2 monolayers under a range of infection conditions. The peptide was shown to have no significant effect on bacterial adhesion to HCE2 cells under the majority of infection conditions, including 4 hr continuous infection with 200 nM peptide; 4 hr non-continuous infection with 20 nM peptide; 1 hr infection with 200 nM peptide; and 1 hr infection with 20 nM peptide. The only exception was a 4 hr non-continuous infection study involving 200 nM peptide. In this experiment, bacterial adhesion was significantly reduced for 800ii-treated cells, with a % bacterial adhesion value of 29.4% ± 8.4. However, a significant reduction in bacterial adhesion was also observed for SCR-treated cells, with a % bacterial adhesion value of 41.1% ± 21.7. This suggests anti-adhesion effects of the peptide may have been non-specific at this concentration. The findings presented in this section, particularly 1 hr infection data, directly contradict the findings of previous laboratory members. Dr Rahaf Issa used a 1 hr infection period in her experiments and consistently observed anti-adhesion effects of the 800ii peptide at a range of peptide concentrations (unpublished data).

There are a number of possible explanations for these experimental differences. Firstly, Dr Issa carried out her experiments approximately 2 years before this study, using the same batch of HCE2 cells. During these experiments, HCE2 cells will have been at lower passage number, and it is possible that genetic drift may have occurred over time, potentially affecting CD9 expression levels. Furthermore, Dr Rahaf Issa has previously compared bacterial adhesion between low and high passage cells and reported lower numbers of cell-associated bacteria for high passage cells (unpublished data), which could explain high levels of background binding in the 800ii peptide studies. However, it should be noted that this was a small-scale study and statistical significance was not calculated. It is also possible that frozen HCE2 stocks may have deteriorated over time. To test this hypothesis, new HCE2 cells were purchased from ATCC but these cells were later abandoned due to subtle differences in cell morphology and a drastically reduced proliferation rate compared to the original HCE2 cell population.

This highlights a major problem with commercially produced immortalised cell lines, which is that there may be variation between batches of cells and when this occurs, it is difficult to determine which cells are most representative of the *in vivo* cell type. It is also possible that problems with the experimental protocol may have masked anti-adhesion effects of the 800ii peptide. Although no significant effect of the peptide was observed under the majority of infection conditions, % bacterial adhesion values were consistently below 100% for 800ii-treated cells. Furthermore, 800ii values were consistently lower than corresponding adhesion values for SCR-treated cells and this was observed during 4 hr continuous infection with 200 nM peptide (90.7% vs 108.7%); 4 hr non-continuous infection with 20 nM peptide (84.6% vs 105.1%); and 1 hr infection with 20 nM peptide (92.7% vs 104.6%). However, this pattern was not observed during 1 hr infection with 200 nM peptide (92.6% vs 88.6%), providing further support for the idea that high peptide concentrations are associated with non-specific anti-adhesion effects. Potential problems with the experimental protocol included sub-optimal cell culture conditions and high levels of background binding, both of which were investigated in **section 5.3.2.1**.

Section 5.3.2.1 describes the use of comparison studies to optimise the bacterial adhesion protocol and assess the suitability of chosen conditions. There were concerns regarding HCE2 cell viability as ATCC recommends the use of fibronectin coating medium (0.01 mg/ml fibronectin, 0.03 mg/ml bovine collagen type I and 0.01 mg/ml bovine serum albumin) for culturing HCE2 cells on tissue culture plastic. However, Dr Rahaf Issa had previously shown that the standard fibronectin coating medium was associated with high levels of non-specific bacterial binding (unpublished data). Therefore, a reduced coating medium of 0.1 mg/ml bovine collagen type I was used in early peptide studies, and this was later replaced by uncoated conditions. SRB assays were used to investigate whether uncoated versus collagen-coated conditions were associated with differences in the number of adherent HCE2 cells. These studies revealed no significant difference between coating conditions in the presence or absence of *S. aureus* infection and so it was concluded that uncoated conditions were suitable for bacterial adhesion assays. Similarly, SRB assays investigating BSA showed that HCE2 cell numbers were unaffected by use of 5% BSA prepared in HBSS, as compared to BSA prepared in KSFM, despite subtle changes in cell morphology. Therefore, no change in the BSA condition was implemented. One potential limitation of the SRB assays is that sulforhodamine B provides a measurement of cell numbers but not cell viability. Therefore, it may have been more beneficial to assess HCE2 monolayers using an LDH or MTT assay, which measure cell lysis and cellular metabolic activity, respectively (Korzeniewski and Callewaert, 1983, Denizot and Lang, 1986). The PBS wash steps carried out after infection were also subjected to optimisation. Four different washing techniques were trialled and CV assays showed no significant difference in numbers of adherent HCE2 cells between wash conditions.

163

CFU/well measurements also revealed no significant difference in bacterial numbers between conditions but wash condition 4 (use of a shaker for each PBS wash) was selected for future experiments due to the reduced variability of results. During washing experiments, bacterial numbers were quantified in the presence of HCE2 monolayers and no cell controls. It is important to note that no significant difference between cells and no cells was observed under any of the four wash conditions. This demonstrates that large numbers of bacteria were adhering non-specifically to tissue culture plastic and these non-cell associated bacteria were not removed by PBS wash steps. Similar findings were also reported during 800ii experiments (**section 5.3.2**) and following 4 hr non-continuous infection of HCE2 monolayers with 20 nM peptide, there was no significant difference between cell and no cell conditions for the majority of MOIs tested. Taken together, these findings suggest that high levels of SH1000-GFP bacteria which were not specifically bound to HCE2 cells, may have masked subtle effects of the 800ii peptide.

In **section 5.3.3**, bacterial adhesion experiments were performed using the 800-cap CD9 peptide. Preliminary experiments identified peptide concentrations of 2 nM and 0.2 nM as the most suitable concentrations for future work and repeat experiments were carried out towards the end of the project. In these final experiments, CFU/well measurements were significantly reduced under no cell conditions and variation between biological replicates was relatively small. These findings were attributed to improvements in experimental technique. For example, extreme care was taken not to introduce bubbles and a timer was used for saponin scraping steps. However, despite reductions in variation, anti-adhesion effects of the 800-cap peptide were not observed. % Bacterial adhesion values for 800-cap-treated cells were lower than corresponding values for SCR-treated cells under both peptide conditions but these differences were not significant and bacterial adhesion was not significantly reduced compared to untreated controls. These findings match data collected by Dr Mahendra Raut using the MRSA6 clinical isolate. Dr Raut observed significant reductions in bacterial adhesion for 800ii at 200 nM, but not 800-cap (unpublished data). Taken together, these findings suggest 800-cap may be less effective than 800ii at inhibiting *S. aureus* adhesion. One possible explanation for this is peptide stability as Dr Luke Green has previously shown that 800-cap is more susceptible to degradation by *S. aureus* SH1000 than 800ii (unpublished data). It would be interesting to repeat the work carried out in **section 5.3.3** using 800ii peptide under the optimised conditions.

5.4.3.2. Unfractionated heparin (UFH)

In **section 5.3.4**, bacterial adhesion assays were used to investigate the effect of 10 U/ml UFH on bacterial adhesion to HCE2 monolayers. CFU/well values were significantly reduced under no cell

conditions for both *S. aureus* and *P. aeruginosa*, demonstrating the occurrence of cell-specific binding and UFH was associated with significant reductions in bacterial adhesion for both bacterial pathogens. For *S. aureus* SH1000-GFP, an 85.3% reduction in bacterial adhesion was observed following UFH treatment. In contrast, a reduction of 68.8% was observed for *P. aeruginosa* PAO1-GFP. These findings demonstrate that UFH is capable of disrupting a major bacterial adhesion mechanism utilised by both *S. aureus* and *P. aeruginosa*. However, this is not the sole adhesion pathway as bacteria were still able to adhere to HCE2 cells following UFH pre-treatment and differences between bacterial species may represent differences in the bacterial adhesins used by these pathogens. For example, UFH has been proposed to inhibit staphylococcal adhesion by displacing cell-associated fibronectin (see **section 1.8.2**). Fibronectin binding proteins (FnBPA and FnBPB) act as major bacterial adhesins in *S. aureus* and fibronectin plays an important role in the adhesion and subsequent invasion of epithelial cells by *S. aureus* (Fowler et al., 2000). Therefore, removal of endogenous fibronectin is expected to cause significant disruption to *S. aureus* pathogenesis. In contrast, flagella and type IV pili constitute the major bacterial adhesins in *P. aeruginosa* (Jurado-Martin et al., 2021). The flagellar protein, FliC, has been shown to bind heparan sulphate proteoglycans (HSPGs) (Bucior et al., 2012) and integrins have been proposed to act as host receptors for type IV pili (Johnson et al., 2011). In contrast, fibronectin-binding has been linked to outer membrane proteins such as OprQ and these proteins are not regarded as major *P. aeruginosa* adhesins (Arhin and Boucher, 2010). Therefore, the reduced effects of UFH on *P. aeruginosa* adhesion, could represent a reduced dependence on fibronectin for host-cell binding. Alternatively, UFH may inhibit *P. aeruginosa* adhesion via a different mechanism which is not directly linked to loss of fibronectin "adhesion nets." For example, removal of fibronectin could cause changes in the structural organisation of membrane microdomains. Fibronectin has a number of partner proteins in the host cell membrane, including integrins (Pytela et al., 1985) and the HSPG syndecan family (Gong et al., 2008) and therefore, *P. aeruginosa* inhibition may be linked to changes in the distribution of important host receptor proteins.

My findings complement previous studies, which show a reduction in bacterial adhesion to epithelial cell lines following addition of heparan sulphate or HS analogues (Chen et al., 1995, Garcia et al., 2016, Rajas et al., 2017). Garcia et al also utilised the HCE2 cell line but an important distinction between my experiments is that heparan sulphate was added directly to the bacterial inoculum. In my experiments UFH was added directly to HCE2 monolayers and was only present in trace amounts during infection, allowing the host-directed effects of UFH to be studied. Findings from Garcia et al. provide support for observed differences between *S. aureus* and *P. aeruginosa* as the authors studied changes in bacterial adhesion to HCE2 cells following treatment with heparinase and/or chondroitinase enzymes. These enzymes are responsible for removing heparan sulphate and/or chondroitin sulphate GAGs from the

epithelial cell surface and associated reductions in bacterial adhesion were significantly increased for Gram positive bacteria compared to Gram negative pathogens. These findings indicate that cell surface GAGs are more important in the bacterial adhesion of Gram positive species such as *S. aureus*. Therefore, a reduced dependence on GAGs could explain why the inhibitory effects of UFH were reduced in *P. aeruginosa* compared to *S. aureus*.

5.4.4. Cytokine expression

In **section 5.3.5**, qPCR was used to measure mRNA expression of IL-6, IL-8, TNFα and CCL20 by HCE2 cells, under a range of *S. aureus* infection conditions. Expression of IL-6, TNFα and CCL20 was detected by infected HCE2 cells under all conditions. In contrast only CCL20 was expressed by uninfected HCE2 cells and mRNA expression was considerably reduced (by approximately 128-fold) compared to infected HCE2 cells. These findings show that mRNA expression of IL-6, TNFα and CCL20 in HCE2 cells is upregulated in response to *S. aureus* infection. Expression data for IL-8 was inconclusive as large Ct values were reported under all infection conditions but a significant difference in Ct values for 800-cap-treated cells and uninfected HCE2 cells was observed. Therefore, this cytokine was either not expressed or expressed at very low levels in infected HCE2 cells. Relative expression of cytokines in infected HCE2 cells was compared between different treatment conditions. Pre-treatment of HCE2 cells with 100 nM 800-cap, 100 nM 800-SCR or 10 U/ml UFH was shown to have no effect on cytokine expression, despite data in **section 5.3.4**, showing that staphylococcal adhesion was significantly reduced in response to UFH. There are a few possible explanations for this. Firstly, in bacterial adhesion studies, HCE2 cells were infected with SH1000-GFP for 1 hr, whereas the infection period was increased to 3.5 hrs for cytokine expression studies. UFH may not retain its effects on *S. aureus* during extended infection periods. Furthermore, even if fewer SH1000-GFP bacteria were adhering to HCE2 cells in the UFH condition, these bacteria were still present in the cell culture medium. Therefore, non-adherent bacteria may have been releasing bacterial products which induced changes in cytokine expression.

Other groups have reported similar changes in cytokine expression in response to *S. aureus* infection of human corneal epithelial cells. This includes the upregulation of IL-6 and TNFα in response to *S. aureus* infection (Heimer et al., 2010) or exposure to *S. aureus* exoproducts (Kumar et al., 2004). These studies also reported upregulation of IL-8 in response to *S. aureus*, and IL-8 represented one of the most abundant secreted products in the HCEC cell line (Heimer et al., 2010). Therefore, there may have been a problem with the specificity of the IL-8 primers. In agreement with my findings, Heimer et al. reported the largest increase in mRNA expression for CCL20, with an expression increase of over

400-fold. This was much larger than my observed increase of 128-fold, but this may be attributable to the increased infection time (6 hrs) used in their study (Heimer et al., 2010). Our group has previously investigated changes in cytokine expression in response to CD9 peptide (Ventress et al., 2016). This study involved the Tissue Engineered skin (TEskin) model, as well as a different subset of cytokines (Interleukin 1α (IL-1α), Monocyte Chemoattractant Protein 1 (MCP1/CCL2), IL-6 and IL-8). However, similar findings were reported and following infection of the TEskin model, there were no significant differences in cytokine expression in the presence or absence of 800 peptide.

5.4.5. Future work

There are a number of additional studies that would be beneficial to complete. Firstly, bacterial adhesion studies involving 800ii could be repeated using optimised techniques and a greater range of peptide concentrations. The 800ii peptide studies were the first experiments carried out using the bacterial adhesion protocol. Compared to UFH experiments and the final 800-cap study, there was greater variation between biological replicates in 800ii studies and a significant difference between cell and no cell conditions was not always observed. The disappearance of these problems in later experiments suggests that changes to PBS wash steps and improvements in experimental technique (e.g., taking care to avoid bubbles) were instrumental in reducing background binding. Therefore, it would be interesting to repeat the 800ii experiments using the optimised techniques. It would also be useful to repeat bacterial adhesion assays with a different strain of *S. aureus*, such as MRSA6 or even a different bacterial species, such as *P. aeruginosa*. There is limited peptide data for SH1000, and experiments performed by Dr Rahaf Issa did not use the optimised bacterial adhesion protocol. For example, a much lower seeding density of 20,000 cells/well was used and 96-well plates were collagen-coated prior to seeding. Therefore, the findings presented in this chapter are not directly comparable with data from early studies. Furthermore, data from Dr Mahendra Raut suggests although CD9 peptides display moderate efficacy against *S. aureus*, they are much more effective in their treatment of other bacterial pathogens such as *P. aeruginosa*. Therefore, future studies could include *P. aeruginosa* PAO1 as a positive control. Finally, it would also be useful to confirm whether CD9-derived tetraspanin peptides are binding to the surface of HCE2 cells. This type of experiment has been performed in the RT4 cell line previously, using fluorescent CD9-derived tetraspanin peptides and confocal microscopy (Albaldi, 2022).

In addition to the CD9 peptide work, bacterial adhesion studies involving UFH could be expanded to include clinical isolates of *S. aureus* and *P. aeruginosa*. Further experiments could also be performed to gain greater mechanistic insight into how UFH inhibits bacterial adhesion, as well as how this

pathway may differ between *S. aureus* and *P. aeruginosa* infection models. For example, knockout cell lines could be used to investigate the effects of different cell surface proteoglycans on bacterial adhesion to HCE2 cells and whether UFH treatment is associated with additive inhibition effects. I could also try supplying HCE2 cells with fibronectin to explore whether high concentrations of fibronectin are able to overcome the inhibitory effects of UFH. Dr Luke Green recently proposed a mechanism for UFH mediated inhibition of staphylococcal adhesion (see **section 1.8.2**), and this mechanism involves displacement of fibronectin from the cell surface. However, the potential role for fibronectin in *P. aeruginosa* infection models requires further investigation. Finally, qPCR experiments could be repeated using different IL-8 primers to confirm whether this cytokine is expressed by infected HCE2 cells. Expression studies could also be conducted in the absence of infection to see whether CD9/UFH treatments alter inflammatory signalling pathways under uninfected conditions.

5.4.6. Conclusion

In summary, the effects of CD9-derived tetraspanin peptides on bacterial adhesion to HCE2 monolayers remain unclear and further investigation is required. However, unfractionated heparin (UFH) has been shown to significantly reduce bacterial adhesion of *S. aureus* and *P. aeruginosa* to HCE2 monolayers under static conditions. The anti-adhesion effects of UFH will be further investigated in **Chapter 7**, under flow conditions.

CHAPTER 6: TRANSWELL INFECTION STUDIES

6.1. Introduction

This chapter describes use of the HCE2 transwell model to investigate *S. aureus* infections in the context of the human corneal epithelium. The HCE2 transwell model is composed of 3-4 cell layers of immortalised human corneal epithelial cells, which have been cultivated on collagen-coated transwell inserts using the optimised cell culture protocol described in **Chapter 3**. Transwell inserts are composed of polyester and contain 0.4 µm pores. These pores are larger than the size exclusion limit for *S. aureus* (0.22 µm) (Hasegawa et al., 2003) and therefore bacteria should be able to enter the transwell pores. In the transwell model, HCE2 cells represent the human corneal epithelium and the coated transwell membrane is intended to mimic the basement membrane of the *in vivo* cornea. Therefore, movement of bacteria into the basal chambers can be likened to infiltration of the corneal stroma. However, this chapter will be focussed on the initial stages of bacterial keratitis that are localised to the corneal epithelium. This includes adhesion to and invasion of corneal epithelial cells by *S. aureus* and a potential role for corneal epithelial cells as non-professional phagocytes.

6.1.1. Virulence mechanisms utilised by *S. aureus* during bacterial keratitis

S. aureus produces a range of virulence factors expected to influence infection progression in the HCE2 transwell model. This includes adhesins belonging to the MSCRAMM family, which facilitate staphylococcal adhesion via their interactions with host Extracellular Matrix (ECM) proteins (Foster et al., 2014). Fibronectin is known to play a major role in *S. aureus* pathogenesis and bacteria bind this ECM molecule via fibronectin binding proteins (FnBPA/B) (Flock et al., 1987). Staphylococcal adhesion was recently investigated using human corneas and a 117-fold increase in bacterial adhesion was observed following superficial corneal injury (Maurin et al., 2021). Increases in bacterial adhesion were attributed to increased exposure of ECM-fibronectin and conversely, anti-fibronectin blocking antibodies were associated with significant reductions in bacterial adhesion. Another *S. aureus* adhesin that has been implicated in bacterial keratitis is collagen adhesin (Cna). This bacterial cell surface protein binds host collagen and a Cna-mutant was associated with reduced infection of rabbit corneas compared to wild-type and rescue strains (Rhem et al., 2000). In addition to these adhesins, *S. aureus* produces several toxins with potent cytolytic effects (O'Callaghan, 2018). Examples include alpha-toxin and gamma-toxin, both of which generate pores in host cell membranes, causing cellular dysregulation and ultimately cell death. Alpha toxin has also been shown to activate ADAM10, a membrane metalloproteinase that cleaves E-cadherin and causes detachment of cells from host membranes (Berube and Wardenburg, 2013). Finally, *S. aureus* is also capable of invading corneal

epithelial cells (Jett and Gilmore, 2002) and the efficacy of bacterial internalization has been linked to bacterial virulence. For instance, during an infection study involving rabbit corneas only one *S. aureus* strain (UMCR1) was shown to initiate infection following topical inoculation with bacteria (Tang et al., 2012). This strain was shown to be highly invasive, highlighting the importance of bacterial internalisation in the initiation of bacterial keratitis. The FnBP-Fn-α5β1 integrin pathway is the major *S. aureus* internalisation pathway and as part of this pathway, *S. aureus* triggers its own uptake by binding host integrin proteins (Fowler et al., 2000). However, the subsequent engulfment of bacteria is an active host process involving reorganisation of the actin cytoskeleton (Jett and Gilmore, 2002, Schroder et al., 2006) and there is evidence to suggest that bacterial internalisation may be protective in the context of the corneal epithelium.

6.1.2. Non-professional phagocytic activity of human corneal epithelial cells

Epithelial cells have been proposed to act as non-professional phagocytes which form the first line of defence against invading pathogens (Gunther and Seyfert, 2018). There are two critical differences between phagocytosis in epithelial cells and professional phagocytes (e.g., neutrophils and macrophages). Firstly, epithelial cells do not express Fc gamma receptors (FcγR) or complement receptors and therefore these cells cannot perform opsonic phagocytosis. Instead, bacterial uptake is triggered by the invading pathogen. Secondly, although bacteria are targeted to phagolysosomes in both professional and non-professional phagocytes, the efficacy of intracellular killing is lower in epithelial cells relative to neutrophils or macrophages. This has been demonstrated by *S. aureus* infection studies involving Mammary Epithelial Cells (MECs) (Gunther et al., 2017). During these infections, *S. aureus* bacteria are rapidly taken up by MECs via an actin-mediated internalisation pathway. Despite the persistence of intracellular bacteria, these infections elicit a weak immune response, becoming chronic in nature. Mechanical disruption of *S. aureus* prior to MEC infection significantly enhanced the host immune response (Bauer et al., 2015) and therefore it has been suggested that the limited efficacy of intracellular killing may be linked to insufficient degradation of *S. aureus* within MEC lysosomes (Gunther and Seyfert, 2018). Human corneal epithelial cells have also been shown to internalise *S. aureus* bacteria (Jett and Gilmore, 2002) and, whilst intracellular clearance mechanisms have not been investigated in the context of bacteria, they have been studied using *Aspergillus flavus* spores (Arunachalam et al., 2021). This study highlighted a number of similarities between professional and non-professional phagocytosis pathways. Although internalisation of Aspergillus spores was mediated by actin rings, the recruitment of early-stage (e.g., CD71) and late-stage (e.g., LAMP1) endosomal markers was observed, revealing the formation of mature phagosomes. Furthermore, these corneal epithelial cell phagosomes underwent acidification,

as observed in professional phagocytes. The efficacy of intracellular *A. flavus* killing was not reported but a previous study involving *Aspergillus fumigatus* showed that less than 3% of intracellular conidia were able to survive within A549 airway epithelial cells (Wasylnka and Moore, 2003). Therefore, pathogen-induced invasion of host cells may confer protective effects in epithelial cells due to intracellular killing. Studies involving epithelial-like cells have also suggested a role for efferocytosis (i.e., the removal of dead cells by host phagocytes) in bacterial clearance. *P. aeruginosa* was shown to exhibit dead cell tropism and following adhesion to apoptotic Madin-Darby Canine Kidney (MDCK) cells, both adherent *P. aeruginosa* and apoptotic cells were engulfed by neighbouring cells (Capasso et al., 2016). Both MDCK cells and *P. aeruginosa* bacteria were then targeted for destruction within efferocytic phagosomes. These findings suggest that efferocytic and non-professional phagocytic clearance mechanisms may play an important role in bacterial clearance at host epithelial surfaces. Finally, another important characteristic of the cornea that may be advantageous for bacterial clearance is the occurrence of cell shedding. Superficial corneal epithelial cells are regularly sloughed from the surface of the cornea (Ren and Wilson, 1996), and this has been proposed to play an important role in the removal of adherent bacteria (Fleiszig et al., 2019). Therefore, it seems highly likely that bacterial internalisation could complement this pathway by sequestering pathogens prior to epithelial desquamation.

6.2. Aims

1. To explore mechanisms of *S. aureus* infection using the HCE2 transwell model of *S. aureus* keratitis.
    a) To assess damage to HCE2 multilayers following *S. aureus* infection.
    b) To study the localisation of *S. aureus* bacteria in the HCE2 transwell model.
2. To study the invasion of HCE2 cells by *S. aureus* and the associated phagocytic activity of HCE2 cells.

6.3. Results

6.3.1. Microscopy reveals the progression of *S. aureus* infection in the HCE2 transwell model.

6.3.1.1. Transmission electron microscopy shows disintegration of HCE2 multilayers during SH1000-GFP infection and the internalisation of SH100-GFP bacteria.

The optimised HCE2 transwell model (see **Chapter 3**) was infected using SH1000-GFP at MOI 10 and progression of infection was visualised at 5 hrs and 9 hrs post-infection by Transmission Electron Microscopy (TEM). At 5 hrs post-infection (**Figure 6-1**), the multilayer architecture of the HCE2 model remained intact and 3 to 4 cell layers were observed (**Figure 6-1A**). However, there were gaps between neighbouring cells in certain regions, and clusters of cell debris revealed HCE2 cell death (**Figure 6-1**). By 9 hrs post infection (**Figure 6-2**), HCE2 multilayers had disintegrated almost entirely and gaps between neighbouring cells became larger. Internalisation of SH1000-GFP bacteria was observed at both 5 hrs and 9 hrs post-infection (**Figure 6-3**). Engulfment of bacteria at the corneal epithelial cell surface was visible (**Figure 6-3A**), as well as the presence of bacteria within HCE2 cells (**Figure 6-3B and C**). Internalised bacteria were observed within the outer layer of HCE2 cells (**Figure 6-3C**), as well as within lower cell layers (**Figure 6-3B**). This indicated that SH1000-GFP bacteria were able to traverse the superficial corneal epithelial cell layer of my model. The PET membranes of transwell inserts were clearly visible in TEM micrographs as dark grey bands (**Figure 6-1B**, **6-3A**, **6-4**). However, transwell pores were more difficult to visualise and were sometimes visible as circles in the PET membrane (**Figure 6-3A**). In a subset of electron micrographs, cellular material was observed within PET membranes (**Figure 6-4**). This material lacked distinct structure or cellular organelles and in **Figure 6-4A**, this material remained attached to the HCE2 monolayer. However, in **Figure 6-4C**, cellular material was observed within the PET membrane at two locations and the larger of these structures appears to have separated from the HCE2 multilayer. It was hypothesised that these structures could represent HCE2 projections or secreted products but further investigation is required.
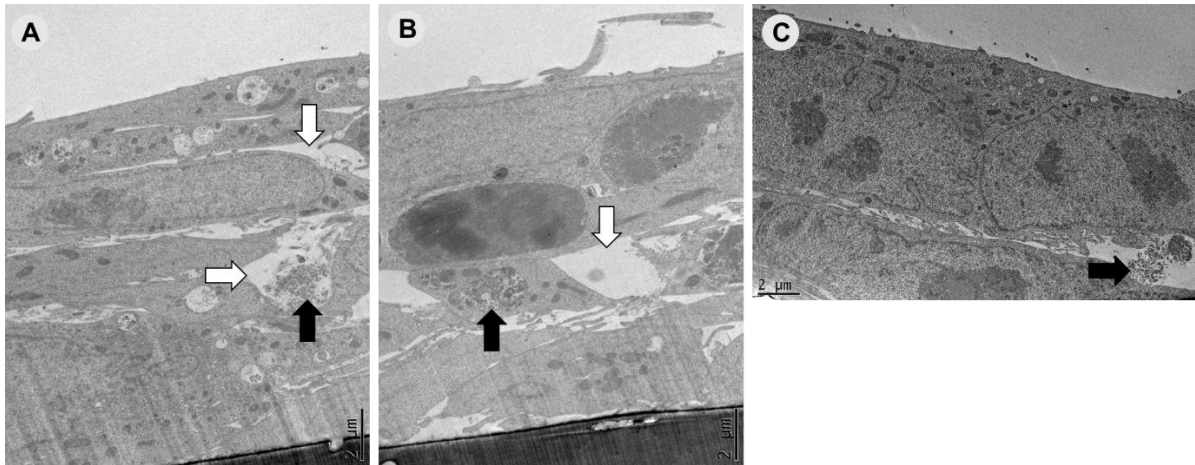
Figure 6-1. Transmission Electron Micrographs of HCE2 multilayers at 5 hrs post-infection with SH1000-GFP. HCE2s were cultured on transwell inserts using the optimised protocol. On day 6 of culture at ALI, HCE2 multilayers were infected with SH1000-GFP at MOI 10. All images were collected 5 hrs post-infection. Gaps between cells are labelled with white arrows. Cell debris and dead/dying cells are labelled with black arrows. Scale bars represent 2 μm. Microscopy was performed by Chris Hill (Cryo-Electron Microscopy Facility, UoS).
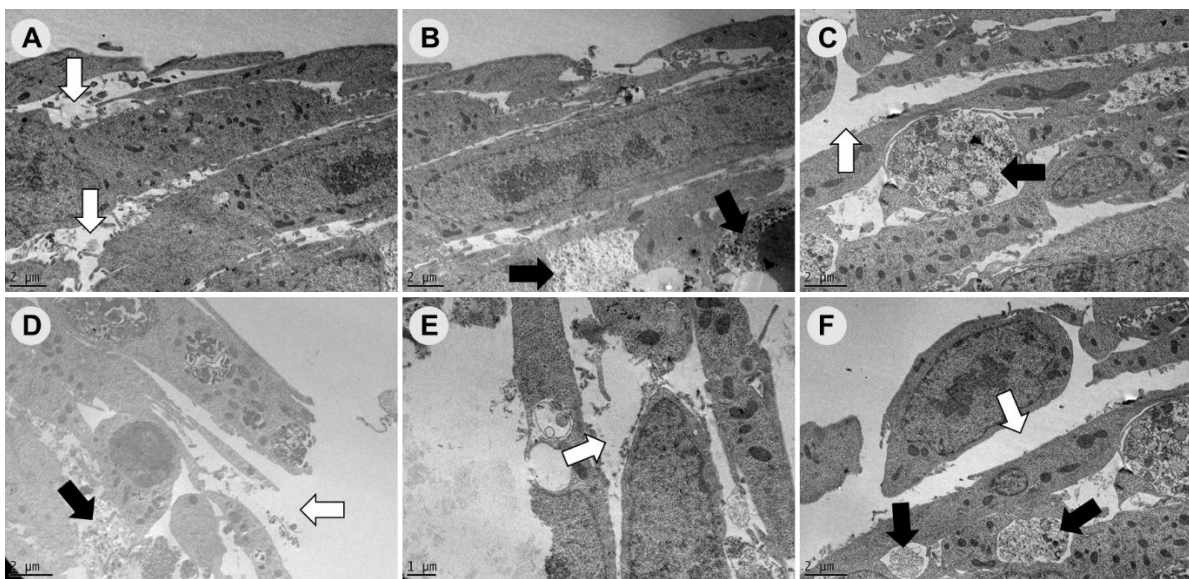
Figure 6-2. Transmission Electron Micrographs of HCE2 multilayers at 9 hrs post-infection with SH1000-GFP. HCE2s were cultured on transwell inserts using the optimised protocol. On day 6 of culture at ALI, HCE2 multilayers were infected with SH1000-GFP at MOI 10. All images were collected 9 hrs post-infection. Gaps between cells are labelled with white arrows. Cell debris and dead/dying cells are labelled with black arrows. Scale bar represents 2 μm for **A-D**, **F** and 1 μm in **E**. Microscopy was performed by Chris Hill (Cryo-Electron Microscopy Facility, UoS).
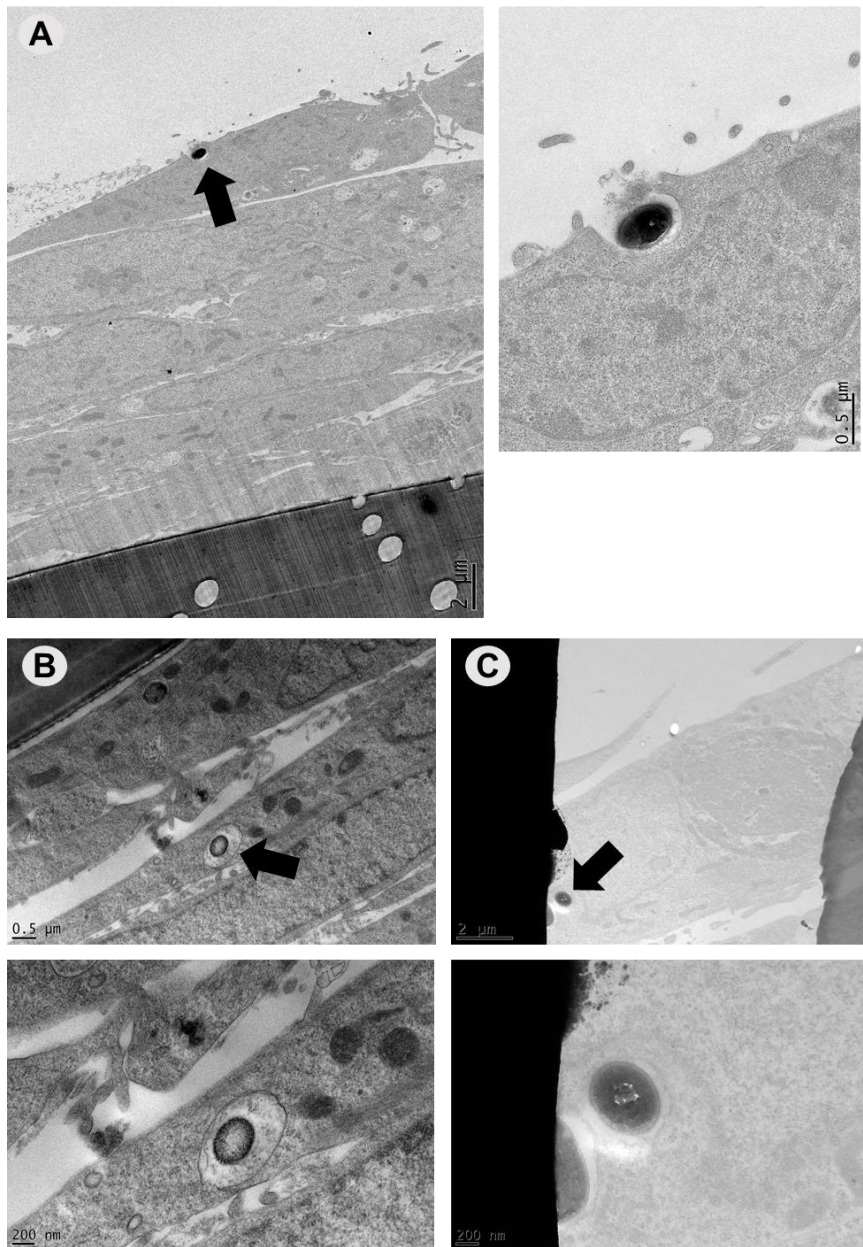
Figure 6-3. Transmission Electron Micrographs of bacterial internalisation by HCE2 multilayers.
HCE2s were cultured on transwell inserts using the optimised protocol. On day 6 of culture at ALI, HCE2 multilayers were infected with SH1000-GFP at MOI 10. Transwells were visualised at 5 hrs (A and B) or 9 hrs (C) post-infection. All images display the engulfment or internalisation of SH1000-GFP, and bacteria are labelled with black arrows. For **A**, scale bars represent 2 and 0.5 μm. For **B and C**, scale bars represent 0.5 μm and 200 nm. Microscopy was performed by Chris Hill (Cryo-Electron Microscopy Facility, UoS).

Figure 6-4. Transmission Electron Micrographs of cellular material in transwell membranes.
HCE2s were cultured on transwell inserts using the optimised protocol. On day 6, HCE2 multilayers were infected with SH1000-GFP at MOI 10. All images were collected at 5 hrs post-infection and display cellular material in PET transwell membranes (labelled with black arrows). Scale bars represent 2 µm for **A-B** and 0.5 µm in **C**. Microscopy was performed by Chris Hill (Cryo-Electron Microscopy Facility, UoS).

6.3.1.2. AiryScan confocal microscopy shows bacterial traversal of HCE2 multilayers.

The optimised HCE2 transwell model was infected using SH1000-GFP at MOI 1 or 10, and the distribution of bacteria was investigated at 5 hrs and 9 hrs post-infection, using AiryScan confocal microscopy. GFP-tagged bacteria were clearly visible on the surface of HCE2 multilayers under all infection conditions and there was a clear increase in bacterial numbers between 5 hrs and 9 hrs post-infection for both MOI conditions, showing that SH1000-GFP bacteria readily proliferate in the HCE2 transwell model (**Figure 6-5**). Bacteria appear to occupy the surface of HCE2 multilayers as clusters, which may represent bacterial microcolonies and therefore the early stages of biofilm formation. DAPI staining revealed potential differences in HCE2 cell viability between 5 hrs and 9 hrs post-infection (**Figure 6-5A**). At 5 hrs post-infection, cell nuclei were clearly visible and possessed typical nuclear morphology (i.e., a rounded nucleus with defined shape). However, by 9 hrs post-infection, nuclei were much harder to distinguish and only a few, relatively small cell nuclei were observed at MOI 10. However, it should be noted that *S. aureus* bacteria were also stained by DAPI and therefore SH1000-GFP may be masking viable HCE2 cells at later time points. Z-stacks were used to study the distribution of SH1000-GFP bacteria within HCE2 multilayers and traversal of host cell layers was observed at MOI 10 (**Figure 6-6**). At 5 hrs post-infection, SH1000-GFP bacteria were visualised at the surface of HCE2 multilayers (**Figure 6-5**), as well as approximately 7 µm below the corneal epithelial cell surface (**Figure 6-6A**). By 9 hrs post-infection, SH1000-GFP bacteria had progressed further into the HCE2 multilayer and clusters of bacteria were visible approximately 15 µm below the corneal epithelial cell surface (**Figure 6-6B**). A single bacterium was also observed at 19 µm. In addition to displaying bacterial traversal over time, comparison of **Figure 6-6A** and **6-6B** revealed differences in the HCE2 transwell model between duplicate wells. CellMask was used to stain HCE2 cell membranes and in **Figure 6-6B**, HCE2 multilayers had an approximate depth of 36 µm, whereas this was only ~30 µm in **Figure 6-6A**. Therefore, reducing multilayer variation will be an important consideration for future work.

(A)

(B)
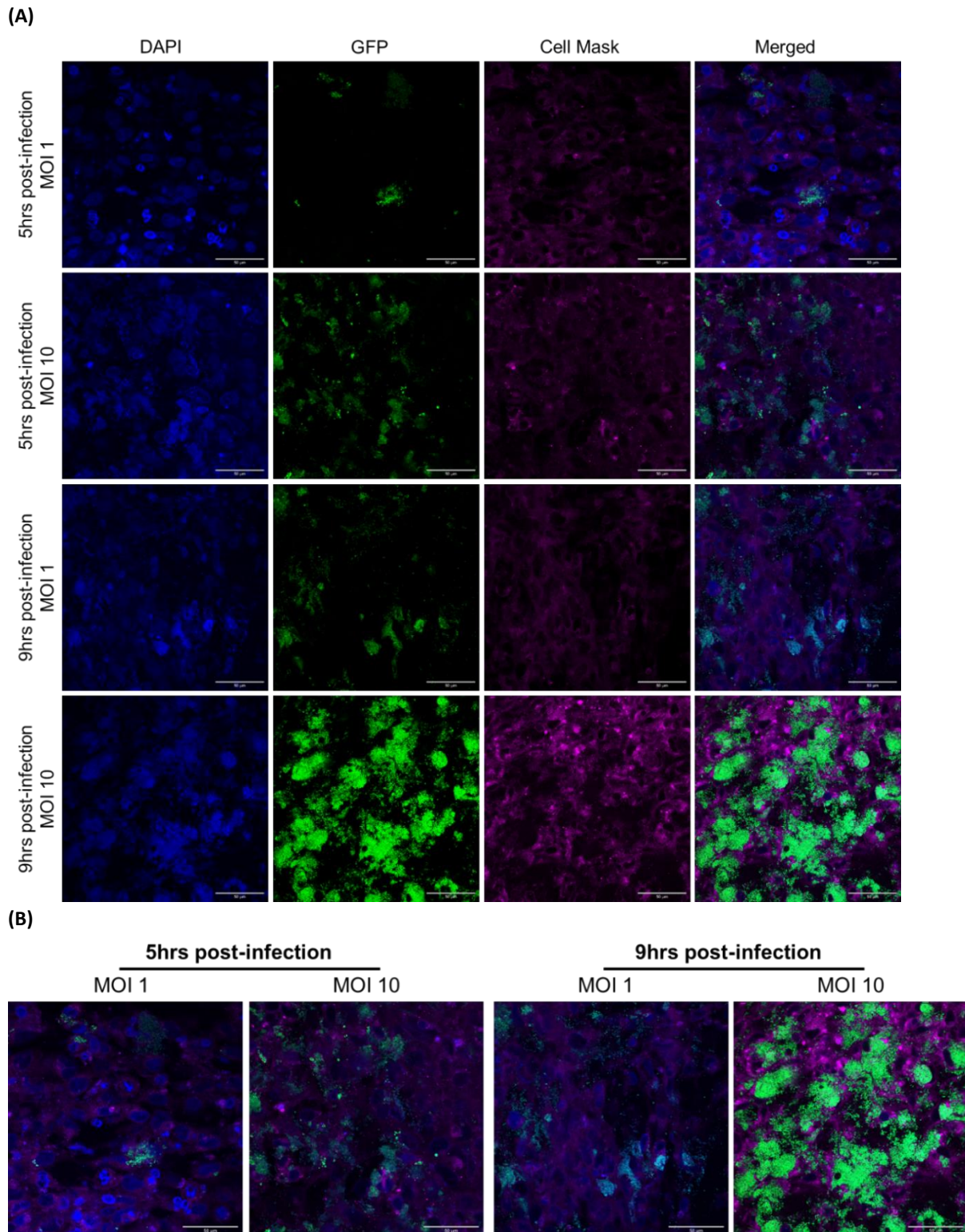
Figure 6-5. AiryScan confocal images showing the distribution of SH1000-GFP bacteria on the surface of HCE2 multilayers. (A) Individual channels. (B) Merged images only.

HCE-2 multilayers were cultured on transwell inserts using the optimised protocol. On day 6 of culture at ALI, HCE2s were infected with SH1000-GFP at MOI 1 or 10. At 5 and 9 hrs post-infection, transwell inserts were fixed and prepared for confocal microscopy. DAPI was used to stain cell nuclei (blue) and CellMask was used to stain cell membranes (magenta). Microscopy images were processed using IMARIS and GFP tagged bacteria are represented by spots (green). Scale bars represent 50 μm.

(A)

(B)
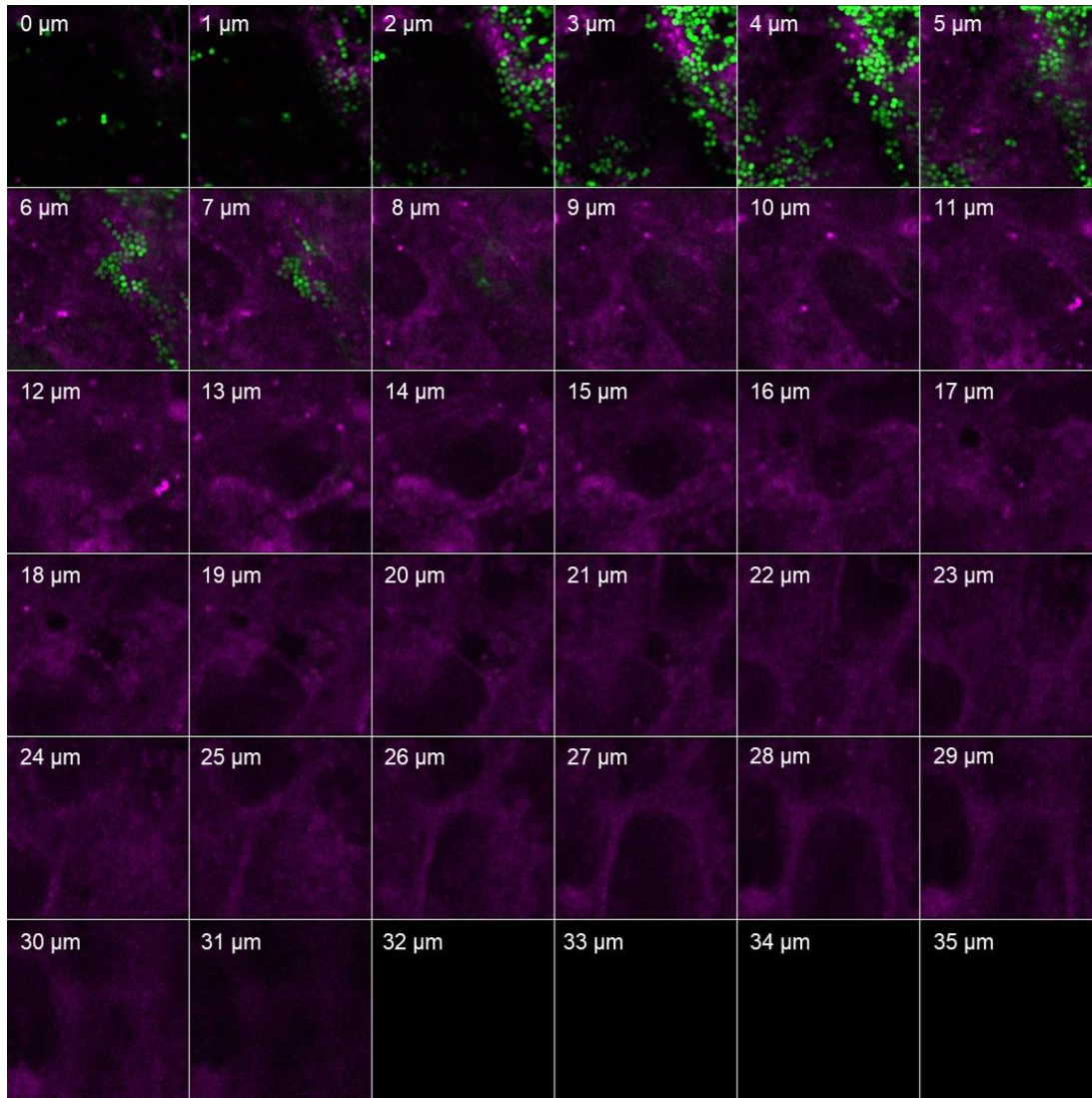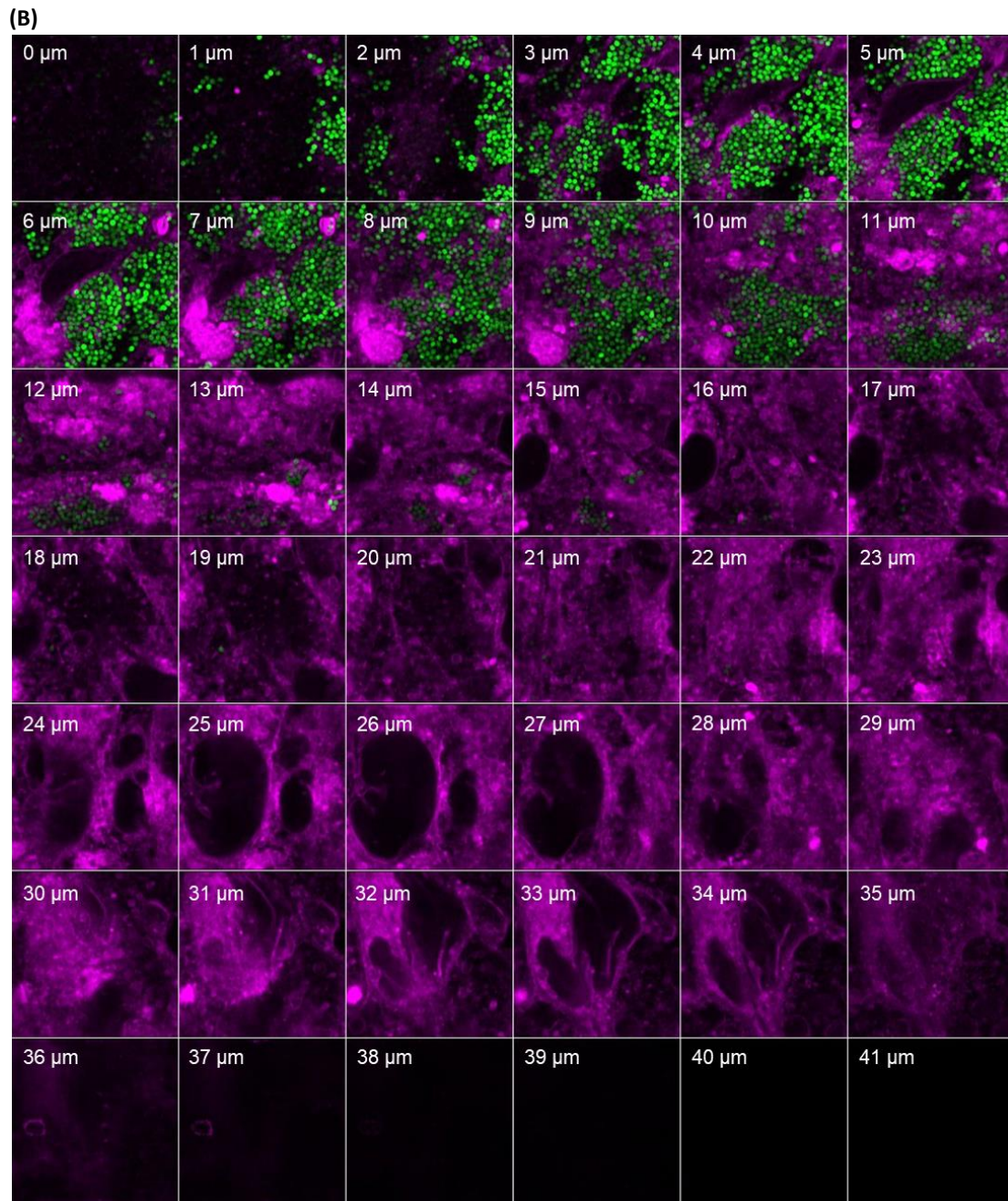
Figure 6-6. AiryScan z-stack images showing the distribution of SH1000-GFP within HCE2 multilayers.
(A) 5 hrs post-infection, MOI 10 (B) 9 hrs post-infection, MOI 10. Microscopy images were processed using IMARIS and GFP tagged bacteria are represented by spots (green). CellMask was used to stain cell membranes (magenta). The first image in each montage represents the surface of the infected HCE2 multilayer (0 µm). Subsequent images were taken within cell multilayers.

6.3.2. Infection of HCE2 multilayers with SH1000-GFP causes low levels of LDH release at early infection time points.

Supernatants were collected from apical and basal chambers during transwell infection studies and used to perform cytotoxicity assays (**Figure 6-7** and **6-8**). These assays provided a quantitative measure of lactate dehydrogenase (LDH) in tissue culture supernatants. LDH is a stable, cytosolic enzyme found within mammalian cells and therefore relative levels of extracellular LDH were used a as a measurement of cell lysis. Transwells containing uninfected HCE2 cells were included to provide a baseline measurement for LDH release under normal conditions and detergent-lysed cells were included to measure complete cell lysis. Finally, transwells containing no HCE2 cells (no cell controls) were included to quantify bacterial LDH release under different MOI conditions. Cumulative LDH measurements showed a small increase in absorbance readings between 1 and 5 hrs post-infection for all conditions (**Figure 6-7**). However, between 5 and 9 hrs post-infection there was a large increase in average absorbance readings for HCE2 cells infected with SH1000-GFP at MOI 1 (1.734 ± 0.802) and HCE2 cells infected at MOI 10 (2.732 ± 0.542). Large increases in absorbance were also observed for transwell inserts containing no cells, following infection at MOI 1 (1.040 ± 0.600) or MOI 10 (1.684 ± 0.345) but absorbance readings remained below corresponding HCE2 readings. In contrast, absorbance readings remained almost identical between 5 and 9 hrs for detergent-lysed cells (0.130 ± 0.017) and there was only a small increase in absorbance readings for uninfected HCE2 cells (0.486 ± 0.148). Once initial absorbance readings had been collected, values for no cell controls (i.e., bacterial LDH) were subtracted from corresponding HCE2 infection conditions and % cytotoxicity calculations were performed (see **section 2.7.3.1**). At 1 hr post-infection, similar % cytotoxicity values were reported for HCE2 cells infected at MOI 1 (4.9% ± 6.9), HCE2 cells infected at MOI 10 (9.9% ± 9.6) and uninfected HCE2 cells (10.7% ± 3.0) (**Figure 6-8**). By 5 hrs, average cytotoxicity values were increased for MOI 1 (9.7% ± 7.1), MOI 10 (20.6% ± 9.1) and uninfected HCE2 cells (19.0% ± 3.3). However, increases were very small and there was no significant difference between conditions at 1 or 5 hrs post-infection ($p > 0.05$ in all cases). Between 5 and 9 hrs post-infection, a much larger increase in % cytotoxicity values was observed for MOI 1 (27.3% ± 8.3), MOI 10 (48.5% ± 3.7) and uninfected HCE2 cells (32.5% ± 9.6). There was a significant increase in cytotoxicity for HCE2 cells infected with SH1000-GFP at MOI 10, as compared to uninfected HCE2 cells ($p= 0.0360$) and there was also a significant increase compared to MOI 1 ($p= 0.0056$). However, no significant difference between MOI 1 and uninfected HCE2 cells was observed ($p > 0.05$, n=3, two-way ANOVA with Tukey's multiple comparisons test).
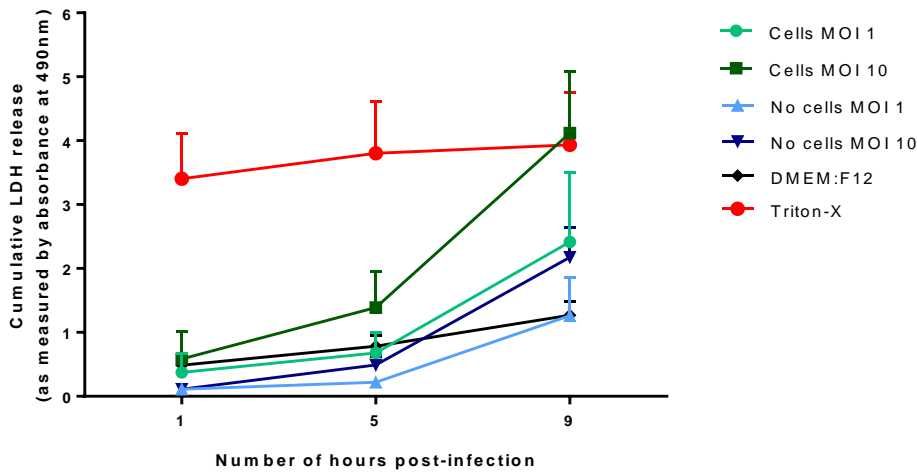
Figure 6-7. Cumulative LDH release following infection of the HCE2 transwell model with SH1000-GFP.
Media supernatants were collected from apical and basal chambers at 1, 5 and 9 hrs post-infection. Supernatants were centrifuged at 200 *xg* to remove any cell debris and then stored at -80°C. The Promega CytoTox 96 Non-Radioactive cytotoxicity assay to detect LDH in supernatant samples, as measured by absorbance at 490 nm. Absorbance readings for the corresponding apical and basal chambers have been combined and the data is presented cumulatively for each time point. Uninfected cell controls treated with cell culture medium (DMEM: F12), were included and Triton-X-treated cells, which were representative of maximum cell lysis. Data represent mean values ± SD, n=3 for all conditions.
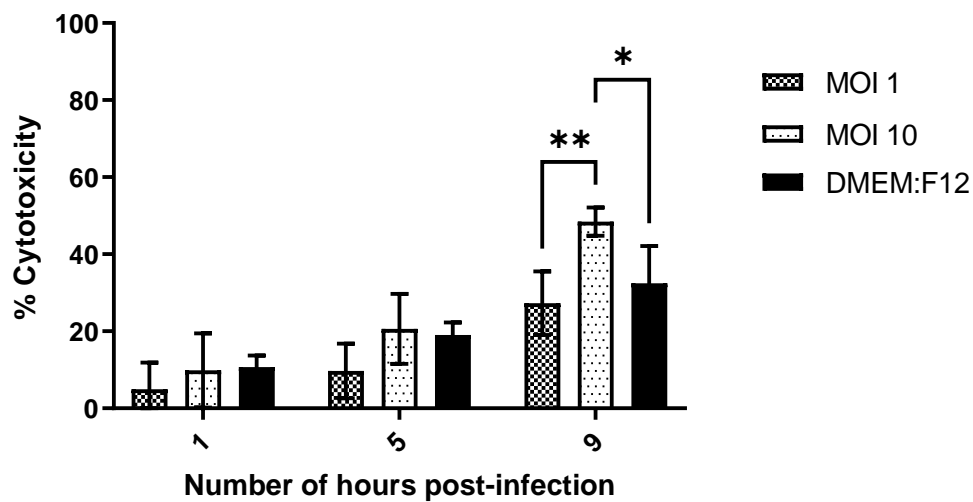
Figure 6-8. % Cytotoxicity calculations for HCE2 multilayers infected with SH1000-GFP.
Cumulative LDH release was used to calculate % cytotoxicity under different infection conditions. Conditions include infection at MOI 1, infection at MOI 10 and uninfected cell multilayers (DMEM: F12). When calculating % cytotoxicity values, LDH values for no cell controls were subtracted to account for bacterial LDH. Data represent mean values ± SD, n=3 for all conditions. Data was analysed by two-way ANOVA with Tukey's multiple comparisons test, *p ≤ 0.05, **p ≤ 0.01.

6.3.3. SH1000-GFP bacteria traverse transwell inserts and traversal is increased in the presence of HCE2 multilayers compared to no cell conditions.

The HCE2 transwell model was infected using SH1000-GFP at MOI 1 or 10, by adding bacteria to the apical chambers of transwell inserts. Transwells containing no HCE2 cells were also included and bacteria in apical and basal chambers were quantified by plating aliquots from the chambers onto LB agar at 1, 5 and 9 hrs post-infection (**Figure 6-9**). At 1 hr post-infection (**Figure 6-9A**), CFU/well values for apical chambers infected at MOI 1, were similar for transwells containing cells ($7.03 \times 10^4 \pm 4.16 \times 10^4$) and no cells ($1.10 \times 10^5 \pm 6.93 \times 10^4$). In contrast, CFU/well values were significantly increased under no cell conditions ($1.66 \times 10^6 \pm 1.56 \times 10^5$) compared to cell conditions ($1.06 \times 10^6 \pm 3.56 \times 10^5$) at MOI 10 (p= 0.0004, n=3, two-way ANOVA with Šidák's multiple comparisons test) and over a ten-fold increase in CFU/well values was observed between MOI 1 and 10. No bacteria were recovered from basal chambers in the MOI 1, cell condition and very low numbers of bacteria were recovered under all other conditions: no cells MOI 1 ($4.17 \times 10^0 \pm 7.22 \times 10^0$), cells MOI 10 ($1.09 \times 10^3 \pm 1.78 \times 10^3$), no cells MOI 10 ($4.17 \times 10^0 \pm 7.22 \times 10^0$).

At 5 hrs post-infection (**Figure 6-9B**), CFU/well values for apical chambers remained over 10-fold higher for MOI 10 than MOI 1. At MOI 10, CFU/well values were significantly increased under no cell conditions ($1.24 \times 10^7 \pm 6.88 \times 10^6$) compared to cell conditions ($3.53 \times 10^6 \pm 2.41 \times 10^6$) (p= 0.0039) whereas no significant difference between cells ($1.89 \times 10^5 \pm 1.34 \times 10^5$) and no cell conditions ($6.37 \times 10^5 \pm 4.25 \times 10^5$) was observed at MOI 1 (p > 0.05). By 5 hrs post-infection, bacteria were recovered from basal chambers under all conditions. There was no significant difference in CFU/well values between conditions (p > 0.05 in all cases, n=3, two-way ANOVA with Šidák's multiple comparisons test) but large variations in average values were reported: cells MOI 1 ($1.77 \times 10^4 \pm 2.56 \times 10^4$), no cells MOI 1 ($1.32 \times 10^3 \pm 1.80 \times 10^3$), cells MOI 10 ($1.98 \times 10^5 \pm 2.85 \times 10^5$), no cells MOI 10 ($2.70 \times 10^3 \pm 1.85 \times 10^3$).

By 9 hrs post-infection (**Figure 6-9C**), CFU/well values for apical chambers were still higher at MOI 10 compared to MOI 1, but a 10-fold difference was no longer observed: cells MOI 1 ($2.56 \times 10^7 \pm 3.30 \times 10^6$), no cells MOI 1 ($3.69 \times 10^7 \pm 6.66 \times 10^6$), cells MOI 10 ($3.74 \times 10^7 \pm 1.10 \times 10^7$), no cells MOI 10 ($9.80 \times 10^7 \pm 3.60 \times 10^7$). As reported at 1 and 5 hrs post-infection, CFU/well values for MOI 10 were significantly increased in the absence of cells (p= 0.0017), whereas there was no significant difference between cells and no cell conditions at MOI 1 (p > 0.05, n=3, two-way ANOVA with Šidák's multiple comparisons test). High numbers of bacteria were recovered from basal chambers under all conditions but compared to the 5-hr time point, variations in average CFU/well values were reduced: cells MOI 1

$(2.16 \times 10^6 \pm 3.29 \times 10^6)$, no cells MOI 1 $(3.89 \times 10^6 \pm 6.68 \times 10^6)$, cells MOI 10 $(1.31 \times 10^7 \pm 2.22 \times 10^7)$, no cells MOI 10 $(4.42 \times 10^6 \pm 6.25 \times 10^6)$.

Upon closer inspection of the data, it was noted that CFU/well values for basal chambers were generally increased in the presence of HCE2 cells and the data was re-plotted to compare cell versus no cell conditions (**Figure 6-10**). At MOI 1, average CFU/well values were increased in the presence of cells versus no cells at 5 hrs post-infection (**Figure 6-10A**). However, no bacteria were recovered at 1 hr post infection under cell conditions and by the 9-hr time point, CFU/well values were highly similar under both conditions. At MOI 10, average CFU/well values were increased in the presence of cells at both 1 and 5 hrs post-infection, but CFU/well values were highly similar by the 9-hr time point. Statistical analysis revealed no significant difference between cells and no cells at any of my chosen time points (data not shown). However, I hypothesised that this was due to large variation and insufficient repeats rather than a true lack of difference between conditions and so I continued to investigate this phenomenon.

It was hypothesised that increased CFU/well values for basal chambers in the presence of HCE2 monolayers could be linked to differences in bacterial adhesion. In initial experiments, apical CFU/well values were significantly increased under no cell conditions at 1, 5 and 9 hrs post-infection for MOI 10 (**Figure 6-9**). It was speculated that fewer input bacteria were adhering to the apical side of transwell inserts in the absence of cells and therefore fewer bacteria were able to move through the transwell pores and into the basal chambers. This hypothesis was tested by using saponin to quantify numbers of adherent bacteria at 5 hrs and 9 hrs post-infection and compare differences in bacterial adhesion between different conditions (**Figure 6-11**). At 5 hrs post-infection, there was no significant difference in CFU/well values for cells $(3.46 \times 10^6 \pm 2.51 \times 10^6)$ versus no cells $(1.28 \times 10^7 \pm 1.48 \times 10^7)$ at MOI 1 $(p= 0.9722)$, nor between cells $(7.38 \times 10^7 \pm 5.04 \times 10^7)$ versus no cells $(4.65 \times 10^7 \pm 1.08 \times 10^7)$ at MOI 10 $(p= 0.6191$, n=3, one-way ANOVA with Tukey's multiple comparisons test) (**Figure 6-11A**). Similar findings were reported at 9 hrs post-infection and CFU/well values were closely matched for cells $(4.14 \times 10^7 \pm 1.66 \times 10^7)$ versus no cell conditions $(4.60 \times 10^7 \pm 7.84 \times 10^6)$ at MOI 1, as well as between cells $(1.18 \times 10^8 \pm 8.02 \times 10^7)$ and no cells $(4.43 \times 10^7 \pm 1.34 \times 10^7)$ at MOI 10 (**Figure 6-11B**). Based on these findings, it was concluded that increased bacterial traversal in the presence of HCE2 cells was not caused by increased bacterial adhesion.

A simplified transwell infection protocol was developed for measuring bacterial traversal (see **section 2.7.7**) and CFU/well measurements for basal chambers were compared under cells versus no cell conditions following 8 hr infection with *S. aureus* (**Figure 6-12**). MOI was increased to MOI 50 to ensure bacterial traversal within the 8-hr time period. A significant increase in basal CFU/well values was

observed for infected HCE2 multilayers ($2.94 \times 10^6 \pm 6.21 \times 10^6$) compared to no cell conditions ($3.92 \times 10^2 \pm 1.17 \times 10^3$) following 8 hr infection with SH1000-GFP (p= 0.0002, n=9) (**Figure 6-12A**). Similar findings were also reported using the *S. aureus* clinical isolate, LVP13 (**Figure 6-12B**) and basal CFU/well values were significantly increased under cells ($2.88 \times 10^6 \pm 3.39 \times 10^6$) versus no cell conditions ($5.44 \times 10^3 \pm 8.55 \times 10^3$) (p= 0.0433, n= 6, Mann Whitney test). These findings confirmed that bacterial traversal of transwell inserts was increased in the presence of HCE2 multilayers. It was hypothesised that increased traversal was mediated by the active uptake of *S. aureus* bacteria by HCE2 cells.
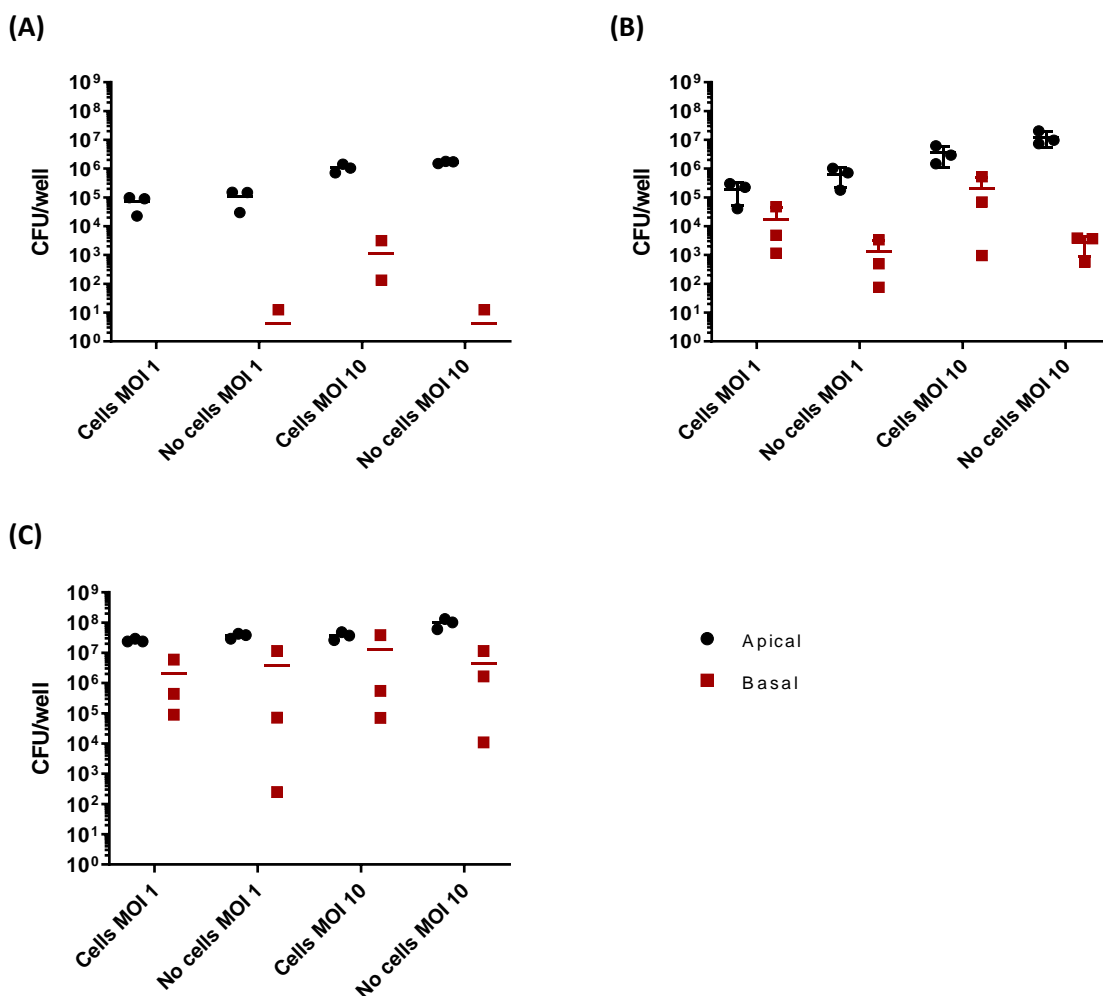
Figure 6-9. Quantification of bacteria in apical and basal chambers following infection of the HCE2 transwell model with SH1000-GFP.

(A) 1 hr post-infection (B) 5 hrs post-infection (C) 9 hrs post-infection. HCE2s were cultured on transwell inserts using the optimised protocol and control wells containing no cells were also included. On day 6 of culture at ALI, HCE2 multilayers were infected with SH1000-GFP at MOI 1 or 10. After 1 hr infection, inoculum was removed from apical chambers and plated on LB agar to calculate CFU/well. Culture medium was also removed from basal chambers and used for CFU/well calculations. All transwells were washed with HBSS and media in apical and

basal chambers was replaced. Further media changes and CFU/well calculations were carried out at 5 and 9 hrs post-infection. Data represent mean values ± SD, n=3 for all conditions.

(A)

(B)
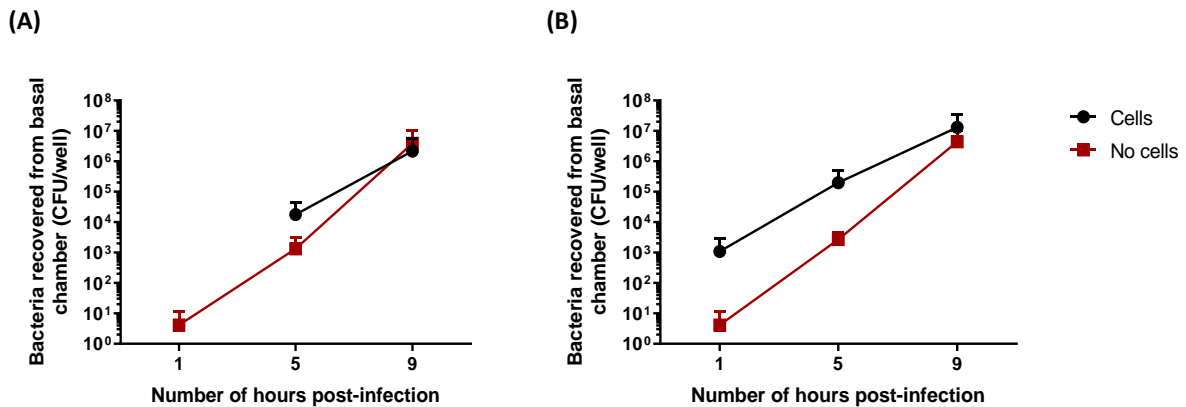
Figure 6-10. Numbers of bacteria present in basal chambers for cells versus no cell conditions.
(A) MOI 1 (B) MOI 10. CFU/well data for the HCE2 transwell infection has been presented in an alternative format. Only CFU/well values for basal chambers are shown to compare the rate of bacterial traversal in the presence of cells versus no cell conditions. Cells refers to transwell inserts containing HCE2 multilayers cultured under optimised conditions. No cell refers to transwell inserts that have been collagen coated but contain no HCE2 cells, only tissue culture medium. Data represent mean values ± SD, n=3 for all conditions.

(A)

(B)
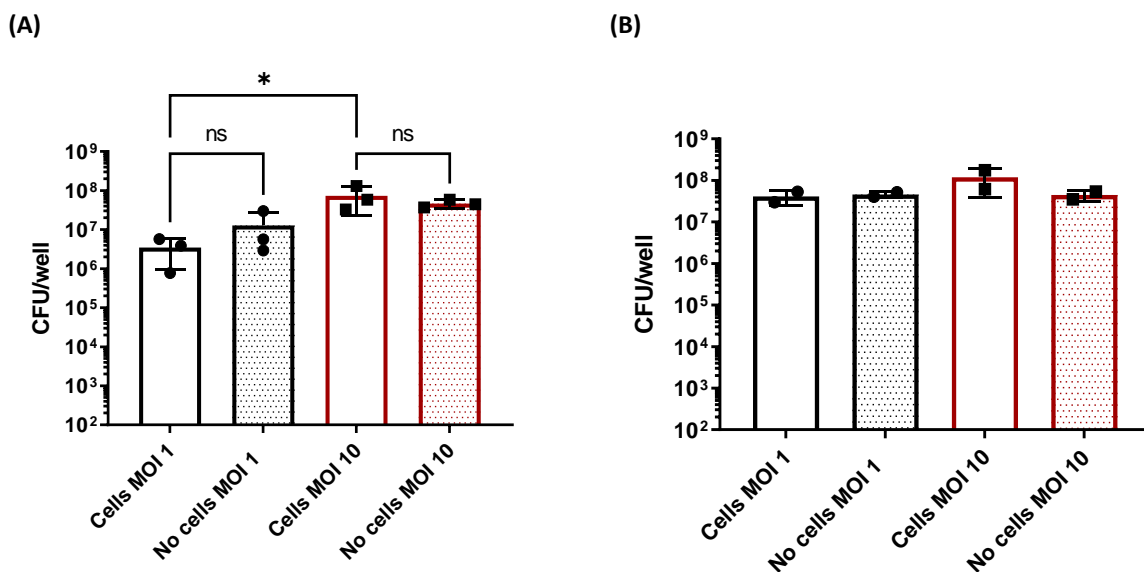
Figure 6-11. Quantification of adherent bacteria following infection of the HCE2 transwell model with SH1000-GFP.
(A) 5 hrs post-infection n=3. **(B) 9 hrs post-infection** n=2. Numbers of adherent bacteria in the infected transwell model were quantified at 5 hrs and 9 hrs post-infection. Tissue culture medium was removed, and non-adherent bacteria were removed by washing. 2% saponin was added to apical chambers and plates were incubated at 37°C for 20 mins to lyse the cells. Cell scraping was used to ensure complete destruction of cell multilayers and lysates were plated to quantify bacteria. Data represent mean values ± SD. Data was analysed by one-way ANOVA with Tukey's multiple comparisons test, *p ≤ 0.05, ns= not significant.

(A)

(B)
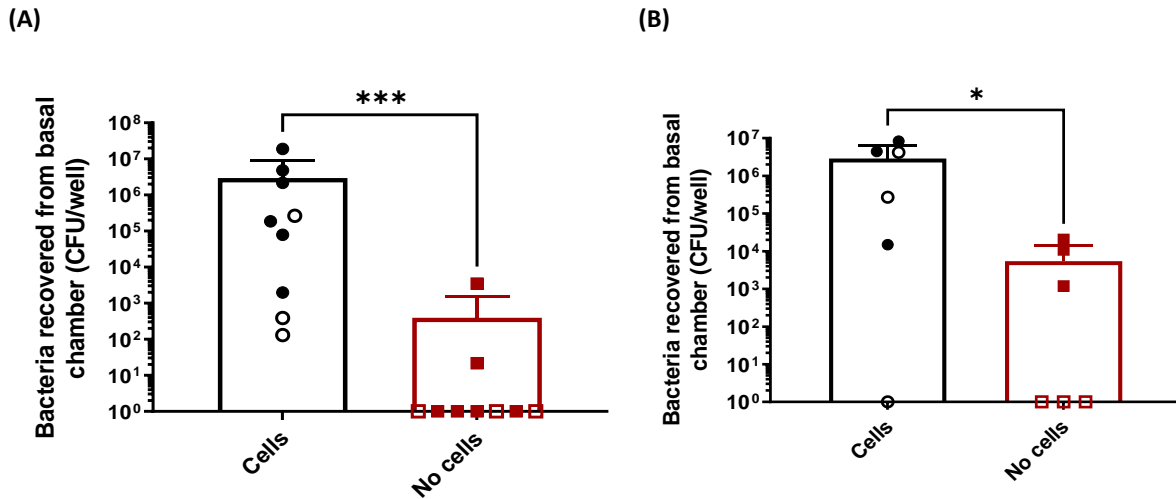
Figure 6-12. Bacterial traversal at 8 hrs post-infection for cells versus no cell conditions.
(A) *S. aureus* **laboratory strain, SH1000-GFP (B)** *S. aureus* **clinical isolate, LVP13.** HCE2 multilayers were cultured on transwell inserts using the optimised protocol and corresponding no cell controls were prepared. These transwells were collagen coated but contained no HCE2s, only tissue culture medium. All transwell inserts were infected for 1 hr with bacteria at MOI 10 (represented by unfilled shapes) or 50 (filled). After 1 hr, inoculum was removed, wells were washed to remove non adherent bacteria and fresh medium was added to apical chambers. Media aliquots were collected from basal chambers at 8 hrs post-infection and aliquots were plated out to calculate CFU/well. Zero values have been changed to 1 so they are visible on log axis. Data represent mean values ± SD, n=9 for SH1000-GFP, n=6 for LVP13. Data was analysed by Mann Whitney test, *p ≤ 0.05, ***p ≤ 0.001.

6.3.4. SH1000-GFP bacteria are internalised by HCE2 cells and comparison with other cell types demonstrates a high level of phagocytic activity.

Flow cytometry was used to measure uptake of GFP-tagged SH1000 by HCE2 cells, following 2 hr infection at a range of MOIs (**Figure 6-13**). Bacterial uptake was observed at all MOIs and differences in cell fluorescence were used to distinguish uninfected HCE2 cells from HCE2 cells containing internalised SH1000-GFP. At MOI 1, 6.9% ± 3.0 of HCE2 cells contained internalised SH1000-GFP (**Figure 6-13A**). This increased to 27.0% ± 9.2 at MOI 10 and 34.1% ± 12.8 at MOI 50. A significant increase in the percentage of cells containing internalised bacteria was observed when MOI was increased from 1 to 10 (p= 0.0317), as well as between MOI 1 and MOI 50 (0.0062) but no significant difference was observed between MOI 10 and MOI 50 (p= 0.5484), suggesting saturation of the system. MFI measurements for the total cell population also provided increasing values with increasing MOI (MOI 1: 108.7 ± 64.5; MOI 10: 123.1 ± 60.1; MOI 50: 187.5 ± 128.1) but there was large variation between experiments and no significant difference was observed between conditions (p > 0.05 in all cases) (**Figure 6-13B**). MFI values from just the infected cell population were also compared and there was no significant difference between MOI conditions (MOI 1= 568.8 ± 278.3; MOI 10= 395.4 ± 99.2; MOI 50= 507.0 ± 179.3) (p > 0.05 in all cases, n=3, one-way ANOVA with Tukey's multiple comparisons test) (**Figure 6-13C**). This suggested the number of SH1000-GFP bacteria internalised by HCE2 cells remained constant between MOI conditions and was likely to represent one bacterium per HCE2 cell.

Bacterial internalisation data for HCE2 cells was compared against equivalent datasets collected using the HaCaT human keratinocyte cell line and primary mouse Bone Marrow Derived Macrophages (BMDMs). Following 2 hr infection with SH1000-GFP, 8.5% ± 9.2 of HaCaT cells contained internalised SH1000-GFP (**Figure 6-14A**). In comparison, 27.0% ± 9.2 of HCE2 cells and 40.9% ± 20.1 of BMDMs contained bacteria. This pattern was mirrored by MFI values for the total cell population: 10.6 ± 15.0 for HaCaT cells, 123.1 ± 60.1 for HCE2 cells, and 446.3 ± 330.4 for mouse BMDMs (**Figure 6-14B**). However, no significant difference between cell types was observed using either measurement (p > 0.05 in all cases). MFI values for the infected cell population were also compared between cell types (**Figure 6-14C**). MFI values were highly similar for HaCaT (372.8 ± 73.9) and HCE2 (395.4 ± 99.2) cells. There was a large increase in average MFI values for BMDMs (835.8 ± 364.4) and the difference between HCE2 cells and BMDMs was close to significance (p= 0.0636, n=4 for HCE2s and n=3 for BMDMs, one-way ANOVA with Tukey's multiple comparisons test).

(A)

(B)

(C)
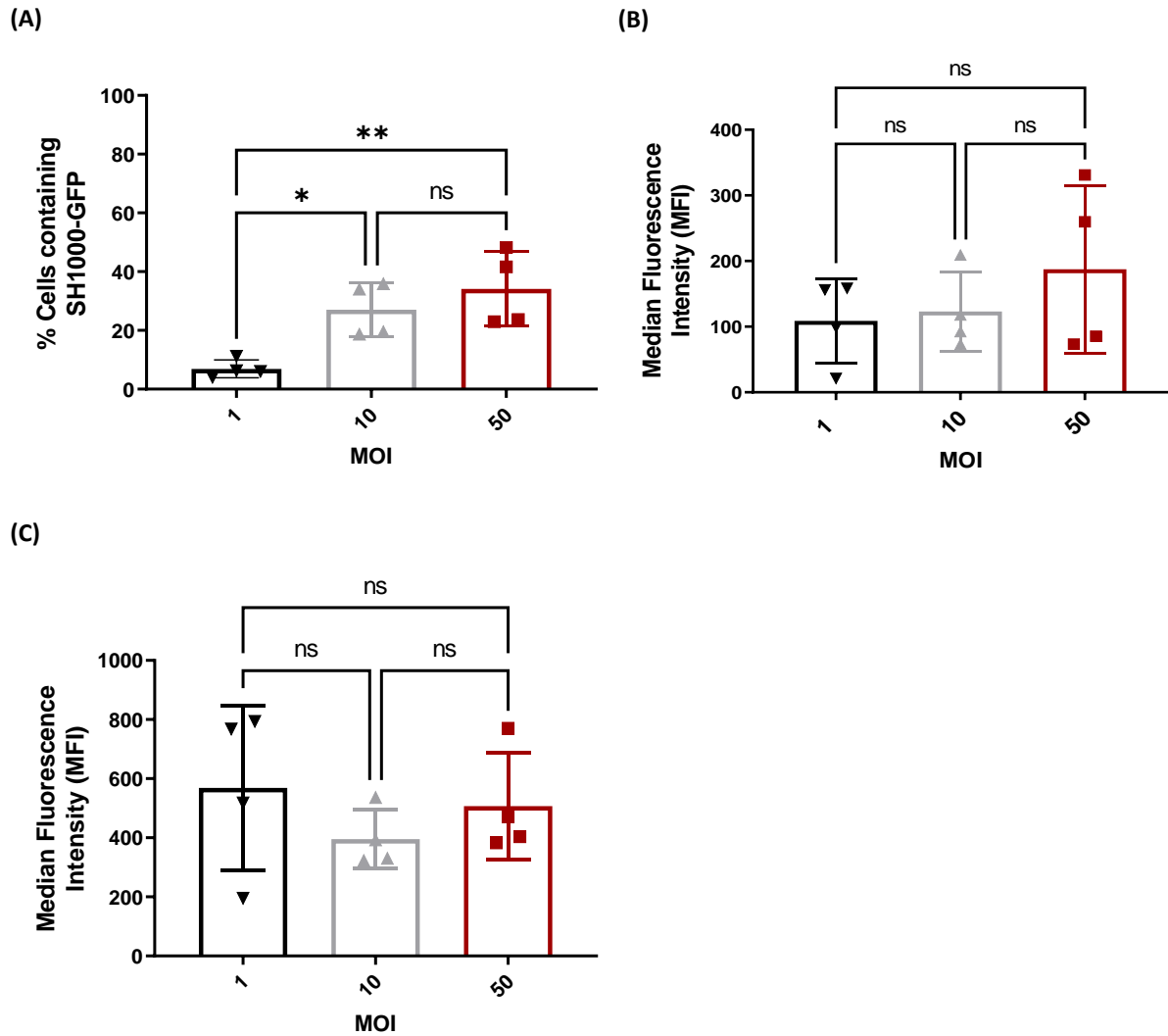
Figure 6-13. Internalisation of SH1000-GFP by the HCE2 cell line.
(A) % HCE2 cells containing SH1000-GFP (B) MFI values for the total cell population (C) MFI values for the infected cell population. Internalisation of *S. aureus* SH1000-GFP was quantified by flow cytometry. HCE2 monolayers were infected with SH1000-GFP at a range of MOIs (1, 10 and 50) for 2 hrs. Uninfected medium only controls were also included. After 2 hrs, extracellular bacteria were killed using 20 µg/ml lysostaphin and infected HCE2s were harvested for flow cytometry. Data represent mean ± SD, n=4. Data was analysed using one-way ANOVA with Tukey's multiple comparisons test, *p ≤ 0.05, **p ≤ 0.01, ns= not significant.

(A)

(B)

(C)
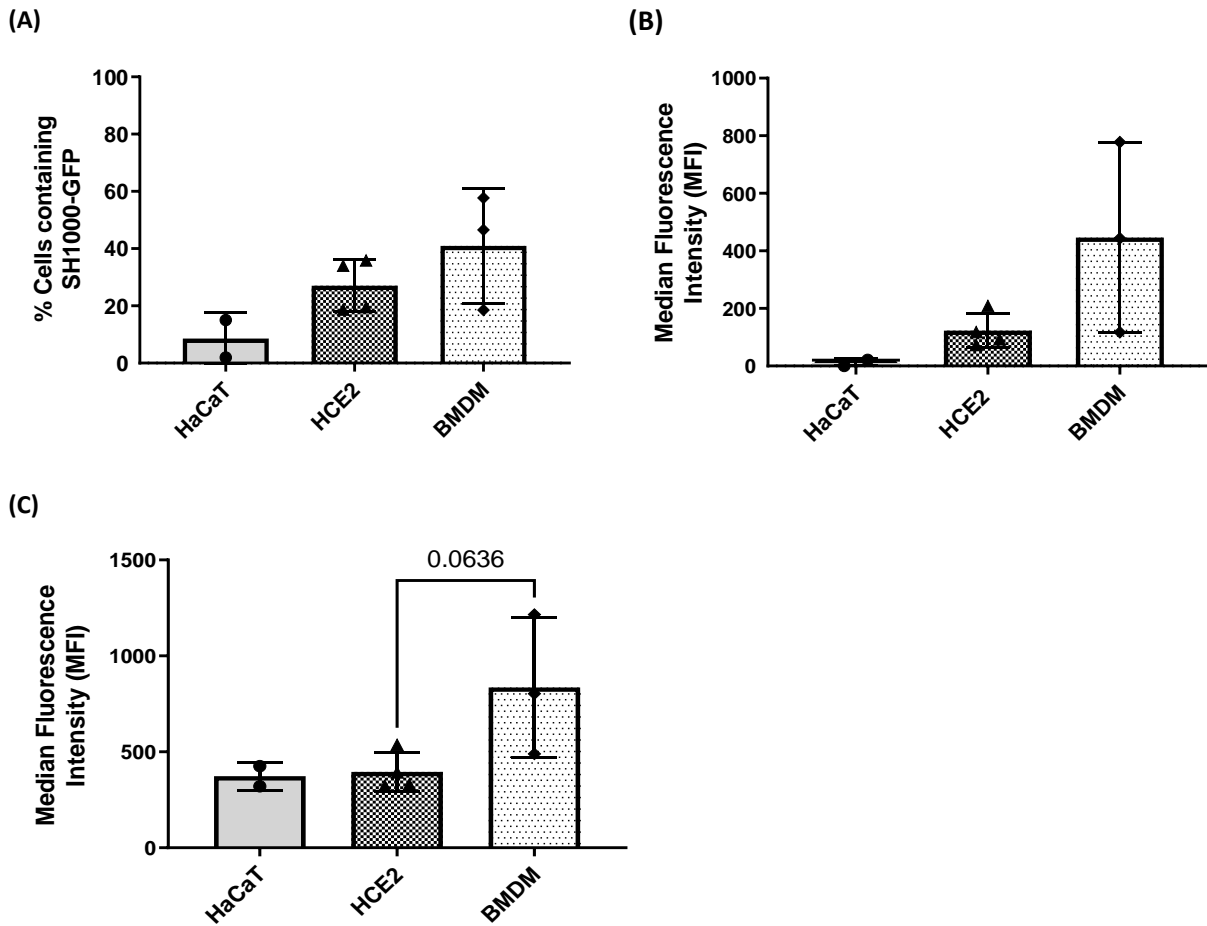
Figure 6-14. Comparing internalisation of SH1000-GFP between different cell types.
(A) % cells containing SH1000-GFP (B) MFI values for the total cell population (C) MFI values for the infected cell population. Internalisation of *S. aureus* SH1000-GFP was quantified by flow cytometry using three cell types: (1) Immortalized human keratinocytes (HaCaT), (2) Immortalized human corneal epithelial cells (HCE2) and (3) Primary Bone Marrow-Derived Macrophages (BMDM) from mice. Cell monolayers were infected with SH1000-GFP at MOI 10 for 2 hrs. Uninfected, medium only controls were also included. After 2 hrs, extracellular bacteria were killed using 20 µg/ml lysostaphin and infected cells were harvested for flow cytometry. Data represent mean ± SD, n=2 for HaCaTs, n=4 for HCE2s, n=3 for BMDMs. Data was analysed using one-way ANOVA with Tukey's multiple comparisons test.

6.3.5. Internalised SH1000-GFP bacteria are not cleared by HCE2 cells.

Flow cytometry was used to quantify internalised SH1000-GFP, and cell fluorescence profiles were compared at 2 and 6 hrs post-infection to measure bacterial clearance (**Figure 6-15**). Cells were cultured in medium containing low-dose lysostaphin between these time points to prevent uptake of extracellular SH1000-GFP bacteria. For uninfected HCE2 and BMDM cells, a single sharp peak was displayed on the fluorescence histogram corresponding to no/very low levels of GFP fluorescence (**Figure 6-15A**). At 2 hrs post-infection, a shift in the histogram population was observed for both cell types, as cells containing SH1000-GFP were detected (**Figure 6-15B**). This shift was more pronounced for BMDM cells, as counts for GFP-fluorescing cells were increased and maximum fluorescence values were larger. By 6 hrs post infection, GFP-positive cells were still detected for both cell types (**Figure 6-15C**). However, maximum fluorescence values had increased for HCE2 cells, whereas this value remained similar for BMDMs. Furthermore, whilst fluorescence histograms showed a decrease in GFP-positive cells for BMDMs, an increase in these cells was observed for HCE2 cells. Data was extracted from fluorescence histograms and GFP-fluorescence values were compared between 2 hrs and 6 hrs post-infection (**Figure 6-16** and **Figure 6-17**). For HCE2 cells, there was a significant increase in the percentage of cells containing SH1000-GFP bacteria between 2 hrs (24.9% ± 2.7) and 6 hrs (43.5% ± 9.6) post-infection (p= 0.0318) (**Figure 6-16A**). MFI values for the total cell population also demonstrated an increase in average values (111.6 ± 41.2 to 263.0 ± 210.0) but this difference was not significant (p= 0.2878) (**Figure 6-16B**). In contrast, when MFI values for the infected cell population were compared, a significant increase in MFI values was observed (325.3 ± 61.5 to 1382.5 ± 142.9) (p= 0.003, n=3, unpaired t-test) (**Figure 6-16C**). Based on these observations, it was concluded that internalised SH1000-GFP were not effectively cleared by HCE2 cells and instead SH1000-GFP bacteria were able to replicate within these cells, resulting in a net increase in GFP-fluorescence over time. For BMDM cells, the percentage of cells containing SH1000-GFP decreased between 2 hrs (40.9% ± 20.2) and 6 hrs (25.9% ± 14.6) post-infection (**Figure 6-17A**). However, the difference between time points was not significant (p= 0.3544). Similarly, a non-significant decrease in MFI values was observed for the whole cell population between 2 hrs (446.3 ± 330.4) and 6 hrs (191.8 ± 177.3) (p= 0.3050) (**Figure 6-17B**). In contrast to the HCE2 cell population, MFI values for the infected BMDM population were highly similar between 2 hrs (835.8 ± 364.4) and 6 hrs (1061 ± 1014) (p= 0.7355, n=3, unpaired t-test) (**Figure 6-17C**). This indicates that SH1000-GFP bacteria were unable to replicate within infected BMDMs and/or rate of intracellular replication was closely matched by rate of intracellular killing.
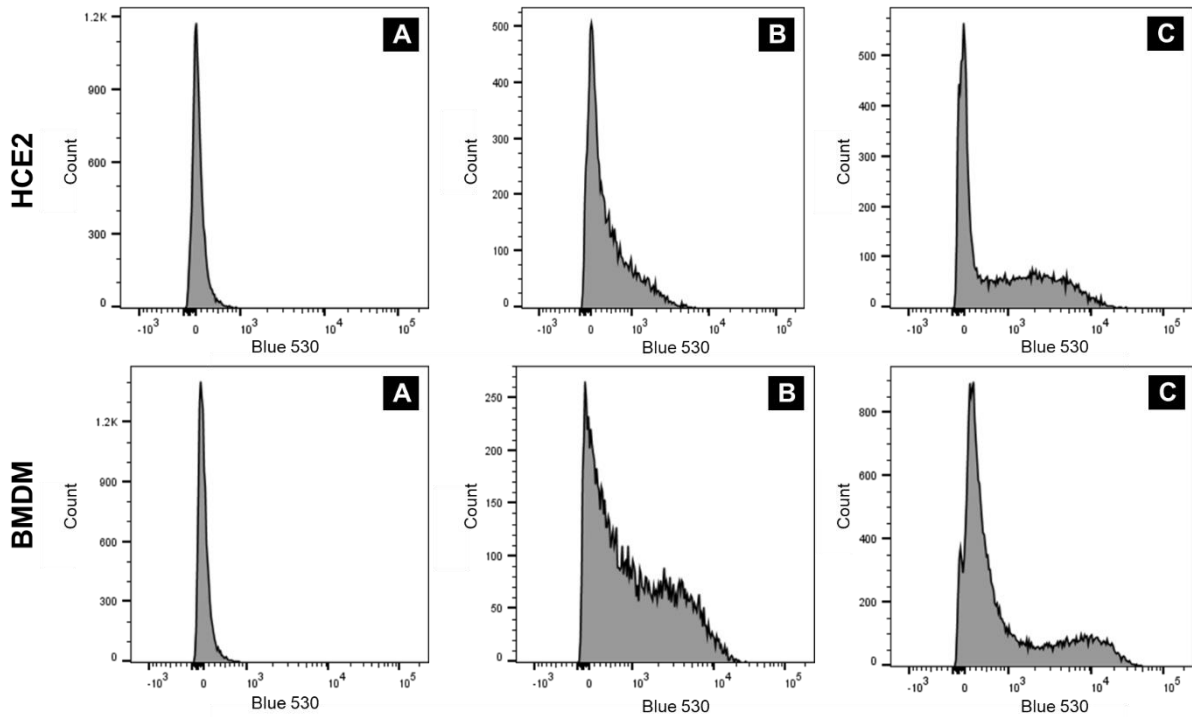
Figure 6-15. Using GFP fluorescence to measure bacterial clearance by flow cytometry.
GFP tagged *S. aureus* S1000 was used to measure initial bacterial uptake and clearance, as measured by GFP quenching over 4 hrs. Representative histograms of GFP fluorescence for different cell populations are shown: **(A) Uninfected cell population (B) 2 hrs post-infection (C) 6 hrs post-infection.** Top panel displays a representative HCE2 data set. Bottom panel displays a representative BMDM data set.

(A)

(B)

(C)
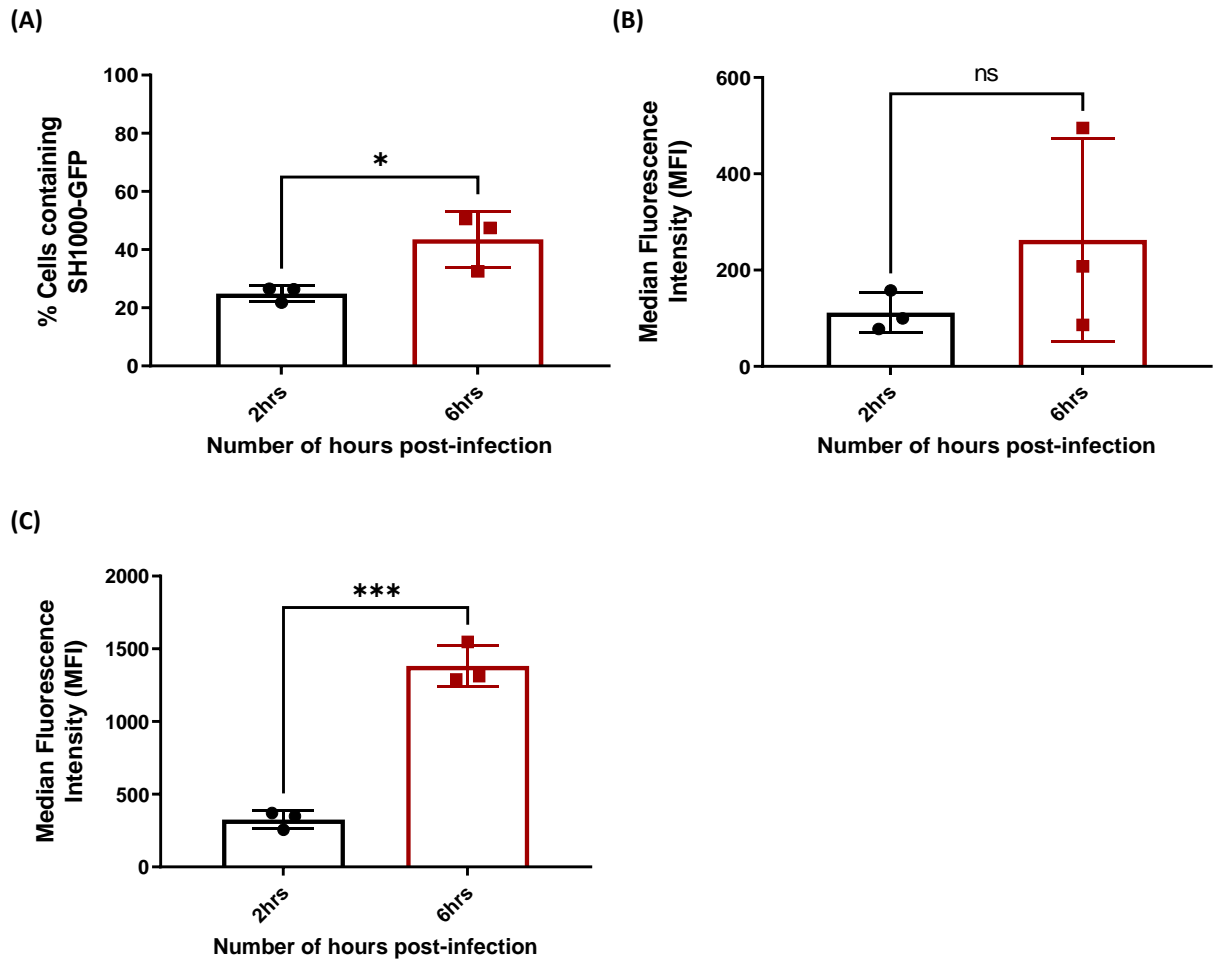
Figure 6-16. Fate of internalised SH1000-GFP in the HCE2 cell line.

(A) % HCE2s containing SH1000-GFP (B) MFI values for the total cell population (C) MFI values for the infected HCE2 population. The number of *S. aureus* SH1000-GFP in HCE2 cells was quantified by flow cytometry. HCE2 monolayers were infected with SH1000-GFP at MOI 10 for 2 hrs. Uninfected medium only controls were also included. After 2 hrs, extracellular bacteria were killed using 20 µg/ml lysostaphin. Infected HCE2s were harvested or incubated in medium containing 2 µg/ml lysostaphin for a further 4 hrs. Data represent mean ± SD, n=3. Data was analysed by unpaired t-test, *p ≤ 0.05, ***p ≤ 0.001, ns= not significant.

(A)

(B)

(C)
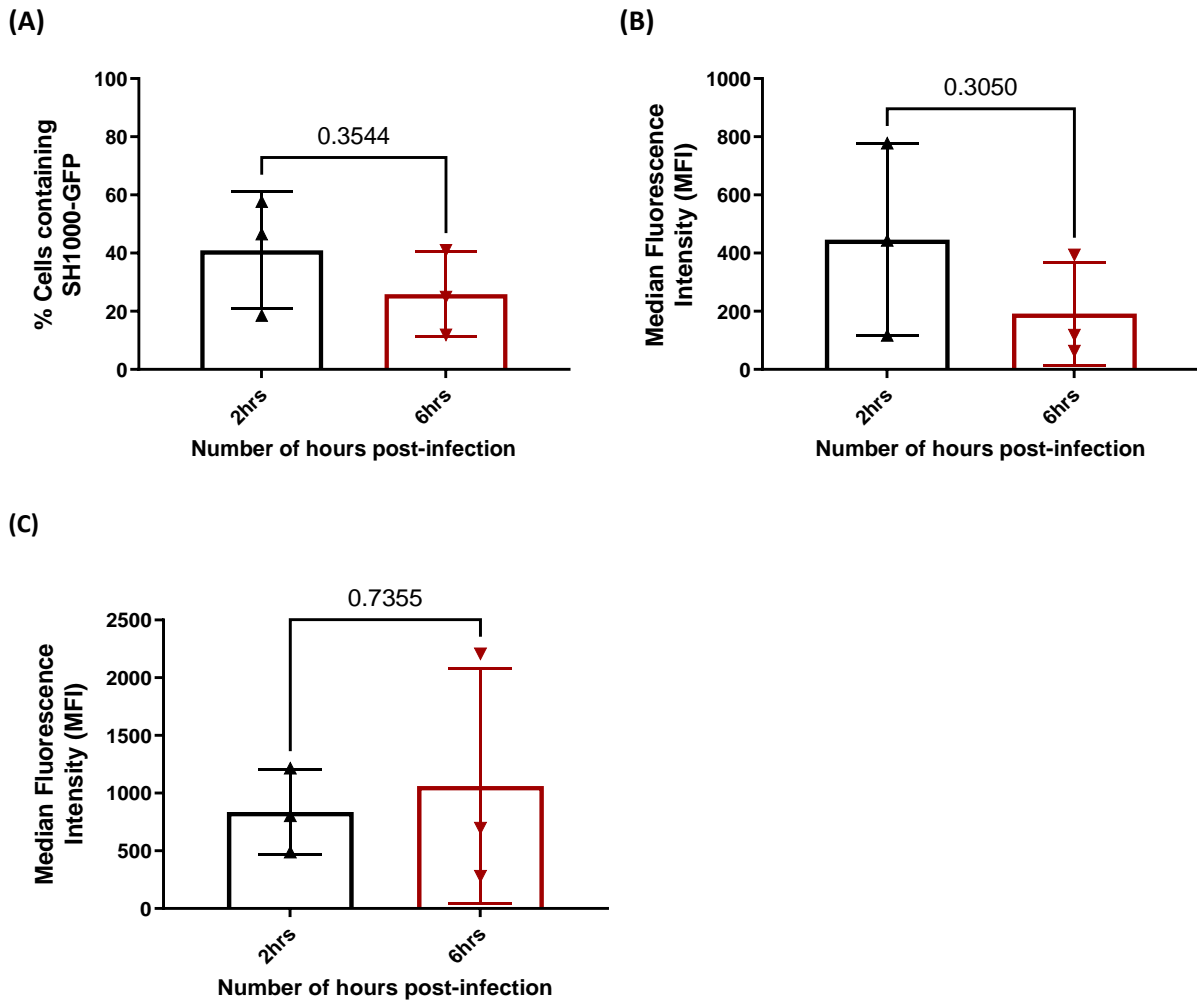
Figure 6-17. Fate of internalised SH1000-GFP by primary mouse BMDMs.
(A) % BMDMs containing SH1000-GFP (B) MFI values for the total cell population (C) MFI values for the infected BMDM population. The number of *S. aureus* SH1000-GFP in primary mouse BMDMs was quantified by flow cytometry. BMDM monolayers were infected with SH1000-GFP at MOI 10 for 2 hrs. Uninfected medium only controls were also included. After 2 hrs, extracellular bacteria were killed using 20 μg/ml lysostaphin. Infected BMDMs were harvested or incubated in medium containing 2 μg/ml lysostaphin for a further 4 hrs. Data represent mean ± SD, n=3. Data was analysed by unpaired t-test.

6.3.6. Increased bacterial traversal in the presence of HCE2 multilayers cannot be explained by active uptake of SH1000-GFP by HCE2 cells.

Following the observation that SH1000-GFP bacteria were internalised by HCE2 cells, bacterial traversal of transwell inserts was investigated using active uptake inhibitors (**Figure 6-18**). Inhibitors included 4% PFA, which inhibits all active cell processes and cytochalasin D, which inhibits actin polymerisation. Rearrangement of the host actin cytoskeleton is essential for the pathogen-induced internalisation of *S. aureus* (Jett and Gilmore, 2002). Bacterial traversal was measured by basal chamber CFU/well measurements in the presence or absence of HCE2 multilayers and CFU/well values were increased in the presence of HCE2 cells under all conditions (**Figure 6-18A**). Under untreated conditions, average CFU/well was $7.98 \times 10^6 \pm 9.76 \times 10^6$, in the presence of cells and $1.17 \times 10^3 \pm 2.03 \times 10^3$, in the absence of cells. For cytochalasin D-treated wells, CFU/well was $4.24 \times 10^6 \pm 6.29 \times 10^6$ for cells, whereas no bacteria were recovered from basal chambers in the absence of cells. For 4% PFA-treated cells, CFU/well was $4.55 \times 10^6 \pm 7.69 \times 10^6$ for cells and $1.15 \times 10^5 \pm 2.00 \times 10^5$ for no cell conditions. Basal CFU/well values were also compared for transwell inserts containing HCE2 multilayers (i.e., cell conditions only) and no significant difference between treatment conditions was observed ($p > 0.05$ in all cases, n=3, one-way ANOVA with Tukey's multiple comparisons test) (**Figure 6-18B**), suggesting increased bacterial traversal in the presence of cells is not mediated by an active process. Flow cytometry was used to confirm that cytochalasin D and 4% PFA treatments prevented bacterial uptake in HCE2 cells (**Figure 6-19**). For untreated, infected HCE2 cells, an average MFI value of 159.3 ± 8.1 was recorded. In contrast, MFI values were decreased for infected HCE2 cells treated using cytochalasin D (78.0 ± 22.3) or 4% PFA (86.1 ± 6.4) and these values were comparable to MFI values for uninfected cells (97.8 ± 3.7).

(A)

(B)
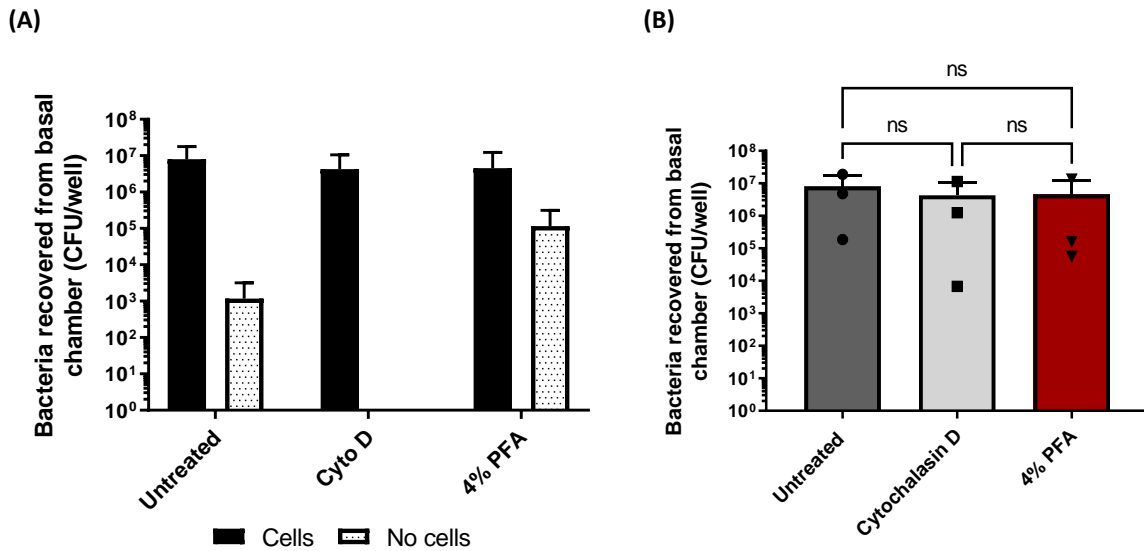
Figure 6-18. Bacterial traversal of transwell inserts in the presence of bacterial internalisation inhibitors.
HCE2 multilayers were cultured on transwell inserts using the optimised protocol; no cell controls were also prepared. On day 6 of culture at ALI, transwells were pre-treated with cytochalasin D or fixed with 4% PFA and infected with SH1000-GFP at MOI 50. The infection protocol for measuring bacterial traversal was followed and aliquots were collected from basal chambers at 8 hrs post-infection. Data represent mean ± SD, n=3. **(A) Comparison of cells versus no cell values for all treatment conditions. (B) Cells values only.** Data was analysed by one-way ANOVA with Tukey's multiple comparisons test, ns= not significant.
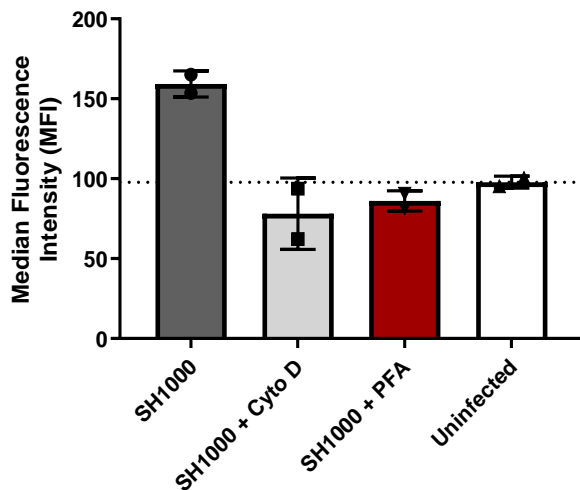
Figure 6-19. Testing inhibitors of bacterial internalisation by flow cytometry.
Flow cytometry was used to measure the uptake of SH1000-GFP by HCE2s. HCE2 monolayers were pre-treated with cytochalasin D or 4% PFA and infected with SH1000-GFP at MOI 10 for 2 hrs. Uninfected HCE2s and untreated cell populations were also included. MFI values for the total cell population are shown. Data represent mean ± SD, n=2.

6.3.7. Bacterial traversal of empty transwell inserts is not affected by choice of coating reagent.

It was hypothesised that increased bacterial traversal in the presence of HCE2 multilayers could be linked to deposition of an extracellular matrix in the presence of HCE2 cells. Therefore, bacterial traversal experiments were repeated under no cell conditions using different coating reagents (**Figure 6-20**). ECM gel was considered the closest representation of the native extracellular matrix generated by HCE2 cells. For transwells infected using SH1000-GFP, basal CFU/well values were similar for collagen-coated ($1.27 \times 10^4 \pm 2.54 \times 10^4$), fibronectin-coated ($2.89 \times 10^1 \pm 5.00 \times 10^1$) and ECM gel-coated ($2.82 \times 10^2 \pm 4.88 \times 10^2$) wells and there was no significant difference between conditions ($p > 0.05$ in all cases, n= 4 for collagen, n=3 for fibronectin and ECM gel) (**Figure 6-20A**). Similar findings were reported for LVP13, with no significant difference between collagen ($2.40 \times 10^4 \pm 4.09 \times 10^4$), fibronectin ($2.17 \times 10^2 \pm 3.75 \times 10^2$) and ECM gel ($1.97 \times 10^4 \pm 2.44 \times 10^4$) conditions ($p > 0.05$ in all cases, n=5 for collagen, n=3 for fibronectin and ECM gel, one-way ANOVA with Tukey's multiple comparisons test) (**Figure 6-20B**). Therefore, increased bacterial traversal in the presence of HCE2 multilayers remains unexplained and this phenomenon warrants further investigation.
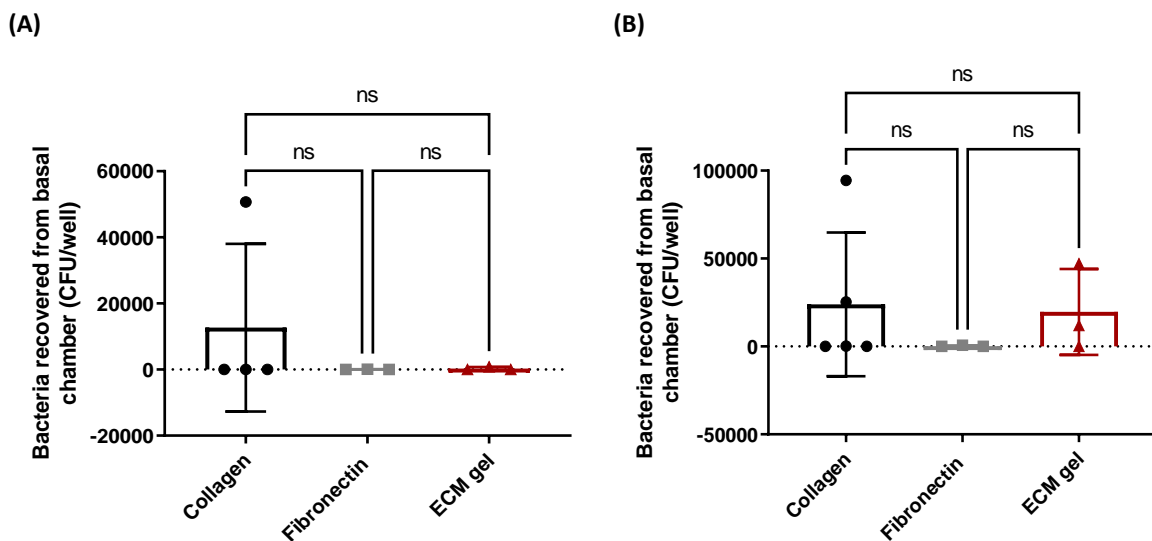
Figure 6-20. Bacterial traversal in the absence of HCE2 multilayers and different transwell coating conditions.

Transwell inserts were coated using 0.1 mg/ml bovine collagen type I, the standard fibronectin coating medium (0.01 mg/ml fibronectin, 0.03 mg/ml bovine collagen type I, 0.01 mg/ml BSA) or ECM gel diluted 1:10 in DMEM. Following removal of the coating medium, empty transwells were incubated in tissue culture medium overnight and the infection protocol for measuring bacterial traversal was followed. Transwells were infected with *S. aureus* at MOI 50 and aliquots were collected from basal chambers at 8 hrs post-infection. Data represent mean ± SD. Data was analysed by one-way ANOVA with Tukey's multiple comparisons test. **(A) SH1000-GFP** n=4 for collagen, n=3 for fibronectin and ECM gel. **(B) LVP13** n=5 for collagen, n=3 for fibronectin and ECM gel.

6.4. Discussion

6.4.1. Summary of results

In this chapter, *S. aureus* infection studies involving the HCE2 transwell model have been described. The first major aim for this chapter was to explore mechanisms of *S. aureus* keratitis using the HCE2 transwell model and this was achieved using a range of different techniques. TEM and cytotoxicity assays were used to study damage to HCE2 multilayers during infection and despite disintegration of multilayers at 9 hrs post-infection, cytotoxicity assays revealed low levels of cell lysis at early time points. TEM images also revealed internalisation of *S. aureus* bacteria by HCE2 cells and the presence of cellular material within PET membranes of infected transwell inserts. Localisation of *S. aureus* bacteria in the infected transwell model was monitored at different time points using TEM, confocal microscopy and bacterial quantification techniques. The HCE2 transwell model was expected to confer significant barrier protection against invading pathogens due to the formation of tight cell junctions (see **Chapter 3**). However, bacteria were able to traverse HCE2 multilayers in relatively little time and bacterial traversal was significantly increased in the presence of HCE2 multilayers compared to no cell conditions. It was hypothesised that increased traversal could be mediated by the active uptake of *S. aureus* by HCE2 cells, allowing bacteria to move into basal chambers via a bacterial transcytosis pathway. In order to test this hypothesis, flow cytometry was used to quantify bacterial internalisation in the presence of HCE2 monolayers. This allowed me to assess the plausibility of the bacterial transcytosis hypothesis whilst also investigating the invasion characteristics of *S. aureus*, thereby achieving the second major aim for this chapter. Flow cytometry confirmed that SH1000-GFP bacteria were internalised by HCE2 cells but that these cells were ineffective in their clearance of bacteria, thereby acting as non-professional phagocytes. These findings provided support for the original bacterial transcytosis hypothesis. However, follow up studies measuring bacterial traversal in the presence of cell inhibitors showed that bacterial traversal was unaffected by cytochalasin D or cell-fixation, despite the inhibition of phagocytosis under these conditions. Therefore, although the phagocytic behaviour of corneal epithelial cells is likely to play a role in *S. aureus* keratitis, it cannot explain why bacterial traversal is increased in the presence of HCE2 cells. The potential role of the ECM was also investigated but ECM mimics were shown to have no effect on bacterial traversal. It may be that ECM mimics were not sufficiently representative of the host ECM, or there may be an alternative explanation which is independent of host cell activity and/or host ECM components. Regardless, increased bacterial traversal in the presence of HCE2 multilayers is an interesting phenomenon that warrants further investigation.

6.4.2. Microscopy techniques

6.4.2.1. Transmission Electron Microscopy

In **section 6.3.1**, microscopy techniques were used to monitor progression of *S. aureus* infection in the HCE2 transwell model. TEM provided major insight into the structural integrity of HCE2 multilayers at 5 and 9 hrs post-infection, following SH1000-GFP infection at MOI 10 (**section 6.3.1.1**). At 5 hrs post-infection, HCE2 multilayers remained relatively intact, and 3-4 cell layers could be observed, as described in the uninfected HCE2 transwell model (**section 3.3.4**). However, gaps were beginning to emerge between neighbouring cells and there was evidence of cell death. By 9 hrs post-infection, widespread disintegration of HCE2 multilayers had occurred and neighbouring cells were completely detached from one another. These findings suggest that *S. aureus* infection causes significant disruption of tight cell junctions and triggers cell death in the HCE2 model. Furthermore, the HCE2 transwell model should not be used to study *S. aureus* infection beyond 9 hrs, as HCE2 multilayers are largely destroyed, meaning the model is no longer physiologically relevant. Longer infection periods would require a significant reduction in MOI.

The deterioration of HCE2 multilayers provides support for the role of *S. aureus* virulence factors in bacterial keratitis. During these infections, corneal damage is caused by the combined effects of bacterial and host cell responses (O'Callaghan, 2018). The bacterial response includes the production of various proteases and cytolytic toxins which damage host tissue and induce cell death (Marquart and O'Callaghan, 2013). Many of these virulence factors (e.g., α-toxin) are upregulated by the Accessory gene regulatory (Agr) system and are repressed by the Repressor of toxins (Rot) global regulatory system (Said-Salim et al., 2003). The Rot system is active during the early stages of *S. aureus* growth and is replaced by Agr activation during the late-log phase (O'Callaghan, 2018). Therefore, the growth-dependent activation of opposing gene regulatory systems could explain why large-scale deterioration of HCE2 multilayers was observed between 5 and 9 hrs post-infection, but not during the initial 5 hr infection period, as increased production of *S. aureus* toxins is expected at later time points. In the infected cornea *in vivo*, host-induced corneal damage is largely attributed to neutrophil infiltration (Livingston et al., 2019). Therefore, the absence of an immune component represents one of the major limitations of the transwell infection model. However, there is evidence to suggest that corneal epithelial cells may also contribute to ocular damage. One study involving a HCE transwell model, showed that exposure of HCE cells to TNFα was associated with significant reductions in Trans-Epithelial Electrical Resistance (TEER) and loss of ZO1 at tight junctions. These changes were observed as early as 2 hrs post-treatment. In the previous chapter, HCE2 cells were shown to express TNFα

following *S. aureus* infection (see **section 5.3.5**). Therefore, proinflammatory cytokines such as TNFα may also contribute to the disruption of multilayer architecture in the infected transwell model.

Another major finding from TEM microscopy studies was the observation that SH1000-GFP bacteria are internalised by HCE2 cells. Engulfment of bacteria was visible at the corneal epithelial cell surface and internalised bacteria were visualised at different positions within the HCE2 multilayer, including within the superficial corneal epithelial layer and within the lower HCE2 cell layers. These images show that bacteria are able to traverse HCE2 cell layers, although the mechanism of traversal is unclear. TEM images also revealed the presence of cellular material, believed to originate from HCE2 cells, in the PET transwell membrane of transwell inserts. It was hypothesised that these cellular bodies, which lacked distinct structure or cellular organelles, could represent HCE2 cell projections or secreted products. Other groups have previously reported internalisation of *S. aureus* by human corneal epithelial cells (Jett and Gilmore, 2002) but the presence of cellular material within PET membranes appears to be a novel finding.

6.4.2.2. Fluorescence Microscopy

Whilst TEM facilitated visualisation of HCE2 multilayers, fluorescence microscopy provided additional information on the distribution of SH1000-GFP bacteria (**section 6.3.1.2**). Microscopy images collected at the surface of infected HCE2 multilayers appeared to show the formation of bacterial microcolonies as early as 5 hrs post-infection and z-stack images displayed an increase in bacterial traversal between 5 and 9 hrs post-infection. At 5 hrs post-infection, bacteria had progressed 7 µm into the HCE2 transwell model and this was increased to 15-19 µm by the 9-hr time point. These measurements equated to 23% and 47% of the total thickness of the HCE2 multilayer, respectively. CellMask staining of HCE2 cells provided total multilayer thickness measurements of 30-36 µm and therefore my *in vitro* model of the corneal epithelium is thinner than the *in vivo* epithelium, which has an approximate thickness of 50 µm (Sridhar, 2018). This matches the previous finding that there are 3-4 cell layers in the HCE2 transwell model (see **section 3.3.4**), whereas the *in vivo* cornea possesses 5-7 cell layers. Another limitation of the HCE2 transwell model identified by epithelial cell staining, was variation in HCE2 multilayer thickness between transwell inserts (i.e., 30 versus 36 µm). In future work, non-invasive techniques such as TEER measurements, could be used to compare epithelial barrier integrity between transwell inserts. Whilst TEER measurements cannot provide a direct measure of multilayer thickness, transwells with similar multilayer architecture should provide similar TEER readings. Therefore, transwell inserts could be selected based on TEER measurements prior to infection work.

Other groups have previously used HCE transwell models to track the movement of *P. aeruginosa* through HCE multilayers (Alarcon et al., 2009b). As in my experiments, fluorescence microscopy was used to visualise GFP-tagged bacteria and z-stacks revealed the accumulation of PAO1-GFP bacteria at transwell membranes by 5 hrs post-infection. Although, bacterial traversal studies have shown that SH1000-GFP is able to traverse HCE2 multilayers within 5 hrs (see **section 6.3.3**), z-stack images indicated that most bacteria were localised to the upper corneal epithelial cell layer at this time point. Furthermore, an increased bacterial inoculum (3 x 10^6 CFU/ml) was used in my infection model compared to the *P. aeruginosa* traversal study (1 x 10^6 CFU/ml). This suggests that *P. aeruginosa* traverses corneal epithelial cell multilayers much more readily than *S. aureus* and different mechanisms of host traversal are likely to exist between species. Therefore, direct comparisons cannot be made. Further support for this is provided by *ex vivo* infection studies. Pinnock et al used human and rabbit corneas to study microbial keratitis and bacteria were inoculated at the site of corneal scratches. Following 24 hr infection with *S. aureus*, the majority of bacteria were observed within the original scratch site, whereas extensive infiltration of bacteria into the surrounding tissue was observed for *P. aeruginosa* (Pinnock et al., 2017). This demonstrates that *P. aeruginosa* is much more invasive in its infection of the cornea and therefore my confocal images, which show limited infiltration of *S. aureus* at the 5-hr time point, are in agreement with previous *ex vivo* findings.

6.4.3. Cytotoxicity assays

In **section 6.3.2**, cytotoxicity assays were used to measure cumulative LDH release as a marker of cell lysis. At 1 and 5 hrs post-infection, levels of LDH release were relatively low under all infection conditions and % cytotoxicity values for infected HCE2 cells were comparable to values for uninfected cells. By 9 hrs post-infection, LDH release was increased, and cytotoxicity values peaked at 48.5% ± 3.7 for HCE2 cells infected at MOI 10. There was a significant increase in cytotoxicity values for infected cells compared to uninfected HCE2 cells at MOI 10, but this was not observed at MOI 1. These findings show that SH1000-GFP does not induce high levels of cell lysis in the HCE2 transwell model. This seemingly contradicts TEM images, which show large-scale deterioration of HCE2 multilayers by 9 hrs post-infection and evidence of cell death at the 5-hr time point.

There are a number of possible explanations for the low cytotoxicity associated with *S. aureus* infections. Firstly, high cytotoxicity values for the DMEM: F12 control condition (in the absence of infection) may have masked the cytotoxic effects of SH1000. High cytotoxicity values for DMEM: F12, particularly at the 9-hr time point, suggest that uninfected HCE2 multilayers may have started to deteriorate. This could be due to the removal of ALI during infection studies or the natural lifespan of

the HCE2 model, which generally peaks on the day of infection. Perhaps if cytotoxicity studies had been carried out at an earlier time point, or in the presence of ALI, a significant difference between infected and uninfected cells would have been observed across multiple conditions. However, it is also possible that low cytotoxicity values are a true reflection of the infection scenario. Other researchers have previously investigated the cytotoxic effects of *S. aureus* and cytotoxicity was shown to depend on cell type and staphylococcal strain (Strobel et al., 2016). Propidium Iodide (PI) staining was used to measure disruption of membrane integrity and *S. aureus* SH1000 was associated with low cytotoxicity compared to other strains. Following 24 hr infection of airway epithelial cells with *S. aureus* SH1000, less than 25% of cells were PI-positive (i.e., non-viable). In contrast, over 75% of A549 cells were PI-positive following infection with *S. aureus* 6850 and the reduced cytotoxicity of SH1000 was linked to the reduced production of cytolytic products such as α-toxin. Therefore, the damage to HCE2 multilayers that was observed by TEM, may be largely attributable to non-cytolytic products such as proteases. For example, *Staphylococcus aureus* Superantigen-Like Protein (SSL1) is a *S. aureus* virulence factor with proteolytic activity which has been shown to play a role in corneal virulence (Tang et al., 2019). SSL1 is upregulated by Rot and downregulated by the Agr system (Benson et al., 2011) and therefore this protease should be present in the medium at early infection time points.

6.4.4. Increased bacterial traversal in the presence of HCE2 multilayers

In **section 6.3.3**, localisation of *S. aureus* bacteria in the HCE2 transwell model was investigated by enumeration of bacteria in apical and basal chambers at different time points. There was an increase in apical CFU/well measurements over time, indicating that *S. aureus* bacteria were able to survive and replicate within the HCE2 transwell model and CFU/well measurements for basal chambers showed that bacteria were able to traverse transwell inserts, generally by 5 hrs post-infection. Preliminary studies suggested bacterial traversal was increased in the presence of HCE2 multilayers compared to no cell controls, but initial results were not significant due to low numbers of repeats. It was hypothesised that increased traversal in the presence of HCE2 cells, could be linked to increased bacterial adhesion and so quantification of adherent bacteria was carried out under different conditions. These studies showed no significant difference between cell and no cell conditions, allowing me to conclude that bacterial traversal was not influenced by bacterial adhesion. These findings also suggested that the HCE2 transwell model would not be suitable for studying the anti-adhesion effects of CD9 peptides and unfractionated heparin, as traditional bacterial adhesion protocols rely on low levels of background binding. Following on from this result, a simplified protocol for measuring bacterial traversal was developed. Both the *S. aureus* laboratory strain, SH1000-GFP and the clinical *S. aureus* isolate, LVP13, were used and bacterial traversal was significantly increased

in the presence of HCE2 multilayers for both staphylococcal species. I concluded that bacterial traversal of transwell inserts was increased in the presence of HCE2 cells and a new hypothesis involving bacterial transcytosis was proposed.

It was hypothesised that increased bacterial traversal in the presence of HCE2 multilayers was mediated by active uptake of *S. aureus* by HCE2 cells. Bacterial transcytosis pathways have previously been implicated in the traversal of invasive *P. aeruginosa* strains (Alarcon et al., 2009a) and the movement of bacteria between host cells has been well documented in other pathogens, e.g., *Listeria monocytogenes* (Gedde et al., 2000). However, the observation that bacterial traversal is increased in the presence of HCE2 multilayers appears to be a novel finding and contradicts a previous study involving *P. aeruginosa* (Alarcon et al., 2009b), which showed increased traversal in the absence of HCE2 multilayers.

6.4.4.1. Phagocytosis studies

In **sections 6.3.4** and **6.3.5**, flow cytometry was used to study internalisation of GFP-tagged SH1000 by HCE2 cells. These experiments were designed to investigate the phagocytic activity of HCE2 cells and determine whether bacterial transcytosis was a plausible explanation for increased bacterial traversal in the presence of HCE2 cells. Initial experiments (**section 6.3.4**) were focussed on bacterial uptake and HCE2 cells were shown to internalise SH1000-GFP bacteria, with approximately 27% of HCE2 cells containing SH1000-GFP bacteria following 2 hr infection at MOI 10. Flow cytometric gating was used to study infected and uninfected cell populations separately and MFI values for infected HCE2 cells were similar across a range of MOIs, suggesting a lack of variation in the number of SH1000-GFP bacteria internalised by HCE2 cells. This indicated that the majority of HCE2 cells contained a single SH1000-GFP bacterium at this time point. The relative phagocytic activity of HCE2 cells was assessed by comparison with the non-phagocytic human keratinocyte cell line (HaCaT) and primary bone marrow-derived macrophages (BMDM) from mice, which represented professional phagocytes. Although significant differences between cell types were not observed, bacterial uptake was increased in HCE2 cells (27%) compared to HaCaT cells (8.5%) and decreased compared to mouse BMDMs (40.9%). This provides support for the idea that HCE2 cells may act as non-professional phagocytes. MFI values for the infected cell population were highly similar for HCE2 and HaCaT cells and there was little variation between biological replicates, indicating that HaCaT cells and HCE2 cells generally take up a single bacterium. In contrast, MFI values were increased for infected BMDM cells, suggesting these cells were capable of internalising multiple SH1000-GFP bacteria during the 2-hr infection period.

In **section 6.3.5**, flow cytometry experiments were extended, and infected cells were cultured in medium containing low dose lysostaphin, to measure bacterial clearance over a 4-hr time period. Clearance data for HCE2s showed a significant increase in the percentage of cells containing bacteria between 2 and 6 hrs post-infection. The use of lysostaphin prevented HCE2 cells from becoming newly infected by extracellular *S. aureus* and therefore there are two possible explanations for this finding. Firstly, HCE2 cell death may have occurred between the two time points, with cell death disproportionately affecting the uninfected cell population. Alternatively, internalised SH1000-GFP bacteria may have been transferred from infected to uninfected HCE2 cells, providing further support for the bacterial transcytosis hypothesis. MFI values for the infected cell population, showed a 4-fold increase in MFI between the 2 and 6 hr time points. This demonstrates the intracellular survival of SH1000-GFP bacteria within HCE2 cells and provides evidence that these bacteria are able to replicate within HCE2 cells. Therefore, HCE2 cells are highly inefficient in their clearance of intracellular *S. aureus* bacteria. Bacterial clearance studies were also performed using mouse BMDMs to validate the protocol and provide comparison with HCE2 cells. Between 2 and 6 hrs post-infection, there was a decrease in the percentage of BMDMs containing SH1000-GFP, as well a decrease in MFI values for the total BMDM population. This reveals a reduction in internalised bacteria between the two time points, with effective clearance of intracellular SH1000-GFP by BMDMs. It should be noted that reductions in internalised bacteria were not significant, but this may be linked to the increased variability of primary cells compared to immortalised cell lines. It is also important to note that bacteria were not opsonised prior to infection and therefore BMDMs are expected to display reduced phagocytic activity compared to *in vivo* macrophages.

The bacterial internalisation data presented within this chapter can be corroborated by previous research findings. For example, internalisation of *S. aureus* has been compared between different cell-types previously and the A549 epithelial cell line was shown to take up high numbers of bacteria (Strobel et al., 2016). In contrast, very low numbers of intracellular bacteria were detected for the HaCaT human keratinocyte cell line, mirroring my data for the HaCaT versus HCE2 cell lines. Furthermore, the internalisation of *S. aureus* by an SV40-immortalised human corneal epithelial cell line has been reported previously (Jett and Gilmore, 2002). However, I cannot make quantitative comparisons with my own data due to differences in methodology. In the aforementioned study, intracellular bacteria were quantified by CFU, whereas my study utilised fluorescence readings that have not been calibrated against actual bacterial numbers. Calibration would be difficult to perform as samples are fixed prior to flow cytometric analysis and therefore this represents a limitation of the flow cytometry protocol. However, this technique also facilitated the measurement of bacterial clearance within human corneal epithelial cells, a phenomenon that has not been reported previously.

My findings suggest that HCE2 cells are inefficient in their clearance of intracellular bacteria. However, discrepancies in the phagocytic activity of immortalised cell lines and primary cell lines have been reported previously (Strobel et al., 2016) and therefore it will be important to repeat this work using primary corneal epithelial cells. If HCE2 findings are replicated in primary cells, this could provide support for two opposing theories regarding the functionality of the human corneal epithelium. Firstly, it may be that corneal epithelial cells are not able to destroy intracellular bacteria, and that their primary role is to protect the ocular surface via shedding. Or alternatively, it may be that corneal epithelial cells are able to provide phagocytic defence against certain ocular pathogens, but that *S. aureus* is able to circumvent these killing mechanisms. Immune evasion remains to be fully characterised in non-professional phagocytes, but *S. aureus* is believed to escape the phagosome via activation of the Agr quorum sensing system. Agr activation results in the upregulation of virulence factors involved in immune evasion (e.g., phenol soluble modulins) and following its release, *S. aureus* is proposed to replicate in the host cytosol (Moldovan and Fraunholz, 2019).

6.4.4.2. Potential explanations for increased bacterial traversal in the presence of HCE2 cells

Phagocytosis experiments showed that SH1000-GFP bacteria were internalised by HCE2 cells but that these cells were ineffective in their intracellular clearance of these bacteria. This provided further support for the bacterial transcytosis hypothesis and bacterial traversal studies were repeated using cell inhibitors. These inhibitors included cytochalasin D, which inhibits actin polymerisation and 4% PFA which inhibits all active cell processes. The chosen treatment conditions were shown to inhibit internalisation of SH1000-GFP by HCE2 monolayers, as measured by flow cytometry and it was hypothesised that bacterial traversal of HCE2 multilayers would be reduced in the presence of these inhibitors. However, neither cytochalasin D nor fixation of cells with 4% PFA was shown to affect bacterial traversal. There was no significant difference in basal CFU/well measurements for untreated, cytochalasin D-treated, or fixed transwells containing HCE2 multilayers and bacterial traversal was consistently increased compared to no cell conditions. This refuted the hypothesis that increased bacterial traversal was mediated by active uptake of *S. aureus* bacteria. An alternative hypothesis was proposed, whereby bacterial traversal was increased in the presence of HCE2 cells due to the deposition of an extracellular matrix (ECM) by HCE2 cells. To test this hypothesis, bacterial traversal was investigated in the absence of HCE2 cells, using different coating reagents intended to represent the extracellular matrix. These reagents included the standard collagen coating medium; a fibronectin coating medium containing fibronectin, collagen type I and bovine serum albumin; and an ECM gel containing laminin, collagen type IV and heparan sulphate proteoglycans. Of these coating reagents,

ECM gel was believed to provide the closest representation of the host ECM. However, choice of coating reagent was shown to have no significant effect on bacterial traversal, with similar basal CFU/well measurements observed under all coating conditions.

Therefore, the mechanism by which bacterial traversal is increased in the presence of HCE2 multilayers remains unexplained. To the best of my knowledge, this is a previously unreported phenomenon. However, bacterial traversal of HCE multilayers has been investigated previously using *P. aeruginosa*. In these studies, rate of bacterial traversal was shown to be increased by twitching motility (Alarcon et al., 2009a) and the phospholipase activity of the secreted exoprotein, ExoU (Ramirez et al., 2012). Based on these findings, alternative mechanisms of bacterial traversal were proposed for the different *P. aeruginosa* pathotypes. Invasive (*exoS* +ve) *P. aeruginosa* strains were shown to traverse HCE multilayers via translocation between epithelial cells and during these infections, TEER values remained relatively unchanged (Alarcon et al., 2009a). In contrast, destruction of tight cell junctions and host cell death were central to multilayer traversal by cytotoxic (*exoU* +ve) *P. aeruginosa* strains and these infections were associated with large reductions in TEER, revealing loss of epithelial barrier function (Ramirez et al., 2012). Based on phagocytosis inhibitor studies and TEM images showing destruction of HCE2 multilayers, we can infer that traversal of HCE2 multilayers by *S. aureus* is more akin to the traversal of cytotoxic *P. aeruginosa* and therefore bacterial proteases and cytolytic toxins are likely to play an important role in *S. aureus* keratitis. However, *P. aeruginosa* traversal studies cannot explain why *S. aureus* traversal is increased in the presence of HCE2 multilayers and this contradicts *P. aeruginosa data* that shows increased bacterial traversal in the absence of cells (Alarcon et al., 2009b).

There are a number of possible explanations for this phenomenon. Firstly, differences between my findings and traversal studies involving *P. aeruginosa* may be linked to pore size. A pore size of 0.4 µm was used in my experiments whereas Alarcon et al used transwell inserts containing 8 µm pores. Both *S. aureus* and *P. aeruginosa* are larger than 0.4 µm but these bacteria possess 'filter infiltration activity' which allows them to move through pores which are smaller than their bacterial size, over extended periods of time (Hasegawa et al., 2003). Infiltration studies involving MF-Millipore filters, showed that the size exclusion limits for *S. aureus* and *P. aeruginosa* were 0.22 µm and <0.22 µm respectively, although the passive movement of bacteria was slow, with *S. aureus* ATCC 25923 taking 96 hrs to passively traverse through 0.45 µm pores. Therefore, I hypothesise that traversal of transwell pores may be increased in the presence of HCE2 cell multilayers due to presence of chemotactic gradients. These gradients may be formed by the secreted products of HCE2 cells, causing bacteria to move towards the basal chambers in the presence of HCE2 multilayers. Alternatively, the presence of HCE2

cells may interfere with the structural integrity of PET membranes, potentially widening transwell pores and/or making it easier for bacteria to pass through. Support for this hypothesis is provided by TEM images showing the presence of cellular material within PET membranes. Finally, it remains possible that bacterial traversal is influenced by ECM components but that selected coating reagents were not sufficiently representative of the host ECM to allow this phenomenon to be detected. The most complex coating reagent was the ECM gel, and this coating material contains significantly fewer components than the native ECM. Furthermore, it is incredibly difficult to replicate the complex structural organisation of the ECM *in vitro* due to the absence of *in vivo* host cell processes. For example, the fibrillogenesis of fibronectin (Yang and Friedl, 2016) and the activity of host matrix metalloproteinases (Couture et al., 2016). Therefore, I cannot definitively conclude that the ECM is not involved in bacterial traversal.

6.4.5. Future work

There are a number of additional experiments that could be completed as part of this chapter. Firstly, the observation that bacterial traversal is increased in the presence of HCE2 multilayers warrants further investigation and it would be interesting to investigate whether this phenomenon is specific to human corneal epithelial cells and/or *S. aureus*. Therefore, repeat experiments could be carried out using an alternative cell line, e.g., A549 airway epithelial cells or the HaCaT human keratinocyte cell line, and a different bacterial species such as *P. aeruginosa*. Furthermore, I cannot conclude that ECM components are not involved in bacterial traversal due to the simplicity of my ECM mimics. To better test this hypothesis, HCE2 multilayers could be cultured on transwell inserts before being removed using trypsin. Trypsin should detach HCE2 cells whilst leaving the ECM relatively intact. Bacterial traversal rates for these transwells could then be compared against empty transwells containing no cells. In addition, *S. aureus* adhesin mutants that exhibit reduced interaction with host ECM components could be incorporated into bacterial traversal assays. If the ECM does mediate bacterial traversal, these mutants would be expected to display reduced traversal rates. Finally, I could further investigate how *S. aureus* SH1000 is able to evade intracellular killing mechanisms within human corneal epithelial cells. In particular, confocal microscopy could be used to study the sub-cellular localisation of *S. aureus* with HCE2 cells as it is currently unclear whether these bacteria replicate within the host cytosol or host autophagosomes (Moldovan and Fraunholz, 2019).

6.4.6. Conclusion

In summary, *S. aureus* is a complex pathogen which is able to disrupt the structural integrity of HCE2 multilayers, traverse transwell inserts in the presence or absence of cells, invade HCE2 cells and evade

intracellular clearance mechanisms. Bacterial traversal of transwell inserts is increased in the presence of HCE2 multilayers compared to no cell conditions and this cannot be explained by bacterial transcytosis. This is a novel observation which warrants further investigation.

CHAPTER 7: BIOFLUX INFECTION STUDIES

7.1. Introduction

This chapter describes use of the BioFlux™ (Fluxion Biosciences, USA) microfluidic system to model bacterial keratitis infections under physiological flow conditions. In the previous chapters, host-pathogen interactions between HCE2 cells and pathogenic bacteria were investigated using simple cell culture models and transwell inserts. One of the major limitations of these models is the presence of static conditions, which are not representative of physiological conditions at the ocular surface. In the *in vivo* cornea, human corneal epithelial cells are continually exposed to shear stress due to the movement of tear film over the corneal epithelium and the role of blinking (Masterton and Ahearne, 2018). The presence of shear stress has important effects on both mammalian and bacterial cell behaviour (see **section 1.7**) and so it is important that mechanical stimuli such as shear stress are incorporated into *in vitro* model systems. Use of the BioFlux microfluidic system to simulate bacterial keratitis is a novel area of work that has not been reported previously and therefore extensive optimisation of BioFlux infection protocols was required. During protocol development, a switch from the BioFlux 1000z to BioFlux 200 system was made and the improved imaging capabilities of the BioFlux 200 system allowed me to identify a number of problems with the original protocol. Therefore, as well as providing optimised BioFlux infection protocols for antimicrobial drug testing, this chapter highlights the importance of rigorous model testing and identifies key experimental variables to consider when using the BioFlux system.

7.1.1. BioFlux microfluidic system

The BioFlux microfluidic system is a benchtop instrument provided by Fluxion Biosciences, which allows biological processes to be studied under physiological flow conditions. Four different BioFlux systems are currently available from Fluxion and the BioFlux 200™ and BioFlux 1000z™ systems were used during this project. These multi-component systems share common elements, including an electropneumatic pump and BioFlux pressure interface, which can be affixed to specialised BioFlux plates (**Figure 7-1A**). Various BioFlux plates are available from Fluxion but 48-well plates with glass-bottomed channels, designed for low-shear stress (0-20 dyn/cm^2) conditions, were used in my experiments. These plates consist of 24 inlet wells and 24 outlet wells, and each pair of wells is connected by a single channel (**Figure 7-1B**). These channels contain a viewing window, which is 75 µm (H) x 350 µm (L), and glass coverslips are positioned beneath the window to facilitate high-resolution microscopy. The region between inlet wells and the viewing window is referred to as the serpentine, as this region of the channel is long and winding. In contrast, the path between the outlet

wells and viewing window is much shorter, with just one bend in the channel. These specialised BioFlux plates, in combination with the electropneumatic pump and pressure interface, allow precise shear stress conditions to be generated. In my experiments, continuous, pulsatile and oscillatory flow conditions were trialled, with shear stress values ranging from 0.2 to 1 dyn/cm^2 (**Figure 7-2**). It should be noted that gravity flow may also be present when using the BioFlux system. This term refers to the uncontrolled movement of fluid due to differences in volume between the inlet and outlet wells. Differences in volume generate pressure which causes fluid to move towards the area of lower volume. However, Fluxion estimates that for a fluid with similar viscosity to water (i.e., tissue culture media), the maximal rate of gravity flow in the BioFlux system is only 2.9 µl/hr. Following the introduction of bacteria into BioFlux channels, progression of infection was monitored by microscopy. The integrated Zeiss Axio Observer microscope was used for BioFlux 1000z studies, whereas a Nikon Ti-E inverted microscope was used in later BioFlux 200 studies. The Nikon Ti-E microscope was set up by the Durham laboratory (School of Biosciences, UoS), as the BioFlux 200 does not include an integrated microscopy system. This microscope offered advanced imaging capabilities compared to the integrated Zeiss system, including the Nikon Perfect Focus System, a 100x magnification lens and the ability to perform phase microscopy. Both BioFlux systems were modified to include an incubation chamber which surrounded the microscope and heating blocks maintained the temperature of the incubation chamber at 37°C. In the BioFlux 1000z system, this chamber was also supplied with 5% CO_2. HCE2 cell monolayers were cultured in microfluidic channels prior to infection work and GFP-tagged strains of *S. aureus* SH1000 and *P. aeruginosa* PAO1 were used to allow visualisation of bacteria by fluorescence microscopy.

(A)

(B)
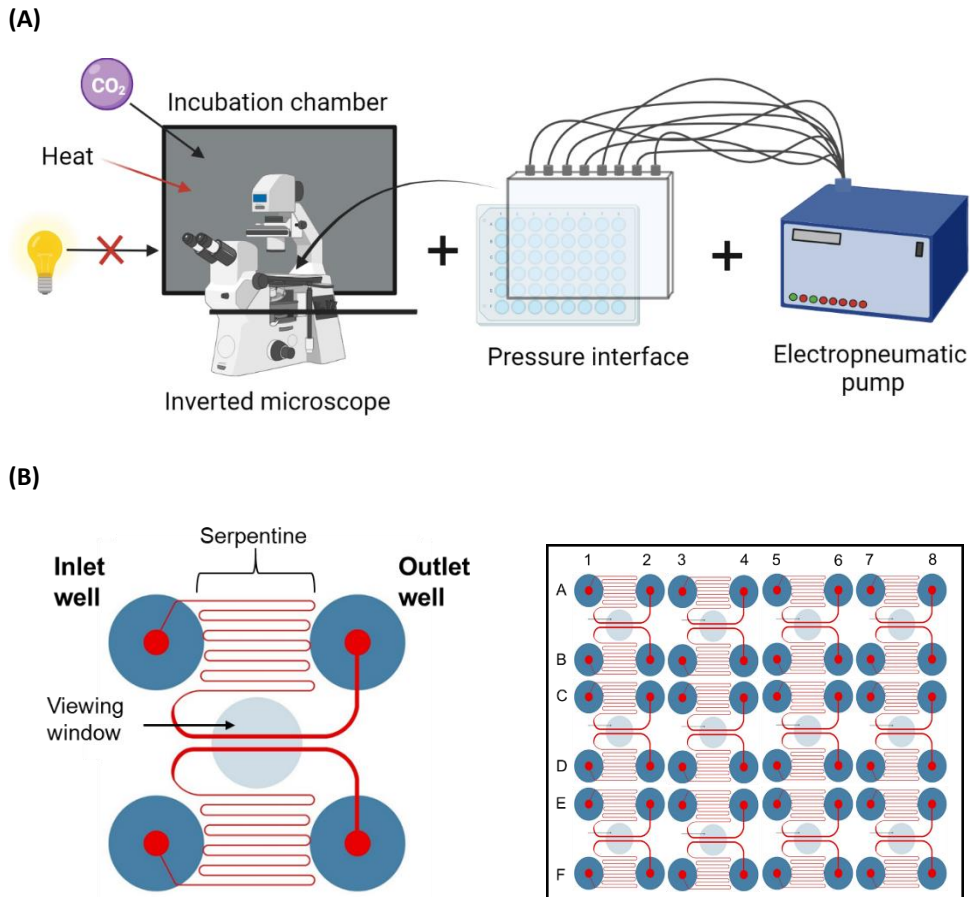
Figure 7-1. BioFlux microfluidic system.

(A) BioFlux components. The BioFlux is composed of 3 major components: (1) an electropneumatic pump which generates shear stress, (2) a pressure interface which connects the pump to specialised BioFlux plates, and (3) an inverted microscope for live cell imaging. Microscopes are surrounded by an incubation chamber which prevents entry of light and maintains optimal cell culture conditions (37°C, 5% CO_2). Created with Biorender.com. **(B) 48-well low shear BioFlux plates.** 48 well plates contain 24 inlet wells and 24 outlet wells. Each pair of wells is connected by a microfluidic channel, with 24 channels and therefore 24 viewing windows per plate. Created using Vectorworks.
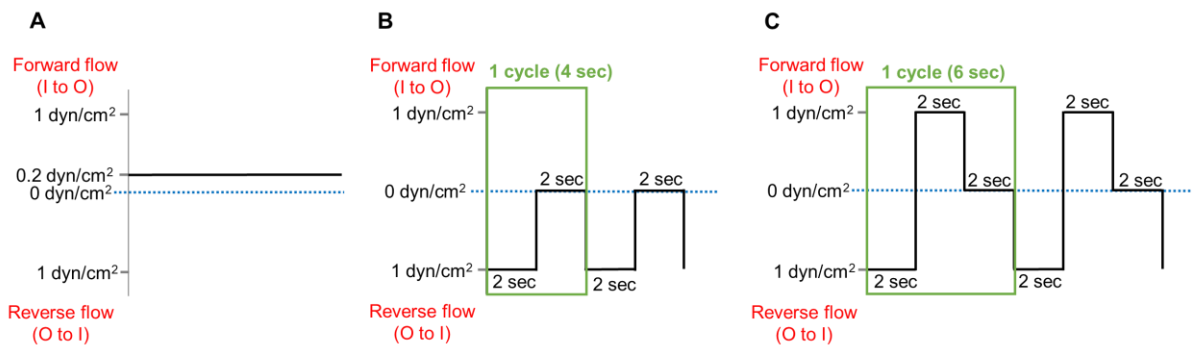
Figure 7-2. Shear flow conditions used in BioFlux experiments.
(A) Continuous: Unidirectional, 0.2 dyn/cm^2 flow in the inlet to outlet direction. **(B) Pulsatile:** 2 seconds of 1 dyn/cm^2 flow in the outlet to inlet direction, 2 seconds of no flow. **(C) Oscillatory:** 2 seconds of 1 dyn/cm^2 flow in the outlet to inlet direction, 2 seconds of 1 dyn/cm^2 flow in the inlet to outlet direction, 2 seconds of no flow. During oscillatory flow there is net flow in the inlet to outlet direction.

7.1.2. Optimisation of BioFlux protocols

Three different infection protocols were used during this chapter and their protocols are summarised in **Figure 7-3** (see **section 2.8** for further details). The preliminary infection (**Figure 7-3A**) and microcolony formation (**Figure 7-3B**) protocols were designed to study the initial stages of biofilm formation on corneal epithelial cells and they were developed using the BioFlux 1000z and BioFlux 200 systems, respectively. The preliminary infection protocol was developed by Dr Mahendra Raut, whereas I developed the microcolony formation protocol following optimisation studies. Both protocols involved inoculation of HCE2 monolayers with small numbers of bacteria, followed by a short incubation period under static conditions to allow bacteria to adhere. Flow conditions were then introduced, and infection progression was monitored over 8 or 24 hrs. In contrast the bacterial adhesion protocol (**Figure 7-3C**) was designed to study just the first stage of infection: bacterial adhesion to host cells. In these studies, HCE2 monolayers were continuously supplied with bacteria under shear flow conditions and the maximum length of infection was 2 hrs. The bacterial adhesion protocol was also used to investigate the putative anti-adhesion effects of unfractionated heparin (UFH). **In Chapter 5**, 10 U/ml UFH was shown to significantly reduce bacterial adhesion to HCE2 monolayers under static conditions (**section 5.3.4**). This was observed for both *S. aureus* SH1000-GFP and *P. aeruginosa* PAO1-GFP and corroborates findings from previous lab members (Green et al., unpublished). However, use of the BioFlux to study the effects of UFH on bacterial adhesion under flow conditions represents an entirely novel area of work.
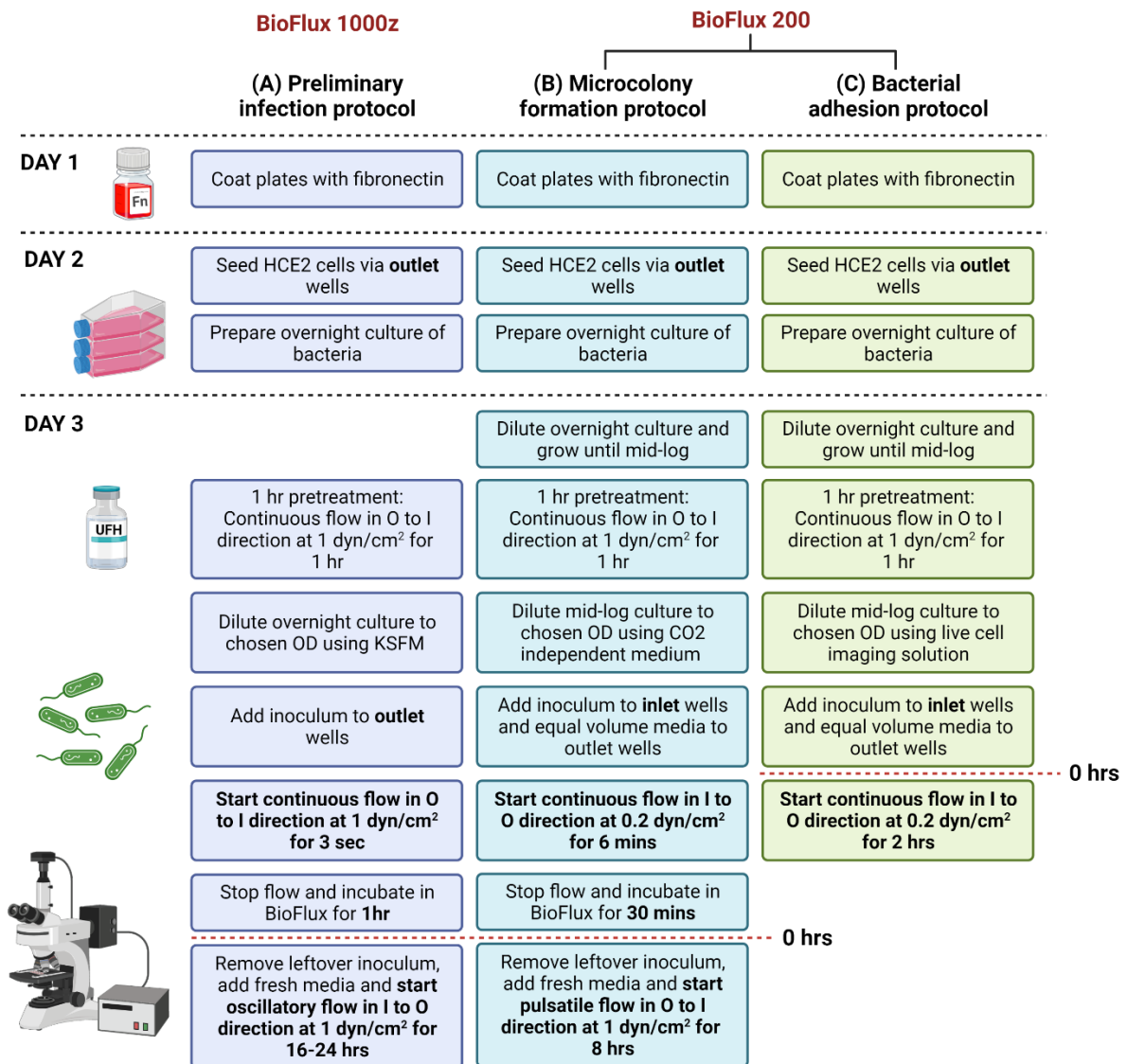
Figure 7-3. A comparison of BioFlux infection protocols.

(A) Preliminary infection protocol. (B) Microcolony formation protocol. (C) Bacterial adhesion protocol. Different protocols used for BioFlux infection work are summarised above. The preliminary infection protocol was developed using the BioFlux 1000z system whereas microcolony formation and bacterial adhesion protocols were optimised using the BioFlux 200. Important differences between protocols are highlighted in bold. In preliminary infection and microcolony formation experiments, the 0-hr time point refers to the end of the static incubation period, immediately before the introduction of oscillatory/pulsatile flow (bacteria already present). In bacterial adhesion experiments, 0 hr refers to the time point immediately before introduction of continuous flow (no bacteria present). I= inlet; O= outlet. Created with Biorender.com.

7.2. Aims

1. To optimise a protocol for measuring biofilm formation on the surface of HCE2 monolayers, under physiological flow conditions.

2. To optimise a protocol for measuring bacterial adhesion to HCE2 monolayers under physiological flow conditions.

3. To use the optimised BioFlux infection protocols to test novel antimicrobials, in particular CD9-derived tetraspanin peptides and unfractionated heparin (UFH).

7.3. Results

7.3.1. BioFlux 1000z experiments

7.3.1.1. Preliminary experiments using the BioFlux 1000z system demonstrated biofilm formation by PAO1-GFP, which was increased in the presence of HCE2 monolayers.

HCE2 monolayers were infected with PAO1-GFP using the preliminary BioFlux infection protocol developed by Dr Mahendra Raut and progression of infection was monitored over 24 hrs using time-lapse microscopy (**Figure 7-4**). HCE2 monolayers were clearly depicted by brightfield microscopy (**Figure 7-4A**) and at 0 hrs, a healthy cell monolayer was observed. Small numbers of rounded cells were visible, which were indicative of cell death and/or cell detachment but the majority of cells possessed normal HCE2 morphology. The appearance of HCE2 monolayers remained relatively unchanged until 6 to 8 hrs post-infection, when large clusters of rounded HCE2 cells began to form. By 9 hrs post-infection the HCE2 monolayer had completely disintegrated and only rounded, dead cells were observed. Between 9 and 24 hrs, remnants of the HCE2 monolayer were no longer visible and HCE2 cells were replaced by large bacterial aggregates. Although later timepoints cannot be used to simulate bacterial keratitis they remain physiologically relevant as they show PAO1-GFP is capable of forming biofilms under flow conditions. PAO1-GFP was visualised using fluorescence microscopy (**Figure 7-4B**). However, autofluorescence contributed to high levels of background fluorescence at early time points. Autofluorescence was proposed to originate from the cell culture medium (KSFM) and/or HCE2 cells and as a result, it was difficult to distinguish GFP-tagged bacteria until around 8 hrs post-infection. By 10 hrs, multiple PAO1-GFP microcolonies were observed and by 15 hrs post-infection, many of these large bacterial clusters had begun to merge together. Between 15 and 24 hrs post-infection, thick bacterial lawns, proposed to represent biofilm populations, were formed.

In **Figure 7-5**, fluorescence microscopy images have been studied in more detail to trace the origin of bacterial populations that were visible at 11 hrs post-infection. Time lapse microscopy images remained relatively similar between 0 and 7 hrs post infection and so only images from 0, 7, 8, 9, 10

and 11 hrs post-infection have been included. Beyond 11 hrs post-infection, distinct bacterial populations were hard to distinguish. Many of the PAO1-GFP microcolonies present at the 11-hr time point corresponded to clear regions of fluorescence at all time points (e.g., population A, labelled in red). In contrast, other clusters of PAO1-GFP bacteria could be traced back to 7 or 8 hrs post-infection but were not clearly visible at the start of the infection (e.g., population B, labelled in yellow). Finally, some populations were not visible at the start of the infection but were clearly visible towards the end of the time lapse series (e.g., population C, labelled in blue). This suggests that some PAO1-GFP microcolonies were formed by adherent PAO1-GFP bacteria present at the start of the experiment, whereas other bacteria adhered to HCE2 monolayers at later infection timepoints, following the introduction of oscillatory flow.

The preliminary BioFlux infection protocol was also used to compare biofilm formation between channels containing HCE2 monolayers and empty microfluidic channels (**Figure 7-6**). The empty microfluidic channels were coated using the standard fibronectin coating medium, but contained no HCE2 cells. Fluorescence microscopy revealed increased adhesion of PAO1-GFP to microfluidic channels in the presence of cells. Under cell conditions, GFP-tagged bacteria were clearly visible at the 8-hr time point and by 12 hrs, PAO1-GFP bacteria occupied the majority of the channel (**Figure 7-6A**). In contrast, no bacteria were visible at 8 hrs under the no cell conditions and by 12 hrs, only small numbers of individual microcolonies were observed (**Figure 7-6B**). This suggests PAO1-GFP preferentially binds to HCE2 monolayers over abiotic surfaces.

(A)

(B)
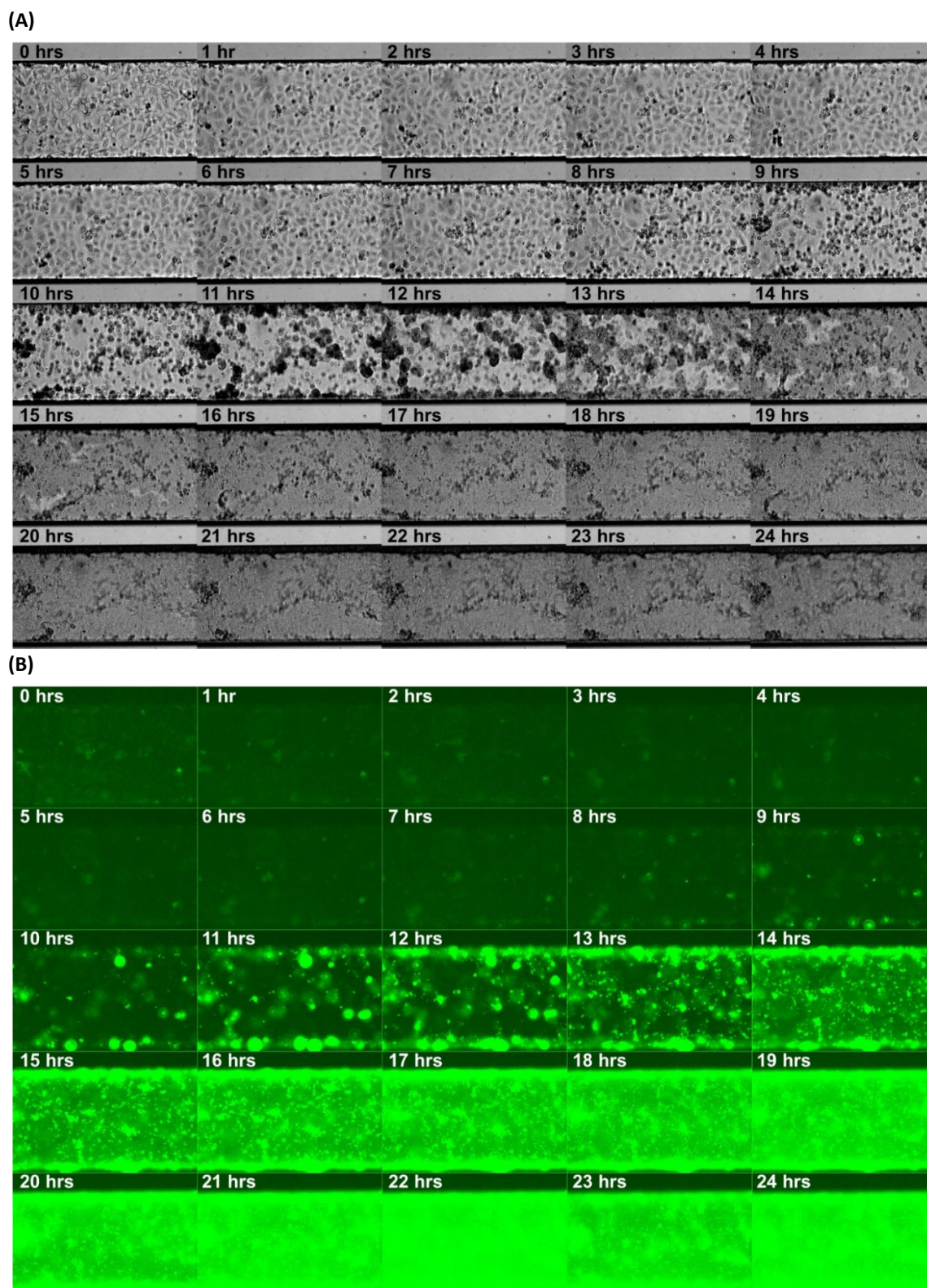
Figure 7-4. Time lapse microscopy images following 24 hr infection of HCE2 monolayers with PAO1-GFP using the preliminary infection protocol.

(A) Brightfield (B) GFP fluorescence. HCE2 monolayers were infected with PAO1-GFP using the preliminary BioFlux infection protocol. Images were collected every 15 minutes at 20x magnification, using brightfield and fluorescence microscopy. The BioFlux 1000z system was used throughout. Images collected at each 1 hr time point (from 0 to 24 hrs post-infection) are displayed.

215
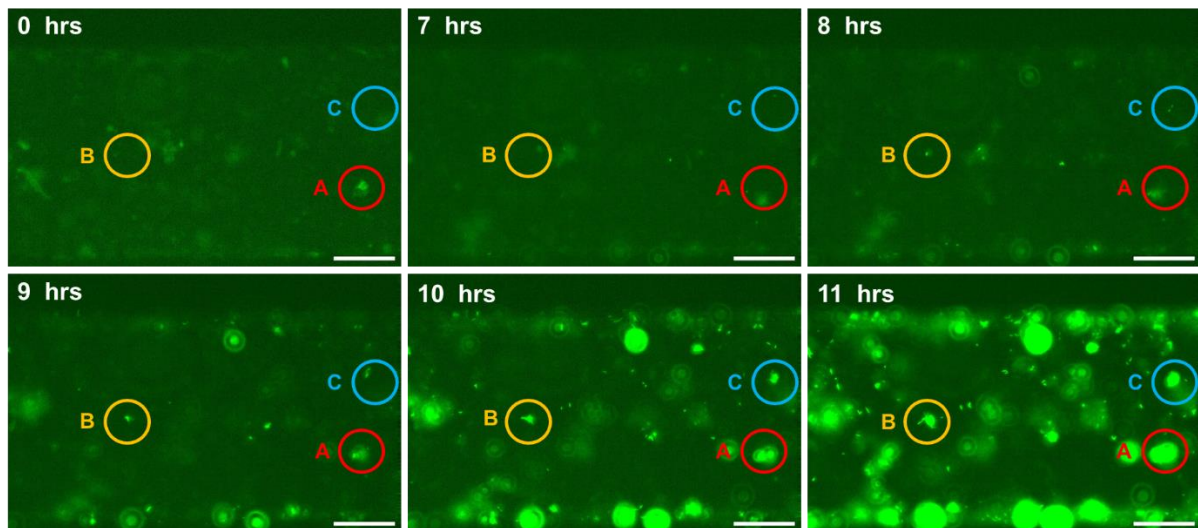
Figure 7-5. Monitoring the formation of PAO1-GFP microcolonies on infected HCE2 monolayers.
Fluorescence microscopy images collected during infection of HCE2 monolayers were studied to trace the origin of PAO1-GFP bacteria visible at 11 hrs post-infection. Images collected at 0, 7, 8, 9, 10 and 11 hrs post-infection are shown. 'A' (red), 'B' (yellow) and 'C' (blue) represent distinct bacterial populations. Scale bars represent 100 µm.
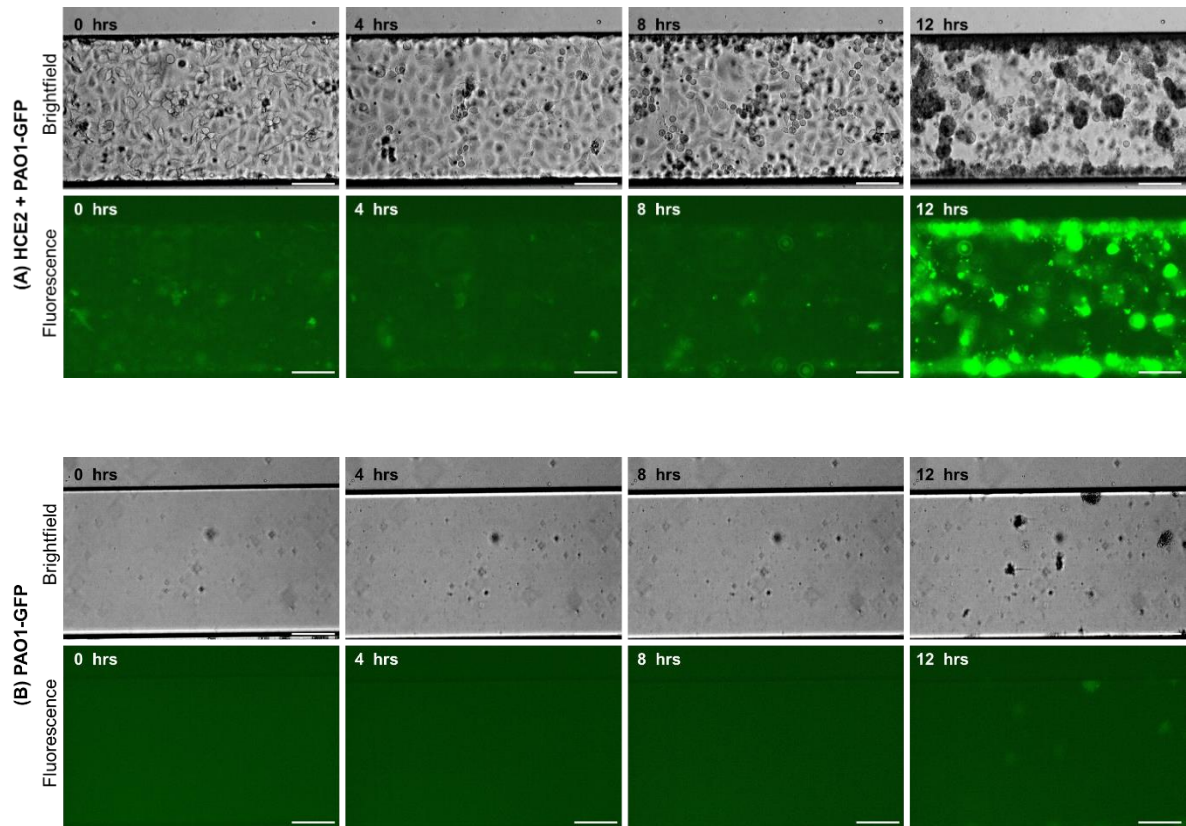
Figure 7-6. Time lapse microscopy images showing the accumulation of PAO1-GFP in the presence or absence of HCE2 monolayers, using the preliminary infection protocol.

(A) HCE2 + PAO1-GFP (B) PAO1-GFP. Microfluidic channels were seeded with HCE2 cells or KSFM only (no cell control) and then infected with PAO1-GFP using the preliminary BioFlux infection protocol. Images were collected every 15 minutes post-infection, using brightfield and fluorescence microscopy at 20x magnification. The BioFlux 1000z system was used throughout. Images collected at 0, 4, 8 and 12 hrs post-infection are displayed above. The same brightness and contrast settings have been applied to all GFP fluorescence images. Scale bars represent 100 µm.

7.3.2. BioFlux 200 experiments

7.3.2.1. Use of the BioFlux 200 system identified numerous problems with the preliminary BioFlux infection protocol.

The preliminary BioFlux infection protocol, which was designed by Dr Mahendra Raut (CBE) using the BioFlux 1000z system, was carried out using the BioFlux 200 system. My original plan was to perform identical repeats of the BioFlux 1000z experiments, using the advanced imaging capabilities of the Nikon Ti-E microscope, as compared to the BioFlux 1000z system, it was much easier to visualise individual bacteria using the BioFlux 200 microscope. Previously high levels of background fluorescence were dramatically reduced and the Perfect Focus System prevented time lapse images from moving out of focus. This was highly advantageous for data collection but it also led to the identification of multiple problems with the preliminary BioFlux infection protocol.

1. **Insufficient inoculation period**

The improved imaging capabilities of the Nikon Ti-E microscope allowed me to track the movement of individual bacteria during bacterial inoculation. As part of the preliminary BioFlux infection protocol, PAO1-GFP bacteria were supplied via the outlet well. The route between the outlet well and the BioFlux viewing window consisted of a short region of straight channel (positions 1 and 2), followed by a single bend in the channel (position 3), followed by entrance into the BioFlux viewing window (position 4) (**Figure 7-7A**). The preliminary BioFlux infection protocol used continuous flow at 1 dyn/cm^2, for approximately 3 seconds, to introduce PAO1-GFP bacteria into the BioFlux viewing window and during initial experiments, these inoculation conditions were assumed to be sufficient. However, when this protocol was repeated using the BioFlux 200 system, fluorescence microscopy revealed that whilst PAO1-GFP bacteria were reaching positions 1 and 2, no bacteria were visible at positions 3 or 4 of the channel (**Figure 7-7B**). The BioFlux plates were then incubated under oscillatory flow conditions and positions 1 and 4 were visualised by fluorescence microscopy for 2 hrs (**Figure 7-7C**). For position 1, bacterial numbers steadily increased throughout the experiment but PAO1-GFP was not observed at position 4 during any of the time points. This confirmed my initial observation, that use of inoculation conditions described in the preliminary infection protocol did not allow PAO1-GFP bacteria to reach the BioFlux viewing windows. This raised additional questions, as large clusters of GFP-tagged bacteria were clearly visible in the BioFlux 1000z experiments, albeit at much later time points (**Figure 7-4B**). Therefore, it was hypothesised that the PAO1-GFP bacterial colonies observed in these experiments were not formed from single, adherent bacteria present at the start of the experiment, but that these bacteria entered the channels at later time points due to oscillatory flow and the presence of leftover inoculum in the outlet wells.

2. Contamination from outlet wells

Support for this hypothesis was provided by visualisation of outlet wells using fluorescence microscopy (**Figure 7-8**). In the preliminary BioFlux infection protocol, the bacterial inoculum was added to outlet wells and any leftover inoculum was removed following a 1 hr static incubation period. The first image shows the appearance of an outlet well immediately after the leftover inoculum was removed (**Figure 7-8A**) and in the second image, the same outlet well was visualised following a PBS wash step (which was not included in the original protocol) (**Figure 7-8B**). PAO1-GFP bacteria were clearly visible in both images and although bacterial numbers were reduced following the PBS wash step, large numbers of PAO1-GFP bacteria remained. Therefore, it seems plausible that the PAO1-GFP bacteria visualised during BioFlux 1000z experiments may have been introduced from outlet wells at later time points. Based on these findings, the use of oscillatory flow was replaced with unidirectional, pulsatile flow and this was initiated in the opposite direction to bacterial inoculation. This was designed to prevent bacteria that had multiplied in the outlet well during the experiment, from entering the channel at later time points.

3. Variations in the initial bacterial inoculum due to HCE2 monolayers

The findings presented in **Figure 7-7** were used to optimise a new infection protocol. Multiple inoculation conditions were trialled and during these stages, an additional problem with the preliminary BioFlux infection protocol was identified. Large variations in bacterial numbers were observed at the 0-hr time point, between adjacent microfluidic channels, despite the use of identical inoculation conditions (**Figure 7-9**). It was hypothesised that variation in the initial bacterial inoculum may be linked to differences in the HCE2 monolayer between channels. Brightfield microscopy images showed the formation of HCE2 monolayers between the BioFlux viewing windows and outlet wells (**Figure 7-7B**, **Figure 7-9**). Therefore, PAO1-GFP bacteria were required to travel over HCE2 monolayers in order to reach the BioFlux viewing region. Differences in the 3D architecture of HCE2 monolayers may have altered the rate of bacterial passage between channels, potentially explaining differences in the size of the initial bacterial inoculum between replicates. To reduce the variation caused by HCE2 monolayers, bacteria were introduced via inlet wells in future experiments. Since HCE2 cells were always seeded via the outlet wells, bacteria introduced via the inlet wells were not expected to encounter HCE2 cells before reaching the BioFlux viewing region.

4. Problems with gravity flow

One final problem with the preliminary BioFlux infection protocol that was identified using the BioFlux 200 system, was the occurrence of gravity flow. Gravity flow refers to the uncontrolled movement of fluid, caused by differences in media volume between the inlet and outlet wells. This was not

accounted for in early experiments but use of the Nikon Ti-E microscope allowed me to visualise the effects of gravity flow and PAO1-GFP bacteria were observed travelling towards the BioFlux viewing window before the initiation of controlled flow. This was a particular problem if bacteria were inoculated via the outlet wells as the route to the BioFlux viewing window was relatively short. Therefore, in the optimised protocol, identical volumes of media were added to inlet and outlet wells to eliminate gravity flow.
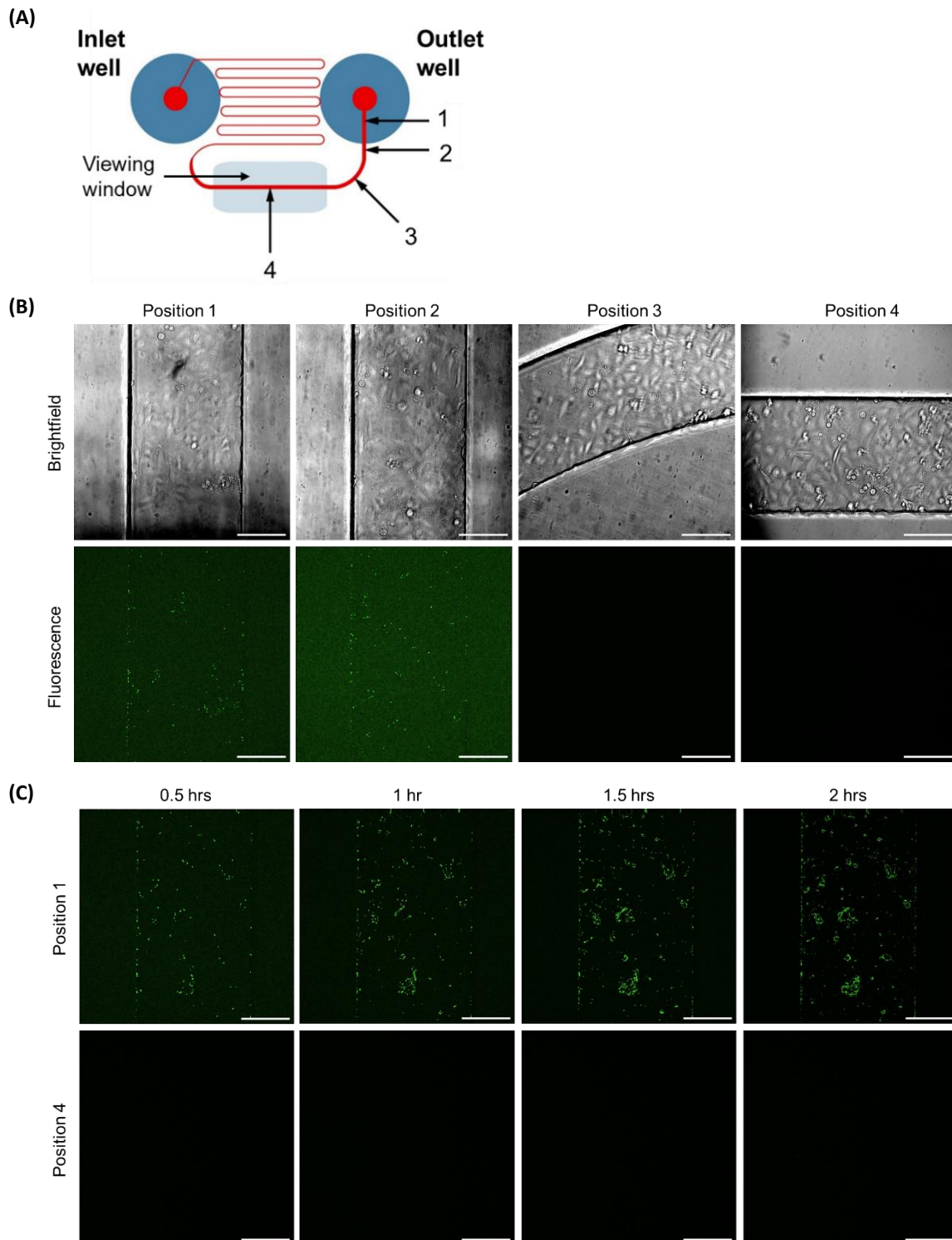
Figure 7-7. Problems with the original bacterial inoculation conditions.
The preliminary BioFlux infection protocol was carried out using the BioFlux 200 system. All microfluidic channels were seeded with HCE2 cells and HCE2 monolayers were infected using PAO1-GFP. **(A) Positions within the BioFlux channel (B) Different channel positions immediately after bacterial inoculation.** Four channel positions were visualised at 0 hrs post-infection, using brightfield and fluorescence microscopy. **(C) Channel positions 1 and 4 at 0.5, 1, 1.5 and 2 hrs post infection.** Infection progression was monitored at position 1 and 4 using fluorescence microscopy. The same brightness and contrast settings have been applied to all fluorescence images in the same figure. Scale bars represent 100 μm.

221
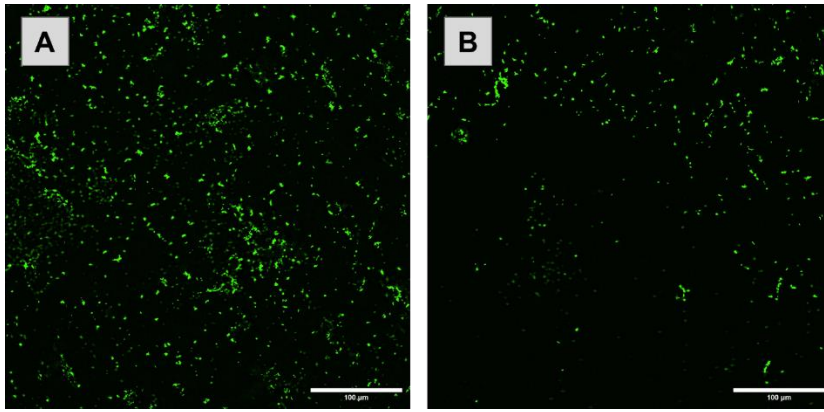
Figure 7-8. Leftover PAO1-GFP bacteria in outlet well.
(A) Before PBS wash (B) After PBS wash. HCE2 monolayers were infected with PAO1-GFP using the preliminary BioFlux infection protocol. Following the 1hr static incubation period, the leftover inoculum was removed and the outlet well was visualised by fluorescence microscopy. Images were collected before and after a PBS wash step. Scale bars represent 100 µm.
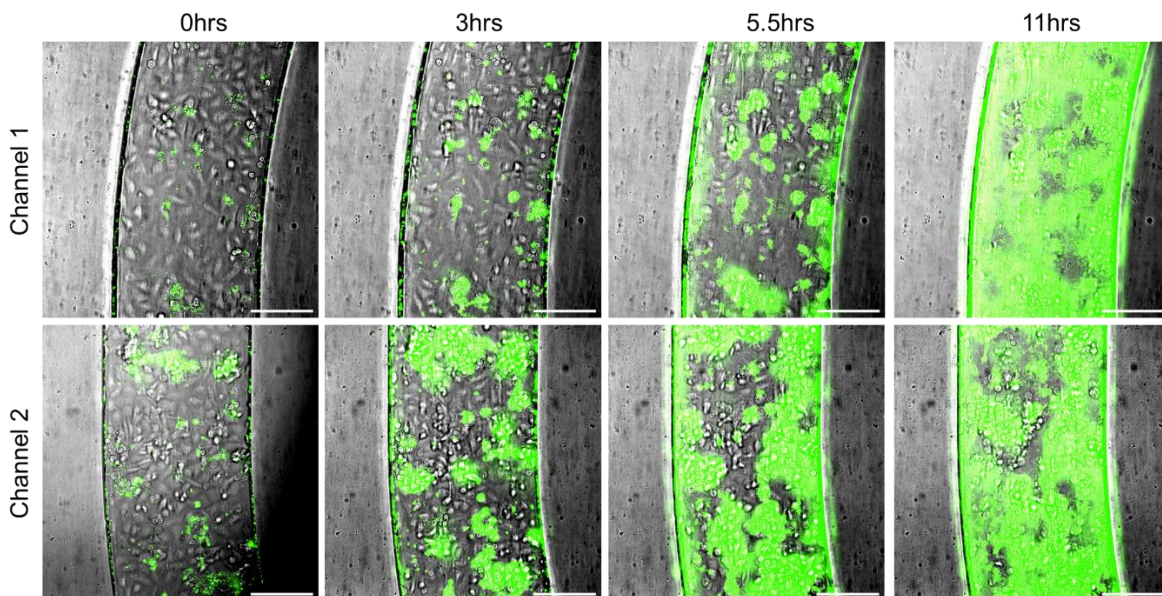
Figure 7-9. Variations in the size of the bacterial inoculum between adjacent BioFlux channels.
Various infection conditions were trialled to optimise the BioFlux infection protocol. In these images, HCE2 monolayers were infected with PAO1-GFP at an increased OD of 0.1-0.12, via the outlet wells. Bacteria were introduced into channels using continuous flow at 0.11 dyn/cm^2, for 4 minutes and then BioFlux plates were incubated under static conditions for 1 hr. After static incubation, infected HCE2 monolayers were incubated for a further 11 hrs under 0.11 dyn/cm^2, pulsatile flow conditions. Progression of infection was visualised using brightfield and fluorescence microscopy. The inoculation conditions used in this experiment did not allow enough bacteria to reach the BioFlux viewing windows and therefore microscopy images were collected between the outlet well and the viewing window, just before the bend in the channel. Merged images from 0, 3, 5.5 and 11 hrs post-infection are displayed. Rows represent adjacent microfluidic channels which were infected using the same bacterial inoculum and infection conditions. Scale bars represent 100 µm.

7.3.2.2. The BioFlux microfluidic system can be used to study the formation of bacterial microcolonies under pulsatile flow conditions.

Following optimisation of inoculation conditions and other changes to the protocol described in **section 7.3.2.1**, a new BioFlux infection protocol was developed using the BioFlux 200 system. This protocol included an 8-hr infection period using pulsatile flow conditions and time lapse microscopy was used to observe microcolony formation on HCE2 monolayers (**Figure 7-10**). A combination of brightfield and fluorescence microscopy were used to visualise HCE2 monolayers and GFP-tagged bacteria, respectively, and images collected at the 0-hr time point confirmed the presence of PAO1-GFP bacteria prior to the introduction of pulsatile flow (**Figure 7-10A**). Approximately 10 individual PAO1-GFP bacteria were visualised by fluorescence microscopy at 0 hrs and the corresponding brightfield image showed a confluent monolayer of HCE2 cells. Merged microscopy images were used to depict progression of infection over 8 hrs (**Figure 7-10B**). PAO1-GFP bacteria were difficult to distinguish between 0 and 2 hrs post-infection, but by 3 hrs post-infection, small microcolonies had begun to form. These microcolonies continued to increase in size throughout the experiment and by 6 hrs post-infection, neighbouring microcolonies had begun to merge together. The spatial location of most microcolonies could be linked to an individual bacterium present at the 0-hr time point. This indicates that microcolonies were formed by the proliferation of existing PAO1-GFP, rather than the arrival of new, preformed clusters of bacteria. In some instances, microcolonies were observed at new positions within the channel but this may have been caused by detachment and reattachment of bacteria from the original population. Visual inspection of HCE2 cells showed that HCE2 monolayers remained largely intact between 0 and 5 hrs post-infection. However, numbers of rounded, dead cells steeply increased after the 3-hr time point and complete destruction of the HCE2 monolayer was observed at the 6-hr time point.

7.3.2.3. GFP-tagged strains of SH1000 and PAO1 demonstrate loss of GFP fluorescence but ubiquitous expression can be achieved by antibiotic selection.

The optimised microcolony formation protocol was used to study infection of HCE2 monolayers with PAO1-GFP and both GFP-tagged and non-fluorescent bacteria were observed (**Figure 7-11**). Microscopy images of individual bacteria showed fluorescent and non-fluorescent bacteria were almost identical in size and shape (**Figure 7-11A**) and time lapse images of microcolonies expressing GFP appeared to show loss of fluorescence over time (**Figure 7-11B**). Therefore, it was hypothesised that the GFP-tagged PAO1 strain was losing its GFP expression plasmid and this hypothesis was tested by flow cytometry (**Figure 7-12**). Flow cytometric analysis of PAO1-GFP bacteria used in BioFlux experiments (**Figure 7-12A**) revealed two distinct populations. These populations were highly similar

223

in terms of their granularity (as measured by side scatter (SSC)), but only one of these populations expressed GFP (as measured by fluorescence with the 530 nm laser). A fluorescence histogram showed that the non-GFP expressing population was around 4-fold larger than the population that retained GFP fluorescence and therefore loss of the plasmid was positively selected for in the bacterial population. To try and restore ubiquitous GFP expression, PAO1-GFP bacteria were cultured on LB agar containing chloramphenicol as the GFP expression plasmid contains a chloramphenicol resistance marker. Analysis of this bacteria provided a single peak on a fluorescence histogram and the vast majority of bacterial cells expressed high levels of GFP (**Figure 7-12B**). Following on from this study, GFP expression in the SH1000-GFP strain was also investigated (**Figure 7-13**). Similarly to PAO1-GFP, two populations were observed when SH1000-GFP was cultured on LB agar and analysed by flow cytometry (**Figure 7-13A**). However, the non-GFP expressing population was much smaller than the population expressing GFP. The SH1000-GFP strain also contains a chloramphenicol resistance marker and so a subset of bacteria were cultured on chloramphenicol-containg agar plates, prior to flow cytometric analysis (**Figure 7-13B**). Flow cytometry provided a single peak on the fluorescence histogram, although there was large variation in the extent of GFP expression compared to PAO1-GFP.

(A)

(B)
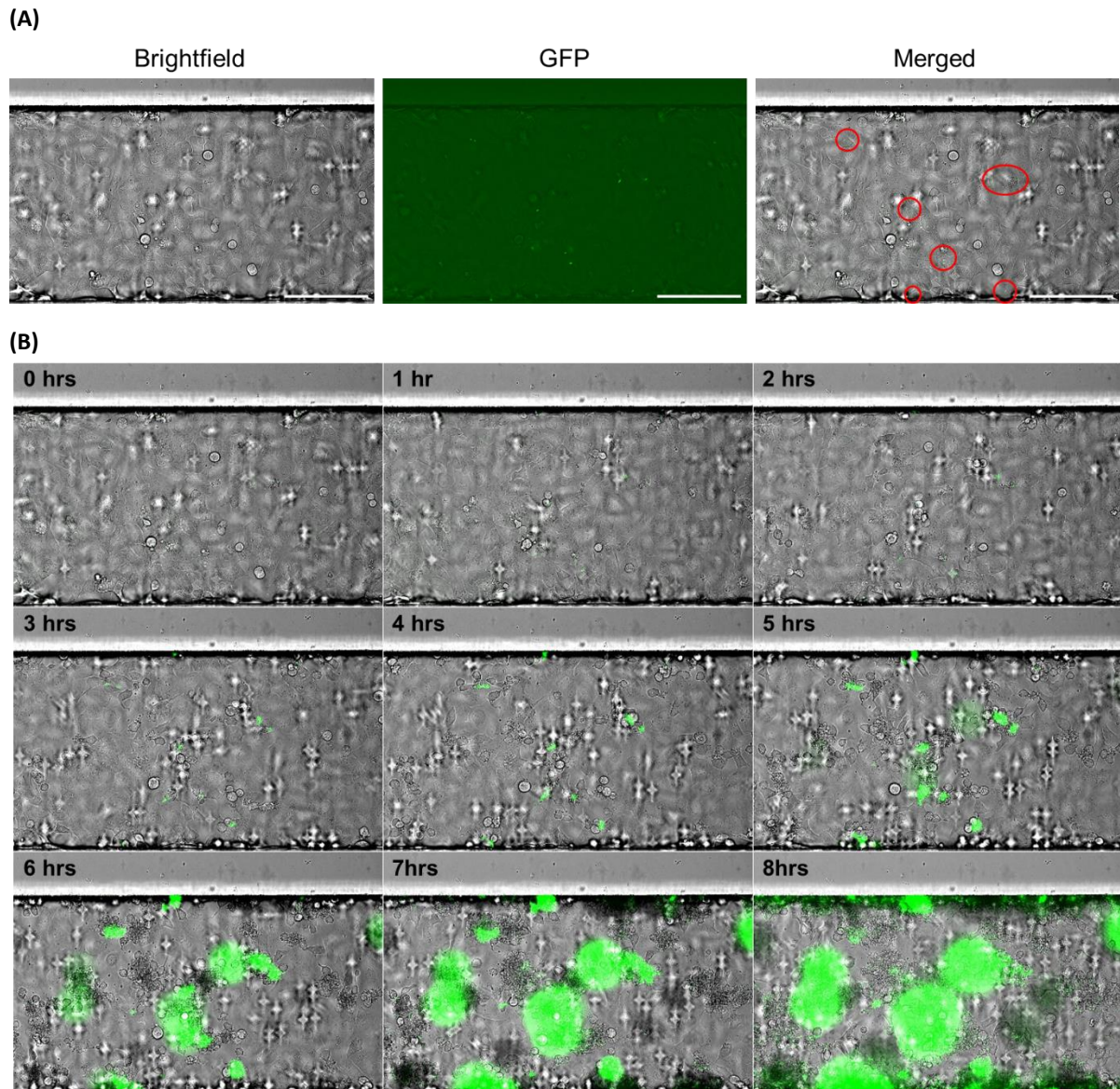
Figure 7-10. Time lapse microscopy images showing infection of HCE2 monolayers with PAO1-GFP using the optimised microcolony formation protocol.
HCE2 monolayers were infected using the microcolony formation protocol and progression of infection was monitored by brightfield and fluorescence microscopy. The BioFlux 200 system was used throughout and images were collected every 15 minutes at 20x magnification. **(A) Brightfield, fluorescence and merged microscopy images showing 0 hrs post-infection.** For the merged image, bacteria present at 0 hrs are circled in red. Scale bars represent 100 µm. **(B) Merged images of 0-8 hrs post-infection.** Each image represents an additional hour post-infection.

(A)

(B)
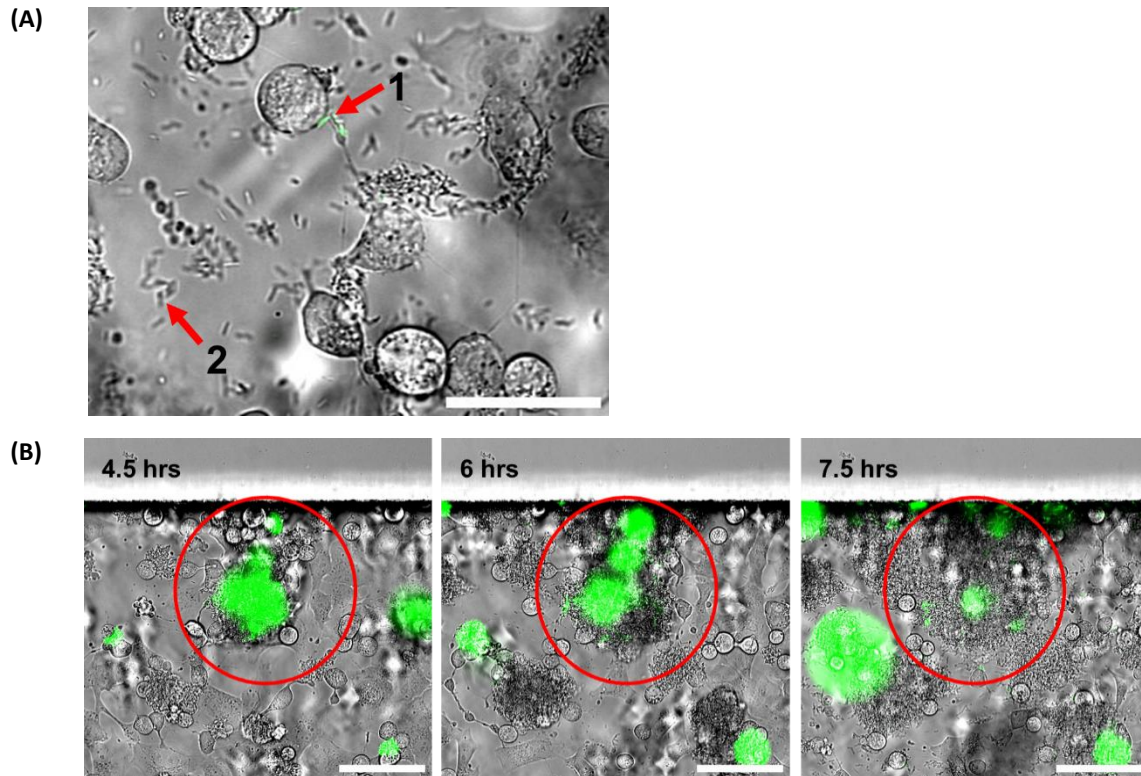
Figure 7-11. Observed loss of fluorescence in the _P. aeruginosa_ PAO1-GFP strain.
Time-lapse microscopy images collected during the microcolony formation experiments were studied for loss of GFP fluorescence. **(A) Individual bacteria.** Image collected at 7.25 hrs post-infection. Arrows have been used to label individual PAO1-GFP bacteria: (1) Retains GFP fluorescence. (2) No GFP expression. Scale bar represents 25 μm**. (B) Microcolonies.** Merged microscopy images of infected HCE2 monolayers at 4.5, 6 and 7.5 hrs post-infection. Scale bars represent 50 μm.

(A)

(B)
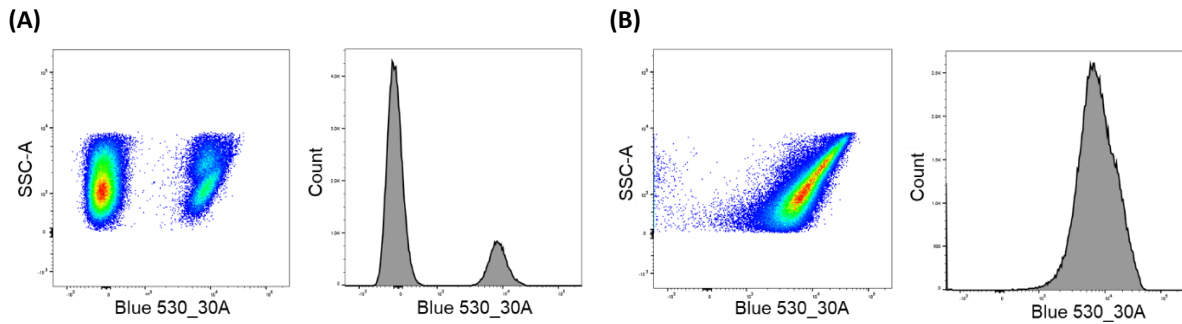
Figure 7-12. PAO1-GFP fluorescence under different growth conditions.
(A) No antibiotics (B) 50 µg/ml chloramphenicol. PAO1-GFP bacteria were plated onto LB agar containing no antibiotics (**A**) or 50 µg/ml chloramphenicol (**B**) and incubated overnight. One or two colonies were selected and transferred to LB (containing no antibiotics) for overnight culture. Bacteria were pelleted, washed and fixed using 4% PFA. GFP fluorescence (Blue 530_30A) was detected by flow cytometry.

(A)

(B)
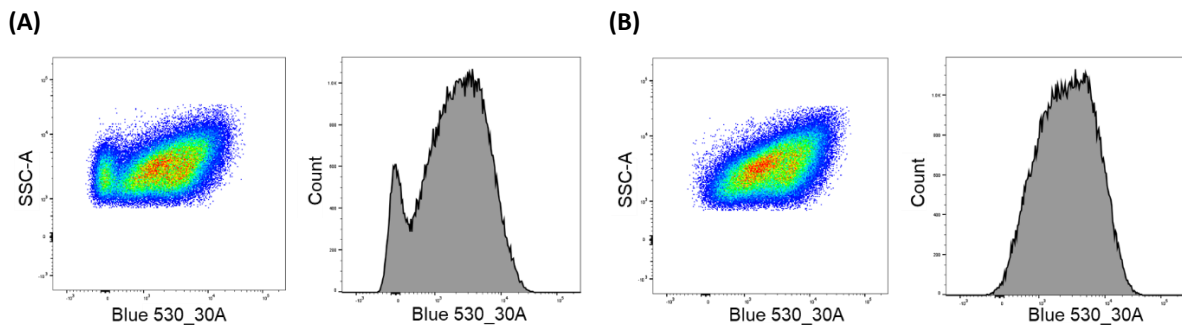
Figure 7-13. SH1000-GFP fluorescence under different growth conditions. (A) No antibiotics (B) 10 µg/ml chloramphenicol.
SH1000-GFP bacteria were plated onto LB agar containing no antibiotics (**A**) or 10 µg/ml chloramphenicol (**B**) and incubated overnight. One or two colonies were selected and transferred to LB (containing no antibiotics) for overnight culture. Bacteria were pelleted, washed and fixed using 4% PFA. GFP fluorescence (Blue 530_30A) was detected by flow cytometry.

7.3.2.4 Bacterial adhesion of PAO1-GFP to HCE2 monolayers under continuous flow conditions is unaffected by pre-treatment of HCE2 monolayers with unfractionated heparin (UFH).

The BioFlux 200 system was used to measure PAO1-GFP adhesion to HCE2 monolayers under continuous flow conditions, following pre-treatment of cells with 10 U/ml unfractionated heparin (UFH) or medium only control. Bacterial adhesion was investigated between 0 and 2 hrs post-infection using time-lapse microscopy (**Figure 7-14**). Brightfield microscopy images revealed the presence of confluent HCE2 monolayers under both conditions and these monolayers remained intact at 2 hrs post-infection (**Figure 7-14A, B**). GFP fluorescence images showed bacterial adhesion to HCE2 monolayers and clusters of PAO1-GFP were visible as early as 30 minutes post-infection. PAO1-GFP bacteria also appeared to adhere to the walls of the microfluidic channels. As well as identifying adherent PAO1-GFP bacteria, non-adherent bacteria were visualised by fluorescence microscopy. Bacteria "in-flow" were easily identifiable as elongated dash shapes and in the optimised protocol, two fluorescence images were collected at each time-point to prevent non-adherent bacteria from being included in bacterial counts. Prior to quantitative analysis, the imageCalculator tool in ImageJ was used to combine paired fluorescence images. This effectively increased the fluorescence intensity of adherent bacteria (which were present in both images), as compared to non-adherent bacteria (only present in one image). Comparison of fluorescence images for UFH-treated and untreated HCE2 monolayers showed similar distribution of PAO1-GFP bacteria under both conditions and visual inspection of time lapse images suggested bacterial numbers were roughly equivalent (**Figure 7-14C**). Further support for this was provided by z-stacks collected at 2 hrs post-infection (**Figure 7-15**). Adjacent z-slices confirmed that the distribution of PAO1-GFP bacteria was highly similar for control (**Figure 7-15A**) and UFH-treated channels (**Figure 7-15B**) at all z-positions tested. Furthermore, visual inspection of maximum intensity z-stack projections revealed no difference between conditions (**Figure 7-15C** and **D**). Similarities in bacterial adhesion of PAO1-GFP to untreated and UFH-treated HCE2 monolayers was confirmed by quantitative analysis (**Figure 7-16**). Bacterial counts were plotted for each 15-minute time point between 0 and 2 hrs post-infection and the resulting plots were highly similar for untreated and UFH-treated cell monolayers (**Figure 7-16A**). Data presented in **Figure 7-16A** was used to perform Area Under the Curve (AUC) calculations and AUC values of 1101 ± 642 (no. bacteria × hrs) and 1166 ± 937 (no. bacteria × hrs) were reported for untreated and UFH-treated HCE2 monolayers, respectively. AUC values measure the accumulation of bacteria over 2 hrs, and in my datsets the units are number of bacteria × time. No significant difference in AUC values was observed between conditions (p= 0.9260, data not shown). Individual time points were then analysed in further detail. At 1 hr post-infection, bacterial counts were highly similar for control (544.6 ± 343.0) and UFH-

228

treated (592.4 ± 485.1) channels, with no significant difference between conditions (p= 0.8957) (**Figure 7-16B**). By 2 hrs post-infection, bacterial numbers had increased for both control (1127.0 ± 666.7) and UFH (1186.0 ± 966.3) conditions, but values remained highly similar (p= 0.9354) (**Figure 7-16C**). Subsequently, bacterial count data was normalised and UFH values were expressed as a percentage of the control condition (100%). At 1 hr post-infection, bacterial adhesion for UFH-treated cells, was calculated as 104.2% ± 27.1 (**Figure 7-16D**). This decreased to 98.0% ± 23.7 by 2 hrs post-infection (**Figure 7-16E**). No significant difference between conditions was observed at 1 hr (p= 0.7996) or 2 hrs (p= 0.8900) post infection (n=3, unpaired t-test).

(A)

(B)

(C)
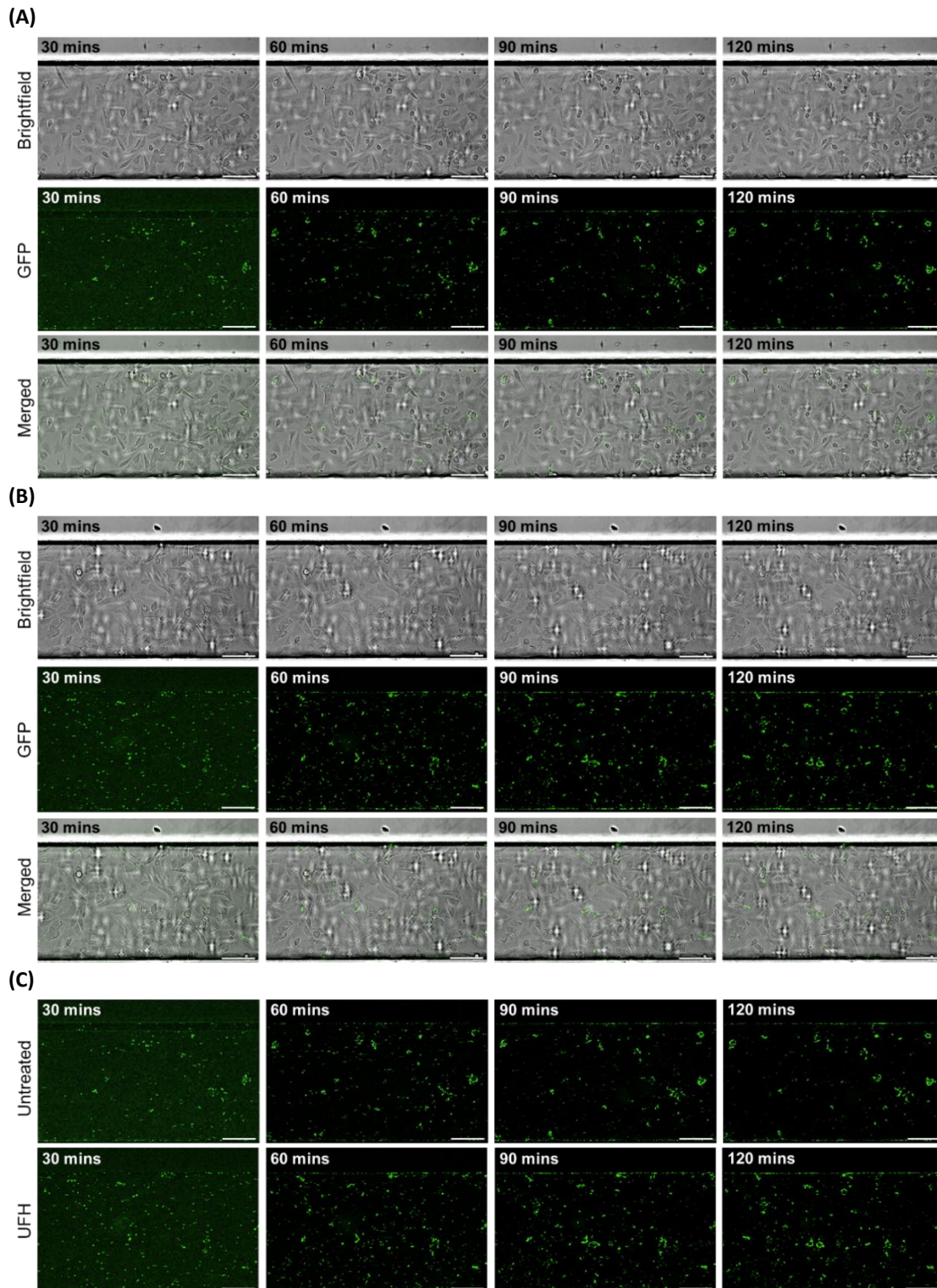
Figure 7-14. Bacterial adhesion of PAO1-GFP to HCE2 monolayers following pre-treatment with UFH or medium only control.
(A) Control (B) 10 U/ml UFH (C) Comparison of treatment conditions. HCE2 monolayers were pre-treated with 10 U/ml UFH or medium only control and infected with PAO1-GFP for 2 hrs under continuous flow conditions (0.2 dyn/cm^2). Images were collected at 20x magnification, every 15 minutes, using brightfield and fluorescence microscopy. Images collected at 30, 60, 90 and 120 mins post-infection are shown above. Scale bars represent 100 μm.

(A)

(B)

(C)

(D)
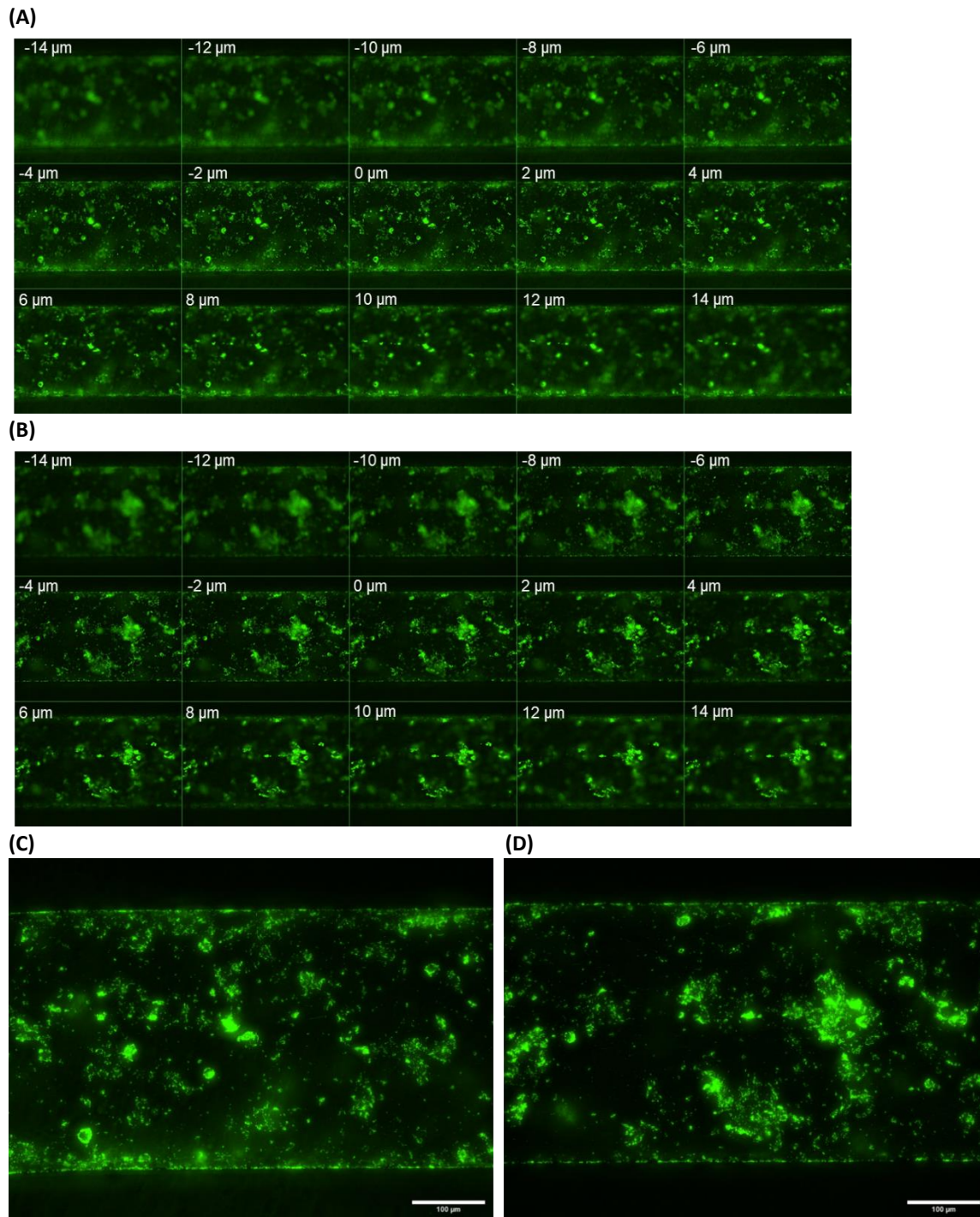
Figure 7-15. Z-stack images showing the distribution of PAO1-GFP in microfluidic channels following pre-treatment with UFH or medium only control.
Infected HCE2 monolayers were visualised using z-stacks at 2 hrs post-infection. 20x magnification and a step increment of 2 μm were used. **(A) Z-stack montage of untreated (control) cells (B) Z-stack montage of UFH-treated cells.** Adjacent z-slices spanning 30 μm are shown. Slices labelled 0 μm represent the z-axis where the majority of PAO1-GFP bacteria were in focus. Increasing positive values represent movement upwards through the channel and vice versa. The same brightness and contrast settings have been applied to all images. **(C) Maximum intensity z-stack projection for untreated (control) cells (D) Maximum intensity z-stack projection for UFH-treated cells.** The same brightness and contrast settings have been applied to both images. Scale bars represent 100 μm.

(A)

(B)

(C)

(D)

(E)
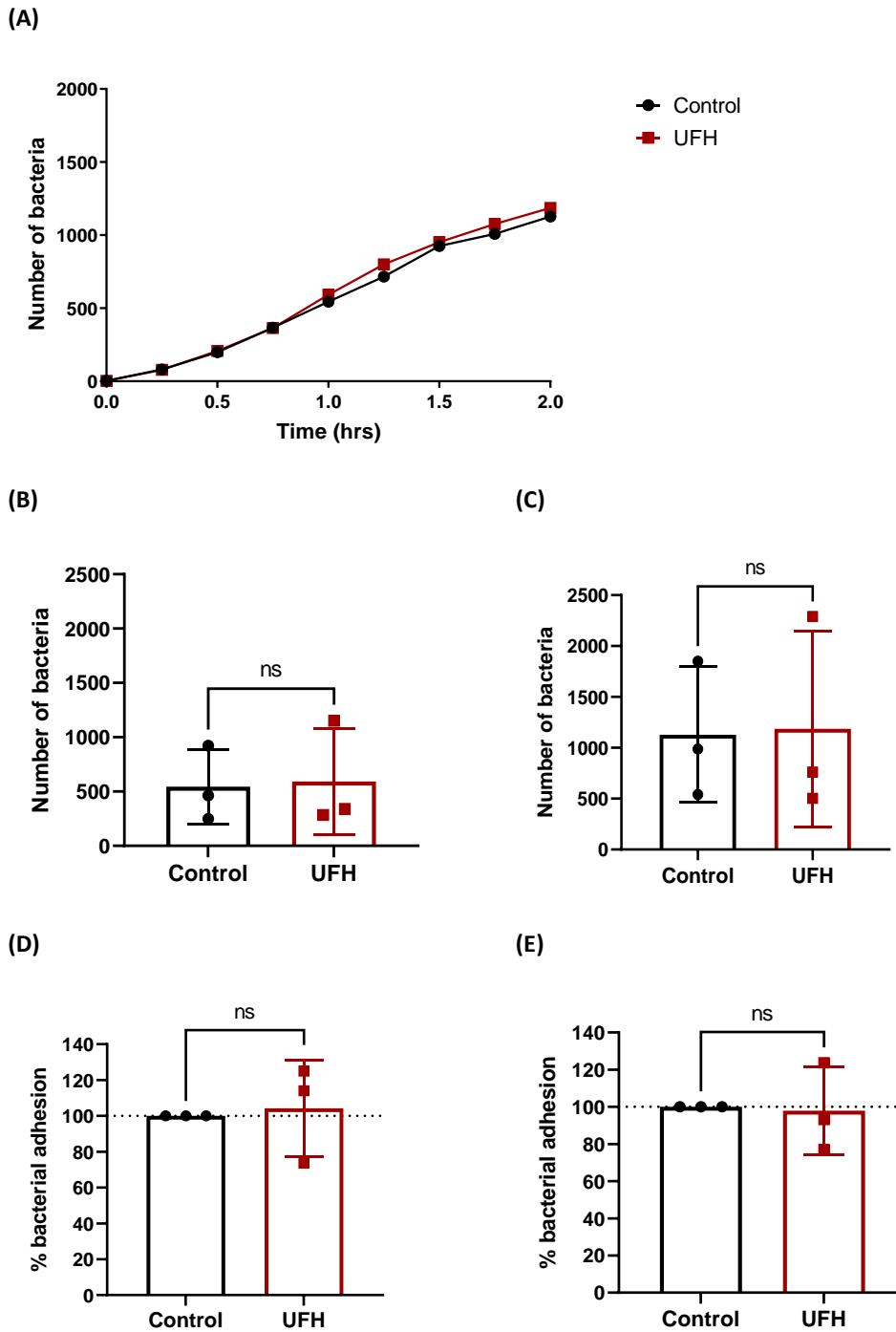
Figure 7-16. Quantification of adherent PAO1-GFP following pre-treatment of HCE2 monolayers with UFH or medium only control.

Fluorescence microscopy images from bacterial adhesion studies were processed in ImageJ and the Feature-Assisted Segmenter/Tracker (FAST) was used to enumerate PAO1-GFP across different frames and treatment conditions in MATLAB. For all time points and conditions, n=3. **(A) PAO1-GFP counts between 0 and 2 hrs post-infection.** Data represent mean values. **(B) PAO1-GFP counts at 1 hr post-infection. (C) PAO1-GFP counts at 2 hrs post-infection.** Data represent mean values ± SD. Data was analysed by unpaired t-test, ns= not significant (p > 0.05) **(D) % bacterial adhesion calculations at 1 hr post-infection (E) % bacterial adhesion calculations at 2 hrs post-infection.** Count data for the UFH condition has been expressed as a percentage of the untreated control. Data represent mean values ± SD. Data was analysed by unpaired t-test, ns= not significant (p > 0.05).

232

7.3.2.5. A significant reduction in bacterial adhesion of SH1000-GFP to HCE2 monolayers under continuous flow conditions, is observed following UFH pre-treatment.

The BioFlux 200 system was used to measure SH1000-GFP adhesion to HCE2 monolayers under continuous flow conditions, following pre-treatment of cells with 10 U/ml unfractionated heparin (UFH) or medium only control. Progression of infection was monitored by time lapse microscopy (**Figure 7-16**). Brightfield microscopy images revealed the presence of confluent HCE2 monolayers, which remained intact throughout the experiment (**Figure 7-17A** and **B**), as observed in earlier PAO1-GFP studies. Fluorescence microscopy revealed the presence of GFP-tagged SH1000 and bacterial adhesion to HCE2 monolayers was observed. However, SH1000-GFP did not adhere to the walls of the microfluidic channels as readily as PAO1-GFP. Both adherent and non-adherent bacteria were visible in fluorescence images and so these images were collected in duplicate, as described previously (**section 7.3.2.4**). Comparison of fluorescence images for UFH-treated and untreated HCE2 monolayers revealed dramatic differences in bacterial adhesion (**Figure 7-17C**). At 30, 60, 90 and 120 minutes post-infection, bacterial numbers were much greater under control conditions. The distribution of bacteria was also markedly different between conditions. Under control conditions, clusters of SH1000-GFP bacteria were visible from 60 minutes post-infection, whereas bacteria did not form visible clusters in the UFH condition. Further support for this was provided by z-stacks collected at 2 hrs post-infection (**Figure 7-18**). Z-stacks were used to visualise SH1000-GFP at multiple z-positions within the channel and visual inspection of these images suggested that bacterial numbers were consistently higher under control conditions (**Figure 7-18A** and **B**). Maximum intensity z-stack projections also revealed a large decrease in overall fluorescence intensity within microfluidic channels following UFH pre-treatment (**Figure 7-18C** and **D**). Phase microscopy was used to investigate bacterial adhesion at increased magnification and the anti-adhesion effects of UFH were demonstrated at low (OD 0.03-0.04) and high (OD 0.1-0.12) bacterial concentrations (**Figure 7-19**). Under both conditions, SH1000-GFP bacteria were visualised on the surface of HCE2 cells and large reductions in adherent bacteria was observed for UFH-treated monolayers. The pre-treatment of HCE2 monolayers with 10 U/ml UFH and its inhibitory effects on bacterial adhesion, were confirmed by quantitative analysis (**Figure 7-20**). Bacterial counts were plotted for each 15-minute time point between 0 and 2 hrs post-infection and large differences were observed for control and UFH conditions (**Figure 7-20A**). At 0.25 and 0.5 hrs post-infection, bacterial counts were highly similar for both conditions but counts began to diverge at 45 minutes post-infection. Between 0.75-2 hrs post-infection, there was a steep climb in bacterial counts for the control condition whereas counts only gradually increased for UFH-treated cells. Data presented in **Figure 7-20A** was used to perform area under the curve calculations and values of 1739 ± 440 (no. bacteria × hrs) and 840 ± 738 (no. bacteria

× hrs) were reported for untreated and UFH-treated HCE2 monolayers, respectively. However, there was no significant difference in AUC values between conditions (p= 0.1441, data not shown), due to large variation in biological replicates. Individual time points were then analysed in further detail. At 1 hr post-infection, bacterial counts were reduced for the UFH condition (395.2 ± 330.5), as compared to the untreated control (811.1 ± 369.5) but no significant difference was observed (p= 0.1444, n=4) (**Figure 7-20B**). By 2 hrs post-infection, bacterial counts were significantly reduced for UFH-treated cells (532.2 ± 438.2), as compared to the control condition (1568.0 ± 134.8) (p= 0.0173, n=3) (**Figure 7-20C**). To account for variation between experiments, count data was normalised and UFH values were expressed as a percentage of the control condition (100%). At 1 hr post-infection, % bacterial adhesion for UFH-treated cells was 44.9% ± 24.2 and bacterial adhesion was significantly reduced compared to the control condition (p= 0.0039, n=4) (**Figure 7-20D**). A significant reduction in % bacterial adhesion for UFH-treated cells was also observed at 2 hrs post-infection (35.0% ± 31.2) (p= 0.0226, n=3, unpaired t-test) (**Figure 7-20E**).

(A)

(B)

(C)
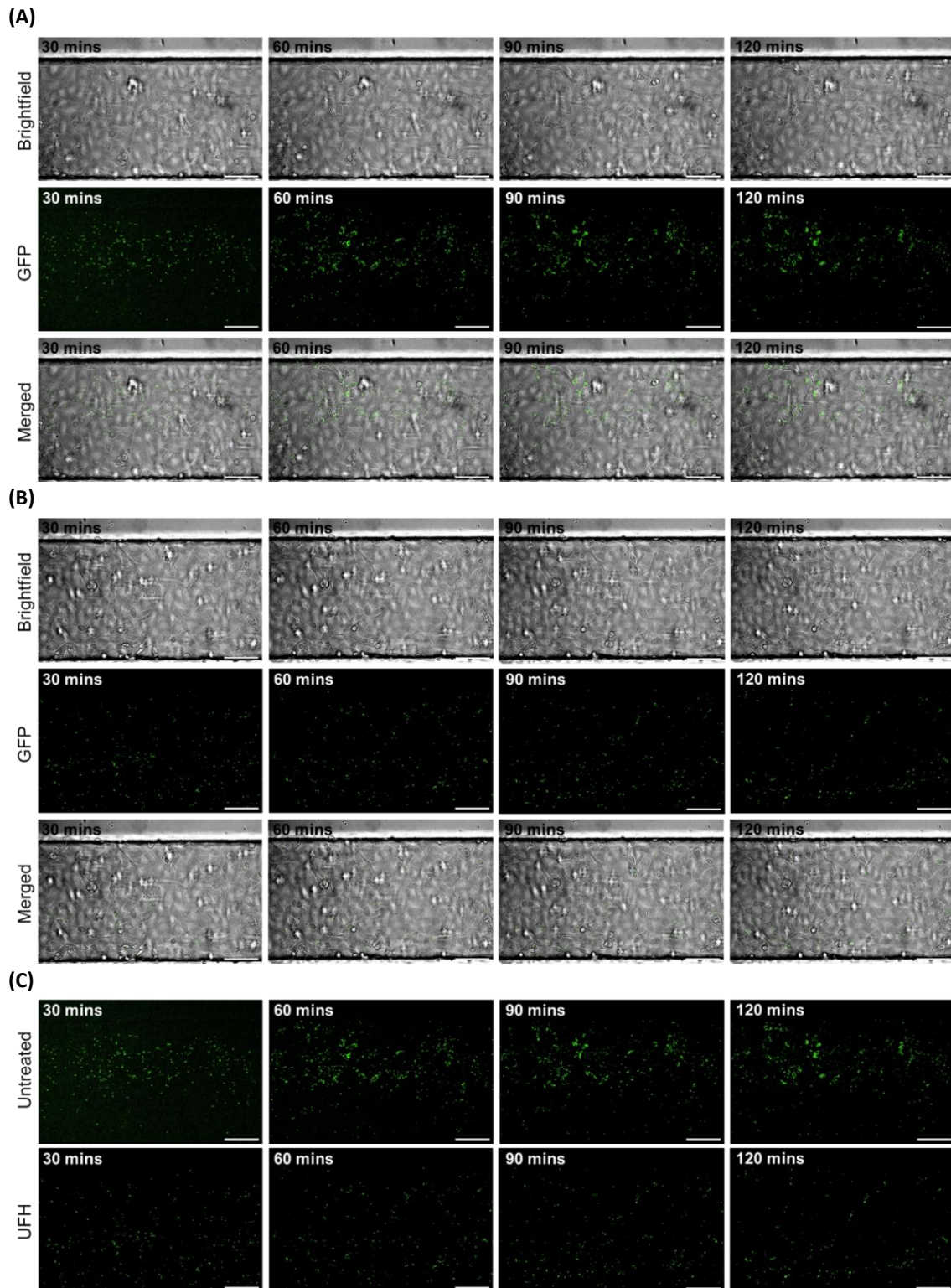
Figure 7-17. Bacterial adhesion of SH1000-GFP to HCE2 monolayers following pre-treatment with UFH or medium only control.
(A) Control (B) 10 U/ml UFH (C) Comparison of treatment conditions. HCE2 monolayers were pre-treated with 10 U/ml UFH or medium only control and infected with SH1000-GFP for 2 hrs under continuous flow conditions (0.2 dyn/cm^2). Images were collected at 20x magnification, every 15 minutes, using brightfield and fluorescence microscopy. Images collected at 30, 60, 90 and 120 mins post-infection are shown above. Scale bars represent 100 μm.

(A)

(B)

(C)

(D)
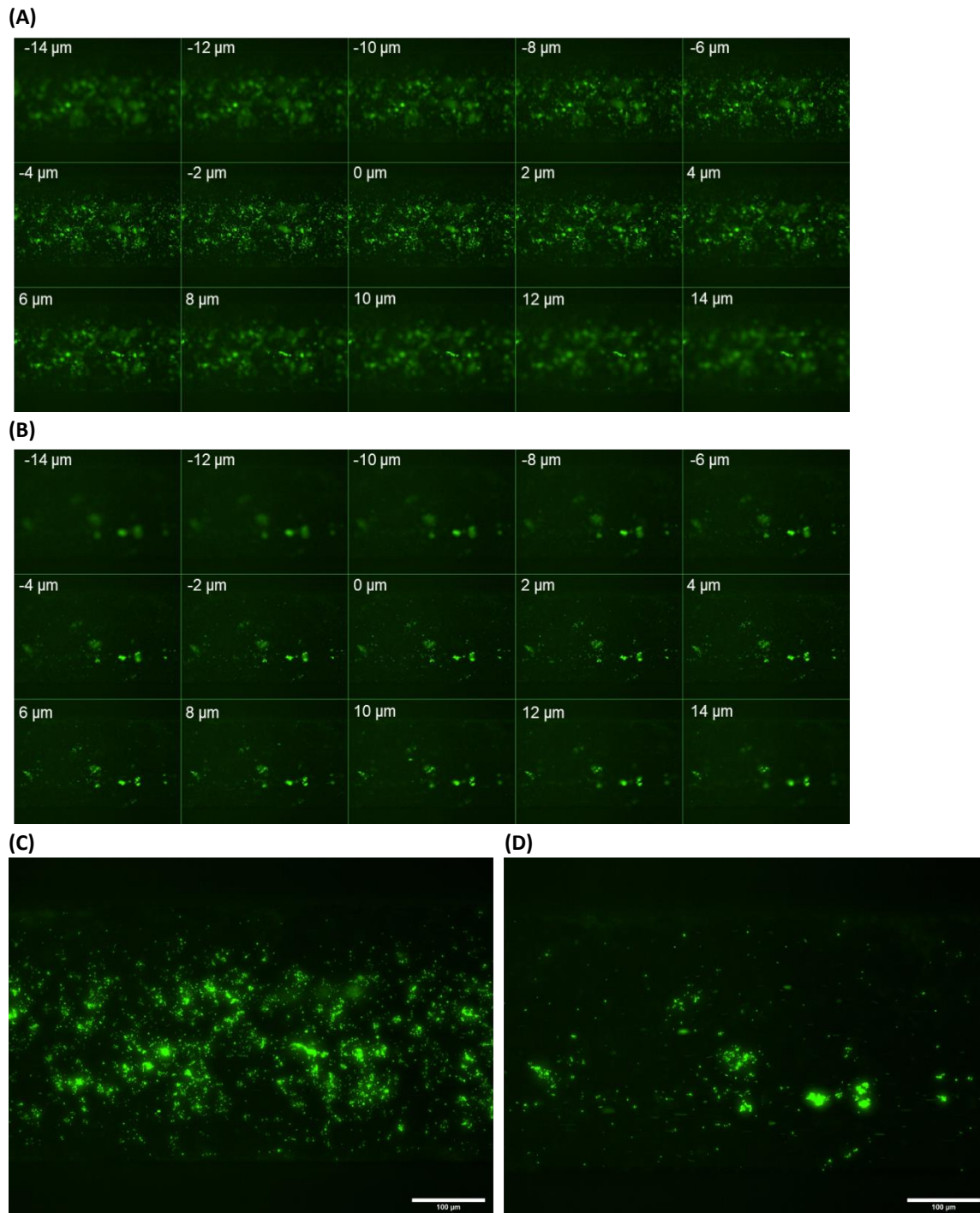
Figure 7-18. Z-stack images showing the distribution of SH1000-GFP in microfluidic channels following pre-treatment with UFH or medium only control.
Infected HCE2 monolayers were visualised using z-stacks at 2 hrs post-infection. 20x magnification and a step increment of 2 μm were used. **(A) Z-stack montage of untreated (control) cells (B) Z-stack montage of UFH-treated cells.** Adjacent z-slices spanning 30 μm are shown. Slices labelled 0 μm represent the z-axis where the majority of SH1000-GFP bacteria were in focus. Increasing positive values represent movement upwards through the channel and vice versa. The same brightness and contrast settings have been applied to all images. **(C) Maximum intensity z-stack projection for untreated (control) cells (D) Maximum intensity z-stack projection for UFH-treated cells.** The same brightness and contrast settings have been applied to both images. Scale bars represent 100 μm.
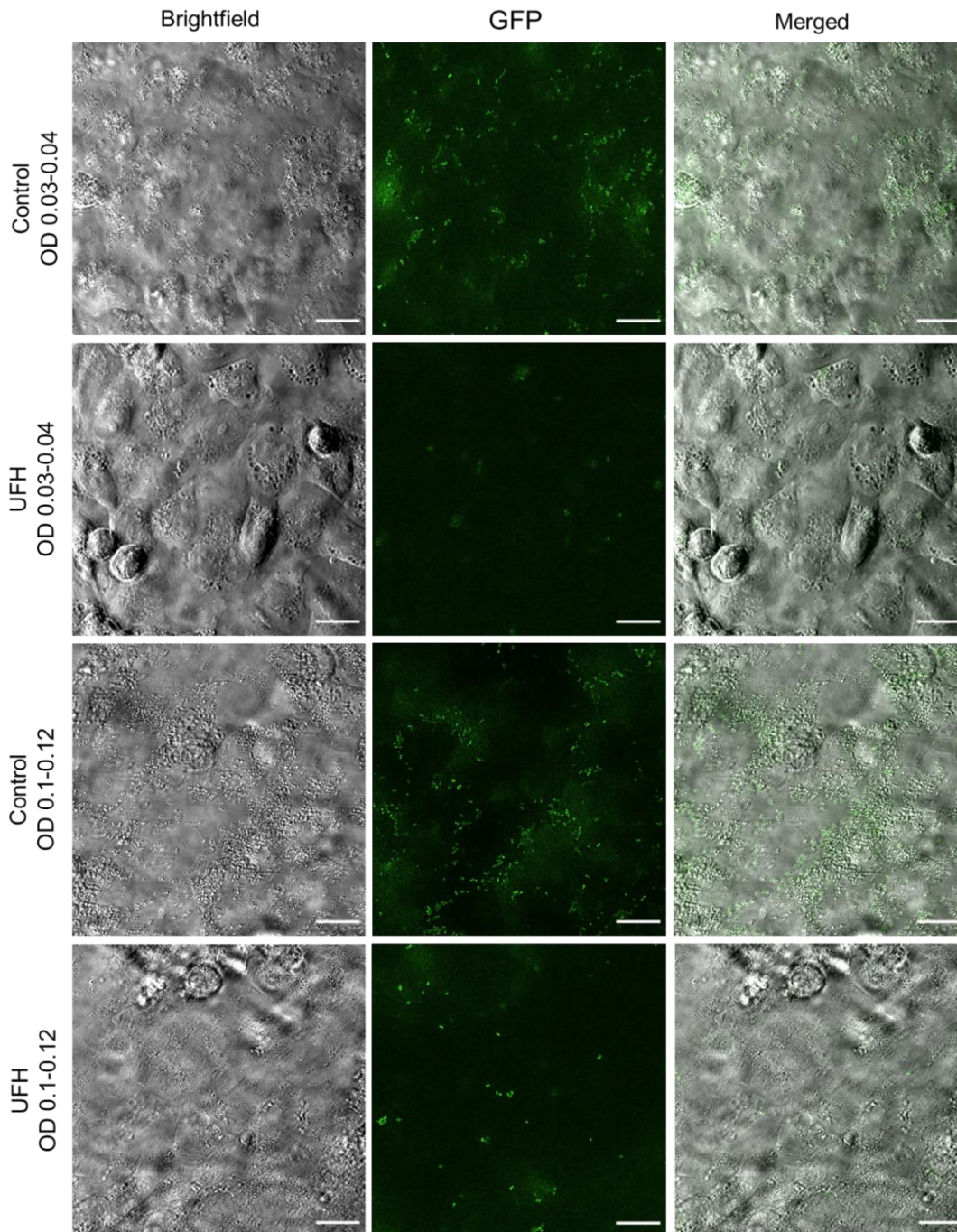
Figure 7-19. Phase microscopy images of infected HCE2 monolayers following pre-treatment with UFH or medium only control.
Infected HCE2 monolayers were visualised at 2 hrs post-infection by phase microscopy at 100x magnification. Two different bacterial inoculums were used, with OD600 values of 0.03-0.04 (standard OD) or 0.1-0.12. Different brightness and contrast settings have been applied to fluorescence images to maximise visibility. Scale bars represent 20 μm.
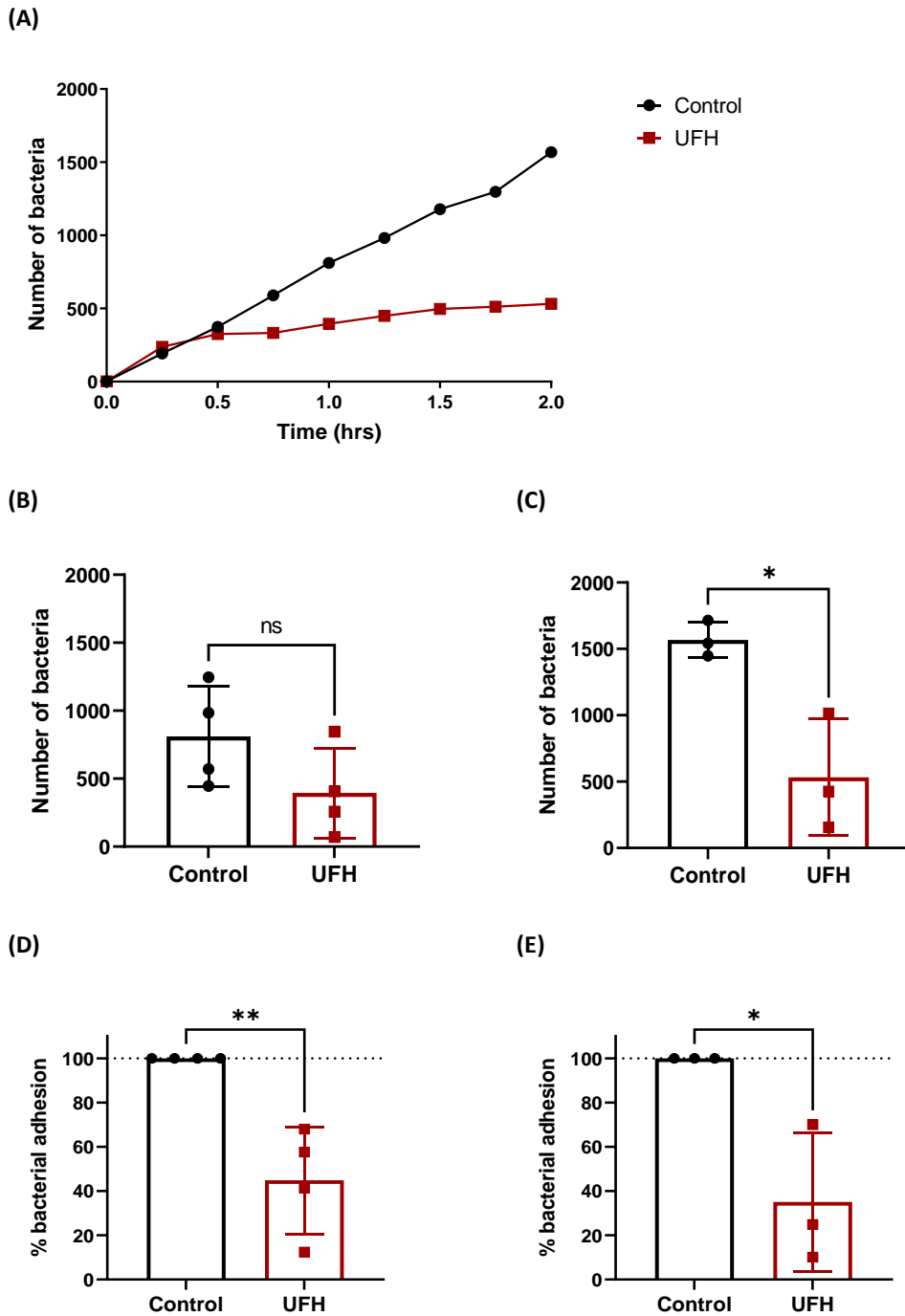
Figure 7-20. Quantification of adherent SH1000-GFP following pre-treatment of HCE2 monolayers with UFH or medium only control.

Fluorescence microscopy images from bacterial adhesion studies were processed in ImageJ and the Feature-Assisted Segmenter/Tracker (FAST) was used to enumerate SH1000-GFP across different frames and treatment conditions in MATLAB. **(A) SH1000-GFP counts between 0 and 2 hrs post-infection.** Data represent mean values, n=3 to 4. **(B) SH1000-GFP counts at 1 hr post-infection. (C) SH1000-GFP counts at 2 hrs post-infection.** Data represent mean values ± SD, n=4 at 1 hr, n=3 at 2 hrs. Data was analysed by unpaired t-test, *p ≤ 0.05, ns= not significant (p > 0.05) **(D) % bacterial adhesion calculations at 1 hr post-infection (E) % bacterial adhesion calculations at 2 hrs post-infection.** Count data for the UFH condition has been expressed as a percentage of the untreated control. Data represent mean values ± SD, n=4 at 1 hr, n=3 at 2 hrs. Data was analysed by unpaired t-test, *p ≤ 0.05, **p ≤ 0.01.

238

7.3.2.6. Pre-treatment of microfluidic channels with UFH does not reduce SH1000-GFP adhesion to empty channels under continuous flow conditions.

The BioFlux 200 system was used to measure SH1000-GFP adhesion to microfluidic channels under continuous flow conditions, following pre-treatment of coated channels with 10 U/ml unfractionated heparin (UFH) or medium only control. As with previous studies, time lapse microscopy was used to monitor bacterial adhesion between 0 and 2 hrs post-infection (**Figure 7-21**) and brightfield microscopy confirmed the presence of empty microfluidic channels, containing no HCE2 cells (**Figure 7-21A**, **B**). Fluorescence microscopy was used to visualise GFP-tagged SH1000 and bacterial adhesion to microfluidic channels was observed under both conditions (**Figure 7-21C**). In the selected images, bacterial numbers appeared to be slightly higher in the presence of UFH, but quantitative analysis of multiple positions within the channel showed that bacterial adhesion rates were approximately equivalent in the presence or absence of UFH (**Figure 7-22**). Bacterial counts were plotted for each 15-minute time point between 0 and 2 hrs post-infection and the resulting curves were highly similar between conditions (**Figure 7-22A**). Data presented in **Figure 7-22A** was used to perform area under the curve calculations and values of 1227 ± 257 (no. bacteria × hrs) and 1292 ± 497 (no. bacteria × hrs) were reported for untreated and UFH-treated microfluidic channels, respectively. Individual time points were then analysed in further detail. At 1 hr post-infection, bacterial counts for control (687.7 ± 177.7) and UFH (670.2 ± 340.1) conditions were highly similar (**Figure 7-22B**). By 2 hrs-post infection, bacterial counts had increased under both conditions but the range of values for control (798.7 ± 115.5) and UFH (972.8 ± 417.0) conditions remained overlapping (**Figure 7-22C**). Statistical significance was not calculated due to low number of repeats (n=2). In **Figure 7-23**, bacterial count data for SH1000-GFP was compared under cells versus no cell conditions. In the absence of UFH, final bacterial counts were increased for HCE2 monolayers compared to no cell conditions, with values peaking at 1568.0 and 972.8, respectively. AUC values of 1739 ± 440 (no. bacteria × hrs) and 1227 ± 257 (no. bacteria × hrs) were recorded. In contrast, bacterial counts for UFH-treated HCE2 monolayers were reduced compared to no cell values, with bacterial numbers peaking at 532.2. An AUC value of 840 ± 738 (no. bacteria × hrs) was recorded.

(A)

(B)

(C)
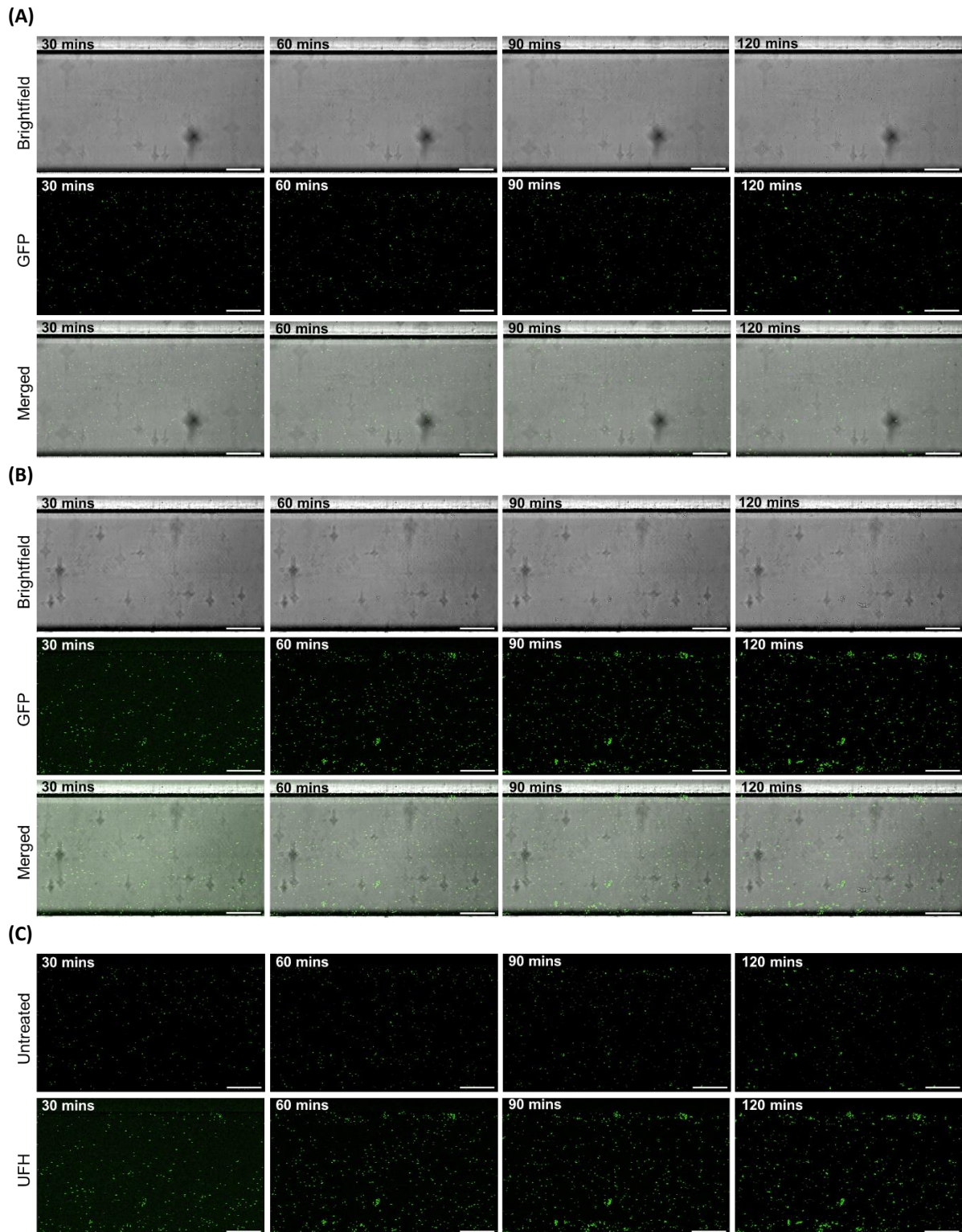
Figure 7-21. Bacterial adhesion of SH1000-GFP to empty microfluidic channels following pre-treatment with UFH or medium only control.
(A) Control (B) 10 U/ml UFH (C) Comparison of treatment conditions. Empty microfluidic channels (containing no HCE2 cells) were pre-treated with 10 U/ml UFH or medium only control and infected with SH1000-GFP for 2 hrs under continuous flow conditions (0.2 dyn/cm^2). Images were collected at 20x magnification every 15 minutes, using brightfield and fluorescence microscopy. Images collected at 30, 60, 90 and 120 mins post-infection are shown above. Scale bars represent 100 μm.

(A)

(B)

(C)
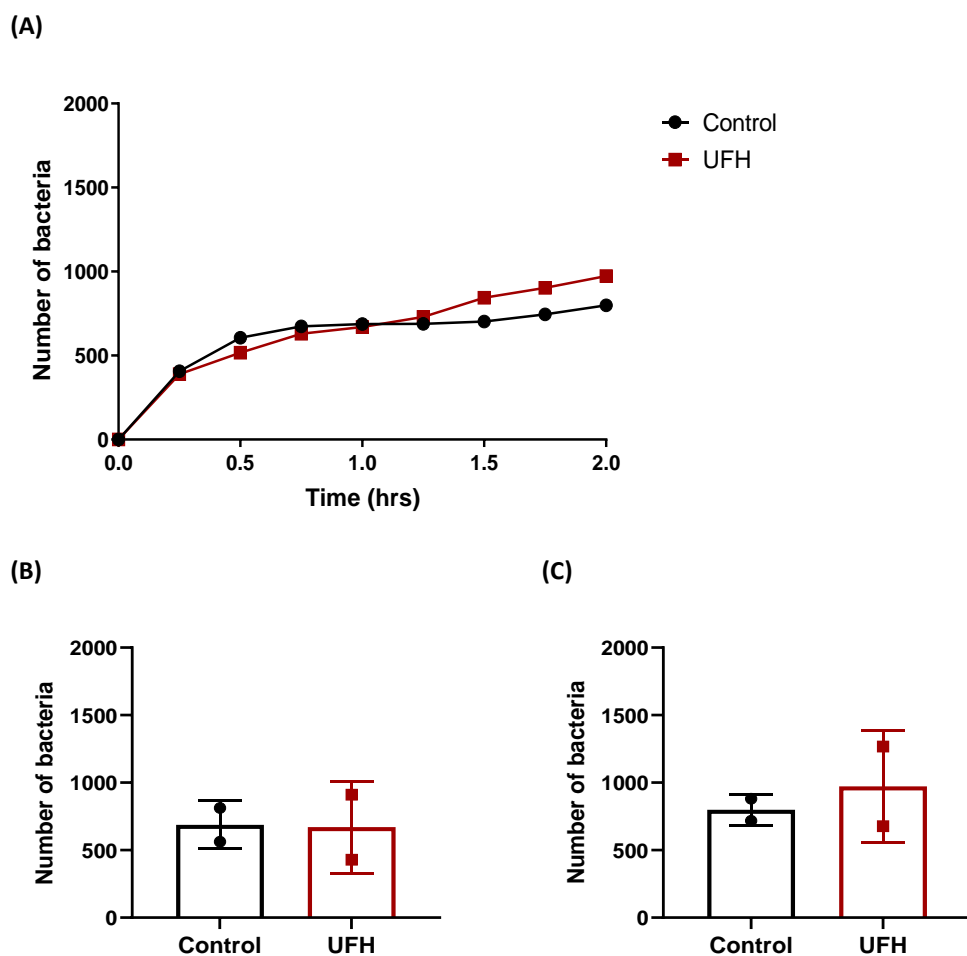
Figure 7-22. Quantification of adherent SH1000-GFP following pre-treatment of empty microfluidic channels with UFH or medium only control.

Fluorescence microscopy images from bacterial adhesion studies were processed in ImageJ and the Feature-Assisted Segmenter/Tracker (FAST) was used to enumerate SH1000-GFP across different frames and treatment conditions in MATLAB. For all time points and conditions, n=2. **(A) SH1000-GFP counts between 0 and 2 hrs post-infection.** Data represent mean values. **(B) SH1000-GFP counts at 1 hr post-infection. (C) SH1000-GFP counts at 2 hrs post-infection.** Data represent mean values ± SD.

(A)

(B)
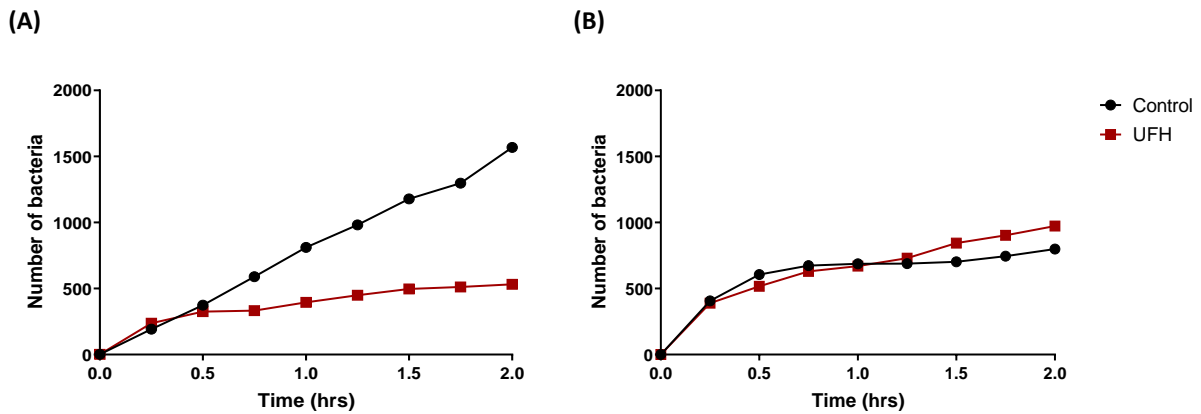
Figure 7-23. Comparison of SH1000-GFP adhesion data for cells versus no cell conditions.
Comparison of the bacterial count data for SH1000-GFP following 2 hr infection in the presence or absence of HCE2 monolayers. Data represent mean values ± SD. **(A) HCE2 monolayers** n=4. **(B) Empty microfluidic channels** n=2.

7.4. Discussion

7.4.1. Summary of results

In this chapter, the BioFlux microfluidic system was used to simulate bacterial keratitis under flow conditions. This is a novel area of work and the BioFlux infection models presented in this chapter represent the first of their kind. As a result, extensive optimisation was required and a switch from the BioFlux 1000z, to the BioFlux 200 system proved critical. Advanced imaging capabilities associated with the BioFlux 200 system, allowed me to visualise individual bacteria and identify multiple problems with the preliminary BioFlux infection protocol. These problems included insufficient inoculation conditions, contamination from outlet wells, variations in the size of the initial bacterial inoculum and the uncontrolled movement of bacteria due to gravity flow. These problems highlight the importance of rigorous model testing and have been provided as a resource for other researchers planning to use the BioFlux. Despite experimental difficulties, two successful BioFlux infection protocols were developed. The first, which is referred to as the microcolony formation protocol, allows infection progression to be monitored over extended periods of time and was designed to study the early stages of biofilm formation. The second protocol is a bacterial adhesion protocol, which involves a short, 2 hr infection period and was designed to study initial attachment of bacteria to human corneal epithelial cells. The development of these protocols has fulfilled the first two aims for this chapter, by facilitating the study of biofilm formation and bacterial adhesion to HCE2 monolayers under flow conditions. In contrast, the final aim for this chapter was only partly achieved. Due to time constraints, the anti-adhesion effects of CD9 derived tetraspanin peptides were not investigated using the optimised BioFlux infection models. However, pre-treatment of HCE2 monolayers with 10 U/ml unfractionated heparin (UFH) was performed and these studies yielded some highly interesting results.

UFH pre-treatment had no effect on *P. aeruginosa* adhesion under flow conditions and inhibition of staphylococcal adhesion was reduced compared to static conditions. This contradicts data from static infection models in **Chapter 5**, which showed inhibition of *S. aureus* and *P. aeruginosa* adhesion in response to UFH pre-treatment. Therefore, my BioFlux infection data suggests a potential role for mechanosensing in bacterial adhesion and demonstrates the importance of using physiologically relevant test models in antimicrobial drug testing.

7.4.2. Preliminary BioFlux 1000z studies

In **section 7.3.1**, the BioFlux 1000z and preliminary BioFlux infection protocol were used to study *P. aeruginosa* infections under oscillatory flow conditions. Brightfield microscopy images revealed deterioration of HCE2 monolayers and fluorescence microscopy displayed the formation of thick, bacterial lawns believed to represent PAO1-GFP biofilms. Healthy HCE2 monolayers and biofilm structures were not observed at overlapping time points and the death of HCE2 cells preceded a rapid increase in bacterial growth at approximately 10 hrs post-infection. Microscopy images showed large numbers of PAO1-GFP bacteria at 11 hrs post-infection and time-lapse images were used to trace the origin of chosen microcolonies. Some populations could be traced back to regions of fluorescence at the 0-hr time point, whereas other bacteria appeared later during the infection. This suggested that new regions of the channel were being colonised following introduction of oscillatory flow. However, based on findings in **section 7.3.2**, BioFlux 1000z images were subject to reinterpretation. In this section, I demonstrated that the original inoculation conditions did not allow bacteria to reach the BioFlux viewing windows and therefore PAO1-GFP bacteria were not present in the channel at the 0-hr time point. Instead, I hypothesise that large, preformed clusters of bacteria were introduced from outlet wells at later time points. Furthermore, regions of fluorescence that were visible between 0 and 7 hrs post-infection may be attributable to HCE2 cells rather than GFP-tagged bacteria, as mammalian cells display low levels of fluorescence, known as autofluorescence (Aubin, 1979). Areas of the channel with high levels of autofluorescence may have corresponded to dead cells as brightfield images showed spatial overlap between rounded HCE2 cells and regions of fluorescence. Furthermore, mammalian cell lines have been shown to display increased autofluorescence in response to cell death and/or severe cell stress (Surre et al., 2018, Kozlova et al., 2020) and *P. aeruginosa* has been shown to preferentially bind dead host cells (Capasso et al., 2016), perhaps explaining why large clusters of PAO1-GFP bacteria were formed at sites of strong autofluorescence. I propose that bacteria first entered the BioFlux viewing region at 8 hrs post-infection, with a sudden influx of bacteria occurring at the 10-hr time point. In contrast, destruction of HCE2 monolayers had occurred by 9 hrs post-

infection and this preceded the main arrival of bacteria. Therefore, I believe that HCE2 cell death was induced by secreted *P. aeruginosa* toxins, which were present in the medium from early time points.

Comparison of cells versus no cell conditions showed that bacterial adhesion was increased in the presence of HCE2 monolayers. This suggests PAO1-GFP preferentially binds to host cell surfaces over abiotic BioFlux channels. This has a number of positive implications for my model. Firstly, it permits the use of HCE2 monolayers which are not 100% confluent, as bacteria are expected to preferentially bind to HCE2 cells instead of gaps in the HCE2 monolayer. This is important as high cell seeding densities can compromise the uniformity of cell monolayers. Secondly, reduced binding to empty channels indicates low levels of non-specific bacterial binding. This is an essential characteristic of bacterial adhesion models (as is discussed in more detail in **Chapter 5**) and allows us to study differences in bacterial-host adhesion in a meaningful way.

7.4.3. Optimising the BioFlux microfluidic system

In **section 7.3.2**, a switch from the BioFlux 1000z to the BioFlux 200 was made. In **section 7.3.2.1**, the preliminary BioFlux protocol developed by Dr Mahendra Raut, was carried out using the BioFlux 200 system and the advanced imaging capabilities of the BioFlux 200, allowed me to identify a number of problems with the preliminary BioFlux infection protocol. These problems included insufficient inoculation conditions, which prevented PAO1-GFP bacteria from reaching the BioFlux viewing region by the 0-hr time point, and the presence of leftover bacteria in outlet wells. As a result, it was hypothesised that PAO1-GFP bacteria observed in the BioFlux 1000z experiments (see **section 7.3.1.1**) were not present in the channels at the start of the experiment but were introduced from outlet wells at later time points. Additional problems included the presence of gravity flow, caused by differences in media volume between inlet and outlet wells, and variations in the size of the initial bacterial inoculum. The latter was attributed to obstruction of BioFlux channels by HCE2 cells, as the preliminary BioFlux infection protocol involved seeding HCE2 cells and introducing PAO1-GFP bacteria, via the outlet wells. Based on my observations in **section 7.3.2.1**, a number of changes to the experimental setup were made and two new infection protocols were developed, a microcolony formation protocol and a bacterial adhesion protocol. The microcolony formation protocol shared a number of similarities with the preliminary BioFlux infection protocol and was designed to study biofilm formation over an extended period of time. However, the bacterial inoculation period was lengthened to ensure PAO1-GFP bacteria were reaching the BioFlux viewing region and oscillatory flow was replaced by unidirectional, pulsatile flow to prevent contamination from the bacterial inoculum at later time points. For both the microcolony formation and bacterial adhesion protocols, bacteria were

introduced via inlet wells to limit obstruction from HCE2 cells and identical volumes of media were used in inlet and outlet wells to prevent gravity flow.

7.4.4. Microcolony formation protocol

In **section 7.3.2.2**, the optimised microcolony formation protocol was used to monitor PAO1-GFP infection of HCE2 monolayers over 8 hrs. Fluorescence microscopy confirmed the presence of individual PAO1-GFP bacteria at the 0 hr-time point and microcolony formation was observed, with clusters of bacteria gradually increasing in size between 0 and 8 hrs post-infection. The spatial distribution of microcolonies corresponded to the location of individual bacteria at the 0-hr time point, confirming that new bacteria were not being introduced from outside of the channel, as in earlier experiments. Furthermore, brightfield microscopy images displayed HCE2 viability until approximately 6 hrs post-infection, with small microcolonies forming on the surface of viable HCE2 monolayers. Therefore, the microcolony formation protocol provides a co-culture model of the early stages of biofilm formation. This allows interactions between live HCE2 cells and biofilm-forming bacteria to be studied in real-time and represents a highly novel area of work. Previous biofilm studies have predominantly investigated biofilm formation in the context of abiotic surfaces or non-living mammalian cell populations (Buhmann et al., 2016) and I am only aware of one other study in which the BioFlux microfluidic system has been used to investigate host-pathogen interactions under flow conditions (Tremblay et al., 2015). In this study, bacterial adhesion of pathogenic *Escherichia coli* to the human colorectal adenocarcinoma cell line (HRT-18) was investigated using the BioFlux 200 system. Infected cell monolayers were incubated for 16 hrs in the presence of unidirectional flow (0.5 dyn/cm^2) and biofilm formation was observed. However, this study appears to have been limited by imaging capabilities and infected monolayers were fixed at the 16-hr time point to facilitate high resolution microscopy. In contrast, I was able to collect high-resolution microscopy images in real-time.

Due to time constraints, the optimised microcolony formation protocol was only performed once and a mixed bacterial population containing fluorescent and non-fluorescent bacteria was observed. This phenomenon was investigated in more detail in **section 7.3.2.3** and flow cytometry indicated the mixed PAO1-GFP population was due to loss of the GFP expression plasmid and not contamination. The SH1000-GFP strain was also analysed by flow cytometry and although two bacterial populations were observed in the absence of antibiotic-selection, the non-GFP expressing population was considerably smaller, demonstrating the improved stability of the SH1000-GFP expression plasmid.

7.4.5. Bacterial adhesion protocol

In **section 7.3.2.4**, the bacterial adhesion protocol was used to investigate changes in *P. aeruginosa* adhesion to HCE2 monolayers following 10 U/ml UFH pre-treatment. Time lapse microscopy images showed similar numbers of adherent PAO1-GFP bacteria in the presence or absence of UFH and this was confirmed by quantitative analysis, which showed no significant difference between the two conditions. At 1 hr post-infection, there was a 4.2% increase in PAO1-GFP adhesion to UFH-treated cells compared to untreated HCE2 monolayers. This directly contradicts findings for static infection models in **section 5.3.4**, which showed a significant reduction (of 68.8%) in bacterial adhesion to HCE2 monolayers following UFH pre-treatment.

There are a number of possible explanations for differences in UFH anti-adhesion effects between static and flow conditions. Firstly, the optimal concentration of UFH may differ between conditions. Only 10 U/ml UFH was included in BioFlux infection studies, as this concentration was shown to display broad-spectrum anti-adhesion activity under static conditions. However, an increased concentration may be required for adhesion inhibition under flow conditions. The mode of action of UFH in *P. aeruginosa* infections remains unclear but we hypothesise that UFH disrupts binding by triggering the reorganisation of bacterial receptor proteins at the host cell surface (see **section 5.4.3.2**). In BioFlux experiments, UFH pre-treatment was carried out under shear stress conditions of 1 dyn/cm^2. The presence of shear stress may have reduced the number of interactions between UFH and HCE2 cell surface proteins, as well as the average interaction time between them. Therefore, an increased UFH concentration may be required to induce equivalent anti-adhesion effects under flow. Furthermore, whereas an MOI of 1 was used in static infection studies, I cannot provide a fixed MOI for the BioFlux infection model as PAO1-GFP bacteria were constantly entering and leaving the channel. Therefore, differences in the ratio of PAO1-GFP bacteria to HCE2 cells may explain differences in anti-adhesion effects.

Alternatively, loss of UFH activity may be linked to mechanosensing effects. Mechanosensing is the process by which bacteria detect and respond to mechanical stimuli in their environment and mechanical cues include surface sensing and fluid flow. Both cues have been shown to influence *P. aeruginosa* behaviour and a common denominator in these mechanosensing pathways is the presence of shear stress (Sanfilippo et al., 2019). Bacteria present in dynamic, fluid environments (e.g., tear film) are continually exposed to shear stress conditions as fluid moves over the bacterial surface, whereas bacteria experience a sudden increase in shear stress following attachment to a surface. Previous mechanosensing studies have largely focussed on surface sensing, and shear stress has been shown to play an important role in initiation of biofilm formation by increasing intracellular cyclic-di-GMP

levels following surface attachment (Rodesney et al., 2017). This study identified the type IV pili protein, PilY1, as an important mechanosensory element and a shear-mediated cyclic-di-GMP response was not observed in PilY1 deletion mutants. This study demonstrates the existence of mechanosensitive *P. aeruginosa* adhesins and these adhesins may explain differences in PAO1-GFP behaviour between static and flow conditions. However, it is important to note that this is an active area of research and there are conflicting reports regarding the role of specific bacterial adhesins. For example, shear stress has been shown to influence the residence time of adherent *P. aeruginosa* on PDMS and glass surfaces (Lecuyer et al., 2011). Residence time increased linearly with increasing shear stress values and this phenomenon was shown to be independent of bacterial appendages such as the flagella and type IV pili proteins. Instead, the authors speculated that increased adhesion in the presence of shear stress was a non-specific phenomenon, caused by global changes in the bacterial cell surface. For example, shear stress may trigger chemical surface modifications that increase the number of electrostatic and/or hydrophobic interactions bacteria can form. More recently, Sanfilippo et al characterised a force-independent mechanosensing pathway (termed rheosensing) which enables *P. aeruginosa* to activate a flow-regulated operon (termed fro) and modulate its behaviour in response to shear stress (Sanfilippo et al., 2019). Differential expression from the fro operon was influenced solely by shear rate (i.e., change in velocity) (see **section 1.7**) and not viscosity and therefore, unlike classical mechanosensing pathways, the rheosensing pathway is independent of mechanical force. Furthermore, deletion of important *P. aeruginosa* adhesins (e.g., *fliC, pilA, pilY1*) had no impact on fro induction, meaning this pathway is independent of the flagella and type IV pili. Instead, the authors speculate that *P. aeruginosa* possesses asymmetrical surface proteins which rotate under flow conditions, effectively acting as molecular water wheels. In summary, there is increasing evidence that shear stress modulates *P. aeruginosa* behaviour via mechanosensing pathways. This is an area of active research but *P. aeruginosa* appears to use multiple mechanosensing pathways (i.e., force-dependent, classical pathways and force-independent, rheosensing pathways) that employ different effector proteins. Therefore, it seems plausible that differences in UFH-activity between static and flow conditions could be linked to mechanosensing effects. Host-pathogen interactions may differ between static and flow conditions (e.g., due to shear-induced conformational changes that alter strength/number of bacterial interactions), meaning interactions typically disrupted by UFH become dispensable.

In **section 7.3.2.5**, the bacterial adhesion protocol was used to investigate changes in *S. aureus* adhesion to HCE2 monolayers following 10 U/ml UFH pre-treatment. Time lapse microscopy images, z-stack projections and phase microscopy images all displayed large reductions in adherent SH1000-GFP bacteria in response to UFH pre-treatment. This was confirmed by quantitative image analysis,

which showed a significant reduction (of 55.1%) in bacterial adhesion to HCE2 monolayers following UFH pre-treatment. This matches data from static infection models (see **section 5.3.4**), which showed an 85.3% reduction in bacterial adhesion at the 1-hr time point. These findings confirm that 10 U/ml UFH has inhibitory effects on staphylococcal adhesion and these effects are not abolished in the presence of flow. Therefore, UFH may be a suitable candidate for preventing *S. aureus* infections at the ocular surface.

In **section 1.8.2**, I outlined a model for UFH-mediated inhibition of staphylococcal adhesion (Green et al., unpublished data). As part of this model, UFH is proposed to reduce staphylococcal adhesion by displacing fibronectin from the host cell surface and I believe this mechanism may be applicable to both static and flow conditions. However, it should be noted that UFH was less effective at inhibiting bacterial adhesion under flow conditions (55.1% versus 85.3% reduction) and there are a number of possible explanations for this. Firstly, reduced efficacy under flow conditions may be linked to differences in the optimal concentration of UFH or differences in MOI between models, as described previously. Alternatively, the presence of shear stress may alter *S. aureus* adhesion characteristics (and therefore the anti-adhesion effects of UFH), via mechanosensing pathways. This has been demonstrated previously using Bovine Aortic Endothelial Cells (BAEC) and shear stress was shown to completely abolish *S. aureus* adhesion to BAECs under shear rate conditions of 10-200 s^{-1} (approx. 0.07-1.4 dyn/cm^2) (Reddy and Ross, 2001). FnBP-Fn binding is the major staphylococcal adhesion mechanism involved in BAEC binding and therefore authors suggested this interaction was disrupted by shear stress. My findings do not indicate shear-mediated abolition of FnBP-Fn binding, as UFH is suspected to target this interaction and therefore if FnBP-Fn binding was completely abolished, no difference between control and UFH conditions would be observed. However, partial disruption of these interactions could explain the reduced efficacy of UFH under flow. Another possibility is that *S. aureus* expresses mechanosensitive proteins that form alternative and/or stronger interactions with host cells in the presence of shear stress, thereby compensating for fibronectin displacement. For example, the *S. aureus* CWA proteins, ClfA and ClfB, have been shown to alter their binding capabilities in response to mechanical tension (Geoghegan and Dufrene, 2018). ClfA and ClfB bind fibrinogen and loricrin, respectively and following increases in mechanical tension, conformational changes in protein structure are observed (Vitry et al., 2017, Herman-Bausier et al., 2018). These changes facilitate formation of strong molecular bonds via the Dock, Lock, Latch (DLL) mechanism, whereas weak molecular bonds predominate under low mechanical stress conditions. These studies demonstrate how *S. aureus* adhesins can act as force-sensitive molecular switches and the mechanosensitive activity of ClfA has been demonstrated in the context of shear stress, with increased ClfA-mediated adhesion to host platelets and von Willebrand factor observed under high shear stress conditions

(Kerrigan et al., 2008, Claes et al., 2017). The cornea is an avascularised, non-keratinised tissue and therefore ClfA/B are unlikely to play a major role in corneal infections. However, the DLL mechanism is utilised by multiple *S. aureus* adhesins (see **section 1.3.1.1**). and so similar mechanosensitive interactions may exist which influence staphylococcal adhesion to corneal epithelial cells under shear stress conditions. Therefore, mechanosensing effects could explain differences in UFH efficacy between static and flow conditions.

In **section 7.3.2.6**, the bacterial adhesion protocol was used to investigate changes in *S. aureus* adhesion to coated BioFlux channels following 10 U/ml UFH pre-treatment. UFH pre-treatment was shown to have no effect on bacterial adhesion, and this provides support for the hypothesis that UFH is a host-directed anti-adhesion therapy. Staphylococcal adhesion was still observed in the absence of HCE2 monolayers but numbers of adherent SH1000-GFP bacteria were reduced and the spatial distribution of bacteria varied between conditions. In the absence of cells, SH1000-GFP were evenly distributed throughout the channel, whereas in the presence of HCE2 monolayers, adherent bacteria formed clusters, highlighting the occurrence of cell-associated adhesion. It should be noted that staphylococcal adhesion under no cell conditions was enhanced by use of fibronectin coating medium, as fibronectin is a major host cell target in *S. aureus* infections (Speziale and Pietrocola, 2020). In the HCE2 BioFlux infection model, fibronectin coating should be shielded by HCE2 monolayers and therefore the no-cell model provides an over-inflated view of non-specific bacterial binding.

7.4.6. Future work

There are multiple additional experiments that could be performed using the optimised BioFlux infection protocols. Due to time constraints the optimised microcolony formation protocol was only performed once. Therefore, it would be highly valuable to repeat this work using both PAO1-GFP and SH1000-GFP. This model could also be used for antimicrobial drug testing. In particular, it would be interesting to investigate the effects of UFH on microcolony formation, as this heparan sulphate analogue has previously been shown to promote biofilm formation in *S. aureus* (Shanks et al., 2005). Therefore, larger SH1000-GFP microcolonies would be expected to form in the presence of UFH. It would also be valuable to expand bacterial adhesion studies to include the CD9-derived tetraspanin peptides and no cell control experiments could be repeated using PAO1-GFP to measure non-specific, *P. aeruginosa* binding to empty BioFlux channels. Finally, it would also be interesting to culture HCE2 monolayers under flow conditions prior to infection. The BioFlux 200 system used in these experiments lacked a CO_2 supply and so following cell seeding, BioFlux plates were placed in an incubator overnight. As a result, HCE2 monolayers were cultivated under static conditions. Previous researchers have shown that shear stress alters the morphology of human corneal epithelial cells

(Molladavoodi et al., 2017) and HCE monolayers display increased mRNA expression of E-cadherin and ZO1 under flow conditions (Hampel et al., 2018). ZO1 is a tight junction protein, and the formation of tight cell junctions plays an important role in intrinsic resistance to infection at the ocular surface (Fleiszig et al., 2019). Therefore, culturing HCE2 cells under flow conditions prior to infection, may alter infection progression and could extend the viability of HCE2 monolayers during microcolony formation assays.

7.4.7. Conclusion

In summary, the BioFlux 200 microfluidic system was used to simulate bacterial keratitis under physiological flow conditions and alternative protocols were developed for studying microcolony formation and bacterial adhesion. These models represent the first of their kind and have the potential to act as valuable tools for antimicrobial drug testing. Bacterial adhesion studies showed that heparin pre-treatment had no effect on *P. aeruginosa* adhesion under flow conditions and inhibition of staphylococcal adhesion was reduced compared to static conditions. These findings implicate a potential role for mechanosensing in bacterial adhesion to host cells and demonstrates the importance of using physiologically relevant test models for antimicrobial drug testing.

CHAPTER 8: FINAL RESULTS SUMMARY

8.1. Summary

In this thesis, I have presented novel *in vitro* models of the human corneal epithelium that were used to simulate bacterial keratitis. Infection studies have provided valuable insight into bacterial pathogenesis at the ocular surface and studies involving putative anti-adhesion therapies have demonstrated the importance of using physiologically relevant models for antimicrobial drug testing.

In **Chapter 3**, an *in vitro* model of the human corneal epithelium, which uses transwell inserts to culture HCE2 cells at an air-liquid interface, was presented. DMEM: F12 medium, supplemented with 10% FBS was identified as the optimal medium condition for culturing differentiated HCE2 cells and a 6-day ALI culture period was selected. Under these conditions, HCE2 cells displayed strong epithelial barrier integrity, as demonstrated by the expression of tight junction proteins and reduced paracellular permeability. HCE2 cells were also shown to express CD9 tetraspanin under a range of culture conditions and this permits the use of HCE2 models for testing CD9-derived tetraspanin peptides. Finally, qPCR was used to detect PAX6 mRNA expression in HCE2 cells. PAX6 is a corneal epithelial cell specific marker and PAX6 mRNA was detected in HCE2 cells under ALI and submerged culture conditions, thereby confirming retention of corneal epithelial cell identity in the HCE2 cell line.

In **Chapter 4**, clinical bacterial keratitis isolates from the LV Prasad Eye Institute in India were characterised by biofilm formation assays, antibiotic susceptibility testing and genome sequencing. A small number of clinical isolates from Northern General Hospital in Sheffield, were also included, as well as previously characterised reference strains. Reference strains were used to optimise protocols and perform quality control, as well as providing useful comparison with clinical isolates from India. Characterisation of clinical isolates allowed me to identify isolates of interest for future work, e.g., isolates with a biofilm-forming phenotype and/or strong antibiotic resistance profile. All LVPEI isolates formed biofilms in tissue culture medium, making them suitable candidates for biofilm infection models and MIC studies identified LVP3 and LVP11 as our most antibiotic resistant strains. *P. aeruginosa* sequencing data was used to identify known antibiotic resistance genes and antibiotic efflux was shown to represent the major antibiotic resistance mechanism in our isolate population. Finally, analysis of virulence factor genes revealed LasA/B, AprA, PASP and PrpL proteases were all highly conserved in our isolate population. The b-type *fliC* allele was more prevalent within our isolate population, as was the invasive (*exoS* +ve) *P. aeruginosa* pathotype and this contradicts previous data from keratitis population studies.

In **Chapter 5**, bacterial adhesion studies were used to study the putative anti-adhesion effects of CD9-derived tetraspanin peptides and unfractionated heparin (UFH). CD9 peptides displayed limited effects on staphylococcal adhesion but there were concerns regarding the experimental protocol and it was hypothesised that high levels of non-specific bacterial binding could be masking anti-adhesion effects. In contrast, pre-treatment of HCE2 monolayers with 10 U/ml UFH significantly reduced bacterial adhesion of *S. aureus* SH1000-GFP and *P. aeruginosa* PAO1-GFP to HCE2 cells. In addition to bacterial adhesion studies, CD9 expression studies were repeated using infected HCE2 cells. CD9 expression was unaffected by infection and therefore changes in CD9 expression should not influence the efficacy of CD9 peptides over time. Finally, qPCR was used to investigate changes in cytokine expression in response to staphylococcal infection and/or anti-adhesion treatment. Expression of IL-6, TNFα and CCL20 were increased in response to infection but neither the CD9 peptides nor UFH were shown to alter mRNA expression levels.

In **Chapter 6**, the HCE2 transwell model developed in **Chapter 3**, was used to simulate *S. aureus* keratitis infections. SH1000-GFP was shown to traverse HCE2 multilayers and extensive destruction of multilayer architecture was observed by 9 hrs post-infection. However, cytotoxicity assays revealed low levels of cell lysis and therefore non-cytolytic bacterial proteases were suggested to play an important role in the early stages of *S. aureus* keratitis. Bacterial traversal studies suggested *S. aureus* was able to pass through 0.4 µm pores in the transwell membrane and bacterial traversal was increased in the presence of HCE2 multilayers compared to no cell conditions. TEM revealed that SH1000-GFP bacteria were internalised by HCE2 cells in the transwell model and so it was hypothesised that increased traversal in the presence of HCE2 multilayers was mediated by active uptake of bacteria. Flow cytometry was used to study bacterial internalisation and HCE2 cells were shown to internalise high numbers of bacteria. However, these cells were inefficient in their clearance of *S. aureus* and intracellular bacteria were able to survive and replicate within HCE2 cells. Therefore, HCE2 cells can be described as non-professional phagocytes. These findings provided support for our active uptake hypothesis but bacterial traversal studies involving phagocytosis inhibitors showed no effect of the inhibitors on bacterial traversal rates. Therefore, an alternative hypothesis was proposed, whereby bacterial traversal is increased in the presence of HCE2 cells due to extracellular matrix components. Preliminary studies failed to identify a link between ECM components and bacterial traversal, but these studies may have been compromised by overly simplistic ECM reagents which fail to mimic the complexity of the ECM *in vivo*. Therefore, the observation that bacterial traversal is increased in the presence of HCE2 multilayers is a novel observation that warrants further investigation.

In **Chapter 7**, the BioFlux™ microfludic system was used to simulate bacterial keratitis infections under physiological flow conditions. Extensive optimisation of the experimental setup was required but ultimately, two infection protocols were developed. The first, which is referred to as the microcolony formation protocol, allows infection progression to be monitored over extended periods of time and was designed to study the early stages of biofilm formation. The second protocol is a bacterial adhesion protocol, which involves a short, 2 hr infection period and was designed to study initial attachment of bacteria to human corneal epithelial cells. The bacterial adhesion protocol was used to study the putative anti-adhesion effects of UFH. Pre-treatment of HCE2 monolayers with 10 U/ml UFH was shown to significantly reduce *S. aureus* adhesion to HCE2 cells under flow conditions. However, the inhibitory effects of UFH were reduced compared to static infection conditions. Furthermore, UFH was shown to have no effect on *P. aeruginosa* adhesion to HCE2 monolayers under flow conditions. This contradicted static infection model data which showed an almost 70% reduction in bacterial adhesion following UFH pre-treatment. Therefore, our BioFlux infection data suggests a potential role for mechanosensing in bacterial adhesion to HCE2 monolayers and demonstrates the importance of using physiologically relevant infection models for antimicrobial drug testing.

8.2. Aims & Objectives

The first major aim of this project (see **section 1.11**) was to develop an *in vitro* cell culture model of the differentiated corneal epithelium, using the HCE2 human corneal epithelial cell line. This aim was successfully achieved in **Chapter 3** and our HCE2 transwell model shares multiple characteristics with the *in vivo* human corneal epithelium, including the presence of cell multilayers, possession of microvilli and the formation of tight cell junctions, which confer epithelial barrier integrity. However, infection of the model with *S. aureus* in **Chapter 6**, was associated with disruption of HCE2 multilayers and bacteria were shown to traverse HCE2 cell layers, indicating loss of epithelial barrier function. The *in vivo* cornea is highly resistant to infection and therefore our HCE2 transwell model requires further optimisation before it can be considered truly representative of the differentiated human corneal epithelium. Important host defence mechanisms present in the *in vivo* cornea that were absent from our HCE2 transwell model, include resident and infiltrative immune cells, the antimicrobial components of tear film and the mechanical protection conferred by blinking. These characteristics will be important considerations for future work.

The second aim for this project was to study clinical isolates obtained from bacterial keratitis patients. This aim was successfully achieved in **Chapter 4**, thanks to our collaboration with researchers and ophthalmologists at the LV Prasad Eye Institute, India. Three clinical staphylococcal isolates and four

P. aeruginosa isolates were initially provided, and these isolates were subjected to phenotypic analysis using growth curves, biofilm formation studies and antibiotic susceptibility testing. Later in the project, Dr Naveen Kumar (CMC, Vellore) provided genome sequencing data for 39 clinical *P. aeruginosa* isolates from LVPEI, and sequence analysis provided valuable insights into conserved virulence factor genes and antibiotic resistance mechanisms used by keratitis isolates. If possible, it will be valuable to continue expanding this isolate library as part of future work.

The final aim for this project was to use *in vitro* HCE2 models to simulate corneal infections and test novel antimicrobials. The use of *in vitro* HCE2 models for studying bacterial keratitis was successfully achieved and there was considerable diversity in the types of infection models used, allowing different aspects of bacterial keratitis to be explored. In **Chapter 5**, simple cell culture models were used to study infection of HCE2 monolayers under static conditions. These models provided cheap, high-throughput systems for performing preliminary testing and identifying suitable drug concentrations. In **Chapter 6**, the HCE2 transwell model was used to study infection of differentiated HCE2 multilayers under static conditions. These studies were particularly useful in studying bacterial traversal. In **Chapter 7**, the BioFlux microfluidic system was used to simulate bacterial keratitis under flow conditions. This allowed me to investigate the effects of shear stress and mimic blinking. Due to time constraints, our aim of using infection models to test novel antimicrobials was only partially achieved. Unfractionated heparin was trialled in simple static infection models and using the BioFlux adhesion protocol, but the effects of UFH on microcolony formation remain to be explored. Furthermore, CD9-derived tetraspanin peptides were only explored in our static infection model and these studies were limited to *S. aureus*. The HCE2 transwell model was not used for antimicrobial drug testing due to time constraints and high levels of non-specific bacterial binding to the transwells.

8.3. Future work

This thesis provides an array of experimental techniques and *in vitro* models that can be used to study bacterial keratitis infections. There are a number of additional experiments that could be carried out to expand on this work, and these are described in more detail in the individual chapter discussions. However, in this section I will highlight key priorities for future work. Firstly, *in vitro* models of the human corneal epithelium must be further improved so that they are more representative of the *in vivo* cornea. For instance, although I have begun to explore the shear-mediated effects of tear film using the BioFlux microfluidic model, these models utilised tissue culture medium, which has a vastly different composition to the human tear film. Human tears contain a multitude of antimicrobial components (e.g., secretory IgA, mucins and AMPs) which are likely to influence host-pathogen

interactions at the ocular surface. Therefore, it would be highly valuable to incorporate actual human tear film from human donors, or an artificial tear film solution, into our models as part of future work. In addition, the role of resident and infiltrative immune cells could be explored using co-culture models and transwell culture conditions could be further optimised to improve barrier function in the presence of bacteria (e.g., using additional media supplements). Secondly, although I have amassed a valuable library of clinical bacterial keratitis isolates, these isolates have not been systematically screened in corneal infection models due to time constraints. Since these isolates were directly retrieved from the human ocular surface, they may display host-adaptations that alter how they interact with human corneal epithelial cells. This may influence the efficacy of host-directed anti-adhesion therapies such as the CD9-derived tetraspanin peptides and therefore, it is important that a range of clinical isolates are incorporated into corneal infection models as part of future work. The BioFlux microfluidic system represents another area of largely untapped potential. My BioFlux adhesion protocol has been used to study unfractionated heparin, but antimicrobial drug testing could be expanded to include the CD9 derived tetraspanin peptides and the microcolony formation protocol could be used to study novel biofilm therapeutics. Differences in the behaviour of bacterial cells and mammalian host cells under static and flow conditions could also be investigated in more detail. Mechanobiology is a rapidly advancing field with potentially important implications in antimicrobial drug testing, and access to the BioFlux microfluidic system puts me in an advantageous position to contribute to this research. One final priority for future work will be to repeat transwell infection work so that mechanisms of increased bacterial traversal in the presence of HCE2 multilayers may be determined. This is a previously unreported phenomenon that may provide novel insights into *S. aureus* pathogenesis at the ocular surface. Additional experiments that could be performed include altering bacterial species and transwell pore size to assess effects on bacterial traversal and the hypothesis that bacterial traversal is facilitated by the host ECM requires further investigation.

REFERENCES

ABHARI, S., EISENBACK, M., KAPLAN, H. J., WALTERS, E., PRATHER, R. S. & SCOTT, P. A. 2018. Anatomic Studies of the Miniature Swine Cornea. *Anatomical Record-Advances in Integrative Anatomy and Evolutionary Biology,* 301**,** 1955-1967.

AGARWAL, P. & RUPENTHAL, I. D. 2016. In vitro and ex vivo corneal penetration and absorption models. *Drug Delivery and Translational Research,* 6**,** 634-647.

AL-MUJAINI, A., AL-KHARUSI, N., THAKRAL, A. & WALI, U. K. 2009. Bacterial keratitis: perspective on epidemiology, clinico-pathogenesis, diagnosis and treatment. *Sultan Qaboos University medical journal,* 9**,** 184-95.

ALARCON, I., EVANS, D. J. & FLEISZIG, S. M. J. 2009a. The Role of Twitching Motility in Pseudomonas aeruginosa Exit from and Translocation of Corneal Epithelial Cells. *Investigative Ophthalmology & Visual Science,* 50**,** 2237-2244.

ALARCON, I., KWAN, L., YU, C., EVANS, D. J. & FLEISZIG, S. M. J. 2009b. Role of the Corneal Epithelial Basement Membrane in Ocular Defense against Pseudomonas aeruginosa. *Infection and Immunity,* 77**,** 3264-3271.

ALARCON, I., TAM, C., MUN, J. J., LEDUE, J., EVANS, D. J. & FLEISZIG, S. M. J. 2011. Factors Impacting Corneal Epithelial Barrier Function against Pseudomonas aeruginosa Traversal. *Investigative Ophthalmology & Visual Science,* 52**,** 1368-1377.

ALBALDI, F. 2022. *An investigation of tetraspanin proteins' role in UPEC infection.* Doctoral dissertation, University of Sheffield.

ALEXANDRAKIS, G., ALFONSO, E. C. & MILLER, D. 2000. Shifting trends in bacterial keratitis in South Florida and emerging resistance to fluoroquinolones. *Ophthalmology,* 107**,** 1497-1502.

ALTSCHUL, S. F., GISH, W., MILLER, W., MYERS, E. W. & LIPMAN, D. J. 1990. BASIC LOCAL ALIGNMENT SEARCH TOOL. *Journal of Molecular Biology,* 215**,** 403-410.

ANANTHARAJAH, A., MINGEOT-LECLERCQ, M. P. & BAMBEKE, F. 2016. Targeting the Type Three Secretion System in Pseudomonas aeruginosa. *Trends in Pharmacological Sciences,* 37**,** 734-749.

ANGUS, A. A., EVANS, D. J., BARBIERI, J. T. & FLEISZIG, S. M. J. 2010. The ADP-Ribosylation Domain of Pseudomonas aeruginosa ExoS Is Required for Membrane Bleb Niche Formation and Bacterial Survival within Epithelial Cells. *Infection and Immunity,* 78**,** 4500-4510.

ANWAR, H., VANBIESEN, T., DASGUPTA, M., LAM, K. & COSTERTON, J. W. 1989. INTERACTION OF BIOFILM BACTERIA WITH ANTIBIOTICS IN A NOVEL INVITRO CHEMOSTAT SYSTEM. *Antimicrobial Agents and Chemotherapy,* 33**,** 1824-1826.

AQUINO, R. S. & PARK, P. W. 2016. Glycosaminoglycans and infection. *Frontiers in Bioscience-Landmark,* 21**,** 1260-1277.

ARAKISASAKI, K., OHASHI, Y., SASABE, T., HAYASHI, K., WATANABE, H., TANO, Y. & HANDA, H. 1995. AN SV40-IMMORTALIZED HUMAN CORNEAL EPITHELIAL-CELL LINE AND ITS CHARACTERIZATION. *Investigative Ophthalmology & Visual Science,* 36**,** 614-621.

ARGUESO, P., WOODWARD, A. M. & ABUSAMRA, D. B. 2021. The Epithelial Cell Glycocalyx in Ocular Surface Infection. *Frontiers in Immunology,* 12.

ARHIN, A. & BOUCHER, C. 2010. The outer membrane protein OprQ and adherence of Pseudomonas aeruginosa to human fibronectin. *Microbiology-Sgm,* 156**,** 1415-1423.

ARORA, S. K., RITCHINGS, B. W., ALMIRA, E. C., LORY, S. & RAMPHAL, R. 1998. The Pseudomonas aeruginosa flagellar cap protein, FliD, is responsible for mucin adhesion. *Infection and Immunity,* 66**,** 1000-1007.

ARUNACHALAM, D., NAMPERUMALSAMY, V. P., PRAJNA, L. & KUPPAMUTHU, D. 2021. Human Corneal Epithelial Cells Internalize Aspergillus flavus Spores by Actin-Mediated Endocytosis. *Infection and Immunity,* 89.

ASKARIAN, F., WAGNER, T., JOHANNESSEN, M. & NIZET, V. 2018. Staphylococcus aureus modulation of innate immune responses through Toll-like (TLR), (NOD)-like (NLR) and C-type lectin (CLR) receptors. *Fems Microbiology Reviews,* 42**,** 656-671.

AUBIN, J. E. 1979. AUTOFLUORESCENCE OF VIABLE CULTURED MAMMALIAN-CELLS. *Journal of Histochemistry & Cytochemistry,* 27**,** 36-43.

AUGUSTIN, D. K., HEIMER, S. R., TAM, C., LI, W. Y., LE DUE, J. M., EVANS, D. J. & FLEISZIG, S. M. J. 2011. Role of Defensins in Corneal Epithelial Barrier Function against Pseudomonas aeruginosa Traversal. *Infection and Immunity,* 79**,** 595-605.

AZGHANI, A. O., IDELL, S., BAINS, M. & HANCOCK, R. E. W. 2002. Pseudomonas aeruginosa outer membrane protein F is an adhesin in bacterial binding to lung epithelial cells in culture. *Microbial Pathogenesis,* 33**,** 109-114.

BAN, Y., DOTA, A., COOPER, L. J., FULLWOOD, N. J., NAKAMURA, T., TSUZUKI, M., MOCHIDA, C. & KINOSHITA, S. 2003. Tight junction-related protein expression and distribution in human corneal epithelium. *Experimental Eye Research,* 76**,** 663-669.

BARBARIGA, M., VALLONE, F., MOSCA, E., BIGNAMI, F., MAGAGNOTTI, C., FONTEYNE, P., CHIAPPORI, F., MILANESI, L., RAMA, P., ANDOLFO, A. & FERRARI, G. 2019. The role of extracellular matrix in mouse and human corneal neovascularization. *Scientific Reports,* 9**,** 12.

BATISTA, A., BREUNIG, H. G., UCHUGONOVA, A., MORGADO, A. M. & KONIG, K. 2016. Two-photon spectral fluorescence lifetime and second-harmonic generation imaging of the porcine cornea with a 12-femtosecond laser microscope. *Journal of Biomedical Optics,* 21**,** 11.

BAUER, I., GUNTHER, J., WHEELER, T. T., ENGELMANN, S. & SEYFERT, H. M. 2015. Extracellular milieu grossly alters pathogen-specific immune response of mammary epithelial cells. *Bmc Veterinary Research,* 11.

BECKERT, U., WOLTER, S., HARTWIG, C., BAHRE, H., KAEVER, V., LADANT, D., FRANK, D. W. & SEIFERT, R. 2014. ExoY from Pseudomonas aeruginosa is a nucleotidyl cyclase with preference for cGMP and cUMP formation. *Biochemical and Biophysical Research Communications,* 450**,** 870-874.

BENNET, D., ESTTACK, Z., REID, T. & KIM, J. 2018. A microengineered human corneal epithelium-on-a-chip for eye drops mass transport evaluation. *Lab on a Chip,* 18**,** 1539-1551.

BENSON, M. A., LILO, S., WASSERMAN, G. A., THOENDEL, M., SMITH, A., HORSWILL, A. R., FRASER, J., NOVICK, R. P., SHOPSIN, B. & TORRES, V. J. 2011. Staphylococcus aureus regulates the expression and production of the staphylococcal superantigen-like secreted proteins in a Rot-dependent manner. *Molecular Microbiology,* 81**,** 659-675.

BENSON, M. A., OHNECK, E. A., RYAN, C., ALONZO, F., SMITH, H., NARECHANIA, A., KOLOKOTRONIS, S. O., SATOLA, S. W., UHLEMANN, A. C., SEBRA, R., DEIKUS, G., SHOPSIN, B., PLANET, P. J. & TORRES, V. J. 2014. Evolution of hypervirulence by a MRSA clone through acquisition of a transposable element. *Molecular Microbiology,* 93**,** 664-681.

BERNIER, S. P., HA, D. G., KHAN, W., MERRITT, J. H. & O'TOOLE, G. A. 2011. Modulation of Pseudomonas aeruginosa surface-associated group behaviors by individual amino acids through c-di-GMP signaling. *Research in Microbiology,* 162**,** 680-688.

BERUBE, B. J. & WARDENBURG, J. B. 2013. Staphylococcus aureus alpha-Toxin: Nearly a Century of Intrigue. *Toxins,* 5**,** 1140-1166.

BHARATHI, M. J., RAMAKRISHNAN, R., MEENAKSHI, R., PADMAVATHY, S., SHIVAKUMAR, C. & SRINIVASAN, M. 2007. Microbial keratitis in South India: Influence of risk factors, climate, and geographical variation. *Ophthalmic Epidemiology,* 14**,** 61-69.

BISPO, P. J. M., HAAS, W. & GILMORE, M. S. 2015. Biofilms in Infections of the Eye. *Pathogens,* 4**,** 111-136.

BJARNSHOLT, T., ALHEDE, M., EICKHARDT-SORENSEN, S. R., MOSER, C., KUHL, M., JENSEN, P. O. & HOIBY, N. 2013. The in vivo biofilm. *Trends in Microbiology,* 21**,** 466-474.

BORKAR, D. S., FLEISZIG, S. M. J., LEONG, C., LALITHA, P., SRINIVASAN, M., GHANEKAR, A. A., TAM, C., LI, W. Y., ZEGANS, M. E., MCLEOD, S. D., LIETMAN, T. M. & ACHARYA, N. R. 2013. Association

Between Cytotoxic and Invasive Pseudomonas aeruginosa and Clinical Outcomes in Bacterial Keratitis. *Jama Ophthalmology,* 131**,** 147-153.

BOUKAMP, P., PETRUSSEVSKA, R. T., BREITKREUTZ, D., HORNUNG, J., MARKHAM, A. & FUSENIG, N. E. 1988. NORMAL KERATINIZATION IN A SPONTANEOUSLY IMMORTALIZED ANEUPLOID HUMAN KERATINOCYTE CELL-LINE. *Journal of Cell Biology,* 106**,** 761-771.

BOURCIER, T., THOMAS, F., BORDERIE, V., CHAUMEIL, C. & LAROCHE, L. 2003. Bacterial keratitis: predisposing factors, clinical and microbiological review of 300 cases. *British Journal of Ophthalmology,* 87**,** 834-838.

BROTHERS, K. M., STELLA, N. A., HUNT, K. M., ROMANOWSKI, E. G., LIU, X. Y., KLARLUND, J. K. & SHANKS, R. M. Q. 2015. Putting on the brakes: Bacterial impediment of wound healing. *Scientific Reports,* 5**,** 14.

BUCIOR, I., PIELAGE, J. F. & ENGEL, J. N. 2012. Pseudomonas aeruginosa Pili and Flagella Mediate Distinct Binding and Signaling Events at the Apical and Basolateral Surface of Airway Epithelium. *Plos Pathogens,* 8**,** 18.

BUHMANN, M. T., STIEFEL, P., MANIURA-WEBER, K. & REN, Q. 2016. In Vitro Biofilm Models for Device-Related Infections. *Trends in Biotechnology,* 34**,** 945-948.

BUILLES, N., BECHETOILLE, N., JUSTIN, V., ANDRE, V., BARBARO, V., DI IORIO, E., AUXENFANS, C., HULMES, D. J. S. & DAMOUR, O. 2007. Development of a hemicornea from human primary cell cultures for pharmacotoxicology testing. *Cell Biology and Toxicology,* 23**,** 279-292.

CABALLERO, A., THIBODEAUX, B., MARQUART, M., TRAIDEJ, M. & O'CALLAGHAN, R. 2004. Pseudomonas keratitis: Protease IV gene conservation, distribution, and production relative to virulence and other Pseudomonas proteases. *Investigative Ophthalmology & Visual Science,* 45**,** 522-530.

CADY, N. C., MCKEAN, K. A., BEHNKE, J., KUBEC, R., MOSIER, A. P., KASPER, S. H., BURZ, D. S. & MUSAH, R. A. 2012. Inhibition of Biofilm Formation, Quorum Sensing and Infection in Pseudomonas aeruginosa by Natural Products-Inspired Organosulfur Compounds. *Plos One,* 7**,** 12.

CAPASSO, D., PEPE, M. V., ROSSELLO, J., LEPANTO, P., ARIAS, P., SALZMAN, V. & KIERBEL, A. 2016. Elimination of Pseudomonas aeruginosa through Efferocytosis upon Binding to Apoptotic Cells. *Plos Pathogens,* 12.

CASSAT, J. E., SMELTZER, M. S. & LEE, C. Y. 2013. Investigation of Biofilm Formation in Clinical Isolates of Staphylococcus aureus. *In:* JI, Y. (ed.) *Methicillin-Resistant Staphylococcus Aureus.* Totowa: Humana Press Inc.

CDC 2013. Antibiotic resistance threats in the United States, 2013.

CHA, S., KIM, J. H. & GOO, Y. 2019. Optimal magnitude of shear stress for human corneal epithelial cell proliferation in microfluidic culture system. *Investigative Ophthalmology & Visual Science,* 60.

CHANG, V. S., DHALIWAL, D. K., RAJU, L. & KOWALSKI, R. P. 2015. Antibiotic Resistance in the Treatment of Staphylococcus aureus Keratitis: a 20-Year Review. *Cornea,* 34**,** 698-703.

CHARRIN, S., JOUANNET, S., BOUCHEIX, C. & RUBINSTEIN, E. 2014. Tetraspanins at a glance. *Journal of Cell Science,* 127**,** 3641-3648.

CHEN, L. H., YANG, J., YU, J., YA, Z. J., SUN, L. L., SHEN, Y. & JIN, Q. 2005. VFDB: a reference database for bacterial virulence factors. *Nucleic Acids Research,* 33**,** D325-D328.

CHEN, T., BELLAND, R. J., WILSON, J. & SWANSON, J. 1995. ADHERENCE OF PILUS(-) OPA(+) GONOCOCCI TO EPITHELIAL-CELLS IN-VITRO INVOLVES HEPARAN-SULFATE. *Journal of Experimental Medicine,* 182**,** 511-517.

CHEN, Y., GOTTE, M., LIU, J. & PARK, P. W. 2008. Microbial Subversion of Heparan Sulfate Proteoglycans. *Molecules and Cells,* 26**,** 415-426.

CHENG, A. G., KIM, H. K., BURTS, M. L., KRAUSZ, T., SCHNEEWIND, O. & MISSIAKAS, D. M. 2009. Genetic requirements for Staphylococcus aureus abscess formation and persistence in host tissues. *Faseb Journal,* 23**,** 3393-3404.

CHEVANCE, F. F. V. & HUGHES, K. T. 2008. Coordinating assembly of a bacterial macromolecular machine. *Nature Reviews Microbiology,* 6**,** 455-465.

CHIDAMBARAM, J. D., PRAJNA, N. V., SRIKANTHI, P., LANJEWAR, S., SHAH, M., ELAKKIYA, S., LALITHA, P. & BURTON, M. J. 2018. Epidemiology, risk factors, and clinical outcomes in severe microbial keratitis in South India. *Ophthalmic Epidemiology,* 25**,** 297-305.

CHO, P. & BOOST, M. V. 2019. Evaluation of prevention and disruption of biofilm in contact lens cases. *Ophthalmic and Physiological Optics,* 39**,** 337-349.

CHU, H. S., HU, F. R. & CHEN, C. T. 2013. Photodynamic antimicrobial chemotherapy for methicillin-resistant Staphylococcus aureus -in vitro, biofilm, and ex vivo bovine keratitis model. *Investigative Ophthalmology & Visual Science,* 54.

CHUA, K. Y. L., STINEAR, T. P. & HOWDEN, B. P. 2013. Functional genomics of Staphylococcus aureus. *Briefings in Functional Genomics,* 12**,** 305-315.

CLAES, J., LIESENBORGHS, L., PEETERMANS, M., VELOSO, T. R., MISSIAKAS, D., SCHNEEWIND, O., MANCINI, S., ENTENZA, J. M., HOYLAERTS, M. F., HEYING, R., VERHAMME, P. & VANASSCHE, T. 2017. Clumping factor A, von Willebrand factor-binding protein and von Willebrand factor anchor Staphylococcus aureus to the vessel wall. *Journal of Thrombosis and Haemostasis,* 15**,** 1009-1019.

CLARKE, S. R., ANDRE, G., WALSH, E. J., DUFRENE, Y. F., FOSTER, T. J. & FOSTER, S. J. 2009. Iron-Regulated Surface Determinant Protein A Mediates Adhesion of Staphylococcus aureus to Human Corneocyte Envelope Proteins. *Infection and Immunity,* 77**,** 2408-2416.

CLEMENS, L. E., JAYNES, J., LIM, E., KOLAR, S. S., REINS, R. Y., BAIDOURI, H., HANLON, S., MCDERMOTT, A. M. & WOODBURN, K. W. 2017. Designed Host Defense Peptides for the Treatment of Bacterial Keratitis. *Investigative Ophthalmology & Visual Science,* 58**,** 6273-6281.

COATES, R., MORAN, J. & HORSBURGH, M. J. 2014. Staphylococci: colonizers and pathogens of human skin. *Future Microbiology,* 9**,** 75-91.

COLLIER, S. A., GRONOSTAJ, M. P., MACGURN, A. K., COPE, J. R., AWSUMB, K. L., YODER, J. S. & BEACH, M. J. 2014. Estimated Burden of Keratitis - United States, 2010. *Mmwr-Morbidity and Mortality Weekly Report,* 63**,** 1027-1030.

COLLIN, S. P. & COLLIN, H. B. 2000. A comparative SEM study of the vertebrate corneal epithelium. *Cornea,* 19**,** 218-230.

COPIN, R., SHOPSIN, B. & TORRES, V. J. 2018. After the deluge: mining Staphylococcus aureus genomic data for clinical associations and host-pathogen interactions. *Current Opinion in Microbiology,* 41**,** 43-50.

CORRIGAN, R. M., RIGBY, D., HANDLEY, P. & FOSTER, T. J. 2007. The role of Staphylococcus aureus surface protein SasG in adherence and biofilm formation. *Microbiology-Sgm,* 153**,** 2435-2446.

COUTURE, C., ZANIOLO, K., CARRIER, P., LAKE, J., PATENAUDE, J., GERMAIN, L. & GUERIN, S. L. 2016. The tissue-engineered human cornea as a model to study expression of matrix metalloproteinases during corneal wound healing. *Biomaterials,* 78**,** 86-101.

CRABBE, A., DE BOEVER, P., VAN HOUDT, R., MOORS, H., MERGEAY, M. & CORNELIS, P. 2008. Use of the rotating wall vessel technology to study the effect of shear stress on growth behaviour of Pseudomonas aeruginosa PA01. *Environmental Microbiology,* 10**,** 2098-2110.

CRESPO-MORAL, M., GARCIA-POSADAS, L., LOPEZ-GARCIA, A. & DIEBOLD, Y. 2020. Histological and immunohistochemical characterization of the porcine ocular surface. *Plos One,* 15**,** 17.

DAS, S., SAMANTARAY, R., MALLICK, A., SAHU, S. K. & SHARMA, S. 2019. Types of organisms and in-vitro susceptibility of bacterial isolates from patients with microbial keratitis: A trend analysis of 8 years. *Indian Journal of Ophthalmology,* 67**,** 49-53.

DAVE, A., SAMARTH, A., KAROLIA, R., SHARMA, S., KARUNAKARAN, E., PARTRIDGE, L., MACNEIL, S., MONK, P. N., GARG, P. & ROY, S. 2020. Characterization of Ocular Clinical Isolates of

Pseudomonas aeruginosa from Non-Contact Lens Related Keratitis Patients from South India. *Microorganisms,* 8**,** 14.

DAVEY, M. E. & O'TOOLE, G. A. 2000. Microbial biofilms: from ecology to molecular genetics. *Microbiology and Molecular Biology Reviews,* 64**,** 847-+.

DE BENTZMANN, S. & PLÉSIAT , P. 2011. The P*seudomonas aeruginosa* opportunistic pathogen and human infections. Environmental Microbiology.

DE LIMA, C. D. M., CALEGARI-SILVA, T. C., PEREIRA, R. M. S., SANTOS, S., LOPES, U. G., PLOTKOWSKI, M. C. M. & SALIBA, A. M. 2012. ExoU Activates NF-kappa B and Increases IL-8/KC Secretion during Pseudomonas aeruginosa Infection. *Plos One,* 7**,** 9.

DEIVANAYAGAM, C. C. S., WANN, E. R., CHEN, W., CARSON, M., RAJASHANKAR, K. R., HOOK, M. & NARAYANA, S. V. L. 2002. A novel variant of the immunoglobulin fold in surface adhesins of Staphylococcus aureus: crystal structure of the fibrinogen-binding MSCRAMM, clumping factor A. *Embo Journal,* 21**,** 6660-6672.

DENIZOT, F. & LANG, R. 1986. RAPID COLORIMETRIC ASSAY FOR CELL-GROWTH AND SURVIVAL - MODIFICATIONS TO THE TETRAZOLIUM DYE PROCEDURE GIVING IMPROVED SENSITIVITY AND RELIABILITY. *Journal of Immunological Methods,* 89**,** 271-277.

DEY, S. 2011. Corneal cell culture models: a tool to study corneal drug absorption. *Expert Opinion on Drug Metabolism & Toxicology,* 7**,** 529-532.

DIEP, B. A., GILL, S. R., CHANG, R. F., PHAN, T. H., CHEN, J. H., DAVIDSON, M. G., LIN, F., LIN, J., CARLETON, H. A., MONGODIN, E. F., SENSABAUGH, G. F. & PERDREAU-REMINGTON, F. 2006. Complete genome sequence of USA300, an epidemic clone of community-acquired meticillin-resistant Staphylococcus aureus. *Lancet,* 367**,** 731-739.

DIGIANDOMENICO, A., WARRENER, P., HAMILTON, M., GUILLARD, S., RAVN, P., MINTER, R., CAMARA, M. M., VENKATRAMAN, V., MACGILL, R. S., LIN, J., WANG, Q., KELLER, A. E., BONNELL, J. C., TOMICH, M., JERMUTUS, L., MCCARTHY, M. P., MELNICK, D. A., SUZICH, J. A. & STOVER, C. K. 2012. Identification of broadly protective human antibodies to Pseudomonas aeruginosa exopolysaccharide Psl by phenotypic screening. *Journal of Experimental Medicine,* 209**,** 1273-1287.

DOAN, T., AKILESWARAN, L., ANDERSEN, D., JOHNSON, B., KO, N., SHRESTHA, A., SHESTOPALOV, V., LEE, C. S., LEE, A. Y. & VAN GELDER, R. N. 2016. Paucibacterial Microbiome and Resident DNA Virome of the Healthy Conjunctiva. *Investigative Ophthalmology & Visual Science,* 57**,** 5116-5126.

DOEING, D. C., BOROWICZ, J. L. & CROCKETT, E. T. 2003. Gender dimorphism in differential peripheral blood leukocyte counts in mice using cardiac, tail, foot, and saphenous vein puncture methods. BMC clinical pathology.

DONLAN, R. M. & COSTERTON, J. W. 2002. Biofilms: Survival mechanisms of clinically relevant microorganisms. *Clinical Microbiology Reviews,* 15**,** 167-193.

DOROSHENKO, N., RIMMER, S., HOSKINS, R., GARG, P., SWIFT, T., SPENCER, H. L. M., LORD, R. M., KATSIKOGIANNI, M., POWNALL, D., MACNEIL, S., DOUGLAS, C. W. I. & SHEPHERD, J. 2018. Antibiotic functionalised polymers reduce bacterial biofilm and bioburden in a simulated infection of the cornea. *Biomaterials Science,* 6**,** 2101-2109.

DREIER, J. & RUGGERONE, P. 2015. Interaction of antibacterial compounds with RND efflux pumps in Pseudomonas aeruginosa. *Frontiers in Microbiology,* 6.

DUA, H. S., FARAJ, L. A., SAID, D. G., GRAY, T. & LOWE, J. 2013. Human Corneal Anatomy Redefined A Novel Pre-Descemet's Layer (Dua's Layer). *Ophthalmology,* 120**,** 1778-1785.

DUROSE, J. B., LI, J., CHIEN, S. & SPECTOR, D. H. 2012. Infection of Vascular Endothelial Cells with Human Cytomegalovirus under Fluid Shear Stress Reveals Preferential Entry and Spread of Virus in Flow Conditions Simulating Atheroprone Regions of the Artery. *Journal of Virology,* 86**,** 13745-13755.

DUTTA, D., COLE, N. & WILLCOX, M. 2012. Factors influencing bacterial adhesion to contact lenses. *Molecular Vision,* 18**,** 14-21.

EHLERS, N., HEEGAARD, S., HJORTDAL, J., IVARSEN, A., NIELSEN, K. & PRAUSE, J. U. 2010. Morphological evaluation of normal human corneal epithelium. *Acta Ophthalmologica,* 88**,** 858-861.

EIDHIN, D. N., PERKINS, S., FRANCOIS, P., VAUDAUX, P., HOOK, M. & FOSTER, T. J. 1998. Clumping factor B (ClfB), a new surface-located fibrinogen-binding adhesin of Staphylococcus aureus. *Molecular Microbiology,* 30**,** 245-257.

EL SOLH, A. A. & ALHAJHUSAIN, A. 2009. Update on the treatment of Pseudomonas aeruginosa pneumonia. *Journal of Antimicrobial Chemotherapy,* 64**,** 229-238.

ELBADAWY, H. M., SALVALAIO, G., PAREKH, M., RUZZA, A., BARUZZO, M., CAGINI, C., PONZIN, D. & FERRARI, S. 2015. A superfusion apparatus for ex vivo human eye irritation investigations. *Toxicology in Vitro,* 29**,** 1619-1627.

ELGAWIDI, A., MOHSIN, M. I., ALI, F., WATTS, A., MONK, P. N., THOMAS, M. S. & PARTRIDGE, L. J. 2020. A role for tetraspanin proteins in regulating fusion induced by Burkholderia thailandensis (vol 81, pg 729, 2020). *Medical Microbiology and Immunology,* 209**,** 643-652.

EMAM, A., YU, A. R., PARK, H. J., MAHFOUD, R., KUS, J., BURROWS, L. L. & LINGWOOD, C. A. 2006. Laboratory and clinical Pseudomonas aeruginosa strains do not bind glycosphingolipids in vitro or during type IV pill-mediated initial host cell attachment. *Microbiology-Sgm,* 152**,** 2789-2799.

EPELMAN, S., STACK, D., BELL, C., WONG, E., NEELY, G. G., KRUTZIK, S., MIYAKE, K., KUBES, P., ZBYTNUIK, L. D., MA, L. L., XIE, X. B., WOODS, D. E. & MODY, C. H. 2004. Different domains of Pseudomonas aeruginosa exoenzyme S activate distinct TLRs. *Journal of Immunology,* 173**,** 2031-2040.

ERIE, J. C., NEVITT, M. P., HODGE, D. O. & BALLARD, D. 1993. INCIDENCE OF ULCERATIVE KERATITIS IN A DEFINED POPULATION FROM 1950 THROUGH 1988. *Archives of Ophthalmology,* 111**,** 1665-1671.

EUCAST. 2021a. Breakpoint tables for interpretation of MICs and zone diameters. http://www.eucast.org.

EUCAST. 2021b. EUCAST reading guide for broth microdilution. http://www.eucast.org.

EUCAST. 2021c. Routine and extended internal quality control for MIC determination and disk diffusion as recommended by EUCAST. http://www.eucast.org.

FANAEI, M., MONK, P. N. & PARTRIDGE, L. J. 2011. The role of tetraspanins in fusion. *Biochemical Society Transactions,* 39**,** 524-528.

FELDMAN, M., BRYAN, R., RAJAN, S., SCHEFFLER, L., BRUNNERT, S., TANG, H. & PRINCE, A. 1998. Role of flagella in pathogenesis of Pseudomonas aeruginosa pulmonary infection. *Infection and Immunity,* 66**,** 43-51.

FERNANDEZ, L. & HANCOCK, R. E. W. 2012. Adaptive and Mutational Resistance: Role of Porins and Efflux Pumps in Drug Resistance. *Clinical Microbiology Reviews,* 25**,** 661-+.

FILLOUX, A. 2011. Protein secretion systems in Pseudomonas aeruginosa: an essay on diversity, evolution, and function. *Frontiers in Microbiology,* 2**,** 21.

FLEISZIG, S. M. J., KROKEN, A. R., NIETO, V., GROSSER, M. R., WAN, S. J., METRUCCIO, M. M. E. & EVANS, D. J. 2019. Contact lens-related corneal infection: Intrinsic resistance and its compromise. *Progress in retinal and eye research***,** 100804.

FLEISZIG, S. M. J., KWONG, M. S. F. & EVANS, D. J. 2003. Modification of Pseudomonas aeruginosa interactions with corneal epithelial cells by human tear fluid. *Infection and Immunity,* 71**,** 3866-3874.

FLOCK, J. I., FROMAN, G., JONSSON, K., GUSS, B., SIGNAS, C., NILSSON, B., RAUCCI, G., HOOK, M., WADSTROM, T. & LINDBERG, M. 1987. CLONING AND EXPRESSION OF THE GENE FOR A FIBRONECTIN-BINDING PROTEIN FROM STAPHYLOCOCCUS-AUREUS. *Embo Journal,* 6**,** 2351-2357.

FOSTER, T. J., GEOGHEGAN, J. A., GANESH, V. K. & HOOK, M. 2014. Adhesion, invasion and evasion: the many functions of the surface proteins of Staphylococcus aureus. *Nature Reviews Microbiology,* 12**,** 49-62.

FOWLER, T., WANN, E. R., JOH, D., JOHANSSON, S. A., FOSTER, T. J. & HOOK, M. 2000. Cellular invasion by Staphylococcus aureus involves a fibronectin bridge between the bacterial fibronectin-binding MSCRAMMs and host cell beta 1 integrins. *European Journal of Cell Biology,* 79**,** 672-679.

FRESCHI, L., VINCENT, A. T., JEUKENS, J., EMOND-RHEAULT, J. G., KUKAVICA-IBRULJ, I., DUPONT, M. J., CHARETTE, S. J., BOYLE, B. & LEVESQUE, R. C. 2019. The Pseudomonas aeruginosa Pan-Genome Provides New Insights on Its Population Structure, Horizontal Gene Transfer, and Pathogenicity. *Genome Biology and Evolution,* 11**,** 109-120.

GARCIA, B., MERAYO-LLOVES, J., RODRIGUEZ, D., ALCALDE, I., GARCIA-SUAREZ, O., ALFONSO, J. F., BAAMONDE, B., FERNANDEZ-VEGA, A., VAZQUEZ, F. & QUIROS, L. M. 2016. Different Use of Cell Surface Glycosaminoglycans As Adherence Receptors to Corneal Cells by Gram Positive and Gram Negative Pathogens. *Frontiers in Cellular and Infection Microbiology,* 6**,** 12.

GARCIA-NUNEZ, M., MARTI, S., PUIG, C., PEREZ-BROCAL, V., MILLARES, L., SANTOS, S., ARDANUY, C., MOYA, A., LINARES, J. & MONSO, E. 2017. Bronchial microbiome, PA biofilm-forming capacity and exacerbation in severe COPD patients colonized by P-aeruginosa. *Future Microbiology,* 12**,** 379-392.

GEDDE, M. M., HIGGINS, D. E., TILNEY, L. G. & PORTNOY, D. A. 2000. Role of listeriolysin O in cell-to-cell spread of Listeria monocytogenes. *Infection and Immunity,* 68**,** 999-1003.

GEOGHEGAN, J. A. & DUFRENE, Y. F. 2018. Mechanomicrobiology: How Mechanical Forces Activate Staphylococcus aureus Adhesion. *Trends in Microbiology,* 26**,** 645-648.

GILL, D. B. & ATKINSON, J. P. 2004. CD46 in Neisseria pathogenesis. *Trends in Molecular Medicine,* 10**,** 459-465.

GIPSON, I. K. & ARGUESO, P. 2003. Role of mucins in the function of the corneal and conjunctival epithelia. *International Review of Cytology - a Survey of Cell Biology, Vol 231,* 231**,** 1-49.

GIPSON, I. K., SPURR-MICHAUD, S., ARGUESO, P., TISDALE, A., NG, T. F. & RUSSO, C. L. 2003. Mucin gene expression in immortalized human corneal-limbal and conjunctival epithelial cell lines. *Investigative Ophthalmology & Visual Science,* 44**,** 2496-2506.

GIPSON, I. K., SPURR-MICHAUD, S., TISDALE, A. & MENON, B. B. 2014. Comparison of the Transmembrane Mucins MUC1 and MUC16 in Epithelial Barrier Function. *Plos One,* 9**,** 12.

GONDELAUD, F. & RICARD-BLUM, S. 2019. Structures and interactions of syndecans. *Febs Journal,* 286**,** 2994-3007.

GONG, W., LIU, Y., HUANG, B., LEI, Z., WU, F. H., LI, D., FENG, Z. H. & ZHANG, G. M. 2008. Recombinant CBD-HepII polypeptide of fibronectin inhibits alpha v beta 3 signaling and hematogenous metastasis of tumor. *Biochemical and Biophysical Research Communications,* 367**,** 144-149.

GRECO, D., VELLONEN, K. S., TURNER, H. C., HAKLI, M., TERVO, T., AUVINEN, P., WOLOSIN, J. M. & URTTI, A. 2010. Gene expression analysis in SV-40 immortalized human corneal epithelial cells cultured with an air-liquid interface. *Molecular Vision,* 16**,** 2109-2120.

GREEN, L. R., MONK, P. N., PARTRIDGE, L. J., MORRIS, P., GORRINGE, A. R. & READ, R. C. 2011. Cooperative Role for Tetraspanins in Adhesin-Mediated Attachment of Bacterial Species to Human Epithelial Cells. *Infection and Immunity,* 79**,** 2241-2249.

GREEN, M., SARA, S., HUGHES, I., APEL, A. & STAPLETON, F. 2019. Trends in contact lens microbial keratitis 1999 to 2015: a retrospective clinical review. *Clinical and Experimental Ophthalmology,* 47**,** 726-732.

GROSSMAN, T. H. 2016. Tetracycline Antibiotics and Resistance. *Cold Spring Harbor Perspectives in Medicine,* 6.

GRUBB, S. E. W., MURDOCH, C., SUDBERY, P. E., SAVILLE, S. P., LOPEZ-RIBOT, J. L. & THORNHILL, M. H. 2009. Adhesion of Candida albicans to Endothelial Cells under Physiological Conditions of Flow. *Infection and Immunity,* 77**,** 3872-3878.

GUINDOLET, D., CROUZET, E., HE, Z. G., HERBEPIN, P., JUMELLE, C., PERRACHE, C., DUMOLLARD, J. M., FOREST, F., PEOC'H, M., GAIN, P., GABISON, E. & THURET, G. 2017. Storage of Porcine Cornea in an Innovative Bioreactor. *Investigative Ophthalmology & Visual Science,* 58**,** 5899-5909.

GUNTHER, J., PETZL, W., BAUER, I., PONSUKSILI, S., ZERBE, H., SCHUBERTH, H. J., BRUNNER, R. M. & SEYFERT, H. M. 2017. Differentiating Staphylococcus aureus from Escherichia coli mastitis: S. aureus triggers unbalanced immune-dampening and host cell invasion immediately after udder infection. *Scientific Reports,* 7.

GUNTHER, J. & SEYFERT, H. M. 2018. The first line of defence: insights into mechanisms and relevance of phagocytosis in epithelial cells. *Seminars in Immunopathology,* 40**,** 555-565.

GUREVICH, A., SAVELIEV, V., VYAHHI, N. & TESLER, G. 2013. QUAST: quality assessment tool for genome assemblies. *Bioinformatics,* 29**,** 1072-1075.

HAHNE, M. & REICHL, S. 2011. Development of a serum-free human cornea construct for in vitro drug absorption studies: The influence of varying cultivation parameters on barrier characteristics. *International Journal of Pharmaceutics,* 416**,** 268-279.

HAIKO, J. & WESTERLUND-WIKSTROM, B. 2013. The role of the bacterial flagellum in adhesion and virulence. *Biology,* 2**,** 1242-67.

HAKKARAINEN, J. J., REINISALO, M., RAGAUSKAS, S., SEPPANEN, A., KAJA, S. & KALESNYKAS, G. 2016. Acute cytotoxic effects of marketed ophthalmic formulations on human corneal epithelial cells. *International Journal of Pharmaceutics,* 511**,** 73-78.

HALEY, P. J. 2003. Species differences in the structure and function of the immune system. *Toxicology,* 188**,** 49-71.

HALL, C. W. & MAH, T. F. 2017. Molecular mechanisms of biofilm-based antibiotic resistance and tolerance in pathogenic bacteria. *Fems Microbiology Reviews,* 41**,** 276-301.

HALOVA, I. & DRABER, P. 2016. Tetraspanins and Transmembrane Adaptor Proteins As Plasma Membrane Organizers - Mast Cell Case. *Frontiers in Cell and Developmental Biology,* 4**,** 14.

HAMPEL, U., GARREIS, F., BURGEMEISTER, F., ESSEL, N. & PAULSEN, F. 2018. Effect of intermittent shear stress on corneal epithelial cells using an in vitro flow culture model. *Ocular Surface,* 16**,** 341-351.

HANKE, M. L. & KIELIAN, T. 2012. Deciphering mechanisms of staphylococcal biofilm evasion of host immunity. *Frontiers in Cellular and Infection Microbiology,* 2**,** 12.

HASEGAWA, H., NAGANUMA, K., NAKAGAWA, Y. & MATSUYAMA, T. 2003. Membrane filter (pore size, 0.22-0.45 mu m; thickness, 150 mu m) passing-through activity of Pseudomonas aeruginosa and other bacterial species with indigenous infiltration ability. *Fems Microbiology Letters,* 223**,** 41-46.

HATAMI-MARBINI, H., ETEBU, E. & RAHIMI, A. 2013. Swelling Pressure and Hydration Behavior of Porcine Corneal Stroma. *Current Eye Research,* 38**,** 1124-1132.

HAUCK, C. R. 2002. Cell adhesion receptors - signaling capacity and exploitation by bacterial pathogens. *Medical Microbiology and Immunology,* 191**,** 55-62.

HAYASHI, S., OSAWA, T. & TOHYAMA, K. 2002. Comparative observations on corneas, with special reference to Bowman's layer and Descemet's membrane in mammals and amphibians. *Journal of Morphology,* 254**,** 247-258.

HAYASHIDA, A., AMANO, S. & PARK, P. W. 2011. Syndecan-1 Promotes Staphylococcus aureus Corneal Infection by Counteracting Neutrophil-mediated Host Defense. *Journal of Biological Chemistry,* 286**,** 3288-3297.

HAYES, S., BOOTE, C., LEWIS, J., SHEPPARD, J., ABAHUSSIN, M., QUANTOCK, A. J., PURSLOW, C., VOTRUBA, M. & MEEK, K. M. 2007. Comparative study of fibrillar collagen arrangement in

the corneas of primates and other mammals. *Anatomical Record-Advances in Integrative Anatomy and Evolutionary Biology,* 290**,** 1542-1550.

HE, C., ZHOU, Y., LIU, F., LIU, H., TAN, H., JIN, S., WU, W. & GE, B. 2017. Bacterial Nucleotidyl Cyclase Inhibits the Host Innate Immune Response by Suppressing TAK1 Activation. *Infection and immunity,* 85.

HEIDARI, H., HADADI, M., EBRAHIM-SARAIE, H. S., MIRZAEI, A., TAJI, A., HOSSEINI, S. R. & MOTAMEDIFAR, M. 2018. Characterization of virulence factors, antimicrobial resistance patterns and biofilm formation of Pseudomonas aeruginosa and Staphylococcus spp. strains isolated from corneal infection. *Journal Francais D Ophtalmologie,* 41**,** 823-829.

HEIMER, S. R., YAMADA, A., RUSSELL, H. & GILMORE, M. S. 2010. Response of corneal epithelial cells to Staphylococcus aureus. *Virulence,* 1**,** 223-235.

HEINIGER, R. W., WINTHER-LARSEN, H. C., PICKLES, R. J., KOOMEY, M. & WOLFGANG, M. C. 2010. Infection of human mucosal tissue by Pseudomonas aeruginosa requires sequential and mutually dependent virulence factors and a novel pilus-associated adhesin. *Cellular Microbiology,* 12**,** 1158-1173.

HELDERMAN, F., SEGERS, D., DE CROM, R., HIERCK, B. P., POELMANN, R. E., EVANS, P. C. & KRAMS, R. 2007. Effect of shear stress on vascular inflammation and plaque development. *Current Opinion in Lipidology,* 18**,** 527-533.

HEMLER, M. E. 2005. Tetraspanin functions and associated microdomains. *Nature Reviews Molecular Cell Biology,* 6**,** 801-811.

HENRIKSSON, J. T., MCDERMOTT, A. M. & BERGMANSON, J. P. G. 2009. Dimensions and Morphology of the Cornea in Three Strains of Mice. *Investigative Ophthalmology & Visual Science,* 50**,** 3648-3654.

HENRIQUES, M., SOUSA, C., LIRA, M., ELISABETE, M., OLIVEIRA, R. & AZEREDO, J. 2005. Adhesion of Pseudomonas aeruginosa and Staphylococcus epidermidis to silicone-hydrogel contact lenses. *Optometry and Vision Science,* 82**,** 446-450.

HERMAN-BAUSIER, P., LABATE, C., TOWELL, A. M., DERCLAYE, S., GEOGHEGAN, J. A. & DUFRENE, Y. F. 2018. Staphylococcus aureus clumping factor A is a force-sensitive molecular switch that activates bacterial adhesion. *Proceedings of the National Academy of Sciences of the United States of America,* 115**,** 5564-5569.

HILL, D., ROSE, B., PAJKOS, A., ROBINSON, M., BYE, P., BELL, S., ELKINS, M., THOMPSON, B., MACLEOD, C., AARON, S. D. & HARBOUR, C. 2005. Antibiotic susceptibilities of Pseudomonas aeruginosa isolates derived from patients with cystic fibrosis under aerobic, anaerobic, and biofilm conditions. *Journal of Clinical Microbiology,* 43**,** 5085-5090.

HILLIAM, Y., KAYE, S. & WINSTANLEY, C. 2020. Pseudomonas aeruginosa and microbial keratitis. Journal of Medical Microbiology.

HOBDEN, J. A. 2002. Pseudomonas aeruginosa proteases and corneal virulence. *DNA and Cell Biology,* 21**,** 391-396.

HOIBY, N., CIOFU, O., JOHANSEN, H. K., SONG, Z. J., MOSER, C., JENSEN, P. O., MOLIN, S., GIVSKOV, M., TOLKER-NIELSEN, T. & BJARNSHOLT, T. 2011. The clinical impact of bacterial biofilms. *International Journal of Oral Science,* 3**,** 55-65.

HOLLOWAY, B. W. 1955. GENETIC RECOMBINATION IN PSEUDOMONAS-AERUGINOSA. *Journal of General Microbiology,* 13**,** 572-581.

HOUANG, E., LAM, D., FAN, D. & SEAL, D. 2001. Microbial keratitis in Hong Kong: relationship to climate, environment and contact-lens disinfection. *Transactions of the Royal Society of Tropical Medicine and Hygiene,* 95**,** 361-367.

HSIAO, Y.-T., FANG, P.-C., CHEN, J.-L., HSU, S.-L., CHAO, T.-L., YU, H.-J., LAI, Y.-H., HUANG, Y.-T. & KUO, M.-T. 2018. Molecular Bioburden of the Lens Storage Case for Contact Lens-Related Keratitis. *Cornea,* 37**,** 1542-1550.

HUBATSCH, I., RAGNARSSON, E. G. E. & ARTURSSON, P. 2007. Determination of drug permeability and prediction of drug absorption in Caco-2 monolayers. *Nature Protocols,* 2**,** 2111-2119.

HUGHES, P., MARSHALL, D., REID, Y., PARKES, H. & GELBER, C. 2007. The costs of using unauthenticated, over-passaged cell lines: how much more data do we need? *Biotechniques,* 43**,** 575-584.

HUME, E. B. H., DAJCS, J. J., MOREAU, J. M., SLOOP, G. D., WILLCOX, M. D. P. & O'CALLAGHAN, R. J. 2001. Staphylococcus corneal virulence in a new topical model of infection. *Investigative Ophthalmology & Visual Science,* 42**,** 2904-2908.

HUMPHREY, J. D., SCHWARTZ, M. A., TELLIDES, G. & MILEWICZ, D. M. 2015. Role of Mechanotransduction in Vascular Biology Focus on Thoracic Aortic Aneurysms and Dissections. *Circulation Research,* 116**,** 1448-1461.

HUTCHINGS, M. I., TRUMAN, A. W. & WILKINSON, B. 2019. Antibiotics: past, present and future. *Current Opinion in Microbiology,* 51**,** 72-80.

JAY, L., BROCAS, A., SINGH, K., KIEFFER, J. C., BRUNETTE, I. & OZAKI, T. 2008. Determination of porcine corneal layers with high spatial resolution by simultaneous second and third harmonic generation microscopy. *Optics Express,* 16**,** 16284-16293.

JENUL, C. & HORSWILL, A. R. 2019. Regulation of Staphylococcus aureus Virulence. *Microbiology Spectrum,* 7.

JETT, B. D. & GILMORE, M. S. 2002. Internalization of Staphylococcus aureus by human corneal epithelial cells: Role of bacterial fibronectin-binding protein and host cell factors. *Infection and Immunity,* 70**,** 4697-4700.

JIAN, H. J., YU, J. T., LI, Y. J., UNNIKRISHNAN, B., HUANG, Y. F., LUO, L. J., MA, D. H. K., HARROUN, S. G., CHANG, H. T., LIN, H. J., LAI, J. Y. & HUANG, C. C. 2020. Highly adhesive carbon quantum dots from biogenic amines for prevention of biofilm formation. *Chemical Engineering Journal,* 386.

JIANG, X. Y., MCCLELLAN, S. A., BARRETT, R. P., ZHANG, Y. F., FOLDENAUER, M. E. & HAZLETT, L. D. 2012. The Role of VIP in Cornea. *Investigative Ophthalmology & Visual Science,* 53**,** 7560-7566.

JINNO, A., HAYASHIDA, A., JENKINSON, H. F. & PARK, P. W. 2020. Syndecan-1 Promotes Streptococcus pneumoniae Corneal Infection by Facilitating the Assembly of Adhesive Fibronectin Fibrils. *Mbio,* 11.

JOHNSON, M. D. L., GARRETT, C. K., BOND, J. E., COGGAN, K. A., REDINBO, M. R. & WOLFGANG, M. C. 2011. Pseudomonas aeruginosa PilY1 Binds Integrin in an RGD- and Calcium-Dependent Manner. Figshare.

JONSSON, K., SIGNAS, C., MULLER, H. P. & LINDBERG, M. 1991. 2 DIFFERENT GENES ENCODE FIBRONECTIN BINDING-PROTEINS IN STAPHYLOCOCCUS-AUREUS - THE COMPLETE NUCLEOTIDE-SEQUENCE AND CHARACTERIZATION OF THE 2ND GENE. *European Journal of Biochemistry,* 202**,** 1041-1048.

JOUANNET, S., SAINT-POL, J., FERNANDEZ, L., NGUYEN, V., CHARRIN, S., BOUCHEIX, C., BROU, C., MILHIET, P. E. & RUBINSTEIN, E. 2016. TspanC8 tetraspanins differentially regulate the cleavage of ADAM10 substrates, Notch activation and ADAM10 membrane compartmentalization. *Cellular and Molecular Life Sciences,* 73**,** 1895-1915.

JURADO-MARTIN, I., SAINZ-MEJIAS, M. & MCCLEAN, S. 2021. Pseudomonas aeruginosa: An Audacious Pathogen with an Adaptable Arsenal of Virulence Factors. *International Journal of Molecular Sciences,* 22**,** 35.

KACKAR, S., SUMAN, E. & KOTIAN, M. S. 2017. Bacterial and Fungal Biofilm formation on Contact Lenses and their Susceptibility to Lens Care Solutions. *Indian Journal of Medical Microbiology,* 35**,** 80-84.

KAHN, C. R. & RHIM, J. 1996. *Human corneal epithelial cell lines with extended lifespan*. 3.

KAHN, C. R., YOUNG, E., LEE, I. H. & RHIM, J. S. 1993. HUMAN CORNEAL EPITHELIAL PRIMARY CULTURES AND CELL-LINES WITH EXTENDED LIFE-SPAN - IN-VITRO MODEL FOR OCULAR STUDIES. *Investigative Ophthalmology & Visual Science,* 34**,** 3429-3441.

KANG, Y. G., SHIN, J. W., PARK, S. H., OH, M. J., PARK, H. S. & KIM, S. H. 2014. Effects of Flow-Induced Shear Stress on Limbal Epithelial Stem Cell Growth and Enrichment. *Plos One,* 9.

KAO, W. W. Y., LIU, C. Y., CONVERSE, R. L., SHIRAISHI, A., KAO, C. W. C., ISHIZAKI, M., DOETSCHMAN, T. & DUFFY, J. 1996. Keratin 12-deficient mice have fragile corneal epithelia. *Investigative Ophthalmology & Visual Science,* 37**,** 2572-2584.

KARLSSON, J. & ARTURSSON, P. 1991. A METHOD FOR THE DETERMINATION OF CELLULAR PERMEABILITY COEFFICIENTS AND AQUEOUS BOUNDARY-LAYER THICKNESS IN MONOLAYERS OF INTESTINAL EPITHELIAL (CACO-2) CELLS GROWN IN PERMEABLE FILTER CHAMBERS. *International Journal of Pharmaceutics,* 71**,** 55-64.

KATO, K., LILLEHOJ, E. P., KAI, H. & KIM, K. C. 2010. MUC1 expression by human airway epithelial cells mediates Pseudomonas aeruginosa adhesion. *Frontiers in bioscience (Elite edition),* 2**,** 68-77.

KAYE, K. S., POGUE, J. M., TRAN, T. B., NATION, R. L. & LI, J. 2016. Agents of Last Resort Polymyxin Resistance. *Infectious Disease Clinics of North America,* 30**,** 391-+.

KAYE, S., TUFT, S., NEAL, T., TOLE, D., LEEMING, J., FIGUEIREDO, F., ARMSTRONG, M., MCDONNELL, P., TULLO, A. & PARRY, C. 2010. Bacterial Susceptibility to Topical Antimicrobials and Clinical Outcome in Bacterial Keratitis. *Investigative Ophthalmology & Visual Science,* 51**,** 362-368.

KAZMIERCZAK, B. I. & ENGEL, J. N. 2002. Pseudomonas aeruginosa ExoT acts in vivo as a GTPase-activating protein for RhoA, Rac1, and Cdc42. *Infection and Immunity,* 70**,** 2198-2205.

KEAY, L., EDWARDS, K., NADUVILATH, T., TAYLOR, H. R., SNIBSON, G. R., FORDE, K. & STAPLETON, F. 2006. Microbial keratitis - Predisposing factors and morbidity. *Ophthalmology,* 113**,** 109-116.

KEAY, L., EDWARDS, K. & STAPLETON, F. 2009. Signs, Symptoms, and Comorbidities in Contact Lens-Related Microbial Keratitis. *Optometry and Vision Science,* 86**,** 803-809.

KERRIGAN, S. W., CLARKE, N., LOUGHMAN, A., MEADE, G., FOSTER, T. J. & COX, D. 2008. Molecular basis for Staphylococcus aureus-mediated platelet aggregate formation under arterial shear in vitro. *Arteriosclerosis Thrombosis and Vascular Biology,* 28**,** 335-340.

KETKO, A. K., LIN, C. H., MOORE, B. B. & LEVINE, A. M. 2013. Surfactant Protein A Binds Flagellin Enhancing Phagocytosis and IL-1 beta Production. *Plos One,* 8**,** 9.

KHAN, M., STAPLETON, F., SUMMERS, S., RICE, S. A. & WILLCOX, M. D. P. 2020. Antibiotic Resistance Characteristics ofPseudomonas aeruginosaIsolated from Keratitis in Australia and India. *Antibiotics-Basel,* 9.

KIMURA, K., TERANISHI, S. & NISHIDA, T. 2009. Interleukin-1 beta-Induced Disruption of Barrier Function in Cultured Human Corneal Epithelial Cells. *Investigative Ophthalmology & Visual Science,* 50**,** 597-603.

KITAZAWA, K., HIKICHI, T., NAKAMURA, T., SOTOZONO, C., KINOSHITA, S. & MASUI, S. 2017. PAX6 regulates human corneal epithelium cell identity. *Experimental Eye Research,* 154**,** 30-38.

KLOTZ, S. A., AU, Y. K. & MISRA, R. P. 1989. A PARTIAL-THICKNESS EPITHELIAL DEFECT INCREASES THE ADHERENCE OF PSEUDOMONAS-AERUGINOSA TO THE CORNEA. *Investigative Ophthalmology & Visual Science,* 30**,** 1069-1074.

KOLPEN, M., BJARNSHOLT, T., MOSER, C., HANSEN, C. R., RICKELT, L. F., KUHL, M., HEMPEL, C., PRESSLER, T., HOIBY, N. & JENSEN, P. O. 2014. Nitric oxide production by polymorphonuclear leucocytes in infected cystic fibrosis sputum consumes oxygen. *Clinical and Experimental Immunology,* 177**,** 310-319.

KONG, C., NEOH, H. M. & NATHAN, S. 2016. Targeting Staphylococcus aureus Toxins: A Potential form of Anti-Virulence Therapy. *Toxins,* 8.

KORZENIEWSKI, C. & CALLEWAERT, D. M. 1983. AN ENZYME-RELEASE ASSAY FOR NATURAL CYTO-TOXICITY. *Journal of Immunological Methods,* 64**,** 313-320.

KOZLOVA, A. A., VERKHOVSKII, R. A., ERMAKOV, A. V. & BRATASHOV, D. N. 2020. Changes in Autofluorescence Level of Live and Dead Cells for Mouse Cell Lines. *Journal of Fluorescence,* 30**,** 1483-1489.

KRACHMER, J. H., MANNIS, M. J. & HOLLAND, E. J. 2010. Cornea and Sclera: Anatomy and Physiology. *Cornea.* 3rd ed.: Elsevier Health Sciences.

KREGER, A. S. & GRAY, L. D. 1978. PURIFICATION OF PSEUDOMONAS-AERUGINOSA PROTEASES AND MICROSCOPIC CHARACTERIZATION OF PSEUDOMONAL PROTEASE-INDUCED RABBIT CORNEAL DAMAGE. *Infection and Immunity,* 19**,** 630-648.

KUGADAS, A., GEDDES-MCALISTER, J., GUY, E., DIGIANDOMENICO, A., SYKES, D. B., MANSOUR, M. K., MIRCHEV, R. & GADJEVA, M. 2019. Frontline Science: Employing enzymatic treatment options for management of ocular biofilm-based infections. *Journal of Leukocyte Biology,* 105**,** 1099-1110.

KUMAR, A., ZHANG, J. & YU, F. S. X. 2004. Innate immune response of corneal epithelial cells to Staphylococcus aureus infection: Role of peptidoglycan in stimulating proinflammatory cytokine secretion. *Investigative Ophthalmology & Visual Science,* 45**,** 3513-3522.

KUNIMOTO, D. Y., SHARMA, S., GARG, P. & RAO, G. N. 1999. In vitro susceptibility of bacterial keratitis pathogens to ciprofloxacin - Emerging resistance. *Ophthalmology,* 106**,** 80-85.

KWONG, M. S. F., EVANS, D. J., NI, M., COWELL, B. A. & FLEISZIG, S. M. J. 2007. Human tear fluid protects against Pseudomonas aeruginosa keratitis in a murine experimental model. *Infection and Immunity,* 75**,** 2325-2332.

LAI, T. & TANG, S. 2014. Cornea characterization using a combined multiphoton microscopy and optical coherence tomography system. *Biomedical Optics Express,* 5**,** 1494-1511.

LAKKIS, C., MENDOZA, M. N., FAN, D., CHAUHAN, A., SRINIVAS, S. P. & FLEISZIG, S. M. J. 2001. Shear stress reduces corneal epithelial cell killing by cytotoxic P-aeruginosa. *Investigative Ophthalmology & Visual Science,* 42**,** S593-S593.

LALITHA, P., MANOHARAN, G., KARPAGAM, R., PRAJNA, N. V., SRINIVASAN, M., MASCARENHAS, J., DAS, M., PORCO, T. C., LIETMAN, T. M., CEVALLOS, V. & KEENAN, J. D. 2017. Trends in antibiotic resistance in bacterial keratitis isolates from South India. *British Journal of Ophthalmology,* 101**,** 108-113.

LAWINBRUSSEL, C. A., REFOJO, M. F., LEONG, F. L., HANNINEN, L. & KENYON, K. R. 1993. EFFECT OF PSEUDOMONAS-AERUGINOSA CONCENTRATION IN EXPERIMENTAL CONTACT LENS-RELATED MICROBIAL KERATITIS. *Cornea,* 12**,** 10-18.

LECUYER, S., RUSCONI, R., SHEN, Y., FORSYTH, A., VLAMAKIS, H., KOLTER, R. & STONE, H. A. 2011. Shear Stress Increases the Residence Time of Adhesion of Pseudomonas aeruginosa. *Biophysical Journal,* 100**,** 341-350.

LEE, K. K., SHETH, H. B., WONG, W. Y., SHERBURNE, R., PARANCHYCH, W., HODGES, R. S., LINGWOOD, C. A., KRIVAN, H. & IRVIN, R. T. 1994. THE BINDING OF PSEUDOMONAS-AERUGINOSA PILI TO GLYCOSPHINGOLIPIDS IS A TIP-ASSOCIATED EVENT INVOLVING THE C-TERMINAL REGION OF THE STRUCTURAL PILIN SUBUNIT. *Molecular Microbiology,* 11**,** 705-713.

LEIGHTON, T. L., BUENSUCESO, R. N. C., HOWELL, P. L. & BURROWS, L. L. 2015. Biogenesis of Pseudomonas aeruginosa type IV pili and regulation of their function. *Environmental Microbiology,* 17**,** 4148-4163.

LEONARD, B. C., YANEZ-SOTO, B., RAGHUNATHAN, V. K., ABBOTT, N. L. & MURPHY, C. J. 2016. Species variation and spatial differences in mucin expression from corneal epithelial cells. *Experimental Eye Research,* 152**,** 43-48.

LEONARD, E. K., PAI, V. H., AMBERG, P., GARDNER, J. & ORWIN, E. J. 2012. Design and validation of a corneal bioreactor. *Biotechnology and Bioengineering,* 109**,** 3189-3198.

LEONG, Y. Y. & TONG, L. 2015. Barrier Function in the Ocular Surface: From Conventional Paradigms to New Opportunities. *Ocular Surface,* 13**,** 103-109.

LI, H. D., LI, X. Y., WANG, Z. L., FU, Y. K., AI, Q., DONG, Y. & YU, J. L. 2015. Autoinducer-2 regulates Pseudomonas aeruginosa PAO1 biofilm formation and virulence production in a dose-dependent manner. *Bmc Microbiology,* 15**,** 8.

LI, J., MA, X., ZHAO, L., LI, Y., ZHOU, Q. & DU, X. 2020. Extended contact lens wear promotes corneal norepinephrine secretion and *Pseudomonas aeruginosa* infection in mice. *Invest Ophthalmol Vis Sci,* 61**,** 17.

LI, M., DU, X., VILLARUZ, A. E., DIEP, B. A., WANG, D. C., SONG, Y., TIAN, Y. R., HU, J. H., YU, F. Y., LU, Y. & OTTO, M. 2012. MRSA epidemic linked to a quickly spreading colonization and virulence determinant. *Nature Medicine,* 18**,** 816-U217.

LI, T. & LU, L. 2005. Epidermal growth factor-induced proliferation requires down-regulation of Pax6 in corneal epithelial cells. *Journal of Biological Chemistry,* 280**,** 12988-12995.

LILLEHOJ, E. P., KIM, B. T. & KIM, K. C. 2002. Identification of Pseudomonas aeruginosa flagellin as an adhesin for Muc1 mucin. *American Journal of Physiology-Lung Cellular and Molecular Physiology,* 282**,** L751-L756.

LIM, T. P., LEE, W., TAN, T. Y., SASIKALA, S., TEO, J., HSU, L. Y., TAN, T. T., SYAHIDAH, N. & KWA, A. L. 2011. Effective Antibiotics in Combination against Extreme Drug-Resistant Pseudomonas aeruginosa with Decreased Susceptibility to Polymyxin B. *Plos One,* 6.

LIU, J. & LI, Z. J. 2021. Resident Innate Immune Cells in the Cornea. *Frontiers in Immunology,* 12.

LIVINGSTON, E. T., MURSALIN, M. H. & CALLEGAN, M. C. 2019. A Pyrrhic Victory: The PMN Response to Ocular Bacterial Infections. *Microorganisms,* 7**,** 35.

MADHU, S. N., JHA, K. K., KARTHYAYANI, A. P. & GAJJAR, D. U. 2018. Ex vivo Caprine Model to Study Virulence Factors in Keratitis. *Journal of Ophthalmic & Vision Research,* 13**,** 383-391.

MAKSIMOV, P., HERMOSILLA, C., KLEINERTZ, S., HIRZMANN, J. & TAUBERT, A. 2016. Besnoitia besnoiti infections activate primary bovine endothelial cells and promote PMN adhesion and NET formation under physiological flow condition. *Parasitology Research,* 115**,** 1991-2001.

MALTSEVA, I. A., FLEISZIG, S. M. J., EVANS, D. J., KERR, S., SIDHU, S. S., MCNAMARA, N. A. & BASBAUM, C. 2007. Exposure of human corneal epithelial cells to contact lenses in vitro suppresses the upregulation of human beta-defensin-2 in response to antigens of Pseudomonas aeruginosa. *Experimental Eye Research,* 85**,** 142-153.

MANTELLI, F. & ARGUESO, P. 2008. Functions of ocular surface mucins in health and disease. *Current Opinion in Allergy and Clinical Immunology,* 8**,** 477-483.

MARIM, F. M., SILVEIRA, T. N., LIMA, D. S. & ZAMBONI, D. S. 2010. A Method for Generation of Bone Marrow-Derived Macrophages from Cryopreserved Mouse Bone Marrow Cells. *Plos One,* 5**,** 8.

MARQUART, M. E. 2011. Animal Models of Bacterial Keratitis. *Journal of Biomedicine and Biotechnology***,** 12.

MARQUART, M. E., CABALLERO, A. R., CHOMNAWANG, M., THIBODEAUX, B. A., TWINING, S. S. & O'CALLAGHAN, R. J. 2005. Identification of a novel secreted protease from Pseudomonas aeruginosa that causes corneal erosions. *Investigative Ophthalmology & Visual Science,* 46**,** 3761-3768.

MARQUART, M. E. & O'CALLAGHAN, R. J. 2013. Infectious Keratitis: Secreted Bacterial Proteins That Mediate Corneal Damage. *Journal of Ophthalmology,* 2013.

MASTERTON, S. & AHEARNE, M. 2018. Mechanobiology of the corneal epithelium. *Experimental Eye Research,* 177**,** 122-129.

MATHERS, W. D. & DALEY, T. E. 1996. Tear flow and evaporation in patients with and without dry eye. *Ophthalmology,* 103**,** 664-669.

MATTICK, J. S. 2002. Type IV pili and twitching motility. *Annual Review of Microbiology,* 56**,** 289-314.

MAURIN, C., COURRIER, E., HE, Z. G., RIGAILL, J., JOSSE, J., LAURENT, F., GAIN, P., THURET, G. & VERHOEVEN, P. O. 2021. Key Role of Staphylococcal Fibronectin-Binding Proteins During the Initial Stage of Staphylococcus aureus Keratitis in Humans. *Frontiers in Cellular and Infection Microbiology,* 11.

MCARTHUR, A. G., WAGLECHNER, N., NIZAM, F., YAN, A., AZAD, M. A., BAYLAY, A. J., BHULLAR, K., CANOVA, M. J., DE PASCALE, G., EJIM, L., KALAN, L., KING, A. M., KOTEVA, K., MORAR, M., MULVEY, M. R., O'BRIEN, J. S., PAWLOWSKI, A. C., PIDDOCK, L. J. V., SPANOGIANNOPOULOS,

P., SUTHERLAND, A. D., TANG, I., TAYLOR, P. L., THAKER, M., WANG, W. L., YAN, M., YU, T. & WRIGHT, G. D. 2013. The Comprehensive Antibiotic Resistance Database. *Antimicrobial Agents and Chemotherapy,* 57**,** 3348-3357.

MCDERMOTT, A. M. 2013. Antimicrobial compounds in tears. *Experimental Eye Research,* 117**,** 53-61.

MEDAWAR, P. B. 1948. IMMUNITY TO HOMOLOGOUS GRAFTED SKIN .3. THE FATE OF SKIN HOMOGRAFTS TRANSPLANTED TO THE BRAIN, TO SUBCUTANEOUS TISSUE, AND TO THE ANTERIOR CHAMBER OF THE EYE. *British Journal of Experimental Pathology,* 29**,** 58-&.

MEEK, K. M., DENNIS, S. & KHAN, S. 2003. Changes in the refractive index of the stroma and its extrafibrillar matrix when the cornea swells. *Biophysical Journal,* 85**,** 2205-2212.

MEENAN, N. A. G., VISAI, L., VALTULINA, V., SCHWARZ-LINEK, U., NORRIS, N. C., GURUSIDDAPPA, S., HOOK, M., SPEZIALE, P. & POTTS, J. R. 2007. The tandem beta-zipper model defines high affinity fibronectin-binding repeats within staphylococcus aureus FnBPA. *Journal of Biological Chemistry,* 282**,** 25893-25902.

MERINDANO, M. D., COSTA, J., CANALS, M., POTAU, J. M. & RUANO, D. 2002. A comparative study of Bowman's layer in some mammals: Relationships with other constituent corneal structures. European Journal of Anatomy.

METRUCCIO, M. M. E., EVANS, D. J., GABRIEL, M. M., KADURUGAMUWA, J. L. & FLEISZIG, S. M. J. 2016. Pseudomonas aeruginosa Outer Membrane Vesicles Triggered by Human Mucosal Fluid and Lysozyme Can Prime Host Tissue Surfaces for Bacterial Adhesion. *Frontiers in Microbiology,* 7.

METRUCCIO, M. M. E., TAM, C., EVANS, D. J., XIE, A. L., STERN, M. E. & FLEISZIG, S. M. J. 2017. Contributions of MyD88-dependent receptors and CD11c-positive cells to corneal epithelial barrier function against Pseudomonas aeruginosa. *Scientific Reports,* 7.

METRUCCIO, M. M. E., WAN, S. J., HORNEMAN, H., KROKEN, A. R., SULLIVAN, A. B., TRUONG, T. N., MUN, J. J., TAM, C. K. P., FRITH, R., WELSH, L., GEORGE, M. D., MORRIS, C. A., EVANS, D. J. & FLEISZIG, S. M. J. 2019. A novel murine model for contact lens wear reveals clandestine IL-1R dependent corneal parainflammation and susceptibility to microbial keratitis upon inoculation with Pseudomonas aeruginosa. *Ocular Surface,* 17**,** 119-133.

MIKKELSEN, H., MCMULLAN, R. & FILLOUX, A. 2011. The Pseudomonas aeruginosa Reference Strain PA14 Displays Increased Virulence Due to a Mutation in ladS. *Plos One,* 6**,** 7.

MILES, A. A., MISRA, S. S. & IRWIN, J. O. 1938. The estimation of the bactericidal power of the blood. *Journal of Hygiene,* 38**,** 732-749.

MOHAMMED, I., SAID, D. G. & DUA, H. S. 2017. Human antimicrobial peptides in ocular surface defense. *Progress in Retinal and Eye Research,* 61**,** 1-22.

MOHAN, R. R., POSSIN, D. E., SINHA, S. & WILSON, S. E. 2003. Development of genetically engineered tet HPV16-E6/E7 transduced human corneal epithelial clones having tight regulation of proliferation and normal differentiation. *Experimental Eye Research,* 77**,** 395-407.

MOLDOVAN, A. & FRAUNHOLZ, M. J. 2019. In or out: Phagosomal escape of Staphylococcus aureus. *Cellular Microbiology,* 21.

MOLLADAVOODI, S., ROBICHAUD, M., WULFF, D. & GORBET, M. 2017. Corneal epithelial cells exposed to shear stress show altered cytoskeleton and migratory behaviour. *Plos One,* 12**,** 16.

MONK, P. N. & PARTRIDGE, L. J. 2012. Tetraspanins- Gateways for Infection. Infectious Disorders-Drug Targets.

MONTIE, T. C., DOYLEHUNTZINGER, D., CRAVEN, R. C. & HOLDER, I. A. 1982. LOSS OF VIRULENCE ASSOCIATED WITH ABSENCE OF FLAGELLUM IN AN ISOGENIC MUTANT OF PSEUDOMONAS-AERUGINOSA IN THE BURNED-MOUSE MODEL. *Infection and Immunity,* 38**,** 1296-1298.

MUN, J., TAM, C., CHAN, G., KIM, J. H., EVANS, D. & FLEISZIG, S. 2013. MicroRNA-762 Is Upregulated in Human Corneal Epithelial Cells in Response to Tear Fluid and Pseudomonas aeruginosa

Antigens and Negatively Regulates the Expression of Host Defense Genes Encoding RNase7 and ST2. *Plos One,* 8**,** 8.

MUN, J. J., TAM, C., KOWBEL, D., HAWGOOD, S., BARNETT, M. J., EVANS, D. J. & FLEISZIG, S. M. J. 2009. Clearance of Pseudomonas aeruginosa from a Healthy Ocular Surface Involves Surfactant Protein D and Is Compromised by Bacterial Elastase in a Murine Null-Infection Model. *Infection and Immunity,* 77**,** 2392-2398.

NAKAMURA, T., NISBIDA, K., DOTA, A. & KINOSHITA, S. 2002. Changes in conjunctival clusterin expression in severe ocular surface disease. *Investigative Ophthalmology & Visual Science,* 43**,** 1702-1707.

NAVARATNAM, J., UTHEIM, T. P., RAJASEKHAR, V. K. & SHAHDADFAR, A. 2015. Substrates for Expansion of Corneal Endothelial Cells towards Bioengineering of Human Corneal Endothelium. *Journal of Functional Biomaterials,* 6**,** 917-945.

NEUMANN, M. & SJOSTRAND, J. 1993. CENTRAL MICROBIAL KERATITIS IN A SWEDISH CITY POPULATION - A 3-YEAR PROSPECTIVE-STUDY IN GOTHENBURG. *Acta Ophthalmologica,* 71**,** 160-164.

NG, A. L. K., TO, K. K. W., CHOI, C. C. L., YUEN, L. H., YIM, S. M., CHAN, K. S. K., LAI, J. S. M. & WONG, I. Y. H. 2015. Predisposing Factors, Microbial Characteristics, and Clinical Outcome of Microbial Keratitis in a Tertiary Centre in Hong Kong: A 10-Year Experience. *Journal of Ophthalmology***,** 9.

NI, M. J., TAM, C., VERMA, A., RAMPHAL, R., HAWGOOD, S., EVANS, D. J. & FLEISZIG, S. M. J. 2008. Expression of surfactant protein D in human corneal epithelial cells is upregulated by Pseudomonas aeruginosa. *Fems Immunology and Medical Microbiology,* 54**,** 177-184.

NUNEZ-ALVAREZ, C. & OSBORNE, N. N. 2019. Enhancement of corneal epithelium cell survival, proliferation and migration by red light: Relevance to corneal wound healing. *Experimental Eye Research,* 180**,** 231-241.

O'CALLAGHAN, R., CABALLERO, A., TANG, A. H. & BIERDEMAN, M. 2019. Pseudomonas aeruginosa Keratitis: Protease IV and PASP as Corneal Virulence Mediators. *Microorganisms,* 7**,** 17.

O'CALLAGHAN, R. J. 2018. The Pathogenesis of Staphylococcus aureus Eye Infections. *Pathogens,* 7.

O'TOOLE, G., KAPLAN, H. B. & KOLTER, R. 2000. Biofilm formation as microbial development. *Annual Review of Microbiology,* 54**,** 49-79.

O'TOOLE, G. A. 2011. Microtiter Dish Biofilm Formation Assay. *Jove-Journal of Visualized Experiments***,** 3.

OJEDA, J. L., VENTOSA, J. A. & PIEDRA, S. 2001. The three-dimensional microanatomy of the rabbit and human cornea. A chemical and mechanical microdissection-SEM approach. *Journal of Anatomy,* 199**,** 567-576.

OKUROWSKA, K., ROY, S., THOKALA, P., PARTRIDGE, L., GARG, P., MACNEIL, S., MONK, P. N. & KARUNAKARAN, E. 2020. Establishing a Porcine Ex Vivo Cornea Model for Studying Drug Treatments against Bacterial Keratitis. *Journal of Visualized Experiments,* 159.

OLIVEIRA, D., BORGES, A. & SIMOES, M. 2018. Staphylococcus aureus Toxins and Their Molecular Activity in Infectious Diseases. *Toxins,* 10.

OLSEN, I. 2015. Biofilm-specific antibiotic tolerance and resistance. *European Journal of Clinical Microbiology & Infectious Diseases,* 34**,** 877-886.

ORANS, J., JOHNSON, M. D. L., COGGAN, K. A., SPERLAZZA, J. R., HEINIGER, R. W., WOLFGANG, M. C. & REDINBO, M. R. 2010. Crystal structure analysis reveals Pseudomonas PilY1 as an essential calcium-dependent regulator of bacterial surface motility. *Proceedings of the National Academy of Sciences of the United States of America,* 107**,** 1065-1070.

OUELLETTE, M. M., MCDANIEL, L. D., WRIGHT, W. E., SHAY, J. W. & SCHULTZ, R. A. 2000. The establishment of telomerase-immortalized cell lines representing human chromosome instability syndromes. *Human Molecular Genetics,* 9**,** 403-411.

PALMER, K. L., AYE, L. A. & WHITELEY, M. 2007. Nutritional cues control Pseudomonas aeruginosa multicellular Behavior in cystic fibrosis sputum. *Journal of Bacteriology,* 189**,** 8079-8087.

PARKINS, M. D., CERI, H. & STOREY, D. G. 2001. Pseudomonas aeruginosa GacA, a factor in multihost virulence, is also essential for biofilm formation. *Molecular Microbiology,* 40**,** 1215-1226.

PASCOLINI, D. & MARIOTTI, S. P. 2012. Global estimates of visual impairment: 2010. *British Journal of Ophthalmology,* 96**,** 614-618.

PENDLETON, J. N., GORMAN, S. P. & GILMORE, B. F. 2013. Clinical relevance of the ESKAPE pathogens. *Expert Review of Anti-Infective Therapy,* 11**,** 297-308.

PERIASAMY, S., NAIR, H. A. S., LEE, K. W. K., ONG, J., GOH, J. Q. J., KJELLEBERG, S. & RICE, S. A. 2015. Pseudomonas aeruginosa PA01 exopolysaccharides are important for mixed species biofilm community development and stress tolerance. *Frontiers in Microbiology,* 6**,** 10.

PETERS, B. M., JABRA-RIZK, M. A., O'MAY, G. A., COSTERTON, J. W. & SHIRTLIFF, M. E. 2012. Polymicrobial Interactions: Impact on Pathogenesis and Human Disease. *Clinical Microbiology Reviews,* 25**,** 193-212.

PFISTER, R. R. 1973. The Normal Surface of Corneal Epithelium: A Scanning Electron Microscopic Study. *Investigative Ophthalmology & Visual Science,* 12**,** 654-668.

PFLUGFELDER, S. C. & STERN, M. E. 2020. Biological functions of tear film. *Experimental Eye Research,* 197.

PINNOCK, A., SHIVSHETTY, N., ROY, S., RIMMER, S., DOUGLAS, I., MACNEIL, S. & GARG, P. 2017. Ex vivo rabbit and human corneas as models for bacterial and fungal keratitis. *Graefes Archive for Clinical and Experimental Ophthalmology,* 255**,** 333-342.

PONCE-ANGULO, D. G., BAUTISTA-HERNANDEZ, L. A., CALVILLO-MEDINA, R. P., CASTRO-TECORRAL, F. I., APARICIO-OZORES, G., LOPEZ-VILLEGAS, E. O., RIBAS-APARICIO, R. M. & BAUTISTA-DE LUCIO, V. M. 2020. Microscopic characterization of biofilm in mixed keratitis in a novel murine model. *Microbial Pathogenesis,* 140**,** 9.

PONNURAJ, K., BOWDEN, M. G., DAVIS, S., GURUSIDDAPPA, S., MOORE, D., CHOE, D., XU, Y., HOOK, M. & NARAYANA, S. V. L. 2003. A "dock, lock, and latch" structural model for a staphylococcal adhesin binding to fibrinogen. *Cell,* 115**,** 217-228.

POSTNIKOFF, C. K., PINTWALA, R., WILLIAMS, S., WRIGHT, A. M., HILEETO, D. & GORBET, M. B. 2014. Development of a Curved, Stratified, In Vitro Model to Assess Ocular Biocompatibility. *Plos One,* 9**,** 12.

PRETOR, S., BARTELS, J., LORENZ, T., DAHL, K., FINKE, J. H., PETERAT, G., KRULL, R., AL-HALHOULI, A. T., DIETZEL, A., BUTTGENBACH, S., BEHRENDS, S., REICHL, S. & MULLER-GOYMANN, C. C. 2015. Cellular Uptake of Coumarin-6 under Microfluidic Conditions into HCE-T Cells from Nanoscale Formulations. *Molecular Pharmaceutics,* 12**,** 34-45.

PYTELA, R., PIERSCHBACHER, M. D. & RUOSLAHTI, E. 1985. IDENTIFICATION AND ISOLATION OF A 140-KD CELL-SURFACE GLYCOPROTEIN WITH PROPERTIES EXPECTED OF A FIBRONECTIN RECEPTOR. *Cell,* 40**,** 191-198.

RAJAS, O., QUIROS, L. M., ORTEGA, M., VAZQUEZ-ESPINOSA, E., MERAYO-LLOVES, J., VAZQUEZ, F. & GARCIA, B. 2017. Glycosaminoglycans are involved in bacterial adherence to lung cells. *Bmc Infectious Diseases,* 17.

RAMIREZ, J. C., FLEISZIG, S. M. J., SULLIVAN, A. B., TAM, C., BORAZJANI, R. & EVANS, D. J. 2012. Traversal of Multilayered Corneal Epithelia by Cytotoxic Pseudomonas aeruginosa Requires the Phospholipase Domain of ExoU. *Investigative Ophthalmology & Visual Science,* 53**,** 448-453.

RAMPHAL, R., MCNIECE, M. T. & POLACK, F. M. 1981. ADHERENCE OF PSEUDOMONAS-AERUGINOSA TO THE INJURED CORNEA - A STEP IN THE PATHOGENESIS OF CORNEAL INFECTIONS. *Annals of Ophthalmology,* 13**,** 421-425.

RANTA, V. P., LAAVOLA, M., TOROPAINEN, E., VELLONEN, K. S., TALVITIE, A. & URTTI, A. 2003. Ocular pharmacokinetic modeling using corneal absorption and desorption rates from in vitro permeation experiments with cultured corneal epithelial cells. *Pharmaceutical Research,* 20**,** 1409-1416.

RASHID, Z., FARZANA, K., SATTAR, A. & MURTAZA, G. 2012. PREVALENCE OF NASAL STAPHYLOCOCCUS AUREUS AND METHICILLIN-RESISTANT STAPHYLOCOCCUS AUREUS IN HOSPITAL PERSONNEL AND ASSOCIATED RISK FACTORS. *Acta Poloniae Pharmaceutica,* 69**,** 985-991.

REDDY, K. & ROSS, J. M. 2001. Shear stress prevents fibronectin binding protein-mediated Staphylococcus aureus adhesion to resting endothelial cells. *Infection and Immunity,* 69**,** 3472-3475.

REDFERN, R. L., REINS, R. Y. & MCDERMOTT, A. M. 2011. Toll-like receptor activation modulates antimicrobial peptide expression by ocular surface cells. *Experimental Eye Research,* 92**,** 209-220.

REDGRAVE, L. S., SUTTON, S. B., WEBBER, M. A. & PIDDOCK, L. J. V. 2014. Fluoroquinolone resistance: mechanisms, impact on bacteria, and role in evolutionary success. *Trends in Microbiology,* 22**,** 438-445.

REICHL, S., KOLLN, C., HAHNE, M. & VERSTRAELEN, J. 2011. In vitro cell culture models to study the corneal drug absorption. *Expert Opinion on Drug Metabolism & Toxicology,* 7**,** 559-578.

REN, H., PETROLL, W., JESTER, J., CAVANAGH, H., MATHERS, W., BONNANO, J. & KENNEDY, R. 1997. Adherence of P*seudomonas aeruginosa* to shed rabbit corneal epithelial cells after overnight wear of contact lenses. *Contact Lens Association of Ophthalmologists Journal,* 23**,** 63-68.

REN, H. W. & WILSON, G. 1996. Apoptosis in the corneal epithelium. *Investigative Ophthalmology & Visual Science,* 37**,** 1017-1025.

REN, H. W. & WILSON, G. 1997. The effect of a shear force on the cell shedding rate of the corneal epithelium. *Acta Ophthalmologica Scandinavica,* 75**,** 383-387.

REYES, R., CARDENES, B., MACHADO-PINEDA, Y. & CABANAS, C. 2018. Tetraspanin CD9: A Key Regulator of Cell Adhesion in the Immune System. *Frontiers in Immunology,* 9**,** 9.

RHEM, M. N., LECH, E. M., PATTI, J. M., MCDEVITT, D., HOOK, M., JONES, D. B. & WILHELMUS, K. R. 2000. The collagen-binding adhesin is a virulence factor in Staphylococcus aureus keratitis. *Infection and Immunity,* 68**,** 3776-3779.

ROBERTS, A. E. L., KRAGH, K. N., BJARNSHOLT, T. & DIGGLE, S. P. 2015. The Limitations of In Vitro Experimentation in Understanding Biofilms and Chronic Infection. *Journal of Molecular Biology,* 427**,** 3646-3661.

ROBERTSON, D. M., LI, L., FISHER, S., PEARCE, V. P., SHAY, J. W., WRIGHT, W. E., CAVANAGH, H. D. & JESTER, J. V. 2005. Characterization of growth and differentiation in a telomerase-immortalized human corneal epithelial cell line. *Investigative Ophthalmology & Visual Science,* 46**,** 470-478.

ROBERTSON, D. M., ROGERS, N. A., PETROLL, W. M. & ZHU, M. F. 2017. Second harmonic generation imaging of corneal stroma after infection by Pseudomonas aeruginosa. *Scientific Reports,* 7.

ROCHE, F. M., MEEHAN, M. & FOSTER, T. J. 2003. The Staphylococcus aureus surface protein SasG and its homologues promote bacterial adherence to human desquamated nasal epithelial cells. *Microbiology-Sgm,* 149**,** 2759-2767.

RODESNEY, C. A., ROMAN, B., DHAMANI, N., COOLEY, B. J., TOUHAMI, A. & GORDON, V. D. 2017. Mechanosensing of shear by Pseudomonas aeruginosa leads to increased levels of the cyclic-di-GMP signal initiating biofilm development. *Proceedings of the National Academy of Sciences of the United States of America,* 114**,** 5906-5911.

ROLANDO, M. & ZIERHUT, M. 2001. The ocular surface and tear film and their dysfunction in dry eye disease. *Survey of Ophthalmology,* 45**,** S203-S210.

ROSSI, E., LA ROSA, R., BARTELL, J. A., MARVIG, R. L., HAAGENSEN, J. A. J., SOMMER, L. M., MOLIN, S. & JOHANSEN, H. K. 2021. Pseudomonas aeruginosa adaptation and evolution in patients with cystic fibrosis. *Nature Reviews Microbiology,* 19**,** 331-342.

ROWE, T. E., AKANDE, J. M. & REED, K. 2010. Measurement and Prediction of Timolol Diffusion With and Without Simulated Tear Flow. *Investigative Ophthalmology & Visual Science,* 51**,** 2.

RYBTKE, M., HULTQVIST, L. D., GIVSKOV, M. & TOLKER-NIELSEN, T. 2015. Pseudomonas aeruginosa Biofilm Infections: Community Structure, Antimicrobial Tolerance and Immune Response. *Journal of Molecular Biology,* 427**,** 3628-3645.

SAFFARI, M., KARAMI, S., FIROOZEH, F. & SEHAT, M. 2017. Evaluation of biofilm-specific antimicrobial resistance genes in Pseudomonas aeruginosa isolates in Farabi Hospital. *Journal of Medical Microbiology,* 66**,** 905-909.

SAGERFORS, S., EJDERVIK-LINDBLAD, B. & SODERQUIST, B. 2019. Infectious keratitis: isolated microbes and their antibiotic susceptibility pattern during 2004-2014 in Region Orebro County, Sweden. *Acta ophthalmologica*.

SAHU, S. K., MITTAL, S. K., FOULSHAM, W., LI, M. S., SANGWAN, V. S. & CHAUHAN, S. K. 2018. Mast Cells Initiate the Recruitment of Neutrophils Following Ocular Surface Injury. *Investigative Ophthalmology & Visual Science,* 59**,** 1732-1740.

SAID-SALIM, B., DUNMAN, P. M., MCALEESE, F. M., MACAPAGAL, D., MURPHY, E., MCNAMARA, P. J., ARVIDSON, S., FOSTER, T. J., PROJAN, S. J. & KREISWIRTH, B. N. 2003. Global regulation of Staphylococcus aureus genes by rot. *Journal of Bacteriology,* 185**,** 610-619.

SANFILIPPO, J. E., LORESTANI, A., KOCH, M. D., BRATTON, B. P., SIRYAPORN, A., STONE, H. A. & GITAI, Z. 2019. Microfluidic-based transcriptomics reveal force-independent bacterial rheosensing. *Nature Microbiology,* 4**,** 1274-1281.

SANTAJIT, S. & INDRAWATTANA, N. 2016. Mechanisms of Antimicrobial Resistance in ESKAPE Pathogens. *Biomed Research International***,** 8.

SARASWATHI, P., AUNG, T., SALLEH, S. & BEUERMAN, R. 2013. An Experimental Model of Biofilm Formation in the Mouse Cornea. *Investigative Ophthalmology & Visual Science,* 54.

SARASWATHI, P. & BEUERMAN, R. W. 2015. Corneal Biofilms: From Planktonic to Microcolony Formation in an Experimental Keratitis Infection with Pseudomonas Aeruginosa. *Ocular Surface,* 13**,** 331-345.

SCHARFMAN, A., ARORA, S. K., DELMOTTE, P., VAN BRUSSEL, E., MAZURIER, J., RAMPHAL, R. & ROUSSEL, P. 2001. Recognition of Lewis x derivatives present on mucins by flagellar components of Pseudomonas aeruginosa. *Infection and Immunity,* 69**,** 5243-5248.

SCHECHTER, J. E., WARREN, D. W. & MIRCHEFF, A. K. 2010. A Lacrimal Gland is a Lacrimal Gland, But Rodent's and Rabbit's Are Not Human. *Ocular Surface,* 8**,** 111-134.

SCHMIDL, D., SCHMETTERER, L., WITKOWSKA, K. J., UNTERHUBER, A., DOS SANTOS, V. A., KAYA, S., NEPP, J., BAAR, C., ROSNER, P., WERKMEISTER, R. M. & GARHOFER, G. 2015. Tear Film Thickness After Treatment With Artificial Tears in Patients With Moderate Dry Eye Disease. *Cornea,* 34**,** 421-426.

SCHNEEWIND, O. & MISSIAKAS, D. 2014. Sec-secretion and sortase-mediated anchoring of proteins in Gram-positive bacteria. *Biochimica Et Biophysica Acta-Molecular Cell Research,* 1843**,** 1687-1697.

SCHRODER, A., SCHRODER, B., ROPPENSER, B., LINDER, S., SINHA, B., FASSLER, R. & AEPFELBACHER, M. 2006. Staphylococcus aureus fibronectin binding protein-A induces motile attachment sites and complex actin remodeling in living endothelial cells. *Molecular Biology of the Cell,* 17**,** 5198-5210.

SCHWARZ-LINEK, U., HOOK, M. & POTTS, J. R. 2004. The molecular basis of fibronectin-mediated bacterial adherence to host cells. *Molecular Microbiology,* 52**,** 631-641.

SEEBER, J. W., ZORN-KRUPPA, M., LOMBARDI-BORGIA, S., SCHOLZ, H., MANZER, A. K., RUSCHE, B., SCHAFER-KORTING, M. & ENGELKE, M. 2008. Characterisation of Human Corneal Epithelial Cell Cultures Maintained Under Serum-free Conditions. *Atla-Alternatives to Laboratory Animals,* 36**,** 569-583.

SEIGNEURET, M., DELAGUILLAUMIE, A., LAGAUDRIERE-GESBERT, C. & CONJEAUD, H. 2001. Structure of the tetraspanin main extracellular domain - A partially conserved fold with a structurally variable domain insertion. *Journal of Biological Chemistry,* 276**,** 40055-40064.

SEWELL, A., DUNMIRE, J., WEHMANN, M., ROWE, T. & BOUHENNI, R. 2014. Proteomic analysis of keratitis-associated Pseudomonas aeruginosa. *Molecular Vision,* 20**,** 1182-1191.

SHANKS, R. M. Q., DONEGAN, N. P., GRABER, M. L., BUCKINGHAM, S. E., ZEGANS, M. E., CHEUNG, A. L. & O'TOOLE, G. A. 2005. Heparin stimulates Staphylococcus aureus biofilm formation. *Infection and Immunity,* 73**,** 4596-4606.

SHARIF, N. A., OFFORD, E. A., TROMVOUKIS, Y., HOWE, W. E., GRIFFIN, B. W., WIERNAS, T. K. & PFEIFER, A. M. A. 1997. Immortalized human corneal epithelial (CEPI) cells for use in ocular inflammation and toxicity studies. *Investigative Ophthalmology & Visual Science,* 38**,** 3349-3349.

SHARMA, P., GUHA, S., GARG, P. & ROY, S. 2018. Differential expression of antimicrobial peptides in corneal infection and regulation of antimicrobial peptides and reactive oxygen species by type III secretion system of &ITPseudomonas aeruginosa&IT. *Pathogens and Disease,* 76**,** 9.

SHARMA, V., SHARMA, S., GARG, P. & RAO, G. N. 2004. Clinical resistance of Staphylococcus keratitis to ciprofloxacin monotherapy. *Indian Journal of Ophthalmology,* 52**,** 287-292.

SILBY, M. W., WINSTANLEY, C., GODFREY, S. A. C., LEVY, S. B. & JACKSON, R. W. 2011. Pseudomonas genomes: diverse and adaptable. *Fems Microbiology Reviews,* 35**,** 652-680.

SINCOCK, P. M., MAYRHOFER, G. & ASHMAN, L. K. 1997. Localization of the transmembrane 4 superfamily (TM4SF) member PETA-3 (CD151) in normal human tissues: Comparison with CD9, CD63, and alpha 5 beta 1 integrin. *Journal of Histochemistry & Cytochemistry,* 45**,** 515-525.

SKEHAN, P., STORENG, R., SCUDIERO, D., MONKS, A., MCMAHON, J., VISTICA, D., WARREN, J. T., BOKESCH, H., KENNEY, S. & BOYD, M. R. 1990. NEW COLORIMETRIC CYTOTOXICITY ASSAY FOR ANTICANCER-DRUG SCREENING. *Journal of the National Cancer Institute,* 82**,** 1107-1112.

SOSNOVA-NETUKOVA, M., KUCHYNKA, P. & FORRESTER, J. V. 2007. The suprabasal layer of corneal epithelial cells represents the major barrier site to the passive movement of small molecules and trafficking leukocytes. *British Journal of Ophthalmology,* 91**,** 372-378.

SOYER, M. & DUMENIL, G. 2012. A Laminar-Flow Chamber Assay for Measuring Bacterial Adhesion Under Shear Stress. *Neisseria Meningitidis: Advanced Methods and Protocols,* 799**,** 185-195.

SPEZIALE, P. & PIETROCOLA, G. 2020. The Multivalent Role of Fibronectin-Binding Proteins A and B (FnBPA and FnBPB) of Staphylococcus aureus in Host Infections. *Frontiers in Microbiology,* 11.

SRIDHAR, M. S. 2018. Anatomy of cornea and ocular surface. *Indian Journal of Ophthalmology,* 66**,** 190-194.

SRINIVAS, S. P., MUTHARASAN, R. & FLEISZIG, S. 2002. Shear-induced atp release by cultured rabbit corneal epithelial cells. *Lacrimal Gland, Tear Film, and Dry Eye Syndromes 3: Basic Science and Clinical Relevance, Pts a & B,* 506**,** 677-685.

SRINIVASAN, B., KOLLI, A. R., ESCH, M. B., ABACI, H. E., SHULER, M. L. & HICKMAN, J. J. 2015. TEER Measurement Techniques for In Vitro Barrier Model Systems. *Jala,* 20**,** 107-126.

STAPLETON, F. & CARNT, N. 2012. Contact lens-related microbial keratitis: how have epidemiology and genetics helped us with pathogenesis and prophylaxis. *Eye,* 26**,** 185-193.

STEINERT, M., RAMMING, I. & BERGMANN, S. 2020. Impact of Von Willebrand Factor on Bacterial Pathogenesis. *Frontiers in Medicine,* 7.

STEWART, P. & COSTERTON, J. W. 2001. Antibiotic Resistance of Bacteria in Biofilms. The Lancet.

STEWART, R. M. K., WIEHLMANN, L., ASHELFORD, K. E., PRESTON, S. J., FRIMMERSDORF, E., CAMPBELL, B. J., NEAL, T. J., HALL, N., TUFT, S., KAYE, S. B. & WINSTANLEY, C. 2011. Genetic Characterization Indicates that a Specific Subpopulation of Pseudomonas aeruginosa Is Associated with Keratitis Infections. *Journal of Clinical Microbiology,* 49**,** 993-1003.

STROBEL, M., PFORTNER, H., TUCHSCHERR, L., VOLKER, U., SCHMIDT, F., KRAMKO, N., SCHNITTLER, H. J., FRAUNHOLZ, M. J., LOFFLER, B., PETERS, G. & NIEMANN, S. 2016. Post-invasion events

after infection with Staphylococcus aureus are strongly dependent on both the host cell type and the infecting S. aureus strain. *Clinical Microbiology and Infection,* 22**,** 799-809.

SULLIVAN, A. B., TAM, K. P. C., METRUCCIO, M. M. E., EVANS, D. J. & FLEISZIG, S. M. J. 2015. The Importance of the Pseudomonas aeruginosa Type III Secretion System in Epithelium Traversal Depends upon Conditions of Host Susceptibility. *Infection and Immunity,* 83**,** 1629-1640.

SUN, Y., KARMAKAR, M., ROY, S., RAMADAN, R. T., WILLIAMS, S. R., HOWELL, S., SHIVE, C. L., HAN, Y. P., STOPFORD, C. M., RIETSCH, A. & PEARLMAN, E. 2010. TLR4 and TLR5 on Corneal Macrophages Regulate Pseudomonas aeruginosa Keratitis by Signaling through MyD88-Dependent and -Independent Pathways. *Journal of Immunology,* 185**,** 4272-4283.

SURRE, J., SAINT-RUF, C., COLLIN, V., ORENGA, S., RAMJEET, M. & MATIC, I. 2018. Strong increase in the autofluorescence of cells signals struggle for survival. *Scientific Reports,* 8.

SUZUKI, T., OKAMOTO, S., OKA, N., HAYASHI, N., GOTOH, N. & SHIRAISHI, A. 2018. Role of pvdE Pyoverdine Synthesis in Pseudomonas aeruginosa Keratitis. *Cornea,* 37**,** S99-S105.

TAM, A. L. C., COTE, E., SALDANHA, M., LICHTINGER, A. & SLOMOVIC, A. R. 2017. Bacterial Keratitis in Toronto: A 16-Year Review of the Microorganisms Isolated and the Resistance Patterns Observed. *Cornea,* 36**,** 1528-1534.

TAM, C., LEDUE, J., MUN, J. J., HERZMARK, P., ROBEY, E. A., EVANS, D. J. & FLEISZIG, S. M. J. 2011. 3D Quantitative Imaging of Unprocessed Live Tissue Reveals Epithelial Defense against Bacterial Adhesion and Subsequent Traversal Requires MyD88. *Plos One,* 6.

TAM, C., MUN, J. J., EVANS, D. J. & FLEISZIG, S. M. J. 2010. The Impact of Inoculation Parameters on the Pathogenesis of Contact Lens-Related Infectious Keratitis. *Investigative Ophthalmology & Visual Science,* 51**,** 3100-3106.

TANG, A., CABALLERO, A. R., MARQUART, M. E. & O'CALLAGHAN, R. J. 2013. Pseudomonas aeruginosa Small Protease (PASP), a Keratitis Virulence Factor. *Investigative Ophthalmology & Visual Science,* 54**,** 2821-2828.

TANG, A. H., BALZLI, C. L., CABALLERO, A. R., MCCORMICK, C. C., TAYLOR, S. D. & O'CALLAGHAN, R. J. 2012. Staphylococcus Aureus Infection of the Rabbit Cornea Following Topical Administration. *Current Eye Research,* 37**,** 1075-1083.

TANG, A. H., CABALLERO, A. R., BIERDEMAN, M. A., MARQUART, M. E., FOSTER, T. J., MONK, I. R. & O'CALLAGHAN, R. J. 2019. Staphylococcus aureus Superantigen-Like Protein SSL1: A Toxic Protease. *Pathogens,* 8.

TANG, A. H., CABALLERO, A. R., MARQUART, M. E., BIERDEMAN, M. A. & O'CALLAGHAN, R. J. 2018. Mechanism of Pseudomonas aeruginosa Small Protease (PASP), a Corneal Virulence Factor. *Investigative Ophthalmology & Visual Science,* 59**,** 5993-6002.

TANG, A. H., MARQUART, M. E., FRATKIN, J. D., MCCORMICK, C. C., CABALLERO, A. R., GATLIN, H. P. & O'CALLAGHAN, R. J. 2009. Properties of PASP: A Pseudomonas Protease Capable of Mediating Corneal Erosions. *Investigative Ophthalmology & Visual Science,* 50**,** 3794-3801.

TAYLOR, A. W. 2016. Ocular Immune Privilege and Transplantation. *Frontiers in Immunology,* 7.

TOROPAINEN, E. 2007. *Corneal Epithelial Cell Culture Model for Pharmaceutical Studies.* Doctoral dissertation, University of Kuopio.

TOROPAINEN, E., RANTA, V. P., TALVITIE, A., SUHONEN, P. & URTTI, A. 2001. Culture model of human corneal epithelium for prediction of ocular drug absorption. *Investigative Ophthalmology & Visual Science,* 42**,** 2942-2948.

TOROPAINEN, E., RANTA, V. P., VELLONEN, K. S., PALMGREN, J., TALVITIE, A., LAAVOLA, M., SUHONEN, P., HAMALAINEN, K. M., AURIOLA, S. & URTTI, A. 2003. Paracellular and passive transcellular permeability in immortalized human corneal epithelial cell culture model. *European Journal of Pharmaceutical Sciences,* 20**,** 99-106.

TOYONO, T., USUI, T., YOKOO, S., TAKETANI, Y., NAKAGAWA, S., KURODA, M., YAMAGAMI, S. & AMANO, S. 2015. Angiopoietin-Like 7 Is an Anti-Angiogenic Protein Required to Prevent Vascularization of the Cornea. *Plos One,* 10.

TRAIDEJ, M., CABALLERO, A. R., MARQUART, M. E., THIBODEAUX, B. A. & O'CALLAGHAN, R. J. 2003. Molecular analysis of Pseudomonas aeruginosa protease IV expressed in Pseudomonas putida. *Investigative Ophthalmology & Visual Science,* 44**,** 190-196.

TREMBLAY, Y. D. N., VOGELEER, P., JACQUES, M. & HAREL, J. 2015. High-Throughput Microfluidic Method To Study Biofilm Formation and Host-Pathogen Interactions in Pathogenic Escherichia coli. *Applied and Environmental Microbiology,* 81**,** 2827-2840.

TUFT, S. & BURTON, M. 2013. *The Royal College Ophthalmologists, Focus: Microbial Keratitis* [Online]. The Royal College of Ophthalmologists: Focus. Available: https://www.rcophth.ac.uk/wp-content/uploads/2014/08/Focus-Autumn-2013.pdf [Accessed 31st March 2020].

UBANI-UKOMA, U., GIBSON, D., SCHULTZ, G., SILVA, B. O. & CHAUHAN, A. 2019. Evaluating the potential of drug eluting contact lenses for treatment of bacterial keratitis using an ex vivo corneal model. *International Journal of Pharmaceutics,* 565**,** 499-508.

UMEDA, R., SATOUH, Y., TAKEMOTO, M., NAKADA-NAKURA, Y., LIU, K. H., YOKOYAMA, T., SHIROUZU, M., IWATA, S., NOMURA, N., SATO, K., IKAWA, M., NISHIZAWA, T. & NUREKI, O. 2020. Structural insights into tetraspanin CD9 function. *Nature Communications,* 11.

UNG, L., BISPO, P. J. M., SHANBHAG, S. S., GILMORE, M. S. & CHODOSH, J. 2019. The persistent dilemma of microbial keratitis: Global burden, diagnosis, and antimicrobial resistance. *Survey of Ophthalmology,* 64**,** 255-271.

URWIN, L., OKUROWSKA, K., CROWTHER, G., ROY, S., GARG, P., KARUNAKARAN, E., MACNEIL, S., PARTRIDGE, L. J., GREEN, L. R. & MONK, P. N. 2020. Corneal Infection Models: Tools to Investigate the Role of Biofilms in Bacterial Keratitis. *Cells,* 9.

VALLAS, V., WIENERKRONISH, J. P., MOSTOV, K. E. & FLEISZIG, S. M. J. 1996. Cytotoxic strains of Pseudomonas aeruginosa can damage the intact corneal surface. *Investigative Ophthalmology & Visual Science,* 37**,** 4026-4026.

VANPUTTEN, J. P. M. & PAUL, S. M. 1995. BINDING OF SYNDECAN-LIKE CELL-SURFACE PROTEOGLYCAN RECEPTORS IS REQUIRED FOR NEISSERIA-GONORRHOEAE ENTRY INTO HUMAN MUCOSAL CELLS. *Embo Journal,* 14**,** 2144-2154.

VARKI, A., CUMMINGS, R. & ESKO, J. 1999. *Essentials of Glycobiology,* Cold Spring Harbor (NY), Cold Spring Harbor Laboratory Press.

VAZQUEZ, V., LIANG, X. W., HORNDAHL, J. K., GANESH, V. K., SMEDS, E., FOSTER, T. J. & HOOK, M. 2011. Fibrinogen Is a Ligand for the Staphylococcus aureus Microbial Surface Components Recognizing Adhesive Matrix Molecules (MSCRAMM) Bone Sialoprotein-binding Protein (Bbp). *Journal of Biological Chemistry,* 286**,** 29797-29805.

VEERACHAMY, S., YARLAGADDA, T., MANIVASAGAM, G. & YARLAGADDA, P. 2014. Bacterial adherence and biofilm formation on medical implants: A review. *Proceedings of the Institution of Mechanical Engineers Part H-Journal of Engineering in Medicine,* 228**,** 1083-1099.

VENKATESH, M., BARATHI, V. A., GOH, E. T. L., ANGGARA, R., FAZIL, M., NG, A. J. Y., HARINI, S., AUNG, T. T., FOX, S. J., LIU, S. P., YANG, L., BARKHAM, T. M. S., LOH, X. J., VERMA, N. K., BEUERMAN, R. W. & LAKSHMINARAYANAN, R. 2017. Antimicrobial Activity and Cell Selectivity of Synthetic and Biosynthetic Cationic Polymers. *Antimicrobial Agents and Chemotherapy,* 61.

VENTRESS, J. K., PARTRIDGE, L. J., READ, R. C., COZENS, D., MACNEIL, S. & MONK, P. N. 2016. Peptides from Tetraspanin CD9 Are Potent Inhibitors of Staphylococcus Aureus Adherence to Keratinocytes. *Plos One,* 11**,** 17.

VERMELTFOORT, P. B. J., VAN KOOTEN, T. G., BRUINSMA, G. M., HOOYMANS, A. M. M., VAN DER MEI, H. C. & BUSSCHER, H. J. 2005. Bacterial transmission from contact lenses to porcine corneas: An ex vivo study. *Investigative Ophthalmology & Visual Science,* 46**,** 2042-2046.

VERSTRAELEN, J. & REICHL, S. 2013. Expression analysis of MDR1, BCRP and MRP3 transporter proteins in different in vitro and ex vivo cornea models for drug absorption studies. *International Journal of Pharmaceutics,* 441**,** 765-775.

VITRY, P., VALOTTEAU, C., FEUILLIE, C., BERNARD, S., ALSTEENS, D., GEOGHEGAN, J. A. & DUFRENE, Y. F. 2017. Force-Induced Strengthening of the Interaction between Staphylococcus aureus Clumping Factor B and Loricrin. *Mbio,* 8.

WALSH, C. 2000. Molecular mechanisms that confer antibacterial drug resistance. *Nature,* 406**,** 775-781.

WAN, S. J., MA, S., EVANS, D. J. & FLEISZIG, S. M. J. 2020. Resistance of the murine cornea to bacterial colonization during experimental dry eye. *Plos One,* 15**,** 9.

WASYLNKA, J. A. & MOORE, M. M. 2003. Aspergillus fumigatus conidia survive and germinate in acidic organelles of A549 epithelial cells. *Journal of Cell Science,* 116**,** 1579-1587.

WATSKY, M. A. & GEISERT, E. E. 2007. Corneal Tetraspanin Expression During Development and Wound Healing. Investigative Ophthalmology and Visual Science

WERTHEIM, H. F. L., MELLES, D. C., VOS, M. C., VAN LEEUWEN, W., VAN BELKUM, A., VERBRUGH, H. A. & NOUWEN, J. L. 2005. The role of nasal carriage in Staphylococcus aureus infections. *Lancet Infectious Diseases,* 5**,** 751-762.

WHITCHER, J. P., SRINIVASAN, M. & UPADHYAY, M. P. 2001. Corneal blindness: a global perspective. *Bulletin of the World Health Organization,* 79**,** 214-221.

WHITELEY, M., LEE, K. M. & GREENBERG, E. P. 1999. Identification of genes controlled by quorum sensing in Pseudomonas aeruginosa. *Proceedings of the National Academy of Sciences of the United States of America,* 96**,** 13904-13909.

WHO. 2017. *WHO publishes list of bacteria for which new antibiotics are urgently needed.* [Online]. World Health Organization website. Available: https://www.who.int/news-room/detail/27-02-2017-who-publishes-list-of-bacteria-for-which-new-antibiotics-are-urgently-needed [Accessed 31st March 2020 2020].

WICK, R. R., JUDD, L. M., GORRIE, C. L. & HOLT, K. E. 2017. Completing bacterial genome assemblies with multiplex MinION sequencing. *Microbial Genomics,* 3.

WILSON, S. E. 2020. Bowman's layer in the cornea– structure and function and regeneration. *Experimental Eye Research,* 195.

WINSTANLEY, C., KAYE, S. B., NEAL, T. J., CHILTON, H. J., MIKSCH, S., HART, C. A. & MICROBIOLOGY OPHTHALMIC, G. 2005. Genotypic and phenotypic characteristics of Pseudomonas aeruginosa isolates associated with ulcerative keratitis. *Journal of Medical Microbiology,* 54**,** 519-526.

WINSTANLEY, C., O'BRIEN, S. & BROCKHURST, M. A. 2016. Pseudomonas aeruginosa Evolutionary Adaptation and Diversification in Cystic Fibrosis Chronic Lung Infections. *Trends in Microbiology,* 24**,** 327-337.

XIN, Y., LU, Q. X. & LI, Q. T. 2010. 14-3-3 sigma controls corneal epithelial cell proliferation and differentiation through the Notch signaling pathway. *Biochemical and Biophysical Research Communications,* 392**,** 593-598.

XU, Z. B., LIANG, Y. R., LIN, S. Q., CHEN, D. Q., LI, B., LI, L. & DENG, Y. 2016. Crystal Violet and XTT Assays on Staphylococcus aureus Biofilm Quantification. *Current Microbiology,* 73**,** 474-482.

XUE, M. L., THAKUR, A., LUTZE-MANN, L. & WILLCOX, M. D. P. 2000. Pro-inflammatory cytokine/chemokine gene expression in human corneal epithelial cells colonized by Pseudomonas aeruginosa. *Clinical and Experimental Ophthalmology,* 28**,** 197-200.

YANEZ-MO, M., BARREIRO, O., GORDON-ALONSO, M., SALA-VALDES, M. & SANCHEZ-MADRID, F. 2009. Tetraspanin-enriched microdomains: a functional unit in cell plasma membranes. *Trends in Cell Biology,* 19**,** 434-446.

YANG, N. & FRIEDL, A. 2016. Syndecan-1-Induced ECM Fiber Alignment Requires Integrin alpha v beta 3 and Syndecan-1 Ectodomain and Heparan Sulfate Chains. *Plos One,* 11.

YEUNG, J., GADJEVA, M. & GEDDES-MCALISTER, J. 2020. Label-Free Quantitative Proteomics Distinguishes General and Site-Specific Host Responses to Pseudomonas aeruginosa Infection at the Ocular Surface. *Proteomics,* 20**,** 14.

YI, X., WANG, Y. & YU, F. S. X. 2000. Corneal epithelial tight junctions and their response to lipopolysaccharide challenge. *Investigative Ophthalmology & Visual Science,* 41**,** 4093-4100.

YU, Z. T., HAO, R., ZHANG, Y., YANG, H. & IEEE. 2021. A HUMAN CORNEA-ON-A-CHIP. 34th IEEE International Conference on Micro Electro Mechanical Systems (MEMS), Jan 25-29 2021 Electr Network. 982-985.

ZEGANS, M. E., DIGIANDOMENICO, A., RAY, K., NAIMIE, A., KELLER, A. E., STOVER, C. K., LALITHA, P., SRINIVASAN, M., ACHARYA, N. R. & LIETMAN, T. M. 2016. Association of Biofilm Formation, Psl Exopolysaccharide Expression, and Clinical Outcomes in Pseudomonas aeruginosa Keratitis Analysis of Isolates in the Steroids for Corneal Ulcers Trial. *Jama Ophthalmology,* 134**,** 383-389.

ZEGANS, M. E., SHANKS, R. M. Q. & TOOLE, G. A. 2005. Bacterial biofilms and ocular infections. *Ocular Surface,* 3**,** 73-80.

ZHOU, J. Z., JIANG, J., WANG, S. H. & XIA, X. B. 2016. Epithelial cell adhesion molecule-1 (ECAM1) is required in the maintenance of corneal epithelial barrier integrity. *Cell Biology International,* 40**,** 49-54.

ZHOU, L., ZHAO, S. Z., KOH, S. K., CHEN, L. Y., VAZ, C., TANAVDE, V., LI, X. R. & BEUERMAN, R. W. 2012. In-depth analysis of the human tear proteome. *Journal of Proteomics,* 75**,** 3877-3885.

ZHU, B., LIU, C. L., LIU, S. H., CONG, H. J., CHEN, Y. H., GU, L. C. & MA, L. Y. Z. 2016. Membrane association of SadC enhances its diguanylate cyclase activity to control exopolysaccharides synthesis and biofilm formation in Pseudomonas aeruginosa. *Environmental Microbiology,* 18**,** 3440-3452.

ZHU, H., CONIBEAR, T. C. R., BANDARA, R., ALIWARGA, Y., STAPLETON, F. & WILLCOX, M. D. P. 2006. Type III secretion system-associated toxins, proteases, serotypes, and antibiotic resistance of pseudomonas aeruginosa isolates associated with keratitis. *Current Eye Research,* 31**,** 297-306.

ZHU, H., KOCHEVAR, I. E., BEHLAU, I., ZHAO, J., WANG, F. H., WANG, Y. C., SUN, X. D., HAMBLIN, M. R. & DAI, T. H. 2017. Antimicrobial Blue Light Therapy for Infectious Keratitis: Ex Vivo and In Vivo Studies. *Investigative Ophthalmology & Visual Science,* 58**,** 586-593.

ZMANTAR, T., KOUIDHI, B., MILADI, H., MANDOUANI, K. & BAKHROUF, A. 2010. A Microtiter plate assay for Staphylococcus aureus biofilm quantification at various pH levels and hydrogen peroxide supplementation. *New Microbiologica,* 33**,** 137-145.

ZONG, Y. N., XU, Y., LIANG, X. W., KEENE, D. R., HOOK, A., GURUSIDDAPPA, S., HOOK, M. & NARAYANA, S. V. L. 2005. A 'collagen hug' model for Staphylococcus aureus CNA binding to collagen. *Embo Journal,* 24**,** 4224-4236.

ZORN-KRUPPA, M., TYKHONOVA, S., BELGE, G., BEDNARZ, J., DIEHL, H. A. & ENGELKE, M. 2005. A human corneal equivalent constructed from SV40-immortalised corneal cell lines. *Atla-Alternatives to Laboratory Animals,* 33**,** 37-45.

ZSCHALER, J., SCHLORKE, D. & ARNHOLD, J. 2014. Differences in Innate Immune Response between Man and Mouse. *Critical Reviews in Immunology,* 34, 433-454.
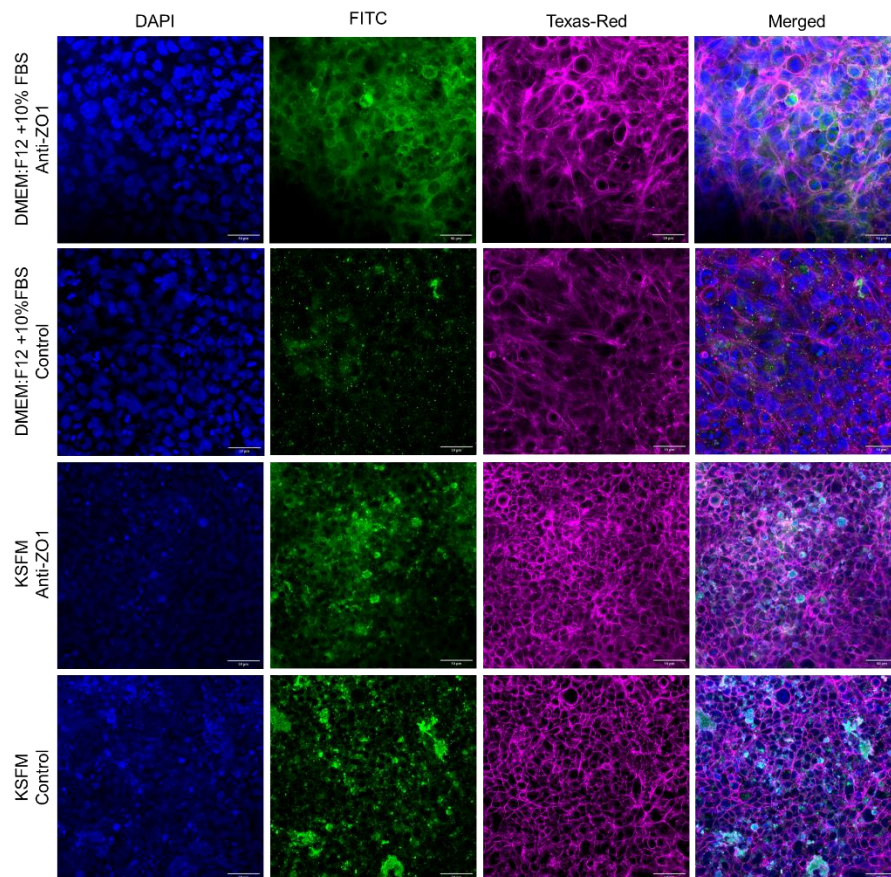
APPENDIX

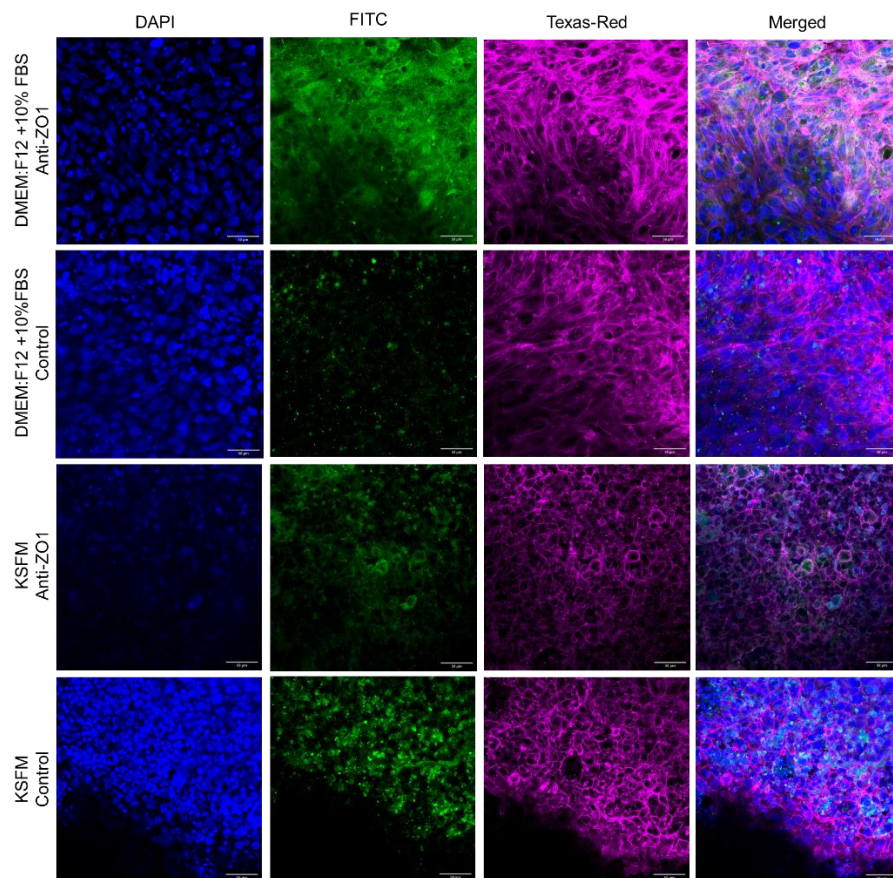**APPENDIX A: Flow cytometry values are not affected by choice of cell detachment technique.**
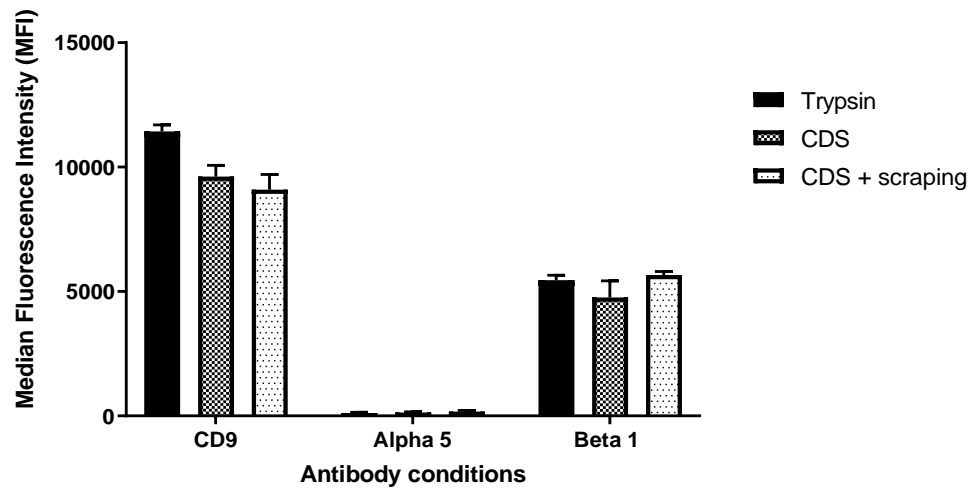
HCE2 expression of tetraspanin CD9, integrin α5 and integrin β1 were quantified by flow cytometry. HCE2 cells were harvested from confluent T-75 flasks using trypsin, Cell Dissociation Solution (CDS) or a combination of CDS treatment and cell scraping. Data represent mean ±SD, n=2.

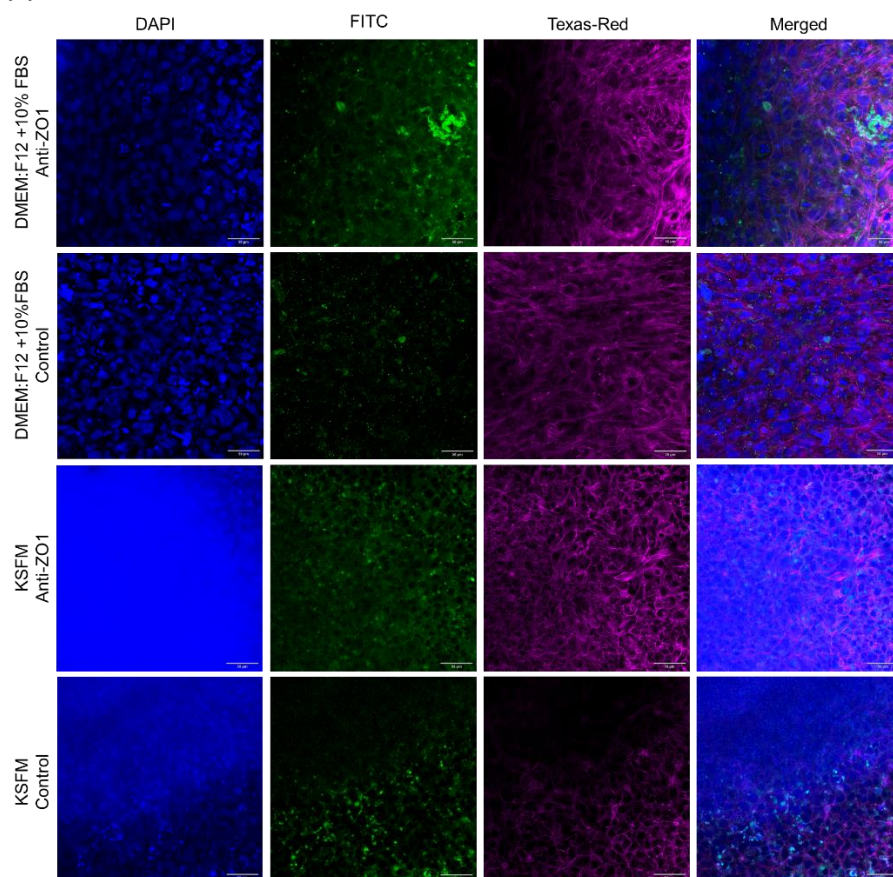**APPENDIX B: Figure 3-10, displayed in blue, green and magenta.**
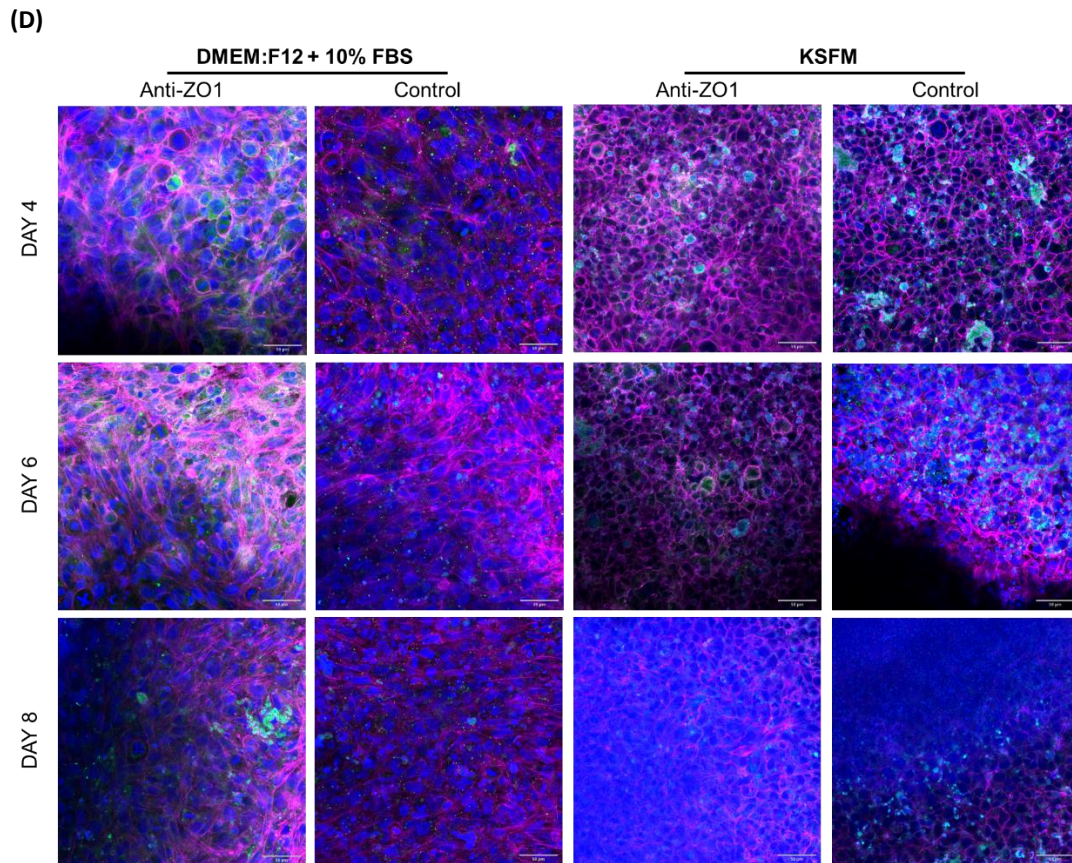
(A)

(B)

(C)

(D)

Figure 3-9. Immunofluorescence staining for ZO1 under different time points and media conditions. (A) Day 4 at ALI (B) Day 6 at ALI (C) Day 8 at ALI (A-C) DAPI, FITC, Texas-Red, Merged (left to right). (D) All time points, merged images only. HCE2s were cultured on transwell inserts. After 72hrs submerged culture in KSFM, ALI was introduced and KSFM was replaced with DMEM: F12 + 10% FBS or KSFM (day 0). Immunofluorescence staining was carried out on days 4, 6 or 8 of culture at ALI. DAPI was used to stain cell nuclei (blue) and FITC-conjugated secondary antibody was used to label anti-ZO1 antibody (green). Texas-Red X phalloidin has been used to stain actin filaments (magenta). Rabbit serum control was included to assess non-specific antibody binding (green). Regions of co-localisation between FITC and Texas-Red are visible (white). The same brightness and contrast settings have been used for all images collected in the same channel, with the exception of Day 8 DAPI-staining **(C-D)** where the brightness of KSFM images has been reduced to improve visibility. Scale bars represent 50 μm.

PUBLICATIONS

1. **Urwin, L.**; Okurowska, K.; Crowther, G.; Roy, S.; Garg, P.; Karunakaran, E.; MacNeil, S.; Partridge, L.J.; Green, L.R.; Monk, P.N. Corneal Infection Models: Tools to Investigate the Role of Biofilms in Bacterial Keratitis. Cells 2020, 9, doi:10.3390/cells9112450.

2. Partridge, L.J.; **Urwin, L.**; Nicklin, M.J.H.; James, D.C.; Green, L.R.; Monk, P.N. ACE2-Independent Interaction of SARS-CoV-2 Spike Protein with Human Epithelial Cells Is Inhibited by Unfractionated Heparin. Cells 2021, 10, doi:10.3390/cells10061419.

3. Green, L.R., Issa, R., Albaldi, F., **Urwin, L.**, Ciani, B., Partridge, L.J. & Monk, P.N. Tetraspanin CD9 organisation of heparan sulphate proteoglycans is required for staphylococcal adhesion to epithelial cells. 2022. *Under review.*

4. **Urwin, L.** & Wheeler, J.H.R.; Durham, W.M.; Green, L.J.; Partridge, L.R.; Monk, P.N. Development of an *in vitro* microfluidic system to study host pathogen interactions at the corneal surface. 2022. *In preparation.*

5. Jadi, P.K.; Dave, A.; Samarth, A.; Issa, R.; Tabassum, K.; Okurowska, K.; Green, L.R.; **Urwin, L.**; Karunakaran, E.; Partridge, L.P.; MacNeil, S.; Garg, P.; Monk, P.N; Roy, S.R. Peptides from Tetraspanin CD9 reduce corneal infection by *Pseudomonas aeruginosa* both *in vitro* and *in vivo*. 2022. *In preparation.*

6. Kumar, N.; **Urwin, L.**; Green, L.R.; Roy, S.; Garg, P.; Karunakaran, E.; Partridge, L.R.; Monk, P.N. Comparative genomic analysis reveals endemicity of *exoU* and *exoS P. aeruginosa* clones in corneal infections. 2022. *In preparation.*

7. Smith, E.F.; **Urwin, L.**; Monk, P.N.; De Vos, K.J. Investigating the roles of C9orf72 in immune related autophagy. 2022. *In preparation.*